Luigi Carrino
Luigi Maria Galantucci
Luca Settineri   *Editors*

Selected Topics in Manufacturing

Emerging Trends from
the Perspective of AITeM's
Young Researchers

A I
Te M

🦅 Springer

Lecture Notes in Mechanical Engineering

Luigi Carrino · Luigi Maria Galantucci ·
Luca Settineri

Editors

Selected Topics
in Manufacturing

Emerging Trends from the Perspective
of AITeM's Young Researchers

Springer

Editors
Luigi Carrino
Dipartimento di Ingegneria Chimica, dei
Materiali e della Produzione Industriale
(DICMaPI)
University of Naples Federico II
Napoli, Italy

Luigi Maria Galantucci ⓘD
Dipartimento di Meccanica Matematica e
Management (DMMM)
Politecnico di Bari
Bari, Italy

Luca Settineri ⓘD
Dipartimento di Ingegneria Gestionale e
della Produzione (DIGEP)
Politecnico di Torino
Torino, Italy

About This Book

This book presents selected contributions on a wide range of scientific and technological areas covered by AITeM (the Italian Manufacturing Association).

First part *AITeM Young Researcher Award 2023* is written by young AITeM associates: the contributions reflect the multifaceted nature of the research in manufacturing, which takes advantage of emergent technologies and establishes interdisciplinary connections with various scientific and technological areas to move beyond simple product fabrication and develop a complex and highly interconnected value creation processes ecosystem pursuing high-value-added products to compete globally. It discusses the following topics: additive manufacturing, materials processing technology, assembly, disassembly and circular economy, manufacturing systems design and management, quality engineering and production metrology, process and system simulation, optimization and digital manufacturing.

An Editorial Committee composed by Luigi Maria Galantucci—Politecnico di Bari (President), Elena Bassoli—Università di Modena e Reggio Emilia, Luca Boccarusso-Università di Napoli Federico II, Davide Campanella—Università di Palermo, Gianni Campatelli—Università di Firenze, Antonio Del Prete—Università del Salento, Enrico Pisino—Competence Center +CIM 4.0 Torino, Loredana Santo—Università di Roma Tor Vergata, Enrico Savio—Università di Padova, Walter Terkaj—STIIMA CNR peer reviewed and selected ten contributions among 25 papers proposed for the Award.

Second part *White Papers* presents five contributions on some Emerging Trends in Manufacturing research. The contributions have been prepared by Working Groups that have formed around strategic research topics in the manufacturing sector, often related to emerging applications: the manufacturing of metallic prosthetic implants, the use of lasers in the production of products and components for electric mobility, digital twins applied to technologies and production systems, joining technologies in naval and marine applications, surface functionalization in biomedical implants. The papers here published aim to provide an overview of the new challenges posed by these frontier areas, demonstrating how only through the multidisciplinary and highly innovative approach that our community offers can these challenges be successfully addressed.

The White Papers underwent a reviewing process led by Prof. Luigi Carrino from the Università di Napoli Federico II to ensure their compliance with AITeM standards and to make their structure consistent.

Contents

AITeM Young Researcher Award 2023

3D Printing of Shape Memory Polymers: Embedding Nichrome-Wires to Enhance Their Performance

Gianni Stano, Antonio Pavone, and Gianluca Percoco

Abstract Shape memory polymers (SMPs) has recently gained popularity in the 3D printing field: the possibility to 3D print polymers capable to change their shape when triggered by a certain temperature, can lead to the fabrication of programmable structures. So far, the usage of solutions such as oven and warm water have been used to activate SMP, resulting in a lack of feasibility and difficult to be employed in real-life scenarios. In the present paper the authors propose a method to embed electrical nichrome-wires inside the 3D printed SMP during the fabrication process, in order to make the activation step easier, more feasible and faster. Several motions were reached when the 3D printed SMPs were activated, resulting appealing for the fabrication of soft robots. Moreover, complex structures made up of SMP material and flexible joint were also manufactured, proving that the proposed manufacturing method can be used to fabricate grippers and walking soft robots.

Keywords Shape memory polymers · 3D printing · Material extrusion · Soft robotics · Smart materials

1 Introduction

Over the years, Additive Manufacturing (AM) technologies have been largely employed for the fabrication of soft robots [1, 2] resulting in a reduction in costs, time and assembly tasks. From an actuation standpoint, 3D printed soft robots are based on pneumatic [3], electromagnetic [4], tendon driven [5], light [6], shape memory polymers (SMP) [7], shape memory alloys (SMA) [8], and hybrid systems [9]. The SMPs are a very promising class of actuators because of (i) lower cost, (ii) possibility to enable greater recovery deformation, (iii) biodegradability, and (iv) possibility to

G. Stano · A. Pavone (✉) · G. Percoco

Department of Mechanics, Mathematics and Management, Polytechnic of Bari, Via Orabona 4, 70125 Bari, Italy
e-mail: antonio.pavone@poliba.it

Interdisciplinary Additive Manufacturing (IAM) Lab, Polytechnic University of Bari, Viale del Turismo 8, 74100 Taranto, Italy

3

respond to more multiple stimuli [10] (even though one of the most studied domain is the temperature stimulus [11]). The SMP working mechanism is here described: its initial shape can be modified to a temporary shape, deforming the SMP at a fixed temperature above the glass transaction (Tg) temperature of the materials, named switching temperature (Ts). Cooling down the SMP, the temporary shape will be fixed: if the polymer is heated again above the Tg temperature, the SMP recover its initial shape [12, 13]. This particularly effect, called shape memory effect (SME) is a complex transformation that involves two class of SMP [14, 15]: (i) traditional one-way SMP (original shape-deforming shape-original shape), and (ii) two-way [16, 17] or more [18] SMP (original shape-deforming shape-original shape-deforming shape), able to remember two different shapes at low- and high-temperature.

On one hand SMPs do not required particular and complicated system to work such as cables, motors or pneumatic compressors, but on the other hand their activation is possible through external heat source [19] (often provided via oven and warm water) resulting in a lack of feasibility for real-life scenarios. A new challenge in soft robotics is the fabrication of SMP smart structures fabricated with embedded resistive wires, to improve SMPs usage [20, 21].

The low Tg (50–65 °C) of Polylactic Acid (PLA) makes it the most used thermoplastic polymers to fabricate SMPs [12] in Fused Filament Fabrication (FFF) technology. In general, FFF printing parameters (infill and pattern) that affect recovery time and recovery rate of SMP structures has been largely studied [14, 22, 23]. Cesarano et al. [24] analyzed the SMP response at different time–temperature combinations and programming parameters. Ehrmann et al. [25] performed mechanical destructive tests and investigate the recovery rate of PLA sample changing infill patterns and percentage. Roudbarian et al. [26] improved the shape memory effect (SME) of PLA by following multi-layered and multi-material approaches. Yang et al. [27] improved physical properties of 3D-printed SMP parts by tuning appropriate process parameters.

Moreover, a new way to exploit the SME in FFF structures is the fabrication of structures composed of SMP parts and links made of non-shape memory material actuated with tendon driven [20]. An hybrid actuation system brings several benefits such as (i) increased bending performance, (ii) use of two materials with different stiffness degrees in the same printing cycle, and (iii) complex movements impossible to achieve using only one actuation system [28, 29].

In the present paper, a multi-material FFF approach has been used to create structures composed of two actuation systems in a single manufacturing cycle: SMP parts connected to soft parts (actuated using a tendon-driven system).

A novel method to enhance the additively manufactured SMP performance is also presented: resistive nichrome (NiCr) wires have been embedded inside the 3D printed SMP during the fabrication process (using the stop and go method), in order to make the SMA activation step easier, more feasible and faster. Several complex motions were obtained when the 3D printed structures (SMP and tendon driven) were activated, resulting appealing for the fabrication of soft robots mimicking animals, and showing that such complex motions are impossible to obtain using only one actuation system.

2 Shape Memory Polymers (SMPs) and Tendon Driven Characterization

The main idea of the present work is the one-shot fabrication of a complex, hybrid-actuated structure combining SMP and tendon driven system, in order to obtained bio-inspired motions [30]. To achieve this goal, a multi-material FFF machine, namely Ultimaker 5 (Ultimaker, The Netherlands) was used. the following parts have been fabricated in the same manufacturing cycle: (i) stiff parts made up with polylactic acid (PLA), with embedded NiCr wire coils (0.6 mm diameter, maximum temperature 1150 °C), (ii) flexible-soft joints made up with thermoplastic polyurethane (TPU). A 0.4 mm nylon tendon and a stepper motor were used to enabling the mechanical driven actuation.

2.1 Shape Memory Polymers: Stiff Parts

Before the fabrication of the complete structure, the SMP structure was studied to choose the best shape for the fabrication of the complex finger actuator. The stiff parts were printed using the process parameters listed in Table 1. In particular, as known from scientific literature [31], low values of printing speed and layer height (lh) increas the quality of the parts: in this work, the printing speed was set at 45 and 25 mm/s respectively for PLA and TPU, and the layer height at 0.1 mm. Moreover, the 45° raster orientation was used to overcome the sinking problem of the empty part (channels to embed resistive wires), and a maximum infill percentage of 100% was used to overcome the low heat diffusivity of the polymer.

PLA is characterized by a glass transaction temperature (Tg) between 55 and 65 °C (technical datasheet). Moreover, the start-and-stop (S&S) method [32] was used to embedded the NiCr wire inside the PLA parts: with a G-code modification it has been possible to pause the print, manually embed the wire and finally resume the manufacturing process to cover the NiCr wire, as shown in Fig. 1. The embedding of NiCr wire during the S&S is a manual process and strongly related to the operator skills, however it took the authors an average of 2 min to accomplish that.

Five different rectangular-sample (R0–) SMA structures, with embedded NiCr wires, have been designed and fabricated to evaluate the best shape in terms of

Table 1 Printing parameters

Printing parameters	PLA (Stiff parts)	TPU (Soft joints)
Printing speed (mm/s)	45	25
Infill percentage (%)	100–Lines	80–Lines
Raster angle (°)	45	45
Printing temperature (°C)	210	235
Layer height (mm)	0.1	0.1
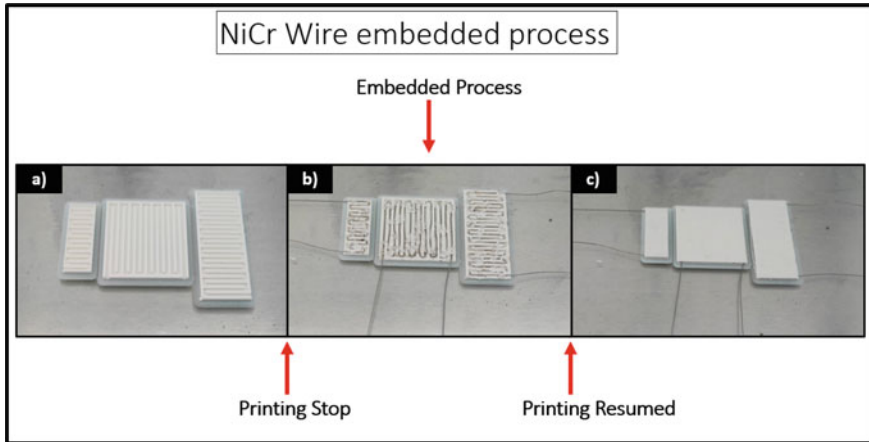
Fig. 1 A NiCr embedded process: **a** 3D printing process stopped when printing of sample channel is finished; **b** embedded NiCr resistance; **c** finale sample with embedded resistance after resumed printed

performance. The different SMP structures have been named R01, R02, R03, R04 and R05, respectively with x–y dimensions of 45×18 mm, 30×30 mm, 28×10 mm, 20×30 mm, 40×10 mm (see Fig. 2), keeping the thickness unchanged (fixed at 1.8 mm). The dimensions of the five different structures have been arbitrarily selected, in order to evaluate (i) the repeatability of the embedding process into different geometries, and (ii) how the dimensions of the structures affect their performance. Every version of the SMP-stiff part has been monolithically fabricated in a single-step printing cycle, resulting time and cost savings: for example, for R01 and R02 the time and cost are respectively 10 and 13 min, and 0.076 and 0.098 euro. It is worth mentioning that the spacing among the channel that housed the NiCr wire, has been set equal to 0.6 mm: this value was experimentally found as the minimum value ensuring a good 3D printing quality.

2.1.1 SMP-Stiff Part Compliance

For the characterization of the SMP-stiff part, the relationship between PLA compliance and local heating is studied. An ad hoc set-up was used to evaluate the compliance factor: (a) a power supply to heat up the embedded NiCr resistance, (b) a thermal imaging camera to evaluate the temperature of the NiCr wire, (c) weight of 50 and 75 g connected to the sample, and (d) a digital camera to take pictures at each increment of temperature to calculate the displacement.

The temperature of NiCr wire was incremented, starting from room temperature $T room$, to $T g$ and the compliance was calculated at 50, 55, 60 and 65 °C: a continuous current of $1.65 A$ (tension of 6.30 V) was applied. Each R-sample was tested three times, calculating the standard deviation of the compliance factor for the different
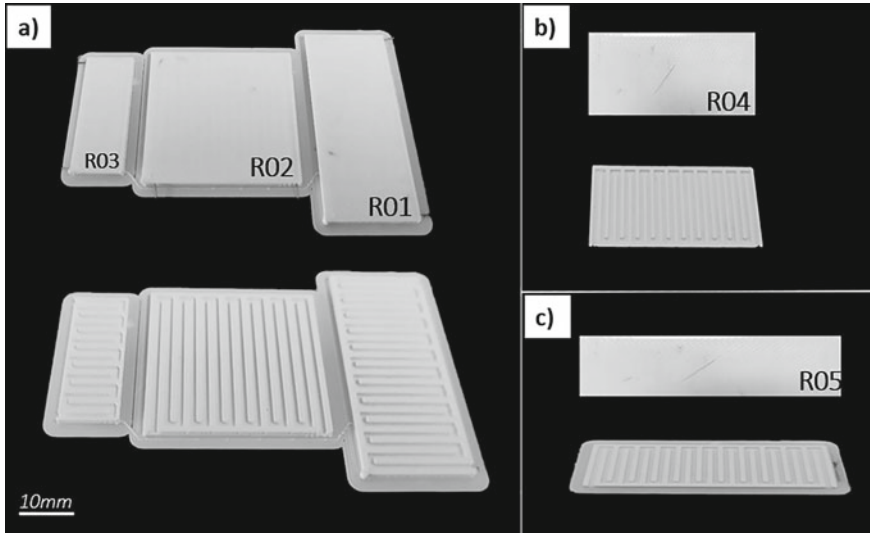
Fig. 2 Printed r-sample finished and internal channels

temperatures setting (see Table 2). Moreover, each sample was activated again to test the recovery shape, according to the SME. The compliance factor $C_m\left[\frac{mm}{N}\right]$ was calculated in according to [20].

$$C_m = \frac{1}{S} \qquad (1)$$

where S is the stiffness of the part, calculated as the ration of the applied force $F[N]$ and the d, sample displacement [mm]:

$$S = \frac{F}{d} \qquad (2)$$

Table 2 PLA stiff R-samples: compliance factor $\Delta C_m/C_{m0}$ versus temperature and load

T (°C)	$\Delta C_m/C_{m0}$ mean (Std. dev)					Load (g)
	R01	R02	R03	R04	R05	
50	2.97 (<0.001)	0.45 (<0.001)	0.43 (<0.001)	1.01 (<0.001)	4.92 (<0.001)	50
	2.31 (0.003)	1.39 (<0.001)	0.60 (0.05)	0.12 (<0.001)	2.68 (<0.001)	75
55	4.02 (<0.001)	1.89 (<0.001)	1.48 (<0.001)	1.22 (0.09)	5.67 (<0.001)	50
	2.92 (<0.001)	2.09 (0.02)	1.36 (<0.001)	1.29 (0.003)	4.40 (<0.001)	75
60	5.89 (0.02)	4.04 (0.02)	1.67 (0.002)	2.63 (0.15)	8.23(0.05)	50
	3.73 (<0.001)	3.43 (0.01)	2.40 (0.002)	3.17 (<0.001)	5.19 (<0.001)	75
65	7.75 (0.12)	6.81 (0.03)	2.24 (0.17)	3.32 (0.02)	9.04 (0.16)	50
	5.12 (0.002)	5.66 (0.02)	4.07 (0.01)	3.98 (0.03)	6.02 (0.06)	75

Starting from $Troom$, associated to C_{m0}, for each tested-temperatures the absolute compliance (ΔC_m) was calculated. R05 is the best in terms of compliance change, showing the maximum absolute compliance factor of 6.02 at $75g$ load and 65 °C. In Fig. 3 the absolute compliance for all the samples is shown.

Additionally, the testing phase has been used to obtain the behavior of the SMP samples at the fist activation (shape transforming phase) and at the second activation (shape recovery phase): such as the compliance testing, two loads (50 and 75 g), respectively generating two forces of $F1 = 0.49$ N and $F2 = 0.74$ N, were used. Firstly, for each rectangular sample, the internal NiCr resistance was heated from $Troom$ to T65 °C switching respectively from the rest position (initial) to final shape position, for each load. Secondly, each sample, after cooling, was re-heated from $Troom$ to T65 °C, respectively from shape position to recovery position (see Fig. 4). For the above-mentioned temperature values (50, 55, 60, and 65 °C) the displacement d was measured for each sample, during each test (see Table 2). $1.65 A$ of current was used. Moreover, the shaping and recovery time were measured to evaluate the actuation time for each sample (see Fig. 6). Particularly, as shown in Fig. 4e), the R05 sample confirms the compliance factor, resulting the only sample with a recovery position almost similar to the initial position. For example, the R05 changes its displacement from starting position to $d_{50g} = 31.12$ mm in 6 s and $d_{75g} = 36.52$ mm in 8 s respectively with 50 and 75 g load (see Fig. 4d). Finally, the R01 and R05 samples was tested in a vertical position to evaluate the bending angle with G-force application, as shown in Fig. 5.

As shown in Figs. 4 and 5, non-uniform deformation have been gotten: this might lead to unwanted failures during the exploitation of the SMP actuator. Due to the extremely huge design freedom offered from Additive Manufacturing (AM), new shapes can be easily fabricated to overcome this issue.

Concluding, R05 sample appears to be the best SMP-sample according to the performances shown. The R05 sample results the best in terms of (i) absolute compliance factor, (ii) SMP behavior with integration of NiCr wire for shape-recovery and (iii) low activation and recovery time. The impact of the manufacturing process on the performance shown by R05 have also been evaluated: five replications of R05 have been fabricated and tested. The standard deviation calculated while applying 75 g for the absolute compliance factor ΔC_m, activation time, and recovery time was respectively 0.7 (mean of 6.3), 1.3 (mean 7.2 s), and 2.1 (mean of 12.8 s). It stands out that the fabrication process is repeatable and has a very low impact on the performance shown from the SMP actuators. Also, from a geometric standpoint the R05 samples shows the highest ratio length/width (40 mm/10 mm): this might be related to the improved performances obtained, however more experiments are needed.

Also, a first attempt to characterize the fatigue life on R05 has been made: 10 consecutive activation cycles have been performed and the activation position, recovery position, activation time and recovery time were evaluated. In particular, all the four outputs shown a very low standard deviation (statistically not significant for every output), suggesting more cycles are needed to further study the fatigue behavior.
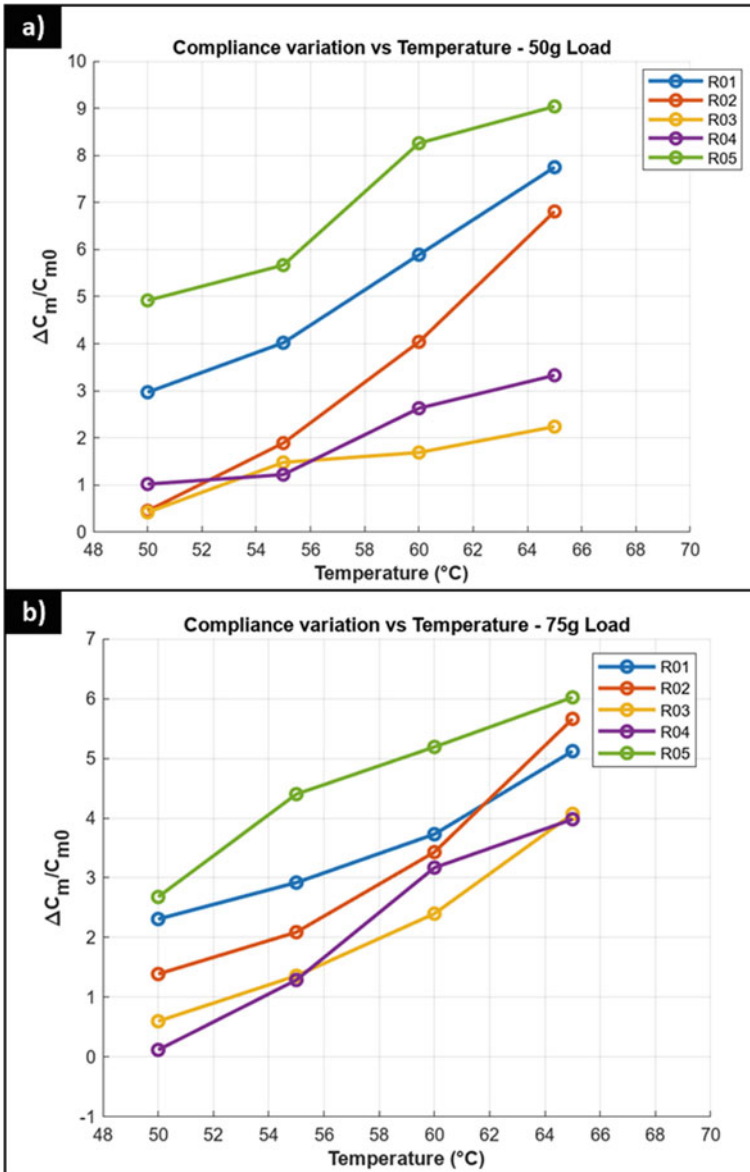
Fig. 3 Tested samples: **a** compliance variation with 50 g load application during temperature variation; **b** compliance variation with 75 g load application during temperature variation
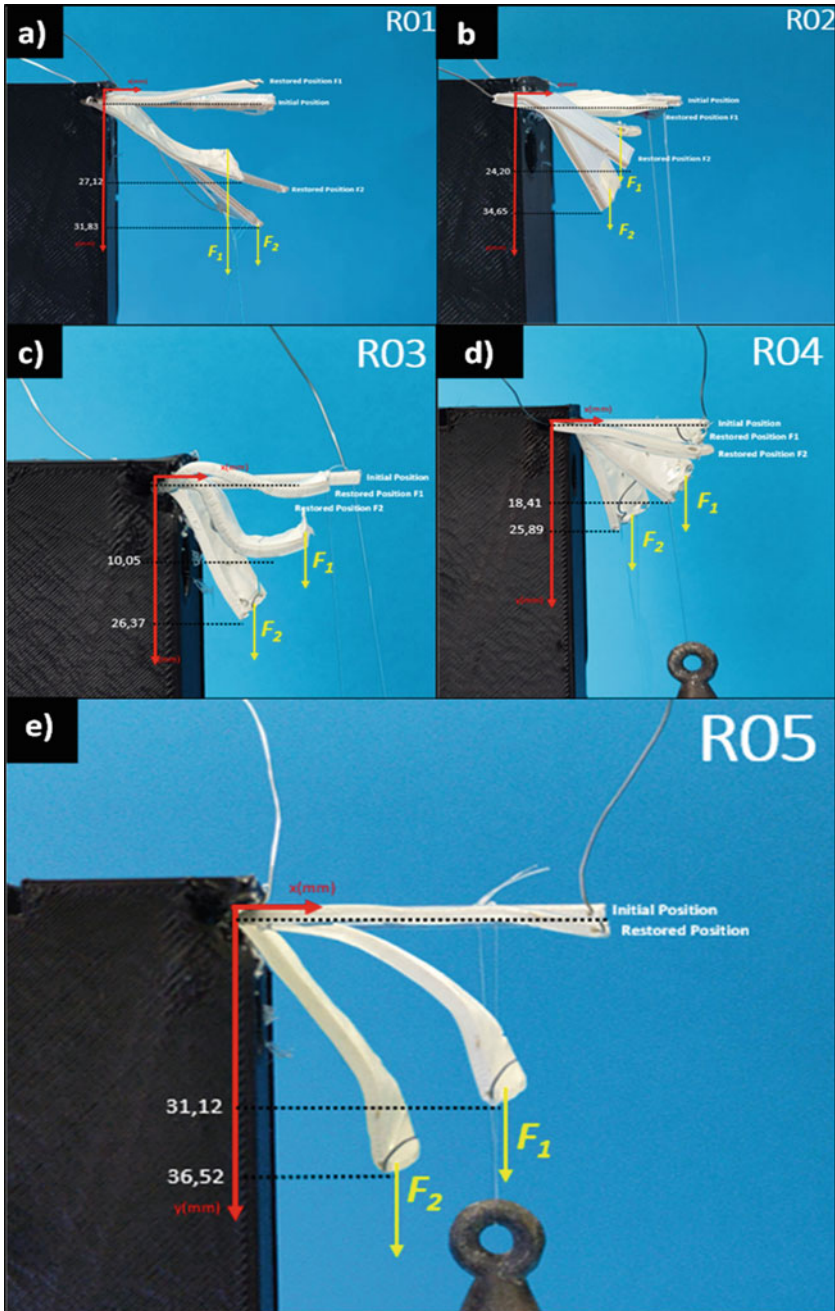
Fig. 4 Shape memory effect of tested samples comparing activation (using 50 and 75 g load) and recovery positions: **a** sample R01; **b** sample R02; **c** sample R03; **d** sample R04; **e** sample R05
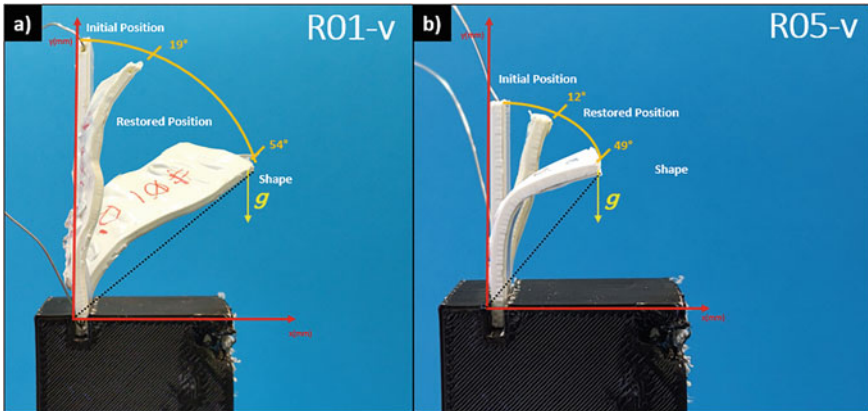
Fig. 5 Shape Memory Effect of tested vertical samples comparing activation (using 50 and 75 g load) and recovery positions: **a** sample R01; **b** sample R05

Since the R05 appear to be the most promising sample, two more variables such as Shape fixity and Shape recovery were evaluated based on 5 consecutive experiments performed on the same R05 sample: when applying 75 g as load, a mean shape fixity of 51° (standard deviation of 4.8°) and shepe recovery of 14° (standard deviation of 1.8°) was found. As shown in Fig. 5, the shape fixity and shape recovery values were calculated with respect to the origin.

2.2 Soft Joint: Tendon Driven Actuation

The SMP part, in the final version of the dual-mode actuator, is connected with a soft joint made up with TPU 95A, activated via a tendon-driven system (see Fig. 8a). In particular, mesh overlapping (mo), infill percentage (ip) and printing temperature of TPU were studied: three values of mesh overlapping were tested (0.15, 0.20, and 0.25 mm) combined to 50 and 80% of i p. In according to [33, 34], a T shape of the contact face between PLA and TPU was designed. After printing, the mesh overlapping and ip were tested with application of three different force of 5, 10, 20 N and 0.25 mm–80% were chosen for the following reasons:

- When a mesh overlapping of 0.15 mm (at 50 and 80% of in fill percentage) is set (Fig. 7a), the adhesion to PLA and TPU was not complete, and it led to the detachment of the joint during the force application
- Increasing the mesh overlapping to 0.20 and 0.25 mm, the adhesion between PLA and TPU increase, although the joint collapse in the range of 10–20 N when 50% of ip was set (see Fig. 7b)
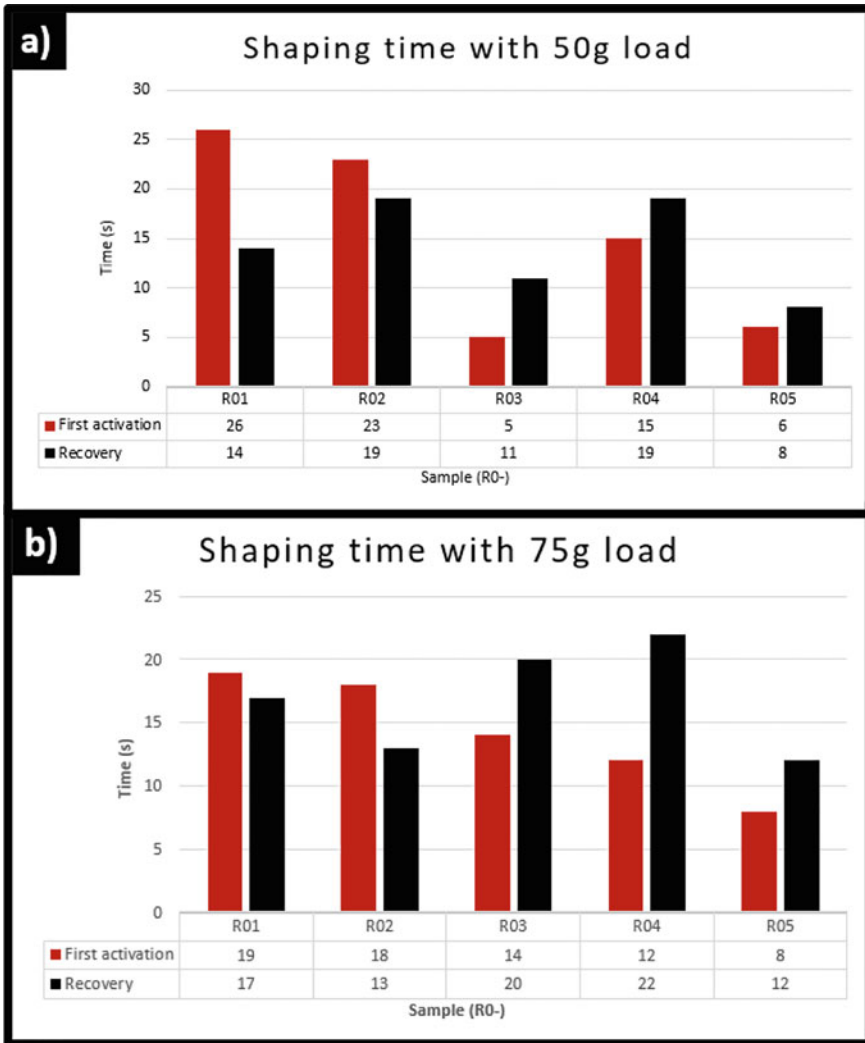
Fig. 6 Shaping time of R-sample during the first activation and during the second activation (recovery): **a** shaping time using 50 g load; **b** shaping time using 75 g load

- The 80% of infill percentage is a good compromise between the soft behaviour of the joint and the adhesion at the interface, setting 0.25 mm mesh overlapping (see Fig. 7c, d).

With a trial-and-error approach, the printing temperature of TPU was set at 240 °C to increase the adhesion to PLA: it is important to note that when temperature increase, proportional to mesh overlapping (set at 0.25 mm) and ip (set at 80%), the
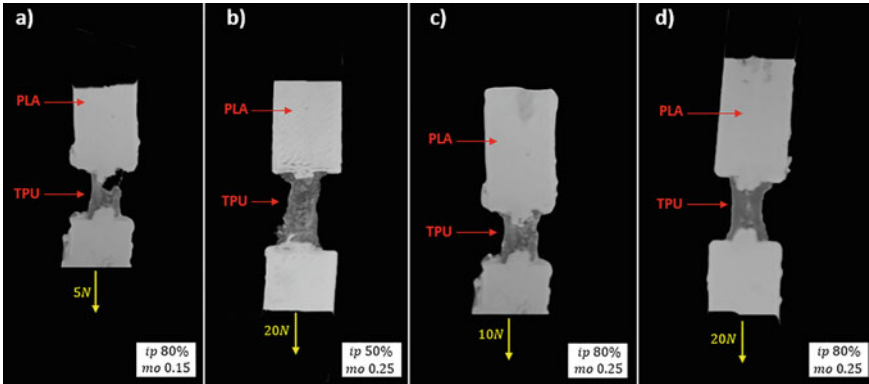
Fig. 7 Interface TPU-PLA tensile test: **a** collapsed joint with application of 5 N and mesh overlapping (mo) sets at 0.15 mm; **b** joint dilatation using 50% infill percentage (ip); **c** 10 N force application using 80% ip and 0.25 mm of mo; **d** 20 N force application
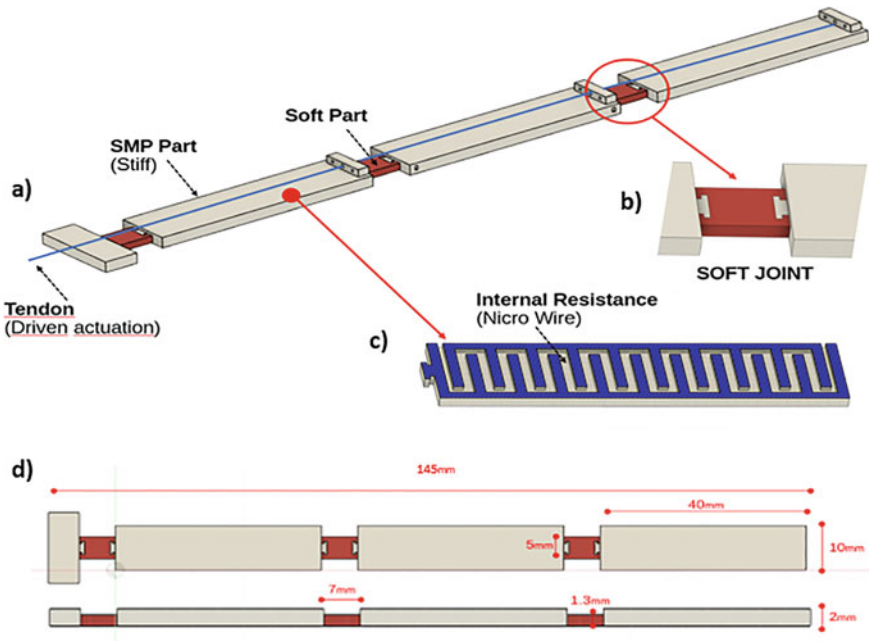
Fig. 8 Computer Aided Design (CAD) of complex finger structure: **a** representation of entirely structure; **b** interface between soft joint and stiff parts; **c** internal resistance channels; **d** dimension of the structure

joint became very functional and this parameters make the interface between PLA and TPU stronger.

3 Characterization of Dual-Activated (SMPs and Tendon-Driven) Structure

The proposed structure takes advantage of two actuation systems (SMP and tendon driven) resulting composed of PLA segments (SMP) and TPU segments (tendon driven) connected each others, as shown in Fig. 8.

The main reason leading to a dual actuation structure is the possibility to achieve complex motions (i.e. bending, twisting) impossible to achieve using a single actuation system. This structure is characterized by a manufacturing time and cost, respectively of 21 min and 0.89 Euro.

The fabricated finger was tested three times for each kind actuation system: (i) SMP actuation, (ii) tendon driven actuation and (iii) both actuation (combination of SMP actuation and tendon driven actuation). The tests were performed starting from resting condition (structure laying on the x-axis of Fig. 9): 1.68 A of current was provided to the NiCr wires to activate the SMP actuation, while a stepper motor was used to pull the tendon wire (tendon-driven actuation). When both the actuation systems were used at the same time, as shown in Fig. 9a), very complex motions were achieved: both bending and twisting were obtained. It is worth mentioning that no damages occurred after the three repetitions, however more tested have to be performed to quantify the fatigue behavior on soft robotics actuators.

It is necessary to note that the following limitations were present in this work:

- the number of the test on the complex actuator are not sufficiently to define a final behavior model, to estimate the right repetition of the movements.
- the tendon driven activation is faster than the SMP activation. An important part of future studies will be the reduction of the cooling time for the SMP by adding external cooling systems such as fan or cold water channels

4 Conclusions

In the present paper, a multi-material FFF approach was used for the monolithic fabrication of a structure able to perform several unconventional movements combining two different types of actuations: SMP system and tendon-driven system. The start and stop method has been successfully used to embed NiCr wires inside SMP structures making them more appealing for real-life scenarios overcoming the high activation time occurring when hot water or oven are used.
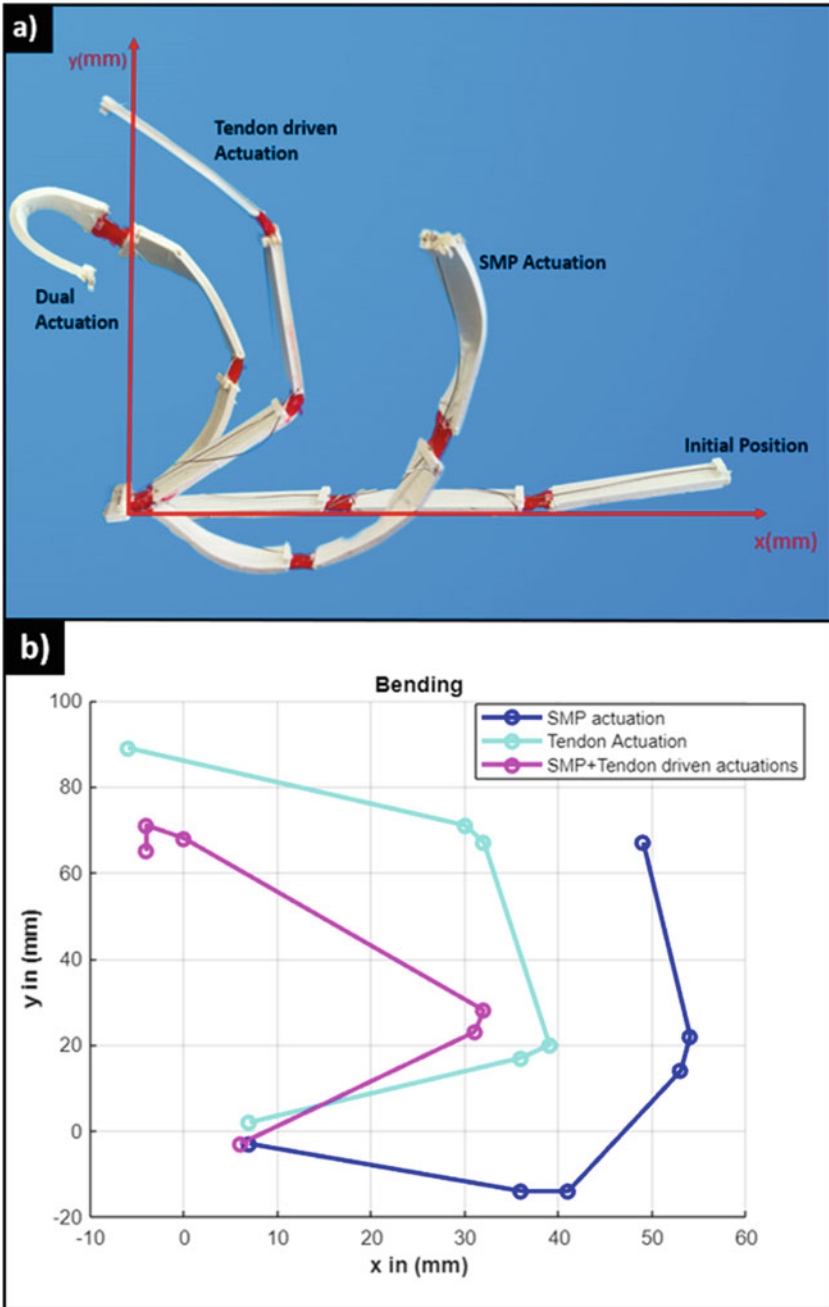
Fig. 9 Motions of complex finger structure, actuated using SMP actuation, Tendon driven actuation and both SMP and Tendon actuation: **a** real bending actuation; **b** software mapping

The present work lays the foundation (i) for an extensively usage of FFF technology to fabricate soft robots performing complex motions and (ii) for the fabrication of SMP-based structures with improved performance. Further investigation based on modelling the behavior of the proposed SMP actuators in relationship with the process parameters set in the slicing software will be performed.

References

1. Stano G, Percoco G (2021) Additive manufacturing aimed to soft robots fabrication: a review. Extrem Mech Lett 42:101079. https://doi.org/10.1016/j.eml.2020.101079
2. Mitchell A, Lafont U, Hołyńska M, Semprimoschnig C (2018) Additive manufacturing—a review of 4D printing and future applications. Addit Manuf 24:606–626. https://doi.org/10.1016/j.addma.2018.10.038
3. Tawk C, Alici G (2021) A review of 3D-printable soft pneumatic actuators and sensors: research challenges and opportunities. Adv Intell Syst 3. https://doi.org/10.1002/aisy.202000223
4. Pavone A, Stano G, Percoco G (2023) One-shot 3D printed soft device actuated using metal-filled channels and sensed with embedded strain gauge, 3D print. Addit Manuf. https://doi.org/10.1089/3dp.2022.0263
5. Tawk C, Gillett A, Spinks GM, Alici G (2019) A 3D-printed omni-purpose soft gripper. 35(5):1268–1275
6. Huang C, Lv JA, Tian X, Wang Y, Yu Y, Liu J (2015) Miniaturized swimming soft robot with complex movement actuated and controlled by remote light signals. Sci Rep 5(July):1–8. https://doi.org/10.1038/srep17414
7. Chen T, Shea K (2018) An autonomous programmable actuator and shape reconfigurable structures using bistability and shape memory polymers, 3D print. Addit Manuf 5(2):91–101. https://doi.org/10.1089/3dp.2017.0118
8. Bodkhe S, Vigo L, Zhu S, Testoni O, Aegerter N, Ermanni P (2020) 3D printing to integrate actuators into composites. Addit Manuf 35:101290. https://doi.org/10.1016/j.addma.2020.101290
9. Aksoy B, Shea H (2022) Multistable shape programming of variable-stiffness electromagnetic devices. Sci Adv 8(21):1–14. https://doi.org/10.1126/sciadv.abk0543
10. Mehrpouya M, Vahabi H, Janbaz S, Darafsheh A, Mazur TR, Ramakrishna S (2021) 4D printing of shape memory polylactic acid (PLA). Polymer (Guildf) 230:124080. https://doi.org/10.1016/j.polymer.2021.124080
11. Ji Q, Wang XV, Wang L, Feng L (2022) Online reinforcement learning for the shape morphing adaptive control of 4D printed shape memory polymer. Control Eng Pract 126:105257. https://doi.org/10.1016/j.conengprac.2022.105257
12. Suethao S, Prasopdee T, Buaksuntear K, Shah DU, Smitthipong W (2022) Recent developments in shape memory elastomers for biotechnology applications. Polymers (Basel). 14(16). https://doi.org/10.3390/polym14163276
13. Koualiarella A et al (2020) Tuning of shape memory polymer properties by controlling 3D printing strategy. CIRP Ann 69(1):213–216. https://doi.org/10.1016/j.cirp.2020.04.070
14. Valvez S, Reis PNB, Susmel L, Berto F (2021) Fused filament fabrication-4d-printed shape memory polymers: a review. Polymers (Basel) 13(5):1–25. https://doi.org/10.3390/polym13050701
15. Leonés A, Sonseca A, López D, Fiori S, Peponi L (2019) Shape memory effect on electrospun PLA-based fibers tailoring their thermal response. Eur Polym J 117(May):217–226. https://doi.org/10.1016/j.eurpolymj.2019.05.014
16. Du L et al (2020) From a body temperature-triggered reversible shape-memory material to high-sensitive bionic soft actuators. Appl Mater Today 18:100463. https://doi.org/10.1016/j.apmt.2019.100463

17. Pandini S et al (2012) Two-way reversible shape memory behaviour of crosslinked poly(ε-caprolactone). Polymer (Guildf) 53(9):1915–1924. https://doi.org/10.1016/j.polymer.2012.02.053

18. Bai Y, Zhang X, Wang Q, Wang T (2014) A tough shape memory polymer with triple-shape memory and two-way shape memory properties. J Mater Chem A 2(13):4771–4778. https://doi.org/10.1039/C3TA15117D

19. Melly SK, Liu L, Liu Y, Leng J (2020) Active composites based on shape memory polymers: overview, fabrication methods, applications, and future prospects. J Mater Sci 55(25):10975–11051. https://doi.org/10.1007/s10853-020-04761-w

20. Stano G, Ovy SMAI, Edwards JR, Cianchetti M, Percoco G, Tadesse Y (2022) One-shot additive manufacturing of robotic finger with embedded sensing and actuation. Int J Adv Manuf Technol 467–485. https://doi.org/10.1007/s00170-022-10556-x

21. Takashima K, Sugitani K, Morimoto N, Sakaguchi S, Noritsugu T, Mukai T (2014) Pneumatic artificial rubber muscle using shape-memory polymer sheet with embedded electrical heating wire. Smart Mater Struct 23(12):125005. https://doi.org/10.1088/0964-1726/23/12/125005

22. Nam S, Pei E (2020) The influence of shape changing behaviors from 4D printing through material extrusion print patterns and infill densities. Materials (Basel) 13(17). https://doi.org/10.3390/MA13173754

23. Huang X, Panahi-Sarmad M, Dong K, Li R, Chen T, Xiao X (2021) Tracing evolutions in electro-activated shape memory polymer composites with 4D printing strategies: a systematic review. Compos Part A Appl Sci Manuf 147:106444. https://doi.org/10.1016/j.compositesa.2021.106444

24. Cesarano F, Maurizi M, Gao C, Berto F, Penta F, Bertolin C (2022) Science direct structural science direct science direct preliminary optimization of shape memory polymers geometric Preliminary optimization shape memory geometric parameters to enhance of the thermal loads' polymers activation range parameters loads' acti. Procedia Struct Integr 42(2019):1282–1290. https://doi.org/10.1016/j.prostr.2022.12.163

25. Ehrmann G, Ehrmann A (2021) Investigation of the shape-memory properties of 3D printed pla structures with different infills. Polymers (Basel) 13(1):1–11. https://doi.org/10.3390/polym13010164

26. Roudbarian N, Baniasadi M, Nayyeri P, Ansari M, Hedayati R, Baghani M (2021) Enhancing shape memory properties of multi-layered and multi-material polymer composites in 4D printing. Smart Mater Struct 30(10). https://doi.org/10.1088/1361-665X/ac1b3b

27. Yang Y, Chen Y, Wei Y, Li Y (2016) 3D printing of shape memory polymer for functional part fabrication. Int J Adv Manuf Technol 84(9–12):2079–2095. https://doi.org/10.1007/s00170-015-7843-2

28. Mao Y, Yu K, Isakov MS, Wu J, Dunn ML, Jerry Qi H (2015) Sequential self-folding structures by 3D printed digital shape memory polymers. Sci Rep 5:1–12. https://doi.org/10.1038/srep13616

29. Yamamura S, Iwase E (2021) Hybrid hinge structure with elastic hinge on self-folding of 4D printing using a fused deposition modeling 3D printer. Mater Des 203:109605. https://doi.org/10.1016/j.matdes.2021.109605

30. Kilbourne BM, Hutchinson JR (2019) Morphological diversification of biomechanical traits: mustelid locomotor specializations and the macroevolution of long bone cross-sectional morphology. BMC Evol Biol 19(1):1–16. https://doi.org/10.1186/s12862-019-1349-8

31. Dey A, Yodo N (2019) A systematic survey of FDM process parameter optimization and their influence on part characteristics. J Manuf Mater Process 3(3). https://doi.org/10.3390/jmmp3030064

32. MacDonald E, Wicker R (2016) Multiprocess 3D printing for increasing component functionality. Science (80) 353(6307):aaf2093. https://doi.org/10.1126/science.aaf2093

33. Dairabayeva D, Perveen A, Talamona D (2022) Investigation on the mechanical performance of mono-material versus multi-material interface geometries using fused filament fabrication. Rapid Prototyp J 29(11):40–52. https://doi.org/10.1108/RPJ-07-2022-0221
34. Stano G, Ovy SMAI, Percoco G, Zhang R, Lu H, Tadesse Y (2023) Additive manufacturing for bioinspired structures: experimental study to improve the multimaterial adhesion between soft and stiff materials, 3D print. Addit Manuf. https://doi.org/10.1089/3dp.2022.0186

Aerosol Jet Printing of 3D Biocompatible Gold Nanoparticle-Based Micro-Structures

Miriam Seiti, Paola Serena Ginestra, and Eleonora Ferraris

Abstract Aerosol Jet® Printing (AJ®P) is an additive manufacturing (AM) technique for the deposition of a functionalized jet on *free-form* substrates. AJ®P is mainly exploited for 2D printed electronics, nevertheless, is gaining attention in the bioelectronic field. Few emerging studies have also established AJ®P as a micro-AM 3D printing technique. In this context, the 3D AJ®P process has not been deeply analysed yet. This work proposes an unique study of novel 3D AJ® printed gold microstructures, as arrays of micropillars ≥ 40 µm, with aspect ratios ARs ≤ 9 and print times ≤ 10 min. Print parameters were investigated via a full factorial design against shape fidelity and resolution, using a layer-by-layer strategy. Specimens were thermally sintered, without any binding. Optical, electrical, and biocompatibility tests were conducted and a flexible 3D microelectrode array was printed as proof-of-concept. Future applications include in-vitro bioelectronics, thermoelectric, and batteries.

Keywords Additive manufacturing · Biomedical applications · Gold nanoparticle ink

1 Introduction

Since the late 1960s, micromanufacturing processes are being continuously investigated and improved for a variety of advanced applications, especially in the electronic, medical, automotive, and biotechnology industries [1]. Representative products of such technologies include (opto)micro-electromechanical systems (MEMS), micro-electronics, microfluidics, and bioelectronics.

M. Seiti (✉) · E. Ferraris
Department of Mechanical Engineering, Campus De Nayer, Leuven, KU, Belgium
e-mail: miriam.seiti@kuleuven.be

M. Seiti · P. S. Ginestra
Department of Mechanical Engineering, University of Brescia, Brescia, Italy

In this context, the development and exploitation of three-dimensional (3D) periodic microstructures with high aspect ratios (ARs) gained a considerable attention, especially for MEMS [2], micro-actuators [3], electrophysiological [4], micro-sensors [5], and scaffolds for cell guidance [6]. The major traditional microfabrication technologies refer to lithography-based processes (photolithography, molding, chemical etching, laser ablation, etc.) and micromachining processes (EDM, micro-extrusion, micro-injection molding, micro-embossing, etc.) [7]. In the last 40 years, Additive Manufacturing (AM) opened up even more possibilities for customized and versatile three-dimensional (3D) microstructures, especially with the use of stereolithography (SLA), fused filament fabrication (FFF), 3D Direct Writing (DW) techniques and hybrid technologies.

Particularly, 3D-DW techniques include droplet-, energy beam-, flow-, and tip-based (or nozzle) writing processes [8]. Among them, 3D-DW nozzle-based techniques (e.g. syringe- or jet-based printing) deal with viscoelastic inks which can be focalized or extruded through a deposition nozzle in a layer-by-layer (LBL) strategy for building up 3D complex and periodic structures at meso- and micro-scales [9]. A wide range of materials, among which metals, polymers, ceramics, and biological compounds, can be singularly or simultaneously printed for multifunctional devices.

Aerosol Jet® Printing (AJ®P) is an AM-DW nozzle-based technique which has been introduced in the market since the 1990s [10]. AJ®P has been conventionally used for the printed electronics (PE) industry, especially for the two-dimensional (2D) deposition of functional inks for passive and active elements on *free-form* substrates (3 or 5-axes platform) [11]. Examples of AJ® printed devices are flexible antennas [12], strain sensors [13], wearable devices [14], electrochemical sensors [15], batteries [16], and so on. The technology concerns the printing of inks in a liquid form which can be further aerosolized by means of a pneumatic or ultrasonic approach. Such inks can have a wide viscosity range of [1–1000] mPas, as long as their loading content has a particle size less than 500 µm. The final printed constructs can feature a size starting from 15 µm, with a minimum thickness of hundreds of nm. Moreover, differently from inkjet printing, AJ®P offers a variable stand-off distance, z [mm], from 1 to 5 mm. Because of such versatility, AJ®P has recently gained attention for life science, and tissue engineering (TE) applications [17–20]. AJ®P commercial inks are typically PE inks, including conductive metal- (such as silver nanoparticles-based, AgNPs inks) and polymer-based dispersions, or (UV curable) dielectrics. Most of those inks derive from inkjet dispersions which have been optimized to work with an AJ®P process. Although the portfolio of AJ®P inks is positively growing, few or even none of the commercial solutions can be currently applied for biomedical applications, especially if they are TE-oriented. Indeed, most of the traditional PE co-solvents applied in the ink formulation (such as xylenes, oils, and specific alcohols or glycols) generally induce a cytotoxic compounds in the cell culture, causing an unhealthy cellular state, which eventually leads to death. Therefore, novel biocompatible solutions have been proposed and successfully 2D AJ® printed, including natural (e.g. collagen [21], silk fibroin [22], gelatin [23]) or synthetic polymers (poly(3,4-ethylenedioxythiophene) polystyrene

sulfonate, PEDOT:PSS [17]), carbon-based (graphene, [24], carbon nanotubes [25], carbon ashes [25]), and also biological compounds (proteins [26]).

Very few among these inks can be exploited for bioelectrical interfaces, such as graphene and PEDOT:PSS-based solutions. Although their competitive cost, a trade-off between electronic/ionic conductivity and biocompatibility is inevitable when compared to precious noble metals, as gold or platinum. For instance, commercial gold nanoparticles (AuNPs)- or platinum nanoparticles (PtNPs)-based inks (mainly available for inkjet printing) have a conductivity 2 or 3 orders of magnitude higher than polymer-based inks. Their use is thus preferred for specific (bio)electronic applications which require high sensing performances and excellent oxidation stability, without compromising the biocompatibility. AuNPs-based inks are unique solutions with outstanding tunable properties (e.g., optical, thermal, electrical) and have been exploited for surface coating and PE, including electrochemical sensors [27], humidity sensors [28], and biosensors [29, 30]. The AuNPs composition can be adjusted for the desired application in terms of shape, size and surface chemistry [31] and the co-solvents can be selected to have low levels of cytotoxicity. In this way, they can be used also in TE, drug delivery and cancer therapy [32–34].

Since 2017, a couple of emerging studies demonstrated the capability to use the AJ®P technology for 3D micro-structuring and micro-fabrication (here referred as 3D AJ®P), including AgNPs-based lattices and micropillars arrays at ARs ~20 [35], AuNPs-based pillars at an AR ~3.5 [30], photo-reactive polymers-based pillars at ARs ≤ 11 [36], and PEDOT:PSS–CNTs-based micropillars at an AR ~3.3 [37]. However, these works lack of a thorough investigation of the effects of 3D AJ®P parameters on the printed microstructures, fundamental for evaluating the repeatability and process window.

Therefore, this manuscript aims to be among the first works that investigate and optimize the 3D AJ®P process via a design of experiment (DOE) approach for the 3D printing of periodic conductive microstructures (micropillars) against shape fidelity and reliability. A novel 3D AJ®P AuNPs-based ink is selected for the study, along with a validation of its conductivity and biocompatibility. Lastly, a flexible 3D microelectrode array chip is printed as proof-of-concept. Such 3D AuNPs-AJ® printed microstructures offer an exciting potential in a vast range of 3D electrical and bioelectrical applications, including energy harvesting devices, (bio)sensors, in-vitro electrophysiology and lab-on-chip devices.

2 Materials and Methods

The AJ®P process atomizes and deposits functional inks on *free-form* substrates, with a resolution scale up to 15 µm in line width and hundreds of nm in thickness [10]. In this study, the AJ®P ultrasonic configuration (U-AJ®P) will be investigated. Figure 1 reports the schematic visualisation of the 3D-AJ®P process, divided into its three main subprocesses: ink atomization and transport, collimation and in-flight jet, and aerosol impaction and impingement. In details, the selected ink is positioned into

an ultrasonic bath and it is sonically excited till the generation of atomized micro-droplets from its surface. The aerosolized mist is then transported via an inert gas (N$_2$) called carrier gas flow, $CGF = [0\text{--}50]$ sccm, into a transport tube. This tube is directly connected to the print head, in which a second inert gas (N$_2$), named sheath gas flow, $SGF = [0\text{--}200]$ sccm, aerodynamically focuses the mist into an aerosol jet. The jet exits the nozzle and the in-flight jet later impacts on the substrate at a decided stand-off distance, z [mm] of 3 mm, following a precise computer-aided design (CAD) file. A post-printing process is usually applied to sinter the printed metal-based structure. CGF and SGF are therefore considered two crucial parameters for the transport and in-flight of the aerosol jet. The ratio between SGF and CGF is known as focusing ratio $R_f = \frac{SGF}{CGF} \geq 1$, for a converged and focused aerosol jet which reduces undesired deposited satellite (or outlier) droplets at the edges of the printed patterns (known as overspray, OS). Moreover, high values of the platen temperature, T [°C] can allow a fast evaporation of the ink (co-)solvents, inducing a pre-sintering process for the building-up of 3D microstructures [39].
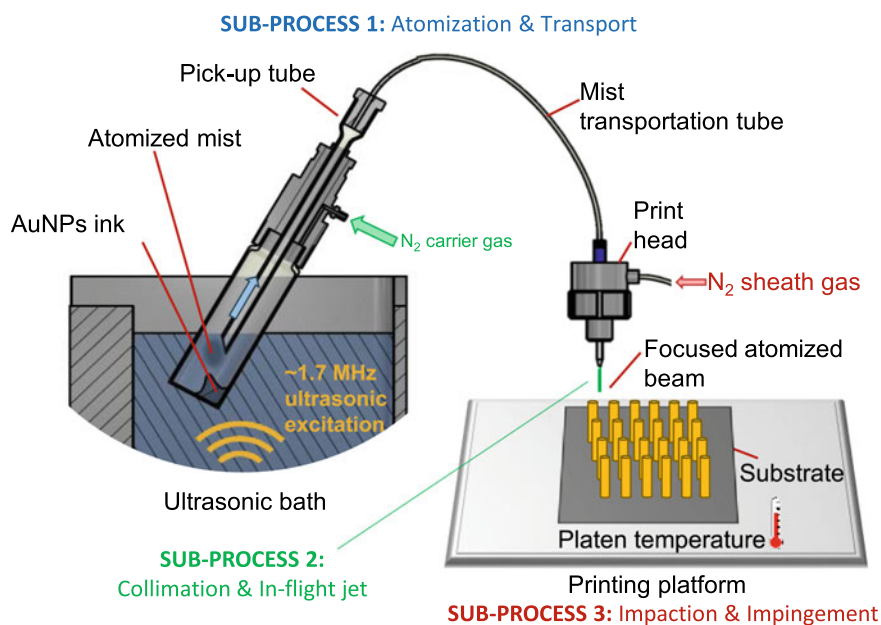
Fig. 1 Schematic figure of the 3D-AJ®P process, highlighting the three main sub-processes: (i) atomization and transport, (ii) collimation and in-flight jet, and (iii) impaction and impingement of the aerosol jet. Figure adapted from Degryse et al., International Conference on Biofabrication, 2021 [38]

2.1   Ink and Substrate

An AuNPs-based ink was developed in partnership with NovaCentrix ($^{©}$NovaCentrix, Austin, TX, USA) and used for U-AJ$^{®}$P. The AuNPs-based ink chosen is a water-based dispersion with 45 wt% loading content and ethylene glycol (EG) as main co-solvent, in order to carry and avoid drying of the aerosol mist during the transport and in-flight phases.

The ink was 2D-AJ$^{®}$ printed for electrical and biocompatibility assays in its standard formulation, while 3D-AJ$^{®}$ printed in a diluted version with MilliQ water, in a ratio of 2:1. The electrical resistance was tested for both formulations. For print investigations, glass slides (Superfrost, VWR, BE) were chosen as reference substrate. Prior to use, the substrates were cleaned with distilled water (DI) and 2-propanol (IPA, Sigma Aldrich, BE) in an ultrasonic bath at $T = 25$ °C for 15 min (EMMI—20 HC, Emag). At same conditions, the ink was sonicated before the print process.

2.2   Process Investigation

The print process was carried out with an AJ$^{®}$P 300 s system ($^{©}$Optomec, Albuquerque, USA) using the ultrasonic configuration. The AJ$^{®}$P print strategy selected is 3D-LBL [39], which is the classic approach used in 3D prototyping following a given CAD pattern.

In this case, the pattern used was an array of 6×4 circles with a diameter of 50 µm and an inter-spacing of 90 µm, which the CAD file was converted in a.prg toolpath code in accordance with VM Tools ($^{©}$VMware inc., USA). A full-factorial design of experiment (DOE) of the type 2^k (k > 0), with k = 3 (three repetitions) was performed in order to investigate the influence of print parameters on the micropillars characteristics. The following factors were analysed: *SGF* (35; 70) sccm, speed *s* (0.4; 0.8) mm/s, and *T* (40, 80) [°C], selected based on the operator experience and preliminary tests. A nozzle with a diameter of $\emptyset = 150$ [µm] and a number of printed layers equal to $n = 25$ were chosen for the investigation. Moreover, the *CGF* was kept fixed at 15 sccm from preliminary trials performed to obtain a continuous and uniform aerosol jet deposition. A Printability and Shape Fidelity Index, Ψ[#], $0 \leq \Psi \leq 1$ was calculated as quantitative response of interest for the full factorial design. More information are reported in the following section.

Table 1 reports an overview about the print parameters investigated at ambient conditions (22 °C, 55% rh). Before printing, the AuNPs-based ink was sonicated in the U-AJ$^{®}$P system for 60 min at 45 V, while the substrate was kept on the print platform for 10 min in order to be thermally in equilibrium with the platen temperature. The green parts were then thermally sintered in an oven at 200 °C for 1.5 h (Heraeus, GmbH) in order to allow solvents evaporation and the obtainment of a continuous and conductive NPs network.

Table 1 AJ® print experimental tests on an AuNPs-based ink. A full factorial design is chosen to investigate the Printability and Shape Fidelity Index, Ψ[#] by varying three factors, that is *SGF*, *s*, and *T*, (two levels each), and three repetitions for every condition (from A to H)

Full factorial design 2^k (k = 3) for 3D printed AuNPs-based micropillars			
Factors	Levels		
Sheath gas flow, *SGF* [sccm]	35		70
Print speed, *s* [mm/s]	0.4		0.8
Platen temperature, *T* [°C]	40		80
Repetitions [#]	3		
Response	Printability and shape fidelity index, Ψ[#]		
Conditions analyzed			
Condition	*SGF* [sccm]	*s* [mm/s]	*T* [°C]
A	35	0.4	40
B	70	0.4	40
C	35	0.4	80
D	70	0.4	80
E	35	0.8	40
F	70	0.8	40
G	35	0.8	80
H	70	0.8	80
Fixed parameters	Values		
Sample design	Array of 6 × 4 circles, Ø = 50 µm		
Substrate	Glass slides, VWR Superfrost® Plus Micro Slide		
Nozzle diameter, Ø [µm]	150		
Stand-off distance, *z* [mm]	3		
Number of layers, *n* [#]	25		
Carrier gas flow, *CGF* [sccm]	15		

2.3 Sample Characterization

Printability and shape fidelity index

For each DOE condition (from A to H), the front raw composed of six 3D-LBL AJ® printed pillars was analyzed. The geometrical and shape fidelity of each pillar was assessed by calculating its height, h [µm], bending angle, α [rad] (from the substrate), middle diameter $Ø_1$ [µm] and top diameter $Ø_2$ [µm].

Three indexes were considered in the evaluation of Ψ[#], that is (i) the uniformity error ε_u[#], (ii) the AR index i_{AR} [#], and (iii) the bending angle error ε_α[#]. Equation (1) defines ε_u as the ratio between the normalized difference of the middle and the top diameter on the middle one, in absolute values.

$$\epsilon_u = \left| \frac{(\emptyset_1 - \emptyset_2)}{\emptyset_1} \right|, 0 \leq \epsilon u \leq 1 \tag{1}$$

It was decided not to consider the base diameter of the pillars due to the unavoidable presence of OS, which accumulates at every printed layers. Equation (2) determines i_{AR} as.

the ratio between the maximum value among the two diameters and the height, in absolute values (e.g. the inverse of the aspect ratio). This means that the processing conditions are optimized for a minimum i_{AR}, which means a maximum AR.

$$i_{AR} = \left| \frac{max(\emptyset_1, \emptyset_2)}{h} \right|, 0 \leq \epsilon AR \leq 1 \tag{2}$$

In this case, the highest value between $\emptyset_1$ and $\emptyset_2$ was selected instead of the mean value due to the presence of a tip narrowing effect, especially for some conditions in which the two values differ of a factor more than 3. Equation (3), instead, describes ε_α as the absolute value of the normalized difference between an angle of $\frac{\pi}{2}$ and the bending angle α.

$$\epsilon_\alpha = \left| \frac{\left(\frac{\pi}{2} - \alpha \right)}{\frac{\pi}{2}} \right|, 0 \leq \epsilon \alpha \leq 1 \tag{3}$$

Finally, Ψ is defined as the normalized sum of the three indexes, as reported in Eq. (4).

$$\Psi = \frac{(\epsilon_u + i_{AR} + \epsilon_\alpha)}{3}, 0 \leq \Psi \leq 1 \tag{4}$$

Therefore, in ideal conditions ($\Psi = 0$) the printed pillar is a similar to a perfect cylinder, with the minimum variation of diameter throughout the height, $\alpha = \frac{\pi}{2}$, and a maximum AR. For each subset, the mean μ [µm] and standard deviation σ (e.g., $\mu \pm \sigma$) of geometrical and error values were computed and analyzed. Statistical analyses and multiple regression modelling were performed via the software Minitab® 2022.

Optical and morphological analysis

Samples were optically inspected via a KH 8700 (©Hirox, Japan) microscope and Tescan Vega 3 scanning electron microscope (SEM) (Tescan Orsay Holding as. Czech Republic). Image analyses were carried out with the software ImageJ.

Electrical analysis

The electrical resistance, $R[\Omega]$, of the ink was validated by 2D-AJ® printing four squares (6×6 mm) with a two-point probe method, three repetitions each (Digital Multimeter 73 III, Fluke). The parameters selected were: $\emptyset_{nozzle} = 300$ µm, $s = 10$ mm/s, $A = 30$ sccm, $S = 40$ sccm, $T = 40$ °C, and 10 layers. The post-process sintering was carried out as previously explained.

Biocompatibility analysis

An immunofluorescence assay on human fibroblasts (HFs) at day 5 was conducted in order to observe their adhesion and morphology (nuclei and cytoskeleton) on AJ® printed AuNPs squares, same as the one used for R testing. Plastic was used as positive control. Before cell seeding, all the substrates were washed three times with a phosphate buffer solution (PBS, 1x, Sigma Aldrich, IT), and further autoclaved for sterilization. HFs (BJ cell line ATCC® CRL-2522™) at a concentration of 5 $\times$ 10^4 cells cm^{-2} were seeded onto the samples and incubated for 30 min. Later, a Dulbecco's modified Eagle's medium (DMEM) was added as medium culture, supplemented with 1% penicillin/streptomycin, 10% fetal bovine serum, and 1% L-glutamine (©Euroclone S.P.A., IT). Afterwards, cells were maintained in the incubator at 37 °C in a saturated humidity atmosphere of 95% air and 5% CO_2. After 5 days of cell culturing, HFs were fixed for 30 min (fixation and permeabilization, 15 min each) with a Fix&Perm Sample Kit® (SIC). Subsequently, cells were incubated for 45 min with a blocking solution (iBind™ 5X Buffer, Invitrogen), further stained with Phalloidin (Sigma Aldrich) for cytoskeletal visualization, and finally counterstained for 5 min with Hoechst 33,342 for nuclei determination. The resulting samples were fixed on glass coverslips and optically analysed with an inverted fluorescence microscope (Olympus IX70) and with Image-Pro Plus software v.7.0 (Media Cybernetics), respectively.

3   Results and Discussion

3.1   *Geometrical Analysis*

Figure 2 shows representative optical images of 3D-LBL AJ® printed AuNPs-based micropillars at the different conditions (from A to H). Moreover, Table 2 reports the data ($\mu \pm \sigma$) of the dimensional analysis (h [μm], α [rad], $\emptyset_1$ [μm], $\emptyset_2$ [μm]) performed for each printing condition selected in the full factorial design 2^k (k = 3, from A to H). Every 3D micropillars printing condition lasted less than 10 min. The maximum pillar height achieved was equal to $h = (435.67 \pm 0.01)$ μm at the condition C (35, 0.4, 80), with the highest $AR_C = 9.3$, while the minimum one, $h = (216.39 \pm 0.01)$ μm, was obtained at the condition F (70, 0.8, 40), with $AR_F = 5.4$. Compared to the expected CAD file (circle with $\emptyset = 50$ μm), the printed pillars generally showed a variation between the middle $\emptyset_1$ and the top $\emptyset_2$ diameter. Overall, a deviation from the CAD fidelity is always expected in every condition, and it was detected less than 6% in the conditions B, C, and D. In this case, it was selected a post-printing thermal treatment. Sintering processes on AJ® printed inks are well-known to induce a shrinkage effect of about 20% [40, 41], which strongly depends on the concentrations of loading particle and co-solvents present in the ink. For this reason, a CAD fidelity factor cannot be considered in the DOE analysis. Finally, α
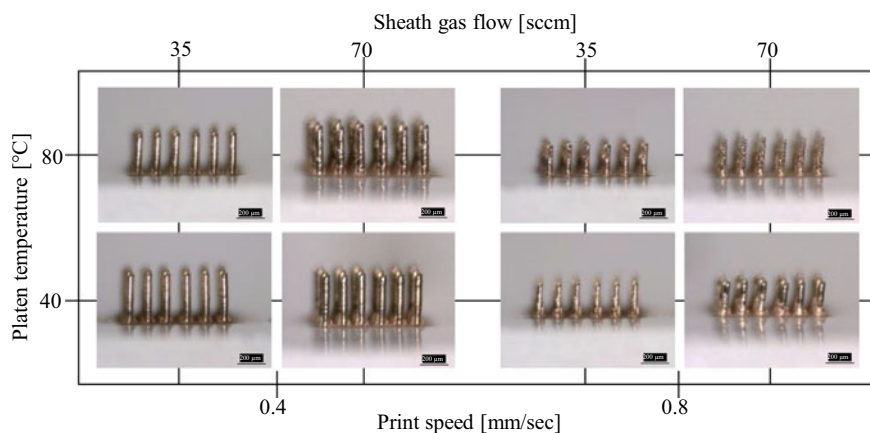
Fig. 2 Representative images and conditions of the full factorial design 2^k (k = 3) performed for 3D AJ® printed AuNPs-based micropillars

Table 2 Geometrical analysis on 3D-LBL AJ® printed AuNPs-based micropillars values of height, h [μm], bending angle, α [rad], middle $\emptyset_1$ [μm] and top $\emptyset_2$ [μm] diameters, based on the different DOE conditions (from A to H)

	Geometrical analysis of 3D-LBL AJ® printed micropillars, ($\mu \pm \sigma$)			
	Height, h [μm]	Bending angle, α [rad]	Middle $\emptyset_1$ [μm]	Top $\emptyset_2$ [μm]
A	355.94 ± 0.01	1.58 ± 0.03	41.36 ± 0.01	41.94 ± 0.01
B	265.78 ± 0.01	1.52 ± 0.21	46.56 ± 0.01	47.83 ± 0.01
C	435.67 ± 0.01	1.55 ± 0.03	47.61 ± 0.01	46.94 ± 0.01
D	345.06 ± 0.01	1.58 ± 0.04	51.28 ± 0.01	47.39 ± 0.01
E	228.61 ± 0.01	1.51 ± 0.24	30.06 ± 0.01	32.52 ± 0.01
F	216.39 ± 0.01	1.57 ± 0.03	39.67 ± 0.01	22.39 ± 0.01
G	248.70 ± 0.01	1.61 ± 0.04	36.44 ± 0.01	33.06 ± 0.01
H	262.61 ± 0.01	1.64 ± 0.04	44.44 ± 0.01	16.17 ± 0.01

ranged between $0.083 \leq \alpha \leq 0.018$. In every condition analyzed, the bending of the pillars was indeed a minor defect, as reported in Table 2.

3.2 Process Investigation Analysis

The print parameters *SGF* (35;70) sccm, *s* (0.4;0.8) mm/s, and *T* (40,80) [°C] were investigated. The errors ε_u, i_{AR}, ε_α, and the final Ψ[#] are reported in Table 3. As first, ε_α has the lowest effect on Ψ, with a range of $0.018 \leq \varepsilon_\alpha \leq 0.083$. This was already evident from the previous data about α values. Instead, a wider range is

obtained for i_{AR}, that is $0.12 \leq i_{AR} \leq 0.19$, and the largest one for ε_u, that is $0.05 \leq \varepsilon_u \leq 0.63$. Therefore, the uniformity error, which measures the shape uniformity of the pillars along the printed layers, is the most variable. The smallest $\Psi = (0.20 \pm 0.05)$ and the highest $\Psi = (0.85 \pm 0.05)$ values were obtained at the conditions C (35, 0.4, 80), and H (70, 0.8, 80), respectively. Visual observations show that s has a stronger effect over Ψ. Particularly, at higher s, the pillars geometry is distorted and deformed, increasing ε_u and i_{AR}. . For instance, at the condition H (70, 0.8, 80), the two diameters measured are equal to $\emptyset_1 = (44.44 \pm 0.01)$ µm and $\emptyset_2 = (16.17 \pm 0.01)$ µm, which means that the tip of the pillar is almost 3 times smaller than the middle diameter, with the maximum $\varepsilon_u = (0.63 \pm 0.03)$. Moreover, ε_α finds its maximum value at $\varepsilon_\alpha = (0.08 \pm 0.14)$ at the condition E (35, 0.8, 40), with the same s but different SGF and T.

Figure 3 reports the results obtained from the statistical analysis. Figure 3a is showing the data normal distribution after Johnson transformation (P = 0.495). As shown in Fig. 3b, the most significant parameter is indeed s, followed by SGF and T. The main effect plot indicates a strong effect of s, also validated by a $P\text{-value}_s \leq 0.000$, compared to the other two parameters, with P-values equal to $P\text{-value}_{SGF} \leq 0.001$ and $P\text{-value}_T \leq 0.611$. Thus, T can be considered almost negligible in the investigated process window, meaning that there is no significant difference in the printed patterns at $T = 40$ or 80 °C. The reason can be found in the normal boiling points NBP of the ink's co-solvent combination, that is water (NBP = 100 °C) and EG (NBP = 197 °C), which are higher than the temperatures used in this study. Values of $T \geq 100$ °C may indeed determine an increase of Ψ, along with a decrease in the micropillars surface quality. As previously mentioned, the tip narrowing effect is more emphasized at a high s. The pillars diameter is indeed more uniform throughout the height at a low $s = 0.4$ mm/s, while a conical-like shape rather than a cylindrical one is recognizable at a $s = 0.8$ mm/s (Fig. 2). This defect is caused by the combined effect of high s and shutter time (e.g., off time between layers), which does not allow the printing of a complete circle. Since z is kept steady, at every layer, the aerosol jet

Table 3 Results of the full factorial analysis on 3D-LBL AJ® printed micropillars, (μ, σ) for the factors ε_u, i_{AR}, ε_α, and the final Ψ[#]

	Full factorial analysis 2^k (k > 0), k = 3 on 3D-LBL AJ® printed micropillars, (μ ± σ)			
	Uniformity error, ε_u	Aspect ratio index, i_{AR}	Bending error, ε_α	Ψ[#]
A	0.09 ± 0.07	0.12 ± 0.01	0.02 ± 0.01	0.24 ± 0.07
B	0.10 ± 0.05	0.19 ± 0.01	0.03 ± 0.01	0.31 ± 0.04
C	0.05 ± 0.04	0.11 ± 0.01	0.04 ± 0.02	0.20 ± 0.05
D	0.08 ± 0.06	0.15 ± 0.01	0.04 ± 0.02	0.27 ± 0.08
E	0.17 ± 0.17	0.14 ± 0.02	0.08 ± 0.14	0.40 ± 0.29
F	0.43 ± 0.14	0.18 ± 0.02	0.02 ± 0.01	0.63 ± 0.16
G	0.17 ± 0.07	0.15 ± 0.01	0.04 ± 0.02	0.37 ± 0.08
H	0.63 ± 0.03	0.17 ± 0.01	0.04 ± 0.02	±0.05

deposited is distributed between the building up of the base and the tip. This effect is more evident at high T and SGF, resulting in the highest values of Ψ, since the jet is more focused and the evaporation of the co-solvents is faster, leading to the deposition of thinner and taller tips. The interaction plot of Fig. 3c indeed confirms that low values of s and T lead to low Ψ. Alternatively, a low SGF, independently from the other two parameters, usually results in a low Ψ. Furthermore, Fig. 3d illustrates the contour plot of Ψ with respect to SGF versus s, validating a decrease of Ψ at low SGF and s. Also from this graph, it is visible the significancy of s, which at the highest values can give $\Psi \geq 0.8$.

Thus, the best conditions achieved in this process window are at a low $s = 0.4$ mm/s with $0.20 \leq \Psi \leq 0.31$, with C (35, 0.4, 80), $\Psi = (0.20 \pm 0.05)$ as best condition, followed by A (35, 0.4, 40), $\Psi = (0.24 \pm 0.07)$. Instead, the worst conditions are achieved at a high $s = 0.8$ mm/s, with $0.37 \leq \Psi \leq 0.85$. A linear regression analysis performed to minimize Ψ also validated the results obtained, with a R-sq = 81.20% and as optimal solution the combination $SGF = 35$ sccm and $s = 0.4$ mm/s, with a final model equation as shown in Eq. (5):

$$min\Psi = 0.274 - 0.006x_1 - 0.307x_2 + 0.020x_1 \times x_2 \tag{5}$$

with $x_1 = SGF$ and $x_2 = s$.
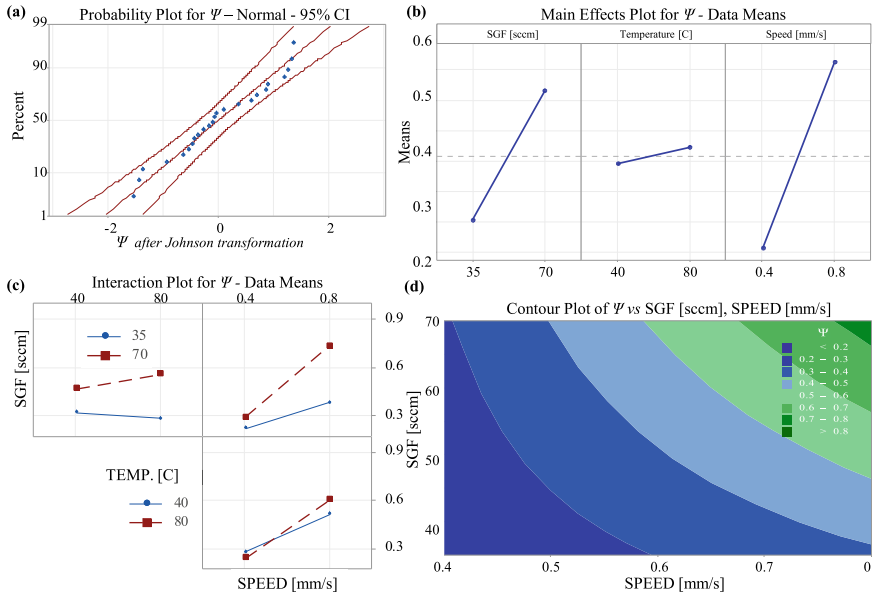
Fig. 3 Results obtained from the statistical analysis of Ψ, indicating **a** the probability plot, **b** the main effects plot, **c** the interaction plot and, **d** the contour plot
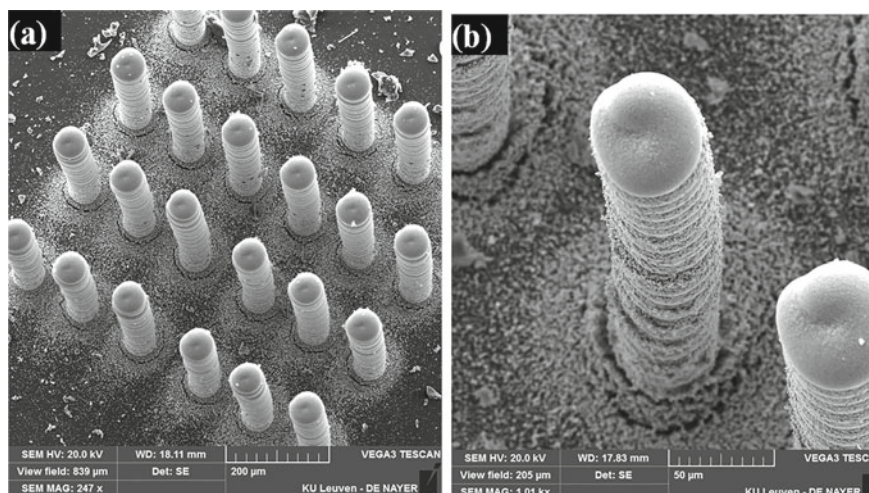
Fig. 4 Scanning electron microscopy (SEM) images of sintered **a** 3D-LBL AJ® printed AuNPs array of micropillars (6 × 4), with **b** zoom on a single pillar with visible printed layers

Figure 4 reports two SEM images at different scales of an array of 3D-LBL AJ® printed AuNPs micropillars at the best condition (C) and $n = 15$. Figure 4a shows an array of fully dense and sintered pillars, with a tip diameter of (51.01 ± 1.71) μm and a single layer thickness of around 5 μm at the last layers (see Fig. 4b). The OS is also visible and radially distributed at the base of each pillar, for a total diameter of ca. 140 μm.

3.3 Electrical and Biocompatibility Analysis

Final values of R in 2D AJ® printed samples were equal to $R = 0.29 \pm 0.01$ Ω, validating the high AuNPs conductivity. Moreover, immunofluorescent assays of HFs at day 5 on plastic and AuNPs-based printed films report a good cellular proliferation (see Fig. 5). Although cells seeded onto the printed films have not reached yet the confluence as the plastic control (Fig. 5a), their protrusions are elongating and spreading over the substrate (Fig. 5b). This is a synonym of a healthy environment for cellular growing and leads to the best proliferation conditions for the cells.
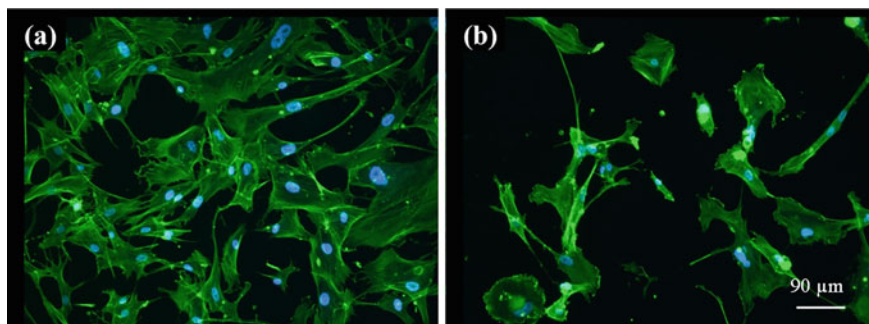
Fig. 5 Fluorescent microscopy images 10X of HFs cultured onto **a** plastic control and **b** AJ®
printed and sintered AuNPs-based films

4 Case Study Test

The best 3D-LBL AJ®P condition C obtained from the DOE was ultimately applied in
a proof-of-concept application for the printing of micropillars on the top of a printed
chip. Specifically, a 3D MEA chip is AJ® printed on a Thermoplastic Polyurethanes
(TPU) foil (Grafityp, Houthalen, BE). The design (interconnects and electrodes) used
refers to the 60MEA chip by ©Multi Channel Systems (MCS, Reutlingen, GmbH).
The chip interconnects were printed with a $\emptyset_{nozzle} = 150\ \mu m$, $s = 3$ mm/s, $CGF =$
15 sccm, $SGF = 35$ sccm, $T = 40$ °C, and 3 layers. Subsequently, micropillars of a
diameter of 50 μm were printed on the top of the electrodes for a total of 15 layers.

A post-process sintering was further applied as previously explained. Figure 6
shows a fully AuNPs-based printed 3D MEA chip on a flexible and transparent TPU
foil. The printing time was less than 15 min. Figure 6a indicates the prototype with
an overall.
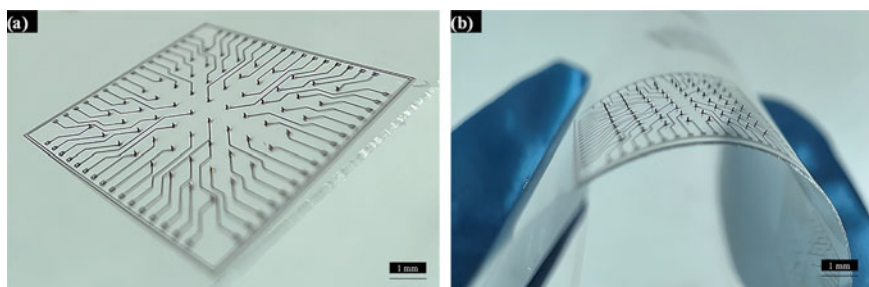
Fig. 6 Representative images of **a** a flat and **b** bended 3D AJ® printed AuNPs-based MEA chip
on a flexible and transparent PET thin film

dimension of 11.5×11.5 mm, with resolution down to 40 ± 0.01 μm and micropillars electrodes in the range of 150 μm in height. Moreover, Fig. 6b demonstrates the ability to bend the 3D chip, a feature of potential interest in lab-on-chip devices, smart textiles and organoid platforms.

5 Conclusions and Future Perspectives

The AM-DW AJ®P process is gaining attention for its versatility to print a wide variety of functionalized inks for PE and biomedical applications. Mainly developed for the 2D deposition of electrical inks, recent case studies demonstrated the ability of the process also as a 3D micro-AM technique. However, an optimization of such 3D AJ®P process has been rarely reported.

In this paper, an innovative conductive AuNPs-based ink is investigated for the novel 3D-LBL AJ®P production of micropillars by means of a full factorial design approach. The electrical properties and biocompatibility of the ink were preliminary verified and the immunofluorescence assay reported healthy conditions of the cells on conductive printed samples.

The print parameters investigated in the process are the sheath gas SGF [sccm], the speed s [mm/s], and the platen temperature T [°C]. The morphology of the samples is evaluated and a Printability and Shape Fidelity Index Ψ[#], $0 \leq \Psi \leq 1$, is selected as response of interest, with $\Psi = 0$ as the ideal condition. Ψ considers the shape uniformity and the bending of the printed samples (ε_u, and ε_α, respectively), and maximizes the AR (minimizes i_{AR}). Results of this DOE show a significant effect of s and SGF on Ψ, while T can be negligible. The best print parameters combination is obtained with $SGF = 35$ sccm, $s = 0.4$ mm/s, $T = 80$ °C ($\Psi = 0.20 \pm 0.05$) for the production of fully dense micropillars in less than 10 min, with a height of $h \sim 436$ μm, a diameter of $\emptyset \sim 47$ μm, and a bending of $\alpha = 1.55$ rads.

Ultimately, as a proof-of-concept application, a 3D MEA chip was 3D-LBL AJ® printed on a flexible PET foil in less than 15 min, with a resolution down to 40 μm. Future studies will be focused on the chip characterization and electrophysiological tests using electro-active cells, such as neural lineages. The potential use of such microstructures is also towards *in-vitro* bioelectronics, smart textiles, and energy harvesting devices.

References

1. Vaezi M, Seitz H, Yang S (2013) A review on 3D micro-additive manufacturing technologies. Int J Adv Manuf Technol 67:1721
2. Le HT, Haque RI, Ouyang Z et al (2021) MEMS inductor fabrication and emerging applications in power electronics and neurotechnologies. Microsyst Nanoeng 71(7):1–22
3. Potekhina A, Wang C (2019) Review of electrothermal actuators and applications. Actuators 8(4):69
4. Liu Y, Li X, Chen J, Yuan C (2020) Micro/nano electrode array sensors: advances in fabrication and emerging applications in bioanalysis. Front Chem 8:1102
5. Nazemi H, Joseph A, Park J, Emadi A (2019) Advanced micro- and nano-gas sensor technology: a review. Sensors 19(6):1285
6. Leclech C, Villard C (2020) Cellular and subcellular contact guidance on microfabricated substrates. Front Bioeng Biotechnol 8:1198
7. Qin Y (2015) Preface, micromanufacturing engineering technology, 2nd edn. Elsevier
8. Hon KKB, Li L, Hutchings IM (2008) Direct writing technology-advances and developments. CIRP Ann Manuf Technol 57(2):601
9. Saadi MASR, Maguire A, Pottackal NT, Thakur MSH, Ikram M, Hart AJ, Ajayan PM, Rahman MM et al (2022) Direct ink writing: A 3D printing technology for diverse materials. Adv Mater 34(28):2108855
10. Wilkinson NJ, Smith MAA, Kay RW, Harris RA (2019) A review of aerosol jet printing—a non-traditional hybrid process for micro-manufacturing. Int J Adv Manuf Technol 105:4599
11. de Souza FM, Gupta RK (2023) Nano-inks: fundamentals, synthesis, and enegy applications. In: Smart multifunctional nano-inks. Elsevier
12. Machiels J, Verma A, Appeltans R, Buntinx M, Ferraris E, Deferme W (2021) Printed Electronics (PE) as an enabling technology to realize flexible mass customized smart applications. Procedia CIRP 96:115–120
13. Agarwala S, Goh GL, Le TD, An J, Peh ZK, Yeong WY, Kim YJ (2019) Wearable bandage-based strain sensor for home healthcare: combining 3D Aerosol jet printing and laser sintering. ACS Sens 4(1):218–226
14. Cooper C, Hughes B (2020) Aerosol jet printing of electronics: an enabling technology for wearable devices. In: Pan pacific microelectronics symposium (Pan Pacific). HI, USA, pp 1–11
15. Cantù E, Tonello S, Abate G, Uberti D, Sardini E, Serpelloni M (2018) Aerosol jet printed 3D electrochemical sensors for protein detection. Sensors 18(11):3719
16. Deiner LJ, Jenkins T, Howell T, Rottmayer M (2019) Aerosol jet printed polymer composite electrolytes for solid-state Li-Ion batteries. Adv Eng Mater 21(12):1900952
17. Seiti M, Ginestra PS, Ferraro RM, Giliani S, Vetrano RM, Ceretti E, Ferraris E (2022) Aerosol Jet® printing of Poly(3,4-Ethylenedioxythiophene): Poly(Styrenesulfonate) onto micropatterned substrates for neural cells in vitro stimulation. Int J Bioprinting 8(1):50–65
18. Gibney R, Ferraris E (2021) Bioprinting of collagen type I and II via aerosol jet printing for the replication of dense collagenous tissues. Front Bioeng Biotechnol 9:1–12
19. Tonello S, Bianchetti A, Braga S, Almici C, Marini M, Piovani G, Guindani M, Dey K, Sartore L, Re F, Russo D, Cantù E, Lopomo NF, Serpelloni M, Sardini E (2020) Impedance-based monitoring of mesenchymal stromal cell three-dimensional proliferation using aerosol jet printed sensors: a tissue engineering application. Materials 13(10):2231
20. Parate K, Pola CC, Rangnekar SV, Mendivelso-Perez DL, Smith EA, Hersam MC, Gomes CL, Claussen JC (2020) Aerosol-jet-printed graphene electrochemical histamine sensors for food safety monitoring. 2D Mater 7(3):034002
21. Gibney R, Patterson J, Ferraris E (2021) High-resolution bioprinting of recombinant human collagen type III. Polym 13(17):2973
22. Xiao Y, Kalaitzidou K, Yao D, Yeo W, Harris TAL (2020) Challenges and advances in aerosol jet printing of regenerated silk fibroin solutions. Adv Mater Interfaces 7(12):1902005

23. Phuah EWC, Hart WL, Sumer H, Stoddart PR (2020) Patterning of biomaterials by aerosol jet printing: a parametric study. Bioprinting 18:e00081

24. Parate K, Rangnekar SV, Jing D, Mendivelso-Perez DL, Ding S, Secor EB, Smith EA, Hostetter JM, Hersam MC, Claussen JC (2020) Aerosol-jet-printed graphene immunosensor for label-free cytokine monitoring in serum. ACS Appl Mater Interfaces 12(7):8592–8603

25. Goh GL, Agarwala S, Tan YJ, Yeong WY (2018) A low cost and flexible carbon nanotube pH sensor fabricated using aerosol jet technology for live cell applications. Sens Actuators, B Chem 260:227–235

26. Giuri A, Striani R, Carallo S, Colella S, Rizzo A, Mele C, Bagheri S, Seiti M, Ferraris E, Esposito Corcione C (2023) Waste carbon ashes/PEDOT:PSS nano-inks for printing of supercapacitors. Electrochim Acta 441:141780

27. Williams NX, Watson N, Joh DY, Chilkoti A, Franklin AD (2020) Aerosol jet printing of biological inks by ultrasonic delivery. Biofabrication 12(2):025004

28. Mekhmouken S, Battaglini N, Mattana G, Maurin A, Zrig S, Piro B, Capitao D, Noel V (2021) Gold nanoparticle-based eco-friendly ink for electrode patterning on flexible substrates. Electrochem Commun 123:106918

29. Su CH, Chiu HL, Chen YC, Yesilmen M, Schulz F, Ketelsen B, Vossmeyer T, Liao YC (2019) Highly responsive PEG/Gold nanoparticle thin-film humidity sensor via inkjet printing technology. Langmuir 35(9):3256–3264

30. Im J, Trindade GF, Quach TT, Sohaib A, Wang F, Austin J, Turyanska L, Roberts CJ, Wildman R, Hague R, Tuck C (2022) Functionalized gold nanoparticles with a cohesion enhancer for robust flexible electrodes. ACS Appl Nano Mater 5(5):6708–6716

31. Ali MA, Hu C, Jahan S, Yuan B, Saleh MS, Ju E, Gao SJ, Panat R (2021) Sensing of COVID-19 antibodies in seconds via aerosol jet nanoprinted reduced-graphene-oxide-coated 3D electrodes., Adv Mater 33(7):2006647

32. Wei Tan J, An J, Chua CK, Tran T (2019) Metallic nanoparticle inks for 3D printing of electronics. Adv Electron Mater 5(5):1800831

33. Kang MS, Lee SY, Kim KS, Han DW (2020) State of the art biocompatible gold nanoparticles for cancer theragnosis. Pharm 12(8):701

34. Shukla R, Bansal V, Chaudhary M, Basu A, Bhonde RR, Sastry M (2005) Biocompatibility of gold nanoparticles and their endocytotic fate inside the cellular compartment: a microscopic overview. Langmuir 21(23):10644–10654

35. Kus-liśkiewicz M, Fickers P, Ben Tahar I (2021) Biocompatibility and cytotoxicity of gold nanoparticles: recent advances in methodologies and regulations. Int J Mol Sci 22(20):10952

36. Saleh MS, Hu C, Panat R (2017) Three-dimensional microarchitected materials and devices using nanoparticle assembly by pointwise spatial printing. Sci Adv 3(3):e1601986

37. Vlnieska V, Gilshtein E, Kunka D, Heier J, Romanyuk YE (2022) Aerosol jet printing of 3D pillar arrays from photopolymer ink. Polymers 14(16):3411

38. Zips S, Grob L, Rinklin P, Terkan K, Adly NY, Weiß LJK, Mayer D, Wolfrum B (2019) Fully printed μ-needle electrode array from conductive polymer ink for bioelectronic applications. ACS Appl Mater Interfaces 11(36):32778–32786

39. Degryse O, Gibney R, Bloemen V, Ferraris E (2021) Collagen composite inks for Aerosol Jet® printing in bone tissue engineering applications. Procedia CIRP 110:180–185

40. Seiti M, Degryse O, Ferraris E (2022) Aerosol Jet® printing 3D capabilities for metal and polymeric inks. Mater Today Proc 70:38–44

41. Schuetz K, Hoerber J, Franke J (2015) Selective light sintering of Aerosol-Jet printed silver nanoparticle inks on polymer substrates. In: AIP conference proceeding, pp 1593, 1, 732

Surface Quality Improvement Techniques for 3D Printed Metal Samples

Mariangela Quarto and Giancarlo Maccarini

Abstract Additive manufacturing technologies can cover the needs for highly customized components characterized by complex shapes in a short lead time. Despite the benefits of AM processes, these techniques are generally characterized by a low-quality surface finish, one of the most important requirements in several industrial fields. Considering this aspect, it is important to define solutions able to improve the surface finish to benefit the low lead times and the elevated level of customization. This study aims to develop surface quality improvement techniques for metal material extrusion (metal-MEX) samples. Specifically, an investigation was carried out to improve the surface finish of AISI630 stainless steel samples fabricated by metal-ME using different approaches (e.g., thermal and mechanical). The techniques were defined avoiding overstressed components that could be damaged and evaluating the processing convenience of processing time.

Keywords Surface quality · Additive manufacturing · Metal-MEX

1 Introduction

In the next two decades, the demand for implantable devices is expected to rise due to the speed with which the world's population grows and ages. This increase in demand is linked to the inherent complexity of the required implant which paired with the differences between patients makes difficult their standardization, originating the challenge of manufacturing high-quality and vastly different implantable devices to modern engineering [1, 2].

Each device must respond to the specific requirements of the patient, and this implies an increment in the customization of the parts. For this reason, it is important to identify new techniques able to produce these kinds of components respecting all the requirements and coping with geometry and texture challenges. A possible

M. Quarto (✉) · G. Maccarini
Department of Management, Information and Production Engineering, University of Bergamo, Via Pasubio 7/B, Dalmine, Italy
e-mail: mariangela.quarto@unibg.it

solution can be represented by Additive manufacturing (AM) techniques able to produce highly customized implants. Among all the AM techniques, metal-Material Extrusion (metal-MEX) is the simplest and most economical technique [3]. It offers the possibility of producing complex metal parts with high structural integrity but, is usually characterized by poor and variable surface finishing [4] that in some cases can affect the technical properties and compromise the required tolerances [5]. In addition to the surface finishing, also the final mechanical properties of metal-MEX parts are still under study due to the presence of uncontrolled porosities and defects [6].

The poor surface quality of the metal-MEX components resulting from a high surface roughness is mostly due to the tracks related to the layer path [7]. The surface quality of 3D printed parts is extremely important for the biological outcomes of both cells and bacteria colonization during in vivo conditions [8]. The improvement of surface roughness and the evaluation of its texture is still a challenging topic related to the production of biomedical devices through AM techniques. Post-processing is a crucial step in additive manufacturing (AM) to enhance the surface finishing and mechanical properties of the final parts. While AM technologies can produce complex geometries with high precision, the surface finish of the parts may not be satisfactory for some applications. Post-processing techniques can be applied to achieve the desired surface quality and texture [9].

Metal-MEX is characterized by anisotropy and poor surface quality due to surface texture and staircase effect. In particular, the surface texture originates from a coarse mesh which approximates the surfaces of the part using too few triangles. This aspect can be overcome by reducing the dimensions of the triangles which allows an improvement in the precision of the geometry. On the other side, the staircase effect is intrinsic to the process and cannot be completely solved since a continuous surface is approximated by layers having a finite height along the build direction.

Many researchers focused attention on the definition of methods to overcome these issues [10–13], and the influence of printing parameters on surface quality was the object of several studies [14–17]. The surface quality of the MEX printed product or part can be enhanced by optimizing the MEX process parameters like raster and contour angle, built orientation, air gap, layer thickness, etc. In particular, the results show that layer thickness and building angle are the most effective factors. Despite this, it is not possible to reach a very smooth surface only by optimizing the printing parameters, especially for the metal-MEX, as further treatments (debinding and sintering) to remove the polymer components are needed [11].

Comparing the metal-MEX to the traditional polymeric MEX the similarities in the process and the printing issues are a lot. Considering the extensive research on improving the surface quality of polymeric parts, in this study similar approach is assessed on the green parts. This means that the treatment for surface quality improvement is placed in the middle of the process chain, treating the printed parts before the removal of the polymeric component. Such as reported in Fig. 1, various kinds of treatment are available and categorized as a function of the methodology applied. The use of hot solvent vapor is one of the most widely use techniques for the improvement of polymeric part surface quality. This success can be related to

the simplicity of the process and the good results obtained [18–20]. Considering that the metal-MEX prints a filament made up of metal powder and polyoxymethylene (POM) matrix, the application of vapor of any kind of organic solvent is not allowed since POM is a thermoplastic polymer nonperishable from acetone. Thus, a thermal approach was selected.

Another approach that is possible to consider is mechanical surface quality improvement using, for example, a non-conventional process such as micro-electrical discharge machining (micro-EDM). The use of micro-EDM for removing a thin layer of material from a workpiece offers the advantage of avoiding the mechanical stress and vibration that is typically generated by traditional machining processes. This is because the micro-EDM process utilizes high-frequency electrical discharges to erode the material, rather than cutting tools that can cause mechanical stress and vibration on the workpiece.

Mechanical
- Manual Sanding
- Abrasive Milling
- Abrasive Flow Machine
- Sand Blasting
- Vibratory Bowl Finsihing
- Hot Cutter Machining
- Ball Burnishing
- Barrel Tumbling
- Friction Stir Processing
- Magnetic Based Finishing

Chemical
- Manual Painting
- Acetone Dipping
- Vapor Smoothing
- Chemical Machining
- Electropolishing

Thermal
- Laser Surface Processing
- CNC Assisted Selective Melting

Hybrid
- Hybrid Additive Process (CNC Assisted Milling, Turning and Grinding)
- Ablation & Remelting (Laser Surface Processing)
- Rolling and Burnishing
- Friction Stir Processing

Fig. 1 The main classification of post-processing treatment for roughness improvement [21]

The absence of contact between the electrode and the workpiece assures the structural quality of the part. Consequently, in this work, thermal and electrical approaches have been selected. In particular, the proposed thermal method tries to improve the surface quality thanks to the assumption that, by providing heat to the target surface, the material approaches its melt state by arranging itself in a less constrained manner to the laid layer leading to the occlusion of the surface cavities associated with the side-by-side of the layer parts. On the other side, the micro-EDM has been applied assuming that it is possible to remove a thinner layer than the one laid in the additive process. The quality improvement is evaluated by considering the surface roughness and the main amplitude parameters by comparing the results of treated parts with the as-built parts.

This paper aims to evaluate the two cited approaches defining their main characteristics, benefits, and limitations. The research investigates and compares the effectiveness of these two methods for improving the surface quality of additive manufactured parts basing the analysis on the main roughness parameters (e.g., R_a, R_{sk}, R_{ku}) and the possibility of generating visible defects. The final goal is the identification of which method results in the most significant improvements.

2 Materials and Methods

2.1 Sample Preparation

Samples were produced by the Material Extrusion (MEX) process extruding a filament made up of AISI630 martensitic stainless-steel powder (90 wt.%), equally distributed in a polymeric matrix composed of polyoxymethylene (POM) and polyolefin. The layer thickness was equal to 0.1 mm, the nozzle temperature is 270 °C and the components were printed on a building plate with a controlled temperature equal to 100 °C. 0° building angle was considered.

The printed parts, called green-part, were sent to an external company for removing the main polymer content (primary binder, i.e. polyoxymethylene) through a catalytic debinding process at 120 °C, obtaining the brown-part, consisting of pure metal particles and a residual binder (backbone).

The brown-part was characterized by the same volume and a reduction in mass with respect to the green-part. The subsequent sintering process at temperatures immediately below the melting point of the metal allowed to remove the secondary binder from the brown-part and to sinter the metal particles, filling the cavities left by the binder. The sintering cycle consisted of two ramps at elevated temperatures with two different holding times which allow reaching the final physical and mechanical characteristics of the parts, generating a volume reduction described by the shrinkage percentages. Further details could not be provided since the post-shaping process instructions are confidential. The material reaches its final properties in terms of hardness, strength, and ductility after the sintering phase. Stainless steel AISI630

samples are characterized by a 40 × 10 mm planar surface chosen as a target for the treatment.

2.2 Thermal Treatment

The thermal treatment was carried out on the green-parts (polymer and metal powder). The thermal treatment experimental equipment (Fig. 2) consists of a hot-air gun placed orthogonally to the target surface. This hot-air gun is a popular tool, widely used in industrial applications for stripping paint and varnish, shaping, welding, and speeding up the drying process of glued connections and plastic shaping. The distance between the hot-air gun and the target surface is kept constant (10 mm) during the experiments in order to compare the results. Due to the dimensions of the tip of the hot-air gun, just a portion of the target surface was exposed to the hot-air flow (ϕ 15mm), an area sufficient for meeting the requirements of UNI EN ISO 21920:2022.

   This method assumes that, like for polymeric material [22, 23], the hot-air flow generates a redistribution of the superficial material reducing the surface asperities. The heat transferred to the target surface allows the remodeling and smoothing of the treated zone generating a modification of the metal particle distribution. The smoothing process is completed when the treatment time is reached. Then, the part was removed from the heating area, and it rests in open air (for 24 h) so that the material can cool down at room temperature and the part definitively re-harden. With regards to treatment time, four levels were tested, from 0 to 70 s. The 0 s exposure time corresponds to the untreated sample, and it represents the reference to compare the effects of the treatment. Moreover, to not compromise the tests with intermediate measurements, one sample for each treatment time level was used. Airflow was set equal to 120 L/min according to the maximum capacity of the hot-air gun. Four levels of temperature were tested (210 °C, 240 °C, 270 °C, and 300 °C) directly setting

Fig. 2 Thermal approach set-up
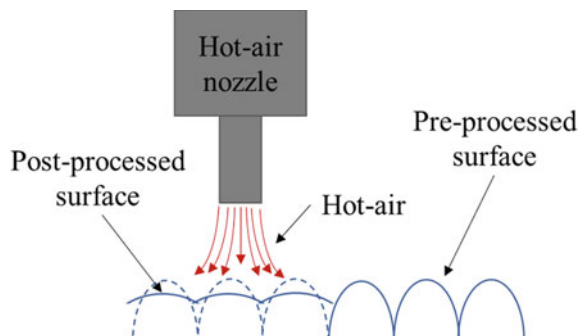
Table 1 Micro-EDM process parameters

Parameters	Pulse shape		
	Short	Medium	Long
Peak current (I)—A	4	13	25
Voltage (V)—V	90	100	130
Frequency—Hz	180	160	130
Discharge width (t_{on})—μs	2	4	5

the hot-air gun. After debinding and sintering processes, the final surface roughness parameters were measured as the average of the different measurements. Three repetitions for each combination of exposure time and temperature were performed.

2.3 Micro-EDM

The micro-electrical discharge machining (micro-EDM) was carried out on the white parts. The printed samples were fixed on a Sarix SX-200 machine and through CAM software, the electrode paths for the generation of micro-features were defined. The process parameters were selected through the execution of preliminary tests able to define parameter combinations able to reduce the probability of short circuits and assuring process stability and repeatability. Three runs for each combination of process parameters were performed.

The micro-EDM process removes material from the target surface generating the typical craters texture of this process. In this way, the waviness and the differences between peaks and valleys decrease since the process reduces the effects of the side-by-side layers. A cylindrical tungsten carbide electrode was tested considering 300 μm in diameter. Hydrocarbon oil was used as a dielectric medium. Three electrical discharge shapes were tested: short, medium, and long pulses. The pulse shapes differ in the peak of current reached during the process and their width.

Table 1 reports the process parameters applied during the micro-EDM process. Square pockets 1 × 1 mm with a depth equal to 20 μm were machined. Since the machine used does not allow to set the real value of the peak of current, their intensity can be evaluated as reported in [24] by means of an oscilloscope and an elaboration of the data through a Matlab code.

2.4 Data Analysis

The samples were analyzed qualitatively and quantitatively. Firstly, the qualitative analysis was conducted for evaluating if all the treated samples were compliant with the quantitative analysis. In this case, compliance is assured if the surface of the sample, at first optical analysis, results to be characterized by no defects and/

or alteration of the starting geometry. This helps to identify defects which can be classified by the UNI EN ISO 21920:2022 as: visible and effective, invisible but effective, visible but ineffective (cosmetic), and invisible and ineffective.

A 3D reconstruction of the treated surfaces was performed by means of Keyence VHX-7000 digital microscope. After the scansion of the area, the raw data were elaborated to obtain a surface description considering surface roughness and amplitude parameters (e.g., R_a, R_{sk}, R_{ku}) as defined by the international standard UNI EN ISO 21920:2022. The amplitude parameters are considered for distinguishing between two profiles having the same roughness. All these parameters together give information about the statistical average properties. Specifically, R_{sk} describes the symmetry of the height distribution histogram, R_{ku} describes the sharpness of the probability density profiles, while R_z is the average value of the absolute values of the heights of the five highest-profile peaks and the depths of the five deepest valleys within the evaluation length.

3 Results and Discussion

After the collection of qualitative and quantitative information, the results were compared for identifying the strengths and weaknesses of the tested methods. Regarding the thermal treatment, it is possible to observe that some sample results unsuitable for the final texture evaluation. These samples were removed from the analysis since they show several major defects on the treated surfaces (UNI EN ISO 21920:2022), affecting the aspect of the surface. Specifically, it is observed that maintaining a constant hot air flow (120 L/min) and changing the temperature and the exposition time can generate a negative effect on the surface.

Figure 3 shows the appearance of surfaces removed from the assessment. These defects can be classified as visible and effective defects since they modify the geometry, the texture and probably the mechanical characteristics of the part. Table 2 reports the results of the qualitative analysis associated with the parameters of the thermal treatment which are clarified in Fig. 4, where it is possible to observe which combination of air flow temperature and exposure time allows to obtain compliant part for the quantitative analysis.

Making a relation between the aspect of the treated surfaces and the parameters applied it was defined a thermal index (TI) as the product of the flow rate (it is kept constant during all tests), exposure time (t) and temperature (T) (Eq. 1). This index does not represent a specific physical quantity, but observing the values assumed by the non-compliant parts, it is possible to identify a maximum value of this index for avoiding the creation of defects. From this index, it is possible to have a general idea of the heat transferred to the surface correlating.

$$TI = flow\,rate \cdot t \cdot T \tag{1}$$
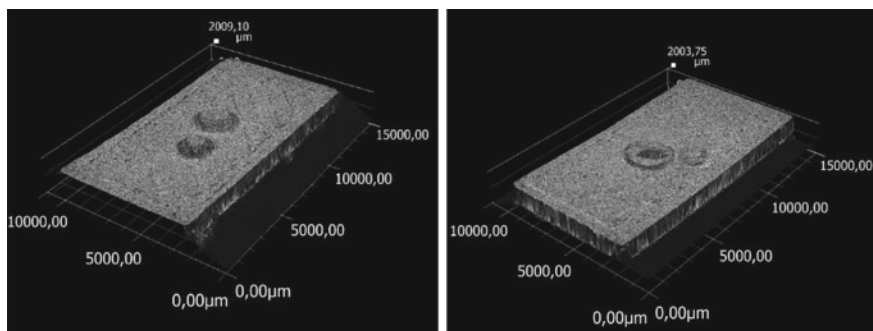
Fig. 3 Example of defects generated on the sample surfaces after the thermal approach. **a** swelling of the surface. **b** surface collapse

Table 2 Parameters and thermal index of thermal treatments

Sample	Air flow temperature (T) [°C]	Exposure time (t) [s]	Thermal index (I)	Surface aspect
1	210	10	4200	OK
2	210	30	12,600	OK
3	210	50	21,000	Swelling
4	210	70	29,400	Swelling
5	240	10	4800	OK
6	240	30	14,400	OK
7	240	50	24,000	Swelling
8	240	70	33,600	Swelling
9	270	10	5400	OK
10	270	30	16,200	Swelling
11	270	50	27,000	Swelling
12	270	70	37,800	Swelling
13	300	10	6000	OK
14	300	30	18,000	Swelling
15	300	50	30,000	Swelling
16	300	70	42,000	Collapse
17	–	–	–	Non treated samples
18	–	–	–	Non treated samples
19	–	–	–	Non treated samples
20	–	–	–	Non treated samples
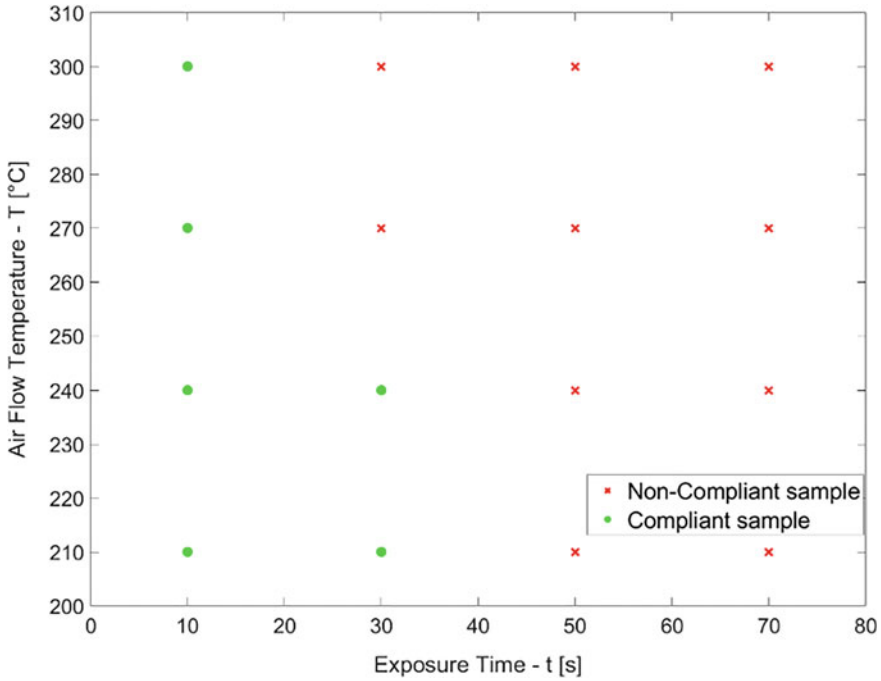
Fig. 4 Compliant and non-compliant samples as a function of thermal treatment parameters

In this way, it is possible to observe that using an index with a value equal to or greater than 16,200 L°C generates surfaces characterized by important defects which cause a scrap of the parts.

Considering the samples suitable for the effectiveness of the thermal treatment, as anticipated the evaluation of three profiles was conducted for collecting data about the main roughness parameters. In general, it was observed that the thermal treatment does not affect the R_a values, but it is able to reduce the Rz (Fig. 5). This indicates that the heat air flow allows the redistribution of the material, in particular the metal powder contained in the green part, reducing the effect of the material distribution along the layer cutting down the asperities and smoothing the treated zone. Furthermore, after the thermal treatment, the skewness (R_{sk}) is kept negative as for the non-treated samples indicating a predominance of sharp valleys and rounded peaks. Regarding the kurtosis, the treated surfaces are platykurtic which means the surface profile has relatively few high peaks and low valleys. This is the contrary compared to the non-treated surfaces, which result to be leptokurtic indicating many high peaks or deep valleys (Fig. 6). These results show the ability of the thermal treatment to reduce the height of peaks and valleys creating a smooth surface.

Concerning the micro-EDM process the improvements in terms of R_a and R_z are evident in Fig. 7. Specifically, an implementation of the R_a value in a range between 80 and 90% is observed. In particular, the entire texture change assumes the typical
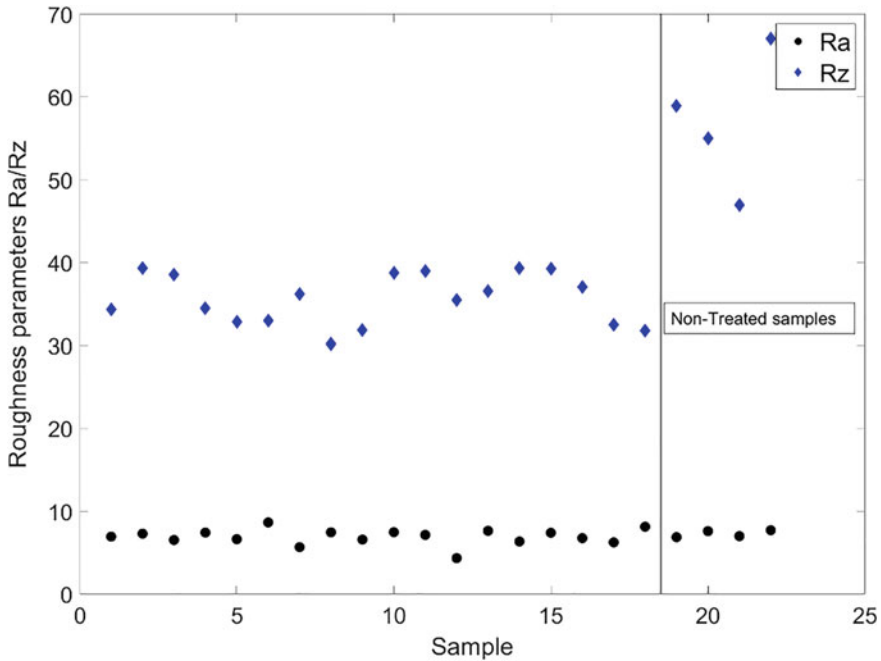
Fig. 5 R_a and R_z for compliant samples after thermal treatment

aspect of the EDMed surface defined by a series of craters. This aspect is visible in the area around the cavity of Fig. 8. Furthermore, the micro-EDM machining generates a reduction in R_z reducing the maximum irregularities of the surface. In this case, the reduction is more variable, short pulses assure a greater reduction due to the smaller craters and consequently less concavity. The longer pulses cause a modification in the amplitude parameters increasing the presence of high peaks and deep valleys ($R_{ku} > 3$) due to the convex geometry of the craters. The short pulses generate a higher implementation in surface roughness maintaining the same distribution and symmetry level of peaks and valleys (Fig. 8).

Compared to the thermal treatment, the non-contact removal material process modifies the surface texture. In fact, the absence of contact between the electrode and workpiece avoids the generation of micro-cracks and damages related to the machining, removing just small layers of materials without spreading them along the entire surface. For these characteristics, some cavities can be observed on the machined surface (Fig. 9) probably owned to the presence of porosity and voids, typical of additive manufacturing processes. It is possible to suppose that this kind of defect belongs to the effective class. This means that defects have a deviation large enough when measured under defined conditions, to influence the measured value and/or the uncertainty of the measurement of interest. Indeed, if further study will confirm that they derive from the typical cavities generated by the additive
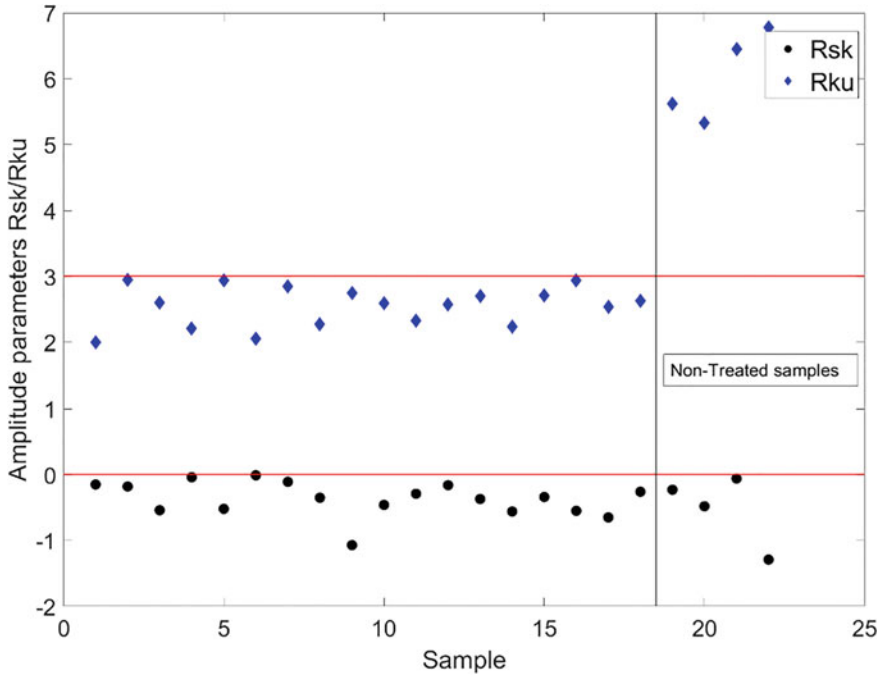
Fig. 6 R_{sk} and R_{ku} for compliant samples after thermal treatment
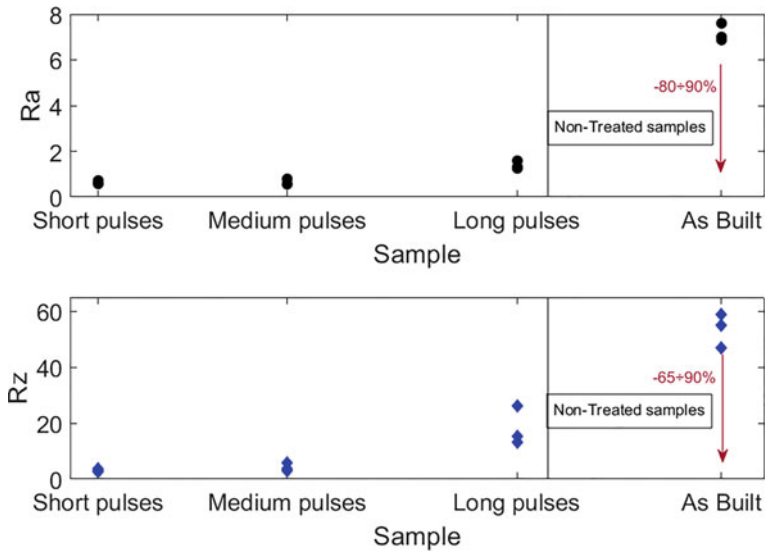
Fig. 7 R_a and R_z after micro-EDM
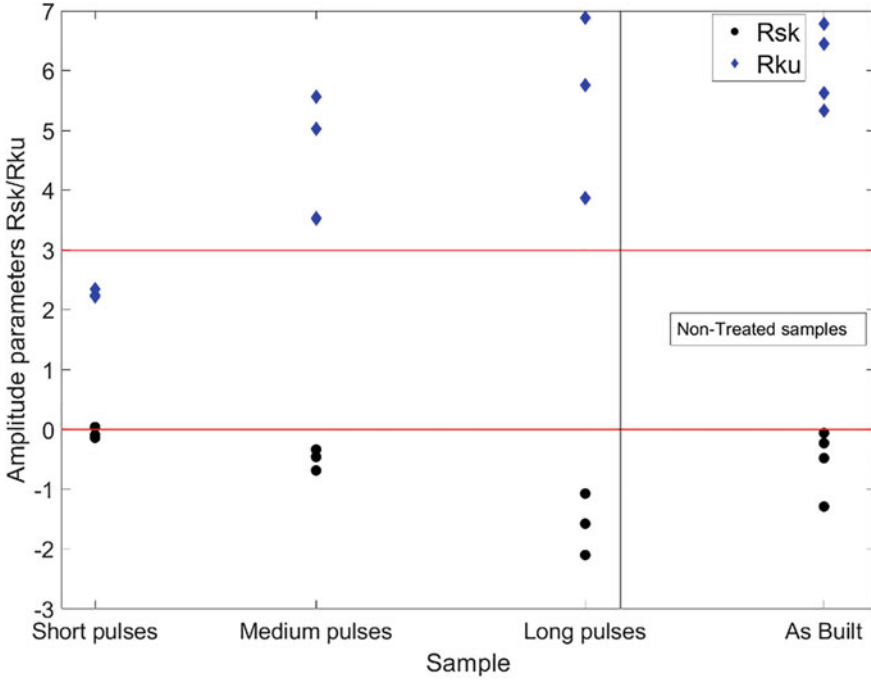
Fig. 8 R_{sk} and R_{ku} after micro-EDM

manufacturing process, they surely affect (important in relation to the functionality of the piece) its mechanical properties, durability, and resistance.

4 Conclusions

This work considers two different approaches for improving the surface texture of metal material extruded parts in stainless steel AISI630. Two approaches were assessed: a thermal and a mechanical approach, respectively. The thermal approach involved heating the surface with a flow of hot air at a constant flow rate and in the various tests the exposure time and temperature of the air flow were modified. The mechanical approach was based on the micro-EDM milling process. different pulse shapes were tested. In both cases, the samples were investigated from the qualitative point of view for identifying if the processes generate defects; furthermore, the implementation of the roughness in terms of R_a and some amplitude parameters were evaluated for defining the effectiveness of the processes.

The results show that the thermal approach is effective non for the R_a implementation, but it generates an improvement in R_z reducing the difference between peaks and valleys demonstrating the possibility to improve the distribution of the metal
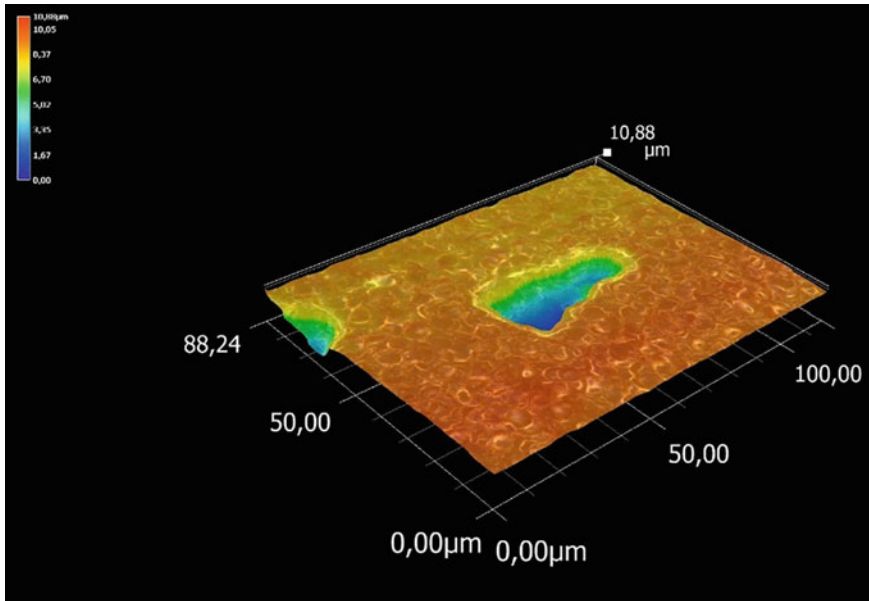
Fig. 9 Example of porosity revealed by the removal of surface material by micro-EDM

powder in the polymer matrix before the debinding and sintering processes. At the same time, this approach can generate high-level defection if the heat input is excessive. Considering the heat index value defined in the work, it is possible to observe that the combination of temperature and exposure time risk generating excessive heating which leads to swelling of the surface making the component unsuitable for analysis and, in the case of finished pieces, for installation.

Micro-EDM milling results generate a more stable process avoiding the generation of additional defects. What can happen in this approach is that the micro-EDM, since it is non-contact machining, removes the surface material highlighting the cavities and porosity present in the first layer of the samples. Furthermore, the mechanical approach generates a great implementation in the roughness parameters, also in terms of R_a.

References

1. Ginestra PS, Ceretti E, Fiorentino A (2016) Potential of modeling and simulations of bioengineered devices: endoprostheses, prostheses and orthoses. https://doi.org/10.1177/0954411916643343
2. Gastaldi D, Parisi G, Lucchini R, Contro R, Bignozzi S, Ginestra PS, Filardo G, Kon E, Vena P (2015) A Predictive model for the elastic properties of a collagen-hydroxyapatite porous scaffold for multi-layer osteochondral substitutes. Int J Appl Mech 7:1550063. https://doi.org/10.1142/S1758825115500635

3. Quarto M, Giardini C (2022) Additive manufacturing of metal filament: when it can replace metal injection moulding. Prog Addit Manuf 1–10. https://doi.org/10.1007/s40964-022-003 48-w

4. Allegri G, Colpani A, Ginestra PS, Attanasio A (2019) An experimental study on micro-milling of a medical grade Co–Cr–Mo alloy produced by selective laser melting. Materials 12:2208. https://doi.org/10.3390/ma12132208

5. Leary M (2017) Surface roughness optimisation for selective laser melting (SLM): accommodating relevant and irrelevant surfaces. Laser Addit Manuf Mater Des Technol Appl 99–118. https://doi.org/10.1016/B978-0-08-100433-3.00004-X

6. Galy C, Le Guen E, Lacoste E, Arvieu C (2018) Main defects observed in aluminum alloy parts produced by SLM: From causes to consequences. Addit Manuf 22:165–175. https://doi.org/10.1016/j.addma.2018.05.005

7. Kaynak Y, Tascioglu E (2018) Finish machining-induced surface roughness, microhardness and XRD analysis of selective laser melted Inconel 718 alloy. Procedia CIRP 71:500–504. https://doi.org/10.1016/j.procir.2018.05.013

8. Brouqui P, Rousseau MC, Stein A, Drancourt M, Raoult D (1995) Treatment of Pseudomonas aeruginosa-infected orthopedic prostheses with ceftazidime-ciprofloxacin antibiotic combination. Antimicrob Agents Chemother 39:2423–2425. https://doi.org/10.1128/AAC.39.11.2423

9. Carminati M, D'Urso G, Giardini C (2023) The enhancement of mechanical properties via post-heat treatments of AISI 630 parts printed with material extrusion. Prog Addit Manuf. https://doi.org/10.1007/s40964-023-00401-2

10. Agarwala MK, Jamalabad VR, Langrana NA, Safari A, Whalen PJ, Danforth SC (1996) Structural quality of parts processed by fused deposition. Rapid Prototyp J 2:4–19. https://doi.org/10.1108/13552549610732034

11. Pandey PM, Thrimurthulu K, Reddy NV (2004) Optimal part deposition orientation in FDM by using a multicriteria genetic algorithm. Int J Prod Res 42:4069–4089. https://doi.org/10.1080/00207540410001708470

12. Peng A (2012) Methods of improving part accuracy during rapid prototyping. In: Advanced materials research. Trans Tech Publications Ltd., pp 760–763. https://doi.org/10.4028/www.scientific.net/AMR.430-432.760

13. Mohan Pandey P, Venkata Reddy N, Dhande SG (2003) Slicing procedures in layered manufacturing: a review. Rapid Prototyp J 9:274–288. https://doi.org/10.1108/13552540310502185

14. Caminero MÁ, Romero Gutiérrez A, Chacón JM, García-Plaza E, Núñez PJ (2022) Effects of fused filament fabrication parameters on the manufacturing of 316L stainless-steel components: geometric and mechanical properties. Rapid Prototyp J 28:2004–2026. https://doi.org/10.1108/RPJ-01-2022-0023

15. Boschetto A, Bottini L, Miani F, Veniali F (2022) Roughness investigation of steel 316L parts fabricated by metal fused filament fabrication. J Manuf Process 81:261–280. https://doi.org/10.1016/j.jmapro.2022.06.077

16. Kumar R, Kumar M, Singh Chohan J, Kumar S (2022) Effect of process parameters on surface roughness of 316L stainless steel coated 3D printed PLA parts. Mater Today: Proc 68:734–741. https://doi.org/10.1016/j.matpr.2022.06.004

17. Butt J, Bhaskar R, Mohaghegh V (2022) Analysing the effects of layer heights and line widths on FFF-printed thermoplastics. Int J Adv Manuf Technol 121:7383–7411. https://doi.org/10.1007/s00170-022-09810-z

18. Castro-Casado D (2021) Chemical treatments to enhance surface quality of FFF manufactured parts: a systematic review. Prog Addit Manuf 6:307–319. https://doi.org/10.1007/s40964-020-00163-1

19. Lavecchia F, Guerra MG, Galantucci LM (2022) Chemical vapor treatment to improve surface finish of 3D printed polylactic acid (PLA) parts realized by fused filament fabrication. Prog Addit Manuf 7:65–75. https://doi.org/10.1007/s40964-021-00213-2

20. Riva L, Fiorentino A, Ceretti E (2022) Characterization of chemical surface finishing with hot acetone vapours on ABS parts fabricated by FFF. Prog Addit Manuf. https://doi.org/10.1007/s40964-022-00265-y
21. Hashmi AW, Mali HS, Meena A (2021) The surface quality improvement methods for fdm printed parts: a review. Presented. https://doi.org/10.1007/978-3-030-68024-4_9
22. Adel M, Abdelaal O, Gad A, Nasr AB, Khalil AM (2018) Polishing of fused deposition modeling products by hot air jet: evaluation of surface roughness. J Mater Process Technol 251:73–82. https://doi.org/10.1016/j.jmatprotec.2017.07.019
23. Heshmat M, Adel M (2021) Investigating the effect of hot air polishing parameters on surface roughness of fused deposition modeling PLA products: ANOVA and regression analysis. Prog Addit Manuf 6:679–687. https://doi.org/10.1007/s40964-021-00190-6
24. Quarto M, Bissacco G, D'Urso G (2019) Machinability and energy efficiency in micro-EDM milling of zirconium boride reinforced with silicon carbide fibers. Materials 12:3920. https://doi.org/10.3390/ma12233920

Arc Oscillation for Microstructural and Geometric Control of Solids Produced by WAAM

Gustavo H. S. F. L. Carvalho and Gianni Campatelli

Abstract Wire arc additive manufacturing (WAAM) is an additive technology with several advantages, such as a high deposition rate, the possibility to manufacture metallic materials, a very low incidence of porosity and excellent mechanical properties. However, there are challenges in WAAM, like the uncontrollable grain growth (due to the prolonged exposure to high temperatures) and the accumulation of impurities or decrease in toughness (due to preferred crystallographic orientation and the grain growth mechanism). These issues are relevant for many materials like steel, aluminium, titanium, and nickel alloys. This work aimed to use arc oscillation in steel that could break this unrestrained grain growth, resulting in a more refined grain structure. The components were characterised morphologically, geometrically, and microstructurally, and the oscillation resulted in microstructures that were equally or more refined than the base material.

Keywords Additive manufacturing · Wire Arc Additive Manufacturing (WAAM) · Arc welding

1 Introduction

Today's engineering faces many challenges when it comes to manufacturing components. In order to reach the current mechanical and sustainability requirements, new manufacturing processes such as additive manufacturing (AM) have been developed and improved. AM is gaining attention because it supports the transition to a more digital and flexible manufacturing solution, it is indeed a strategy promoted by many national Industry 4.0 initiatives and represents a sustainable solution for many applications [1].

Among the AM technologies, the wire arc additive manufacturing (WAAM) stands out as one of the most important direct energy deposition (DED) processes. In this

G. H. S. F. L. Carvalho (✉) · G. Campatelli
Department of Industrial Engineering, University of Florence, Via di Santa Marta 3, 50139 Firenze, Italy
e-mail: gustavo.carvalho@unifi.it

process, an electric arc (welding) is used to melt the wire (filler metal) and build the component through the deposition of successive beads or layers [2]. So, a welding process that uses a wired filler metal is used to build the component instead of being used to join the materials. The main processes are GMAW, GTAW, and PAW [3].

GMAW-based WAAM, the Gas Metal Arc Welding acronym, has some singular characteristics that differentiate it from other additive manufacturing processes. It has a very high deposition rate compared to other WAAM processes [4], it is capable of building large and massive components, and excessive porosity is not an intrinsic issue of the process resulting in components with excellent mechanical properties.

However, despite its advantages, GMAW-based WAAM has some limitations. One is the geometrical accuracy, which is usually reported in the literature [5–7] as not being easy to control. In automatic WAAM processes, the deposition is programmed in advance. However, some geometric variations may occur during deposition and disturb the deposition. Due to the nature of the WAAM-GMAW process, the final layer dimensions will differ from the programmed one to some degree. The magnitude of this variation will depend on aspects such as material, welding parameters and path. These parameters affect the bead's accommodation, which, in turn, accommodates differently in the longitudinal or transverse deposition direction. Thus, after a bead deposition, its final dimension will differ from the programmed one to different degrees in the length and width of the bead. It is difficult to predict these changes and add them to the toolpath program in advance.

Another frequent problem is caused by prolonged heating during the deposition of the various layers of material, which can lead to excessive grain growth, impairing the mechanical properties of the materials [8–11].

There are some ways to control the microstructure, such as heat treatments, the use of workpiece vibration [12], and thermomechanical procedures, such as interlayer cold working [13] or laser shock peening [14]. However, despite presenting good results, most of these procedures lead to a greater expenditure of time and energy and, consequently, a larger carbon footprint and cost. Therefore, this article will suggest a different approach to face the microstructural problems of uncontrolled grain growth to avoid post-processing, with the use of arc oscillation. Regarding the geometry, it is proposed to use a narrow bead deposition capable of improving the accuracy and the deposition versatility by increasing the possible toolpaths to make the deposition. The narrow bead will be achieved by increasing and optimising the travel speed without decreasing wire feed speed (WFS) to not compromise its deposit rate and productivity.

The arc oscillation technique has already been applied to other alloys and processes (usually by magnetic arc oscillation) with promising results [15–18]. The main idea is to change the temperature gradient direction during deposition, constantly changing the solidification direction of the grains, "disturbing" their growth and limiting their sizes. At the same time, it avoids defects such as hot cracks [19, 20], which occur due to the accumulation of impurities and low-melting-point elements in the same zone.

In the present work, several arc oscillations are tested using a narrow bead to bring versatility to the deposition, increasing the path possibilities during the manufacture of the part. The narrow bead will be achieved by speeding up the deposition and reducing the heat input (which provides faster cooling rates and does not favour grain growth) [21, 22]. Then solids with and without oscillation will be manufactured and compared, using a continuous deposition, without an idle time between layers. The assessment of the deposition strategies of the solids will include geometrical and metallurgical evaluations. For the geometrical evaluation, the deposition symmetry, accuracy, and efficiency will be analysed. For the metallurgical evaluation, the microstructures will be analysed to verify if the oscillations were able to lead to better, or at least similar, microstructures with respect to the base material, i.e. without excessive grain growth, defects or brittle phase transformations.

2 Material and Methods

The depositions were performed using a GMAW-based WAAM process with the CMT technology. The base material used was a 5 mm-thick low-carbon steel plate (designation EN10025:2 grade S235JR), and the filler metal was a low-carbon steel AWS ER70S-6 Ø0.8 mm wire produced by SAF-FRO (Filcord C). Table 1 shows the substrate and filler metal typical compositions.

The welding depositions were performed using a Fronius TPS 320i welding machine on a DMU 75 Monoblock 5-axis AC table machining centre (manufactured by DMG Mori) used to ensure proper control of the deposition velocity, torch positioning and path [24]. The torch was perpendicular to the substrate with a direct current electrode positive (DCEP) polarity. The shielding gas was 18% CO_2 and 82% argon, using a flow of 15 L/min).

First, it was investigated the most suitable welding parameters to perform a non-oscillated narrow bead. Thus, the travel speed was optimised to a high value based on previous works [25]. With faster deposition, a lower heat input is obtained. For materials that do not have the problem of martensitic formation, it is a helpful strategy to preserve a smaller grain size. Table 2 presents the welding parameters that have been kept constant for all the tests. The heat input was calculated according to the conventional equation considering the efficiency [26, 27].

Figure 1 presents the two oscillations used in this work. The first oscillation runs the path of a sinusoidal wave (Fig. 1a), and the second runs the path of a square wave (Fig. 1b). The oscillation parameters were a proportion of the width (b) of the

Table 1 Chemical composition of the base metal and the filler metal (% weight)

	C	Mn	Si	P	S	N	Cu	Fe
S235JR steel [23]	0.19	1.50	–	0.045	0.045	0.014	0.60	Bal
Filcord C/ER70S-6	0.08	1.50	0.90	0.025	0.025	–	–	Bal

Table 2 Welding parameters

Current (A)	Voltage (V)	WFS (m/min)	Travel speed (mm/min)	Heat input (J/mm)	Arc power (kW)	CTWD (mm)	bead width "b" (mm)
82	14.8	6.0	1050	58.3	1.2	14	3

where "WFS" is the wire feed speed, and "CTWD" is the contact tip to work distance

single bead without oscillation. Table 3 shows the parameters for the sinusoidal and square wave oscillations. The types and dimensions tested were chosen based on our experimentation and results found in the literature[16, 18–20] that were suitable to our application and test dimensions. The combinations of amplitude and wavelength/wave distance were selected to obtain reasonably uniform and straight beads, since some oscillation combinations may lead to excessive material stacking or lack of material. The GCODE of the paths were generated using MATLAB®. After the experiments with the single oscillated beads, they were analysed, and the best sets of parameters were used for the deposition of the solids.

The metallographic preparation was performed according to ASTM E3-11, and 2%Nital and 10%Nital were used for the microstructural and macrostructural etching, respectively. A Nikon Eclipse LV150 optical microscope was used to observe the welds. The quantitative metallography followed the ASTM E112 standard for grain size measurement.

Fig. 1 The two types of tested oscillations. Sinusoidal wave (**a**) and square wave (**b**). "$A_{peak-peak}$" is the peak-to-peak amplitude, "λ" is wavelength and "d" wave distance
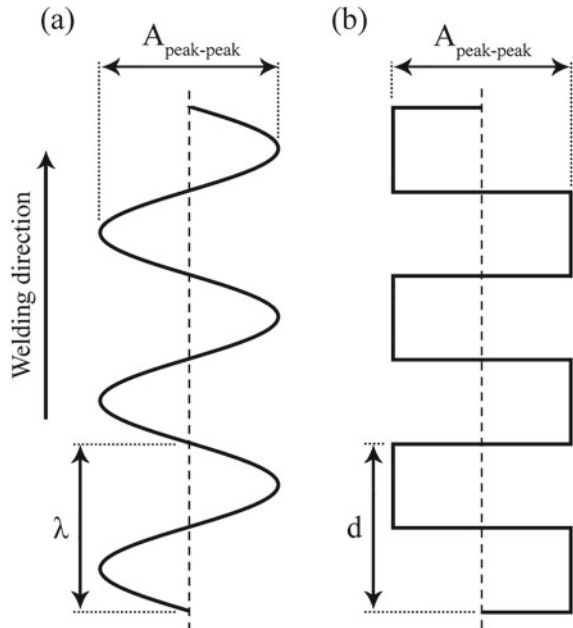
Table 3 Oscillation parameters

Bead ID	Oscillation type	$A_{peak-peak}$		d or λ	
		Ratio	(mm)	Ratio	(mm)
SB	No oscillation	–	–	–	–
SQ-1	Square wave	1.2 · b	3.6	1.2 · b	3.6
SQ-2		1.6 · b	4.8	1.2 · b	3.6
SQ-3		2.0 · b	6.0	1.2 · b	3.6
SQ-4		1.6 · b	4.8	0.8 · b	2.4
SQ-5		1.6 · b	4.8	1.6 · b	4.8
SQ-6		1.2 · b	3.6	0.8 · b	2.4
SQ-7		2.0 · b	6.0	0.8 · b	2.4
SIN-1	Sinusoidal wave	1.6 · b	4.8	1.2 · b	3.6
SIN-2		1.2 · b	3.6	1.2 · b	3.6
SIN-3		2.0 · b	6.0	1.2 · b	3.6
SIN-4		1.6 · b	4.8	0.8 · b	2.4
SIN-5		1.6 · b	4.8	1.6 · b	4.8
SIN-6		1.2 · b	3.6	0.8 · b	2.4
SIN-7		2.0 · b	6.0	0.8 · b	2.4

where "$A_{peak-peak}$", d and "λ" are presented in Fig. 1, and "b" is the width of the bead without oscillation

3 Results and Discussion

3.1 Oscillation Optimisation and Solids Manufacturing

Figure 2 shows the macroscopic aspect of the beads. The SB sample is the bead without oscillation. The two types of oscillations detailed in Fig. 1 did not show a significant difference in terms of surface finish when comparing samples with similar dimensional parameters (for example, SIN-3 to SQ-3 or SIN-7 to SQ-7). However, with the same amplitude and distance ("d" equal to "λ"), the square wave path is longer, which leads to a slight increase in the amount of deposited material and a wider bead.

The parameters selected to produce the solids were based on the results obtained for the single beads, considering as selection criteria arc stability, weld surface appearance, the macrostructural influence of the oscillation (i.e. whether the oscillation produced a macroscopically relevant oscillation), and the presence or absence of defects.

Regarding the external aspect, the wavelength/wave distance parameters for samples SIN-5 to SQ-5 were too long, and the bead edges were not smooth. If the edge is too much irregular, this location may be a preferential spot for welding defects like the inclusion of impurities or lack of fusion. In the case of multipass

Fig. 2 Aspect of the narrow bead without oscillation (SB) and the oscillated beads

welding, this problem is even more probable. Also, some oscillations did not represent a significant stir in the bead's progression, such as in SIN-1, SIN-2, SQ-1 and SQ-2. The oscillations that were considered for the manufacturing of the solids are SQ-3, SQ-7 and SIN-3.

For the deposition of a massive part that requires a multi-bead and multi-layer deposition, additional variables must be considered: the stepover between each bead; the angle between each bead (called work angle); and the direction/sense of each layer's deposition.

Based on the study performed by Baffa et al. [25], a stepover of 60% between beads was selected. A perpendicular work angle (flat weld position) was chosen to maintain a flat position for the deposition. Regarding the direction/sense of each layer's deposition, three approaches were tested, depicted in Fig. 3. The first was the rotation of 0° between each layer, i.e. welding every layer in the same direction and sense. The second was a 180° rotation between each layer, i.e. welding each
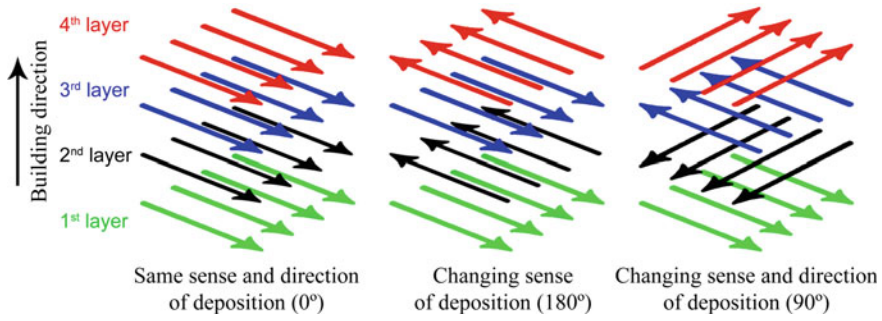
Fig. 3 The strategies of deposition. After the fourth layer, the sequence repeats

Table 4 Oscillation parameters of the solids

Solid ID	Â$_{layer}$	Oscillated single bead parameter (Table 3)	A$_{peak-peak}$		d or λ	
			Ratio	(mm)	Ratio	(mm)
CUB-SB	0°	SB	–	–	–	–
CUB-SQ3	0°	SQ-3	2.0 · b	6.0	1.2 · b	3.6
CUB-SQ7	0°	SQ-7	2.0 · b	6.0	0.8 · b	2.4
CUB-SQ7-90	90°	SQ-7	2.0 · b	6.0	0.8 · b	2.4
CUB-SIN3-180	180°	SIN-3	2.0 · b	6.0	1.2 · b	3.6

where "Â$_{layer}$" is the rotation angle between each layer deposition, see Fig. 3

layer in the same direction but in opposite senses. The third approach was a 90º rotation between layers, i.e. welding with each layer perpendicular to the previous one following a clockwise direction.

Four quadrangular-based solids of approximately 40 mm × 40 mm × 40 mm were manufactured using the abovementioned parameters, varying the welding direction/ sense and the oscillation parameters. All solids were manufactured without idle time, i.e. without no waiting time between layers to cool the part. Table 4 details the parameters tested.

3.2 Geometrical Issues and Uniformity

One of the major challenges in WAAM is the lack of geometric precision. This happens because the layer deposition by welding has some undesirable geometrical effects that are intensified as the number of deposited layers increases. These issues can be divided into longitudinal or transversal, based on how they affect the geometry of the solids.

The longitudinal effect can be seen through the progression of the bead/layer. It happens because of the height difference between the start and end of the layer caused by the difference in volume deposited at the starting and ending spots of the bead deposition. The transversal effect can be observed through a transversal view of the layer. It happens due to the height difference between the layer's centre and edges (the rounding of the solid's edges), caused by the rounded shape of the beads and their accommodation after melting.

The first issue can be assessed by observing the longitudinal welding progression of the beads, while the second can be assessed by observing the beads/layers transversally. Figure 4 details the aspect of the produced solids and the spots of observation for the geometrical analysis.

The height difference between the beginning and end of the bead/layer deposition due to the difference in the amount of material deposited in the arc-striking and arc-extinguishing locations is observed in several studies [5, 28]. This issue has an accumulative effect, which means that layer after layer, this difference becomes increasingly significant. Thus, it is also a process problem in WAAM production.

From a process standpoint, this difference will cause problems in programming the torch path in GMAW-WAAM deposition because the beginning, middle and end of the bead/layer will have different heights. This results in variations in the distance between the torch and the substrate throughout the welding progression. Expressive and uncorrected torch height/CTWD variations may significantly affect the welding results or even lead to the appearance of defects [29].

Some approaches can alleviate or eliminate this issue without directly changing the welding parameters. One of the most effective is changing the welding path to eliminate/reduce the arc striking/extinction spots by designing a continuous deposition. Of course, this is not feasible for every type of material and geometry. Another straightforward way of changing the welding path to optimise the geometry is to

Fig. 4 Aspect of the solids after deposition and the observation spots for the geometrical analysis
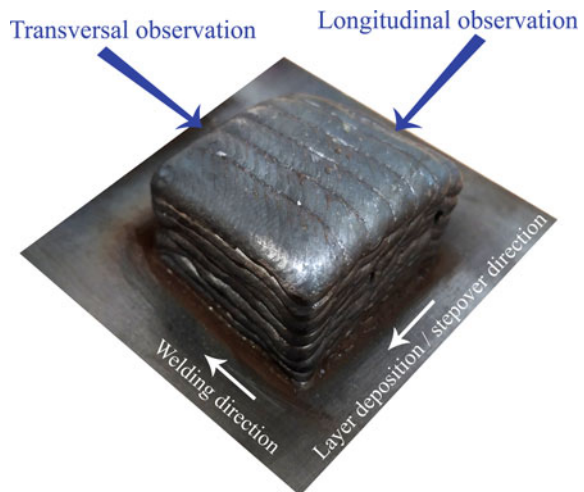
change the starting point of each layer instead of eliminating/reducing the starting/ending points. The two most commonly used ways based on this approach are to place the weld start at the previous end location and alternate this each layer (180° rotation represented in Fig. 3), and change the weld deposition point every time in each layer (such as the 90° rotation exemplified in Fig. 3).

Figure 5 presents the longitudinal observation of the solids, indicating the height variation between the starting and ending point of the layer deposition (∆h). The first observation regards the bad overall result for the deposition without oscillation (CUB-SB). The use of narrow beads gives flexibility from the point of view of programming the torch path. However, the GMAW-CMT process, despite its advantages, may present issues in low heat input multi-bead welding because some beads may attach laterally to the preceding one instead of melting the base material. This phenomenon was observed using the narrow bead parameter (CUB-SB in Fig. 5), resulting in a problematic and erratic deposition. Many beads did not attach to the base material but to the preceding adjacent bead (more heated), which resulted in many defects. So, due to the high level of defects, instability and poor visual appearance, the deposition was interrupted after some layers before reaching the desired height (40 mm). Also, the height difference (∆h) was the most pronounced because it was interrupted before, alleviating the cumulative effect of the height difference. This fact proves the difficulty in depositing narrow/low heat input beads using the GMAW-CMT technology.

The oscillation improved the uniformity of the geometry from the longitudinal observation and allowed the use of a low heat input deposition. It is particularly relevant because using narrow beads was not possible. However, it is also evident that using the same bead/layer starting and ending point (CUB-SQ3 and CUB-SQ7) presented a significant height difference, unlike the solids built changing starting and ending spots (CUB-SQ7-90 and CUB-SIN3-180). No defect was detected for the solids produced using arc oscillation.

Changing the start position (either 90º or 180º) avoided the repeated deposition in the same starting point, which would mean a systematic deposition of the highest part of the layer over the highest part of the previous layer. Figure 5 illustrates that the solids changing the starting point presented much better overall symmetry longitudinally, indicating that the strategies of changing the starting of the weld between layers are efficient. The longitudinal observation detected no pronounced difference between 90º (CUB-SQ7-90) and 180º (CUB-SIN3-180) rotation regarding the overall symmetry.

Regarding the issue of the difference between the middle beads and the start/end bead, a transversal observation is required. Thus, a transversal cross-section macrograph of the solids was prepared (transversal observation in Fig. 4). Figure 6 shows the transversal section of the solids' upper part of the deposition (the analysis of the solid without oscillation was limited to the external aspect in Fig. 5 due to the high quantity of defects and unsatisfactory results). All samples exhibit the typical phenomenon of being higher at the middle beads without major differences.

One of the reasons for the difference between the middle and external sides is the accommodation of the first and last bead. The central beads do not have much space
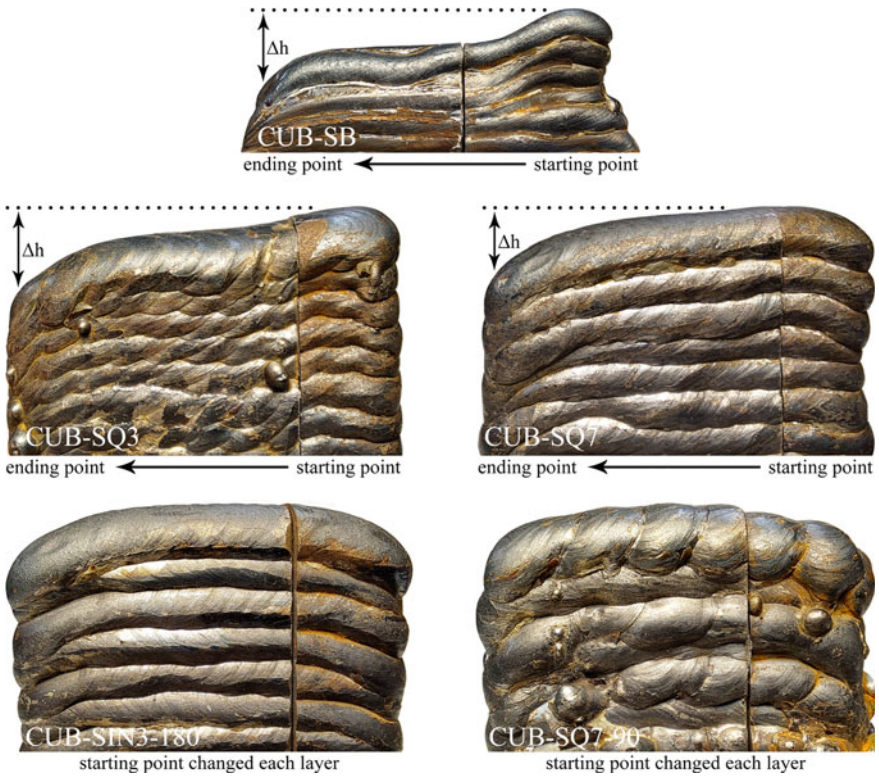
Fig. 5 Longitudinal observation of the manufactured solids
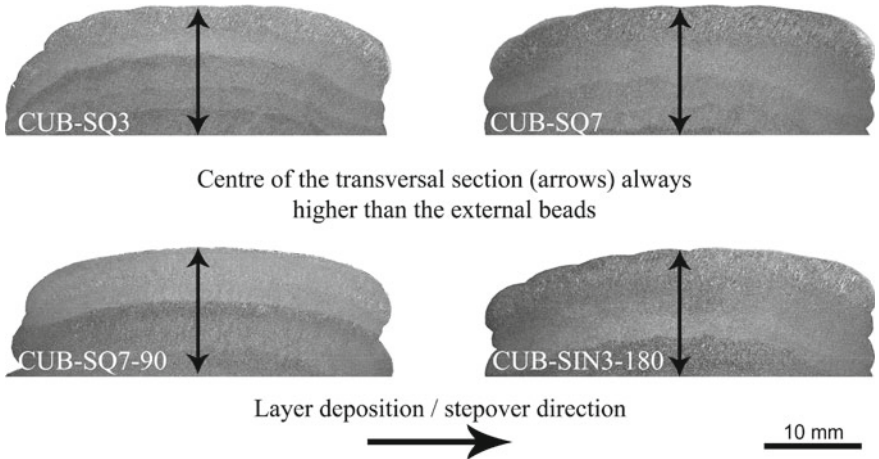
Fig. 6 Transversal macrography of the solids

to accommodate compared to the external beads that always have one free external side. Thus, the layer's central part is higher than the external, where the beads can drip and accommodate after melting. This effect is enhanced by each welded layer.

3.3 Geometrical Uniformity and Machinability Efficiency

It is known that geometrical accuracy is not one of the WAAM strengths, especially using GMAW. This chapter will analyse which of the strategies used to manufacture the solids produces the most uniform and accurate geometry. Also, a brief assessment regarding an eventual machining step will be evaluated. Based on image analysis, two main approaches will be used.

The first considers how far the deposition was from a square geometry, since the path of the programmed deposition follows the geometry of a cube. This will provide a metric to evaluate how far the programmed path is from the desirable geometry, giving valuable information on how much more deposition would be necessary to achieve the desired geometry.

The second approach is regarding an estimation of required machining operations, evaluating how much material would be necessary to remove to obtain a flat surface. This will constitute an evaluation of the geometry accuracy, uniformity and material waste (efficiency).

Figure 7 presents the image analysis of the transversal section from Fig. 6. The percentages represent how close the deposition was to a complete square section (hatched area). Solid CUB-SQ7 was the closest to a completely square section. However, the solids are not extremely different from each other regarding this aspect, considering that the minimum and maximum values were 86 and 91% of filling, respectively. The irregularities and differences in height between the centre and the external beads will lead to the need for more deposition followed by machining if a squared section is desired.
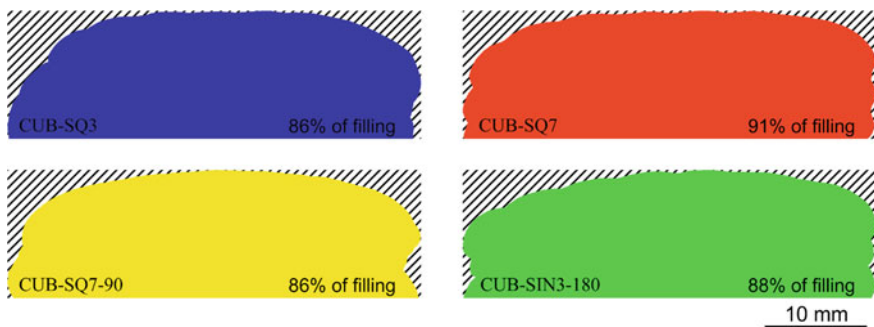
Fig. 7 Image analysis of the upper part of the transversal cross-sections

Regarding the uniformity and eventual machining steps, Fig. 8 illustrates the lateral surface of each transversal cross-section. The hatch represents how much material would have to be machined to have a flat surface, and the percentage represents how much more material needs to be machined compared to the material that needs the least material removal (CUB-SQ3). In other words, compared to CUB-SQ3 (solid with the least need for material removal to obtain a flat surface), CUB-SQ7 needs 41% more material removal, CUB-SQ7-90 93% more material removal and CUB-SIN3-180 6% more material to be removed. This measurement represents the uniformity of the deposition of each layer, as well as the maximum difference between the most extensive section and the smallest section. The solids CUB-SQ7 and CUB-SIN3-180 are very similar and the most uniform. The solid with the 90º (CUB-SQ7-90) rotation between layers presented the worst uniformity and accuracy.

As mentioned, in automatic WAAM processes the final dimensions will differ from the programmed ones to some degree and it is not straightforward to predict and correct these differences when programming the toolpath. This issue proved relevant when the 90º rotation between each layer deposition was used. As shown in Fig. 8, the sample with the 90º rotation presented very irregular deposition, especially between layers. On the other hand, the 180° rotation presented much more regular and uniform deposition. Notably, the uniformity of the profiles followed the oscillated beads' width (wider beads led to more irregular solids).

3.4 Metallographic Analysis

Figure 9 compares the microstructure of the unaffected base material and the solids produced with the different deposition strategies in the transverse direction according to Figs. 4 and 6. Their average grain sizes (Øavg) are indicated next to each image.

The microstructures of the solids are mostly uniform regarding the microconstituents. All samples presented essentially equiaxed ferritic microstructure, with pearlite in some spots. They were all similar to each other and to the base material, as shown in Fig. 9. Unlike the base material, the solids are characterised by a grain size variation throughout the building direction due to the thermal history of the deposition. The maximum variation in the average grain size between different regions of the solids was 7 μm.

Naturally, the upper region of the manufactured solids showed more difference from the base material since the last welded layer is not subjected to the thermal cycle of a subsequent deposition. Nevertheless, it is a region close to the surface, and in some cases, most of these regions are removed in subsequent machining.

Regarding the grain size, all solids presented an average grain size similar to or smaller than the unaffected base metal. The slight difference in grain size between the samples does not represent a change that could mean pronounced differences in mechanical properties according to several examples in the literature [30, 31]. From the Hall–Petch relationship between the yield stress "σ_y" and the grain size "d" (Eq. 1), the same results are obtained. Considering it is the same material, every
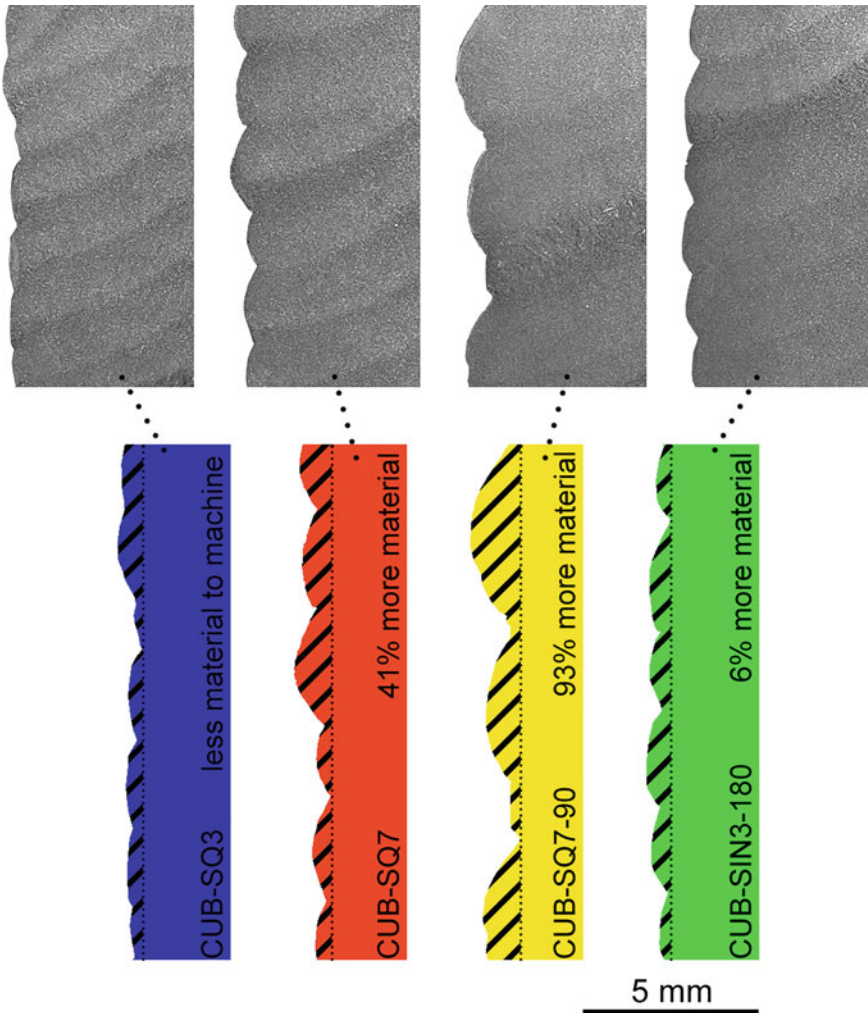
Fig. 8 Lateral side of the transversal profiles

parameter of the right part of the equation would be the same except the grain size. Even the largest grain size difference (9.4 and 11.4 µm) would not change the Yield Strength (σ_y) significantly. Based on the Hall–Petch relationship (Eq. 1), the influence solely of the grain size on the Yield Strength (σ_y) for these solids would be approximately 5% (using σ_0 and k according to [32, 33] and the minimum and maximum grain size found: 9.4 and 11.4 µm). Therefore, using any of the presented deposition strategies it is possible to obtain a grain size similar in size to the original base material (or even smaller) without the use of pauses during deposition to lower the temperature between layers or post-welding heat treatment.
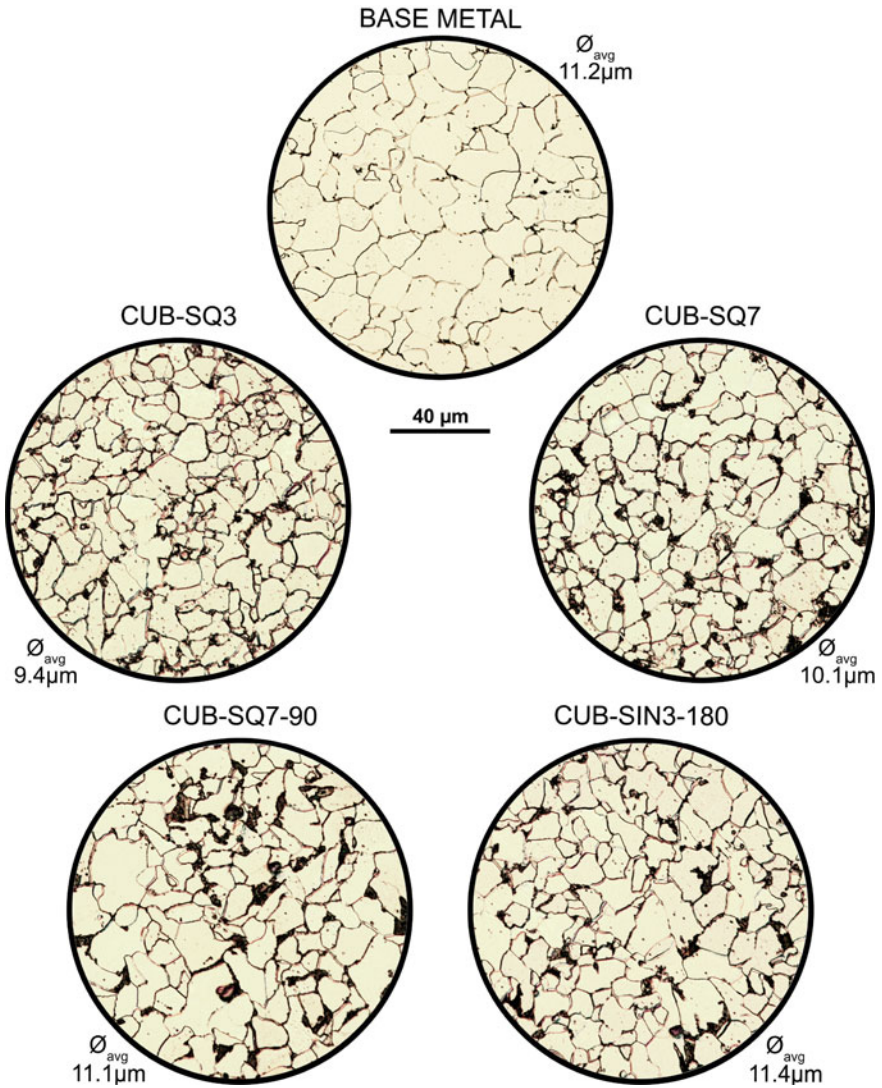
Fig. 9 Microstructure of the base material and the manufactured solids (transverse to the welding direction, as indicated in Fig. 4 and performed in Fig. 6)

$$\sigma_y = \sigma_0 + kd^{-1/2} \tag{1}$$

where "k" is a constant, "d" is the average grain diameter, and σ_0 is the yield stress of a single crystal.

3.5 Heat Input and Energy Analysis

The heat input is a critical parameter to measure the energy applied to the process. However, since it measures the energy per unit length, it is the same when we analyse the heat input for the oscillated beads because their travel speeds were the same. So, the calculated values do not give all the information regarding the energy applied in each case. Thus, in this chapter a different calculation of the applied energy will be shown, considering the entire length travelled (since with oscillation, the path travelled is longer).

Despite the overall length of the individual beads being the same (i.e. the linear length from the starting and ending point of the bead), the oscillation causes the total path length to differ. Thus, one way to obtain the energy is to calculate the toolpath's total length (i.e. the total path travelled for the bead deposition considering the oscillation and not just the starting and ending point). For the square wave, the calculation is simple, just adding the straight parts of the wave until the final length of the bead. For the total path using the sinusoidal waves, the calculation is more complex and follows Eq. 2, where "a" and "b" are the limits for one cycle of oscillation (from 0 to the wavelength value). The general sinusoidal function is given in Eq. 3.

$$Arc\ Length\ =\ \int_{a}^{b} \sqrt{1 + \left(\frac{dy}{dx}\right)^2}\, dx \qquad (2)$$

$$y = A\sin\left(\frac{2\pi}{B}(x - C)\right) + D \qquad (3)$$

where A is the amplitude, B is the wavelength, C is the left/right shift and D is the up/down shift.

After calculating the bead's total length, it is possible to calculate the heat input in two ways. The first is considering the bead velocity (speed to perform the total bead—not the travel speed itself), and the second is using the total path, multiplying it by the heat input to obtain the bead deposition energy.

Table 5 shows the result of the calculation, indicating that the energies are proportional to the deposited area (greater deposition energies obtained in oscillations that have a longer path and deposited a greater amount of material). Thus, the microstructural results were not significantly different. From the point of view of total energy for the deposition of the solids, there is no significant difference. This is because although the energy of each bead changes due to differences in the path, two considerations must be observed: first, the welding progression speed is the same, and second, the beads with the longest path (and which take the longer to be deposited) are wider, which results in a smaller number of beads to reach the final dimension of the solid. However, it gives a more correct indication of the energy used for each bead than the calculation of the traditional heat input. Since low heat input provides high cooling rates and less grain growth [21, 22], oscillations can also be used to change

the number of required beads without sacrificing the low heat input microstructural advantages. This is especially interesting because the deposition of the narrow beads (also capable of low-heat input deposition) did not result in a consistent deposition free of defects.

Therefore, the oscillations allowed keeping the grain size similar to the original and reducing the susceptibility to hot cracking by changing the solidification direction along the bead. The test of the different strategies allowed verifying the differences from the microstructural and geometrical accuracy point of view based on the type and parameters of oscillation. From the microstructural point of view, although the CUB-SQ3 sample showed the best result (smallest grain size), the difference between the samples was not significant. Regarding the geometric accuracy (a factor that can alter the efficiency from the point of view of post-processing), the solid CUB-SIN3-180 had the best overall result. However, disregarding the strategy of changing the welding start/end point (since it is a strategy that can be used regardless of the oscillation types), samples CUB-SIN3-180 and CUB-SQ3 showed the best overall results. Better geometric accuracy and uniformity result in less material to be machined/wasted, which makes the process more energy efficient and sustainable. Furthermore, the deposition strategies allows the continuous deposition without idle time between layers to cool the part. That said, it is important to optimise the

Table 5 Energy estimation for each type of oscillation. Oscillations SQ-3, SQ-7 and SIN-3 were the ones used to manufacture the solids

Bead ID	Oscillation type	$A_{peak-peak}$ (mm)	d or λ (mm)	Bead's total length (mm)	Bead velocity "BV" (mm/min)	Heat input based on BV (J/mm)	Bead's total deposition energy (kJ)
SB	–	–	–	60	1050	58.3	3.50
SQ-1	Square wave	3.6	3.6	180	350	169.1	10.15
SQ-2		4.8	3.6	220	286	210.7	12.64
SQ-3		6.0	3.6	260	242	243.2	14.59
SQ-4		4.8	2.4	300	210	287.7	17.26
SQ-5		4.8	4.8	180	350	167.4	10.04
SQ-6		3.6	2.4	240	263	238.3	14.30
SQ-7		6.0	2.4	360	175	359.1	21.55
SIN-1	Sinusoidal wave	4.8	3.6	175	360	166.9	10.02
SIN-2		3.6	3.6	138	456	132.5	7.95
SIN-3		6.0	3.6	213	296	205.0	12.30
SIN-4		4.8	2.4	251	251	249.5	14.97
SIN-5		4.8	4.8	138	456	131.7	7.90
SIN-6		3.6	2.4	194	325	180.9	10.85
SIN-7		6.0	2.4	310	203	307.4	18.44

oscillation for each case to obtain a bead that has a relevant oscillation (capable of presenting the microstructural advantages) and is narrow enough to promote good geometric accuracy.

4 Conclusions

This work analysed different deposition strategies regarding their geometrical performance and final microstructure, achieving the following conclusions:

- The solid manufactured with narrow and low heat input parameters without oscillation presented many defects and instability during deposition;
- The solids produced with arc oscillations did not present any defect and showed an average grain size and microstructure similar to the original base metal. The CUB-SQ3 sample (square wave oscillation) presented the smallest grain size;
- Changing each layer's starting and ending point is crucial to obtain a more uniform and accurate geometry. However, the 180º rotation is preferred because it is easier to program than the 90º rotation due to a more predictable path;
- All strategies tested are capable of producing satisfactory solids with similar microstructures in a continuous depositions, i.e. without idle time between layers. The best overall solid was the CUB-SIN3-180, i.e. deposition made with a 180º rotation between layers, with a sinusoidal oscillation.

References

1. Hegab H, Khanna N, Monib N, Salem A (2023) Design for sustainable additive manufacturing: a review. Sustain Mater Technol 35:e00576
2. Kumar Sinha A, Pramanik S, Yagati KP (2022) Research progress in arc based additive manufacturing of aluminium alloys—a review. Meas J Int Meas Confed 200:111672
3. Wu B, Pan Z, Ding D, Cuiuri D, Li H, Xu J, Norrish J (2018) A review of the wire arc additive manufacturing of metals: properties, defects and quality improvement. J Manuf Process 35:127–139
4. Li Y, Su C, Zhu J (2022) Comprehensive review of wire arc additive manufacturing: Hardware system, physical process, monitoring, property characterization, application and future prospects. Results Eng 13:100330
5. Le VT, Mai DS, Doan TK, Paris H (2021) Wire and arc additive manufacturing of 308L stainless steel components: optimization of processing parameters and material properties. Eng Sci Technol Int J 24:1015–1026
6. Rosli NA, Alkahari MR, bin Abdollah MF, Maidin S, Ramli FR, Herawan SG (2021) Review on effect of heat input for wire arc additive manufacturing process. J Mater Res Technol 11:2127–2145
7. Li F, Chen S, Shi J, Zhao Y, Tian H (2018) Thermoelectric cooling-aided bead geometry regulation in wire and arc-based additive manufacturing of thin-walled structures. Appl Sci 8:207
8. Singh S, Sharma SK, Rathod DW (2021) A review on process planning strategies and challenges of WAAM. Mater Today Proc 47:6564–6575

9. Zhuo Y, Yang C, Fan C, Lin S, Chen Y, Chen C, Cai X (2021) Grain refinement of wire arc additive manufactured titanium alloy by the combined method of boron addition and low frequency pulse arc. Mater Sci Eng A 805:140557

10. Chen C, Chen F, Yang Y, Zhang H (2021) Study on appearance and mechanical behavior of additively manufacturing of Ti–6Al–4V alloy by using cold metal transfer. CIRP J Manuf Sci Technol 35:250–258

11. Nagasai BP, Malarvizhi S, Balasubramanian V (2022) Effect of welding processes on mechanical and metallurgical characteristics of carbon steel cylindrical components made by wire arc additive manufacturing (WAAM) technique. CIRP J Manuf Sci Technol 36:100–116

12. Zhang C, Gao M, Zeng X (2019) Workpiece vibration augmented wire arc additive manufacturing of high strength aluminum alloy. J Mater Process Technol 271:85–92

13. Gu J, Ding J, Williams SW, Gu H, Bai J, Zhai Y, Ma P (2016) The strengthening effect of inter-layer cold working and post-deposition heat treatment on the additively manufactured Al–6.3Cu alloy. Mater Sci Eng A 651:18–26

14. Sun R, Li L, Zhu Y, Guo W, Peng P, Cong B, Sun J, Che Z, Li B, Guo C, Liu L (2018) Microstructure, residual stress and tensile properties control of wire-arc additive manufactured 2319 aluminum alloy with laser shock peening. J Alloys Compd 747:255–265

15. Yuan T, Luo Z, Kou S (2016) Grain refining of magnesium welds by arc oscillation. Acta Mater 116:166–176

16. Syed AK, Zhang X, Davis AE, Kennedy JR, Martina F, Ding J, Williams S, Prangnell PB (2021) Effect of deposition strategies on fatigue crack growth behaviour of wire + arc additive manufactured titanium alloy Ti–6Al–4V. Mater Sci Eng A 814:141194

17. Lara M, Díaz VV, Camus M, Da Cunha TV (2020) Effect of transverse arc oscillation on morphology, dilution and microstructural aspects of weld beads produced with short-circuiting transfer in GMAW. J Brazilian Soc Mech Sci Eng 42:449

18. Yan Z, Yuan T, Chen S (2019) Microstructural refinement of 6061 and 5052 aluminium alloys by arc oscillation. Mater Sci Technol 35:1651–1655

19. Kou S, Le Y (1985) Grain structure and solidification cracking in oscillated arc welds of 5052 aluminum alloy. Metall Trans A 16:1345–1352

20. Kou S, Le Y (1985) Alternating grain orientation and weld solidification cracking. Metall Trans A 16:1887–1896

21. Turichin G, Kuznetsov M, Pozdnyakov A, Gook S, Gumenyuk A, Rethmeier M (2018) Influence of heat input and preheating on the cooling rate, microstructure and mechanical properties at the hybrid laser-arc welding of API 5L X80 steel. Procedia CIRP 74:748–751

22. Liu D, Yang J, Zhang Y, Qiu Y, Cheng G, Yao M, Dong J (2021) Effect of welding heat input on the microstructure and impact toughness of HAZ in 420 MPa-grade offshore engineering steel. Front Mater 8:1–14

23. BS EN 10025–2 (2019) Hot rolled products of structural steels - Part 2: Technical delivery conditions for non-alloy structural steels, British Standards Institution, United Kingdom

24. Campatelli G, Venturini G, Grossi N, Baffa F, Scippa A, Yamazaki K (2021) Design and testing of a WAAM Retrofit kit for repairing operations on a milling machine. Machines 9:322

25. Baffa F, Venturini G, Campatelli G, Galvanetto E (2022) Effect of stepover and torch tilting angle on a repair process using WAAM. Adv Manuf

26. Richardson RW, DuPont JN, Farson DF, Lyttle KA, Meyer DW (2001) Physics of welding. In: Jenney CL, O'Brien A (eds) AWS Weld. Handb, vol 1—Weld. Sci. Technol., 9th edn. American Welding Society, Miami, USA, pp 51–85

27. DuPont JN, Marder AR (1995) Thermal efficiency of arc welding processes. Weld J 74:406s–416s

28. Huang J, Liu G, Yu X, Wu H, Huang Y, Yu S, Fan D (2022) Microstructure regulation of titanium alloy functionally gradient materials fabricated by alternating current assisted wire arc additive manufacturing. Mater Des 218:110731

29. Carvalho GHSFL, Venturini G, Campatelli G, Galvanetto E (2023) Development of optimal deposition strategies for cladding of Inconel 625 on carbon steel using wire arc additive manufacturing. Surf Coatings Technol 453:129128

30. Nag S, Sardar P, Jain A, Himanshu A, Mondal DK (2014) Correlation between ferrite grain size, microstructure and tensile properties of 0.17 wt% carbon steel with traces of microalloying elements. Mater Sci Eng A 597:253–263
31. Ohring M (1995) How engineering materials are strengthened and toughened. In: Engineering materials science. Elsevier, pp 431–500
32. Seok M-Y, Choi I-C, Moon J, Kim S, Ramamurty U, Jang J (2014) Estimation of the Hall-Petch strengthening coefficient of steels through nanoindentation. Scr Mater 87:49–52
33. Asahi H, Yagi A, Ueno M (1993) Effects of strengthening mechanisms on sulfide stress cracking resistance of low strength steels. ISIJ Int 33:1190–1195

Pre-process Optimisation of Filament Feed Rate in Fused Filament Fabrication by Using Digital Twins and Machine Learning

Arianna Rossi, Michele Moretti, and Nicola Senin

Abstract One of the limitations of fused filament fabrication (FFF) in mass customisation is the long trial and error process required to optimise process parameters under frequent changes of geometries, materials and structural/mechanical requirements. Extrusion parameters may also need to be changed in-process, for example to address different requirements of skin and internal regions within the same part. This work explores the possibility of making a FFF machine capable of autonomous optimisation of extrusion parameters, currently for use in pre-process optimisation, but in future also applicable to in-process adaptive optimisation and control. Through a combination of machine learning and digital twinning, the proposed solution is able to automatically modify a part program optimising extrusion parameters to improve uniformity of widths of the extruded strands. The solution learns how to modify the part program using data from example depositions (tests runs) and simulation models. The proposed approach is demonstrated through the application to a test case.

Keywords Additive manufacturing · Machine learning · Fused filament fabrication

1 Introduction

1.1 Scenario

In the overall challenge of transitioning from automation to autonomy in manufacturing, an overarching question is: can a CNC machine tool learn to write a part program without assistance, and then execute it whilst controlling part quality during operation?

A. Rossi (✉) · M. Moretti · N. Senin
Department of Engineering, University of Perugia, 06125 Perugia, Italy
e-mail: arianna.rossi2@studenti.unipg.it

We have been looking into such question with a specific focus on an additive process known as fused filament fabrication (FFF), a material extrusion process based on thermal reaction bonding (MEX-TRB [1]). In FFF, the polymer or composite material is provided as filament, and deposited in layers, stacked upon each other to form the final part [2].

It is generally recognised [3, 4] that for a CNC machine to achieve autonomy of process planning and execution, the following challenges must be addressed:

(i) *self-observation*: the CNC machine must be able to sense itself, collecting and storing information about its current and past operation. For FFF specifically, this means being able to sense and record axes movements, temperature, vibrations and any other internal variables deemed relevant to manufacturing performance;

(ii) *part-observation*: the CNC machine must be able to observe the part as it is being fabricated, in order to collect information on consequences of current and past actions. For FFF specifically, this implies the machine being able to observe the part at multiple temporal and spatial scales, ranging from the strand of material currently being deposited, to the layer deposited so far, to the portion of part built;

(iii) *reasoning*: the machine needs multiple layers of automated data elaboration. At a lower-level, the machine must be capable of processing sensor data (ranging from point to imaging sensors) in order to extract relevant information. At a higher-level, the machine must be capable of forming its own internal "mental models" linking its own behaviour to results, useful both as partial replacement of further experiential data, and as a decision support tool, when operating in predictive mode.

We envision that solving the above challenges of self-sensing, part-sensing and reasoning would lead to improved machine autonomy, intended both as the capability of autonomous process planning (choice of process parameters and automatic programming of the manufacturing operations, without the need of a man-made part program), and as the capability of real-time reaction to anomalies during operation: at a smaller temporal scale, by immediate change of process parameters/adaptive control and optimisation; at a longer temporal scale, by adaptive replanning of the remaining parts of the fabrication process.

The work presented here illustrates recent our research progress in the three challenge areas of self-sensing, part-sensing and reasoning, as illustrated above, focusing on the specific objective of developing a FFF machine capable to autonomously learn optimal extrusion parameters through previous deposition experience, thus ultimately being capable of bypassing (or recalibrating) prescriptions provided via the part program.

1.2 The Extrusion Problem

The extrusion system considered in this work is summarized in Fig. 1. A filament is driven into the melting chamber at feed rate F_F (referred to as: *filament feed rate*) by a motorized cogwheel (Bowden architecture [5]). The material is melted, brought to a temperature T, and forced out through the nozzle orifice at speed v_z. The nozzle is located above the deposition plane to achieve the desired layer thickness h. During the fabrication process, the extruder head translates over the x, y plane at travel speed $F_{x,y}$ (referred to as: *extruder travel speed*). Assuming an incompressible material and flow conservation, for a given extruder geometry, extrusion temperature T, and layer thickness h, the filament feed rate F_F and the extruder travel speed $F_{x,y}$ determine the width w of the deposited strand.

When fabricating a part through FFF, it is common [2] to choose different fabrication speeds for different portions of the part program. In particular, the outer walls (skin) of the part, as well as the first and the last layer, are fabricated using reduced speeds over the deposition plane, in order to ensure more uniform adhesion between deposited strands and better surface finish. Conversely, the inner regions of the part are usually fabricated using higher fabrication speeds in order to shorten manufacturing time.

In contemporary CAM/slicer software, filament feed rate F_F and extruder travel speed $F_{x,y}$ are usually modified in synch, so that at steady-state, the targeted width w for the deposited strands is achieved no matter the extruder travel speed. The values for both the F_F and $F_{x,y}$ parameters are usually computed using simple flow conservation models which do not take into proper account the dynamics of the extrusion process. Because the models focus on steady-state, during transients, constancy
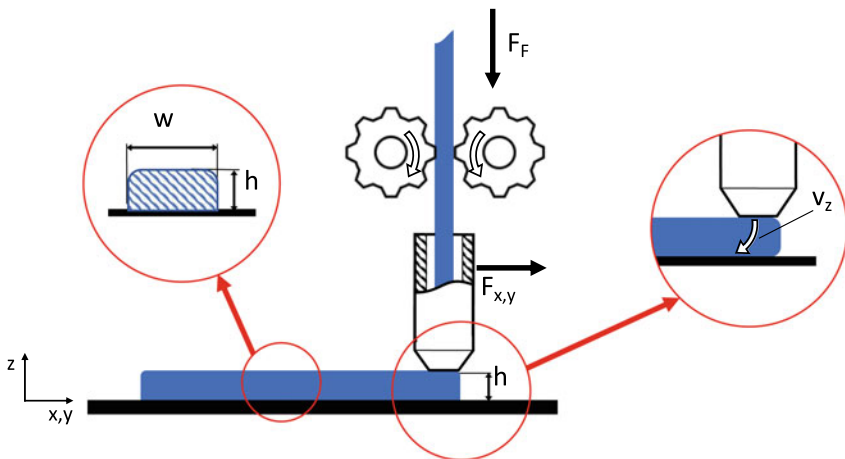
Fig. 1 Schematics of the extrusion system

of strand width is not respected. For example, the slicer software Cura [6] generates g-code with two simultaneous upwards steps for F_F and $F_{x,y}$ when extruder travel speed must be increased, and two simultaneous downwards steps when it must be decreased. In both conditions, the transient dynamics of the extrusion process generate temporary changes of deposited strand width w. These are referred to as temporary *under-extrusion* (strand thinning) when the extruder switches to higher travel velocities, and temporary *over-extrusion* (strand thickening) when the extruder is slowed down. Although both effects are typically temporary, while they last, they are detrimental for final part quality. In particular, under-extrusion increases the likelihood of incomplete merging between adjacent strands, with consequences for geometry, overall structural integrity and mechanical properties of the final parts [7]. Issues caused by over-extrusion concerns geometry accuracy, in particular in corners and holes and poorer surface finish [8]. Material excess may also lead to layer drooping, stringing and to the presence of blobs [9].

1.3 State of the Art

The great variety of materials, geometries and processing conditions a FFF machine may encounter justifies the idea of developing a learning mechanism for the machine to autonomously find an optimal solution for each operating condition, based on previous operational experience in that condition. This in turn leads back to addressing the challenges of *self-observation*, *part-observation* and *reasoning* discussed in Sect. 1.1.

The problem of how to equip FFF machines with a wide array of devices for self-sensing is being extensively researched in the literature, and multiple solutions have been presented to acquire and record information on machine movements through axes encoders [10, 11], temperature [12–15] and extrusion pressure [16, 17]. The use of customized hot-ends has been explored to investigate the evolution of process variables related to melting and transport phenomena inside the extruder [11, 15]. The use of acoustic emissions has been explored [18, 19], as well as the observation of the current absorbed by the filament feeder stepper motor [20, 21] to detect phenomena preventing uniform material extrusion, e.g., nozzle clogging. Elsewhere, the temperature and flow profile of the material passing internally through the extruder have been investigated using particle tracking on pigmented filaments and embedding a thermocouple into the filament [22].

The challenge of observing the result of the extrusion and deposition process has equally been investigated at multiple scales. With this aim, vision systems have been used to observe the small region close to the nozzle in order to monitor the newly deposited material, both from the side [23, 24] and from above [25, 26], also using a thermal camera to investigate the cooling process [27]. Other sensing strategies focused on phenomena occurring inside the part after the deposition, through embedding sensors in the artefact during its fabrication. For example, in [28, 29], fibre Bragg gratings have been used to measure the residual strains inside the part,

while the use of embedded thermocouples has also been explored to investigate the internal temperature profile [28].

A significant portion of research which could be ascribed to machine "reasoning" has addressed the interpretation of sensor data. Frequent in the literature is the use of mathematical modelling and numerical simulations [30–33]. At the same time digital twins, i.e., simulation models designed to be fed with in-process data and capable of providing a digital reproduction of the actual system [34], have been widely used to support signal interpretation in FFF processes. Some examples can be found in [35–39] where digital replicas of the process have been used to predict the quality of the final part, detect anomalies, evaluate process variables and enhance the detection of layer contours. Machine reasoning covers also the development of correlation models linking actions to effects, in our specific case: extrusion parameters to properties of the deposited material. Studies have focused on the material being extruded, the deposited strands, and the entire part. Finite element methods models and experimental tests have been used to find relationship between the filament extrusion rate and interlayer bonding and void presence [40]. Localised anomalies have been also analysed in relation to different velocity profiles using CFD simulation to estimate under- and over-extrusion in corners [32]. The part mesostructure has been simulated using CFD to investigate how layer thickness and distance between adjacent strands may influence it [41]. Concerning the entire part, models considering feed rate, layer thickness and temperature have been developed to estimate dimensional accuracy and surface roughness [42]. The material exiting the nozzle has been studied in simulations aimed at investigating the die swelling effect in relation to different extrusion temperatures and flow rates [43].

As stated earlier in the introduction, in this work we address the problem of creating a reasoning system for an FFF machine, capable of learning optimal extrusion parameters through deposition experience. However, for the time being, the results of such learning are not meant to be applied in real-time during fabrication, but rather translated into the machine capability of automatically modifying its part program ahead of its next execution. In such a context, it is useful to mention notable literature work on g-code optimisation/automated generation in FFF. In [44] irregularities in the geometry of strands deposited along curved paths are reduced through modifications of the extrusion rate depending on local tangential velocity of the extruder on the part. Others authors have focused into optimising extrusion and deposition parameters in correspondence of specific features that must be built (e.g., holes, thin walls, [45]). Issues related to reducing the irregularity of deposited strands, discussed earlier in Sect. 1.2, have been addressed by some authors for different MEX processes. For example, in [46] for silicone extrusion (MEX-CRB/P/Silicone [1]), the g-code is modified ahead of execution in order to reduce the under-extrusion observed when the extruder begins depositing, due to it taking some time to ramp-up to a steady flow-rate. In [47], the modifications are more radical: the CNC architecture of a FFF machine is replaced by an industrial robot and a custom post-processor is proposed that converts the part-program to the new architecture, enabling smoother traversal speeds for the extruder and resulting in a more uniform deposited strand. Machine learning technologies are increasingly being used

to optimise part programs. For example, in [48] an approach based on reinforcement learning is proposed to optimise the part program dedicated to the realisation of thin-walled structures. However, the solution is not for FFF, but rather for wire arc additive manufacturing.

2   Methods

2.1   Targeted Process Parameters and Variables

The objective of this work was to develop an element of machine intelligence specifically dedicated to learning new strategies for modifying filament feed rate F_F in order to reduce transient under and over-extrusion phenomena taking place when a change of extruder travel speed $F_{x,y}$ is programmed within the part program (written in g-code). In this investigation, the default upwards and downwards step-like changes of $F_{x,y}$ introduced by Cura [6] are left untouched. However, future research will look into ways for the machine to also learn how to modify $F_{x,y}$ (along with F_F) so that both parameters can be optimised to reduce under- and over-extrusion. An even further research step would target the implementation of strategies for changing F_F and $F_{x,y}$ in-process and in real-time, to address disturbances, or to implement adaptive optimisation of process parameters if anything changes during fabrication.

2.2   Solutions for Self-sensing and Part-Sensing

For use in this and other projects, we have been developing a number of custom extruder heads equipped with multiple sensors [11, 39, 49, 50]. The first of the two FFF prototypes used in this work is a custom machine featuring a three-axis Cartesian architecture (Fig. 2). The build platform moves along x, y direction, while the extruder is mounted on a horizontal gantry which moves along the vertical direction. The extruder is equipped to process filaments with a diameter of 1.75 mm, while the nozzle has a diameter of 0.4 mm. The extrusion system has a Bowden configuration, in which cold end and hot end are physically separated. Sensors include thermocouples (for temperature in the melting chamber and at the nozzle exit), load cells (to measure filament compression as it enters the melting chamber), and optical rotary encoders to monitor the rotation of the motor-powered and driven cogwheels that determine filament feed rate. The travel path and speed of the extruder head over the x, y build platform is also monitored through optical rotary encoders.

Whilst the aforementioned sensors cover the self-sensing functionality required for the FFF machine, in this specific work the challenge of making the machine also capable of observing the results of its operation (i.e., part-sensing) involved the
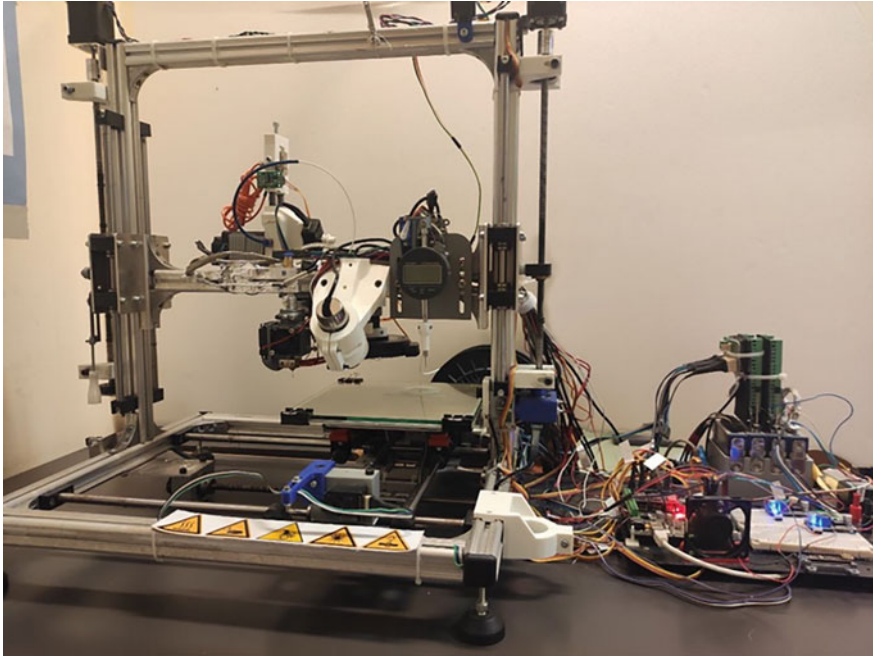
Fig. 2 One of the two FFF prototypes used in this work. Complete FFF machine featuring multiple sensors on the Cartesian axes and extruder head

possibility to observe (and measure) the width of deposited strands using a non-contact solution.

The problem of observing the strand is a challenging one: the main hurdles are related to access and observability, considering that the extrusion process implies moving parts that may need to be tracked, the deposition event may be temporarily occluded from view depending on extruder trajectory (if observed from a specific side), while—if observing from above—the extrudate may exit the nozzle in different directions on the x, y plane, depending on current travel direction. Whilst we are working on custom machine architectures specifically dedicated to support real-time deposited strand observation, for the purpose of this specific work we relied on a more indirect approach, making use of another dedicated experimental FFF machine, consisting of a stationary extruder that releases material in-air, and a high-speed optical camera (DMK 33UP2000 [51]) featuring a 1920 × 1200 pixel CMOS sensor, which observes the extrudate as it leaves the nozzle orifice with a resolution of 914 pixel/mm and a FoV of 2.1 × 1.6 mm [49]. Ths second experimental FFF machine features a Bowden extruder identical to the one mounted on the other machine, and also extrudes a 1.75 mm diameter filament through a 0.4 mm nozzle. The combined use a particle-laden filament and in-house built software for particle tracking [49] allows to measure extrudate vertical speed v_z at the nozzle exit, whilst at the same time recording filament feed rate F_F through optical rotary encoders (Broadcom-Avago
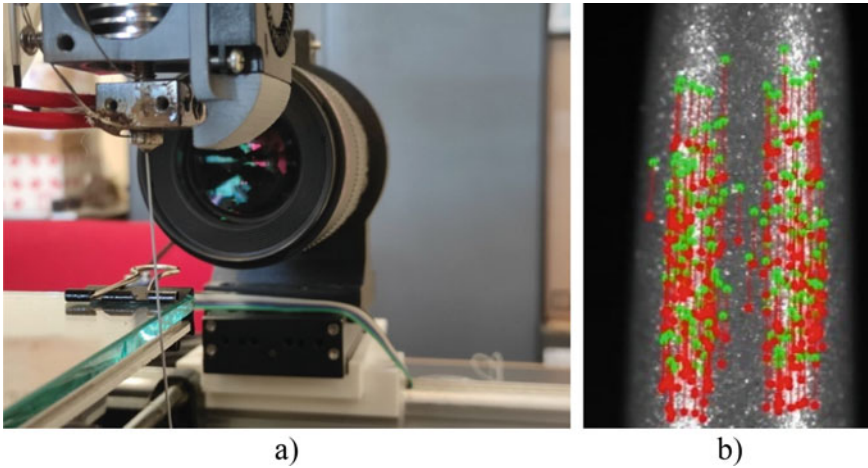
Fig. 3 Second FFF prototype used in this work; **a** custom multi-sensor FFF extruder head for in-air extrusion at fixed-position, paired with high-speed optical camera; **b** detail of extrudate speed measurement v_z using particle tracking [49]

AEDM-5810-Z12, 5000 ppr [52]) mounted on the filament-driving cogwheels (see Fig. 3).

For the specific purpose of this work, the problem of observing the actual width of the deposited strand was only solved indirectly: (i) we started from a numerical simulation of the extrusion process developed in previous work [49] to identify a first model linking F_F and v_z; (ii) the simulation parameters were then calibrated using experimental data collected from the in-air extrusion apparatus shown in Fig. 3 [49]; (iii) the calibrated simulation was turned into a digital twin, capable of predicting v_z in real-time from $F_{x,y}$ and F_F data provided by g-code or in-process sensors. (iv) to make the digital twin faster at estimating v_z, we used a previously developed method [53] based on deep learning to teach a non-linear autoregressive model with exogenous variables (NARX) to replicate the results of the original simulation. Once properly fitted, the NARX is able to mimic the behaviour of the original twin at a fraction of the computational time; (v) as the prediction stops at v_z, we extended the twin by adding an algebraic model based on flow conservation [49] to compute strand width w from v_z. This latter model works under the assumptions of constant gap h between the orifice and the surface underneath. This solution is only temporary, as our prediction for strand width w cannot take into account actual fluctuations of the gap h, and will be replaced by direct, optical observation of deposited strand width on the build plate (in progress).

Despite the limitations, the method illustrated above allowed to obtain a serviceable digital twin capable of predicting strand width once provided with F_F and $F_{x,y}$ values. The twin was then transferred to the other experimental FFF machine (Fig. 2) dedicated to performing actual strand deposition test runs, to experiment with different automated decision systems, all supported by the digital twin to predict

consequences of choosing different F_F modification strategies. Since the machines used in this work are all based on a Bowden extruder architecture, the applicability of the developed digital twin is limited to machines using the same architecture. With the Bowden architecture though, the digital twin can be adapted to operate on any machine, as long as properly tuned using data from that machine.

2.3 Solution for Filament Feed Rate Optimisation

The filament feed rate optimiser plays the role of the "reasoning" system within the conceptual framework of autonomous FFF machine, although it is limited to intervening on only one process parameter (the filament feed rate F_F) in order to influence only one process variable (deposited strand width w). The intended mode of operation is referred to as "model-supported" reasoning, as the optimiser ultimately identifies the optimal values for F_F by using the digital twin (Sect. 2.2.) to predict the effects of choosing different F_F values on deposited strand width w. Although in future implementations we will be exploring the use of such an optimiser in real-time "reactive" mode (i.e. the optimiser decides new values for F_F in-process, consequent to detecting changes in w through real-time observation/simulation), for the purpose of this work, we have been only exploring the possibility of using the optimiser to modify the g-code ahead of execution (pre-process optimisation), making use of w predictions (from the digital twin) to estimate the benefits of any change introduced in the g-code.

In its current configuration, the optimiser is powered by a genetic algorithm. Training is performed as follows: (i) portions of g-code containing changes in $F_{x,y}$ are isolated from the part program, considering a time window of fixed width, containing the step change; (ii) for each window, a full time-series for $F_{x,y}$ is generated, containing the step-wise transition (Fig. 4a); (iii) for each window, an equal length time-series for F_F is generated also from the instructions contained in the original g-code (Fig. 4b). Because the slicer (Cura) implements simultaneous step-changes, the steps in the F_F and $F_{x,y}$ time histories are time-aligned. The two time-series shown in Fig. 4a, b represent the behaviour of the two process parameters according to the original g-code in relation to a specific time window. The behaviour of the targeted process variable w (deposited strand width) is computed by the digital twin over the same time interval (Fig. 4c). The twin is interrogated with the time series shown in Fig. 4a, b to produce the result shown. Figure 4, is actually showing an episode of acceleration in the deposition, temporarily causing under-extrusion.

The objective function for the genetic algorithm consists of the area between w_0 (the target, ideally constant strand width) and the real width w (referred to as *cumulative width error*).

The search consists of exploring the infinite time series which can be adopted for F_F (departing from the initial synchronous step) in order to minimize the cumulative width error. Note that in Fig. 4c in addition to the transient region for the real width w, another element of consistent differentiation is visible between w and w_0: the real

Fig. 4 a Time series corresponding to a step-wise transition for $F_{x,y}$ as generated from the g-code; **b** simultaneous step-change in F_F, also from the g-code; **c** deposited strand width w resulting from the simultaneous step-wise transitions of $F_{x,y}$ and F_F
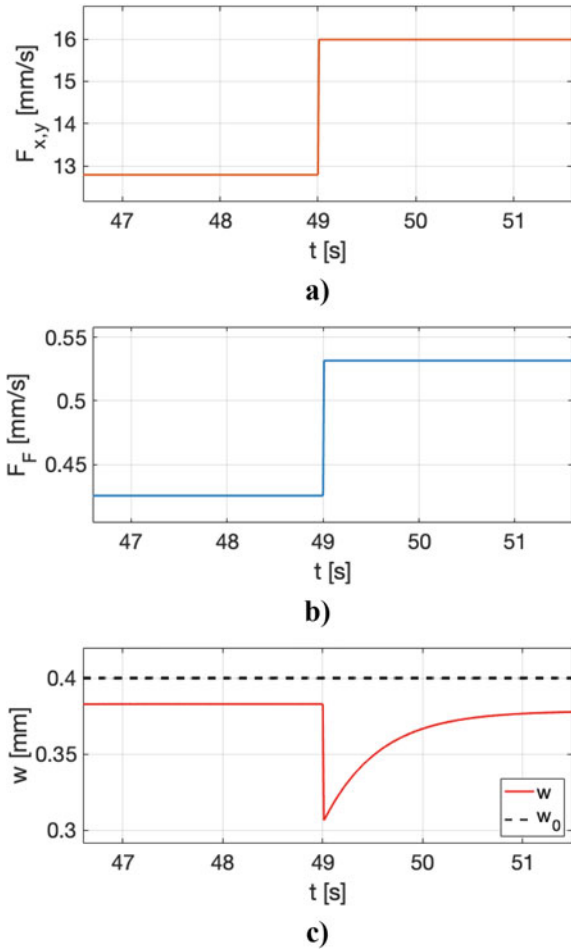
width is consistently smaller than the reference set by Cura because the slicer does not consider filament slippage, which reduces overall material flow and causes under-extrusion [7]. On the contrary, slippage is included in the digital twin [49]. Hence, the genetic algorithm optimiser discussed in this work operates both to minimize w variations and to compensate for slippage.

For the time being, we have further constrained the search space by only allowing time series for F_F which feature two consecutive step changes, as summarized in Fig. 5. As illustrated in the figure, the genetic algorithm considers only four independent search variables, representing respectively: time instant to initiate the first step (t_1); filament feed rate to be reached in the first step ($F_{F,1}$); time instant to initiate the second step (t_2) and filament feed rate to be reached ($F_{F,2}$) and kept stationary. Note that, no constraint is imposed to whether the two steps should be upwards or downwards-oriented, the optimiser is free to decide autonomously. In designing the

Fig. 5 Search variables for the genetic algorithm: time instants to initiate the two steps t_1 and t_2, and filament feed rates to be reached in the first ($F_{F,1}$) and in the second ($F_{F,2}$) step
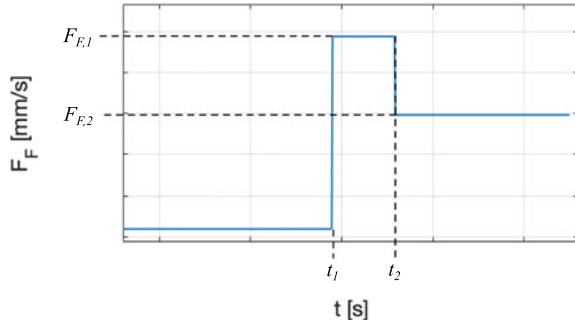
optimisation problem, we had originally explored also ramp-like and freeform transients for F_F. However, we have currently decided against such types of transients, as preliminary optimisation tests seemed to indicate convergence towards double-step transients anyways. Importantly, the inclusion of the filament feed rate to be reached ($F_{F,2}$) as the fourth search variable, implies that the optimiser is free to operate also on the F_F values that apply to steady-state conditions, potentially overriding the choice of the slicer software even in such scenarios (important to minimize slippage, as discussed above). Note in fact that $F_{F,2}$ optimised for any step-like transition is also the initial steady-state filament feed rate for the next step-like transition.

The genetic algorithm currently uses a population of 50 individuals, and runs 200 generations, or fewer, if one of the early termination criterions is satisfied. Early termination is triggered if (i) the cumulative width error is $\leq 10\%$ of the cumulative width error computed pre-optimisation; or (ii) the average change of cumulative width error between two consecutive generations is less than 10^{-6}. The crossover operator (crossover—scattered) and the mutation operator (mutation—gaussian) are run with 0.8 and 1.0 probabilities, respectively. Three individuals are chosen at the end of each generation to generate the offspring (elitist model NSGA-II [54]). Once the genetic algorithm optimisation has been run on all the step-like changes of $F_{x,y}$ found in the part program, the produced, optimal F_F time series are used to update the g-code. The whole optimisation is executed off-line.

3 Results

The test case consisted of a part program (g-code) containing 17 step changes for $F_{x,y}$ and a corresponding number of simultaneous step changes for F_F. The part program was processed by the optimiser off-line. The optimiser was run separately on each step, by selecting a window covering a time interval of -2.5 s before and $+2.5$ s after the step change. The x, y and F_F time series for the time interval were generated as illustrated in Sect. 2.3, by simulating parameter evolution over time at 0.01 s sampling rate (100 Hz), corresponding to the sampling rate of the encoders dedicated to observing the same variables (rotary optical encoders on the x, y axes,

and rotary optical encoder on the motor-driven cogwheel driving the filament into the melting chamber (Sect. 2.2 and Fig. 2). The step changes for the extruder travel speed $F_{x,y}$ were processed by the optimiser in a sequential manner. This is because the last of the four parameters altered by the optimisation applied to a specific step (i.e., $F_{F,2}$, Sect. 2.3), corresponds to the filament feed rate being enacted by the extruder when the next step is reached.

In Fig. 6, an example run for the optimiser is shown, applied to a upwards step for $F_{x,y}$. Figure 7 shows an equivalent example for a downwards step. In both figures the leftmost panel indicate the time series before the optimisation, the rightmost panel those after the optimisation. Note that $F_{x,y}$ is unchanged as it is not altered by the optimisers, whilst F_F changes from its default step-like appearance (as originally programmed by the slicer) to the two-step configuration computed by the optimiser. The plots for the deposited strand width w are obtained by interrogating the digital twin with the original and updated F_F time series. For the specific cases illustrated in Fig. 6 the cumulative width error (Sect. 2.3) changed from 1.64 mm^2 to 0.48 mm^2 (over the 5 s time window). For the step in Fig. 7, the error changed from 42.49 mm^2 to 4.23 mm^2 over the 5 s time window. Similar results were obtained for the other steps, resulting in an average error reduction which often got closer to one order of magnitude with respect to the original values.
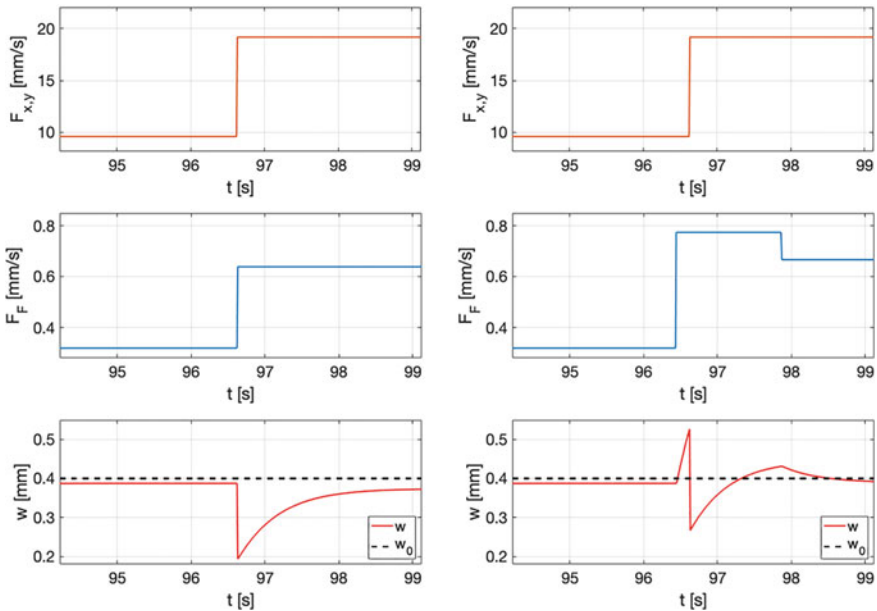
Fig. 6 Operation of the optimiser on one of the $F_{x,y}$ upwards steps in the test g-code. Left panel: before optimisation; right panel: after optimisation. In both panels: top: $F_{x,y}$; middle: F_F; bottom: w and w_0
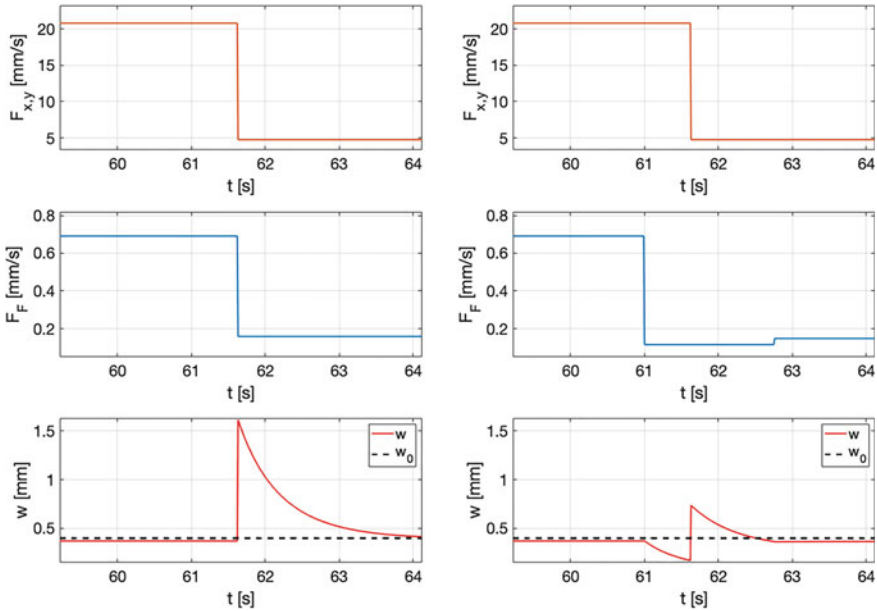
Fig. 7 Operation of the optimiser on one of the $F_{x,y}$ downwards steps in the test g-code. Left panel: before optimisation; right panel: after optimisation. In both panels: top: $F_{x,y}$; middle: F_F; bottom: w and w_0

Note that, as illustrated in Sect. 2.3, the digital twin is interrogated multiple times during optimisation to test for alternatives corresponding to all the individuals of the population managed by the genetic algorithm, and for each generation of the evolving population. For our current configuration of the optimiser, the twin is interrogated on average 4000 times for each individual step-wise change to be optimised. Replacing the original twin with a NARX powered by machine learning helped significantly reducing the temporal overhead (each original simulation run took on average 50 s for a time-history of 5 s, whilst the NARX equivalent took 0.08 s per run).

4 Conclusions

In this work we have illustrated the development of a solution for a FFF machine to learn optimal extrusion parameters using data from previous depositions. The solution does not allow for in-process correction, and is currently limited to providing a means for the g-code to be optimised ahead of its next execution. G-code optimisation itself is currently focused solely on making the deposited strand more uniform in width, compensating over and under-extrusion effects which normally occur as in default operation filament feed-rate is not ideally optimised with respect to current extruder traversal speed over the deposition surface. Our optimiser currently only

operates by modifying filament feed-rate within the g-code. Another limitation is that our FFF machine does not really learn to perform a better extrusion and deposition process by observing all the involved variables. Rather, it uses a mixture of observations (time-series from sensed extruder travel speed and filament feed rate, collected in previous depositions), and simulated data, consisting of deposited strand widths computed by a digital twin, validated in previous work.

Our current results are clearly work in progress towards a future goal of implementing a more comprehensive sensing and learning system, in particular so that the reliance on simulated predictions is balanced by using more information directly captured from the process. Our solution is currently based on a combination of methods using deep learning, genetic algorithms and digital twinning. Despite the aforementioned limitations, the implemented g-code optimisation system was capable of achieving a reduction of over- and under-extrusion phenomena of approximately one order of magnitude with respect to the initial unoptimised state, when applied to the test case. Our solution can currently operate only as a pre-optimiser of the part program. We envision the future possibility to reach to a full in-process, real-time system for strand width control and adaptive optimisation during deposition. To achieve this longer-term aim, we are developing technologies for in-process strand measurement, and in-process learning of correlation models better capturing the relationships between extrusion process parameters and geometric results for the deposited part.

References

1. International Organization for Standardization (2022) ISO/ASTM 52900:2021-Additive manufacturing—General principles—Fundamentals and vocabulary
2. Gibson I, Rosen DW, Stucker B (2014) Additive manufacturing technologies, vol 17. Springer, Cham, Switzerland
3. Ezenkwu CP, Starkey A (2019) Machine autonomy: definition, approaches, challenges and research gaps. In: Arai K, Bhatia R, Kapoor S (eds) Intelligent computing: proceedings of the 2019 computing conference, vol 1. Springer International Publishing, pp 335–358
4. Liu C, Vengayil H, Zhong RY, Xu X (2018) A systematic development method for cyber-physical machine tools. J Manuf Syst 48:13–24
5. Hoque M, Kabir H, Jony MH (2018) Design and costruction of a bowden extruder for a FDM 3D printer uses 1.75 mm filament. Int J Tech Res Sci 3:282–288
6. Ultimaker Cura. https://ultimaker.com/software/ultimaker-cura. Last accessed 28 Feb 2023
7. Moretti M, Rossi A (2021) Closed loop filament feed control in fused filament fabrication. 3D Print Addit Manuf
8. Butt J, Bhaskar R, Mohaghegh V (2022) Investigating the influence of material extrusion rates and line widths on FFF-printed graphene-enhanced PLA. J Manuf Mater Process 6(3):57
9. Butt J, Bhaskar R, Mohaghegh V (2021) Investigating the effects of extrusion temperatures and material extrusion rates on FFF-printed thermoplastics. Int J Adv Manuf Technol 117(9–10):2679–2699
10. Weiss B, Storti D, Ganter M (2015) Low-cost closed-loop control of a 3D printer gantry. Rapid Prototyp J 21(5):482–490

11. Moretti M, Bianchi F, Senin N (2020) Towards the development of a smart fused filament fabrication system using multi-sensor data fusion for in-process monitoring. Rapid Prototyp J 26(7):1249–1261
12. Seppala JE, Hoon Han S, Hillgartner KE, Davis CS, Migler KB (2017) Weld formation during material extrusion additive manufacturing. Soft Matter 13(38):6761–6769
13. Pollard D, Ward C, Herrmann G, Etches J (2017) Filament temperature dynamics in fused deposition modelling and outlook for control. Procedia Manuf 11:536–544
14. Coogan TJ, Kazmer DO (2020) Prediction of interlayer strength in material extrusion additive manufacturing. Addit Manuf 35:101368
15. Anderegg DA, Bryant HA, Ruffin DC, Skrip SM, Fallon JJ, Gilmer EL, Bortner MJ (2019) In-situ monitoring of polymer flow temperature and pressure in extrusion based additive manufacturing. Addit Manuf 26:76–83
16. Coogan TJ, Kazmer DO (2019) In-line rheological monitoring of fused deposition modeling. J Rheol 63(1):141–155
17. De Backer W, Sinkez P, Chhabra I, Van Tooren M, Bergs A (2020) In-process monitoring of continuous fiber additive manufacturing through force/torque sensing on the nozzle. In: AIAA scitech 2020 forum, p 1632
18. Li H, Yu Z, Li F, Kong Q, Tang J (2022) Real-time polymer flow state monitoring during fused filament fabrication based on acoustic emission. J Manuf Syst 62:628–635
19. Tlegenov Y, Hong GS, Lu WF (2018) Nozzle condition monitoring in 3D printing. Robot Comput-Integr Manuf 54:45–55
20. Kim C, Espalin D, Cuaron A, Perez MA, Macdonald E, Wicker RB (2015) A study to detect a material deposition status in fused deposition modeling technology. In: 2015 IEEE international conference on advanced intelligent mechatronics (AIM). IEEE, pp 779–783
21. Tlegenov Y, Lu WF, Hong GS (2019) A dynamic model for current-based nozzle condition monitoring in fused deposition modelling. Prog Addit Manuf 4:211–223
22. Peng F, Vogt BD, Cakmak M (2018) Complex flow and temperature history during melt extrusion in material extrusion additive manufacturing. Addit Manuf 22:197–206
23. Shen H, Sun W, Fu J (2019) Multi-view online vision detection based on robot fused deposit modeling 3D printing technology. Rapid Prototyp J 25:343–355
24. Jin Z, Zhang Z, Gu GX (2020) Automated real-time detection and prediction of interlayer imperfections in additive manufacturing processes using artificial intelligence. Adv Intell Syst 2(1):1900130
25. Liu C, Law ACC, Roberson D, Kong Z (2019) Image analysis-based closed loop quality control for additive manufacturing with fused filament fabrication. J Manuf Syst 51:75–86
26. Jin Z, Zhang Z, Gu GX (2019) Autonomous in-situ correction of fused deposition modeling printers using computer vision and deep learning. Manuf Lett 22:11–15
27. Caltanissetta F, Dreifus G, Hart AJ, Colosimo BM (2022) In-situ monitoring of material extrusion processes via thermal videoimaging with application to Big Area Additive Manufacturing (BAAM). Addit Manuf 58:102995
28. Kousiatza C, Karalekas D (2016) In-situ monitoring of strain and temperature distributions during fused deposition modeling process. Mater Des 97:400–406
29. Kantaros A, Karalekas D (2013) Fiber Bragg grating based investigation of residual strains in ABS parts fabricated by fused deposition modeling process. Mater Des 50:44–50
30. Zhang Y, Chou YK (2006) Three-dimensional finite element analysis simulations of the fused deposition modelling process. Proc Inst Mech Eng, Part B: J Eng Manuf 220(10):1663–1671
31. Xia H, Lu J, Tryggvason G (2018) Fully resolved numerical simulations of fused deposition modeling. Part II—solidification, residual stresses and modeling of the nozzle. Rapid Prototyp J 24:973–987
32. Comminal R, Serdeczny MP, Pedersen DB, Spangenberg J (2019) Motion planning and numerical simulation of material deposition at corners in extrusion additive manufacturing. Addit Manuf 29:100753

33. Stewart SR, Wentz JE, Allison JT (2015) Experimental and computational fluid dynamic analysis of melt flow behavior in fused deposition modelling of poly(lactic) acid. In: ASME international mechanical engineering congress and exposition, vol 57359. American Society of Mechanical Engineers, p V02AT02A010
34. DebRoy T, Zhang W, Turner J, Babu SS (2017) Building digital twins of 3D printing machines. Scripta Mater 135:119–124
35. Sun H, Rao PK, Kong ZJ, Deng X, Jin R (2017) Functional quantitative and qualitative models for quality modeling in a fused deposition modeling process. IEEE Trans Autom Sci Eng 15(1):393–403
36. Chhetri SR, Faezi S, Canedo A, Faruque MA (2019) QUILT: Quality inference from living digital twins in IoT-enabled manufacturing systems. In: Proceedings of the international conference on internet of things design and implementation, pp 237–248
37. Balta EC, Tilbury DM, Barton K (2019) A digital twin framework for performance monitoring and anomaly detection in fused deposition modeling. In: IEEE 15th international conference on automation science and engineering (CASE). IEEE, pp 823–829
38. Kim Y, Alcantara D, Zohdi TI (2022) Thermal state estimation of fused deposition modeling in additive manufacturing processes using Kalman filters. Int J Numer Meth Eng 123(13):3021–3033
39. Moretti M, Rossi A, Senin N (2020) In-process monitoring of part geometry in fused filament fabrication using computer vision and digital twins. Addit Manuf 37:101609
40. Ghorbani J, Koirala P, Shen YL, Tehrani M (2022) Eliminating voids and reducing mechanical anisotropy in fused filament fabrication parts by adjusting the filament extrusion rate. J Manuf Process 80:651–658
41. Serdeczny MP, Comminal R, Pedersen DB, Spangenberg J (2019) Numerical simulations of the mesostructure formation in material extrusion additive manufacturing. Addit Manuf 28:419–429
42. Haghbin N, Bone D, Young K (2021) Controlled extrusion-based 3D printing of micro-channels with the geometric modelling of deposited roads. J Manuf Process 67:406–417
43. Van Waeleghem T, Marchesini FH, Cardon L, D'hooge DR (2022) Melt exit flow modelling and experimental validation for fused filament fabrication: from Newtonian to non-Newtonian effects. J Manuf Process 77:138–150
44. Ertay DS, Yuen A, Altintas Y (2018) Synchronized material deposition rate control with path velocity on fused filament fabrication machines. Addit Manuf 19:205–213
45. Papazetis G, Vosniakos G-C (2019) Feature-based process parameter variation in continuous paths to improve dimensional accuracy in three-dimensional printing via material extrusion. Proc Inst Mech Eng, Part B: J Eng Manuf 233:2241–2250
46. Tian X, Li Y, Ma D, Han J, Xia L (2022) Strand width uniformly control for silicone extrusion additive manufacturing based on image processing. Int J Adv Manuf Technol 119:3077–3090
47. Castelli K, Zaki AMA, Balakrishnappa AY, Carnevale M, Giberti H (2021) A path planning method for robotic additive manufacturing. In: 3rd international congress on human-computer interaction, optimization and robotic applications (HORA). IEEE, Ankara, Turkey, pp 1–5
48. Petrik J, Bambach M (2023) Reinforcement learning and optimization based path planning for thin-walled structures in wire arc additive manufacturing. J Manuf Process 93:75–89
49. Moretti M, Rossi A, Senin N (2021) In-process simulation of the extrusion to support optimisation and real-time monitoring in fused filament fabrication. Addit Manuf 38:101817
50. Moretti M, Senin N (2022) In-process monitoring of part warpage in fused filament fabrication through the analysis of the repulsive force acting on the extruder. Addit Manuf 49:102505
51. The image source 2020. https://www.theimagingsource.com. Last accessed 10 May 2023
52. Broadcom: High Resolution 3-channel Housed Encoder Module Kits with Snap-on Cover 2019. https://www.broadcom.com/products/motion-control-encoders/incremental-encoders/transmissive-encoders/aedm-5xxx. Last accessed 10 May 2023
53. Rossi A, Moretti M, Senin N (2022) Neural networks and NARXs to replicate extrusion simulation in digital twins for fused filament fabrication. J Manuf Process 84:64–76

54. Kalyanmoy D (2001) Multi-objective optimization using evolutionary algorithms. England, Chichester

Unlocking New In-Situ Defect Detection Capabilities in Additive Manufacturing with Machine Learning and a Recoater-Based Imaging Architecture

Matteo Bugatti, Marco Grasso, and Bianca Maria Colosimo

Abstract Additive manufacturing (AM) has the potential to revolutionize the way products are designed and produced in a wide range of industries. However, ensuring the quality and reliability of AM parts remains a challenge, as defects can occur during the building process. In-situ monitoring is a promising approach for detecting and classifying these defects for in-process part qualification. In this paper, we present a novel approach for in-situ monitoring of laser powder bed fusion (LPBF) processes using a recoater-based imaging sensor and machine learning algorithms. The new sensor architecture is a recoater-mounted contact image sensor (CIS) and allows for high-resolution imaging of the build area during the recoating process, enabling the observation of a wide range of part and process-related defects. We demonstrate the effectiveness of using machine learning for image analysis on a series of experiments on a commercial AM system, showing significant improvements in defect detection accuracy compared to existing methods. Our results demonstrate the potential of the recoater-based sensor architecture for unlocking new capabilities for in-situ monitoring and quality control in powder bed-based AM processes.

Keywords Additive manufacturing · In-situ monitoring · Recoater-based imaging sensor

1 Introduction

Quality assurance of AM products is crucial to ensure functionality and safety of the products. Metal AM can suffer from a wide range of defects such as porosity, cracks, and inclusions. These defects are often generated during the AM process itself and it can be challenging to detect them in the final product. This is especially true when dealing with complex structures that are more difficult to inspect with

M. Bugatti (✉) · M. Grasso · B. M. Colosimo
Dipartimento Di Meccanica, Politecnico Di Milano, Via La Masa 1, 20156 Milano, MI, Italy
e-mail: matteo.bugatti@polimi.it

traditional non-destructive testing (NDT) methods [1]. Over the past several years, there has been a growing interest in in-situ monitoring of AM processes to detect and classify defects in real-time. This approach leverages the "openness" of the AM process, which allows for the observation of the build area during the process, and it is considered to have the potential to significantly reduce the cost of quality control and, in the future, improve the overall quality of AM parts via a combination of in-situ monitoring and process control.

A wide variety of monitoring techniques have been explored in the literature, both image (e.g. optical, thermal and x-ray imaging) and non-image based methods (e.g. acoustic emission and ultrasonic) [2]. However, most of these methods suffer from one or more of the following limitations: (i) low spatial resolution, (ii) small field of view or (iii) limited applicability to industrial AM processes. Optical imaging methods are among the most popular in-situ monitoring techniques for AM processes. Newer industrial machines are usually equipped with one external camera pointed at the build platform. The camera is used to take images of the printed area and of the surrounding powder bed throughout the build process. These images can be used to detect some powder bed inhomogeneities, such as incomplete spreading, powder streaking or recoater hopping. However, these methods are limited to detecting large-scale defects and are not suitable for smaller powder bed defects, such as contaminations. In addition, the low resolution does not allow to perform part reconstruction or detect small-scale defects that may appear on the top surface of the printed part (e.g., open pores, balling etc.).

To unlock the full potential of optical imaging for AM in-situ monitoring, it is necessary to combine high-resolution imaging with a field of view that is large enough to cover the entire build area. In a recent work [3], we demonstrated the implementation of a recoater-mounted contact image sensor (CIS) for in-situ monitoring of LPBF processes. The type of sensor, which is often used in other quality control applications, and its position in the build chamber offer several advantages over the traditional external camera. In addition to the large field of view and higher resolution, the CIS offers the ability to capture color images and, thanks to the integrated lighting system, provides a more homogeneous illumination across the scene. These two additional features contribute to significantly improve the image quality compared to external cameras. Other authors [4], using a similar architecture, have also demonstrated that by leveraging an additional feature of the sensor, i.e., the extremely short focal length, a pseudo height map can be reconstructed from the images. This allows to detect out-of-plane defects in the powder bed and on the printed parts, but the accuracy is limited and the "direction" of the deviation (e.g., whether the out-of-plane is a peak or a valley) cannot be determined.

In this paper, we explore the impact of this new sensor architecture on the performance of a machine learning algorithm for detecting dimensional and geometrical deviations in the printed part. A comparative study between the recoater-mounted CIS and the external camera is also presented to highlight differences and potential limitations of the two architectures.

2　Equipment and Experimental Setup

The case study investigated in this paper is a test print of a series of bridge samples printed with different support structures. The test print was performed on a commercial LPBF system (3D-NT) equipped with a recoater-mounted CIS and an external camera module. The specifications of the two sensors are summarized in Table 1.

The four samples were printed using the same process parameters reported in Table 2.

The only difference between the samples is the support strategy used. The bridge-like geometry was specifically designed to enhance the stress-induced deformation. Table 3 summarizes the main characteristics of the four support structures shown in Fig. 1.

The standard support strategy (Fig. 1a) serves as a baseline to compare against the other, increasingly weaker, support structures.

Table 1　Monitoring equipment

	CIS	Camera
Working distance (WD) [mm]	14	500
Resolution [µm/px]	21	100
Mode	Color	Mono
Depth	8-bit	8-bit

Table 2　Process parameters

Parameter	Value
Power [W]	200
Scan speed [mm/s]	1000
Hatch distance [µm]	90
Scan strategy	Hatching
Layer thickness [µm]	25
Build plate material	AlSi10Mg
Focal position f [mm]	0
Beam waist diameter D4σ [mm]	0.05

Table 3　Types of support structures

	Standard	Pillar 0.6	Pillar 0.3	Single line
Shape	Lattice wall	Pillar	Pillar	Lattice wall
Thickness/diameter [mm]	0.5	0.6	0.3	0.5
Distance btw. walls/pillars [mm]	5	5	5	–
Support-Part connection	Triangular	Rounded	Rounded	Triangular
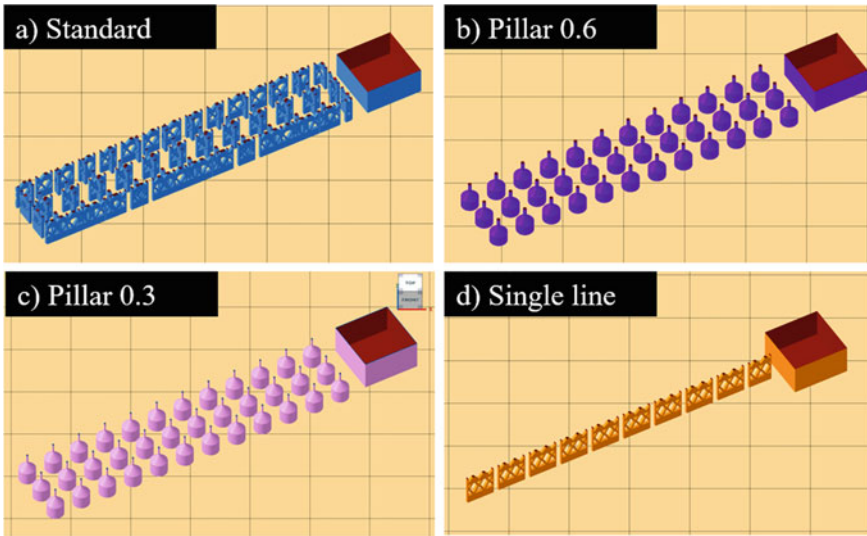
Fig. 1 Types of support structures

This experiment investigates the well-known trade-off between buildability and post-processing costs. Robust support structures make it easier to print the part, but they add complexity to the post-processing operations (i.e., support removal).

On the other hand, weaker support structures simplify the post-processing and increase the cost-effectiveness of production, but they are more likely to fail under residual stress load. If some supports fail, the printed part will lack fixed anchor points, which can lead to geometrical and dimensional deviations from the original design. Excessive deviations result in a part that is out of tolerance and must be scrapped, thus increasing the cost of production, and reducing the overall efficiency of the process.

In this scenario, the application of in-situ monitoring can be beneficial and allow to monitor the integrity of support structures to prevent the onset of critical deviations and stop the build process to prevent the production of a defective part and minimize waste.

To validate the results of the in-situ monitoring method developed in this work, the geometrical and dimensional deviations of the samples were measured ex-situ via CT-scan.

3 Methodology

The integrity of support structures can be monitored either directly or indirectly. Direct monitoring of the support structures consists in observing the support structures during the build process. Due to the typical size of the support stuctures, direct monitoring is only possible with high-resolution sensors, such as the recoater-mounted CIS.

The indirect way of monitoring the support structures consists in observing the behavior of the supported part during the build process. When the support fails under residual stress load, the supported part will start warping. As soon as the warping exceeds the powder bed thickness (typically less than 0.1 mm), the recoater will fail to spread the powder over the warped portion of the part and the part will remain exposed. The incomplete powder spreading can be observed in the layerwise images, and it can be used to infer the integrity of the support structures, or the lack of support structures altogether.

In the literature, there are several examples of algorithms capable of detecting defects associated to powder bed inohomogenities. For example, Zhang et al. [5], report they can detect height differences in each printed layer, while Zur Jacob-smuhlen et al. [6, 7] in two different studies specifically worked on super-elevated edges, and developed a method to classify them into critical and non-critical classes. Scime et al. [8, 9] developed a classifier based on deep convolutional neural networks to identify recoating defects, such as streaking, hopping and super-elevation.

In this work, a new method was developed to automatically detect part warping and other phenomena that affect the powder spreading using the in-situ images. The main steps of the algorithm are briefly outlined in the following:

1. *Pre-processing*: perspective and flat field correction.
2. *Masking*: the regions of interest (RoI) corresponding to each printed part at layer i are isolated in the corresponding post-deposition image using the nominal slice of layer i as a reference.
3. *Empirical probability density function (PDF)*: the histogram of the region of interest was extracted.
4. *Dimensionality reduction*: the simplicial functional principal component analysis (SFPCA) is performed to find the directions along which the dataset displays the maximum variability. The first K principal components are retained based on the percentage of explained variability.
5. *Scores calculation*: the first K scores are then used to analyze the dataset.

In a preliminary step, flat field and perspective corrections (homography) are applied to the layerwise images obtained from the recoater-mounted CIS and the external camera to get a top-down view of the build area, similar to the nominal layerwise images. The images are then registered and cropped to match the size of the corresponding nominal slice and the position of the parts. After registration, the images are smoothed and the pixel intensity is modified to correct for broad illumination inhomogeneities.

Compared to the external camera images (Fig. 2), the unprocessed CIS images (Fig. 3) already provide a close to perfect top-down view of the build platform. Only minor corrections must be performed to adjust for alignment errors when mounting the CIS on the recoater. This results in a final image that is less distorted and higher quality.

After the preliminary steps and the image pre-processing is complete, the masking step is performed (Fig. 4). This operation makes the method completely shape-agnostic and exploits the nominal slice shape as prior knowledge about the area where to look for powder bed inhomogeneity anomalies. A "dilated" version of the
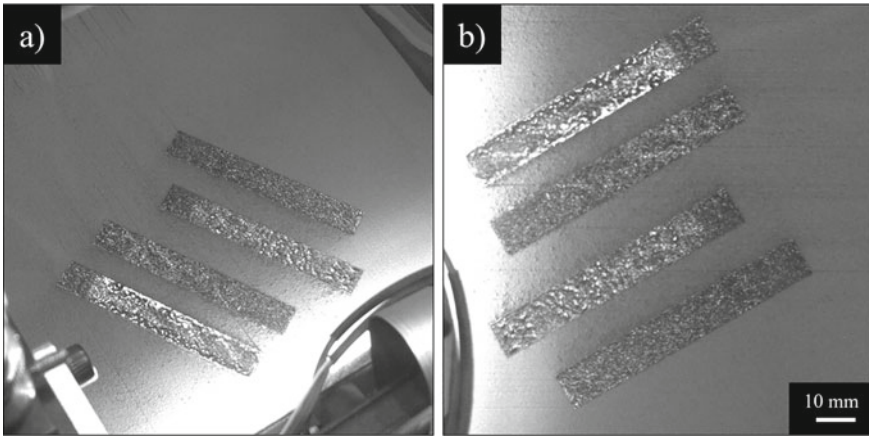
Fig. 2 Homography operation on external camera images, before (**a**) and after (**b**)
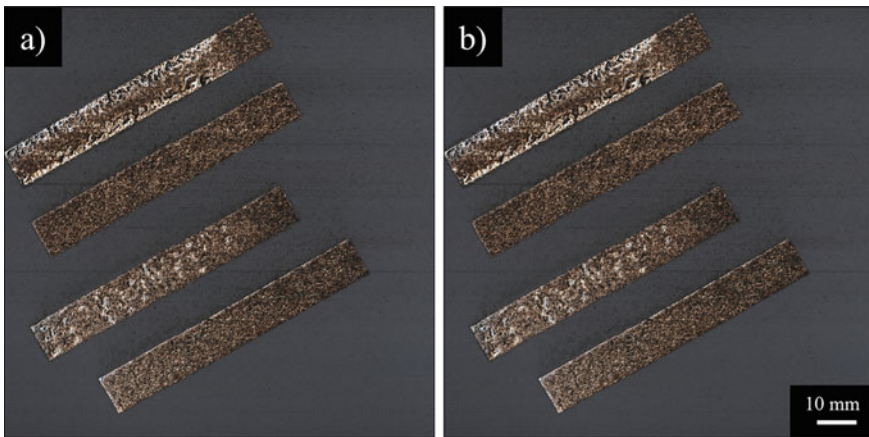
Fig. 3 Perspective correction on CIS images, before (**a**) and after (**b**). Almost no correction is required in this case
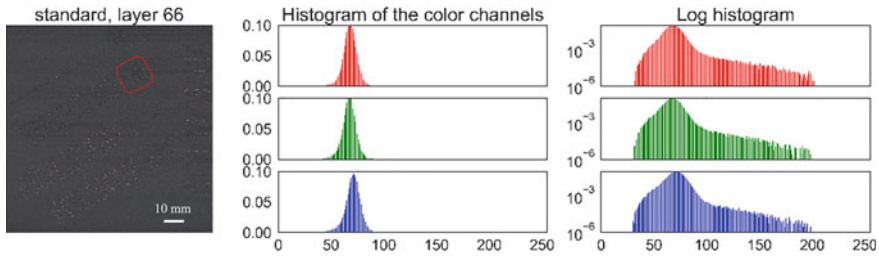
Fig. 4 Extraction of the empirical PDF function from the ROI

mask of each part is applied to make sure to include some of the surrounding powder for reference.

The extraction of the empirical PDF is then performed for each individual masked area (i.e., each individual part). The intuition behind this approach is that functional data that represent the empirical PDF will differ when the ROI under analysis contains only an homogeneous powder layer (i.e., in control condition) or powder and a portion of the part (i.e., out-of-control condition).

However, dealing with functional datasets can be complex due to the intrinsic high dimensionality (Fig. 4). For this reason, a dimensionality reduction step was implemented. Simplicial functional principal component analysis (SFPCA) [10] was used for this task. SFPCA is a specific counterpart of the traditional FPCA which is performed within the space of density functions (Bayes space B2), and allows to obtain a high-quality approximation of PDFs, while preserving their constraints. This method was originally developed by Menafoglio et al. [11] to monitor the quality of metal foams from the empirical PDF of specific variables of interest. In this work, the same approach SFPCA-based was used to reduce the dimensionality of the dataset.

The SFPCA procedure finds the directions in B^2 along which the variability of the dataset is maximized. Using the associated eigenvalues, ρ_i, computed from the SFPCA, it is possible to identify the minimum number, K, of SFPCs needed to retain a specific amount of the total variability, according to Eq. (1):

$$\sum\nolimits_{i=1}^{K} \rho_i \Big/ \sum\nolimits_{i=1}^{\infty} \rho_i \tag{1}$$

The first K scores, i.e., the projection of the original empirical PDFs along the first K principal directions, were then used to study the problem in a low dimensional space with respect to that of the original functional dataset.

4 Discussion of Results

Two main types of defects were found during the print, i.e., the presence of warping (Fig. 5) or incomplete recoating of the part (Fig. 6).
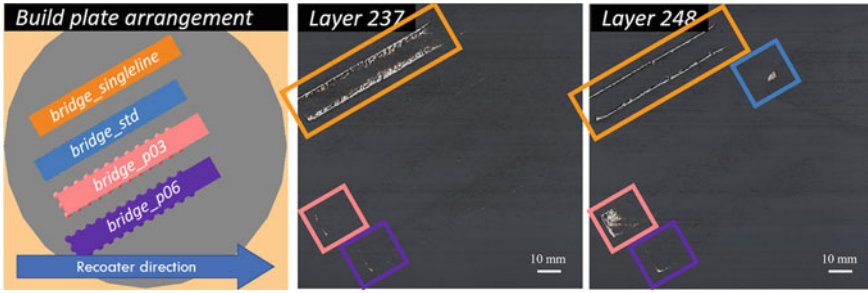
Fig. 5 Post-deposition images showing different stages of the warping defect in the sample with single line support
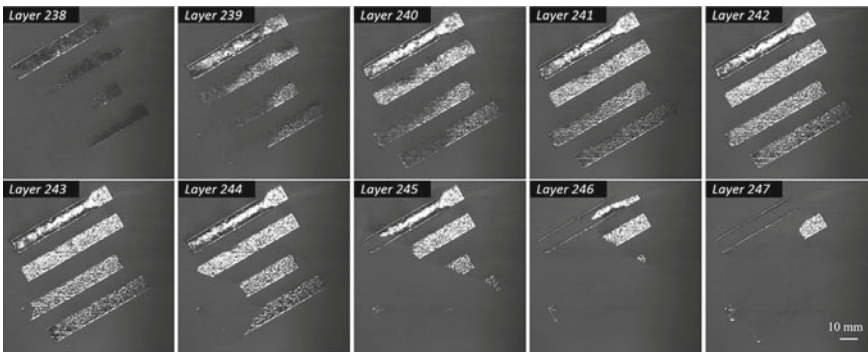
Fig. 6 Incomplete spreading due to insufficient powder feed (layer 238–247)

The detected anomalies match very closely the defects observed in the CT-scan (Figs. 7 and 8).

The samples printed with the standard and the pillar 0.6 mm support structures (Fig. 7a, b) showed no significant deviations from the nominal shape. All the supports were intact at the end of the print, which confirms that the support structures were robust enough to withstand the residual stress load.

Significant warping was observed immediately after printing the first overhang layers of the least supported sample, i.e., the bridge with single line supports. The lack of anchor points on the sides of the sample resulted in a visible deformation and consequent deviation from the nominal shape.

The bridge with 0.3 mm pillar supports showed an intermediate behavior. The supports were able to withstand the residual stress load for the first few layers, after which the supports subjected to the highest load (i.e., near the edge) started to fail. The final deformation of the bridge exceeds 2 mm near its most extreme region.

The incomplete spreading, on the other hand, led to a thicker layer of powder being deposited when powder supply was restored. Since the energy density was not sufficient to fully melt such a thick layer of powder, gaps and delaminations are
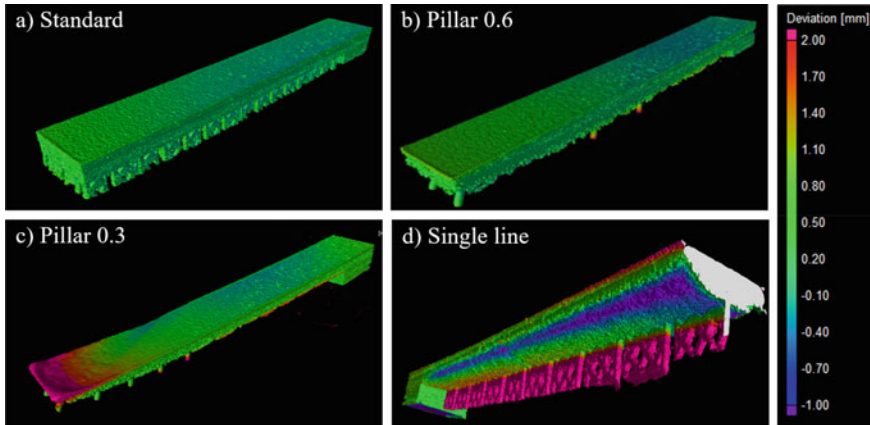
Fig. 7 CT-scan of the bridge samples. The most supported samples, i.e., standard (**a**) and pillar 0.6 (**b**), show little to no deformation, unlike the least supported ones, i.e., pillar 0.3 (**c**) and single line (**d**)
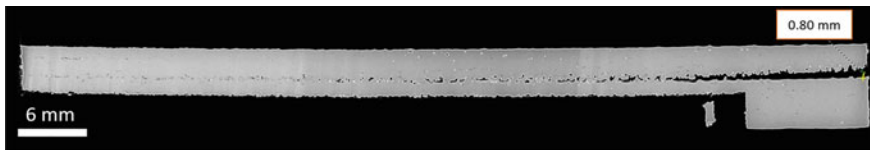
Fig. 8 Lack-of-fusion and delamination in the standard supports sample due to incomplete spreading from layer 238 to 247

observed at that specific layer height due to lack-of-fusion and incomplete bonding between the new layer and the existing part (Fig. 8).

When large deviations occur, i.e., an extended region of the part is not covered by the new powder layer, the empirical PDFs show a significant departure from the standard unimodal distribution that is expected in the histogram of a well recoated region. The empirical PDFs extracted from two different groups of images, in-control (from layer 50–70) and out-of-control (from layer 230–250) are show in Fig. 9.

After applying the SFPCA procedure and computing the eigenvalues and eigenfunctions, it is possible to see that the only first 2 SFPCs are necessary to retain almost 90% of the total variability (Fig. 10).

The scores for the two sets of observations (in-control and out-of-control) are shown in Fig. 11. Two well separated clusters are clearly visible in the scatterplot. This means that, just by using the first 2 scores of the SFPCA, in-control and out-of-control PDFs can be immediately identified.

The same approach was tested on the external camera images, but the results were not on par with the CIS (Fig. 12). The separation between in-control and out-of-control clusters is not as clear and some out-of-control observations fall close to the in-control ones.
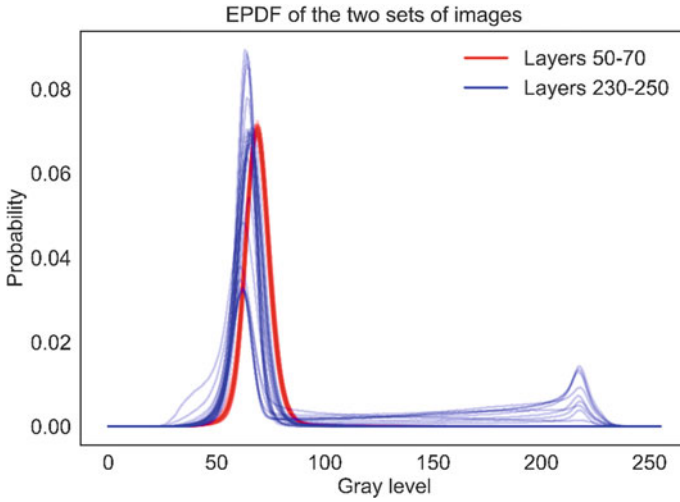
Fig. 9 Comparison between the in-control (layer 50–70) and out-of-control (layer 230–250) empirical PDFs (CIS images) of the standard supports sample
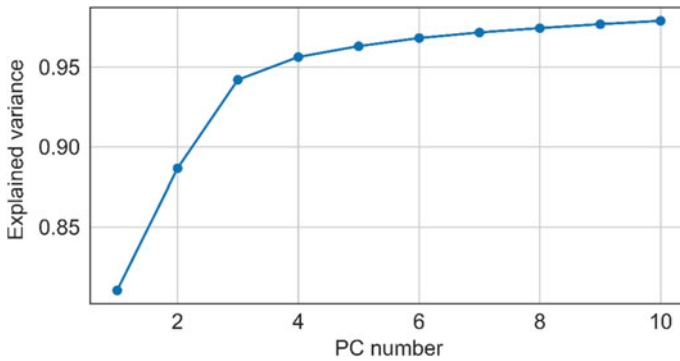
Fig. 10 Explained variance of each PC

Despite the layers under analysis being the exact same, the difference in performance is most probably related to the lower quality images acquired by the external camera. The empirical PDFs extracted from the camera images (Fig. 13) show a noisier distribution, even when considering only the in-control conditions. This is likely the root cause of the lower precision of the external camera at detecting shifts in the distribution using principal components scores.

A direct comparison between the images of the two sensors is shown in Fig. 14. The CIS allows to inspect the part at an unprecedented resolution, giving the ability to observe surface patterns that are not visible to the external camera. The images of the recoater-mounted CIS provide a better contrast between the powder and the
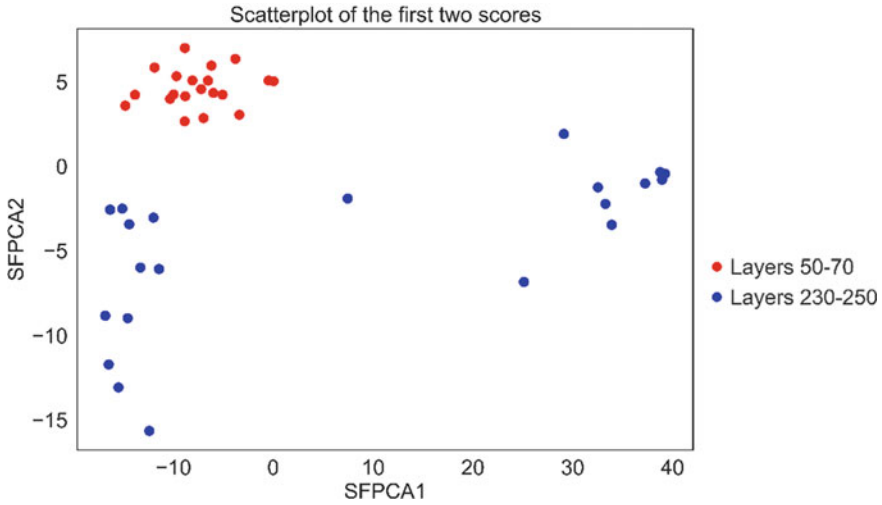
Fig. 11 First 2 scores of the in-control and out-of-control empirical PDFs extracted from the CIS images
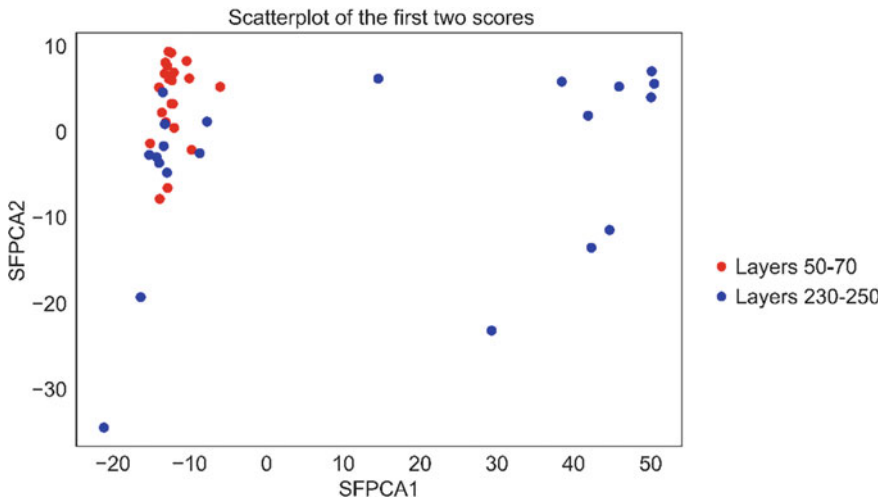
Fig. 12 First 2 scores of the in-control and out-of-control empirical PDFs extracted from the external camera images

printed part, and three distinct types of surface patterns can be observed, depending on the phase of the powder, i.e., (i) fully melted powder, (ii) partially melted powder, and (iii) unmelted powder. On the other hand, the images of the external camera show a more uniform surface, with no visible differences between some surface pattern (e.g., unmelted and partially melted powder).
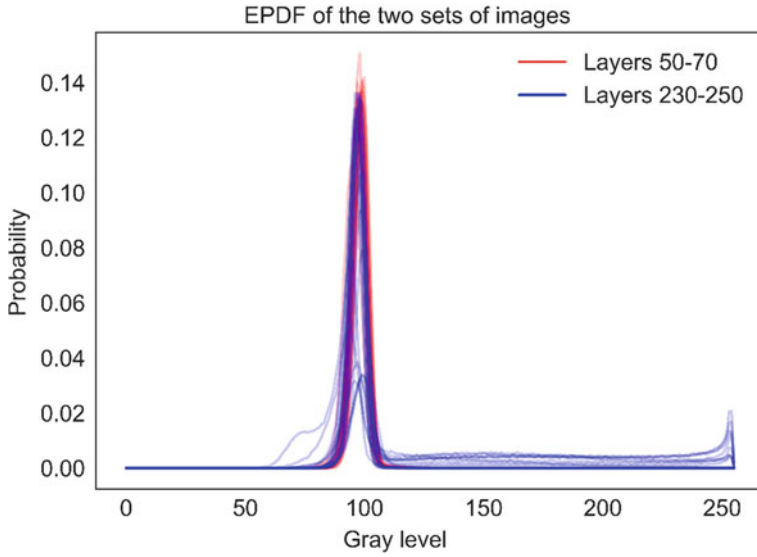
Fig. 13 Comparison between the in-control (layer 50–70) and out-of-control (layer 230–250) empirical PDFs (external camera images) of the standard supports sample
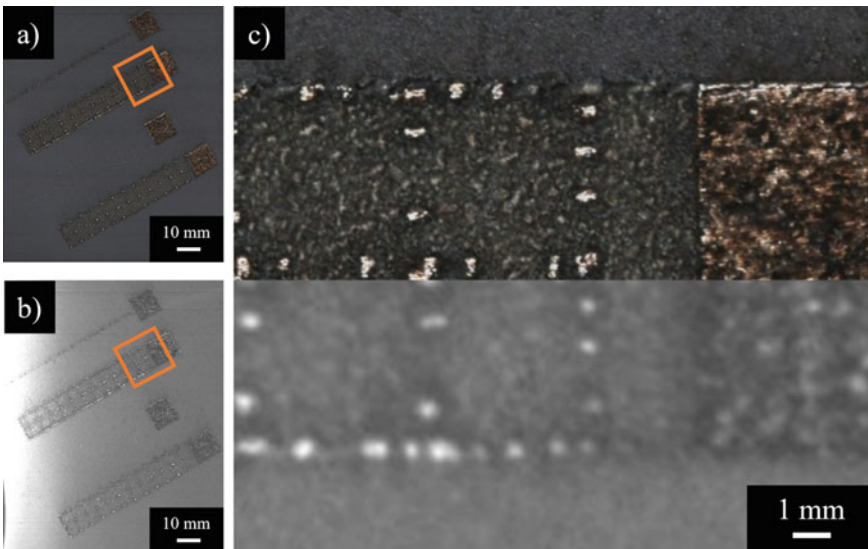
Fig. 14 Image quality comparison. Full images from the CIS (**a**) and the external camera (**b**) and side by side comparison (**c**) (CIS on the top, and camera on the bottom)

5 Conclusion and Future Work

In this paper, we have presented a comparative study between the recoater-mounted CIS and the external camera for in-situ monitoring of LPBF processes. The results of this study show that the recoater-mounted CIS is a promising sensor architecture for in-situ monitoring of LPBF processes and it can be used to detect the onset of critical deviations in the printed part. Compared to the external camera, the recoater-mounted CIS is more precise at detecting critical deviations in the image composition that are not as clear to the external camera. This translates to a quicker detection of deviations before they exceed the tolerance limits, and the part needs to be scrapped. This higher precision can be used to act earlier on the process and, when possible, adjust the printing strategy to recover from the deviation and save the part rather than stopping its production altogether.

This study primarily concentrated on identifying large-scale deviations in the components. However, the high-resolution images obtained by the recoater-mounted CIS can be utilized to detect small-scale defects by implementing the empirical PDF-based technique on smaller areas of the powder bed. Future research will focus on detecting other types of defects, such as spatters and contamination, which are not visible to conventional inspection methods but are known to cause the development of porosity and inclusions in the finished product.

References

1. Colosimo BM, Huang Q, Dasgupta T, Tsung F (2018) Opportunities and challenges of quality engineering for additive manufacturing. J Qual Technol 50(3):233–252
2. Grasso M, Remani A, Dickins A, Colosimo BM, Leach RK (2021) In-situ measurement and monitoring methods for metal powder bed fusion: an updated review. Meas Sci Technol 32(11):112001
3. Bugatti M, Colosimo BM (2022) The intelligent recoater: a new solution for in-situ monitoring of geometric and surface defects in powder bed fusion. Addit Manuf Lett 3:100048
4. Seita M (2019) A high-resolution and large field-of-view scanner for in-line characterization of powder bed defects during additive manufacturing. Mater Des 164:107562
5. Zhang B, Ziegert J, Farahi F, Davies A (2016) In situ surface topography of laser powder bed fusion using fringe projection. Addit Manuf 12:100–107. https://doi.org/10.1016/j.addma.2016.08.001
6. Zur Jacobsmuhlen J, Kleszczynski S, Schneider D, Witt G (2013) High resolution imaging for inspection of Laser Beam melting systems. In: 2013 IEEE international instrumentation and measurement technology conference, pp 707–712. https://doi.org/10.1109/I2MTC.2013.6555507.
7. Zur Jacobsmuhlen J, Kleszczynski S, Witt G, Merhof D (2015) Detection of elevated regions in surface images from laser beam melting processes. In: IECON 2015-41st annual conference of the ieee industrial electronics society, pp 1270–1275. https://doi.org/10.1109/IECON.2015.7392275
8. Scime L, Beuth J (2018) A multi-scale convolutional neural network for autonomous anomaly detection and classification in a laser powder bed fusion additive manufacturing process. Addit Manuf 24:273–286

9. Scime L, Siddel D, Baird S, Paquit V (2020) Layer-wise anomaly detection and classification for powder bed additive manufacturing processes: a machine-agnostic algorithm for real-time pixel-wise semantic segmentation. Addit Manuf 36:101453
10. Hron K, Menafoglio A, Templ M, Hrůzová K, Filzmoser P (2016) Simplicial principal component analysis for density functions in Bayes spaces. Comput Stat Data Anal 94:330–350
11. Menafoglio A, Grasso M, Secchi P, Colosimo BM (2018) Profile monitoring of probability density functions via simplicial functional PCA with application to image data. Technometrics 60(4):497–510

Preliminary Study on the Feasibility of Electrically Assisted Direct Joining of Titanium and PEEK

Silvia Ilaria Scipioni, Alfonso Paoletti, and Francesco Lambiase

Abstract The present study introduces an electrically assisted direct joining process for hybrid metal-polymer connections. The process consists of the adoption of an electrical current to heat the metal component, which is pressed against a thermoplastic polymer. Titanium grade 2 and Polyetheretherketone were selected for the preliminary testing campaign. An instrumented equipment was developed to control and measure the main process parameters such as the voltage and the current during the joining process. The investigation was carried out to determine the feasibility of the process. To this end, preliminary experimental tests were performed by varying the main process parameters. The metal surface's laser texturing was performed before joining to promote micromechanical interlocking. Quality assessment of the connections was carried out through single lap shear tests and fracture surface analysis.

Keywords Resistance welding · Polymers · Hybrid joints

1 Introduction

It is increasingly common in great many fields, such as transportation, biomedical and structural [1], to use multi-material structures, composed by polymers (or reinforced polymers) and metals. Even though joining such different materials brings considerable advantages e.g. reduction of structures' weight, it also involves different issues from a processing perspective. Indeed, metals and polymers, show different physical, mechanical, and thermal properties and this can introduce some constraints and limitations.

Traditionally, mechanical fastening or adhesive bonding have been used to join dissimilar materials. These processes are characterized by significant problems in terms of durability, energy efficiency, and environmental impact due to the use

S. I. Scipioni (✉) · A. Paoletti · F. Lambiase
Department of Industrial and Information Engineering and Economics, University of L'Aquila, Via G. Gronchi 18, Zona Industriale Di Pile, 67100 L'Aquila, AQ, Italy
e-mail: silviailaria.scipioni@graduate.univaq.it

of chemicals. Regarding productivity, both processes require pre or post-treatment phases: in mechanical joining, drilling is required, while in adhesive bonding, surface pre-treatment and curing times are often needed. Then, concerning mechanical properties, mechanical fastening shows high-stress concentrations and the requirement of external components, which increase weight and costs. Therefore, given the great demand from different manufacturing fields, severe efforts are being expended to overcome the limitations of traditional joining processes. For these reasons, different joining processes have been developed in recent years. Among them, heat-assisted joining processes, such as laser-assisted joining (LAJ) [2], friction-assisted joining (FAJ) [3], friction spot joining [4], and ultrasonic joining [5–7], have been greatly used to join dissimilar materials.

These processes involve two different steps to make the joining occur: heating the interface and applying external pressure to create the bonding, producing a tight connection between the substrates. In the LAJ process, the transparency of the polymer at the laser wavelength is exploited to directly heat the interface. The joining mechanisms achieved by these processes can be chemical (e.g. CO bonds), physical (Van der Waals forces), or mechanical. In addition, the process has high efficiency and reduced joining times, due to the use of confined heat sources. These processes, which have been subjected to recent studies, have also demonstrated their feasibility in bonds where composites with thermoset or thermoplastic matrices [8, 9] and engineering plastics (such as PEEK [10]) were used.

On the other hand, in the FAJ process, the upper material is metallic. A rotating tool is plunged into the top face and it is due to the rotation and vertical force applied by the tool that the joint is generated. Several pretreatments exist to increase the bond strength [11], including anodization of the metal substrate [12–14], grafting [15], formation of macroscopic [16], and microscopic structures on the metal substrate [17]. Such pretreatments promote the formation of CO bonds and the increase of mechanical interlocking. To reduce the formation of porosity [18], which can damage the joint formation, ultrasonic systems can be adopted [19].

The joint formation is strongly influenced by the thermal and mechanical characteristics of the substrates. Currently, only a few studies have been conducted to investigate the possibility of joining techno-polymers. In [20] the feasibility of joining PEEK and AA5053 aluminum alloy sheets was investigated, demonstrating how it is possible to obtain high mechanical strength, with a maximum shear strength of 47 MPa.

In the present study, the possibility of joining titanium and PEEK was investigated; these materials are mostly employed in various sectors, including aeronautics, aerospace, and biomedical, owing to their biocompatibility and high strength/weight ratio. The joint between titanium and PEEK was produced through an electrically assisted direct joining process. To this end, prototypal equipment was developed by modifying an existing resistance spot welder machine. The machine was modified to be controlled by an external interface by remotely controlling proportional relays connected to a commercial IO board and a LabVIEW program.

Preliminary experimental tests were conducted using a thermal imaging camera to observe the temperature trend during the process. This enabled the identification of

a suitable processing window to perform preliminary joining tests. Therefore, some joining tests were performed with the aim of determining the main characteristics of the joints. Mechanical characterization and fracture surface morphology were carried out on the joints produced to perform a quality assessment.

2 Electrically Assisted Direct Joining

Electrically assisted direct joining of dissimilar material such as metals and thermoplastics (or reinforced thermoplastics) is a thermomechanical joining process [21] which exploits the Joule's heating effect through a material as a heating medium. To this end, an overlapping configuration can be used, as schematized in Fig. 1. During the process, the electrodes come into contact with the upper (conductive) material, which is rapidly heated through the Joule's effect. Thus, the temperature at the metal-polymer interface also steeply rises leading to joint formation. After the current flow, the metal rapidly cools down leading to joint consolidation. The joint formation is due to different joining mechanisms, which depend on the materials involved, the surface morphology, the pressure, and the temperature distribution. The joining mechanisms include the formation of physical and chemical bonding as well as mechanical microinterlocking [22].

Compared to the other thermomechanical joining processes, electrically assisted joining provides different advantages. Indeed, it does not produce beam reflections and it is not affected by laser radiation absorption such as laser-assisted joining. During the joining operation, the electrodes are in tight contact with the components; thus, the process is not characterized by movable tools or high processing forces (such as friction-assisted joining). In addition, electrically assisted direct joining can be easily integrated within existing assembly lines since it requires minor machine modifications. Since the process is based on Joule's effect, electrically assisted direct joining is best suited for metals with relatively low electrical conductivity, such as steel or titanium alloys.

3 Materials and Methods

3.1 Experimental Prototypal Apparatus

A prototypal apparatus was developed to conduct experimental tests (Fig. 2). A common spot welder machine was modified to integrate into an Industry 4.0 context and have better control of the process parameters as well as higher process reliability. The original machine was modified in order to be controlled remotely and to perform online current and voltage measurements by dynamic control of the current supplied during the process. The proposed system has been enriched with an Open
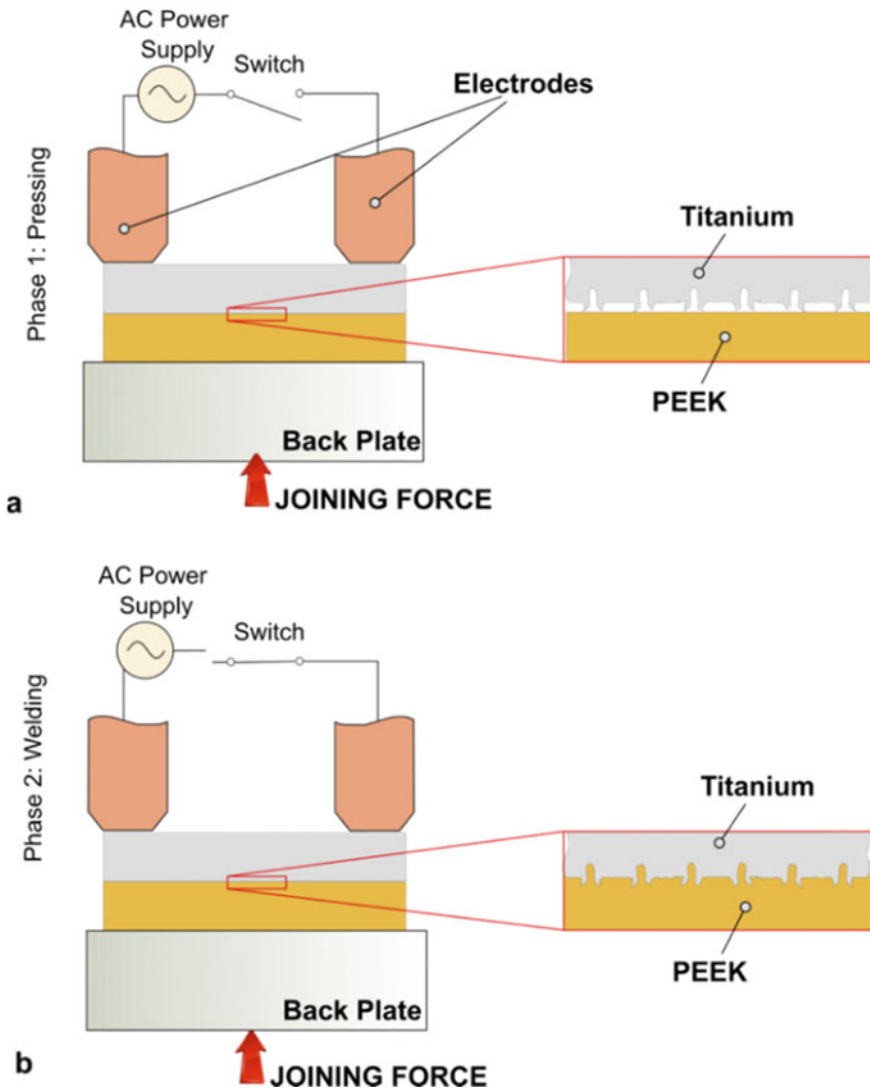
Fig. 1 Main phases of electrically assisted direct joining

Platform Communications Unified Architecture (OPC-UA) interface that enables data exchange with other systems both hardware (i.e. P. L. C., Industrial P.C., etc..) and software (i.e. S. C. A. D. A., ad-hoc software, etc.). The entire system was implemented using LabVIEW software from National Instruments.

An USB-6002 board from national Instruments developed by LabVIEW was used to convert the manually controlled welding machine to an automatically controlled one. The board is a multifunction DAQ that allows for exclusive control of the welding

Fig. 2 Experimental equipment and the clamping equipment
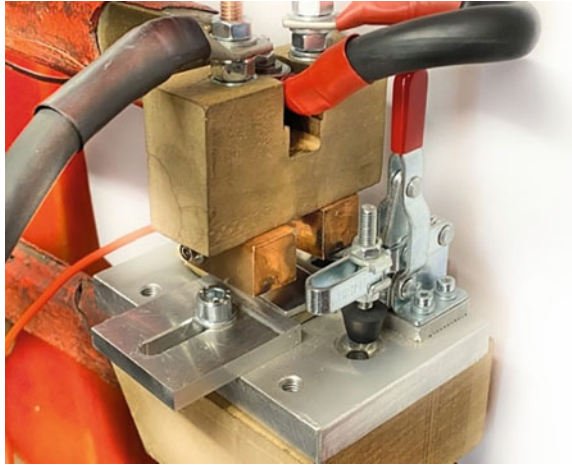
voltage and current. The welding voltage and current are controlled by a Crydom P. M. P. series solid-state relay, designed specifically for industrial power applications. Through this relay, it is possible to bias the waveform of the voltage input to the machine based on an analog input between 0 and 5 V.

National Instruments' USB-6002 board has USB connections for the computer interface and measures voltage and current via analog inputs connected to sensors placed by creating threads on the welding electrodes (for voltage measurement) and on the copper-clad brass bar (for current measurement), which was used as a shunt (Fig. 3).

The integration of the old machine archetype with the new control system was aimed at developing a system capable of different control strategies including fixed "aperture" of the relays, constant voltage, and constant current. Indeed, during the welding procedures, the materials undergo significant temperature rise that determines a proportional variation of the electrical resistivity of the material. Thus, during the joining process, when the fixed relay aperture was adopted, both the current and the voltage may change, depending on the variation of material resistivity.

3.2   Software Development for Measurement and Control

The adopted USB-6002 board is compatible with National Instruments' LabVIEW programming software, this enables to control the proportional relays and measure the main processing signals (voltage and current) during the joining process. Welding voltage and current are controlled by a solid-state relay, which is much more efficient, durable, and reliable than a mechanical relay since it contains only fixed parts. These relays are commonly used in all industrial processes that require precise and reliable

handling. Such relays allow the waveform of the machine input voltage to be partialized according to an analog input between 0 and 5 V. In the control screen, shown in Fig. 4, it is possible to enter a voltage value ranging from 0 to 100% of full-scale (almsot 2.1 V). The National Instruments board generates the signal and measures current, voltage, energy and power during joint formation as shown in Fig. 5.

The general scheme of the system consists of several elements:

- An interface that allows the system to receive control and configuration commands, shown in Fig. 4;
- A central system that manages the control and measurement instrument;
- A driver that interfaces the central system with the input/output board;
- Two servers where welding profiles and collected measurement data are stored.

Each weld consists of five distinct phases, corresponding to a different row within the LabView program. These phases are: pressing time, rise up time, welding time, fall time, releasing time. Each joining process is therefore identifiable with an ennuple in which the time intervals of the waveform and the maximum value to be achieved are represented. Within the database, each weld is contained within a row uniquely identified by a private key. The database specifically stores the following values:
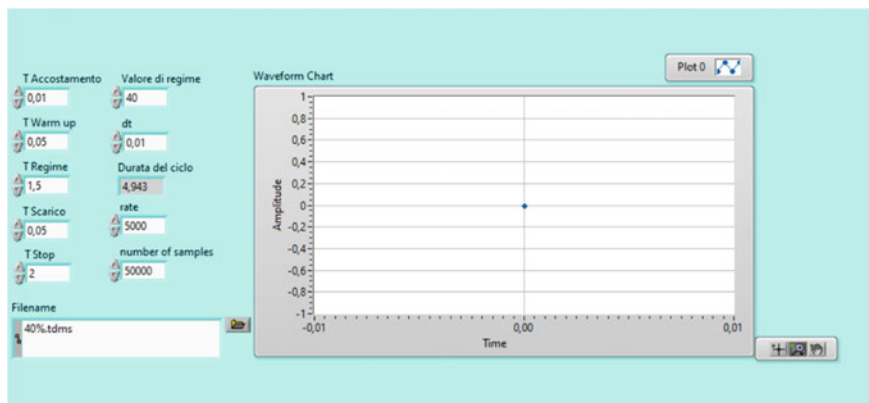
Fig. 4 LabVIEW control panel
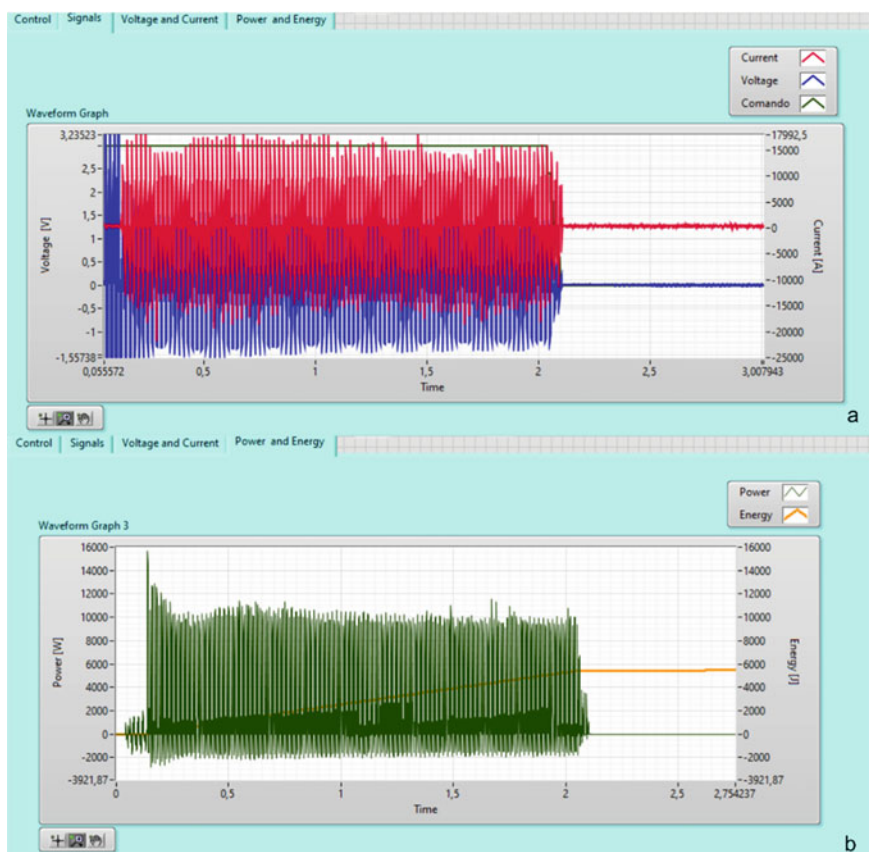
Fig. 5 Current, tension, energy and power during joining

1. "Amplitude": it is the field that describes the maximum value generated by the National Instruments board. The value is expressed in percent from 0 to 100 of the maximum input value;
2. "Pressing Time": is the time when the electrodes go down but there is still no power;
3. "Rise Up Time" is the time interval of the ramp when ramping from the value 0% to the value set in the amplitude field;
4. "Welding Time": is the time interval in which the system holds the output value constant at the value specified in the amplitude field;
5. "Fall Time": is the time interval of the ramp when it goes from the value set in the amplitude field to the value set at 0%;
6. "Releasing Time": is the interval in which the system holds the output value at 0% before notifying the end of the welding cycle.

A welding profile can be defined as a sequence of welding processes by joining different welding types. The values of current and voltage recorded during the joints are saved in a file system. The files are organized and managed by another database which will track the performed welding profile, welding times, maximum and minimum power values recorded, and link this information with the file containing the performed recordings.

3.3 Specimen Preparation

Rolled sheets of 2 mm of thickness of titanium grade 2 were joined to polyetheretherketone (PEEK) supplied by Victrex (PEEK 450 G) with 5 mm of thickness. PEEK (polyetheretherketone) is a semi-crystalline thermoplastic with a service temperature of up to 250 °C and a melting temperature of 343 °C.

The main mechanical characteristics of the materials were identified through tensile tests which were conducted complying with the ASTM standards E08 [23] for the titanium and D638 for the PEEK E08 [24]. Besides, physical tests were conducted on the PEEK with the aim of determining the characteristic temperatures of the polymer. Thermogravimetric tests were conducted to investigate the decomposition temperature of the PEEK material by means of a machine model L81/1550 by LINSEIS. The tests were conducted at the highest heating rate allowed by the machine 40 °C/min. The main mechanical and thermal properties of the materials are summarized in Table 1.

Laser texturing was performed on the titanium surface before joining. To this end, a pulsed 30 W fiber laser YLP-RA30-1-50-20-20 by IPG was adopted. Laser texturing was performed under the following conditions: power: 30 W, pulse frequency 30 kHz, scanning speed 1.0 m/s, the distance between consecutive scans: 0.3 mm, and 20 repetitions. Such texturing conditions were selected on the bases of preliminary experiments. A fine laser texturing optimization was behind the scope of the present paper.

Table 1 Mechanical and thermal parameters of materials

Material	Titanium	PEEK
Young modulus [GPa]	120	4
Yield strength, $\sigma_{y0.2}$ [MPa]	394	–
Tensile strength, σ_{max} [MPa]	450	98
Compressive strength [MPa]	–	125
Elongation at ropture [%]	20	45
Melting temperature [°C]	1670	343
Thermal decomposition temperature [°C]	–	520

3.4 Joining Procedure

Overlap joining experiments were performed by using the abovementioned proto-typal machine. The tests were conducted using different values of the amplitude in a range between 20 and 80% of and the current value; welding time duration has been fixed for each test at 1 s.

In these preliminary tests, other process conditions such as the rise-up time, the fall time, and the releasing time were kept fixed at 0.5, 0.5 and 0.5 s respectively. Figure 6 shows the current trend during the above-described steps of the welding process.

The electrode force P was determined [25] by Eq. 1.

$$P = 2.5 \cdot t \cdot \sqrt{\frac{\sigma_t}{300}} \tag{1}$$
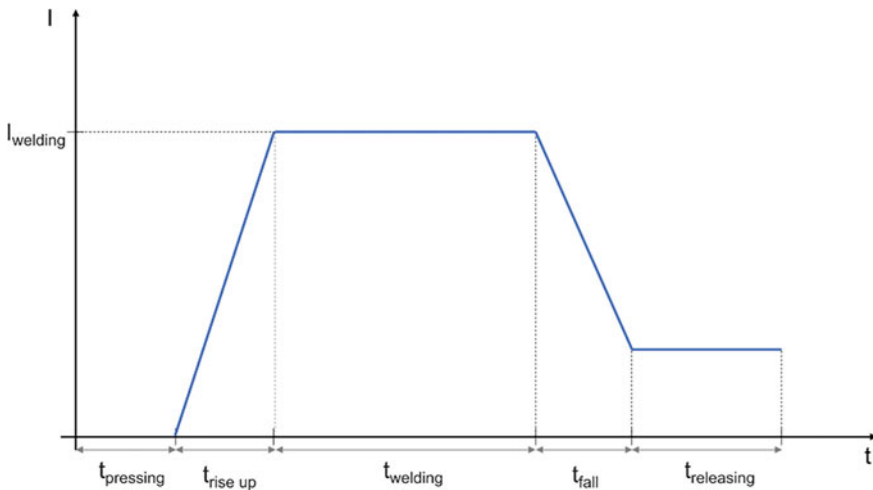
Fig. 6 Current steps during EAJ process

where t represents the thickness in mm and σ_t represents the tensile strength in MPa. The weaker material (PEEK) was considered; thus, the electrode force was 7.2 N. The distance between the electrodes was 8 mm.

3.5 *IR Thermography*

Infrared (IR) measurements were performed to determine the temperature variation during the joining experiments. This also enabled us to determine a suitable set of process conditions that enabled us to avoid excessive temperature rise. Excessive temperature (above 520 °C) potentially leads to thermal degradation of the polymer. Besides, titanium is a highly reactive material; thus, a temperature above 600 °C would easily lead to the formation of sparks and flames.

To this end, an IR thermal camera model T1020 by Flir was used during the experiments. This IR camera is characterized by a maximum acquisition rate of 50 Hz and a maximum measurable temperature of 1500 °C. The IR camera was placed at 0.3 m from the sample at an inclination angle of 30°. The surface emissivity of the titanium was set to 0.4. A picture of the setup is reported in Fig. 7.

Fig. 7 Picture of the IR camera positioned over the equipment for temperature measurement

Fig. 8 Schematic of the sample used for mechanical characterization (single lap shear tests)
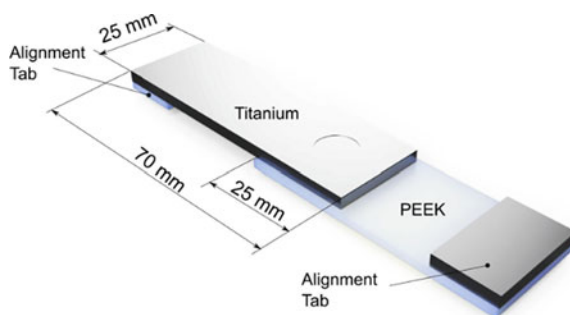
3.6   Mechanical Testing and Fracture Surface Analysis

Mechanical characterization tests were conducted to perform a preliminary analysis of the influence of the process parameters on the quality of the joints. To this end, single lap shear tests were conducted. The sample used in the tests, along with the main sample dimensions, is schematized in Fig. 8

The tests were conducted under quasistatic conditions, using a universal testing machine model C43.504 by MTS at 2 mm/min of traverse speed. For each process condition, the tests were replicated three times. After mechanical tests, optical microscopy analysis was conducted on the fractured surfaces to determine the bonding area and to better understand the failure conditions of the specimens. To this end, a stereoscope model M205 by LEICA was used along with a 3D surface reconstruction software.

4   Results

4.1   Temperature Analysis and Control of Process Conditions

During the EAJ process, the quality of the joint depends largely on the penetration of metal teeth into the polymeric material as well as the presence of porosities and eventually thermal degradation.

These phenomena strictly depend on the processing temperature. Figure 9 shows the IR temperature map recorded during the electrically assisted direct joining. The temperature is measured over the titanium sheet surface.

After the temperature acquisitions, a rectangular region of Interest (ROI) was placed over the titanium surface. Then, for each frame, the mean temperature over the ROI was calculated. This enables to determine the variation of the temperature history with time. Figure 10 shows the temperature variation recorded during preliminary joining tests conducted under different processing conditions. As can be observed, the variation of the current set by the developed interface enables to determine severe
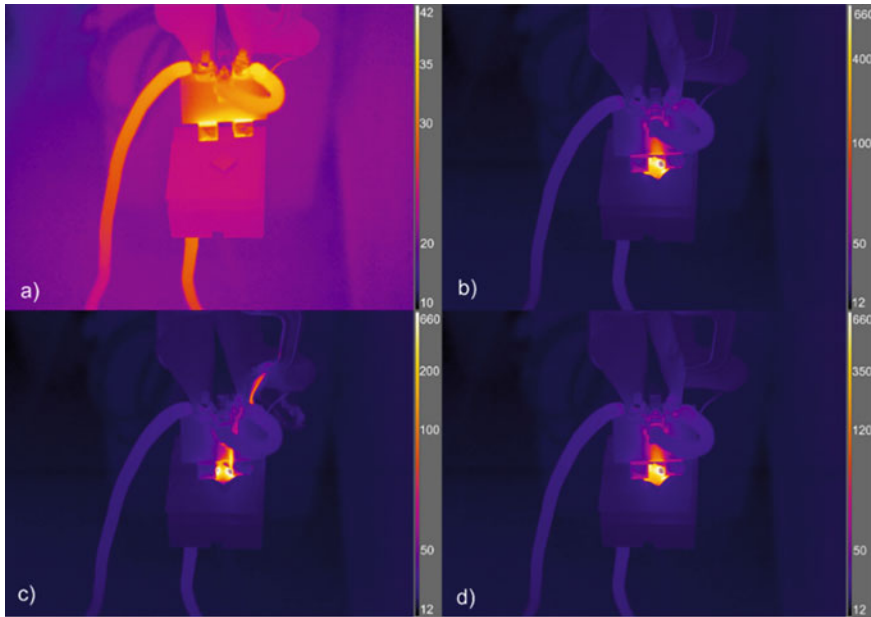
Fig. 9 IR temperature map after **a** 0 s, **b** 0.5 s, **c** 1 s and **d** 1.5 s (showing flame development)

temperature changes in a few seconds. The tests conducted at 20 and 40% of the amplitude did not generate enough heating for the joint to be successful. Indeed, as shown in Fig. 10, the temperature reached for the yellow curve is lower than 100 °C. The best conditions, instead, were performed at 60% of the amplitude. Under this condition, the joining occurred, in agreement with previous findings reported in [26] which indicated that the minimum temperature for joining PEEK through thermomechanical joining should be at least 300 °C, but still below the degradation temperature of the PEEK (520 °C).

The test conducted at 80% of the amplitude generated temperature above 600 °C, leading to the degradation of PEEK. Figure 9 shows the temperature map during the EAJ process at an amplitude of 80%; as can be observed in Fig. 9c, the temperature reached led to the develop of flames. Considering the phenomena occurred during the test with 80% of the amplitude, in this discussion, the trends of temperature and other electrical quantities of interest related to the test conducted with maximum amplitude were not included. the adoption of still higher value of voltage (100%) resulted in complete degradation of PEEK. During the tests performed the values of electrical parameters of interest were recorded and analyzed. Figure 11 shows the trend of current, voltage, energy and power during Electrically Assisted Direct Joining process. Voltage, energy and power showed a quasi-linear increasing trend with the increase in amplitude, as showed also in Fig. 12. On the other hand, for the current, the test performed with an amplitude of 80% showed not higher values than the others. This was due to the bad contact between the electrode and the upper

Fig. 10 Temperature variation during preliminary joining tests
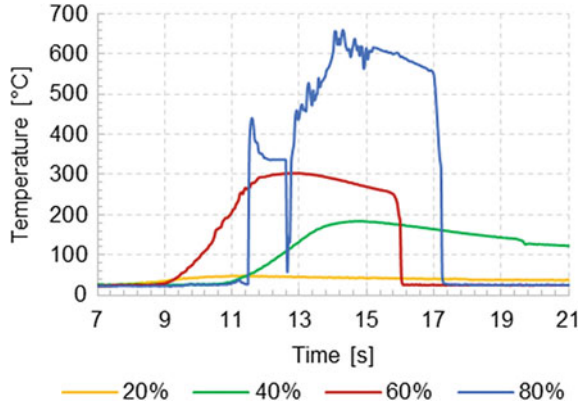
surface of the titanium sheet. By reducing the contact area, the resistance increased; the value of the voltage, instead, was imposed by proportional relays.
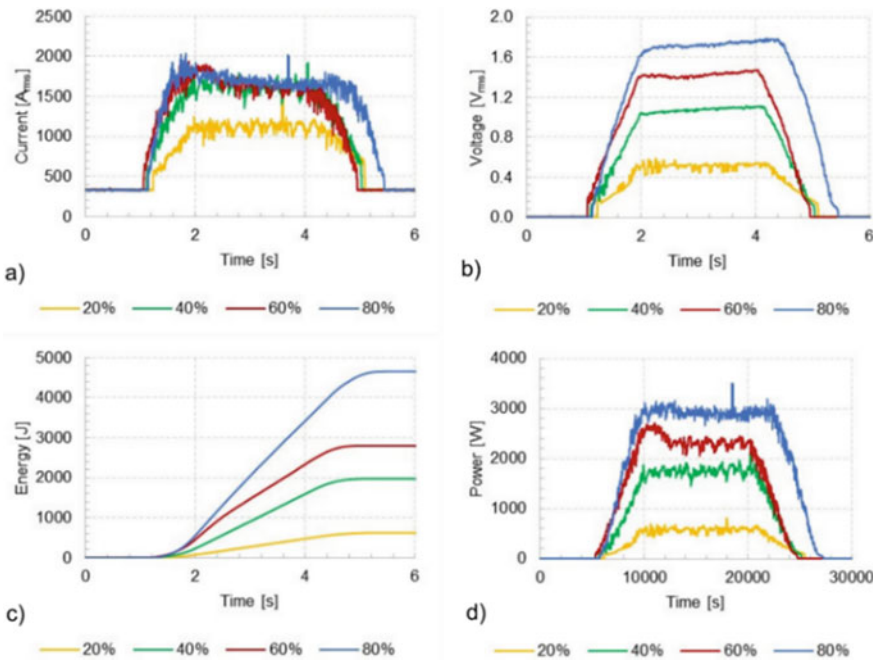
Fig. 11 Electrical parameters during joining for the different levels analyzed
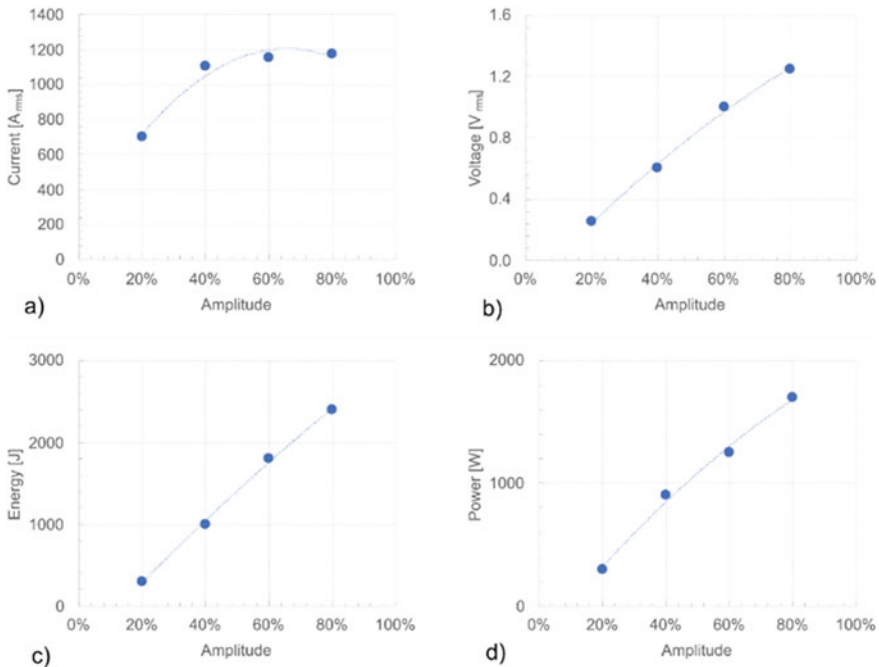
Fig. 12 Trends of average value of current (**a**), voltage (**b**), Energy (**c**) and power (**d**) with four different level of amplitude analyzed

4.2 Preliminary Assessment of Joints Quality

Preliminary tests conducted showed that the optimum temperature for successful joining is about 350 °C. An excessive temperature leads to the degradation of PEEK. Figure 13a shows the correctly realized joint and Fig. 13b shows a PEEK fracture surface.

In Fig. 14 is reported a load–displacement curve obtained during single lap shearing tests.

After performing single lap shear test, it was possible to analyze the fracture surfaces; in Fig. 15a is shown the PEEK surface, instead Fig. 15b shows the titanium surface.

5 Conclusions

The present study investigated the process of electrically assisted direct joining for producing hybrid metal-polymer joints. The processing conditions, namely the current and voltage were analyzed to determine a suitable processing window
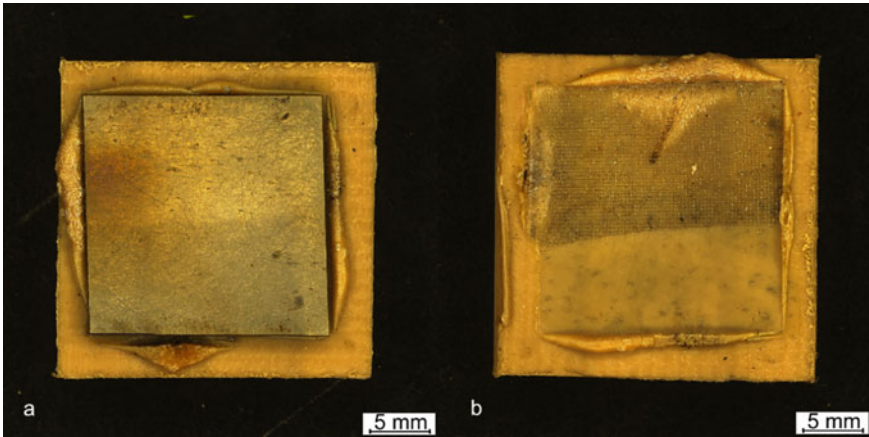
Fig. 13 Ti-PEEK joint (**a**), PEEK fracture surface (**b**)

Fig. 14 Load–displacement curve obtained during single lap shearing tests
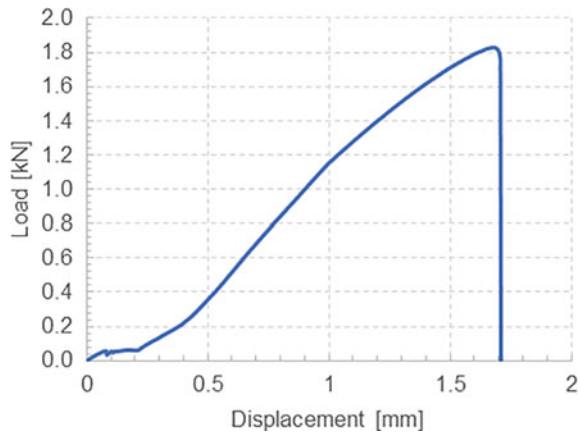
to perform joining tests. To this end, a prototypal apparatus was developed for conducting the experimental tests. The apparatus was also equipped with an IR thermal camera which enabled the determination of the rapid variation of the temperature during the joining process. The main achievements of the study are as follows:

- the update of the old traditional spot-welding machine through the integration of a proportional relays and remote control by the USB IO board and the software developed in LabVIEW enabled a fine control of the process conditions during all the phases of the joining process.
- the mean temperature achieved during the steady state phase was highly depending on the value of the aperture set on the proportional relays.
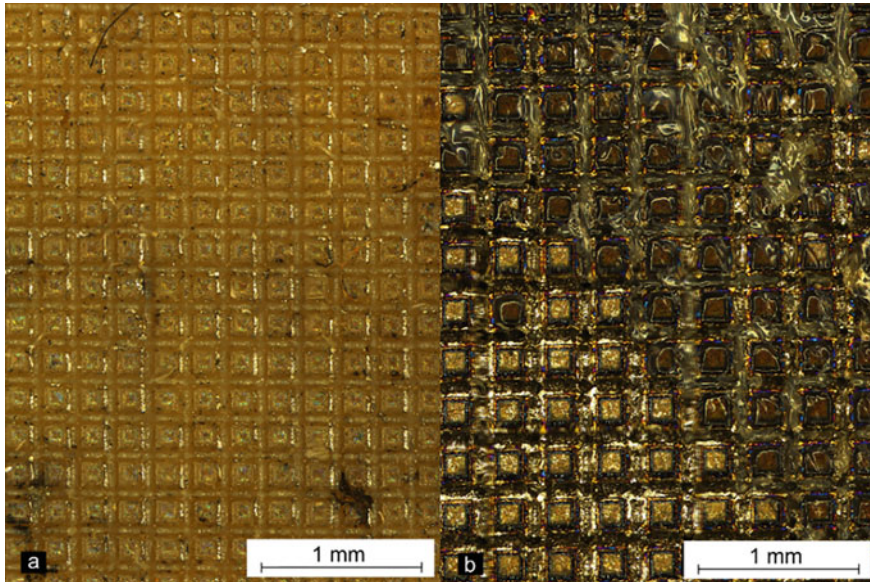
Fig. 15 PEEK surface (**a**), Titanium surface (**b**) after performing single lap shearing test

- the heating time achievable through the electric ally assisted direct joining process was extremely short (lower than 1 s) indicating the great potential of the process to join dissimilar materials such as metals and polymers.

In order to realize a greater joint uniformity through EAJ process, further work can be done on the implementation of an improved coupling system that allows fixed positioning of the specimens to be joined. The temperature control assumes a crucial role during the process for the correct realization of the joint; in future work it will be possible to proceed by controlling the temperature achieved, in relation to current and voltage imposed by the remote control. Future work could also include the improvement of the described apparatus in order to create a continuous joint by developing a two-axis cartesian movement system.

References

1. Chan C-W, Smith GC (2016) Fibre laser joining of highly dissimilar materials: commercially pure Ti and PET hybrid joint for medical device applications. Mater Des 103:278–292
2. Katayama S, Kawahito Y (2008) Laser direct joining of metal and plastic. Scripta Mater 59(12):1247–1250
3. Lambiase F et al (2017) Friction assisted joining of aluminum and PVC sheets. J Manuf Process 29:221–231
4. Amancio-Filho S et al (2011) On the feasibility of friction spot joining in magnesium/fiber-reinforced polymer composite hybrid structures. Mater Sci Eng, A 528(10–11):3841–3848

5. Lionetto F et al (2018) Ultrasonic spot welding of carbon fiber reinforced epoxy composites to aluminum: mechanical and electrochemical characterization. Compos B Eng 144:134–142
6. Lionetto F, Balle F, Maffezzoli A (2017) Hybrid ultrasonic spot welding of aluminum to carbon fiber reinforced epoxy composites. J Mater Process Technol 247:289–295
7. Backe D, Balle F (2016) Ultrasonic fatigue and microstructural characterization of carbon fiber fabric reinforced polyphenylene sulfide in the very high cycle fatigue regime. Compos Sci Technol 126:115–121
8. Lambiase F et al (2017) Laser-assisted direct-joining of carbon fibre reinforced plastic with thermosetting matrix to polycarbonate sheets. Opt Laser Technol 94:45–58
9. Genna S, Lambiase F, Leone C (2018) Effect of laser cleaning in laser assisted joining of CFRP and PC sheets. Compos B Eng 145:206–214
10. Lambiase F, Genna S (2014) Experimental analysis of laser assisted joining of Al-Mg aluminium alloy with Polyetheretherketone (PEEK). Int Des 59:448–453; (2018) J Adhes Adhes 84:265–274
11. Arai S, Kawahito Y, Katayama S, Effect of surface modification on laser direct joining of cyclic olefin polymer and stainless steel. Materials
12. Zhang Z et al (2016) Effect of anodizing pretreatment on laser joining CFRP to aluminum alloy A6061. Int J Adhes Adhes 70:142–151
13. Jung D-J, Cheon J, Na S-J (2016) Effect of surface pre-oxidation on laser assisted joining of acrylonitrile butadiene styrene (ABS) and zinc-coated steel. Mater Des 99:1–9
14. Yusof F et al (2012) Effect of anodizing on pulsed Nd: YAG laser joining of polyethylene terephthalate (PET) and aluminium alloy (A5052). Mater Des 37:410–415
15. Zhang Z, Shan J, Tan X (2018) Evaluation of the CFRP grafting and its influence on the laser joining CFRP to aluminum alloy. J Adhes Sci Technol 32(4):390–406
16. Schricker K et al (2014) Macroscopic surface structures for polymer-metal hybrid joints manufactured by laser based thermal joining. Phys Procedia 56:782–790
17. Tamrin K, Nukman Y, Zakariyah S (2013) Laser lap joining of dissimilar materials: a review of factors affecting joint strength. Mater Manuf Processes 28(8):857–871
18. Tan X et al (2015) Characteristics and formation mechanism of porosities in CFRP during laser joining of CFRP and steel. Compos B Eng 70:35–43
19. Chen Y, Yue TM, Guo Z (2016) A new laser joining technology for direct-bonding of metals and plastics. Mater Des 110:775–781
20. Lambiase F, Paoletti A (2018) Mechanical behavior of AA5053/polyetheretherketone (PEEK) made by friction assisted joining. Compos Struct 189:70–78
21. Li Y-F et al (2019) Solid-state dissimilar joining of stainless steel 316L and Inconel 718 alloys by electrically assisted pressure joining. Mater Charact 154:161–168
22. Lambiase F, Grossi V, Paoletti A (2022) High-speed joining of hybrid metal-polymer joints during the friction-assisted joining process. Compos Struct 280:114890
23. ASTM, ASTM E8/E8M
24. ASTM, ASTM D638
25. Nasir Z, Khan M (2016) Resistance spot welding and optimization techniques used to optimize its process parameters. Int Res J Eng Technol (IRJET) 3(5):887–893
26. Lambiase F, Paoletti A (2018) Friction assisted joining of titanium and polyetheretherketone (PEEK) sheets. Thin-Walled Struct 130:254–261

Milling Cutting Force Model Including Tool Runout

Lorenzo Morelli, Niccolò Grossi, and Antonio Scippa

Abstract   Tool radial runout is an inevitable phenomenon which significantly affects the cutting conditions in a milling operation. Indeed, tool runout causes irregular spacing between cutter teeth creating uneven engagement conditions. This aspect may limit the accuracy and reliability of the predictive approaches dealing with important phenomena in milling such as chatter, surface errors and tool wear. For these predictions, a cutting force model, which includes tool runout, is essential, but it requires complex formulations which limit its application. This paper presents a simplified cutting force model for an endmill with generic geometry then adapts it to represent the effect of radial runout on a regular endmill. The model thus obtained expresses the cutting forces as a Fourier series considering the effect of tool runout on the cutting force frequency components, and it is easy to apply to other predictive models. The proposed formulations are validated, and an application is presented.

Keywords   Milling · Predictive model · Tool geometry

1   Introduction

Cutter runout is a common condition occurring in milling operations with multiple flutes. Indeed, tool geometric centre generally deviates from the spindle axis generating the eccentricity (i.e., runout) which causes uneven engagement conditions among the flutes involved in the cut [1]. Consequently, cutting forces are directly affected by the tool runout in terms of shape and magnitude [2]. Furthermore, the effect of runout on the cutting forces has influences on other important aspects of the cutting process such as tool wear [3] machined surface [4] and process stability (i.e., chatter) [5] For this reason, an accurate cutting force representation including tool runout is essential for predictive approaches dealing with those aspects with the aim of improving process accuracy and productivity. In literature, cutting force

L. Morelli (✉) · N. Grossi · A. Scippa

Department of Industrial Engineering, University of Firenze, Via di Santa Marta 3, 50139 Firenze, Italy

e-mail: lorenzo.morelli@unifi.it

representation is largely based on mechanistic models which assume cutting force is related to the instantaneous chip thickness though the cutting coefficients [6]. In this context, the two most adopted types of cutting models are the lumped shear force model, based on only one cutting coefficient [7] and the dual mechanism force model, which uses two separate coefficients (i.e., the cutting coefficient and the edge coefficient) [8]. These models provide a time domain representation of the cutting forces, and they include the effect of runout by predicting the actual undeformed chip thickness which is defined as the difference between the radii of the flute considered and the one preceding it, using geometric expressions [9]. These approaches provide good results, but they are limited to conditions in which chip thickness depends only on two consecutive flutes. Chen et al. [10] presented a method to fill this gap with different formulations for the undeformed chip thickness according to the radial depth of cut, feed per tooth and runout. The proposed method is effective, yet the need of formulations for each combination of parameters makes the approach not easy to extend to cutters with more than two flutes. On the other hand, Gao et al. [11] analysed the effect of runout on the radial engagement for a two fluted endmill. In detail, the authors proposed formulations for each flute cutter radius, pitch angle, engagement angles and feed per tooth according to runout. Unlike the other approaches, the Gao et al. approach analyses the effect of runout on the process parameters giving a deeper insight on the impact of runout on cutting forces. Nonetheless, the reliability of the method is limited to cutting conditions in which chip thickness is related to the radius of the flute analysed and the one preceding it, like previously mentioned methods. For a more accurate cutting force representation in time domain able to include tool runout, literature highlight models which consider the cycloidal trajectories of the flutes, known as "trochoidal models". In this context, Kunmanchik and Schmitz [12] proposed a trochoidal model for generic tools. In the proposed method, the authors considered a generic tool geometry with different flutes radii and pitch angles, and they developed expression of both chip thickness and process parameters considering the actual flutes paths. This model was then adapted to model runout on an ideal endmill with even flute radii and pitch angles using dedicated runout parameters in the chip thickness expressions. Moreover, the authors identified the boundary beyond which the proposed model does not return accurate results since chip thickness is no longer related to the radius of the flute analysed and the previous radius. The model developed by the authors is more accurate and general compared to the others, yet its reliability is limited by the boundary identified by the authors. The models described, despite their accuracy are not easy to couple with other models which aim at coupling the cutting forces with the dynamic of the milling system [4, 5] because, due to the complexity of the formulations adopted for the chip thickness, the frequency content of the cutting forces including runout cannot be derived analytically, and it can be found only through a Fast Fourier Transform (FFT) of the cutting forces in the time domain. In this context, a frequency domain representation of the cutting forces including runout could be useful, but very few studies deal with this topic. Wang et al. [13] used the convolution analysis and a mechanistic cutting force model including runout to develop a closed form formulation for cutting forces in the frequency domain. These formulations present the same limitations of the

approaches previously mentioned regarding the undeformed chip thickness. In this work, a Fourier series representation of the cutting forces in the frequency domain (as in [14]) for an endmill with generic geometry (i.e., with uneven flute radii and pitch angles) is developed. In detail, analytical formulations for Fourier coefficients considering the actual flutes sequence during the cut and which flutes are responsible for chip thickness formation. Then, following the same steps of the approach by Kunmanchik and Schmitz [12], the proposed formulations are adapted to represent the effect of radial runout on an ideal endmill (i.e., with even flute radii and pitch angles). The formulations thus obtained allow to directly evaluate the frequency content of the cutting forces for an ideal endmill in presence of runout, and they are easy to apply to other predictive approaches.

1.1 Runout Identification State of the Art

As an application of the developed formulations, a technique to identify runout through the measured cutting force spectrum is proposed. To contextualize this application, this section analyses the state of art about runout identification strategies. Indeed, independently from the cutting model considered, the inclusion of runout in the cutting force prediction is obtained through runout parameters which become additional input of the cutting force prediction method. These parameters are usually the runout length and the orientation angle, and they must be either measured or calibrated for an accurate prediction. In literature two main measuring strategies are found: direct and indirect method; the direct methods measure runout parameters using both contact [15, 16] and non-contact [17–19] measuring devices. These methods allow an offline identification of the runout parameter, but in the actual cutting process the geometry of the cut may be different and the measured runout parameters may present limited reliability. Instead, indirect methods estimate runout parameters from the analysis of input signals, such as cutting forces or cutting power. For example, Niu et al. [5] developed a linear mechanistic cutting force model combined with a non-linear identification algorithm to identify both cutting coefficients and runout parameters for variable pitch and variable helix milling tools; Krüger and Denkena [20] adopted the cutting energy distribution to identify runout geometry with results characterized by a variance smaller than 3% to the measured values. Seethaler and Yellowley [21] formulated a general expression of the runout between each couple of two consecutive flutes in the form of a discrete Fourier series in end milling. Herman et al. [22] proposed a method based on the frequency domain representation of cutting forces. The force component at the spindle rotational frequency is used to adaptively identify the runout parameters every digitalisation period. Wang and Zheng [13] developed a method for the identification of runout parameters using the FFT of the measured milling forces at the spindle rotational frequency without the need of prior knowledge regarding cutting coefficients. The identified parameters were quite consistent, but the identification requires

other constants (shearing constants) which must be identified through two preliminary milling tests. All the mentioned identification approaches require either cutting coefficients or other constants to be known or calibrated, limiting the application of these indirect techniques. In this regard, this paper presents an indirect method based on cutting forces spectrum to identify runout parameters without the need of cutting coefficients or calibration tests. The proposed approach was validated both experimentally and numerically, and it showed to be a promising starting point for a force-based runout identification solution.

2 Proposed Approach

This study is divided in two parts. In the first part analytical formulations describing the frequency content of cutting forces for an endmill with generic geometry (i.e., flutes with different radius and pitch angles) are presented. In the second part, the developed formulations are adapted to model runout on a tradition endmill (i.e., evenly spaced flutes with equal pitch angles) and applied in a method to identify runout parameters without any prior knowledge on cutting coefficients or any calibration tests.

2.1 Cutting Force Model

First, analytical equations that predict frequency content of cutting forces in a milling process are presented. These formulations are built for an endmill with a generic geometry assuming that the generic i-th flute is identified by a radius R_i and a pitch angle ϕ_{zi}, as it is shown in Fig. 1, where D_m is the maximum tool diameter, N is the number of flutes characterizing the endmill, α_{el} is the helix angle, while a_r and a_p are the radial and the axial depth of cut respectively.
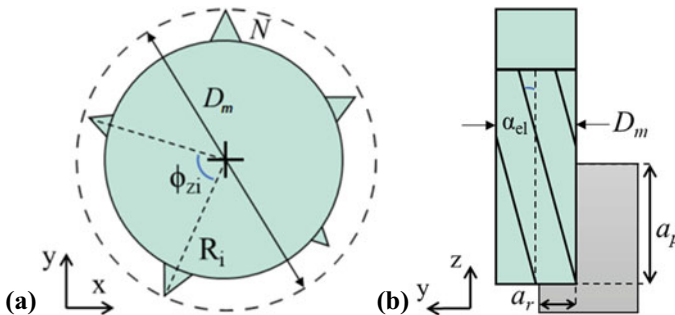
Fig. 1 Generic endmill geometry

The formulations presented are based on a simple mechanistic force model that relates forces linearly to chip thickness with a cutting force coefficient (i.e., lumped shear model). In detail, the radial cutting F_r, the tangential cutting force F_t and the axial cutting force F_a are expressed according to Eq. 1.

$$F_t(\phi) = \sum_{i=1}^{N} K_{tc} a_p h_i(\phi_i)$$

$$F_r(\phi) = \sum_{i=1}^{N} K_{rc} a_p h_i(\phi_i) \tag{1}$$

$$F_a(\phi) = \sum_{i=1}^{N} K_{ac} a_p h_i(\phi_i)$$

where K_{tc}, K_{rc} and K_{ac} are the tangential, the radial and the axial cutting coefficients respectively; h_i is the chip thickness for the ith flute which can be computed following Eqs. 2 and 3.

$$h_i = f_{zi} \sin(\phi_i) \text{ with } \phi_i = \phi + \phi_{zi} \; i = 1, 2, \ldots, N \tag{2}$$

$$\phi = wt \tag{3}$$

where f_{zi} and ϕ_i are respectively the feed per tooth the engagement angle of the ith flute, with ϕ being the engagement angle variable, which is related to the spindle speed w and the time variable t, and ϕ_{zi} representing the pitch angle of the ith flute. Introducing a coordinate system as in Fig. 2 with x representing the feed direction and y the cross-feed direction, the total in-plane cutting force F_{xy} is expressed as:

$$F_{xy}(\phi) = \sqrt{F_t^2(\phi) + F_r^2(\phi)} = \sqrt{F_x^2(\phi) + F_y^2(\phi)} = \sqrt{K_{tc}^2 + K_{rc}^2} \sum_{i=1}^{N} a_p h_i(\phi_i) \tag{4}$$

where F_x is the total cutting force along the feed direction and F_y is the total cutting force in the cross-feed direction. It is worth noting that F_{xy} and F_a differs only for

Fig. 2 Cutting force overview
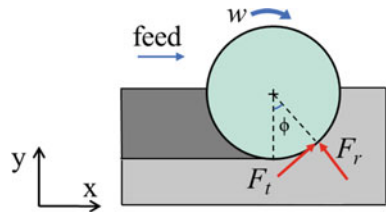
the term related to the cutting coefficients, as it is shown in Eqs. 4 and 1, therefore the following formulations are also appliable to the axial cutting force.

According to Eq. 1, the evaluation of the cutting force depends on the chip thickness, which is related to the feed per tooth and pitch angle of each flute characterizing the endmill geometry. Therefore, to define f_{zi} and ϕ_{zi} for the generic ith flute, it is important to identify the sequence in which flutes follow one another during the cut. Assuming a clockwise numeration of the flutes starting from one of the flutes chosen freely, the flute sequence S is defined as it follows according to the cutting strategy (Fig. 3)

$$S = 1, N, N - 1, N - 2, \ldots, 1 \quad \text{down-milling} \tag{5}$$

$$S = 1, 2, \ldots, N, 1 \quad \text{up-milling} \tag{6}$$

Knowing the sequence S, and assuming for the starting flute (S_1) a pitch angle ϕ_{z1} equal to 0 the pitch angle ϕ_{zi} according to the flute sequence can be expressed as:

$$\phi_{zi} = \sum_{1}^{i} \phi_{zi} i = 1, 2, \ldots, N \tag{7}$$

With these assumptions the pitch angle is referred to the sequence accomplished by the flutes during the cut. To evaluate the cutting forces the chip thickness of each flute should be evaluated within the range between cutter entry angle (ϕ_{in}) and cutter exit angle (ϕ_{out}) which are identified according to the cutting strategy (down-milling or up-milling) and the radial depth of cut (a_r); however, due to the different flutes radii characterizing the generic geometry of the endmill, each flute is characterized by its own entry and exit angle according to the cutting strategy. In detail, for down-milling the ith flute entry angle is evaluated according to the radius of the flute considered R_i and a_r, as it is shown in Eq. 8. Instead, the ith flute exit angle is evaluated by analysing the intersections between the circular trajectory of the considered flute and the trajectories of all the preceding flutes according to the flute sequence.

For each intersection an angle is found, and the minimum is chosen (Eq. 9) since it is representing the first moment at which the flute stops cutting.
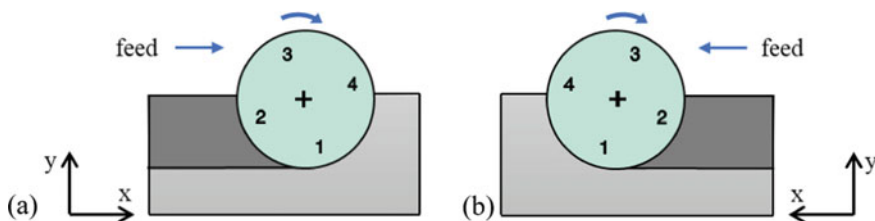
Fig. 3 Example of flute sequence for a 4 fluted endmill **a** Down-milling **b** Up-milling

$$\phi_{in_i} = \pi - a\cos(D_m - 2a_r/2R_i) \quad \text{down-milling} \tag{8}$$

$$\phi_{out_i} = \min\left(-\frac{3\pi}{2} + a\cos\left(\frac{R_i^2 + if_z^2 - R_j^2}{2R_iif_z}\right)\right) \text{down-milling} \tag{9}$$

$$j = S_{i-1}, S_{i-2}, \ldots, S_{i-N} \tag{10}$$

where j represents the indexes of the flutes preceding the i-th flute according to the flute sequence S and f_z is the commanded feed per tooth. An example of the procedure is shown in Fig. 4 for a two fluted endmill where the exit angle of the flute 1 (red trajectory) is found by analysing the intersections (red points) between the trajectory of flute 2 and the trajectory of flute 1 of the previous revolution. Following an analogous procedure, the engagement angles for up-milling are found:

$$\phi_{in_i} = \min\left(-\frac{\pi}{2} + a\cos\left(\frac{R_i^2 + if_z^2 - R_j^2}{2R_iif_z}\right)\right) \text{up - milling} \tag{11}$$

$$\phi_{out_i} = a\cos(D_m - 2a_r/2R_i) \quad \text{up - milling} \tag{12}$$

$$j = S_{i+1}, S_{i+2}, \ldots, S_{i+N} \tag{13}$$

In this case, the trajectories analysed are the ones belonging to the flutes following the one considered, as it is shown in Eq. 13. The variation among the flute radii not only affect the flute entry and exit angles but also the feed per tooth, since it changes the actual distance between flutes moving in the feed direction, as it is described in [11]. Indeed, the actual feed per tooth f_{zi} for the ith flute is found with the following equation:

$$f_{zi} = if_z + \sqrt{R_i^2 - \frac{D_m^2}{4}\cos(\phi)^2} - \sqrt{R_v^2 - \frac{D_m^2}{4}\cos(\phi)^2} \tag{14}$$

$$v = S_{i-1} \text{ down - milling} \quad v = S_{i+1} \text{ up - milling} \tag{15}$$

Fig. 4 Example of exit angle evaluation in down-milling for the flute 2 of a two fluted tool
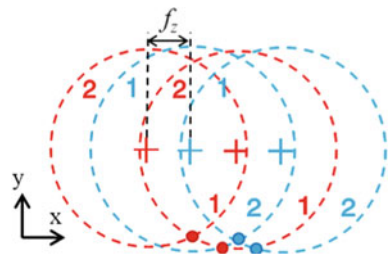
where v is the index referring to the flute radius preceding the ith flute in down-milling and the one following the ith flute in up-milling. In the method proposed by Gao et al. [11] the actual feed per tooth was assumed constant and equal to the maximum of Eq. 14, while in the proposed approach the variation of the actual feed per tooth with the engagement angle ϕ is considered. Furthermore, it is important to note that depending on the magnitude of the feed per tooth f_z and the difference between R_i and R_v some flutes may not participate in the cut, therefore f_{zi} may not be related to the radius of the vth flute but to another one in the flute sequence. In this study, to identify the actual feed per tooth for the ith flute, a procedure based on the chip area formed by the ith flute and the other j flutes of the flute sequence is adopted. In detail, for each i and j combination a value A_{ij} for the chip area is found according to the following equation:

$$A_{ij} = \int_{\phi_{in_i}}^{\phi_{out_i}} \left(i f_z + \sqrt{R_i^2 - \frac{D_m^2}{4} \cos(\phi)^2} - \sqrt{R_j^2 - \frac{D_m^2}{4} \cos(\phi)^2} \right) \sin(\phi) d\phi \quad (16)$$

The flute k_i which identify the correct flute in the cutting sequence to be combined with the ith flute to evaluate the correct value of the actual feed per tooth is obtained from the minimum of the chip area values given by Eq. 16:

$$k_i = \min(A_{ij}) \quad (17)$$

An example of this procedure for a two fluted tool is shown in Fig. 5, where the chip areas considered for the evaluation of the correct value of the feed per tooth for the flute 2 (blue trajectory) are shown. In this case, the flute k_i for the correct evaluation of the actual feed per tooth is the flute 1 (Fig. 5a).

At this point, the chip thickness for the i-th flute for an endmill with a generic geometry can be expressed as:

$$h_i = \left(i f_z + \sqrt{R_i^2 - \frac{D_m^2}{4} \cos(\phi)^2} - \sqrt{R_{k_i}^2 - \frac{D_m^2}{4} \cos(\phi)^2} \right) \sin(\phi_i) \quad (18)$$
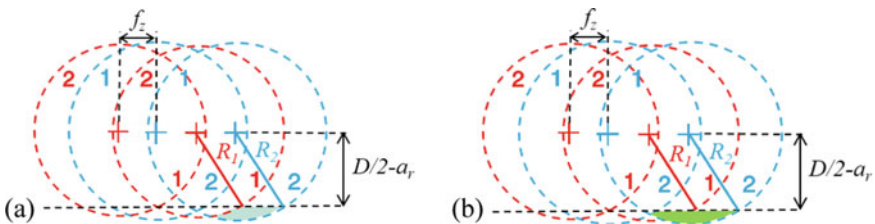
Fig. 5 Example of actual feed per tooth evaluation in Down-milling for the flute 2 of a generic two fluted tool

The total in-plane cutting force F_{xy} becomes:

$$F_{xy}(\phi) = \sqrt{F_t^2(\phi) + F_r^2(\phi)} = \sqrt{K_{tc}^2 + K_{rc}^2}$$

$$\sum_i^N \left(i f_z + \sqrt{R_i^2 - \frac{D_m^2}{4}\cos(\phi)^2} - \sqrt{R_{k_i}^2 - \frac{D_m^2}{4}\cos(\phi)^2} \right) \sin(\phi_i) \quad (19)$$

Following the same procedure presented by Grossi et al. [14] for an ideal endmill with equally spaced flutes, the cutting force F_{xy} for an endmill with a generic geometry considering the tool helix can be formulated in the frequency domain as a Fourier series with the following equations:

$$F_{xy}(\phi) = \sum_i^N a^*_{xy0_i} a_p + \sum_{i=1}^N \sum_{n=1}^\infty \left(\left(\left(\frac{a^*_{xyn_i}}{nk_b} \sin nk_b a_p + \frac{b^*_{xyn_i}}{nk_b} \cos nk_b a_p - \frac{b^*_{xyn_i}}{nk_b} \right) \cos n\phi_i \right. \right.$$

$$\left. \left. + \left(-\frac{a^*_{xyn_i}}{nk_b} \cos nk_b a_p + \frac{a^*_{xyn_i}}{nk_b} + \frac{b^*_{xyn_i}}{nk_b} \sin nk_b a_p \right) \sin n\phi_i \right) \right) \quad (20)$$

where a^*_{xy0i} is the Fourier coefficients at zero frequency for the i-th flute, while a^*_{xyni}, b^*_{xyni} are the coefficients couples which define the real and imaginary components of the forces at the frequency n-multiple of the rotation frequency (n integer) for the i-th flute. In addition, k_b is a geometric parameter related to the tool helix angle thorough the following equation:

$$k_b = 2\tan(\alpha_{hel})/D_m \quad (21)$$

The proposed formulations (Eq. 20) evaluate cutting forces in the frequency domain considering the helix angle through direct expressions, without the need of a specific discretization. Furthermore, such expressions allow to isolate the cutting coefficients from the Fourier coefficients obtaining the following expressions:

$$a^*_{xy0_i} = a^{**}_{xy0_i} \cdot \sqrt{K_{tc}^2 + K_{rc}^2} \quad (22)$$

$$a^*_{xyn_i} = a^{**}_{xyn_i} \cdot \sqrt{K_{tc}^2 + K_{rc}^2} \quad (23)$$

$$b^*_{xyn_i} = b^{**}_{xyn_i} \cdot \sqrt{K_{tc}^2 + K_{rc}^2} \quad (24)$$

With these simplifications, the Fourier series components for F_{xy} become:

- For the constant term (zero frequency)

$$A_{xy0} = \sum_i^N a^{**}_{xy0_i} \cdot \sqrt{K_{tc}{}^2 + K_{rc}{}^2} \cdot a_p \qquad (25)$$

- For the spindle rotational frequency and its harmonics

$$C_{xyn} = \sum_i^N \frac{1}{2}\sqrt{K_{tc}^2 + K_{rc}^2} \cdot \left(\left(\frac{a^{**}_{xyn_i}}{nk_b}\sin(nk_b a_p) + \frac{b^{**}_{xyn_i}}{nk_b}\cos(nk_b a_p) - \frac{b^{**}_{xyn_i}}{nk_b} \right) \right.$$
$$\left. -i\left(-\frac{a^{**}_{xyn_i}}{nk_b}\cos(nk_b a_p) + \frac{a^{**}_{xyn_i}}{nk_b} + \frac{b^{**}_{xyn_i}}{nk_b}\sin(nk_b a_p) \right) \right) \qquad (26)$$

Following the cutting model previously described the Fourier coefficients are found according to Eqs. 27, 28 and 29.

$$a^{**}_{xy0_i} = \int_{\phi_{in_i}}^{\phi_{out_i}} \left(if_z + \sqrt{R_i^2 - \frac{D_m^2}{4}\cos(\phi)} - \sqrt{R_{k_i}^2 - \frac{D_m^2}{4}\cos(\phi)} \right)\sin(\phi)d\phi \quad (27)$$

$$a^{**}_{xyn_i} = \int_{\phi_{in_i}}^{\phi_{out_i}} \left(if_z + \sqrt{R_i^2 - \frac{D_m^2}{4}\cos(\phi)} - \sqrt{R_{k_i}^2 - \frac{D_m^2}{4}\cos(\phi)} \right)\sin(\phi)\sin(n\phi)d\phi \qquad (28)$$

$$b^{**}_{xyn_i} = \int_{\phi_{in_i}}^{\phi_{out_i}} \left(if_z + \sqrt{R_i^2 - \frac{D_m^2}{4}\cos(\phi)} - \sqrt{R_{k_i}^2 - \frac{D_m^2}{4}\cos(\phi)} \right)\sin(\phi)\cos(n\phi)d\phi \qquad (29)$$

It must be pointed out that due to the complexity of these expression the evaluation of Fourier coefficients (Eqs. 27, 28 and 29) implies the use of numerical integration techniques. Nonetheless, the proposed formulations allow to include the evolution of the actual feed per tooth with ϕ in the chip thickness evaluation obtaining a model that is closer to complex models [12] since it better represents the trajectories of the flutes. Furthermore, the proposed model allows to directly compute the frequency content of the cutting force without the need of signal processing.

2.2 Runout Parameters Estimation

In the previous section a frequency cutting force model for an endmill with generic geometry was presented. The proposed model can be easily adapted to model the effect caused by runout in an ideal endmill.

As it shown in Fig. 6, starting from an ideal endmill (Fig. 6a) runout causes a deviation between the geometric centre of the tool and the spindle axis (Fig. 6b).

This deviation is identified by the length of runout ρ and the orientation angle λ. Using these runout parameters, the flutes radius (R_i) and the pitch angles (ϕ_{zi}) for the ith flute related to the tool runout (Fig. 6c) are found with the following equations:

$$R_i = \sqrt{(D/2)^2 + \rho^2 - \rho D \cos(i\phi_z - \lambda)} \qquad (30)$$

$$\phi_{z_i} = \mathrm{acos}(\frac{\sqrt{(\frac{D}{2})^2 + R_i^2 - d^2}}{D R_i}) \qquad (31)$$

$$d = \sqrt{(D/2)^2(1 - 2\cos(\varphi_z))} \qquad (32)$$

In this case φ_z is the pitch angle of the ideal endmill and given by $2\pi/N$, and D is the nominal endmill diameter. The obtained flutes radius and pitch angle are related to the runout parameters (ρ and λ) and become the input for the frequency domain representation described in the previous Sect. 2.1. With this solution a model to add runout to the cutting model in the frequency domain is obtained.

This new model not only adjust the process parameters according to runout, but it considers the flute sequence and their trajectories selecting for each flute the corresponding flute, which allow the formation of the chip with the correct feed per tooth, overcoming the limitation of the cutting models described in the state of the art. Starting from this runout model, an application of the proposed formulations is presented. The aim of this application is developing a method to identify the runout parameters (ρ and λ) from the measured cutting forces using the proposed formulations. In this application only the total in-plane cutting force F_{xy} is used for two reasons:

- it allows to release the information regarding cutting forces from the one related to their directions.
- It is more significant in terms of magnitude compared to F_a, so it is easier to measure and less sensitive to external factors.
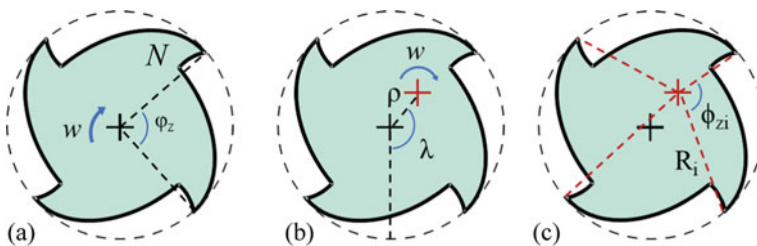
Fig. 6 a Ideal endmill **b** endmill with runout **c** flutes radii and pitch angles for an endmill with runout

Computing the ratio between the zero-frequency component of the cutting force A_{xy0} and the other frequency components C_{xyn} a new parameter (V_n) is found:

$$V_n = \frac{C_{xyn}}{A_{xyo}} = \sum_i^N \frac{1}{a_p a_{xy0_i}^{**}} \left(\left(\frac{a_{xyn_i}^{**}}{nk_b} \sin(nk_b a_p) + \frac{b_{xyn_i}^{**}}{nk_b} \cos(nk_b a_p) - \frac{b_{xyn_i}^{**}}{nk_b} \right) \right.$$
$$\left. - i \left(-\frac{a_{xynn_i}^{**}}{nk_b} \cos(nk_b a_p) + \frac{a_{xyn_i}^{**}}{nk_b} + \frac{b_{xyn_i}^{**}}{nk_b} \sin(nk_b a_p) \right) \right) \tag{33}$$

This parameter is extremely interesting because it does not depend on the cutting coefficients, and since it is based on the total cutting force, it is not affected by the cutting force direction. Moreover, V_n depends on the tool geometry (D, N, α_{el}), the cutting parameters $(a_r, a_p$ and $f_z)$ and the runout parameters $(\rho$ and $\lambda)$. Therefore, assuming the tool geometry and the cutting parameters as given inputs known by the operator, the runout parameters could be identified by comparing the experimental V_n and the predicted one. To achieve this goal, an optimization algorithm is adopted to minimize the following error function v_0:

$$v_o = \frac{\|V_{np} - V_{nm}\|^2}{\|V_{nm}\|^2} n = 2, 3, \ldots, c \tag{34}$$

where c is the number of Fourier coefficients considered, V_{np} and V_{nm} are the predicted and measured values of the ratio formulated in Eq. 33 and the symbol "‖" indicates the 2-norm of the vector. Since V_n is composed by a real and an imaginary part, both will be included in the identification procedure. It is interesting to note that generally cutting forces are represented with good accuracy using only few Fourier coefficients, therefore the runout parameter estimation process is possible exploiting only a limited set of Fourier coefficients.

3   Numerical Validation

First, the proposed formulations were tested numerically in different cutting conditions with the purpose of predicting the cutting forces given the runout parameters. The predicted cutting forces were compared with the ones obtained by other approaches found in the state of the art.

Secondly the proposed method to identify runout parameters was tested adopting as measured forces numerical cutting forces obtained from time domain simulation according to the methods found in state of the art.

3.1 Formulations Comparison

A series of cutting conditions in down-milling with different runout parameters and feed per tooth were tested, as it is summarized in Table 1, with the aim of assessing accuracy of the proposed formulations compared to others found in the state of the art. For these cutting conditions, a four fluted endmill with 12 mm of diameter and 45° of helix angle was considered, and spindle speed was set to 6366 rpm. Moreover, the selected cutting conditions allow to investigate the impact of runout parameters on different cutting force shapes considering that force shape changes according to the cutting parameters, as it was shown in previous studies [23, 24].

The cutting forces predicted with the developed formulations were compared, in both time domain and frequency domain, with the ones obtained from the trochoidal model described in [12], hereafter called "trochoidal", and the method proposed by Gao et al. [11], which will be referred as "fz_m". In detail, for the developed formulations 60 Fourier coefficients for the spindle rotational frequencies and its harmonics were considered. On the other hand, for the fz_m model, which presented only the different expressions for feed per tooth and flute radius according to runout parameter, the same 20 coefficients were considered following the same procedure by Grossi et al. [14]. Instead, for the trochoidal model, which consider the actual flutes trajectories and the tool helix, a sampling frequency of 530,500 Hz with 5000 points per period and 2000 steps for axial discretization were adopted.

In Fig. 7 the comparison between the proposed formulations and the methods found in the state of the art for an ideal case without runout is shown. In this condition force presents a triangular shape, and no appreciable difference is found between the considered methods, as expected. If runout is considered (Fig. 8), differences are found between the methods considered. Indeed, runout affects the evolution of the cutting forces over the speed rotational period, and each flute presents a different triangular shape. Even if all the three methods proposed presents the same evolution among the flutes, the approach proposed by Gao et al. slightly differs from the others because it assumes a constant feed per tooth during the engagement. The proposed method instead is perfectly in agreement with the trochoidal model, which is assumed to be the most accurate since it considers the actual flute trajectories for the chip thickness evaluation. In test 3 (Fig. 9), with the high radial depth of cut ($a_r \geq D/2$), cutting force assume trapezoidal shape, and, due to runout each flute presents its own trapezoidal shape. In detail, the proposed formulations well match with the trochoidal model unlike the fz_m approach. However, it is interesting to note that the rising edge of the cutting force is in good agreement for all the three models because

Table 1 Test overview for force prediction validation

Test id	f_z (mm)	ρ (mm)	λ (degree)	a_r (mm)	a_p (mm)
1	0.05	0	0	3	5
2	0.1	0.01	45	3	5
3	0.1	0.05	0	7	2
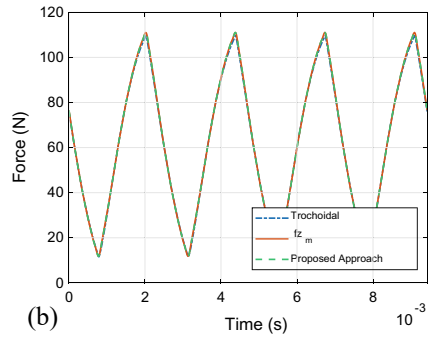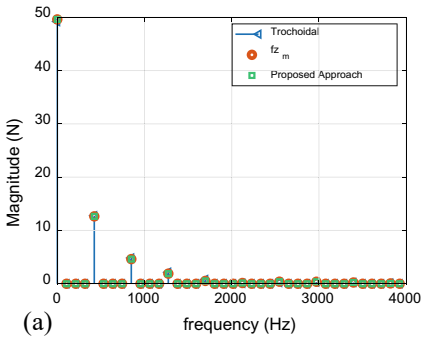
Fig. 7 Predicted cutting forces for test 1 **a** frequency domain **b** time domain

at the beginning of the cut the feed per tooth reaches its maximum and the approach by Gao et al. matches the other models.
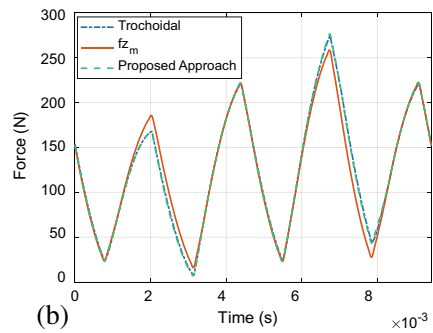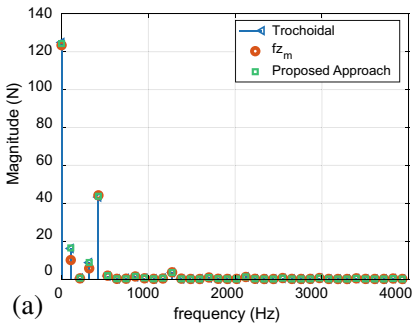
Fig. 8 Predicted cutting forces for test 2 **a** frequency domain **b** time domain
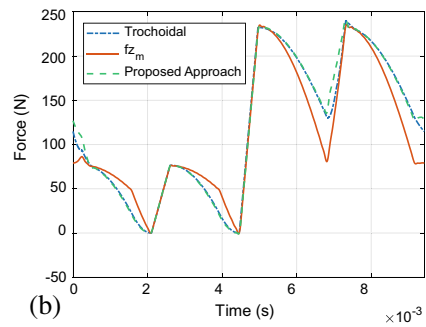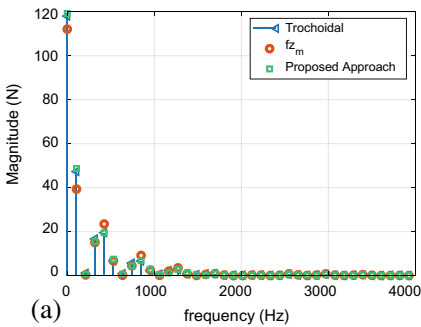
Fig. 9 Predicted cutting forces for test 3 **a** frequency domain **b** time domain

Table 2 Numerical validation for runout parameters identification method

Test	a_r (mm)	a_p (mm)	f_z (mm)	ρ (mm)	λ (degree)	ρ_e (mm)	λ_e (degree)	e_ρ (%)	e_λ (%)
1	3	5	0.1	0.01	45°	0.0098	45.5	2.0	1.1
2	6	3	0.1	0.05	0°	0.0496	0	0.8	0.0
3	3	4	0.1	0.02	60	0.0197	60.5	1.5	1.1
4	2	10	0.05	0.01	15	0.0097	15.3	1.5	2.0
5	1	6	0.05	0.015	30	0.0142	31.5	5.3	5.0

3.2 Runout Identification

The proposed formulations were used to identify runout as presented in Sect. 2.2 for different cutting conditions in terms of depths of cut (a_r and a_p) and runout (ρ and λ) using the same endmill previously described. The FFT of the cutting forces simulated with the trochoidal model [12] were adopted as measured signals. These forces were simulated using a sampling frequency of 530,500 Hz with 5000 points per period and 2000 steps for axial discretization. For the optimization process a genetic algorithm with 1000 population and 25 generation was used to minimize objective function provided in Eqs. 20, 33 Fourier coefficients according to the spindle rotational frequencies and its harmonics were considered. The results obtained are summarized in Table 2 where ρ_e and λ_e represent the runout parameters obtained from the identification method while e_ρ and e_λ are the relative errors between the input runout parameters and the estimated ones. Overall, the proposed method manages to estimate runout parameters with good accuracy and reliability (maximum error 5%). The discrepancies are attributed to the differences between the trochoidal model, and the model used in the proposed approach.

4 Experimental Validation

The identification approach was also experimentally validated. A DMG MORI DMU 75 machine tool was employed to perform three tests in peripheral milling on Aluminium (6082-T4) using a four-fluted end-mill (Garant 202552) with 12 mm diameter and 45° helix angle. Aluminium was chosen since it allows to select a wider range of cutting parameters and avoid tool wear which may alter significantly cutting force shape. For all the three tests, a spindle speed of 2191 rpm and feed per tooth f_z of 0.1 mm were used. The other cutting parameters selected are summarized in Table 3. A Kistler 9257A table dynamometer was used to measure cutting forces in the feed and cross-feed direction. Measured cutting forces were post processed to reduce the distortions derived by the system dynamics using the approach proposed by Scippa et al. [25], and the total cutting force was computed by combing the measured cutting forces. For the optimization procedure the same genetic algorithm previously described was used considering 20 Fourier coefficients.

Table 3 Experimental validation tests and estimated runout parameters

Test	a_r (mm)	a_p (mm)	ρ_e (mm)	λ_e (degree)
1	2	3	0.0065	0°
2	2	8	0.0064	−5.5°
3	1	12	0.0071	14.5°

In Table 3 are reported the results obtained from the identification for ρ and λ in the three tests; the estimated parameters show good coherence being similar one to another according to the fact that all three cutting tests were conducted with the same tool at the same spindle speed. This aspect confirms the consistency of the proposed identification approach. Furthermore, a comparison in terms of force shape and root mean squared deviation (RMSD) between the measured normalized total force and the normalized cutting forces obtained with the proposed formulations and the estimated runout parameters is shown in Fig. 10 for all the three tests. In test 2 and 3, the predicted and measured normalized cutting forces are overall in agreement with a good fitting and relatively small deviation errors (i.e., less than 10%) despite discrepancies. Nonetheless, in test 1 higher errors are presents. These inaccuracies are related to the portions of the signal close to zero which cause high errors values. The discrepancies affecting all the three tests may be related to the fact that an ideal endmill and only radial runout were considered in the prediction neglecting differences in the starting endmill geometry (e.g., uneven spaced flutes) or the presence of a tilt angle generated in the setup phase.

As a second validation, using an on board optical measuring device BLUM-LC series Micro Compact NT, the maximum flute radius R_{max} and minimum flutes radius R_{min} were measured obtaining a R_{max} of 5.977 mm and a R_{min} of 5.964 mm. These two values are not enough to identify experimentally the runout parameters, yet, assuming for the setup adopted in the tests a λ value of 0° (in line with the ones identified), an approximation of the experimental value of ρ could be estimated as $(R_{max} - R_{min})/2$, which gives a ρ of 0.0065 mm. This value is close to the ones found by the proposed method, and it proves that the identification method has potential.

5   Conclusions

In this paper, frequency content of the cutting forces in milling was investigated starting from a generic geometry endmill to an ideal endmill affected by runout. The highlights of this study may be summarized, as it follows:

- Formulations based on Fourier series to directly predict the cutting forces in the frequency domain for an endmill with generic geometry were developed.
- The proposed formulations consider the variations of feed per tooth and engagements angle caused by the different flutes radii, their sequence during the cut and which flutes contribute to the chip formation overcoming the limitations of the
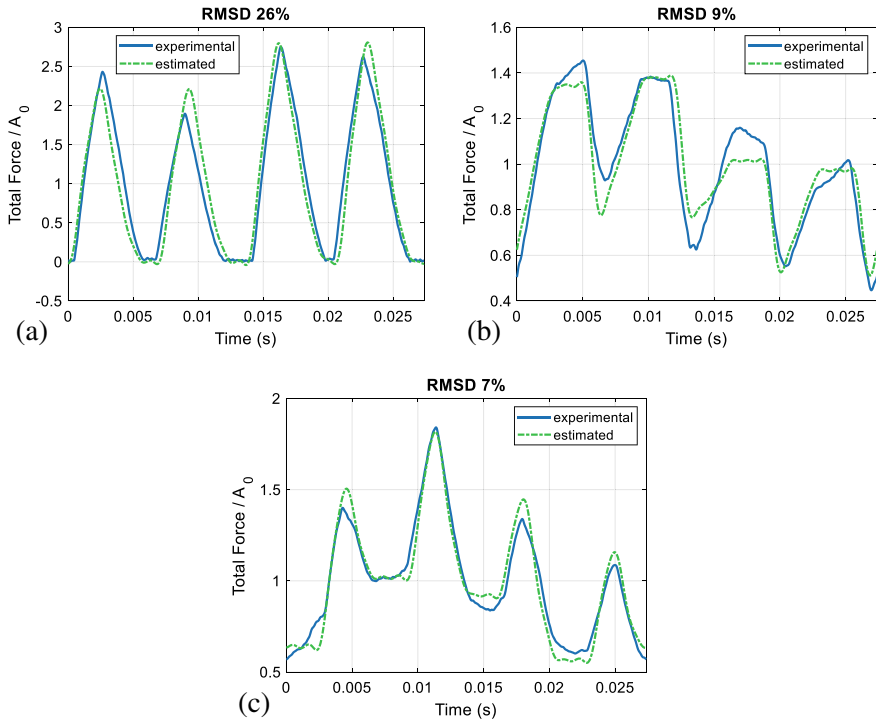
Fig. 10 Comparison between predicted and measured total force **a** test 1 **b** test 2 **c** test 3

models found in the state of the art. However, a direct solution of the proposed formulations is not available yet, limiting their potential.

- Developed formulations were adapted to model the effect of runout on an ideal endmill, obtaining dedicated formulations for cutting force spectra.
- Developed formulations of cutting force spectra for an ideal endmill with runout were applied to develop an approach to identify runout parameters.
- The proposed identification approach does not require any prior knowledge of the cutting coefficients or any calibration test.
- The identification approach was tested both numerically and experimentally with promising results.

Future activities will be focused on trying to simplify the proposed formulations to avoid numerical integration for the Fourier coefficients and extending the experimental validation, including an accurate measure of the runout parameters.

References

1. Lee KY, Kim HM, Park SS (2007) A run-out measuring method using modeling and simulation in four-fluted end milling. J Mater Process Technol 187–188:207–211
2. Matsumura T, Tamura S (2017) cutting force model in milling with cutter runout. In: Procedia CIRP. Elsevier B.V., pp 566–571
3. Zhu K, Zhang Y (2017) Modeling of the instantaneous milling force per tooth with tool run-out effect in high speed ball-end milling. Int J Mach Tools Manuf 118–119:37–48
4. Schmitz TL, Couey J, Marsh E, Mauntler N, Hughes D (2007) Runout effects in milling: surface finish, surface location error, and stability. Int J Mach Tools Manuf 47:841–851
5. Niu J, Ding Y, Zhu LM, Ding H (2017) Mechanics and multi-regenerative stability of variable pitch and variable helix milling tools considering runout. Int J Mach Tools Manuf 123:129–145
6. Wan M, Zhang WH, Tan G, Qin GH (2016) New algorithm for calibration of instantaneous cutting-force coefficients and radial run-out parameters in flat end milling 221:1007–1019. https://doi.org/10.1243/09544054JEM515
7. Wan M, Zhang WH, Dang JW, Yang Y (2009) New procedures for calibration of instantaneous cutting force coefficients and cutter runout parameters in peripheral milling. Int J Mach Tools Manuf 49:1144–1151
8. Chen D, Zhang X, Xie Y, Ding H (2018) Precise estimation of cutting force coefficients and cutter runout in milling using differential evolution algorithm. Procedia CIRP 77:283–286
9. Li G, Xian C, Xin H (2021) Identification of eccentricity for disc milling cutter of indexable two sided inserts. Adv Mech Eng 13
10. Chen Y, Lu J, Deng Q, Ma J, Liao X (2022) Modeling study of milling force considering tool runout at different types of radial cutting depth. J Manuf Process 76:486–503
11. Gao H, Shen H, Liu X, Li R (2020) Mechanics and dynamics research considering the tool radial runout effect in plunge milling. Int J Adv Manuf Technol 106:2391–2402
12. Kumanchik LM, Schmitz TL (2007) Improved analytical chip thickness model for milling. Precis Eng 31:317–324
13. Wang JJJ, Zheng CM (2003) Identification of cutter offset in end milling without a prior knowledge of cutting coefficients. Int J Mach Tools Manuf 43:687–697
14. Grossi N, Morelli L, Scippa A, Campatelli G (2022) A frequency-based analysis of cutting force for depths of cut identification in peripheral end-milling. Mech Syst Signal Process 171
15. Urbikain G, Artetxe E, López de Lacalle LN (2017) Numerical simulation of milling forces with barrel-shaped tools considering runout and tool inclination angles. Appl Math Model 47:619–636
16. Diez E, Perez H, Guzman M, Vizan A (2013) An improved methodology for the experimental evaluation of tool runout in peripheral milling. Int J Adv Manuf Technol 65:283–293
17. Jing X, Tian Y, Yuan Y, Wang F (2017) A runout measuring method using modeling and simulation cutting force in micro end-milling. Int J Adv Manuf Technol 91:4191–4201
18. Zhang X, Zhang J, Zhang W, Li J, Zhao W (2018) A non-contact calibration method for cutter runout with spindle speed dependent effect and analysis of its influence on milling process. Precis Eng 51:280–290
19. Nakatani K, Yauchi M, Matsubara A, Yamaji I (2021) Improvement of machining accuracy by measurement and adjustment of dynamic runout of end mill. Procedia CIRP 101:306–309
20. Krüger M, Denkena B (2012) Model-based identification of tool runout in end milling and estimation of surface roughness from measured cutting forces. Int J Adv Manuf Technol 65(5):1067–1080
21. Seethaler RJ, Yellowley I (1999) The identification of radial runout in milling operations. J Manuf Sci Eng 121:524–531
22. Herman KA, Liang SY (1997) In-process monitoring of end milling cutter runout. Mechatronics 7:1–10
23. Grossi N, Morelli L, Venturini G, Scippa A (2021) Forces shapes in 3-axis end-milling: classification and characteristic equations. J Manuf Mater Process 5:117. 5, 117

24. Yang L, DeVor RE, Kapoor SG (2005) Analysis of force shape characteristics and detection of depth-of-cut variations in end milling. J Manuf Sci Eng 127:454–462
25. Scippa A, Sallese L, Grossi N, Campatelli G, Scippa A, Sallese L, Grossi N, Campatelli G (2015) Improved dynamic compensation for accurate cutting force measurements in milling applications. MSSP 54:314–324

Manufacturing and Testing of Shape Memory Polymer Composite Actuators

Leandro Iorio, Denise Bellisario, and Fabrizio Quadrini

Abstract Shape memory (SM) polymer composite (PC) actuators have been manufactured by using carbon fibre reinforced (CFR) prepregs and by integrating flexible heaters. The smart device has the structure of a composite sandwich with CFR plies as external skins, an embedded heater and SMP layers in between. Small epoxy foam tablets were also inserted in the laminate centre to increase the maximum attainable deformation during the memory step. These foams were produced by a solid-state process. The sandwich consolidation was obtained in one moulding step. For comparison, a second CFR-SMPC actuator was manufactured without the SMPC foams, thus reducing the final laminate thickness. SM performances of the SMPC devices were evaluated by thermo-mechanical cycling in bending configuration. Memory, constrained-recovery and free-recovery tests were carried out. Shape fixity and shape recovery were extracted as well as recovery loads. Results show the optimal SM behaviour of the new sandwich architecture.

Keywords Smart materials · Actuators · Composites

1 Introduction

Shape memory polymer composites (SMPCs) are smart materials with unique functional properties, in combination with typical structural performances of composites. They can be used to design and manufacture new-concept actuators.

In particular, carbon fibre reinforced (CFR) SMPCs maximize the structural properties of the smart laminates and take advantage of the technological development of the manufacturing procedures of CFR structures in aeronautics and aerospace. In

L. Iorio (✉) · F. Quadrini
Department of Industrial Engineering, University of Rome "Tor Vergata", Rome, Italy
e-mail: leandro.iorio@uniroma2.it

D. Bellisario
Faculty of Economics, Universitas Mercatorum, Rome, Italy

fact, many applications are reported for these sectors in the scientific literature such as morphing structures, deployable hinges, booms, antennas and reflectors [1].

SMPCs behave as stimuli responsive materials and the activation stimulus is mainly heat. For thermosets, the characteristic temperature for the shape transition is the glass transition temperature. In many cases, the SM behaviour of the smart composites depends on their matrix which consists of a shape memory polymer (SMP). Fibres remain elastic during heating and do not provide any SM contribution [2]. The typical memory-recovery cycle of a SMPC laminate is shown in Fig. 1. The composite shape, at the end of the manufacturing process, is the equilibrium shape, apart from small distortions related to the relaxation of residual stresses from manufacturing. This shape can be changed in a memory cycle where the laminate is heated and contemporarily deformed under loads and constraints. Because of heating, the composite material softens and is easy to be deformed. Subsequently, the laminate is left to cool under constraints. In the end of cooling, the constraints can be removed and most of the applied deformation remains frozen into a non-equilibrium shape. In order to recover the equilibrium shape, it is necessary to heat again the laminate in absence of any constraint. If some constraints are present, a recovery load is exerted on them. In the end of a free recovery step, the equilibrium shape is preserved also after cooling, and it is possible to apply a new frozen configuration only by repeating the memory step. For this reason, SMPCs are considered one-way SM materials.

This unique behaviour of SMPCs can be exploited to manufacture new-concept actuators which are integrated into the composite structure during manufacturing or are assembled in the end. These actuators are suitable for those cases where light multi-functional structures are requested with one-way slow-rate movements. The best example is the manufacturing of self-deploying space structures which are packed before the launch and are deployed one time in absence of gravity.

CFR-SMPC recovery has been tested in Space under microgravity [3] with the aim of designing actuators [4], self-deployable structures [5], antennas [6], and solar sails [7] but some efforts are still necessary for increasing the technology readiness level
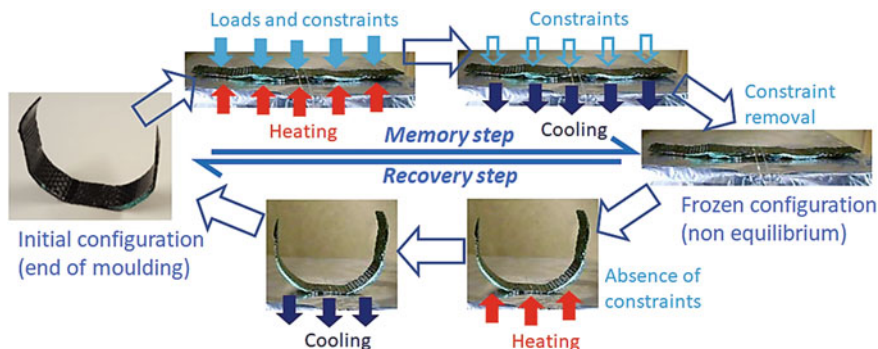
Fig. 1 The memory-recovery cycle for a CFR-SMPC laminate (results from the Horizon 2020 SMARTFAN project, GA No.760779)

of this innovation. In the last years, many studies have focused on the improvement of mechanical properties of SMPCs without affecting their SM behaviour. In fact, quasi-static properties of composites are generally enhanced by reducing molecular mobility of the matrix which is, instead, responsible for shape memory. Balancing structural and SM characteristics of SMPCs is a very complex task, and an important role is played by long carbon fibres [8], arranged in woven fabrics or unidirectional (UD) tapes [9]. CFR-SMPC are stiffer at room temperature and apply higher recovery loads in comparison with SMPs [10]. Nevertheless, UD CFR-SMPC exhibits local micro-buckling during bending deformation [11].

After transition, CFR-SMPCs exhibit high deformability and complex shapes can be frozen as shown in Fig. 2. A 2-ply CFR-SMPC spiral was manufactured and, subsequently, flattened. During free recovery by hot air, the initial equilibrium shape of the spiral is restored. Enhancing the laminate formability during the memory step is another important goal toward an effective application of SMPCs as more and more complex shapes can be frozen. A method to increase the laminate deformability takes advantage of the multi-layer nature of laminates, by inserting soft layers which work as rubbery cushions for the rigid CFR plies. For example, polystyrene interleaf layers have been inserted between CFR laminae [12]. Another advantage of this solution is that commercial CFR prepregs are used for SMPC manufacturing, as well as other commercial materials that do not need modification. Nevertheless, the structural properties of the CFR SMPC can be affected by the hybrid thermoplastic-thermoset polymer interface.

A recent innovation in CFR-SMPCs consists of inserting SMP epoxy interlayers between adjacent CFR layers during composite lamination [13]. Co-curing of these functional SMP layers and CFR prepregs is possible because the SMP polymer is available in the shape of a free uncured powder [14]. High performance CFR-SMPCs have been also manufactured by using commercial aeronautical prepregs [15] and tested under multiple memory-recovery cycles [16].

By increasing the number of CFR plies, the maximum allowable strain during the memory step strongly reduces. A further improvement can be originated with the

Fig. 2 Free recovery of a CFR-SMPC spiral (results from the Horizon 2020 SMARTFAN project, GA No.760779)

integration of SMP foams. In fact, the cellular structure amplifies the SM behaviour because of the cell-collapsing mechanism [17]. Important results have been found by using the same SM epoxy resin for laminate interlayers and foam inserts of the SMPC laminates [18]. This innovation has been possible thanks to the adoption of an innovative foaming process, namely solid-state foaming, which allows producing foams from thermosetting powders in absence of any foaming agent. These epoxy SM foams have been studied extensively for possible use in Space. They were tested under simulated microgravity and hyper-gravity [19], and their shape recovery was carried out under real micro-gravity in an experiment the International Space Station [20], and on the BION-M1 unmanned module [3].

In order to manufacture a CFR-SMPC actuator, the last aspect to consider is the integration of the heating system as most of the experiment on CFR-SMPC laminates and sandwiches have been carried out by thermal convection. Integrated flat heaters were used for the deployment of a SMPC hinge for space structures [21]. At the state of the art, CFR-SMPC sandwiches have been microscopically tested [22], and used to manufacture an integrated device with embedded heater [23]. A flexible heater was inserted during the composite lamination in the middle-plane of the SMPC sandwich, consisting of 4 CFR plies, 2 SMP foam cores, and 1 SMP interlayer. This unit had a limited size (20×45 mm^2) but was able to apply a recovery load about 7.4 N, almost independently from the recovery temperature. However, the reduced size poses serious limitations in its integration into self-deployable structures.

The aim of the current study is overcoming the current state-of-the-art of SMPC actuators by proposing a different architecture, according to Fig. 3. The length of this device is one of the largest ever manufactured for CFR-SMPC sandwich laminates, and combines all the discussed technological improvements: using an SMP foam to extend the laminate deformability; co-curing the SMP interlayers and the CFR prepreg plies; using commercial materials for SMP elements and CFR plies; embedding a flexible heater into the SMPC sandwich. A CFR-SMPC device needs uniform heating during memory and recovery steps. Embedded heaters reach this goal but are generally limited in size. A second actuator with only 2 CFR plies and an SMP interlayer has been manufactured for comparison. Memory-recovery cycles and free recovery tests have been performed for testing.

Fig. 3 Architecture of the CFR-SMPC actuator
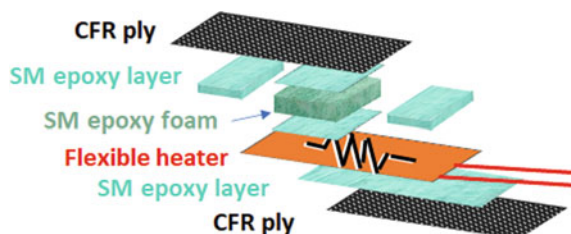
2　Materials and Methods

A CFR-SMPC actuator with a sandwich structure has been manufactured by using commercial raw materials and components. For comparison, a CFR-SMPC laminate has been also produced and tested. For design and optimization, 3-ply CFR laminates without SMP interlayer have been moulded before the actuators.

2.1　Supplied Materials

The SM epoxy resin (Scotchkote 206N) for functional interlayers and foams was supplied by 3M in the shape of an uncured thermosetting powder. It was combined with a 0/90 woven fabric prepreg (Solvay Cycom 132 977–2), designed for autoclave moulding. The flexible heaters (KHLVA-0504/10) were supplied by OMEGA and consisted of an Inconel etched circuit which was encapsulated between two layers of polyimide films. In order to maximize the size of the actuator, a large flexible heater has been acquired and the CFR-SMPC devices were laminated on it. These heaters have a thickness of 150 μm and a size of 13 $\times$ 90 mm^2. The nominal resistance is 40 Ω, and the maximum voltage is limited to 28 V which corresponds to a power of 19.6 W. At higher voltages, the heater temperature overcomes 200 °C that is the maximum allowable temperature, according to the device datasheet.

2.2　CFR Prepreg Characterization

Preliminary moulding and mechanical tests were performed to characterize the mechanical performances of the supplied CFR prepregs, and to find the optimal processing conditions of the lab-scale moulding process. The adopted moulding configuration is shown in Fig. 4a: 3-ply CFR laminates were compression moulded on a heating plate, by applying the pressure through a universal material testing machine (MTS Alliance RT/50), equipped with a 10 kN load cell and a compression platen on the crosshead. This number of plies was selected as a compromise to have thin laminates but flat and enough stiff to be tested up to failure by bending.

Prepreg plies were cut with the shape of 15 $\times$ 100 mm^2, and laminated into an aluminium mould, between two release films. The mould consisted of a bottom plate, a rectangular chamber, and a top punch. A soft rubber insert was inserted between the top release film and the punch to allow pressure distribution during moulding. A spring was located between the punch and the compression platen of the testing machine.

The role of the spring was compensating the thickness reduction of laminates due to agglomeration, as the machine crosshead was fixed during moulding. For
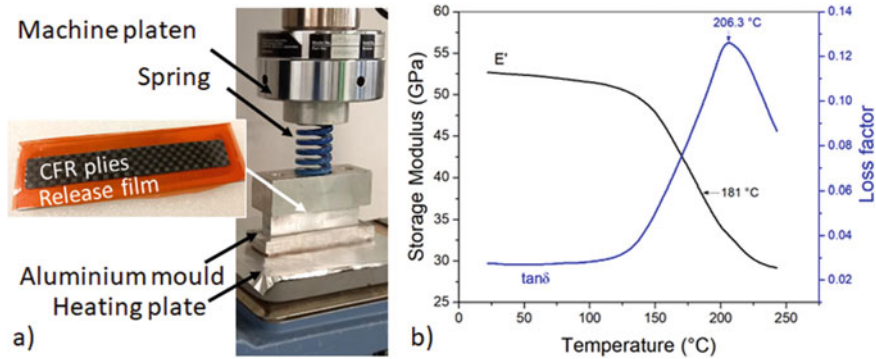
Fig. 4 Compression moulding configuration of CFR composite samples (**a**) and DMA test of a CFR laminate (**b**)

curing, process parameters were initially inferred from suggested parameters of autoclave molding by the prepreg datasheet, and partially modified. In order to move to compression molding, a higher temperature was selected (200 °C) with a lower pressure (2 bar) and shorter holding time (30 min).

In order to verify that the adopted moulding procedure would be able to consolidate the CFR laminates, mechanical tests were carried out (by MTS Insight 5) in a 3-point bending configuration, with a span length of 30 mm, and a testing rate of 10 mm/min up to break. Testing parameters were selected to have sample failure during bending. Results on 5 samples showed the optimal agglomeration of the laminates. In fact, their average thickness was 0.66 ± 0.01 mm, with a cured ply thickness of 220 μm. The resulting bending strength was 840 ± 70 MPa, the maximum strain $2.3 \pm 0.2\%$, and the elastic modulus 47 ± 4 GPa.

The CFR prepreg characterization was concluded with a dynamic mechanical analysis (DMA) test to evaluate its suitability to be integrated into a CFR-SMPC device with the embedded heater. The risk was that the heater would be not able to provide sufficient heat for laminate softening. The test (by Netzsch DMA 242C) was carried out on a single 3-ply CFR sample with a 3-point bending configuration as well. A temperature scan from room temperature to 250 °C was performed at the rate of 5 °C/min, the span length of 40 mm, and the oscillation frequency of 10 Hz. Results are reported in Fig. 4b. The glass transition temperature of the cured CFR laminate can be extracted from the inflection point of the storage modulus (181 °C) and the peak of the loss factor (206 °C). It has been discussed that this glass transition temperature reduces into a CFR-SMPC laminate because of the interaction with the SMP resin [23]. Therefore, it is expected that the CFR plies of the SMPC actuators will soften by the heat of the flexible heater without exceeding its maximum temperature of 200 °C.

2.3 CFR-SMPC Actuator Manufacturing

The CFR-SMPC devices were manufactured in one-step curing process with the same moulding procedure of the neat CFR laminates. The architecture of Fig. 3 was used for the sandwich configuration. Some details of the SMP foam core preparation are reported in Fig. 5. A tablet with the height of 10 mm and the diameter of 20 mm was made by cold compression moulding of the uncured SMP powder. This tablet was solid-state foamed in oven at 320 °C for 8 min into a steel mould.

The foam was cut into 2 mm thick slices from which foam blocks with the nominal size of 13×13 mm^2 were extracted. Higher thicknesses would lead to excessive reduction of the sandwich stiffness. Instead, the width was the same of the selected flexible heater of the actuator. In fact, for the lamination of the CFR-SMPC devices, the CFR plies were cut with the same nominal size of the flexible heater (13×90 mm^2). The CFR-SMPC sandwich actuator was laminated into the mould by using a single CFR ply for the external skins. As shown in Fig. 6, a layer of SMP powder was distributed on the bottom CFR ply, having a mass of 0.17 g which corresponds to a nominal thickness of the SMP interlayer of 100 μm [16]. Subsequently, the heater was placed on it, and two foam tablets on the heater. The volumes before and after the foam tablets were filled with uncured SMP powder: 1.2 g for each side, as calculated by the value of the nominal volume to fill and the cured resin density (1.4 g/cm^3).
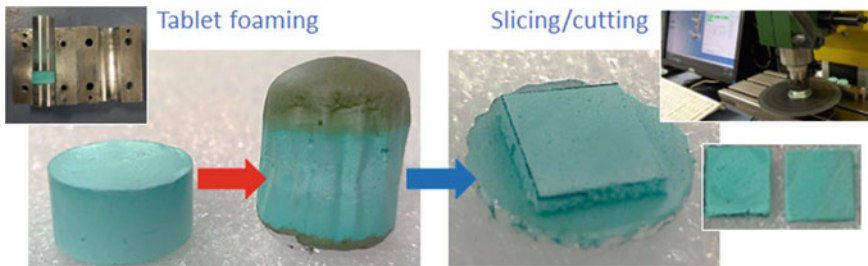
Fig. 5 Preparation of the SMP foam cores of the CFR-SMPC sandwich device
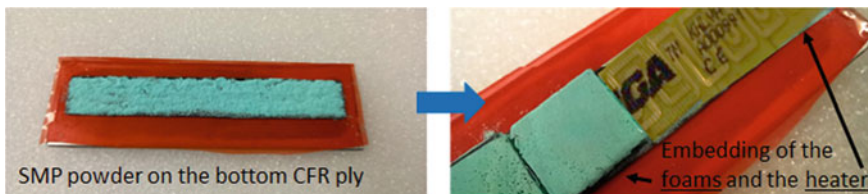
Fig. 6 Main steps of the lamination procedure for the CFR-SMPC sandwich device
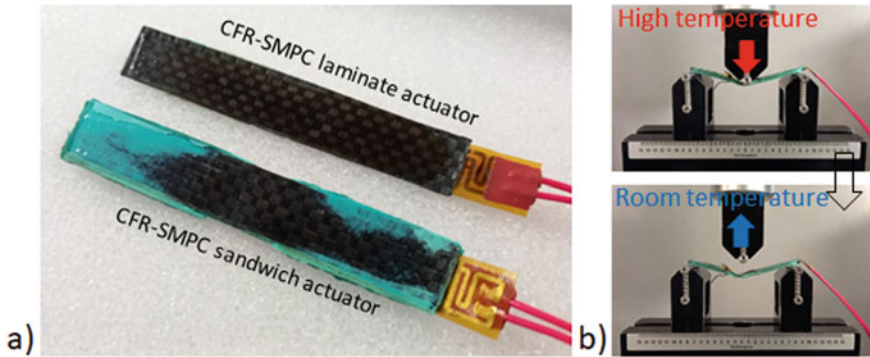
Fig. 7 Manufactured CFR-SMPC devices (**a**) and steps of memory testing in bending configuration and hot deformation mode for the CFR-SMPC sandwich actuator (**b**)

The lamination procedure ended by placing another layer of SMP resin and the top CFR ply. Subsequently, the punch was added to close the mold for curing under the machine platen.

For comparison, a 2-ply CFR-SMPC actuator with embedded heater was moulded with the same procedure of the neat CFR samples and the SMPC sandwich device. In this case, the flexible heater was placed in the neutral axis of the laminate and joined with the external CFR plies by two SMP interlayers, each one with the nominal thickness of 100 μm. The 2 manufactured CFR-SMPC devices are shown in Fig. 7a. The one-step molding procedure has been able to consolidate both the actuators.

2.4 Shape Memory Testing

Shape memory properties of the manufactured actuators were tested by memory, constrained-recovery and free-recovery tests, under the bending configuration.

The memory test was carried out in the so-called "hot deformation mode" [23]. In this case, the samples to test are heated up to their soft state before testing. Subsequently the load is applied according to the selected loading scheme. In this study, the 3-point bending configuration was chosen with a span length of 80 mm, and the softened actuators were bent at the rate of 10 mm/min up to 5 and 10 mm in 2 consecutive tests. The same testing parameters were selected for the laminate and the sandwich device for comparison. SMPC softening occurred by heating up the devices with the embedded heater at the voltage of 26 V (93% of the maximum allowable). A current of 0.63 A resulted for a power of 16.4 W. After loading in the MTS Insight 5 machine, the heater was switched off and the machine crosshead was fixed for the time of 5 min, which was sufficient to cool the devices down to the room temperature, approximately. The testing procedure ends by un-loading the samples to measure the residual elastic recovery. In Fig. 7b, the holding step of the CFR-SMPC
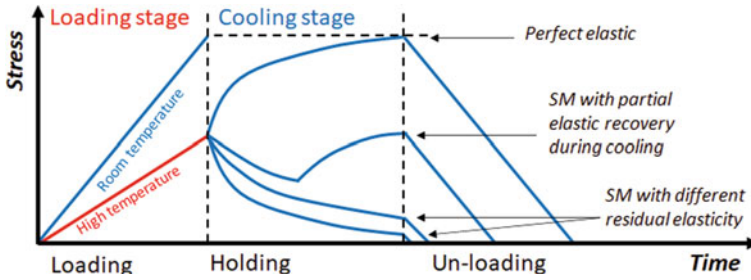
Fig. 8 Theoretical behaviour of perfect elastic and SM materials in a memory test with the hot deformation mode

sandwich device is shown together with the final deformed configuration in the case of 10 mm of nominal inflection. This 3-step testing procedure of the "hot deformation mode" (hot loading, holding under cooling, and un-loading) allows recognising the behaviour of the tested material, and quantifying its SM performances. The response of a generic material to this kind of test is represented by the curves of Fig. 8 in terms of stress versus time.

In the loading stage, the stress increases linearly, and the slope of this line is related to the sample stiffness. As the material softens under heating, this stiffness is lower than the case of room temperature testing. In the end of loading, the heating is interrupted, and the material starts to cool. A perfectly elastic material increases its stiffness up to reach the stress level that would have had in the case of a room temperature loading. In the final un-loading step, the full deformation is recovered with the same slope of the loading stage. If the material is a SMP, most of the stress is forgot during the cooling stage, and the applied deformation is mostly frozen as well. During un-loading, a small amount of residual elastic stress is recovered as well as a part of the applied deformation. Good SMPs show high initial stresses in the end of the loading stage together with very low residual elastic stresses in the end of the cooling stage, without the occurrence of any damage. From a conceptual point of view, the residual elasticity could be zero in the end of testing, but that is a very rare occurrence and only for very soft polymers.

Between these two opposite behaviours (perfect elastic and SMP), it is possible that the stress decrease in the cooling stage is partially compensated by a small elastic stress increase at low temperature. This behaviour is typical of SM samples with high stiffness or with strong contribution of non-SM elements. An example is the manufactured CFR-SMPC actuator with sandwich architecture because of the high device thickness and the presence of the carbon fibres in the external skins.

In the experimentation, during the memory tests, a type-J thermocouple was placed at the device intrados to monitor the temperature during time. The SMPC sandwich device was placed with the foamed tablets from the side of the punch. After each memory test at 5 mm or 10 mm, constrained recovery tests were carried out too. In this case, after un-loading from the memory test, a small pre-load (1 N) was applied by the punch on the device with the frozen configuration. Subsequently, the machine

Fig. 9 Initial and final configuration of the SMPC laminate device during the free recovery test (case of 10 mm of inflection by bending) and difference between the considered maximum displacement in the memory and free recovery test

crosshead was stopped and the heater was switched on with the same voltage of the memory step (26 V). Due to heating, the devices would recover the shape but, for the presence of the constraints, they remain deformed and apply a recovery load to the punch. After 5 min, the heaters were switched off and the devices were left to cool under constraints. Constrained recovery tests were carried out by monitoring the temperature at the device intrados as the memory tests. The tests ended when the device temperature approached again the room temperature. The un-loading phase was not recorded.

However, after load removal, a further elastic stress recovery was observed as well as a reduction of the frozen deformation, in addition to those of the memory test. In order to close the SM testing, at the end of each constrained-recovery test, a free recovery test was also performed by heating the devices with the same voltage (26 V) but in absence of constraints. Free recovery was camera recorded to extract the displacement of the inflection point during time. In this case, the displacement was measured from the device ends and not from the supports as in the previous tests. In the end of the free recovery test, a small residual displacement can be present. The case of the free recovery of the SMPC laminate device is shown in Fig. 9, together with the description of the difference between the maximum displacement from the memory tests and in the free recovery tests.

In order to quantify the loss of deformation during the memory-recovery cycle, it is possible to consider the shape fixity R_f and the shape recovery R_r:

$$R_f = \frac{\varepsilon_u}{\varepsilon_m}.100 \tag{1}$$

$$R_r = \frac{\varepsilon_r}{\varepsilon_m}.100 \tag{2}$$

where ε_u is the frozen strain after load removal, and ε_r is the recovered strain. The term ε_r is calculated as the difference between the maximum applied strain in the memory test ε_m, and the final residual strain after the free recovery test. An optimal SMP shows both parameters, R_f and R_r, close to 100% as R_f expresses the ability of the sample to store the applied without elastic stress recovery, and R_r measures the possibility of recovering the initial equilibrium configuration, without residual deformation in the end of free recovery.

3   Results and Discussion

The CFR-SMPC laminate device has an average thickness of 0.89 mm and a weight of 5.7 g. By considering the thickness of the embedded heater (150 µm) and the thickness of cured CFR plies from the characterization tests (220 µm), the thickness of 150 µm for the SMP interlayer is extracted, 50% more than the expected nominal thickness of 100 µm. This discrepancy may be accepted as a laboratory procedure has been adopted and some errors can be originated by the assumption that the same thickness of the single cured ply is present in the 3-ply neat CFR laminates and in the device CFR skins. Moreover, the nominal thickness for the flexible heater has been used. For the sandwich actuator, which has a final average thickness about 2.68 mm with 2 mm thick foam tablets, a thickness of 90 µm can be inferred for the SMP interlayer between the heater and the bottom CFR ply. In both cases, similar SMP interlayers can be discussed for the 2 actuators.

In terms of weight, the sandwich architecture leads to an increase. In fact, the CFR-SMPC sandwich has a weight of 8.2 g, 44% more than the laminate. As the heater has a weight about 5 g, and both devices have the same number of CFR plies, the sandwich actuator has an amount of 2.5 g more of SM resin.

This additional SMP weight is in the form of foam, filling volume, and interlayer (30% of the device weight). The goal of the design of the new architecture (Fig. 3) is increasing the stiffness at room temperature of the actuator as well as its deformability in the soft state. The bending stiffness of the SMPC laminate at room temperature, with the span length of 80 mm, is 2.2 N/mm which corresponds to the bending modulus of 25.7 GPa. The SMPC sandwich has a lower modulus (10.5 GPa) but a higher stiffness (22.6 N/mm), 10 times the laminate. For the deformability of the device in the soft state, the use of a higher amount of SMP in comparison with the laminate is already a first solution. Nevertheless, the related increase of the device thickness leads to higher stresses in the CFR skins.

For this reason, the use of foams localized in the centre of the actuator helps in reducing memory stresses by the mechanism of cell collapsing. The instrumented memory-constrained recovery-free recovery cycle has been implemented to understand if this new architecture is really valid in comparison with the traditional 2-ply laminate with a SMP interlayer. Results from memory and constrained recovery tests are shown in Fig. 10 in the case of 10 mm of applied inflection.

Reported stresses were calculated by the Euler–Bernoulli beam equation. The comparison between stress values is not possible on the same graph because of the big difference in achieved maximum values (being 10 times higher for the laminate). Before the memory test, both devices reached a comparable temperature at intrados: exactly 181 °C for the laminate and 185 °C for the sandwich. Similar values of temperature (177, and 176 °C respectively) were also reached in the end of the constrained recovery step. These values of temperatures are able to soft the CFR plies according to data of Fig. 4b. However, by comparing the temperature curves of the constrained recovery test, it is possible to observe the effect of the thicker section of the sandwich device on the heating rate. In fact, the thin laminate needs only 1
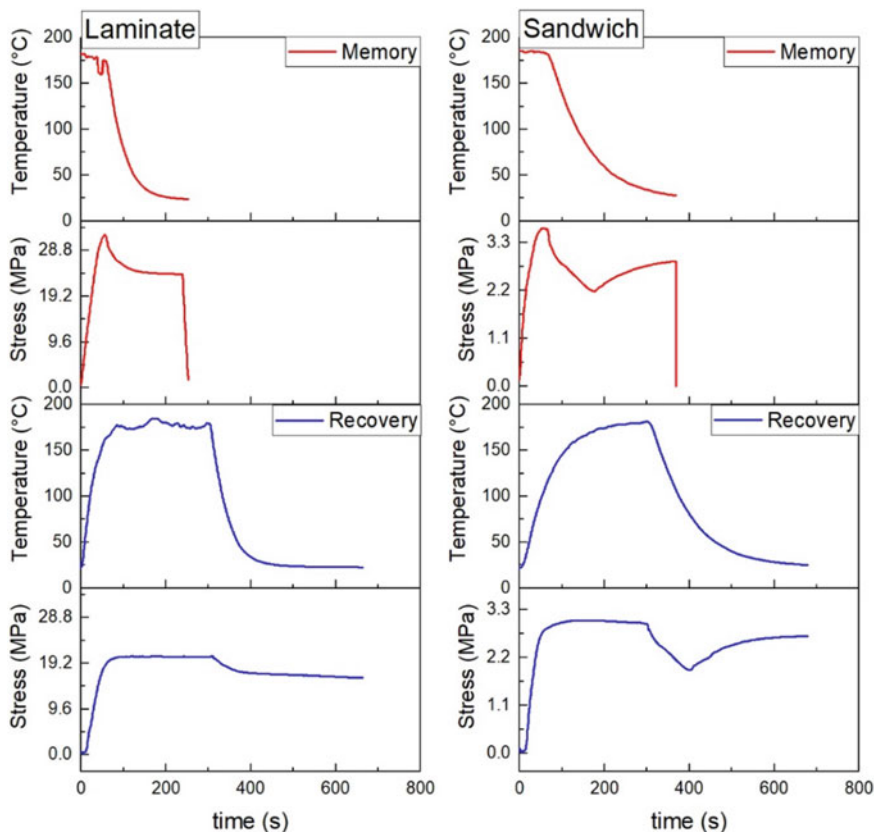
Fig. 10 Temperature and stress curves for the memory and constrained recovery tests of CFR-SMPC actuators in the case of 10 mm of maximum applied displacement

min to exceed the temperature of 170 °C whereas this threshold is exceeded after 3 min by the SMPC sandwich.

In the memory test, the SMPC laminate, shows a typical behaviour of SMPs with a continuous stress decay during cooling. Unfortunately, the stress level is high, starting from 32.2 MPa and is only partially reduced by the SM behaviour of the SMPC, with the consequence of a large displacement recovery in the un-loading step. In the case of the SMPC sandwich, the discussed partial elastic recovery during cooling (Fig. 8) is observed both in the memory and the constrained recovery test. This occurrence is related to the higher stiffness of the CFR-SMPC sandwich device and is responsible to increase the stress in the final plateau zone over the value of the initial applied stress, at the end of the loading stage. Nevertheless, it is important to note that stresses of Fig. 10 are normalized stresses at the intrados/extrados of the bent samples, and do not consider possible local densification because of the rubbery state of the SMP interlayers and foams. It is expected that the real applied stresses

are lower than those numerically calculated in the hypothesis of uniform bending, and much lower for the thick sandwich rather than the thin laminate.

In quantitative terms, the comparison between the two SMPC devices is proposed in Table 1 for both applied displacements (5 and 10 mm) in the memory test. One test was performed for each condition. For the SMPC laminate, the peak load is higher than the sandwich at similar displacement, but the plateau load (in the end of the cooling stage) is comparable because of the elastic stress recovery during cooling of the sandwich. However, the applied stresses remain always low for the SMPC sandwich during both the loading and the cooling stage, with positive effects on the shape fixity.

In fact, the shape fixity is 98% on average for the CFR-SMPC actuator, much higher than 77% of the laminate. As expected, the proposed architecture of the sandwich device combines high stiffness at room temperature with very good ability to freeze the non-equilibrium shape after the memory test. This advantage is paid in terms of the observed weight increase. There could be the further disadvantage of the reduction of the recovery load, which is very important to provide an efficient actuation. Instead, quantitative data of Table 2 on results from the constrained recovery tests, at both applied displacements, show that the recovery loads of the SMPC sandwich are comparable or slightly lower than the laminate. Moreover, the optimal SM behaviour of the sandwich architecture is confirmed by the low decrease of the shape fixity in the end of the constrained recovery test. In fact, it is expected that SMPs and SMPCs always recover a small part of the frozen displacement at each heating over the characteristic temperature. This loss of frozen displacement leads to a reduction of the shape fixity. In the case of the laminate, the shape fixity passes from 77% on average to 63% with a loss of 14% of the applied deformation whereas this loss is only 3% for the sandwich. This fact allows predicting that the CFR-SMPC sandwich actuators could be used under multiple cycling with small decrease of the SM behaviour.

Being more elastic than the sandwich configuration, it can be expected that the CFR-SMPC laminate could show an higher shape recovery, as confirmed by the results of the free recovery tests. Displacement and recovery rate curves are shown for both actuators in Fig. 11 for the case of 10 mm of applied displacement in the memory test. The SMPC laminate take 1 min for full recovery, almost half than the

Table 1 Experimental data from memory tests of the CFR-SMPC actuators

Sample	Nominal applied displacement	Peak load	Peak stress	Plateau load	Plateau stress	Shape fixity
ID	mm	N	MPa	N	MPa	%
Laminate	5	3.5	25.4	2.7	19.6	75.5
	10	5.8	32.2	4.3	23.9	78.5
Sandwich	5	2.6	3.1	2.6	3.0	97.3
	10	3.1	3.6	2.5	2.9	98.1

Table 2 Experimental data from recovery tests of the CFR-SMPC actuators

Sample	Nominal applied displacement	Constrained			Free		
		Peak load	Peak stress	Shape fixity	Maximum displacement	Recovery rate	Shape recovery
ID	mm	N	MPa	%	mm	mm/s	%
Laminate	5	2.3	16.7	60.8	4.2	0.04	97.4
	10	3.6	20.7	65.5	7.6	0.06	98.4
Sandwich	5	2.5	2.9	93.1	4.8	0.02	92.1
	10	2.6	3.1	95.9	9.8	0.04	97.3

sandwich. Curves also show that both actuators recover the equilibrium configuration differently, more uniformly for the SMPC laminate, probably due to the lower time necessary to reach a stable temperature distribution. The SMPC sandwich reaches higher speeds but needs more time for full recovery.

In Table 2, quantitative data from free recovery tests are reported and the higher average speed of the SMPC laminate is visible, being 0.05 mm/s on average in comparison with 0.03 mm/s for the sandwich. In general, these rates are very low, and this is a typical characteristic of the SMPC actuators. The shape recovery of the SMPC laminate is higher than the sandwich, as expected, but a difference of 3% of applied deformation is only present. This difference is acceptable by considering the very high shape fixity which has been reached by the same CFR-SMPC sandwich actuator.
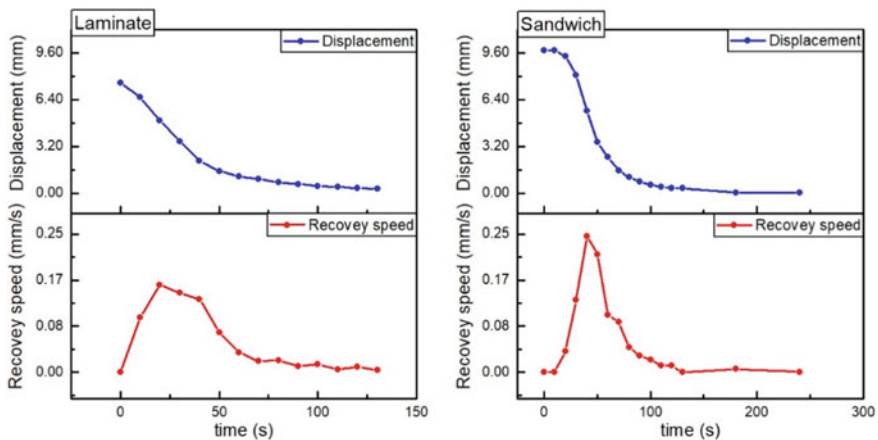
Fig. 11 Displacement and recovery rate curves for the free recovery tests of CFR-SMPC actuators in the case of 10 mm of maximum applied displacement

4   Conclusion

The proposed architecture of the CFR-SMPC sandwich actuator reaches the target of increasing the room temperature stiffness of the actuator together with its deformability in the memory step without affecting excessively the recovery loads. Moreover, very high shape fixity values have been obtained for the SMPC, also after multiple heating–cooling cycles.

The discussed prototypes of the CFR-SMPC actuators represent some of the largest ever manufactured in the state-of-the-art and have a size already interesting for some industrial uses, mainly for self-deploying of space structure. This result has been reached thanks to the one-step manufacturing procedure with lamination of the CFR plies and the SMP layers and foams directly on the flexible heater.

During testing, small displacements have been applied to the CFR-SMPC devices (5 and 10 mm) because of the need to provide a correct comparison between them. Under bending, the maximum strain is applied at the intrados and extrados of the middle cross-section of the bent samples. This solution is very effective to characterize the SM behaviour of the CFR-SMPC devices but it could provide the wrong perception that these materials can undergo small shape changes during actuation. Instead, by spreading the same maximum strain over the entire device length, it is possible to obtain quite large shape-changes. From a theoretical point of view, by applying a curvature equal to $1/R$ to a laminate with thickness t, at a distance y from the neutral axis, the applied deformation ε is equal to y/R.

Therefore, for the CFR-SMPC sandwich actuator (with a thickness of 2.68 mm) a uniform curvature radius of 50 mm leads to a maximum strain of 2.5%, the same of the memory step with 10 mm of inflection. In Fig. 12, the CFR-SMPC sandwich device is shown with a frozen configuration with a curvature radius of 25 and 50 mm. In the case of the lower curvature, the SMPC laminate is shown for comparison. These images show the ability of this device to undergo important shape changes without damaging.
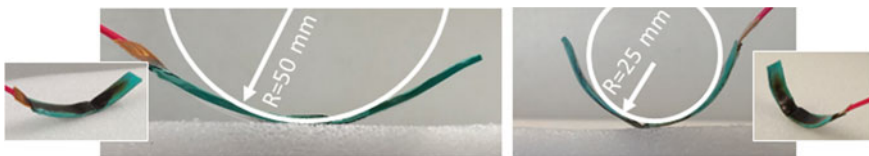
Fig. 12   Shape change ability of the CFR-SMPC actuators

References

1. Liu Y, Du H, Liu L, Leng J (2014) Shape memory polymers and their composites in aerospace applications: a review. Smart Mater Struct 23(2), art. n°:023001
2. Leng J, Lan X, Liu Y, Du S (2011) Shape-memory polymers and their composites: stimulus methods and applications. Prog Mater Sci 56(7):1077–1135
3. Santo L, Quadrini F, Ganga PL, Zolesi V (2015) Mission BION-M1: results of Ribes/Foam2 experiment on shape memory polymer foams and composites. Aerosp Sci Technol 40:109–114
4. Ameduri S, Ciminello M, Concilio A, Quadrini F, Santo L (2019) Shape memory polymer composite actuator: modelling approach for preliminary design and validation. Actuators 8(3), art. n°:5
5. Santo L, Quadrini F, Accettura AG, Villadei W (2014) Shape memory composites for self-deployable structures in aerospace applications. Procedia Eng 88:42–47
6. Santo L, Quadrini F, Bellisario D (2016) Shape memory composite antennas for space applications. IOP Conf Ser Mater Sci Eng 161(1), art. n°:012066
7. Santo L, Bellisario D, Iorio L, Quadrini F (2019) Shape memory composite structures for self-deployable solar sails. Astrodynamics 3(3):247–255
8. Liu Y, Guo Y, Zhao J, Chen X, Zhang H, Hu G, Yu X, Zhang Z (2019) Carbon fiber reinforced shape memory epoxy composites with superior mechanical performances. Compos Sci Technol 177:49–56
9. Li F, Scarpa F, Lan X, Liu L, Liu Y, Leng J (2019) Bending shape recovery of unidirectional carbon fiber reinforced epoxy-based shape memory polymer composites. Compos A Appl Sci Manuf 116:169–179
10. Basit A, L'Hostis G, Durand B (2019) The recovery properties under load of a shape memory polymer composite material. Materialwiss Werkstofftech 50(12):1555–1559
11. Lan X, Liu L, Liu Y, Leng J (2020) Thermomechanical properties and deformation behavior of a unidirectional carbon-fiber-reinforced shape memory polymer composite laminate. J Appl Polymer Sci 137(14), art. n°:48532
12. Robinson P, Bismark A, Zhang B, Maples HA (2017) Deployable, shape memory carbon fibre composites without shape memory constituents. Compos Sci Technol 145:96–104
13. Tedde GM, Santo L, Bellisario D, Iorio L, Quadrini F (2018) Frozen stresses in shape memory polymer composites. Materiale Plastice 55(4):494–497
14. Santo L, Iorio L, Tedde GM, Quadrini F (2018) Shape memory behavior of carbon composites with functional interlayer. In: ASME 2018 13th international manufacturing science and engineering conference, MSEC 2018, vol 2. American Society of Mechanical Engineers (ASME), pp V002T04A013
15. Quadrini F, Bellisario D, Iorio L, Santo L (2019) Shape memory polymer composites by molding aeronautical prepregs with shape memory polymer interlayers. Mater Res Express 6(11), art. n°:115711
16. Quadrini F, Iorio L, Bellisario D, Santo L (2022) Durability of shape memory polymer composite laminates under thermo-mechanical cycling. J Compos Sci 6(3), art. n°:91
17. Squeo EA, Quadrini F (2010) Shape memory epoxy foams by solid-state foaming. Smart Mater Struct 19(10), art. n°:105002
18. Santo L, Quadrini F, De Chiffre L (2013) Forming of shape memory composite structures. Key Eng Mater 554–557:1930–1937
19. Quadrini F, Tedde GM, Santo L, Van Loon JJWA (2018) Solid-state foaming of epoxy resin under hypergravity and simulated microgravity. Adv Polym Technol 37(7):2616–2624
20. Santo L, Quadrini F, Squeo EA, Dolce F, Mascetti G, Bertolotto D, Villadei W, Ganga PL, Zolesi V (2012) Behavior of shape memory epoxy foams in microgravity: experimental results of STS-134 mission. Microgravity Sci Technol 24(4):287–296
21. Dao TD, Goo NS, Yu WR (2018) Blocking force measurement of shape memory polymer composite hinges for space deployable structures. J Intell Mater Syst Struct 29(18):3667–3678

22. Bellisario D, Quadrini F, Iorio L, Santo L, Zhang Z, Li X, Dong H, Semitekolos D, Konstantopoulos G, Charitidis CA (2022) Microscopic testing of carbon fiber laminates with shape memory epoxy interlayer. Mater Today Commun 32, art n°:103854
23. Quadrini F, Iorio L, Bellisario D, Santo L (2021) Shape memory polymer composite unit with embedded heater. Smart Mater Struct 30(7), art. n°:075009

Control Policy for Production Capacity Modulation with Waiting-Time-Constrained Work in Process

Matteo Mastrangelo, Maria Chiara Magnanini, and Tullio A. M. Tolio

Abstract Reducing scrap is one of the key objectives of manufacturing companies to increase production efficiency and sustainability. Although many causes of scrap can be attributed to deviations at level of single processes, there are other causes inevitably related to dynamics at system level, as in presence of perishable material. In such situations the amount of time material waits in buffers, and therefore its level of degradation, is a consequence of the interaction among dynamics of the different production resources. This work presents an analytical model of a two-stage production system with perishable work in process. The model includes a control policy that modulates production capacity of parallel machines based on buffer and machines state, to reduce average waiting time and therefore scrap. Results from an industrial case in the semiconductor manufacturing sector show the usefulness of the policy in reducing scrap when the maximum waiting time of work in process is constrained.

Keywords Manufacturing systems · Quality · Control policies

1 Introduction

Manufacturing companies face a more complex and demanding environment today than in the past. They must satisfy market demands while remaining competitive, all while decreasing the environmental impact of the industrial sector. These objectives can be achieved by pursuing a more sustainable production, which involves creating top-quality products while minimizing resource usage, including energy and materials [1].

Sustainable production necessarily involves improved production efficiency. With modern manufacturing systems becoming increasingly integrated, final performance results from the interaction of a multitude of factors: production planning and

M. Mastrangelo (✉) · M. C. Magnanini · T. A. M. Tolio
Department of Mechanical Engineering, Politecnico di Milano, Milan, Italy
e-mail: matteo.mastrangelo@polimi.it

scheduling, material flow management, inventory control, equipment efficiency, availability of workforce, maintenance practices, quality inspection methods, scrap and waste management policies, and others. To enhance production efficiency, the combined effects of such factors must be considered through integrated approaches that address the interdependence between key manufacturing functions as, for example, logistics, maintenance and quality [2]. It is crucial to have performance evaluation models that can take into account the numerous factors that affect a production system. Performance evaluation serves as a vital tool in comprehending how a system behaves in novel scenarios or estimating the impact of changes to its configuration and/or management policies [3]. Therefore, performance evaluation represents the foundation for optimization and continuous improvement.

One way to enhance production sustainability and efficiency is by improving quality and reducing scrap, which often stems from localized deviations in individual processes such as tool wear, incorrect part positioning, overheating damage, and unwanted vibrations. Process monitoring and control methods are typically utilized to identify and correct such deviations. Although the sources of defects are not directly connected to other manufacturing functions, interaction effects between quality control methods and production logistics may arise. It is critical for instance to evaluate how material flow dynamics can impact the detection and correction of process deviations [4].

However, for production systems involving perishable materials, production logistics can directly contribute to scrap. Perishable materials are susceptible to contamination from the production environment and deterioration over time due to their intermediate state and storage conditions. Extended waiting periods at crucial locations in the production system can negatively impact the quality of work in process. In these situations, it is important to manage production resources effectively to facilitate smooth material flow throughout the factory and prevent excessive accumulation of work in progress.

This paper proposes a control policy for modulating production capacity in presence of parallel unreliable machines and perishable work in process. Manufacturing systems frequently incorporate parallel machines to increase production capacity and balance stages in multi-stage systems. Despite the widespread use, performance evaluation of systems that include parallel machines continues to be an area of interest for researchers [5]. This paper is centered on the definition of a semi-Markov model that incorporates the proposed policy into a two-stage manufacturing system with an inter-operational buffer. The two-stage system serves as the fundamental modeling unit for developing decomposition-based approaches to assess the performance of more extensive systems [6]. Within the reference system, the control policy activates and deactivates machines based on the state of both the buffer and the machines themselves.

The remainder of the paper is organized as follows. Section 2 presents an analysis of the relevant state of the art. Section 3 describes the problem under analysis and Sect. 4 presents the adopted modeling approach. Section 5 describes a case study where the proposed policy is applied to a semiconductor manufacturing system. Section 6 provides conclusions and suggestions for future research.

2 State of the Art

The focus of this paper is on two key subjects that are significant in the state of the art. From an industrial perspective, the management of perishable work in process in production systems is addressed. From the modeling point of view, the work is related to the development of performance evaluation models that integrate production logistics and quality control.

2.1 Perishable Work in Process in Production Systems

Perishability of work in process is a relevant issue in different industrial sectors. In the food processing industry products are subject to perishability, due to possible external contamination and degradation of the material itself, while stored in buffers. Production control in this sector requires accurate determination of quantity to produce based on customer demand [7]. Analogously, the pharmaceutical sector is characterized by deterioration of both finished products and intermediate materials due to chemical nature of processes and products. Accurate inventory control is necessary in order to avoid waste of possibly harmful material [8].

Electronics and semiconductor manufacturing processes are frequently performed at a microscopic scale, resulting in strict limits on the acceptable level of impurities present in incoming parts, as in the diffusion operation in wafer fabrication [9]. Accumulation of large quantities of impurities over long periods of time may cause work in process material to be scrapped or reworked. Thus, inventory control policies are usually focused on keeping low inventory levels, considering the high value of the inventory as well [10].

The majority of studies on control of perishable inventories concentrate on the supply chain [11]. Literature includes works that deal with this problem under various assumptions, including constant [12] or intermittent demand [13], and material with fixed expiration time [14] and or continuous deterioration over time [15]. Outcomes from these works are well-suited for production planning, where time horizons are usually in the order of several days, allowing for possible variations of the control parameters over time [16]. Implementation of these policies can be challenging in contexts where variations occur within hours or even minutes, such as in the shop floor. In such contexts, it would be more practical to implement policies to manage the flow of material based on fixed control points.

2.2   Performance Evaluation Models Integrating Quality

Performance evaluation is an essential step towards improvement of manufacturing systems and involves estimating the effect of various factors on performance indicators such as throughput, work in process level, efficiency, among others. Quality is considered one of the most critical factors that can influence system behavior and performance. Therefore, efforts for their integration in performance evaluation models start with including production resources that may produce parts with imperfect quality [17]. The presence of out-of-control states, potentially producing large numbers of defective parts, is accounted in [18] for small systems including SPC methods and extended in [19] to larger systems. Other contributions include the evaluation and improvement of systems including quality-quantity coupled operations, where the quality of parts as output of manual operations decreases as the operation cycle time decreases [20].

Besides, the issue of quality deterioration, caused by machine stoppages and long waiting times, is not new to the literature. Scrapping policies in response to machine failures are analyzed for instance in [21], considering buffer-less systems with both presence and absence of deterioration memory, in [22], analyzing scrapping policies resulting from stoppages of pharmaceutical production systems, and [23], differentiating between long lasting failures, causing deterioration, and rapid failures that do not influence the quality of parts. Although such works represent valuable contributions to management of deteriorating products in different real scenarios, they do not consider material perishing that is caused by minor stoppages and delay, which are much more frequent during ordinary operation of manufacturing systems.

3   Problem Description

The reference manufacturing system is composed of two production stages decoupled by an inter-operational buffer with finite capacity. The material waiting in the buffer is perishable, meaning that its quality deteriorates as the waiting time increases, possibly leading to scrap. This represents the minimum system configuration allowing to account for the effect of material flow dynamics on quality of perishable material. The concepts that will be presented for the reference system could be applied to larger systems, with the help of decomposition-based performance evaluation approaches [6]. The upstream stage is made of parallel machines that perform the same operation. The downstream stage may be either made of a single machine or multiple machines. All machines are subject to random failures. The system is shown in Fig. 1, where blue squares represent machines and the yellow circle represents the buffer.

To reduce the amount of material being scrapped because of perishability, it is important to control the amount of time material spends waiting inside the buffer. Although one could simply increase productivity of the downstream stage to speed

up material outflow from the buffer, e.g. improving machines availability, this would
lead to poor improvement in case the downstream stage itself is the bottleneck of
the system. Therefore, in many cases it is preferable to act on the upstream stage to
improve control over the level of work in process and keep it as low as possible. This
translates in a reduction of the overall productivity of the upstream stage, so that the
buffer fills up more slowly on average and the average filling rate gets closer to the
average emptying rate, determined by the downstream stage. Productivity reduction
at the upstream stage can be obtained either by decreasing its production rate or by
increasing the amount of non-productive time.

In a production stage that consists of multiple parallel machines, the first action
can be obtained by switching off some of them, so that the overall material flow
from the upstream stage to the buffer is reduced. The second action instead can be
achieved by switching off all machines and keeping them inactive for extended time
windows, differently from what usually happens in production systems with finite
buffers. Indeed, it is common practice to keep machines idle just until enough free
space in the following buffer becomes available.

To exploit the beneficial effects of both actions, they can be combined in a control
policy that modulates the production capacity of the upstream production stage
depending on the level of the work in process and the state of machines. Specifi-
cally, machines are activated or deactivated in correspondence of predefined levels
of the buffer, also called buffer thresholds. Initially, all parallel machines are opera-
tional and the buffer fills up at the maximum possible rate. As buffer level increases
machines are sequentially switched off in correspondence of consecutive thresholds,
namely switching points. At the last switching point all machines are deactivated and
buffer level starts decreasing. The control then lets buffer level decrease and reacti-
vates all machines as soon as buffer level reaches another threshold, namely restart
point. The described system behavior is depicted in Fig. 2 considering a system with
two parallel machines at the upstream stage.

It must be noticed that, in presence of unreliable machines, further reductions in
productivity of a production stage induced by control policies may be detrimental to
the overall performance of the system. A buffer level that is consistently low increases
the likelihood of complete buffer draining when failures occur at the upstream stage,
thus causing starvation of the downstream stage. This situation should be avoided,
particularly in case the downstream stage is the bottleneck. Therefore, a trade-off
exists between the benefits, in terms of reduced waiting time and scrap, and the
drawbacks, in terms of bottleneck starvation.

4 Methods

The problem is approached in two steps: first, a control policy that includes the features mentioned in the previous section is formalized; second, the control policy is included in a steady-state performance evaluation model of the two-stage system under analysis. The control policy is described by means of event graphs, to provide a practical representation of the sequences of states and events involved in control loops. Then the control policy is included in a steady-state performance evaluation of manufacturing systems based on mixed-state Markov Chains, where the buffer level is approximated as a continuous variable [24].

4.1 Formulation of the Control Policy

The control is formalized starting from the set of states the reference system can assume and the set of events that allow transitions among these states. Each parallel machine is characterized by three states: operational, or up (U), failed, or down (D), and idle (I). The idle state represents the machine being not operational because it has been stopped by a control action. Events that change the state from up to down and vice versa, i.e. failure (f) and repair (r), are random and non-controllable. Events that change the state from up to idle and vice versa are controlled. Figure 3a shows the event graph of one upstream machine. Random events are depicted in red and controlled events are depicted in green.

For simplicity, a system with two parallel machines at the upstream stage is considered. However, the control formalization outlined below can be applied to systems with any number of parallel machines by increasing the number of control points. Given this simplification, the buffer state space is discretized in four macro-states: empty (E), restart point (R), first switching point (S_1) and second switching point
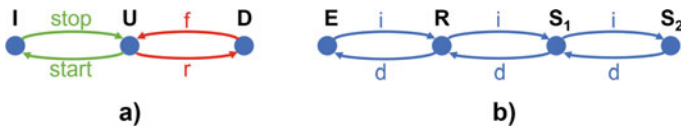
Fig. 3 Event graph of a single machine (**a**) and event graph of the buffer (**b**)

(S_2). The discretized state of the buffer changes when the buffer level hits the corresponding threshold value, either due to an increase (i) or a decrease (d) event. Such events depend on the state of the upstream machines: buffer level increases whenever the upstream stage is productive and decreases when it is not. Figure 3b shows the event graph of the buffer. Events depending on machine states are depicted in blue.

The control loop changes according to the state of the upstream stage. Figure 4 shows the three possible loops: "UU" indicates that both machines are up, "DU" and "UD" indicate that the first and second machines are failed respectively. Control loop (a) is applied when both machines are operational: while the upstream stage is productive and the buffer level increases, machines are stopped sequentially when the respective switching points are reached; when both machines are idle the buffer level decreases until both machines are restarted in correspondence of the restart point.

Control loops (b) and (c) are applied when the first and second machines are failed, respectively. Like in loop (a), the buffer level increases while the upstream stage is productive, but the first switching point has no effect; the operating machine is stopped in correspondence of the second switching point; then the buffer level decreases until the available machine is restarted in correspondence of the restart point. When both machines are failed the buffer level can only decrease, eventually going to zero (E), and no control action is executed.
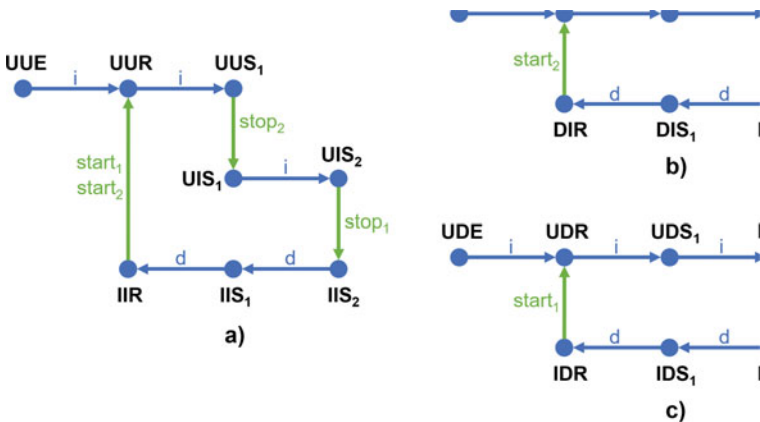
Fig. 4 Control loops **a** with both machines operational, **b** with first machine failed and **c** with second machine failed
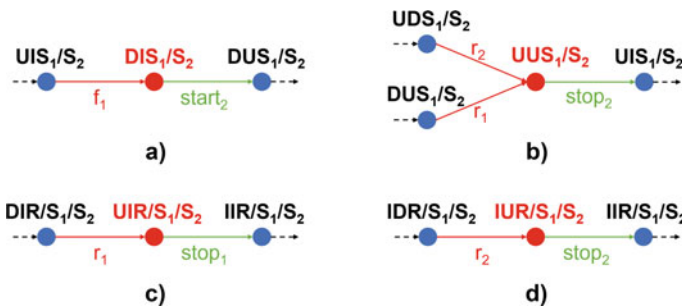
Fig. 5 Various effects of random events (failures and repairs) on control loops

As soon as one machine fails, control loop switches from (a) to (b) or (c) depending on which machine is down. However, when a failure of the first machine occurs after the first switching point has already been reached, and so the state of upstream machines is "UI", a control command to restore productivity of the upstream stage is immediately issued and the idle machine is restarted, as depicted in Fig. 5a. The system is then in control loop (c).

Whenever one of the two machines is down and control loop (b) or (c) is in the upper part, i.e. upstream stage is supposed to be productive, a control action to stop the second machine is immediately issued upon repair of the failed machine, so that the upstream stage produces at the rate imposed by control loop (a), as depicted in Fig. 5b.

Similarly, when one machine is down the system follows control loop (b) or (c). If the second switching point has been passed and the upstream stage is supposed to be non-productive, as soon as the failed machine is repaired a control action to stop it is immediately issued, so that the upstream stage remains non-productive, as depicted in Fig. 5c, d. In this way, control switches to loop (a).

4.2 Performance Evaluation Model

In the following, a stochastic analytical model for the steady-state performance evaluation of the two-stage production system is introduced. The model is based on the state-based Markovian representation of production resources. The combination of the states of the two production stages, namely the joint state, defines the direction and rate of change of the buffer level, which is modeled as a continuous variable. The model is based on the following assumptions:

1. The upstream stage is never starved and the downstream stage is never blocked;
2. Processing times of machines are deterministic and may be different among machines;
3. Machines are unreliable and subject to operation-dependent failures;
4. Time to failure and time to repair are exponentially distributed;

5. The buffer capacity is finite;
6. The system is asynchronous, i.e. each machine can start or finish at any time without synchronization with other machines;
7. The dispatching policy is First In First Out (FIFO).

Figure 6a provides a graphical representation of the Markovian state-based model of one machine with two states, an up state (U) and a down state (D). The failure and repair rates are denoted as p and r respectively. The service rate when the machine is up is denoted as μ. Figure 6b provides the representation of the state-based model of a production stage made of two parallel machines, obtained as the combination of states and transitions of the two machines. Combining the state space of the upstream stage with that of the downstream stage and with the buffer level, the overall state space of the system is obtained. The performance evaluation model includes buffer thresholds that allow to model the dynamics induced by the control policy [25]. The different threshold values represent activation points determining an instantaneous transition between specific joint states at predefined levels of work in process. Figure 7 provides graphical representations of the modeled dynamics. Specifically, Fig. 7a shows the control loop in case both upstream machines are operational and Fig. 7b, c show the control loops in case one machine is failed, i.e. the first switching point has no effect. Joint states are denoted with the combined state of upstream parallel machines between brackets, followed by the state of the downstream machine. For example, state "(UU)U" denotes the joint state where both machines at the upstream stage are operational and the downstream machine is also operational.

Two types of behaviors are defined in [25]: internal behavior, i.e. dynamics occurring within a certain buffer range delimited by two threshold values, and threshold behavior, i.e. dynamics occurring on specific threshold levels. Internal behavior is characterized by a mixed continuous-discrete state space, with buffer level representing the continuous part and joint states representing the discrete part. Buffer
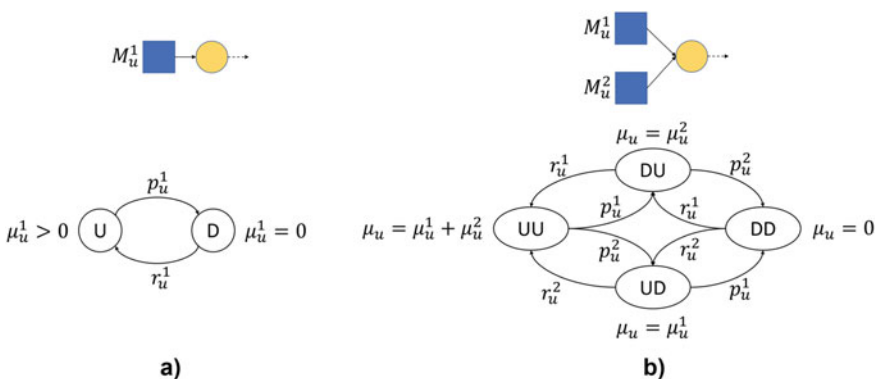
Fig. 6 Graphical representation of the state space of one machine feeding a buffer (**a**) and a production stage with two machines feeding the same buffer (**b**)
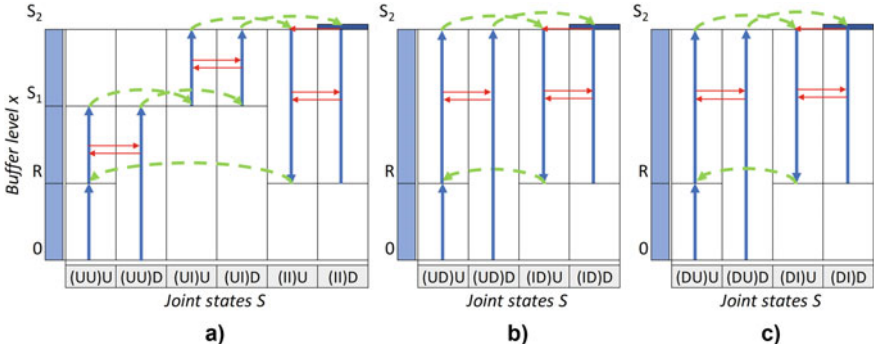
Fig. 7 Representation of the state space of a two-stage system including the proposed control policy, with two parallel machines at the upstream stage and a single machine at the downstream stage. Control loops considering both upstream machines operational (**a**), one upstream machine failed (**b–c**)

level can change at a rate that depends on the joint state. Internal states are represented in Fig. 7 with blue lines. Lines with an arrow indicate buffer level changing in a specific direction. Lines without an arrow indicate buffer level not allowed to change in that joint state. Internal states are characterized by differential equations defining probability density functions of the buffer level for every joint state, denoted as $f(x, S_u S_d)$. The probability of being exactly at a specific buffer level in a given joint state is therefore equal to zero.

On the contrary, the threshold behavior is characterized by a discrete state space and includes those states where the buffer remains steady in correspondence of a given threshold value. Threshold states are characterized by non-zero probability values $\pi(x^*, S_u S_d)$. Threshold states are represented in Fig. 7 with blue boxes. Red arrows among joint states indicate stochastic state transitions due to failures and repairs. For simplicity, only the most significant transitions are reported, to avoid repetitions.

Green dashed arrows indicate state changes determined by the control policy, occurring in correspondence of specific thresholds. It is possible to notice that, with respect to the machine characterization reported in Fig. 6, additional states "I" are present for the upstream production stage, one for every parallel machine, as described in Sect. 4.1. Transitions to and from these states are exclusively determined by control actions. The control behavior described in Sect. 4.1 can be translated into the following probability balance equations in the performance evaluation model:

1. Deactivation of the second upstream machine at the first switching point, denoted with x_s^1, if both machines are not failed:

$$f\left(x_s^1, (UU)S_d\right) \cdot v((UU)S_d) = f\left(x_s^1, (UI)S_d\right) \cdot v((UI)S_d) \qquad (1)$$

2. Deactivation of the only operational machine at the second switching point, denoted with x_s^2:

- Deactivation of the first machine if the second one is idle:

$$\begin{cases} f\left(x_s^2, (UI)U\right) \cdot \nu((UI)U) = f\left(x_s^2, (II)U\right) \cdot \nu((II)U) \\ \quad f\left(x_s^2, (UI)D\right) \cdot \nu((UI)D) = \pi\left(x_s^2, (II)D\right) \cdot r_d \end{cases} \quad (2)$$

- Deactivation of the first machine if the second one has failed:

$$\begin{cases} f\left(x_s^2, (UD)U\right) \cdot \nu((UD)U) = f\left(x_s^2, (ID)U\right) \cdot \nu((ID)U) \\ \quad f\left(x_s^2, (UD)D\right) \cdot \nu((UD)D) = \pi\left(x_s^2, (ID)D\right) \cdot r_d \end{cases} \quad (3)$$

- Deactivation of the second machine if the first one has failed:

$$\begin{cases} f\left(x_s^2, (DU)U\right) \cdot \nu((DU)U) = f\left(x_s^2, (DI)U\right) \cdot \nu((DI)U) \\ \quad f\left(x_s^2, (DU)D\right) \cdot \nu((DU)D) = \pi\left(x_s^2, (DI)D\right) \cdot r_d \end{cases} \quad (4)$$

3. Reactivation of all non-failed upstream machines at the restart point, denoted with x_r:

- Reactivation of both machines, if they are not failed:

$$f(x_r, (II)S_d) \cdot \nu((II)S_d) = f(x_r, (UU)S_d) \cdot \nu((UU)S_d) \quad (5)$$

- Reactivation of the first machine, if the second one has failed:

$$f(x_r, (ID)S_d) \cdot \nu((ID)S_d) = f(x_r, (UD)S_d) \cdot \nu((UD)S_d) \quad (6)$$

- Reactivation of the second machine, if the first one has failed:

$$f(x_r, (DI)S_d) \cdot \nu((DI)S_d) = f(x_r, (DU)S_d) \cdot \nu((DU)S_d) \quad (7)$$

In Eqs. 1–7, $\nu(S_u S_d)$ denotes the rate at which the buffer level increases or decreases, given by the combination of upstream and downstream stages, i.e. $\nu(S_u S_d) = \mu_u(S_u) - \mu_d(S_d)$. Product $f(x^*, S_u S_d) \cdot \nu(S_u S_d)$ represents the probability flow of exiting or entering a given joint state in correspondence of a specific threshold value. In Eqs. 2, 3 and 4, r_d is the repair rate of the downstream machine and represents the transition allowing to exit from threshold states. Indeed, as soon as the downstream machine is repaired, the buffer level starts decreasing.

Another effect of the control policy is the introduction of stochastic transitions between states "(UI)S_d" and "(DU)S_d" and the transition from state "(UD)S_d" to "(UI)S_d" in the buffer range above the first switching point. The first one results from the requirement of having at least one operational machine, if not failed. Therefore, if the first machine fails, the state changes from "(UI)S_d" to "(DI)S_d", but the control immediately reactivates the second machine, changing to state "(DU)S_d". As soon as the first machine is repaired, state changes to "(UU)S_d" but the control immediately switches the second machine back off, changing to state "(UI)S_d". Similarly, the

transition from "(UD)S$_d$" is present because the repair of the second machine changes the state to "(UU)S$_d$", but the control immediately deactivates the second machine, changing to "(UI)S$_d$". Balance equations of these internal states and all other internal states are formulated according to the method reported in [25].

The performance evaluation model defines a system of differential and algebraic equations. Solution of the system of equations provides the probability distribution function of every joint state, denoted as $f(x, S_u, S_d)$, and probability masses of threshold states, denoted as $\pi(x^*, S_u S_d)$. Through these probability distributions it is possible to compute the throughput of the system as in Eq. 8 and the average buffer level as in Eq. 9:

$$th = \sum_{S_u} \sum_{S_d} \mu_d(S_d) \left[\int_0^N f(x, S_u, S_d) dx + \pi\left(x^*, S_u S_d\right) \right] \tag{8}$$

$$\bar{x} = \sum_{S_u} \sum_{S_d} \left[\int_0^N x \cdot f(x, S_u, S_d) dx + x^* \cdot \pi\left(x^*, S_u S_d\right) \right] \tag{9}$$

To determine the fraction of the work in process that exceeds a certain waiting time limit, the waiting time distribution is approximated through the expected value of waiting time conditional to material entering the buffer at a certain level x as in Eq. 10:

$$wt(x) = \frac{x}{\frac{1}{F(x)} \sum_{S_d} F(x, S_d) \cdot \mu_d(S_d)} \tag{10}$$

where the denominator represents the weighted sum of the downstream processing rate, with weights represented by the state probabilities between buffer levels 0 and x. The term $F(x)$ is the probability of buffer level being lower than level x and is computed as in Eq. 11:

$$F(x) = \sum_{S_u} \sum_{S_d} \int_0^x f(x, S_u, S_d) dx \tag{11}$$

The term $F(x, S_2(j))$ represents the probability of the downstream stage being in state j between buffer levels 0 and x and is computed as in Eq. 12:

$$F(x, S_d) = \sum_{S_u} \int_0^x f(x, S_u, S_d) dx \tag{12}$$

Then, the defect rate is equal to the probability of exceeding a certain time limit TL and is computed as in Eq. 13:

$$d = P(wt > TL) = 1 - F\left(x^*\right), x^* | wt\left(x^*\right) = TL \tag{13}$$

Finally, the throughput of good parts and the yield are obtained from Eqs. 14 and 15 respectively:

$$th_g = th \cdot (1 - d) \tag{14}$$

$$y = \frac{th_g}{th} \tag{15}$$

5 Industrial Case Study

5.1 Description of the Production System

The control policy and related performance evaluation model presented in the paper have been analyzed as an application to a real production system in the semiconductor manufacturing sector. The case study is represented by the cleaning and diffusion stages of a wafer fabrication facility. Thermal and chemical operations carried out at the diffusion stage have very strict requirements in terms of wafers surface contamination and therefore cleaning is needed beforehand. Although the entire wafer fabrication process is carried out in a clean room, wafers are still exposed to a small residual fraction of impurities, which can cause defects if they accumulate on the wafer surface for extended periods of time. A waiting time limit is therefore imposed to wafers in queue for diffusion. Wafers exceeding such limit must be reworked at the cleaning stage.

A preliminary analysis on the material flow in the area revealed an almost linear material flow involving specific cleaning machines and groups of diffusion ovens, despite the physical resources are arranged in a job shop layout. This is not unexpected, given that the wafer fabrication process involves building layers with varying characteristics onto silicon wafers, each requiring specific setting of process parameters, namely recipes. Each recipe is typically qualified to be executed only on a subset of machines due to hardware restrictions and costs [26]. In the case under analysis, qualification restrictions at both the cleaning and diffusion stages result in a linear flow of material between groups of resources. Therefore, the system is modeled as a set of five two-stage sub-systems, each with one or two cleaning machines at the upstream stage and multiple diffusion furnaces at the downstream stage. Given the usually high traffic intensity in this part of the system, the cleaning stage is supposed to be never starved, while storage space is assumed to be infinite after the diffusion stage.

The buffer of every sub-system is modeled as a container of planned diffusion hours, and not as a container of wafers. Consequently, the processing rate of every diffusion furnace is equal to 1 [diffusion hours/hour] and processing rates of the upstream machines are rescaled accordingly. Table 1 provides the number

Table 1 Composition of the five two-stage sub-systems: number of machines and buffer capacity

Sub-system	Nr. upstream machines	Nr. downstream machines	Time buffer [diffusion hours]
1	2	10	283
2	2	11	305
3	2	9	252
4	1	4	111
5	1	4	110

of machines at both stages and capacity of the buffer for every two-stage sub-system. Numerical values concerning buffer capacity and system performance are transformed for confidentiality.

5.2 Results

The control policy described in the previous sections is implemented in the different sub-systems. In particular, for sub-systems 1, 2 and 3 the policy is implemented with two switching points, one for every cleaning machine, and one restart point, that restarts both cleaning machines. For sub-systems 4 and 5 the policy is implemented with just one switching point and one restart point, since only one machine is present.

The first stage of the analysis is the performance evaluation of every sub-system with the proposed modeling approach without including any control policy, to imitate the behavior of the original system. The throughput estimated by the analytical model is compared with the actual throughput obtained from production data to assess the accuracy of the modeling approach. The analytical approach exhibits an average error of 1.75% as reported in Table 2.

The second stage of the analysis is the application of the control policy to the system to evaluate its impact. Figure 8 shows the effect of varying the values of the intermediate switching point and the restart point on yield and throughput of good parts of one sub-system. The main results can be summarized in a range of variation that is approximately 1.5% for the yield and 2% for the throughput of good parts. From the obtained response surfaces it is possible to observe, on one side, that both

Table 2 Throughput comparison between model results (with no policy) and real system data

Sub-system	th_{data} (parts/h)	th_{mod} (parts/h)	Error (%)
1	287.29	295.11	+2.72
2	327.91	323.12	−1.46
3	237.54	240.90	+1.41
4	156.50	159.85	+2.14
5	164.32	166.00	+1.02
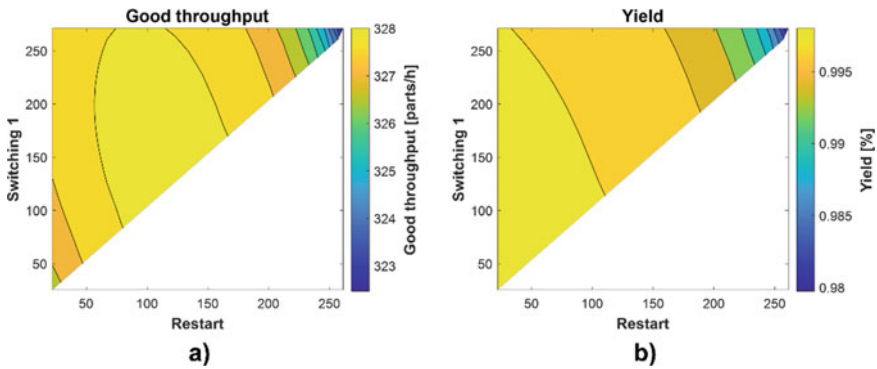
Fig. 8 Behavior of throughput of good parts (**a**) and yield (**b**) against different values of restart point and intermediate switching point, with fixed value of the last switching point

Table 3 Throughput and yield comparison between systems with and without policy

Sub-system	$th_{g,old}$ (parts/h)	Δth_g (%)	y_{old} (%)	Δy (%)
1	295.11	+1.57	98.01	+1.62
2	323.12	+1.50	98.24	+1.48
3	240.90	+1.26	98.38	+1.24
4	159.85	+1.09	98.32	+1.15
5	166.00	+1.00	98.47	+1.04

performance indicators strongly decrease as the control points increase, caused by the higher inventory level. On the other side, the throughput of good parts is negatively affected by a low value of the control points, causing a consistently low buffer level and increasing the risk of starvation of the downstream stage due to buffer emptying.

The trade-off between increasing the quality yield and reducing system productivity highlights the need to search for optimal values of control points that maximize the throughput of good parts. Compared to a system with no control policy, optimizing the control points results in an average increase of 1.3% in both performance indicators. This translates to a reduction in the number of reworked wafers by over 80,000 units per year, considering 220 production days. Details on the results in terms of percentage increase are available in Table 3.

6 Conclusions and Future Research

This work presents a control policy for production capacity modulation of parallel machines in presence of perishable work in process. The proposed policy aims at better controlling work in process to minimize scrap. The policy combines switching points, sequentially deactivating machines as inventory increases, and restart points,

activating machines when inventory goes below a certain value. The policy is formalized by means of event graphs, to provide indications for practical application. The main requirement in this sense is the availability, in real systems, of technological solutions to monitor machine state and buffer level.

The policy is integrated within an analytical performance evaluation method based on the Markovian representation of machines and continuous approximation of material flow. The proposed method allows exhaustive analysis of the policy impact on system behavior and performance. Indeed, a multitude of alternative combinations of system and control parameters can be quickly evaluated to construct response surfaces. The method provides steady-state estimate of performance indicators, aiming at a long-term evaluation of the system, and is not suitable for evaluation of transient periods.

Although the methodology can be easily generalized to systems with arbitrary number of machines, the main limitation of the model lies in the possible occurrence of numerical errors as the number of states increases. Further study must be conducted to identify solutions to this issue, exploiting state reduction techniques.

Finally, the developed performance evaluation method is adopted for the analysis of an industrial case study regarding the diffusion stage in semiconductor wafer fabrication. Results show the benefit obtained with the application of the policy in a critical stage of manufacturing system, in terms of both quality yield and throughput of good parts.

Future research includes the adoption of the formalized two-stage system model as a building block in decomposition-based performance evaluation approaches. This would allow to evaluate the policy impact in multi-stage manufacturing systems with arbitrary number of production stages. Furthermore, integration of the performance evaluation method with optimization methods should be pursued to address complex control optimization problems.

References

1. Machado CG, Winroth MP, Ribeiro da Silva EHD (2020) Sustainable manufacturing in Industry 4.0: an emerging research agenda. Int J Prod Res 58(5):1462–1484
2. Colledani M, Tolio T, Fischer A, Iung B, Lanza G, Schmitt R, Váncza J (2014) Design and management of manufacturing systems for production quality. CIRP Ann 63(2):773–796
3. Adane TF, Bianchi MF, Archenti A, Nicolescu M (2019) Application of system dynamics for analysis of performance of manufacturing systems. J Manuf Syst 53:212–233
4. Colledani M, Tolio T (2006) Impact of quality control on production system performance. CIRP Ann 55(1):453–456
5. Diamantidis A, Lee J-H, Papadopoulos CT, Li J, Heavey C (2020) Performance evaluation of flow lines with non-identical and unreliable parallel machines and finite buffers. Int J Prod Res 58(13):3881–3904
6. Magnanini MC, Tolio T (2023) A Markovian model of asynchronous multi-stage manufacturing lines fabricating discrete parts. J Manuf Syst 68:325–337
7. Pauls-Worm KGJ, Hendrix EMT, Alcoba AG, Haijema R (2016) Order quantities for perishable inventory control with non-stationary demand and a fill rate constraint. Int J Prod Econ 181:238–246

8. Vila-Parrish AR, Ivy JS, King RE (2008) A simulation-based approach for inventory modeling of perishable pharmaceuticals. In: 2008 winter simulation conference. IEEE, pp 1532–1538
9. Mathirajan M, Sivakumar AI (2006) A literature review, classification and simple meta-analysis on scheduling of batch processors in semiconductor. Int J Adv Manuf Technol 29:990–1001
10. Wu JZ (2013) Inventory write-down prediction for semiconductor manufacturing considering inventory age, accounting principle and product structure with real settings. Comput Ind Eng 65(1):128–136
11. Bakker M, Riezebos J, Teunter RH (2012) Review of inventory systems with deterioration since 2001. Eur J Oper Res 221(2):275–284
12. Polotski V, Gharbi A, Kenne J-P (2021) Production control of unreliable manufacturing systems with perishable inventory. Int J Adv Manuf Technol 116:2473–2496
13. Kırcı M, Biçer I, Seifert RW (2019) Optimal replenishment cycle for perishable items facing demand uncertainty in a two-echelon inventory system. Int J Prod Res 57(4):1250–1264
14. Balugani E, Lolli F, Gamberini R, Rimini B, Babai MZ (2019) A periodic inventory system of intermittent demand items with fixed lifetimes. Int J Prod Res 57(22):6993–7005
15. Dolgui A, Tiwari MK, Sinjana Y, Kumar SK, Son Y-J (2018) Optimising integrated inventory policy for perishable items in a multi-stage supply chain. Int J Prod Res 56(1–2):902–925
16. Polotski V, Gharbi A, Kenne J-P (2022) Production control in manufacturing systems with perishable products under periodic demand. J Manuf Syst 63:288–303
17. Tempelmeier H, Bürger M (2001) Performance evaluation of unbalanced flow lines with general distributed processing times, failures and imperfect production. IIE Trans 33(4):293–302
18. Kim J, Gershwin SB (2005) Integrated quality and quantity modeling of a production line. OR Spectr 27:287–314
19. Colledani M, Tolio T (2011) Integrated analysis of quality and production logistics performance in manufacturing lines. Int J Prod Res 49(2):485–518
20. Arinez J, Meerkov SM, Zhang L (2010) Quality/quantity improvement in an automotive paint shop: a case study. IEEE Trans Autom Sci Eng 7(4):755–761
21. Liberopoulos G, Kozanidis G, Tsarouhas P (2007) Performance evaluation of an automatic transfer line with wip scrapping during long failures. Manuf Serv Oper Manag 9(1):62–83
22. Dogan-Sahiner E, Altiok T (1998) Blocking policies in pharmaceutical transfer lines. Ann Oper Res 79:323–347
23. Magnanini MC, Tolio T (2018) A threshold-based control policy for scrap reduction of perishable in-process inventories. Procedia CIRP 78:184–189
24. Gershwin SB (1994) Manufacturing systems engineering. Prentice Hall
25. Tolio TAM, Ratti A (2018) Performance evaluation of two-machine lines with generalized thresholds. Int J Prod Res 56(1–2):926–949
26. Rowshannahad M, Dauzère-Pérès S, Cassini B (2015) Capacitated qualification management in semiconductor manufacturing. Omega 54:50–59

White Papers

Conventional and Innovative Aspects of Bespoke Metal Implants Production

Paola Ginestra, Antonio Piccininni, and Ali Gökhan Demir

Abstract Advances in Manufacturing of metal implants may offer solutions to several challenges. Considering the current state of bespoke manufactured implants alongside clinical and industrial perspectives, this review seeks to illuminate where key advances are being made in a laboratory setting and what is being done to translate them to use in future implants. Especially, additive manufacturing is a core business in producing customized implants but its application in industrial field is yet to be fully exploited. On the other side, sheet forming and laser processing are two main techniques for the fabrication of bespoke metal parts with high dimensional accuracy and surface finishing that can be integrated within a functional chain leading to clinical applications. The exploited processes are here presented, together with a focus on implant customization strategies and standardization processes, key factors for the industrialization of custom-built rather than mass-produced devices.

Keywords Additive manufacturing · Laser processing · Metals · Forming processes

1 Introduction

The metal implants production allows the direct realization of functional parts with complex shapes starting from digital models.

P. Ginestra (✉)
Dipartimento di Ingegneria Meccanica e Industriale, Università Degli Studi Di Brescia, Via Branze, 38 25123 Brescia, Italy
e-mail: paola.ginestra@unibs.it

A. Piccininni
Dipartimento di Meccanica Matematica e Management, Politecnico di Bari – Campus, Via Orabona 4, 70126 Bari, Italy
e-mail: antonio.piccininni@poliba.it

A. G. Demir
Dipartimento di Meccanica, Politecnico Di Milano, Via La Masa 1, 20156 Milano, Italy
e-mail: aligokhan.demir@polimi.it

The aim of this work is to describe additive manufacturing (with particular focus on powder bed techniques), sheet metal forming and laser processing technology, which in recent years found space in many fields of application, particularly in the medical field, through the production of metal orthopedic prostheses. Thanks to powerful equipment and starting from different and newly developed metals, it is possible to process samples in a short time, at sustainable costs and on measure, customizing them according to the customer's requests.

The crucial aspects concerning traditional and innovative manufacturing are presented in order to understand the context in which the present study was carried out and to learn the relative theoretical and technical information. This review presents the main characteristics and advantages of bespoke production in the orthopedic field, comparing traditional and additive production systems, followed by the current progresses to tailor the processes for orthopedic metal implant applications. Subsequently, the added biomaterials such as 316L stainless steel, titanium-6aluminium-4vanadium (Ti–6Al–4V) and cobalt-chromium (Co–Cr) were highlighted, exploring their limits and potential, compared to the materials used in traditional production.

Implants production is nowadays dealing with complication rates caused by defined key issues especially related to mechanical incompatibility, weak wear and fatigue properties, long lead time for bespoke implants and infections. An ideal perspective would take into account: the mechanical mimicking of healthy tissue properties, the geometrical mimicking of a healthy anatomy, the possibility to custom building on demand with low lead time, the mechanical mimicking of specific anatomical districts with a specific focus on wear and fatigues properties and an antimicrobial aspect.

Typically, metallic implants have been manufactured by formative techniques such as casting, or subtractive methods such as milling or machining. However, the past decade has seen increasing interest in using additive manufacturing techniques as well as flexible and versatile sheet metal forming processes, and their potential to enable novel implant geometries or properties. Additive Manufacturing (AM) techniques are those that produce parts from 3D data, by joining of raw materials in a layer-by-layer process. The most used and therefore analyzed powder bed fusion technologies for the production of metal implants are Selective Laser Melting (SLM) and Electron Beam Melting (EBM). Innovative sheet metal forming processes, exploiting the superior elongation achievable by some metallic materials under specific working conditions or thanks to the local interaction between the blank and a rotating tool, have been proposed as promising solutions to ensure the level of complexity needed in an advanced bespoke implant.

Laser based manufacturing processes have been already employed in biomedical implant manufacturing. Laser based manufacturing processes are inherently adaptable to flexible manufacturing being based on a digital tool itself. Lasers can be used for surface to bulk processing, to cut or join materials based on CAD/CAM systems. In particular, laser cutting, and welding are largely employed in mass produced conventional metallic implants and devices [1, 2]. On the other hand their

use in customized implants is relatively less explored. Moreover, the use of relatively less explored texturing, polishing, and heat treatment processes can open up new possibilities for tailored properties for the patient-specific devices [3].

This review seeks to give perspectives on three areas:

1. The research impact that customized manufacturing is having on metal implants production
2. Current process and industrial challenges for implant metal forming and additive manufacturing, and the challenges faced to further industrialization
3. Recent advances in literature and their possible future clinical impact.

2   Shape Customization

Metal implants are commonly used in various orthopedic interventions, such as fracture fixation, spinal instrumentation, joint replacement and bone cancer surgery. Unlike custom orthopedic implants, standard implants have the advantage of being less expensive, less time consuming in mass production, greater surgical flexibility with different sizes and lengths. Traditionally, patients may need to adapt to the fixed dimensions of standard implants. This may result in sub-optimal adaptation to the host bones and consequently possible adverse clinical results. Standard traditional implants may not be able to address reconstructive challenges such as severe bone deformity or bone loss after implant loosening and bone cancer resection [4].

Traditionally, metal orthopedic implants are produced by subtractive processing, in which the material is then removed from a solid metal block until it reaches the desired shape. The other traditional manufacturing method is metal forming. Mechanical forces are applied to the raw material to give it the desired shape, such as melting or forging. Currently, most of the commercial activity in orthopedics has been for standard size implants produced using traditional manufacturing methods.

However, in recent years, with the advent of digital technologies in medical imaging, computer programming in three-dimensional modeling (3D) and computer-assisted instruments for precise implant placement, interest in using patient-specific implants for complex orthopedic reconstruction has increased. Bespoke production has gained popularity in the medical sector and new applications are rapidly evolving into various orthopedic procedures [5].

The technologies used for customized implants needs to entail a flexible process that does not require multiple production steps or additional equipment with inventory. Reduces the cost of producing a small batch of complex plants. The implant can then be customized according to anatomical (patient specific) and surgical (disease specific) needs using the patient's medical images, such as computed tomography (CT) or magnetic resonance imaging (MRI) (Fig. 1).

Patient-specific bespoke implants have the potential to reduce surgical time and provide superior comfort with faster recovery. Customized implants with porous
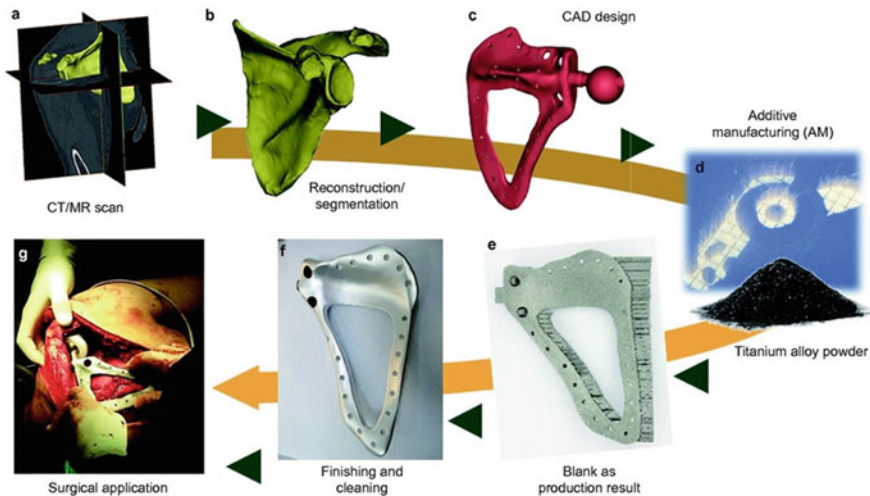
Fig. 1 3D production process of a specific implant in a patient undergoing resection and reconstruction of scapular tumor [5]

internal structures not only promote osseointegration, but also reduce the misalignment of rigidity between natural bone and implant. It can minimize stress-related bone resorption and improve the longevity of orthopedic implants. Although porous materials were clinically useful before the additive manufacturing era, the new technology allows the integration of porous structures with other geometric complexities, such as fine surface characteristics, internal porous interconnectivity and nonporous structures in a single manufacturing process. On the customization aspect, the comparison between traditional orthopedic implants and AM orthopedic implants is shown in Table 1 [4].

Although studies have suggested that bespoke metal structures are good engineering structures for bone replacement, not much is available on the results of the new type of implants, which combine both traditional and innovative production processes and methods. Specifically, the lack of demonstrated performance and regulatory standards of customized implants are some of the concerns that may prevent their use in orthopedic practice.

2.1 Clinical Impact

In general, mass-produced implants with conventional methods can effectively serve most of the patient population. However, when mass-produced implants do not fit into clinical scenarios, such as bone cancer surgery and severe bone loss in joint revision surgery, surgeons are forced to adapt implants to the patient's anatomy by unnecessary bone removal and other additional surgical procedures to build bone

Table 1 Comparison between aspects related to the traditional orthopedic implants and AM orthopedic implants production

	Implants manufactured in the traditional way	Implants realized with additive manufacturing
Materials	–Titanium and cobalt-chromium based alloys of medical grade	–Like traditional implants
Production methods	–Subtractive machining: The material is then removed from a solid block until the desired shape is achieved, such as turning, milling, drilling –Forming: Mechanical forces are applied to the material to give it the desired shape, such as bending, casting, forging, forging, pressing –Need for design, development and production of specific tools –Suitable for mass production –More mature technology compared to plants made with additives	–Additive manufacturing is a process of joining metallic materials layer by layer to create objects from the 3D model data to the construction of the final plant –Flexible supply chains as no specific tools are needed for this process –Ideal for both prototyping and low volume patches (up to one if needed)
Mechanical properties	–Cast or forged implants with sufficient mechanical resistance for load-bearing orthopedic applications –Usually better than implants made with additives	–Better than cast implants and can approach the strength of forged implants
Complexity of the project	–The design must take into account the manufacturing constraints related to processing or casting at each stage, so the design of the plant should not be so complex and complicated that it cannot be manufactured	–The freedom to design complex geometries allows porous implants and solid parts to be integrated into a single plant –The porous implant must be open-cell to allow removal of unmelted metal powder
Porosity	–Difficult in machining application because it is based on a laser that removes material from a solid part or from an applied secondary material –Problems of stress shielding	–The porosity can be integrated into the design and manufactured with precision –Reduce stiffness to fit the module of the surrounding bone structure and minimize stress protection
Osteointegration	–Modify the implant surface with secondary procedures such as porous surface coating, hydroxyapatite plasma spray coating	–Interconnected open porous structures with optimized pore sizes and porosity
Post-processing stages	–Milling, finishing, labelling, cleaning and sterilization	–Like traditional implants

Table 1 (continued)

	Implants manufactured in the traditional way	Implants realized with additive manufacturing
Plant size	–Standardized and approximated to patient geometry –Patients adapt to the implant and the necessary adjustments (bone trimming) are made during the surgical procedure	–Customize based on bone defect and patient position –Appropriate adjustments are minimal during surgery
Regulatory requirements	–Regulatory standards are available for production quality assurance	–Regulatory standards are currently limited to ensure that AM plants are safe and effective
Clinical applications	–Standard implants with different sizes to serve most of the patient population –Increased flexibility during surgery –Long-term clinical evidence is available to support the fact that implants are safe and effective	–Restricted to patients as a one-off implant when a standard implant cannot meet the surgical requirements –Less flexibility during surgery –Only small series of short-term cases are available to evaluate the clinical results of implants

loss. Thanks to the versatility of the design and additive manufacturing, patient-specific implants can be manufactured to meet the unique geometry of a bone defect that is not available in the mass-produced form. Therefore, bespoke implants can reduce operating time in the reconstruction of complex bone defects. It minimizes the impact that the surgery must have on the surrounding tissue and reduces the patient's recovery time after surgery. In addition, newly introduced manufacturing process could allow the integration of a porous structure into the design at the time of manufacture. It contrasts with the conventional manufacturing process where the addition of porosity is a secondary process and is limited to a predetermined structure with limited shapes and porosity of the designed metal. This is very advantageous in a complex surgery with varying amounts of bone loss. Customized implants can not only match the specific bone geometry but can also be optimized in design to match the microscopic 3D structure with the desired porosity and rigidity in the surgical sites that are best for internal bone growth and long-term fixation of the implant. To date, there are few publications on the clinical use of specific implants for patients. The first series of cases are encouraging in various fields of complex orthopedic procedures, such as bone cancer surgery, hip revision surgery, spinal implants and traumatic fracture fixation and reconstruction. The manufacturing technologies that allow a full customization of the products, can address the reconstructive challenges that standard series implants cannot provide due to implant size or disease-specific surgical needs.

In bone sarcoma surgery, tumor resection causes unique bone defects that often require reconstruction to restore continuity and skeletal function. Specifically designed metal implants have the great potential to customize restorative needs at various points in the patient's skeleton. Patient-specific implants have recently been

applied for the reconstruction of clavicular, scapular, calcaneal, pelvic and sacral bone tumors, which have a complex bone geometry and no standard implants for bone reconstruction are available [6–9].

Advanced bespoke implant design can include virtual biomechanical simulation using patient-specific modeling and finite element analysis to evaluate implant performance [8]. It can optimize and modify the design of the system before the actual realization. It can help surgeons provide the most personalized implant for a single patient. The use of patient-specific implants requires close collaboration between orthopedic surgeons and biomedical implant engineers. When planning implants, engineers must design, based on surgeons' comments on surgical requirements that include the surgical approach, the bone defects to be reconstructed, the optimal alignment of the implants needed to achieve, the bone fixation sites and the porous implant for internal bone growth. Therefore, the desired implant geometry can not only be achieved with one production technology but can be an effective combination of the mechanical and physical properties required for surgical applications. Effective collaboration between surgeons and engineers must be established over time and will improve as technology advances.

2.2 Requirements and Limits of Orhopedic Implants

The surface quality and the pore size of an implant are essential for optimal bone growth, which has been promoted with pores in the range 200–400 μm [10, 11]. Pores of 100–350 μm diameter are suitable for cellular colonization and vascularization [10, 12]. The size range has also facilitated the migration of cells into porous and promoted bone regeneration [13]. On the other hand, a porous implant with pore size <100 μm is unfavorable for bone regeneration and leads to the formation of fibrous tissue or non-mineralized bone tissue, as the pore size of 5–15 μm was only suitable for the growth of fibroblasts [14], 70–120 μm for chondrocytes [15]. For internal bone growth, the minimum interconnected porosity of the implant should be at least 40% for sufficient cell infiltration [16]. High porosity can reduce the rigidity of the implant and thus the stress shielding of the surrounding bone. Studies have shown that the Ti–6Al–4V implant gave less stress shielding than traditional samples of the same size [17]. However, the increased porosity of the implant also compromises its mechanical properties, which are not optimal for orthopedic applications. The compression test was conducted on five Ti–6Al–4 V cellular samples manufactured with EBM [18]. It was found that these Ti–6Al–4 V samples with a porosity of about 66% had a maximum compressive strength of 116 MPa and an elastic modulus of 2.5 GPa, which are comparable to the mechanical properties of human bone [18]. The study showed that Ti–6Al–4 V parts manufactured with controlled internal pore architecture can meet the functional requirements of orthopedic implants.

Parts of functionally classified materials (FGM) have also been proposed to address the problem of misalignment of stiffness between host bones and implants [19, 20]. FGM parts are heterogeneous objects with material composition and

microstructure that gradually change with the positions within the parts [19, 20]. Instead of homogeneous porosity over the entire structure, the porosity can be functionally graded and varied to match the porosity of the adjacent bones after implantation. Additive fabrication therefore allows the fabrication of implants with complex geometries with a gradient of porosity perpendicular to the longitudinal axis of the implant, which allows the selection of the distribution of properties to obtain the desired biomechanical functions. Titanium implants with appropriate macro and porous microstructure have been shown to have intrinsic osteoinductive capacity without the need for additional osteogenic cells or osteoinductive agents [21, 22]. Another recent study shared these results. Hydroxyapatite (HA) coatings have been used to stimulate osteogenesis without the need for additional osteogenic cells or bone morphogen proteins (BMP) [21]. The results showed that the HA coating of a porous titanium implant did not significantly increase osteogenicity and that uncoated titanium implants were also osteoinductive [23]. These implants were then implanted in the femoral condyle of the sheep. Extensive osteoinductions and osseointegrations (70% bone growth) were observed, confirming the intrinsic capacity of porous titanium implants produced for bone regeneration [23]. To further accelerate and improve bone growth, a thin layer of bioactive calcium phosphate can be deposited on the surface of metal porous implants [24]. Therefore, current studies show that bespoke production can allow the fabrication of an implant with complex geometries that adapt to the patient's bone anatomy and the combination of porous implants for osseointegration.

Designers and manufacturers must take into account the cleaning requirements of the installations at the design stage. Parts with porous implants represent a major challenge. The pores must be interconnected, open and large enough to allow removal of metal residual. In addition, the process of cleaning up residual debris and removing unwanted backing material must be safe and reproducible. Special tools such as ultrasonic cleaners are available, but ultrasonic cleaning systems and systems are also available. Although bespoke implants offer great promise due to their ability to address reconstructive challenges that go beyond the scope of standard implants, there are some limitations for this emerging technology. The first obstacle to overcome is the demonstration of clinical performance. Like any other new surgical technology in the initial introduction phase, the long-term clinical results of using innovative implants compared to traditional techniques are lacking in orthopedic applications. It remains to be seen whether the potential recognized benefits of the technology can translate into better clinical outcomes for patients. Designing and building bespoke implants requires 3D engineering software and specialized skills that most surgeons do not have. The high cost of the implant, thanks to the unique and personalized use, the software and the investment of the machine further hinder the popularity of the use of the new technology among orthopedic surgeons. Clinical research is necessary to demonstrate safety, clinical effectiveness and cost-effectiveness for patients, surgeons and payers alike. Secondly, there are some regulatory concerns in the design and manufacture of patient-specific implants for clinical applications, as there are currently limited regulatory standards that do not guarantee safe and effective customized implants. The design of a patient-specific implant is based on

the patient's anatomy and clinically proven designs that meet the user's needs. Validation of the results of these installations can only be carried out after their installation. Prospective studies have limitations because it is not possible to compare patient-specific implants in different patients. The design of implants and the accuracy of the planning process can be validated by comparing postoperative CT with preoperative design planning. However, this is normally not done due to unnecessary radiation exposure when capturing CT images. The clinical performance of a patient-specific implant can only be partially validated by comparing the results of patients treated with implants with similar design characteristics. Therefore, the current use of patient-specific implants is limited to patients when a standard implant cannot meet the surgical requirements. Regulatory considerations should include:

- design control (from design inputs, from the design process to the design output) in the predictive production phase.
- the raw materials, the technical process to ensure consistency between the constructions and the post-production quality assurance in the production phase of the additives.
- cleaning, finishing, biocompatibility and sterilization in the post-additive production phase [25]. Since the current workflow of bespoke implants requires various software and steps from the acquisition of preoperative medical images to the final realization of the implant, most orthopedic surgeons are not familiar, and it is not easy to master the process. An integrated and unified IT platform should be developed to allow easy planning and communication between radiologists, orthopedic surgeons, engineers and implant companies.

3   Material Needs for Customized Metal Implants

The choice of the different materials for the realization of orthopedic implants by means of additive manufacturing is a crucial step of the production process. Each of them has specific characteristics that make it suitable for use in specific areas both in absolute terms and compared to traditional techniques.

316L stainless steel. This material is low-cost and easily available, making it suitable for the medical industry as a biocompatible metal bone implant. Combined with additive manufacturing, it is suitable for these applications, as implants or prostheses can be customized with relatively low costs. In mass production, in large volumes, they allow to obtain economies of scale and, consequently, economic advantages, compared to traditional production.

Yang et al. studied the optimization of manufacturing accuracy and density of orthodontic products using a self-developed machine and were able to achieve the required surface quality and mechanical properties [26]. Li et al. studied the possibility of making parts in 316L stainless steel with gradient porosity where the dense part is designed for strength and the porous part is designed to improve tissue growth in biocompatible implants [27]. Bibb et al. reported prosthetic structures with the same material [28]. Bibb et al. also presented 4 case studies on surgical guides

Table 2 Tensile forces and microhardness of AM and Forging 316L stainless steel cast

Property	AM	Forging
Maximum tensile strength (MPa)	480–760	450–818
Yield strength (MPa)	350–640	150–230
Elongation (%)	10–30	50–62
Microhardness (HV)	220–279	133–140

in different maxillo-facial surgeries (jaw and face) [29]. Kruth et al. published on a biocompatible metal framework for dental prostheses [30] and Wehmoller et al. reported on bodily cortical bone implants, mandibular canal segment and SLM 316L stainless steel tubular or support bone structures.

The mechanical properties characterizing this type of material are:

- Resistance and hardness

Steel is often used in many applications due to its strength. It should be noted that the steel components produced by additive processes are stronger and less malleable than their forged counterparts. The rapid cooling in the AM process results in a refined microstructure that increases tensile strength with reduced ductility. Table 2 shows the breaking load, yield strength, elongation and microhardness of 316L stainless steel parts produced by AM and forging.

- Surface roughness

It is common to achieve different roughness values depending on the technique used to process the material. Post-processing such as sandblasting, shot peening or manual sanding is often required to achieve a smooth, shiny surface. However, for 316L stainless steel, Delgado et al. were able to achieve a surface roughness of 5.82 mm without any further processing [31]. Kruth's group, which experimented with laser remelting, was able to achieve surface roughness of up to 2 mm for 316L stainless steel [30].

Titanium-6Aluminium-4 Vanadium (Ti–6Al–4V). Most research on titanium and its alloys is guided by its potential application as a body prosthesis due to its biocompatibility. Ti–6Al–4V are of great interest for their applications in the aerospace and biomedical industry [31]. This group of metallic materials has been widely used for various orthopedic implants due to their good biocompatibility, superior corrosion resistance and high mechanical strength. In addition, they have high specific strength and elastic modulus closer to the bone than Co–Cr alloys and stainless steel. Performance requirements for Ti–6Al–4V alloy implants are specified by ASTM and US FDA standards. Ti–6Al–4V components can be produced with different microstructures depending on the alloy processing method. For example, casting, processed ingots and powder metallurgy give three different microstructures for Ti–6Al–4V.

Research on Ti–6Al–4V body implants has been conducted by several groups. Lin et al. studied the structure and mechanical properties of an inter-cellular fusion

cage Ti–6Al–4V [32], Murr et al. focused their attention on the microstructure and mechanical properties of 3D printed Ti–6Al–4V for biomedical applications [33] and Warnke et al. conducted cellular experiments and demonstrated that porous implants Ti–6Al–4V allow total growth of osteoblasts (bone cells) [34].

Table 3 shows the highest tensile strength reported for Ti–6Al–4V, together with the respective yield and elongation strengths for SLM, EBM and cast parts.

The tensile strength and microhardness of the Ti–6Al–4V parts produced by EBM are lower than the Ti–6Al–4V produced by SLM. This is due to the difference in the microstructure of the parts produced by the two processes, caused by different cooling processes.

Cobalt Chromium (Co–Cr). The Co–Cr has been designed by various groups for implant applications. In terms of hardness, modulus of elasticity and strength, Ayyildiz et al. concluded that the Co–Cr is especially suitable for dental applications [35].

Table 4 shows the highest reported tensile strength for the CoCr, together with the respective yield strength and elongation for the parts produced by SLM and casting.

New materials. Magnesium and its alloys have great potential for orthopedic applications as they have been shown to be completely bioabsorbable, have mechanical properties aligned to the bone and do not induce any inflammatory response. In addition, they are also osteo-conductive, promote bone growth and play a role in cellular attack. Zhang et al. [36] examined the use of magnesium for light weight applications in biodegradable and bio-resorbable orthopedic implants [36].

There are recent studies that aim to replace Ti–6Al–4V with other titanium-based alloys. Chlebus et al. have studied the possibility of using Ti–6Al–7Nb for medical implants as it replaces vanadium with niobium in its chemical composition and this alloy has greater resistance to corrosion and biotolerance than Ti–6Al–4V. Further studies on this new titanium alloy have been carried out by Marcu et al. on

Table 3 Tensile forces and microhardness of SLM, EBM and Ti–6Al–4V cast

Property	SLM	EBM	Casting
Maximum tensile strength (MPa)	1250–1267	830–1150	934–1173
Yield strength (MPa)	1110–1125	915–1200	862–999
Elongation (%)	6–7	13–25	6–7
Microhardness (HV)	479–613	358–387	294–360

Table 4 Tensile forces and microhardness of molten SLM, EBM and Co–Cr cast

Property	SLM	EBM	Casting
Maximum tensile strength (MPa)	562–884	960	296–568
Yield strength (MPa)	951–1308	560	296–568
Elongation (%)	10.2–16.4	20	8.0–10.7
Microhardness (HV)	458.3–482.0	325.5	324.0–384.8

endosseous implants [37]. Szymczyk et al. also examined cultivated cell growth of Staphylocuccus aureus on Ti–6Al–7Nb implant which demonstrated the potential of this titanium alloy in this application [38]. The processing of Ti–24Nb–4Zr–8Sn was examined by Zhang et al. as an improvement over Ti–6Al–4V as it is an alloy of lower modulus. This results in a greater correspondence of the modules between the implant and the surrounding bone and therefore have more possibilities to prevent bone resorption, which causes implant loosening.

Tantalum is a biomaterial with unique mechanical properties. With the designed porosity, it can achieve an elastic modulus similar to that of the bone, which minimizes the protection from stress [39]. Thijs et al. tested the use of pure tantalum for AM fabrication and achieved a relative density of 99,6%. The yield strength of AM Ta is also higher than that of conventional methods [40].

In general, both traditional and AM technologies offer the opportunity to build cellular lattice structures to achieve the desired designs and porosity levels. However, there is a limit to which the osteoinductive potential can be increased by increasing the microporosity as a mechanically stable surface of the material is required to facilitate new bone formation. In addition, the current plants consist of a single material, sometimes with a coating layer, which is essentially uniform in composition and structure in the longitudinal direction. This leads to consistent properties, such as strength and biocompatibility throughout the implant. However, a single composition with a uniform structure cannot meet all the requirements for implants. For specific bone tissues, such as long bones, they are structurally organized so that the bone porosity varies from the outer perimeter to the inner section to achieve normal bone function. In this case, the mechanical strength of the bone gradually decreases from the external to the internal regions and can therefore be considered as a functional structure. Therefore, the concept of functionally classified materials (FGM) [41] and multimaterial processing may be suitable for implants. These parts have the distinctive characteristic of non-homogeneity with respect to strength properties, including yield strength, fracture toughness, fatigue and creep behavior.

4 Manufacturing Solutions for Customized Metal Implants

4.1 Additive Manufacturing

AM of metals can be divided in different sub-categories based on the material charging method: powder bed systems, where materials are added in a layer-by-layer method, powder fed systems, where materials are added through a nozzle and wire fed systems, where materials are added unrolling a wire.

Powder bed systems are the most common and are divided based on the power source and the degree of fusion of the material. The powder bed systems are selective laser melting (SLM), selective laser sintering (SLS) and electron beam melting (EBM) [42].

Selective laser melting and selective laser sintering. An SLM system consists in a roller, two platforms and a laser. A CAD model of the object is loaded in the machine, then a software divides the model in cross sectional layers [43]. Once this process is completed the roller pushes a layer of metallic powder, on the building platform, then the laser melts the powder following the cross section of the designed object [45]. Once the layer has been completely melted and solidified the building platform moves down, the feeding platform rises, and the roller spreads another layer of powder (Fig. 2). The laser melts the second layer of powder that will adhere to the lower layer. The process continues until the object has been built. To detach the object from the building platform the most common technique is electrical discharge machining (EDM) in which the part is put in a dielectric liquid and a wire is charged with a negative electrical potential in relation to the object. When the wire approaches the work piece the dielectric liquid breaks, an electric current flows through it and the electrons generate a plasma arc that melts the material.

Once the process is completed the unmelted powder is collected with a vacuum cleaner to be reused.

The most important printing parameters are laser power, scan speed, layer thickness and hatch spacing, and they play a main role on the properties that the object will show. Also, to build fully dense parts these parameters must be perfectly combined because, for example, a high laser power and low scanning speed can result in extensive material evaporation and in the keyhole effect [44].
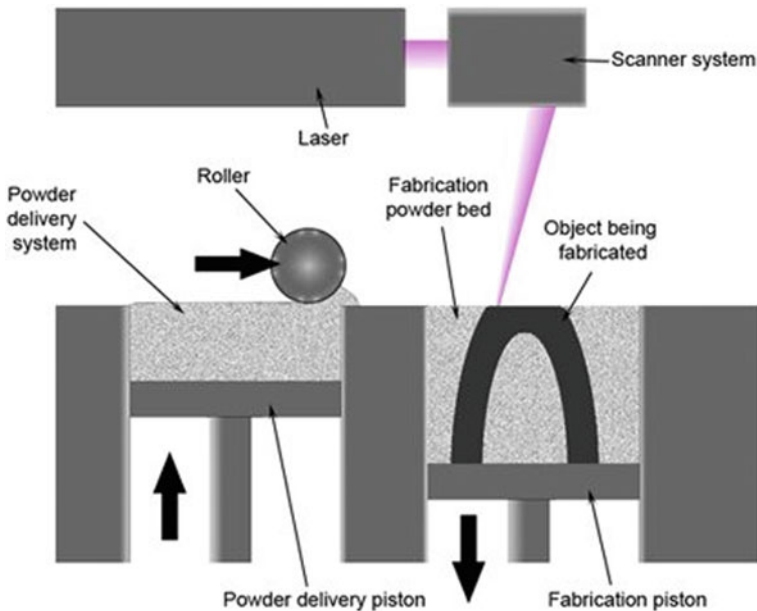
Fig. 2 Scheme of the SLM process

To prevent oxidation, the process is often carried out in Argon or Nitrogen atmosphere. The most common materials for SLM are Copper, Aluminum, Stainless Steel, Titanium and Cobalt-Chromium alloys in form of pure or alloyed metal powder.

Selective laser sintering was the first powder bed fusion process to be developed. It has the same building mechanism of SLM but differs from it by the method used to merge the powder together, in fact this process does not completely melts the powder, but it sinters it [42]. Through sintering the powder do not melt but it fuses together on a molecular level. The energy density of the laser beam is lower than in SLM, so the final parts are weaker due to the presence of voids. SLS allows the control of the porosity of the material, porosity that however require a post-treatment by infiltration to harden the final part [45].

Electron Beam Melting. EBM is similar to SLM, but the powder fusion is achieved through a very hot electron beam (up to 1000 °C). In order to work properly, EBM needs a vacuum environment to prevent the collision between the electrons and the gas molecules, so that the high quality of the beam is maintained [47]. The electrons are accelerated through two controlled magnetic fields. The beam then is focused and directed on the building table with magnetic coils. Figure 3 shows a schematic of the EBM process.

The building of each layer is divided in two stages: the preheating stage and the melting stage [43]. In the preheating stage the powder is heated up to 40–60% of the melting temperature with a high speed and high current beam. In the melting
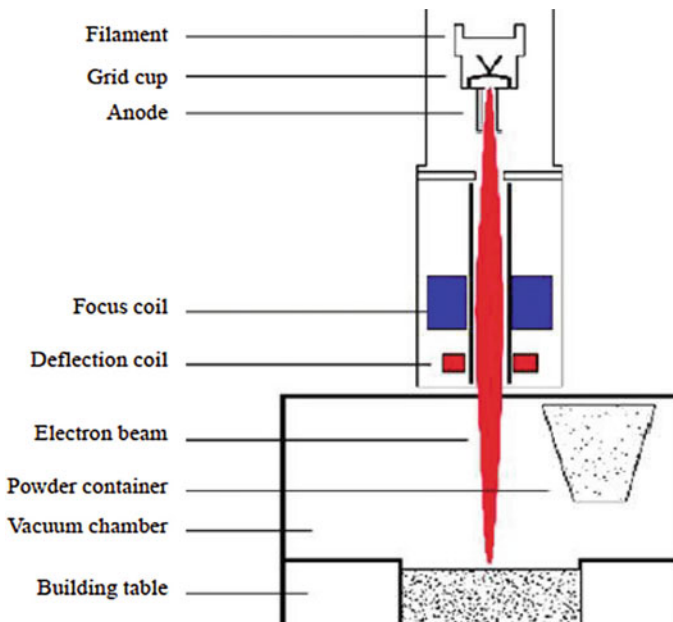
Fig. 3 A figure caption is always placed below the illustration. Short captions are centered, while long ones are justified. The macro button chooses the correct format automatically

stage the complete fusion is achieved with a low speed and low current beam. The preheating of the powder also reduces the residual stresses in the object because the thermal gradient is lower, making any post processing heat treatment unnecessary. The main materials for EBM are Titanium, Stainless Steel and Magnesium alloys.

SLM versus EBM. SLM and EBM follow the same procedure to produce the objects, but the two technologies are very different from each other.

Firstly, the environment of the building chamber is different: SLM works in an inert gas environment with the building plate at room temperature or at most at 200 °C while EBM works with the powder at 600–1000 °C in a vacuum chamber [46]. Due to this high temperature the object cannot be removed instantly from the EBM chamber and has to be left cooling overnight.

Secondly, both the particles and layers sizes differ. SLM particles have a smaller average dimension varying from 20 up to 60 μm while EBM particles go from 45 to 105 μm. Particle's geometry must have as close as possible as a spherical shape to assure a good flowability and homogeneous spread across the building plate. For SLM, layer thickness should cover the height of few powder particles, so it has a range between 30 and 100 μm. EBM, instead, usually works with a layer thickness of 50 μm.

Finally, EBM has a high energy beam with a faster scanning speed that make it faster in building full dense objects, however the beam has to pass multiple time on each layer to preheat and melt the material, thus, the sintering time increases. On the other hand, SLM can be installed with multiple laser sources that work simultaneously reducing the building time considerably.

Due to all these differences in the processes, the choice of which technology use in order to build a component must be made based on the material and the final application. Moreover, due to the lower temperature at which the building is kept, the SLM components are subjected to a higher cooling rate that produces a finer microstructure, resulting usually in higher strength but lower ductility of the parts. Despite that, the high cooling rate is inappropriate to work with brittle materials because can produce stresses and cracks in the object [47].

SLM offers the opportunity to change the process parameters during the building, thus the microstructure and the properties of the object can be modified.

EBM has a higher number of process parameters to control, the optimization for a specific material requires more time resulting in a smaller material choice. Although this gap can be reduced with an intense work of research, it can be time consuming and subsequently expensive.

However, these two processes share similar advantages and are actively considered for the production of orthopedic implants. These advantages include:

- Realization of complex products, innovative shapes, hollow structures and materials with functional gradient that are not otherwise achievable.
- Efficient approach that reduces production costs and time to market for high-value components.
- Excellent material properties, almost no porosity, possibility to combine different materials, significant reduction of material waste.

- Reduction of expensive equipment.

Several studies have also shown that with careful control of mechanical and surface properties, SLM and EBM offer the possibility of producing implants with anisotropic biological properties and responses, equal or higher than conventional plants.

With the advancement of AM technologies, SLM and EBM offer the orthopedic sector the possibility of mass customizing implants at a lower cost thanks to their ability to produce parts with complex and intrinsic designs specific to individual patients.

Despite the advantages of these two processes, they also have limitations, such as the limited materials that can be processed and the restriction of using only one material for construction. These limits can be overcome in the near future with further improvements in SLM and EBM systems, such as reducing the spot size of the laser beam or electron beam for greater accuracy, detailed research on the interaction of the laser beam or electron beam with powders to minimize powder adhesion.

In conclusion, SLM and EBM have great potential in the field of orthopedic applications but have not yet been widely adopted due to some of the limitations mentioned above.

Characteristics of orthopedic implants. Additive manufacturing allows for unique characteristics of orthopedic implants that cannot be achieved by conventional manufacturing methods. Conventional methods can address some of the complex bone geometries but have difficulty in fully adapting to the host bone due to the mismatch between the microstructure and the mechanical and physical properties. Additive manufacturing has the advantage of design freedom and flexibility to create a patient-specific implant. In general, the success of an AM orthopedic implant depends not only on its physical and mechanical properties, but also on the integration of interconnected pores in the design that promotes vascularization with an efficient exchange of nutrients and waste necessary for normal cell proliferation and differentiation [10]. In this regard, additive manufacturing can customize a plant so that:

- matches the patient's bone anatomy and defect using the patient's bone CT data.
- provides mechanical properties reproducing those of the host bone with sufficient strength for load-bearing applications and similar elastic modulus to minimize stress protection and subsequent bone resorption.
- Provide 3D implants with interconnected porosity and pores.

A series of three patients with clavicular, scapular and pelvic bone sarcoma underwent tumor resection and bone defects were reconstructed with titanium prostheses made with EBM. With additional clinical action of 21–48 months, all patients had satisfactory limb functions and no surgical complications were reported, including discrepancy in limb length, screw loosening and implant rupture. A series of 35 patients underwent resection of a pelvic tumor and reconstruction with AM tumor prostheses. Since the pelvis is a highly load-bearing area, the porous surface has been designed and constructed at the implant-bone junction to facilitate bone growth.

The study concluded that additive production could promote precise coupling and osseointegration between implants and host bone. The AM prosthesis for bone defect reconstruction after pelvic cancer elimination was safe, without further complications, and gave good functional results in the short term [39]. Therefore, AM tumor implants can be the ideal option to accurately reconstruct the unique anatomy of any patient with specific bone defects in bone sarcoma surgery. The plates and screws can be customized to ensure the initial stability of the implant fixation, while the porous implant favors the osseointegration of the host bone to ensure the long-term stability of the implant. In addition, the porosity of the implant can be optimized to reduce the modulus and rigidity of the implants that most closely match the bone. It can minimize plant loosening related to stress protection [6–8]. Recently, AM implants have been reported as a hip replacement for severe hip deformities. 57 cases of conventional hip arthroplasty were compared with 17 cases of AM hip arthroplasty. The results showed that the functional scores of patients in the AM group were better than those in the conventional group. However, post-operative infection and loosening rates were higher in the AM group [40]. AM spinal implants have recently been proposed in the treatment of the upper cervical spine, in complex spinal disorders such as craniocervical junction tumor or complex congenital spinal deformity and resection of the sacral tumor [4]. The patient-specific fastener allowed the depth and orientation of the screw path to be determined, based on preoperative 3D planning based on CT [41]. The implant not only reduced overall operating time, but also improved safety with a reduced risk of neurovascular injury. Patient-specific implants that combine vertebral bone defects with incorporated fixation have facilitated surgery, as they have avoided further complex reconstructions such as the collection of rib or fibular grafts and the intraoperative modelling of these grafts to adapt them to the defects [42, 43]. The treatment of complex acetabular fractures and post-traumatic skeletal deformities and defects can also benefit from this technology. Patient-specific titanium plates have been manufactured with additives that can be customized for both pelvic shape and type of acetabular fracture [44]. You save the operating time to shape the standard size plates to the local anatomy, sometimes difficult. AM titanium trellis cages have been used to address the complex problem of segmental bone loss often associated with post-traumatic limb deformities [45]. The lattice structure has a reticle for positioning the bone graft to facilitate internal bone growth. Traditional intramedullary nails or locking plates can also be incorporated into the design of the lattice cages for stable bone fixation. Therefore, the implants are mechanically stable with the minimum mass that allows an immediate and load-bearing movement.

4.2 Sheet Forming

The fully customized geometry for the implantable prostheses is necessary to ensure a perfect coupling with the bone geometry surrounding the damaged region to be healed: in fact, allowing relative micro-displacement at the bone/implant interface can imply potential sites for localized infections [48]. Therefore, it becomes

of paramount importance to find technological solutions capable of achieving the necessary geometrical accuracy. The subtractive manufacturing approaches have been extensively considered over the past years, but with the rise of new advanced biomaterials (e.g., the Mg-based alloys) they've shown some limitations: notable vibrations, formation of different-sizes chips, appearance of the built-up edge have remarkably hindered the use of traditional machining processes. Furthermore, intense wear phenomena, varying loads with a subsequent lack of geometrical accuracy have been also encountered during the machining of NiTi-based and Ti-based alloys [49]. Overcoming such limitations has paved the way to more performing technological solutions, as in the case of the forming processes. As an example, a combination of hot radial shear rolling and rotary forging has been proposed for the manufacturing of metastable beta Ti–18Zr–14Nb alloy for bone implants [50]. Using the same alloy, an artificial hip stem was manufactured by hot forging and its static and fatigue performance analysed [51]. Despite the promising results, bulk forming processes can ensure a limited geometrical complexity. Therefore, being the shape complexity one of the key aspects to be assessed for a fully customized implant, sheet metal forming processes—in particular, Superplastic Forming (SPF) and Single Point Incremental Forming—are the most promising solution to meet such a requirement.

Superplastic Forming (SPF). The Superplastic Forming is based on a peculiar property of some alloys called "superplasticity". A formal definition of superplasticity was for the first time stated at the International Conference on Superplasticity in Advanced Materials held in Osaka, Japan, in 1991 (ICSAM-91): "Superplasticity is the ability of a polycrystalline material to exhibit, in a generally isotropic manner, very high elongations prior to failure". The study of the superplasticity has been, and currently is, facing significant challenges because it represents the base for the development and optimization of the industrial SPF process where very complex parts are formed from superplastic sheet metals for several applications, from automotive to aerospace and biomedicine. It is widely reported in literature that superplastic flow can be achieved if: (1) the material is characterized by a very small grain size, smaller than 10 microns [52, 53] and (2) since superplasticity is a diffusion-based process, working temperature is at or above half of the absolute melting temperature of the material [54]. During the SPF process, the tools are heated up at high temperature—which is usually the one at which the superplastic behaviour is emphasized and changes according to the material—and, once reached, the blank is inserted between them and clamped. The blank is basically subjected to the action of a pressurized gas, whose profile is properly designed to deform the material under an optimal strain rate [55, 56]. The process is schematically shown in Fig. 4.

The geometry of the prosthesis to be manufactured is defined in a previous step, mainly based on CAD techniques. In the case of the cranial prostheses, the approach can be schematized by the workflow in Fig. 5 [57]: the geometry of the prosthesis is usually defined using several mirroring techniques able to retrieve the implant's geometry from the morphology of the sound bone. The workflow is completed by checking the coupling of the designed geometry with the bone damaged area: the defined geometry becomes then the output for the design of the manufacturing process.
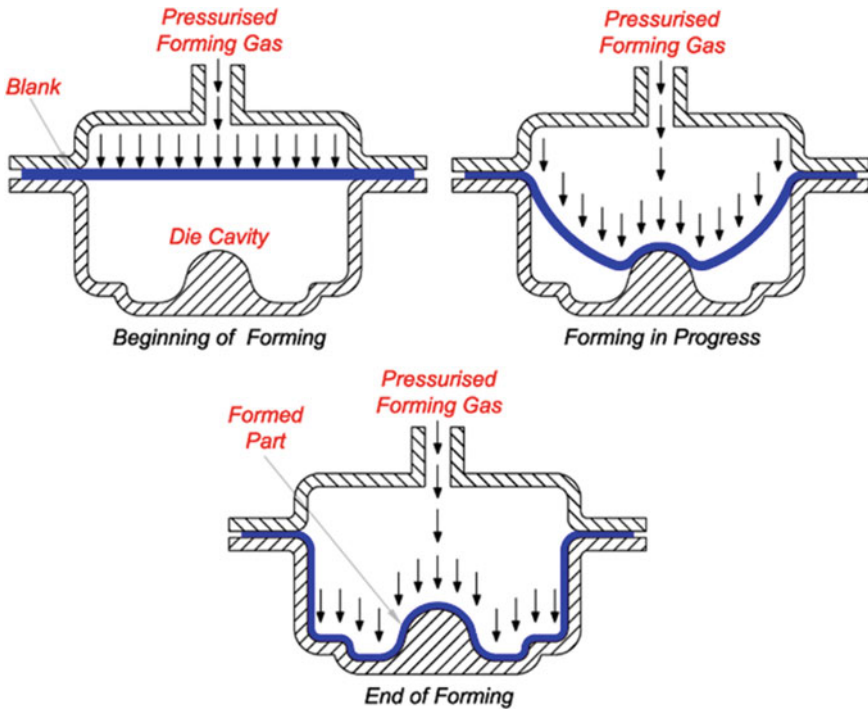
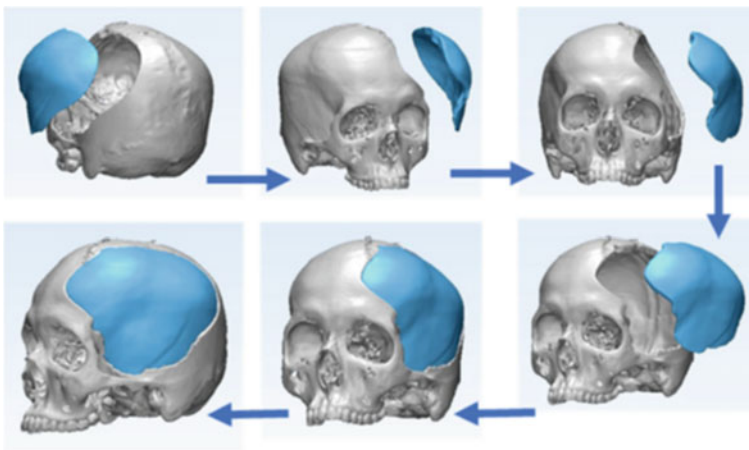**Fig. 4** A schematic overview of the industrial SPF process

Fig. 5 CAD workflow for the definition of the implant geometry [57]

When moving to the process design, several aspects have to be taken into account: the SPF is a complex process and, thus, needs the adoption of an accurate methodology able to limit the waste of time and money. An approach based on the Finite Element (FE) simulation has been widely reported as the most promising solution, especially to calculate the gas presure profile that is one of the unknown quantities. The construction of a reliable FE model passes through the definition of an accurate material model to properly describe the behavior in the superplastic regime. One of the most widely adopted among the several constitutive equations reported in literature is the power-law proposed by Backofen, that relates the equivalent stress state with the equivalent strain rate ($\sigma = C\varepsilon^m$) where the strain rate sensitivity index (the exponent m) is strictly related to the necking behaviour of the alloy. Other formulations have shown good capabilities, as those based on hyperbolic sine law [58] or as the viscoplastic model proposed by Johnson–Cook that has been adopted to satisfactorily model the superplastic behavior of a Ti–6Al–4 V alloy [59]. Nevertheless, as it has been previously underlined, the superplastic behavior is mainly dependent on the material microstructure: not only an average grain size should be below 10 microns, but it should remain as stable as possible [53]. Since grain growth has a detrimental effect on the superplastic behavior, researchers have provided more refined constitutive equations integrating also the kinetics of the grain growth, both static and dynamic [60]. Regardless of the type and complexity of the constitutive equations, material's constants are usually calibrated using data from specific experimental tests: the characterization of superplastic alloys has been initially based on uniaxial tensile tests [61] and in particular on the strain rate jump tests to evaluate the strain rate sensitivity index m [62]. Nevertheless, there's plenty of published papers underlining that the investigation of the material behavior in a biaxial tension mode, rather than uniaxial, is more accurate since being closer to what happens during the industrial superplastic process. Therefore, bulge tests in superplastic conditions have gained more reliability and are widely [63]. In such tests, circular specimens are clamped between tools heated up at the test temperature and are deformed under the action of a pressurized gas. Material's constants can be eventually calibrated by means of analytical approaches, as the one proposed by Enikeev [64], or more advanced techniques such as those relying on the Genetic Algorithms (GA) [65]. In fact, the calibration of unknown parameters in a constitutive equation can be treated as an optimization problem: if the experimental setup is completely reproduced within a CAE environment, an error function—describing the discrepancy between the experimental and numerical data—can be easily calculated and subsequently minimized. It has been also demonstrated that the accuracy of the equation's constants in reproducing the material behavior is strictly related to the choice of the target data [66]. The characterization of the material's behavior in superplastic conditions has also the advantage of identifying the "process window" (mainly in terms of temperature and applied strain rate) in which the alloy emphasizes its superplastic "attitude". As a consequence, the process is designed to respect such a window: in particular, the gas pressure profile is numerically calculated in order to induce the optimal strain rate during the forming operations. Once calculated, the process profile is usually replicated during a set of experimental trials and the predicted geometry (in terms of

shape accuracy and/or final thickness distribution) is compared with the experimental one to validate the numerical predictions. As for the application of the SPF process to real case studies, dental fixtures have been documented as the first application of the superplastic forming for customized implants [67] (Fig. 6).

The achievement of a complex part without any defect becomes possible thanks to a proper selection of the process parameters: despite being one of the first applications of the technology for the fabrication of a customized implant, the adoption of a Finite Element approach has been regarded as an unavoidable step on the way to a successful manufacturing of a sound component. The SPF process has also proved its capabilities also in the case of averagely larger implants: remarkable results have been achieved in the case of customized cranial prostheses. Also in this case, the process design based on numerical simulation demonstrated its effectiveness. In fact, thanks to (i) a preliminary extensive material characterization based on bulge tests covering a wide span of loading conditions and (ii) an accurate Finite Element model, the gas pressure profile was calculated at different values of the target strain rate target: moreover, it was demonstrated that the numerical approach could effectively predict the final distribution of thickness even at different levels of the strain rate target [68]. Figure 7b shows the clear dependence of the final thickness distribution on the applied strain rate during forming: when increasing the strain rate to reduce the forming time, the uniformity of the thickness distribution worsens as a consequence of the lower value of the strain rate sensitivity index m.

The numerical approach, in addition, gave the possibility to design the whole process under a different perspective: the uniformity in the final thickness distribution, which is usually considered a good indicator of the overall quality of the formed component, has to be matched with the minimization of the forming time. As a consequence, the increase in the applied strain rate to reduce the forming time overcomes the need of a strictly uniform part to limit as possible the exposure to the oxygen and the subsequent alloy contamination.
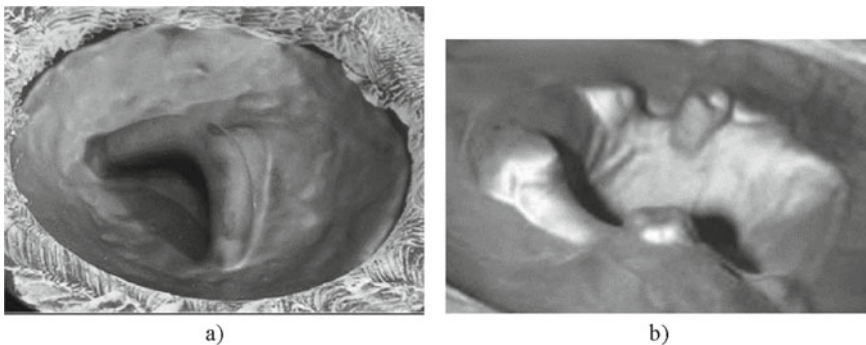

a)   b)

Fig. 6 First application of the SPF on biomedical component: **a** dental implant at the end of the forming stage. **b** internal surface of partial upper denture base [66, 67]
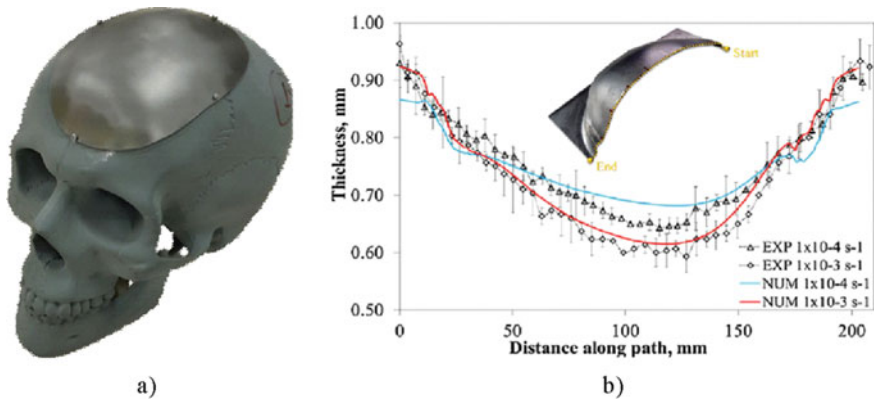
Fig. 7 SPF applied to cranial prosthesis: **a** the investigated case study, **b** numerical vs. experimental comparison of the final thickness distribution at two strain rate levels [68]

Another important aspect related to the SPF process has to be discussed: the manufacturing of a fully customized component implies the availability of a single metallic die for each patient-related case study. Such an aspect, combined with the longer forming time (if compared with a more conventional stamping process), makes the SPF an extremely costly process. Preliminary investigations regarding the super-plastic forming of dental fixtures have revealed the promising performance offered by phosphate bonded investment materials when used for SPF dies [69]. Similar results were also achieved when using a ceramic insert (fabricated by investment casting) as an expendable die for the SPF manufacturing of a Mg-based resorbable cheekbone prosthesis. As a general rule, starting from a pattern obtained by stereolithography (reporting the geometry of the component to be manufactured), a flexible resin pattern replica can be obtained and used for the final casting of the ceramic die [70]. Such a solution not only allows a sensible reduction of the process-related costs (the SPF die can be thus composed of a metallic frame and several interchangeable expendable ceramic inserts) but also makes possible the manufacturing of complex geometries with undercuts.

Single Point Incremental Forming (SPIF). Single point incremental forming (SPIF) is considered a relatively-new sheet metal forming process particularly suitable for rapid prototyping applications and/or for limited batches of production. A general scheme of the SPIF process is reported in Fig. 8 [71].

The blankholder is used to clamp and hold in position the metal blanks while it is deformed by the local action of a rotating single point forming tool whose trajectory is usually optimized according to the geometry to be manufactured [72]. During the forming operations, there is no backup die supporting the back surface of the sheet. Thanks to the excellent formability that can be achieved due to the local contact between the rotating tool and the blank as well as the high level of customization, SPIF has been considered as a suitable solution to overcome the limitations of conventional processes in the manufacturing of fully customized biomedical implants. The design
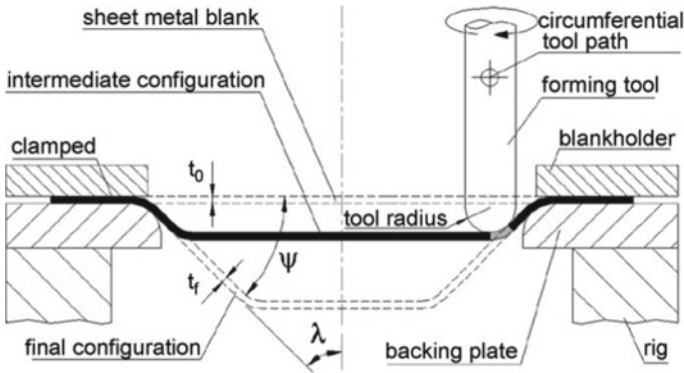
Fig. 8 A schematic view of the SPIF process

and manufacturing of customized implants via SPIF follows a predefined sequence of steps not too different from the one described for the SPF process (see Fig. 9) [73, 74].

The process begins with the creation of a three-dimensional CAD model, usually generated by a reverse approach based on acquisition and modeling operations. Digital data is generally obtained from a scan of the patient's physical model or from CT and MRI scanners. Resulting clouds of data are then processed in a CAD environment software and converted into surfaces or 3D shapes. The 3D model
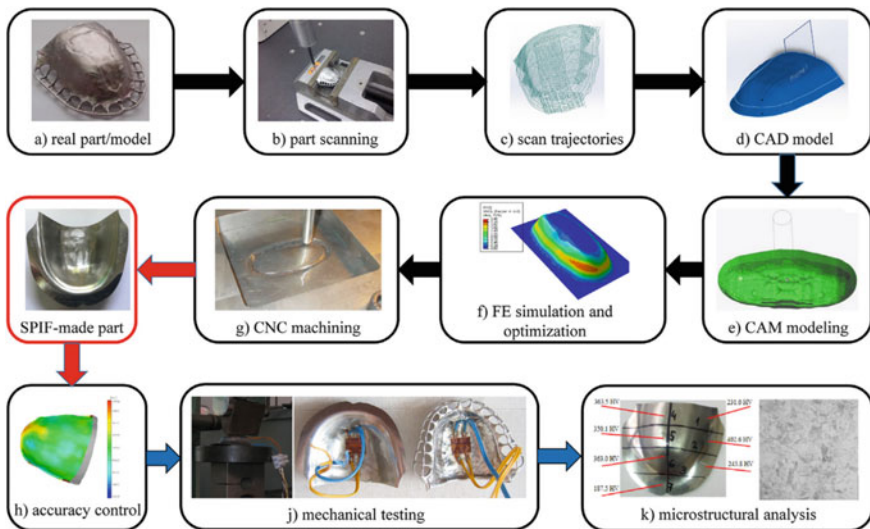
Fig. 9 The predefined sequence of steps for the SPIF process design [Characterisation of geometrical and physical properties of a stainless steel denture framework manufactured by single-point incremental forming, JMR&T Milutinovic 2021]

is then imported in a CAD/CAM environment where several processing strategies are analyzed in terms of accuracy and formability of the parts, surface quality and processing time [75, 76]. A dedicated framework has been proposed to optimize to tool's path using a network analysis methodology based on topological conceptual graphs to capture the effects of different phenomena on the final accuracy of a sheet metal part manufactured by SPIF [77]. The feasibility of the optimized tool's path is then checked during the process design based on numerical simulation: also in this case, the approach based on an accurate Finite Element model is of paramount importance to reduce as possible the waste of time and material. As also underlined in the previous section, the accuracy of the numerical prediction is strictly related to the capability of the constitutive equation to effectively reproduce the material behavior. Several researchers report the satisfactory results obtained by implementing the constitutive model proposed by Johnson and Cook to numerically design the manufacturing of a dental prosthesis [78] and an artificial hip joint component [79].

The big advantage coming from the numerical simulation has led to a more performing process design in which the critical aspects related to the material deformation can be easily identified without excessively wasting time and material: in such a way, the flexibility of the process has led to the correct manufacturing of several customized implants for maxillofacial, denture and cranial applications (Fig. 10).

4.3 Laser Processing

Laser based manufacturing processes are extensively employed in the manufacturing of biomedical implants. The laser beam being flexible tool in terms of its spatial and temporal control allows to interact with the material in different ways providing the means to heat up, melt, vaporize, or ablate. Such phenomena have been used for cutting, engraving, annealing, and welding purposes. A laser process for biomedical implant manufacturing can be essentially designed by selecting the appropriate laser source determining its wavelength, emission type, and beam size along with the beam handling means. The laser process is directly adaptable to CAD/CAM systems facilitating a direct integration. Moreover the processes are inherently open to real time process monitoring especially via the use of optical monitoring methods rendering them directly adaptable to the Industry 4.0 applications. Laser based manufacturing processes in the biomedical field are often related to the micromachining processes. A highly focused laser beam with dimensions typically between $10\,\mu m$ and $50\,\mu m$ is used. Commonly pulsed wave (PW) lasers are employed, where the pulse duration is chosen from ms level down to fs depending on the type of laser-material interaction required. In terms of a generic categorization ms to μs pulse durations are suited to melting based welding and cutting applications, ns pulses are suited to marking and cutting, while the ps to fs pulsed ultrafast systems have been used extensively from cutting to texturing applications. Beyond the previously described use of lasers in
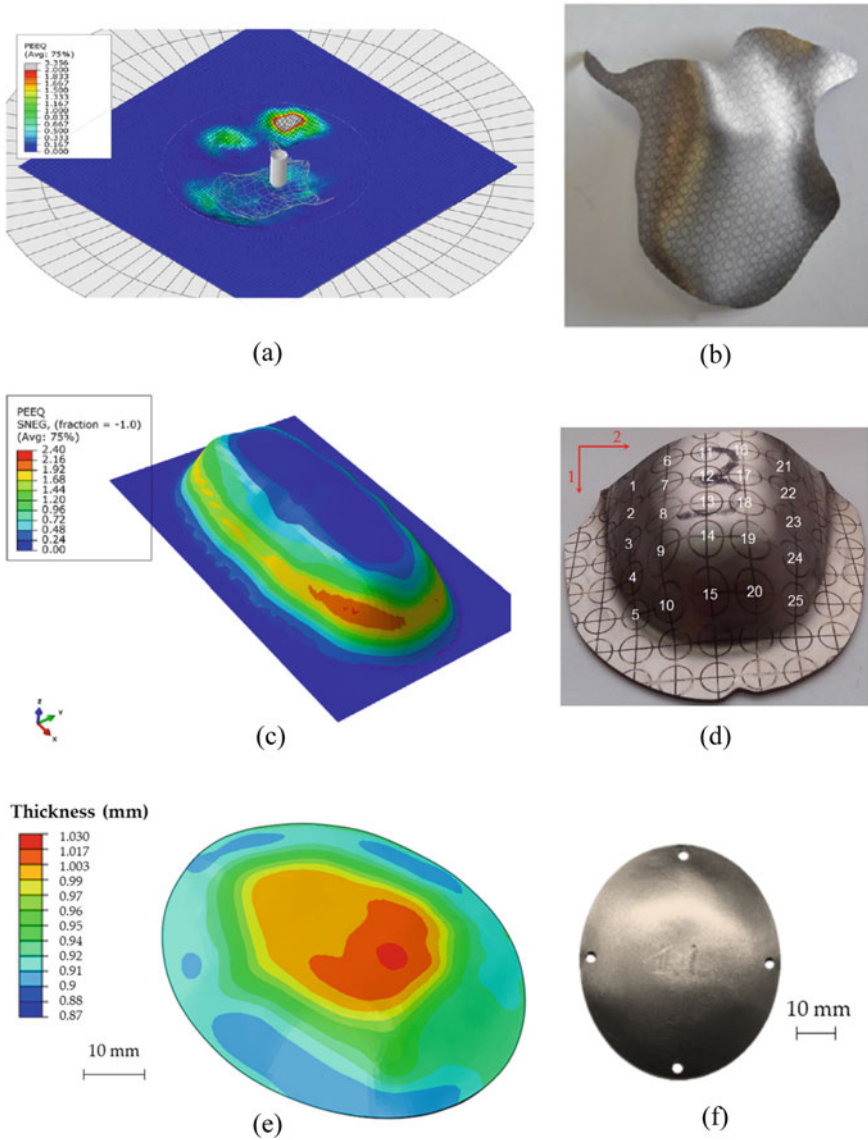
Fig. 10 SPIF in biomedical applications: **a** and **b** customized maxillofacial implant [80]; **c** and **d** maxillary denture base plate [73]; **e** and **f** cranial implant for in-vivo test [81]

additive manufacturing, laser based manufacturing processes are used conventionally in the manufacturing of stents, pace makers, catheters, and packaging of devices. While such processes are aimed to produce large production lots, the lasers indeed open to several possibilities in terms of personalized implant manufacturing. In the

following paragraphs some of the most suitable techniques for personalization and functionalization of biomedical implants are summarized.

Laser microcutting of prototype devices. Laser microcutting is carried out both by means of a proximity processing head that blows the process gas on the cut region or a remote processing head based on a galvanometric scanner. Laser microcutting is widely employed in the cutting microtubes 1–5 mm diameter and 0.05–0.25 mm in thickness for the manufacturing of metallic and polymeric stents. The use of a CAD/CAM system provides ease of switching between different designs rapidly. In terms of testing new device models or novel material types a common bottleneck is the production of dedicated microtubes. Flat precursors such as thin sheets are relatively easier to manufacture. Laser cutting of such precursors in proximity or remote configurations can open up to new possibilities. Recent studies showed the use of laser microcutting of flat sheets to produce foldable/expandable devices. Such designs are often inspired by origami/kirigami providing new dimensions to the flat precursor by cutting, folding, or expansion. Figure 11 shows the concept of an expandable stent after laser cutting of a flat sheet. The design relies on the cutting of a specific design, which allows the passage of a guide wire and a ballooned catheter to expand towards a 3D shape. The final results is a tubular structure after expansion. The approach is exploitable for the testing of new alloys used in metallic stents.

Laser precision welding and heat treatment. Laser welding is highly flexible in terms of materials, thicknesses, and joint configurations. The process can be adapted to keyhole or conduction mode processing and used in both autogenous condition or with filler material. Laser welding is widely exploited in the biomedical device manufacturing [2]. The advantage of the technology regarding personalized implants regards the need to adapt to patient specific geometries freely. The applied weld patterns can be varied from single spots to intricate joint designs following the geometry of the implant. The process can be also adapted to weld dissimilar materials where required [84]. The limited heat affected zone also provides a strong advantage against local corrosion. Laser heat treatment can be seen as an extension of the welding process and potentially applied with the same laser system concerning the biomedical implants. The use of a laser for heat treatments in biomedical implants
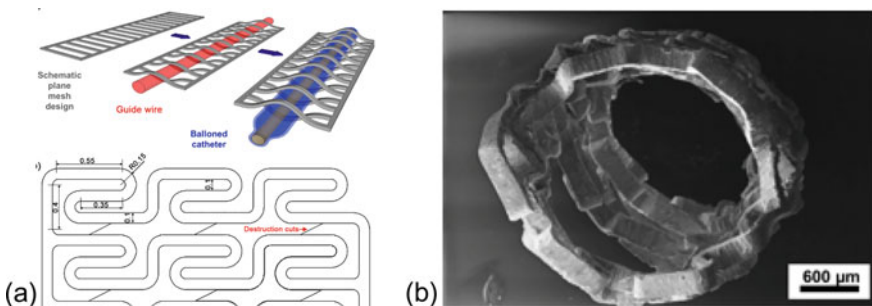

Fig. 11 **a** Concept of an expandable stent after the laser cutting of a flat sheet [82]. **b** Example of an inflated stent mesh in AZ31 Mg alloy [83]

can provide locally improved strength, toughness, or anti-wear behavior. An important application regards the use of laser heat treatment for annealing and shape setting shape memory alloys. The use of lasers can provide customized implant geometry starting from wire feedstocks adapted to the patient geometry freely without the need for complex shape setting dies used for furnace heating [85, 86].

Laser surface functionalization via geometrical and chemical modifications. Laser based surface treatments have been widely explored in many applications and in particular for biomedical implants. While most of the research regards their use in the modification of the entire implant their use can open up new possibilities in bespoke implant production. As a matter of fact the surface of the implant can also be personalized. Such personalization can be carried out on the entire surface of the implant or locally depending on the requirements [87]. The advantage of laser based treatments relies on the possibility to adapt the region of the treatment on patient's anatomical requirements in a flexible manner compared to bulk processing technologies. Concerning surface functionalization treatments lasers can achieve principally geometrical and/or chemical modifications. One of the most widely studied methods regards the variation of the microtopography of the biomedical devices via a direct writing approach (see Fig. 12). Laser surface texturing (LST) has been widely studied employing surface features (eg. dimples, lines, grooves) [88]. Such features can help modify or improve the interaction with the surrounding environment that encompasses both the living tissue but also possible coating applications. LST can improve the cell adhesion, biocompatibility but also can improve the adhesion of a surface coating, reduce the friction during implantation, and control biodegradation processes [89]. While the direct writing based approaches approach dimensional limits in the proximity of a few µm, novel methods such as direct laser interference patterning (DLIP) and laser induced periodic surface structures (LIPSS) can generate sub-micrometric structures beyond the diffraction limit of the laser beam (see Fig. 13) [90, 91].

The use of a laser beam for surface modifications may involve also the reduction of surface asperities (see Fig. 14). Laser micropolishing is a process that generates a very shallow remolten layer that solidifies rapidly filling in surface asperities that are derived from the previous manufacturing processes (see Fig. 3) [92]. The laser
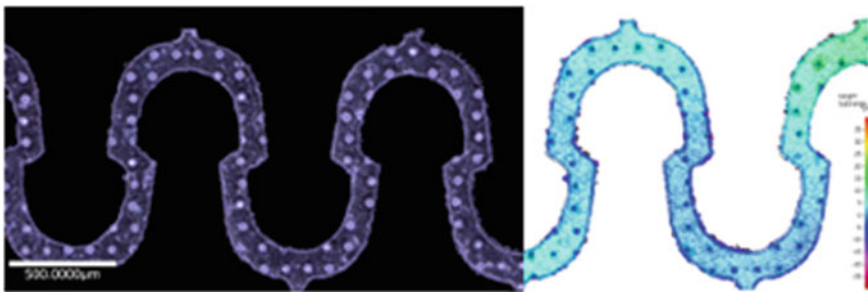
Fig. 12 Laser surface texturing of a stent mesh [95]

Fig. 13 Submicrometric
laser texturing by direct laser
interference patterning on
AZ31 Mg alloy [96]
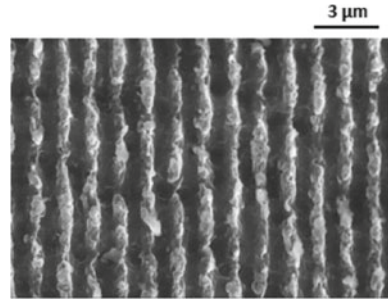
Fig. 14 Laser
micropolishing of AISI 304
stainless steel showing the
transition from untreated to
the laser treated flat region
[97]
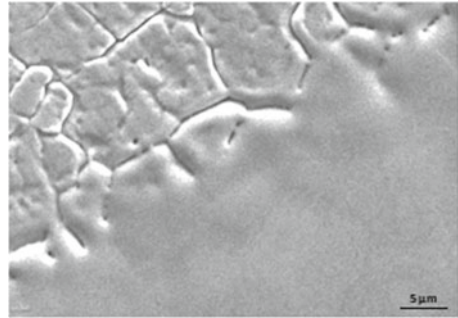
micropolishing technique has been shown to reduce the surface roughness to less
than Ra = 0.5 µm. Such surface features can be exploited to modulate the wetting
behaviour, while antibacterial properties have also been found to be effective [93].
Lasers can also modify the surface chemistry without inducing geometrical changes.
The use of localized laser oxidation of Ti-alloys and stainless steels is an approach
that is already exploited for the permanent marking of biomedical devices. It has
been shown that laser based surface heating can allow to enrich the surface with O
and N that can be regulated to improve biocompatibility [94].

5 Standardization

5.1 Mechanical Characterization of 3D Printed Samples

Performances Considering the overarching context of orthopedic application, the
compression test is the most used to characterize these structures but in the last few
years, tensile, fatigue and bending tests have been carried out to broaden the knowl-
edge of lattices mechanical response. The test standards followed for the characteri-
zation of AM specimens are related to the standard applied to traditionally processed
metals. The compression test is, for example, usually carried out following the ISO

13314 (related to compression tests for porous and cellular metals) that, although it is not specific for additively manufactured samples [27, 27, 27], provides good indications on which parameters to use during the test. For other characterization tests, there is not a specific standard for additively manufactured samples. In the absence of a specific international standard regarding the mechanical characterization of these structures, the researchers need to point out which are the methodologies, instrumentations and parameters most used by the researchers around the world to provide a possible useful guideline for further developments in design, evaluation and applications of metal AM.

5.2 Biomedical Certification

European regulation for medical device follow several ISO's:

ISO 13485, which specifies requirements for a quality management system (QMS), where an organization with the ability to provide medical devices and related services that consistently meet customer and applicable regulatory requirements. Such organizations can be involved in one or more stages of a 3D-printed implant life-cycle, including design, development, production, storage, distribution, installation, and servicing of a medical device, and more.

ISO 11737–1:2018 sterilization of health care products:

Microbiological methods—Part 1: Determination of a population of microorganisms on products. This specifies requirements and guides the enumeration and microbial characterization of the population of viable microorganisms on or in a health care product, component, raw material, or package.

ISO 11737—2009 Sterilization of medical devices—Microbiological methods—Part 2: Tests of sterility performed in the definition, validation, and maintenance of a sterilization process. This document specifies requirements and test methods for materials, preformed sterile barrier systems, sterile barrier systems, and packaging systems that are intended to maintain sterility of terminally sterilized medical devices until the point of use.

ISO 11607—2019 regulates the packaging for terminally sterilized medical devices part I: requirements for materials, sterile barrier systems and packaging systems, shelf life.

The European Union considers 3D-printed implants a custom-made medical device under the old 93/42/CE Directive (MDD 93/24/CE). However, the new Medical Device Regulation MDR (EU) 2017/745 states that 3D printed implants are not considered custom made medical devices under the CE mark. It also says that these devices should still follow all the directives according to their risk classification. A bone substitute was considered as class IIB previously, but they were forced to change to class III because they were resorbable, and this would cause changes in the body.

It is common to see some of the 3D-printed implants being sterilized in an autoclave. However, an autoclave is not an authorized sterilization system for an

implantable medical device. 3D printed implants open new problems during the manufacturing of medical devices because until now, the product was already certified by the supplier. 3D printing implant companies should develop GMP (good management practices) to avoid contamination of the product. Such GMP includes dedicated machines, clean rooms, and consistent internal analysis to ensure the purity of the core of the device. Cleaning of the surface should be done in dedicated cleanrooms, and analysis should confirm your process has no biological or physical contamination. Finally, using certified blisters and controlled sterilization either by ETO or gamma radiation.

5.3 Definition of New Pre-clinical Protocols

The certification protocols, in general, should be also completed by accurate information regarding the prosthesis's load-bearing capacity. Such an aspect is detailed and regulated by dedicated ISO standards: as an example, the ISO 10328:2016 [98] reports all the limit loads—both static and dynamic—that a lower limb implant must respect. On the other hand, when focussing on the other type of implants, the lack of harmonized standards moves the attention on the definition of new testing protocols taking into account several loading conditions. Most of the researches available in literature underlines the paramount importance of certificating the strength of cranial implants when subjected to impact an loading, thus reproducing undesired/unexpected situations like accidents, falls [99] or sport-related events [100]. More in details, accurate experimental conditions have been proposed to physically simulate the impact at a velocity from 3.5 m/s to 7 m/s that represent the loading conditions related to a fall from bed or in the case of a bicycle impact (Fig. 15).

Even more challenging is the definition of a pre-clinical protocol when sport-related events are accounted for: the damage caused by a cricket ball directed at a speed of 110 km/h on a 3D printed head model has been experimentally and numerically investigated, highlighting the remarkable level of the equivalent von Mises stress concentrated in the brain region close to the impact [103] (Fig. 16).

The provided examples can be considered valid alternatives for the exact definition of the loading conditions to be tested in a pre-clinical protocol. Nevertheless, there is a lack of information regarding the same impact loading condition on demonstrative head model on which a customized prosthesis has been already anchored on. The drop test tower has been recently proposed (Fig. 17) as a valid solution to evaluate the strength level of cranial prosthesis when subjected to impact load conditions [104].

As shown in Fig. 17, a customized cranial implant was anchored on a purposely-made PMMA support reproducing the upper portion of a defected skull. When subjected to an impact load condition using a drop-test tower machine, no implant failure has been detected after the impact. Moreover, the drop-test results have also suggested that the maximum implant deflection (as a result of the impact) is strictly related to the blank thickness in the region of the impact. Such a consideration opens a new perspective on the design of customized prosthesis: in fact, beside ensuring the
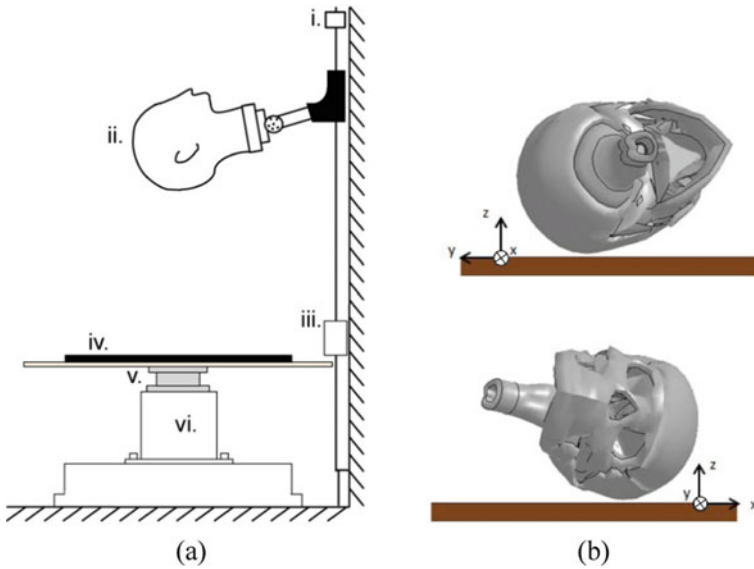
Fig. 15 Definition of representative set-up to investigate impact loading on skull in the case of a fall from bed [101] (**a**) or a bicycle accident [102] (**b**)
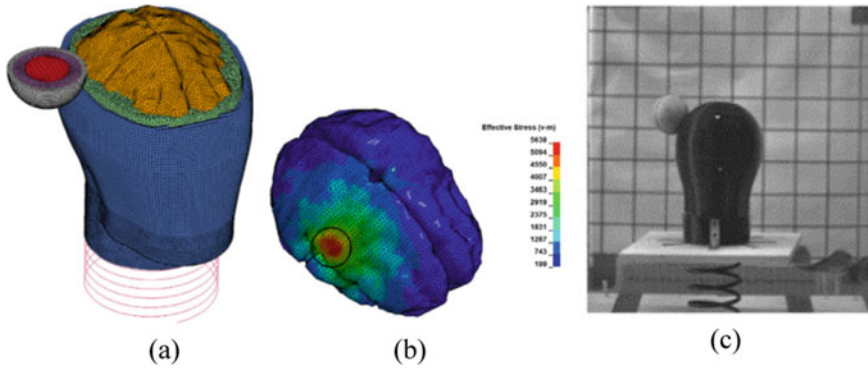
Fig. 16 Definition of a pre-clinical protocol for sport-related accidental events: **a** FE model of the impact, **b** equivalent von Mises stress on the brain region close to the impact, **c** high speed camera acquisition

aesthetical requirements (perfect fit with the surrounding bone), the manufacturing process can be designed and optimized to satisfy specific target requirements in terms of implant's strength. Therefore, in the case of the SPF, the applied strain rate can be tailored in order to ensure a higher thickness in the blank region where the impact is more likely to occur, so that a higher indentation resistance can be obtained. As for the SPIF, the same results can be obtained if the tool's path is optimized to obtain

Fig. 17 Definition of a pre-clinical protocol based on impact loading using a drop test tower

a thicker final blank in the region of a possible impact. Such an approach, recently documented in literature [105], can remarkably improve the conventional prosthesis design that is mostly based on geometrical and process feasibility issues. Moreover, the versatility of tailoring the impact performance according to the post-forming properties of a customized implant can be ideally applied to any type of implant for any patient's anatomy, thus representing a powerful tool for a more robust design and a higher level of customisation of medical prostheses.

6 Conclusions

- Manufacturing of bespoke metal implants has the potential to alter how implants are not only manufactured, but the clinical approach to metallic implants and their functionality
- This has been demonstrated in patient specific implants, and in lab settings, but so far the forays into mass-market implants have been limited in impact.
- Alongside bringing lab research to industrial viability, there needs to be a concerted effort to translate advances made in other high specification industries (e.g. aerospace) into the medical supply chain.

In addition to being anatomically adapted to the patient's anatomical and surgical needs, bespoke implants can incorporate porous scaffolds and solid components

into a single monoblock with reduced implant rigidity and facilitate osseointegration. With the advancement of technologies, you are now able to directly manufacture fully functional parts. In particular, additive manufacturing, sheet forming and laser processing offer the orthopedic sector the possibility of mass customization of implants at a lower cost thanks to their ability to produce parts with complex and intrinsic designs specific to individual patients. A long-lasting plant can be achieved by selecting the optimal combination of surface roughness, pore size and porosity, values that can be achieved through a careful selection of the machining parameters.

The key challenges and future directions of customizing technologies are as follows:

- A comprehensive and reliable database containing detailed information on the mechanical and biological properties of human bones has yet to be created. This database should include bone properties for different ages, gender groups and in different locations. This information is necessary as a "target" of the design process of optimization of the topology.
- The long-term biological performance of metal implants designed through topology optimization techniques must be rigorously evaluated in order to ascertain the advantages and disadvantages of such implants. There is a lack of detailed studies on long-term performance based on aspects of fracture mechanics. The occurring time of the implant's failure is another cause of concern. Because revision surgery after implant failure creates many unnecessary discomforts and pain for the patient.
- Material research. New alloy systems capable of improving the mechanical and biological performance of porous metal implants are in great demand, along with new post-treatment technologies to improve bioactivity and biocompatibility.

References

1. Steen WM, Mazumder J (2020) Laser material processing, vol.1. https://doi.org/10.1007/978-1-84996-062-5
2. Quazi MM, Ishak M, Fazal MA, Arslan A, Rubaiee S, Aiman MH et al (2021) A comprehensive assessment of laser welding of biomedical devices and implant materials: recent research, development and applications. Crit Rev Solid State Mater Sci 46:109–151. https://doi.org/10.1080/10408436.2019.1708701
3. Kurella A, Dahotre NB (2005) Review paper: surface modification for bioimplants: the role of laser surface engineering, vol 20. https://doi.org/10.1177/0885328205052974
4. Wong KC, Scheinemann P (2018) Additive manufactured metallic implants for orthopaedic applications. Sci China Mater 61:440–454. https://doi.org/10.1007/s40843-017-9243-9
5. Wong KC (2008) 3D-printed patient-specific applications in orthopedics. Orthop Res Rev 57–66
6. Fan H, Fu J, Li X, Pei Y, Li X, Pei G et al (2015) Implantation of customized 3-D printed titanium prosthesis in limb salvage surgery: a case series and review of the literature. World J Surg Oncol 13:1–10. https://doi.org/10.1186/s12957-015-0723-2
7. Imanishi J, Choong PFM (2015) Three-dimensional printed calcaneal prosthesis following total calcanectomy. Int J Surg Case Rep 10:83–87. https://doi.org/10.1016/j.ijscr.2015.02.037

8. Wong KC, Kumta SM, Geel NV, Demol J (2015) One-step reconstruction with a 3D-printed, biomechanically evaluated custom implant after complex pelvic tumor resection. Comput Aided Surg 20:14–23. https://doi.org/10.3109/10929088.2015.1076039

9. Wei R, Guo W, Ji T, Zhang Y, Liang H (2017) One-step reconstruction with a 3D-printed, custom-made prosthesis after total en bloc sacrectomy: a technical note. Eur Spine J 26:1902–1909. https://doi.org/10.1007/s00586-016-4871-z

10. Karageorgiou V, Kaplan D (2005) Porosity of 3D biomaterial scaffolds and osteogenesis. Biomaterials 26:5474–5491

11. Kumar A, Nune KC, Murr LE, Misra RDK (2016) Biocompatibility and mechanical behaviour of three-dimensional scaffolds for biomedical devices: process–structure–property paradigm. Int Mater Rev 61:20–45. https://doi.org/10.1080/09506608.2015.1128310

12. Shim JH, Kim SE, Park JY, Kundu J, Kim SW, Kang SS et al (2014) Three-dimensional printing of rhBMP-2-loaded scaffolds with long-term delivery for enhanced bone regeneration in a rabbit diaphyseal defect. Tissue Eng Part A 20:1980–1992. https://doi.org/10.1089/ten.tea.2013.0513

13. Sanz-Herrera JA, Garcia-Aznar JM, Doblaré M (2009) On scaffold designing for bone regeneration: a computational multiscale approach. Acta Biomater 5:219–229

14. Klawitter JJ, Hulbert SF (1971) Application of porous ceramics for the attachment of load bearing internal orthopedic applications. J Biomed Mater Res 5:161–229. https://doi.org/10.1002/jbm.820050613

15. Griffon DJ, Sedighi MR, Schaeffer DV, Eurell JA, Johnson AL (2006) Chitosan scaffolds: interconnective pore size and cartilage engineering. Acta Biomater 2:313–320. https://doi.org/10.1016/j.actbio.2005.12.007

16. Bragdon CR, Jasty M, Greene M, Rubash HE, Harris WH (2004) Biologic fixation of total hip implants. Insights gained from a series of canine studies. J Bone Joint Surg Am 86-A Suppl:105–117

17. Harrysson OLA, Cansizoglu O, Marcellin-Little DJ, Cormier D, West HA (2008) Direct metal fabrication of titanium implants with tailored materials and mechanical properties using electron beam melting technology. Mater Sci Eng C 28:366–373

18. Li X, Wang C, Zhang W, Li Y (2009) Fabrication and characterization of porous Ti6Al4V parts for biomedical applications using electron beam melting process. Mater Lett 63:403–405. https://doi.org/10.1016/j.matlet.2008.10.065

19. Muller P, Mognol P, Hascoet J-Y (2013) Modeling and control of a direct laser powder deposition process for Functionally Graded Materials (FGM) parts manufacturing. J Mater Process Technol 213:685–692. https://doi.org/10.1016/j.jmatprotec.2012.11.020

20. Bobbio LD, Otis RA, Borgonia JP, Dillon RP, Shapiro AA, Liu Z-K et al (2017) Additive manufacturing of a functionally graded material from Ti–6Al–4V to Invar: Experimental characterization and thermodynamic calculations. Acta Mater 127:133–142. https://doi.org/10.1016/j.actamat.2016.12.070

21. Fujibayashi S, Neo M, Kim H-M, Kokubo T, Nakamura T (2004) Osteoinduction of porous bioactive titanium metal. Biomaterials 25:443–450. https://doi.org/10.1016/s0142-9612(03)00551-9

22. Fukuda A, Takemoto M, Saito T, Fujibayashi S, Neo M, Pattanayak DK et al (2011) Osteoinduction of porous Ti implants with a channel structure fabricated by selective laser melting. Acta Biomater 7:2327–2336. https://doi.org/10.1016/j.actbio.2011.01.037

23. Tamaddon M, Samizadeh S, Wang L, Blunn G, Liu C (2017) Intrinsic osteoinductivity of porous titanium scaffold for bone tissue engineering. Int J Biomater 2017:5093063. https://doi.org/10.1155/2017/5093063

24. Reigstad O, Franke-Stenport V, Johansson CB, Wennerberg A, Røkkum M, Reigstad A (2007) Improved bone ingrowth and fixation with a thin calcium phosphate coating intended for complete resorption. J Biomed Mater Res B Appl Biomater 83:9–15. https://doi.org/10.1002/jbm.b.30762

25. Morrison RJ, Kashlan KN, Flanangan CL, Wright JK, Green GE, Hollister SJ et al (2015) Regulatory considerations in the design and manufacturing of implantable 3D-printed medical devices. Clin Transl Sci 8:594–600. https://doi.org/10.1111/cts.12315

26. Yang Y, Lu J, Luo Z, Wang D (2012) Accuracy and density optimization in directly fabricating customized orthodontic production by selective laser melting. Rapid Prototyp J 18:482–489. https://doi.org/10.1108/13552541211272027

27. Li R, Liu J, Shi Y, Du M, Xie Z (2010) 316L Stainless steel with gradient porosity fabricated by selective laser melting. J Mater Eng Perform 19:666–671. https://doi.org/10.1007/s11665-009-9535-2

28. Bibb R, Eggbeer D, Williams R (2006) Rapid manufacture of removable partial denture frameworks. Rapid Prototyp J 12:95–99. https://doi.org/10.1108/13552540610652438

29. Bibb R, Eggbeer D, Evans P, Bocca A, Sugar A (2009) Rapid manufacture of custom-fitting surgical guides. Rapid Prototyp J 15:346–354. https://doi.org/10.1108/13552540910993879

30. Kruth J, Mercelis P, Van Vaerenbergh J, Froyen L, Rombouts M (2005) Binding mechanisms in selective laser sintering and selective laser melting. Rapid Prototyp J 11:26–36. https://doi.org/10.1108/13552540510573365

31. Marin E, Pressacco M, Fusi S, Lanzutti A, Turchet S, Fedrizzi L (2013) Characterization of grade 2 commercially pure trabecular titanium structures. Mater Sci Eng C Mater Biol Appl 33:2648–2656. https://doi.org/10.1016/j.msec.2013.02.034

32. Lin C-Y, Wirtz T, LaMarca F, Hollister SJ (2007) Structural and mechanical evaluations of a topology optimized titanium interbody fusion cage fabricated by selective laser melting process. J Biomed Mater Res A 83:272–279. https://doi.org/10.1002/jbm.a.31231

33. Murr LE, Quinones SA, Gaytan SM, Lopez MI, Rodela A, Martinez EY et al (2009) Microstructure and mechanical behavior of Ti–6Al–4V produced by rapid-layer manufacturing, for biomedical applications. J Mech Behav Biomed Mater 2:20–32. https://doi.org/10.1016/j.jmbbm.2008.05.004

34. Warnke PH, Douglas T, Wollny P, Sherry E, Steiner M, Galonska S et al (2009) Rapid prototyping: porous titanium alloy scaffolds produced by selective laser melting for bone tissue engineering. Tissue Eng Part C Methods 15:115–124. https://doi.org/10.1089/ten.tec.2008.0288

35. Ayyıldız S, Soylu EH, Ide S, Kılıç S, Sipahi C, Pişkin B et al (2013) Annealing of Co–Cr dental alloy: effects on nanostructure and Rockwell hardness. J Adv Prosthodont 5:471–478. https://doi.org/10.4047/jap.2013.5.4.471

36. Zhang LC, Klemm D, Eckert J, Hao YL, Sercombe TB (2011) Manufacture by selective laser melting and mechanical behavior of a biomedical Ti–24Nb–4Zr–8Sn alloy. Scr Mater 65:21–24. https://doi.org/10.1016/j.scriptamat.2011.03.024

37. Marcu T, Todea M, Maines L, Leordean D, Berce P, Popa C (2012) Metallurgical and mechanical characterisation of titanium based materials for endosseous applications obtained by selective laser melting. Powder Metall 55:309–314. https://doi.org/10.1179/1743290112Y.0000000007

38. Szymczyk P, Junka A, Ziółkowski G, Smutnicka D, Bartoszewicz M, Chlebus E (2013) The ability of S.aureus to form biofilm on the Ti–6Al–7Nb scaffolds produced by selective laser melting and subjected to the different types of surface modifications. Acta Bioeng Biomech 15:69–76

39. Alvarez K, Nakajima H (2009) Metallic scaffolds for bone regeneration. Materials (Basel) 2:790–832. https://doi.org/10.3390/ma2030790

40. Thijs L, Montero Sistiaga ML, Wauthle R, Xie Q, Kruth J-P, Van Humbeeck J (2013) Strong morphological and crystallographic texture and resulting yield strength anisotropy in selective laser melted tantalum. Acta Mater 61:4657–4668. https://doi.org/10.1016/j.actamat.2013.04.036

41. Watari F, Yokoyama A, Omori M, Hirai T, Kondo H, Uo M et al (2004) Biocompatibility of materials and development to functionally graded implant for bio-medical application. Compos Sci Technol 64:893–908. https://doi.org/10.1016/j.compscitech.2003.09.005

42. Rayna T, Striukova L (2016) From rapid prototyping to home fabrication: How 3D printing is changing business model innovation. Technol Forecast Soc Change 102:214–224. https://doi.org/10.1016/j.techfore.2015.07.023

43. Gibson I, Rosen D, Stucker B (2015) Additive manufacturing technologies 3D printing, rapid prototyping, and direct digital manufacturing
44. Calderan P (2015) Stampa 3D Il manuale per hobbisti e maker
45. Beltrametti L, Gasparre A (n.d.) 3D printing as a new technological challenge to manufacturing work. Acts XXVI Annu Conf Synerg Manuf What Futur
46. Petrick IJ, Simpson TW (2013) 3D printing disrupts manufacturing: how economies of one create new rules of competition. Res Manag 56:12–16. https://doi.org/10.5437/08956308X5606193
47. Kietzmann J, Pitt L, Berthon P (2015) Disruptions, decisions, and destinations: enter the age of 3-D printing and additive manufacturing. Bus Horiz 58:209–215. https://doi.org/10.1016/j.bushor.2014.11.005
48. Wazen RM, Currey JA, Guo H, Brunski JB, Helms JA, Nanci A (2013) Micromotion-induced strain fields influence early stages of repair at bone-implant interfaces. Acta Biomater 9:6663–6674. https://doi.org/10.1016/j.actbio.2013.01.014
49. Davis R, Singh A, Jackson MJ, Coelho RT, Prakash D, Charalambous CP, et al (2022) A comprehensive review on metallic implant biomaterials and their subtractive manufacturing, vol 120. Springer, London. https://doi.org/10.1007/s00170-022-08770-8
50. Sheremetyev V, Kudryashova A, Cheverikin V, Korotitskiy A, Galkin S, Prokoshkin S et al (2019) Hot radial shear rolling and rotary forging of metastable beta Ti–18Zr–14Nb (at. %) alloy for bone implants: microstructure, texture and functional properties. J Alloys Compd 800:320–326. https://doi.org/10.1016/j.jallcom.2019.06.041
51. Yoshimitsu Okazaki JM (2021) Mechanical performance of artificial hip stems manufactured. Mater 4:732
52. Elias CN, Meyers MA, Valiev RZ, Monteiro SN (2013) Ultrafine grained titanium for biomedical applications: an overview of performance. J Mater Res Technol 2:340–350. https://doi.org/10.1016/j.jmrt.2013.07.003
53. Lu Z, Huang X, Huang J (2021) Role of grain size and shape in superplasticity of metals. Front Mater 8:1–7. https://doi.org/10.3389/fmats.2021.641928
54. Langdon TG (2009) Seventy-five years of superplasticity: historic developments and new opportunities. J Mater Sci 44:5998–6010. https://doi.org/10.1007/s10853-009-3780-5
55. Abu-Farha FK, Khraisheh MK (2008) An integrated approach to the superplastic forming of lightweight alloys: towards sustainable manufacturing. Int J Sustain Manuf 1:18–40. https://doi.org/10.1504/IJSM.2008.019225
56. Wang G (2022) Superplastic Forming (SPF) of Complex Sheet Metal Parts and Structures. In: Caballero FGBT-E of MM and A (eds) Elsevier, Oxford, pp 417–434. https://doi.org/10.1016/B978-0-12-819726-4.00016-8
57. Abdullah JY, Abdullah AM, Hueh LP, Husein A, Hadi H, Rajion ZA (2021) Cranial implant design applying shape-based interpolation method via open-source software. Appl Sci 11. https://doi.org/10.3390/app11167604
58. Lin J (2002) Selection of material models for predicting necking in superplastic forming. Int J Plast 19:469–481. https://doi.org/10.1016/S0749-6419(01)00059-6
59. Gao F, Li W, Meng B, Wan M, Zhang X, Han X (2017) Rheological law and constitutive model for superplastic deformation of Ti–6Al–4V. J Alloys Compd 701:177–185. https://doi.org/10.1016/j.jallcom.2017.01.096
60. Carpenter AJ, Antoniswamy AR, Carter JT, Hector LG, Taleff EM (2014) A mechanism-dependent material model for the effects of grain growth and anisotropy on plastic deformation of magnesium alloy AZ31 sheet at 450 C. Acta Mater 68:254–266. https://doi.org/10.1016/j.actamat.2014.01.043
61. Balasubramanian M, Stalin B, Ramanathan K, Ravichandran M (2020) Hot tensile test for determining the material constant on superplastic 5083Al alloy sheet. Mater Today Proc 21:324–328. https://doi.org/10.1016/j.matpr.2019.05.453
62. Khraisheh MK, Abu-Farha FK, Nazzal MA, Weinmann KJ (2006) Combined mechanics-materials based optimization of superplastic forming of magnesium AZ31 alloy. CIRP Ann Manuf Technol 55:233–236. https://doi.org/10.1016/S0007-8506(07)60405-3

63. Aksenov SA, Kolesnikov AV, Mikhaylovskaya AV (2016) Design of a gas forming technology using the material constants obtained by tensile and free bulging testing. J Mater Process Technol 237:88–95. https://doi.org/10.1016/j.jmatprotec.2016.06.003

64. Enikeev FU, Kruglov AA (1995) An analysis of the superplastic forming of a thin circular diaphragm 37:473–483

65. Sorgente D, Palumbo G, Piccininni A, Guglielmi P, Tricarico L (2017) Modelling the superplastic behaviour of the Ti6Al4V–ELI by means of a numerical/experimental approach. Int J Adv Manuf Technol 90:1–10. https://doi.org/10.1007/s00170-016-9235-7

66. Piccininni A, Sorgente D, Palumbo G (2018) Genetic Algorithm based inverse analysis for the superplastic characterization of a Ti–6Al–4V biomedical grade. Finite Elem Anal Des 148:27–37

67. Curtis R, Majo DG, Soo S, Disilvio L, Gil A, Wood RD et al (2008) Superplastic forming of dental and maxillofacial prostheses. In: Curtis RV, Watson TFBT-DB (eds) Woodhead publishing series in biomaterials. Woodhead Publishing, pp 428–474. https://doi.org/10.1533/9781845694241.428

68. Sorgente D, Palumbo G, Piccininni A, Guglielmi P, Aksenov SA (2018) Investigation on the thickness distribution of highly customized titanium biomedical implants manufactured by superplastic forming. CIRP J Manuf Sci Technol 20:29–35. https://doi.org/10.1016/j.cirpj.2017.09.004

69. Juszczyk AS, Radford DR, Curtis RV (2007) Deformation of phosphate-bonded investment materials at elevated temperatures. Dent Mater 23:579–585. https://doi.org/10.1016/j.dental.2006.03.017

70. Guglielmi P, Cusanno A, Bagudanch I, Centeno G, Ferrer I, Garcia-Romeu ML et al (2021) Experimental and numerical analysis of innovative processes for producing a resorbable cheekbone prosthesis. J Manuf Process 70:1–14. https://doi.org/10.1016/j.jmapro.2021.07.060

71. Martins PAF, Bay N, Skjoedt M, Silva MB (2008) Theory of single point incremental forming. CIRP Ann Manuf Technol 57:247–252. https://doi.org/10.1016/j.cirp.2008.03.047

72. Behera AK, Lauwers B, Duflou JR (2015) Tool path generation for single point incremental forming using intelligent sequencing and multi-step mesh morphing techniques. Int J Mater Form 8:517–532. https://doi.org/10.1007/s12289-014-1174-y

73. Milutinovic M, Lendjel R, Baloš S, Zlatanovic DL, Sevšek L, Pepelnjak T (2021) Characterisation of geometrical and physical properties of a stainless steel denture framework manufactured by single-point incremental forming. J Mater Res Technol 10:605–623. https://doi.org/10.1016/j.jmrt.2020.12.014

74. Boulila A, Ayadi M, Marzouki S, Bouzidi S (2018) Contribution to a biomedical component production using incremental sheet forming. Int J Adv Manuf Technol 95:2821–2833. https://doi.org/10.1007/s00170-017-1397-4

75. Tera M, Breaz RE, Racz SG, Girjob CE (2019) Processing strategies for single point incremental forming—a CAM approach. Int J Adv Manuf Technol 102:1761–1777. https://doi.org/10.1007/s00170-018-03275-9

76. Wang J, Li L, Zhou P, Wang X, Sun S (2019) Improving formability of sheet metals in incremental forming by equal diameter spiral tool path. Int J Adv Manuf Technol 101:225–234. https://doi.org/10.1007/s00170-018-2911-z

77. Behera AK, Lauwers B, Duflou JR (2014) Tool path generation framework for accurate manufacture of complex 3D sheet metal parts using single point incremental forming. Comput Ind 65:563–584. https://doi.org/10.1016/j.compind.2014.01.002

78. Sbayti M, Bahloul R, Belhadjsalah H (2018) Numerical modeling of hot incremental forming process for biomedical application. Lect Notes Mech Eng 881–891. https://doi.org/10.1007/978-3-319-66697-6_86

79. Sbayti M, Ghiotti A, Bahloul R, BelhadjSalah H, Bruschi S (2022) Effective strategies of metamodeling and optimization of hot incremental sheet forming process of Ti6Al4Vartificial hip joint component. J Comput Sci 60:101595. https://doi.org/10.1016/j.jocs.2022.101595

80. Araujo R, Teixeira P, Montanari L, Reis A, Silva MB, Martins PA (2014) Single point incremental forming of a facial implant. Prosthet Orthot Int 38:369–378. https://doi.org/10.1177/0309364613502071

81. Palumbo G, Ambrogio G, Crovace A, Piccininni A, Cusanno A, Guglielmi P et al (2022) A structured approach for the design and manufacturing of titanium cranial prostheses via sheet metal forming. Metals (Basel) 12. https://doi.org/10.3390/met12020293

82. Catalano G, Demir AG, Furlan V, Previtali B (2018) Prototyping of biodegradable flat stents in pure zinc by laser microcutting and chemical etching. J Micromechanics Microengineering 28:095016. https://doi.org/10.1088/1361-6439/aac83d

83. Catalano G, Demir AG, Furlan V, Previtali B (2017) Laser microcutting of sheet metal for prototyping expandable stent-like structures in permanent and biodegradable alloys. In: RTSI 2017—international forum on research and technologies for society and industry. https://doi.org/10.1109/RTSI.2017.8065982.

84. Quazi MM, Ishak M, Fazal MA, Arslan A, Rubaiee S, Qaban A et al (2020) Current research and development status of dissimilar materials laser welding of titanium and its alloys. Opt Laser Technol 126:106090. https://doi.org/10.1016/j.optlastec.2020.106090

85. Biffi CA, Casati R, Tuissi A (2015) Laser shape setting of thin NiTi wires. Smart Mater Struct 25. https://doi.org/10.1088/0964-1726/25/1/01LT02

86. Biffi CA, Coduri M, Tuissi A (2020) On the microstructure and superelastic evolution of laser annealed thin NiTinol wires. Smart Mater Struct 29. https://doi.org/10.1088/1361-665X/aba6cf

87. Menci G, Demir AG, Waugh DG, Lawrence J, Previtali B (2019) Laser surface texturing of β-Ti alloy for orthopaedics: effect of different wavelengths and pulse durations. Appl Surf Sci 489:175–186. https://doi.org/10.1016/j.apsusc.2019.05.111

88. Purnama A, Furlan V, Dessi D, Demir AG, Tolouei R, Paternoster C et al (2018) Laser surface texturing of SS316L for enhanced adhesion of HUVECs. Surf Eng 1–10. https://doi.org/10.1080/02670844.2018.1495408

89. Demir AG, Taketa TB, Tolouei R, Furlan V, Paternoster C, Beppu MM et al (2015) Laser surface structuring affects polymer deposition, coating homogeneity, and degradation rate of Mg alloys. Mater Lett 160:359–362. https://doi.org/10.1016/j.matlet.2015.07.159

90. Furlan V, Biondi M, Demir AG, Previtali B, Pariani G, Bianco A (2018) Two-beam interference patterning of biodegradable magnesium alloy: Influence of number of passes and spots overlap. J Vac Sci Technol B Nanotechnol Microelectron 36. https://doi.org/10.1116/1.4996504

91. Soldera M, Fortuna F, Teutoburg-Weiss S, Milles S, Taretto K, Lasag AF (2020) Comparison of structural colors achieved by laser-induced periodic surface structures and direct laser interference patterning. J Laser Micro Nanoeng 15:97–103. https://doi.org/10.2961/jlmn.2020.02.2004

92. Nüsser C, Wehrmann I, Willenborg E (2011) Influence of intensity distribution and pulse duration on laser micro polishing. Phys Procedia 12:462–471. https://doi.org/10.1016/j.phpro.2011.03.057

93. De Giorgi C, Furlan V, Demir AG, Tallarita E, Candiani G, Previtali B (2017) Laser micropolishing of AISI 304 stainless steel surfaces for cleanability and bacteria removal capability. Appl Surf Sci 406:199–211. https://doi.org/10.1016/j.apsusc.2017.02.083

94. Khafaji NY, Demir AG, Vitali L, Fustinoni D, Niro A, Previtali B et al (2017) Optical characterization of laser coloured titanium under different processing atmospheres. Surf Coatings Technol 321:156–163. https://doi.org/10.1016/j.surfcoat.2017.04.043

95. Furlan V, Demir AG, Previtali B (2015) Micro and sub-micron surface structuring of AZ31 by laser re-melting and dimpling. Opt Laser Technol 75:164–172. https://doi.org/10.1016/j.optlastec.2015.06.030

96. Furlan V, Biondi M, Demir AG, Pariani G, Previtali B, Bianco A. Sub-micrometric surface texturing of AZ31 Mg-alloy through two-beam direct laser interference patterning with a ns-pulsed green fiber laser. Appl Surf Sci 2017;423. https://doi.org/10.1016/j.apsusc.2017.06.138.

97. De Giorgi C, Furlan V, Demir AG, Tallarita E, Candiani G, Previtali B (2017) Laser micropolishing of AISI 304 stainless steel surfaces for cleanability and bacteria removal capability. Appl Surf Sci 406. https://doi.org/10.1016/j.apsusc.2017.02.083

98. ISO/TC 168 Prosthetics and orthotics (2016) ISO 10328:2016—Structural testing of lower-limb prostheses—Requirements and test methods

99. Zong Z, Lee HP, Lu C (2006) A three-dimensional human head finite element model and power flow in a human head subject to impact loading. J Biomech 39:284–292. https://doi.org/10.1016/j.jbiomech.2004.11.015

100. Mainwaring L, Ferdinand Pennock KM, Mylabathula S, Alavie BZ (2018) Subconcussive head impacts in sport: a systematic review of the evidence. Int J Psychophysiol 132:39–54. https://doi.org/10.1016/j.ijpsycho.2018.01.007

101. Wright AD, Laing AC (2012) The influence of headform orientation and flooring systems on impact dynamics during simulated fall-related head impacts. Med Eng Phys 34:1071–1078. https://doi.org/10.1016/j.medengphy.2011.11.012

102. Fahlstedt M, Baeck K, Halldin P, Van Der Sloten J, Goffin J, Depreitere B et al (2012) Influence of impact velocity and angle in a detailed reconstruction of a bicycle accident. IRCOBI Conf Proc Int Res Counc Biomech Inj 2012:787–799

103. Mohotti D, Fernando PLN, Zaghloul A (2018) Evaluation of possible head injuries ensuing a cricket ball impact. Comput Methods Programs Biomed 158:193–205. https://doi.org/10.1016/J.CMPB.2018.02.017

104. Ambrogio G, Palumbo G, Sgambitterra E, Guglielmi P, Piccininni A, De Napoli L et al (2018) Experimental investigation of the mechanical performances of titanium cranial prostheses manufactured by super plastic forming and single-point incremental forming. Int J Adv Manuf Technol 98:1489–1503. https://doi.org/10.1007/s00170-018-2338-6

105. Palumbo G, Piccininni A, Ambrogio G, Sgambitterra E (2020) Design of custom cranial prostheses combining manufacturing and drop test finite element simulations. Int J Adv Manuf Technol. https://doi.org/10.1007/s00170-020-06213-w

Challenges and Opportunities for Laser Applications in Electric Vehicle Manufacturing

Ali Gökhan Demir, Johannes Kriegler, Alessandro Fortunato, Leonardo Caprio, Christian Geiger, Lucas Hille, Michael Karl Kick, Alessandro Ascari, Erica Liverani, and Michael F. Zaeh

Abstract The ever-growing demand for electric vehicles in the world and Europe will result in a significant socio-economical change. The electrification changes the material types, usage, manufacturing, and vehicle design. The contemporary electric drives are being used in various vehicles, such as automobiles, drones, trains, airplanes, and ships. These vehicles will require a lower weight, an extended maximum range, and faster recharging as the number of vehicles in use increases.

A. G. Demir (✉) · L. Caprio
Dipartimento di Meccanica, Politecnico di Milano, Via Privata Giuseppe La Masa, 1, 20156 Milano, MI, Italy
e-mail: aligokhan.demir@polimi.it

L. Caprio
e-mail: leonardo.caprio@polimi.it

J. Kriegler · L. Hille · M. K. Kick · M. F. Zaeh
Technical University of Munich, Munich, Germany
e-mail: johannes.kriegler@iwb.tum.de

L. Hille
e-mail: lucas.hille@iwb.tum.de

M. K. Kick
e-mail: michael.kick@iwb.tum.de

M. F. Zaeh
e-mail: michael.zaeh@iwb.mw.tum.de

C. Geiger
TUM School of Engineering and Design, Department of Mechanical Engineering, Technical University of Munich, Munich, Germany
e-mail: christian.geiger@iwb.tum.de

J. Kriegler · C. Geiger · L. Hille · M. K. Kick · M. F. Zaeh
TUM School of Engineering and Design, Department of Mechanical Engineering, Institute for Machine Tools and Industrial Management (iwb), Boltzmannstrasse 15, 85748 Garching, Germany

A. Fortunato · A. Ascari · E. Liverani
Dipartimento di Ingegneria Industriale, Università Degli Studi di Bologna, Bologna, Italy
e-mail: alessandro.fortunato@unibo.it

Compared to vehicles powered with combustion engines, fewer components will be placed with increased demand in flexible welding, heat treatment, cutting, trimming, and texturing applications. The need for rapid changes in the vehicle models and the variety of components will be resolved through highly digitalized, flexible, adaptable, and reliable manufacturing processes. From this point of view, laser-based manufacturing is an essential solution, placing this family of processes as the conventional method in electric vehicle manufacturing. Today, lasers are used in various applications, such as hairpin stripping and welding, cutting and texturing of Lithium-ion electrodes, welding of battery busbars, and cutting of composite materials. The rapid reduction of the costs of laser sources, optics, and components in the last decade facilitated the adoption of laser systems in electric vehicle manufacturing. Although laser technology has reached the required maturity, the system developers and the end-users still need to catch up with the pace of the growing demand in electric vehicle manufacturing. This white paper highlights the challenges and opportunities regarding the main laser-based manufacturing processes for electric vehicle production.

1 Introduction

Owing to the direct correlation between fuel consumption and the amount of CO_2 and other greenhouse gas emissions directly linked with the climate change phenomenon, the automotive industry has been focusing on alternative drivetrains [1]. In order to reach this goal, a significantly increased share of electric vehicles (EVs) and hybrid-electric vehicles (HEVs) is required. As a matter of fact, by 2025, one in every four new cars worldwide will have an electricfied powertrain. By as early as 2030, one in every two new vehicles worldwide is foreseen to be electrically propelled. It is forecasted that by 2040 the e-mobility will see a climax with up to 54% of car sales and 33% of the global car fleet being electric [2]. However, changing over to electromobility (e-mobility) signifies a radical transformation of production technology. The increasing dynamic in the electrification of vehicles and drive technology will require flexible manufacturing processes able to adapt to the new models to produce reliable and affordable electric vehicles in large volumes.

The fast-growing market of electric vehicles (EVs) comprises hybrid electric vehicles (HEVs), plug-in hybrid electric vehicles (PHEVs), and full electric vehicles (full-EVs). While automotive leads the global change over the electrification in mobility, several other vehicle types, such as air taxis, drones, trains, motorcycles,

E. Liverani
e-mail: a.ascari@unibo.it

and ships, must be produced using novel manufacturing solutions. Several established vehicle manufacturers and new brands are facing similar difficulties related to the lack of experience in the manufacturing technologies to be adopted [3].

In particular, introducing new key components into automotive mass production leads to fundamental changes in the established supply chain. It must be considered that these new challenges, required to be in pace with the ongoing revolution, overburden the known great efforts necessary in the automotive business in terms of speed and competitiveness. The individual mobility concepts of the near future will be a combination of progressively smaller internal combustion engines and electric drives [4]. Figure 1 shows the global electric automobile manufacturing sites and the related brands. Figure 2 illustrates the laser source manufacturers around the globe. The similar global distribution of electric car and laser source manufacturers also exhibits that the automotive industry is amongst the main users of industrial laser sources. While the availability of laser systems increases and the costs per power unit are reduced, the integration of laser sources in automotive and other vehicle manufacturing industries broadens. As a matter of fact, the novel electric vehicles have fewer components in the traction system with more assemblies by welding, an increased number of material thicknesses (0.01–5 mm), and types (Cu-, Al-, Mg-alloys, steel, and composite materials) recalling flexible and digital manufacturing tools. In a conventional power train of a car powered by an internal combustion engine, the number of weld seams surpasses 30 with a total weld length of 0.1 m. In comparison, in an electric power train, the total number of welds can exceed 1200 with a total length up to 20 m [5]. Accordingly, several parts in traction and battery systems are designed and developed with laser-based manufacturing processes in mind. For instance, the total weld length produced by laser beam welding on the BMW iX body and power train exceeds 50 m [6].

Fig. 1 Global distribution and residence of hybrid electric/electric car manufacturers

Fig. 2 Global distribution of the industrial laser source and component manufacturers

While the global demand for electric vehicles increases so does the demand for laser systems in manufacturing along with the technological know-how. Laser-based manufacturing finds itself in the heart of the fast-growing electromobility sector, where process knowledge and trained personnel can become an enabler or a bottle-neck. The need for a collaborative network for e-mobility manufacturing in Europe and worldwide becomes evident from this perspective. The LaserEMobility section of AITeM—Italian Manufacturing Association was formed to fulfill this knowledge gap as an international collaborative group. The present document aims to overview laser-based manufacturing processes used in some of the most important EV components, underlining challenges and opportunities. The document collates wide laser-based manufacturing literature providing insights into how the laser-material interaction can be manipulated for novel manufacturing needs, as well as reporting the most recent works from academia and industry. Finally, the white paper proposes open questions, which were found to be relevant through a panel of experts during the LaserEMobility Workshop 2022 held in Bologna, Italy between 10th and 11th March 2022.

2 Laser-Based Manufacturing in Electric Vehicles Production

2.1 Laser systems as Digital Manufacturing Tools

Laser radiation provides different material interaction mechanisms that can transform and transport material for industrial manufacturing means. Such mechanisms can be manipulated to heat, melt, evaporate, or ablate the material. Different processes can be achieved with the correct choice of laser wavelength and by controlling the temporal and spatial behavior of the laser emission. Laser-based manufacturing processes,

such as welding, cutting, heat treatments, and ablation-based material removal, has been long applied, especially in the automotive industry. Conventionally, laser-based manufacturing processes have been used to improve the quality and productivity of state-of-the-art production chains. In electric vehicle production, several components are designed with laser-based manufacturing processes as the main tool. The laser component manufacturers provide a wide palette with various wavelengths, power, and beam quality ranges highly exploitable in electric vehicle manufacturing. As a matter of fact, the rise of electrification in the mobility industry comes at a moment of maturity for the industrial laser industry. The solid-state high brilliance fiber and disc lasers have proven to be the stable workhorse for many industrial applications. Diode and CO_2 laser systems have improved stability and power ranges, while Nd:YAG laser sources have reliable applications, especially in ablation-based applications.

An EV, compared to a vehicle with an internal combustion engine, has fewer parts, more welded joints, and a wider use of different metals and non-metal materials together. The fast-changing vehicle designs require a rapid adaptation of the manufacturing methods. Hence, using a laser-based manufacturing tool to join, separate, or modify the components of an electric vehicle is a perfect match. The laser industry provides several options for more flexible manipulation of the digital tool for previously unused wavelengths and beam shapes. The main advantages of applying contemporary laser sources for manufacturing in the e-mobility sector are summarized in the following:

- Material variety: Laser wavelengths, power ranges, and beam sizes can be opportunely selected to process some of the most widely used metallic and polymeric materials as well as their combinations in electric vehicles (e.g., copper, aluminium, steel, PMMA, or PEEK). Through temporal and spatial beam manipulation, non-linear absorption mechanisms can be exploited to process materials that are transparent or reflective to the laser wavelength.
- Robustness and reliability: Contemporary laser sources maintain their power levels and beam quality in very tight ranges throughout their lifetime. Most of the laser sources and beam deflection units are equipped with sensors able to carry out self-diagnostics, signaling issues in the event of their occurrence. Such features enhance the precision and the repeatability of the processes.
- Adaptability: The laser sources are often coupled to beam deflection units, cartesian axes, or robots. All combinations provide a quick adaptation to new forms, geometries, and materials to be processed.
- Addressability: The contemporary laser sources are optoelectronic devices that are rapidly controlled via electronic signals synchronizing laser emission and beam motion. The fast addressability of the lasers allows manipulating the process parameters on the same component to be produced.
- Compactness and efficiency: Contemporary laser sources have a small footprint allowing them to be integrated to the system of a station within the production line easily. The solid-state laser sources provide energy conversion efficiencies toward 50% rendering these solutions more eco-friendly.

- Monitoring and control: The laser manufacturing processes provide direct integration with inline monitoring and control means. Laser systems can be easily synchronized with process monitoring sensors by embedding them in a digital platform, and feedback control schemes can be opportunely developed. All of the mentioned advantages of contemporary lasers also provide more reliable and easier integration of monitoring and control strategies.

2.2 Overview of the Studies on Electric Vehicle Manufacturing

In an EV, several components require the use of laser manufacturing tools. Figure 3 shows some of the main components that are processed by laser-based manufacturing methods. These main components can be categorized most generically as follows:

1. Traction systems that are composed of the electric drive and the transmission components
2. Energy storage systems that are mainly battery modules or fuel cell systems
3. Lightweight structural components that are often made of lightweight alloys or composite materials

While the pull for the laser-based manufacturing methods from the e-vehicle industries increases, the number of academic works around this theme also rises. In order to have a general view of the literature trends, an analysis based on keywords was carried out on the Scopus database. As displayed in Fig. 4, some of the main
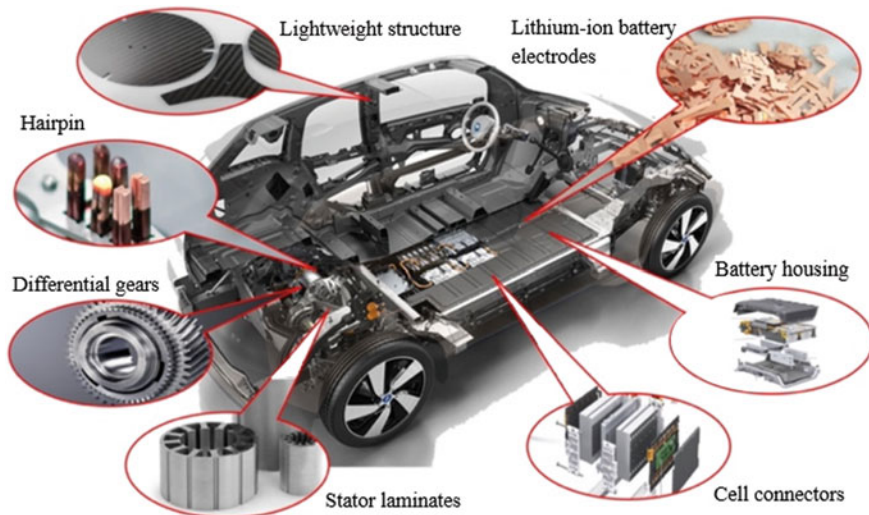

Fig. 3 Overview of components in an electric vehicle where laser-based manufacturing processes are established

keywords regarding e-mobility and their combination were searched. As a starting point, the "e-mobility" keyword was searched along with its alternatives (electric mobility, e-vehicle, electric vehicle). As shown in Fig. 4, a consistent exponential increase of published works is present since 1990. The largest fraction of these works regards the e-drives, then batteries, followed by fuel cells. The intersection of e-mobility with lasers remains a smaller fraction, where a constant growth is visible after 2002. The interest in manufacturing processes, namely welding, cutting, and ablation, has appeared from 2010 onward. It can be argued that such a rise in the manufacturing works coincides with the wider use of high-brilliance solid-state fiber and disc lasers in the industry as well as the increased demand for EVs. Despite the significant growth, the relatively smaller number of works may also signal the need to improve the knowledge base of laser-based manufacturing in the e-mobility field. Indeed, research communities have long been working on combining laser wavelengths and materials similar to what is used in e-mobility applications. These works provide the theoretical basis for the development of new applications. Moreover, the use of newer laser systems requires benchmarking works that are currently lacking in the literature. In the following sections, some of the key laser-based manufacturing applications are defined, referring to the literature both from the theoretical basis and the novel application perspectives.
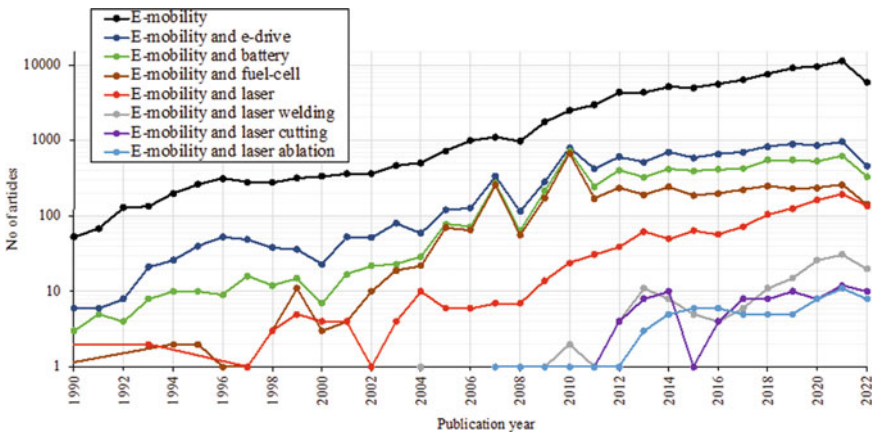
Fig. 4 Overview of published works in literature over the years with respect to the main research themes in laser-based manufacturing for e-mobility; data based on Scopus (last access on 18 July 2022)

2.3 Laser-Based Manufacturing for Lithium-Ion Battery Systems

Battery cells for automotive applications are distinguished by a hierarchical structure presented in Fig. 5 and described below [7, 8]:

- Cell level: The cell is the "basic" part of the battery system, consisting of a prismatic, pouch-encased, or cylindrical geometry. Internally, a series of foils (often made of copper and aluminum) coated with active chemical components make up a cell. These foils are separated from each other by a dielectric separator and submerged in an electrolyte. The battery cathode is made by electrically connecting all aluminum foils, while the anode is formed by joining the copper foils.
- Module level: A module is made up of numerous cells of the same geometry that are connected in series and/or parallel. Although this sub-assembly has a higher
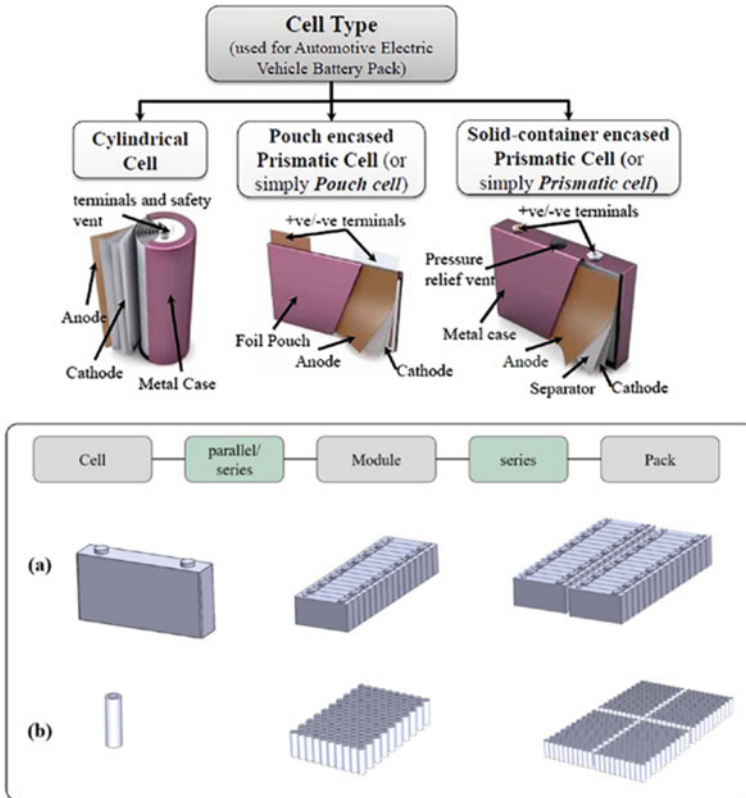
Fig. 5 Cell, module, and pack types in different cell formats used in battery electric vehicles (BEVs) [7, 8]

voltage and capacity than a single cell, it is typically not regarded as the complete battery assembly.

- Pack level: Several modules are connected in series and/or parallel to set the pack's final voltage, capacity, and general shape.

Finally, to enable monitoring and management of all parameters involved in the operating life of the battery, all modules are capsuled in a housing constructed of sheet metal or another material and combined with sensors and controls.

Electrode processing

Cutting: The separation of electrode material is a well-established process in the production chain for lithium-ion batteries [9]. Several process variants exist, depending on the cell format to be produced. For the production of cylindrical cells, e.g., 18,650 cells or 21,700 cells, a slitting process is necessary to generate electrode strips from an electrode coil. These are subsequently winded to produce electrode rolls. For the slitting process, mainly mechanical roll knives are used. For prismatic cells, notching is the most common process, which is the shaping of the current collector foil to create current collector flags. After flat-winding the electrode strips, these current collector flags are welded to obtain an electrical connection between the electrodes. A complete contour cut along the electrode circumference is necessary if a cell stack for pouch cells shall be fabricated from discrete electrodes. Among the presented process variants, this is the most challenging as a tri-layer of a current collector in between two electrode coatings needs to be processed. Usually, aluminum and copper current collector foils with thicknesses between 6 and 16 µm are used for the cathode and the anode, respectively. The coating thicknesses range between 40 and 120 µm depending on the chosen cell design. Laser cutting is an alternative to mechanical cutting processes, fine blanking, for instance, which has gained more interest in the last years and is increasingly becoming the industrial standard for notching and contour cutting [10–12]. The advantages of laser cutting are the geometric flexibility and the non-contact working principle, which prevents tool wear. A challenge is the relatively high investment costs, which require carefully selecting the system components, including the laser sources, the scanning unit, and the sensor systems. Furthermore, high cutting speeds of more than 1 ms^{-1} are required to compete with fine blanking, where the processing speed is independent of the electrode circumference. Additionally, the quality of the cut edge must be maintained when scaling the process. Important quality characteristics are the heat-affected zone (HAZ) around the cutting kerf, particle and spatter contamination, as well as burr formation [13]. Figure 6 illustrates the most important quality criteria for laser cutting of electrodes using a graphite anode scheme.

Commonly, infrared nanosecond-pulsed laser sources with average powers of more than 200 W are used for the laser separation of electrodes in industrial cell production. These laser sources show the advantages of a comparably low heat impact, competitive cutting speeds, and reasonable cost. In academia, continuous wave [13–15] and ultrashort-pulsed [13, 16, 17] laser sources have also been tested. While ultrashort-pulsed laser processes do not allow high cutting speeds, continuous

Fig. 6 Schematic representation of quality criteria concerning laser cutting of electrodes; particles (**a**), spatters (**b**), burrs (**c**), clearance width w_c (**d**), chamfer width (**e**), unequal ablation of the upper and the lower layer (**f**), heat-affected zone (HAZ) (**g**) [13]
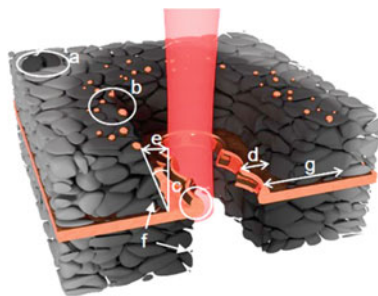
wave and short-pulsed lasers have been shown to fulfill the throughput requirements with cutting velocities of up to $10\,\text{ms}^{-1}$ [13–15]. Thereby, a multi-pass strategy based on ablation cutting by subsequent scan cycles can result in an improved cutting quality [13, 14]. Different approaches address the insufficient cutting speeds, while maintaining the high quality of the cut-edge resulting from the utilization of ultrashort laser pulses. Recently, the potential of megahertz pulse bursts of ultrashort laser pulses was shown [16]. Another rather new approach is an interference pattern by the superposition of two laser beams. Baumann et al. have shown that the resulting higher peak intensity contributes to a faster cutting process [14]. Despite the low absorptivity of the metallic substrate foils [15], usually, infrared laser radiation is employed. Ultraviolet [18] and green laser radiation [19] were investigated but have not yet been established in industrial production due to the higher costs and the lower average powers.

Analytical models have been developed to better understand the underlying process mechanisms and to faster identify suitable process parameters [20–24]. These models include physical phenomena, such as fluid flow, heat transfer, recoil pressure, multiple reflections, capillary and thermo-capillary forces, and phase changes, to investigate the melt pool flow, the geometry, and the temperature distribution on the workpiece [22]. Due to the high variability in the applied electrode coatings, e.g., in the material composition, the porosity, and the coating thickness, the experimental effort when introducing a new electrode system in production can be reduced using such computational models.

The electrode cut edge was proven to influence battery quality and performance. On the one hand, burrs on the cut-edge and particles are suspected of punctuating the separator and causing electrical short-circuits, followed by highly safety-critical thermal runaways of the battery. On the other hand, it was also concluded that an insufficient cut-edge quality negatively influences the electrochemical functionality of lithium-ion batteries, by accelerating capacity fading over the cell lifetime, for instance [25]. Carbonari et al. demonstrated that electrochemical impedance spectroscopy is a feasible method to determine the cut edge quality via the cell-internal resistance [26]. In general, despite the mentioned studies, there remains a research gap in the literature concerning the impact of the cut edge quality on cell functionality.

Future trends will be the utilization of high-power ultrashort-pulsed laser systems. Furthermore, material-specific cutting strategies need to be developed considering
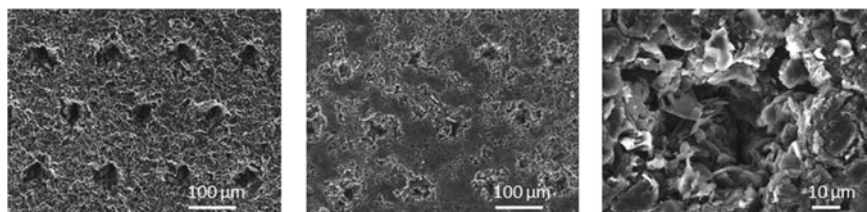
Fig. 7 Schematic scanning electron microscopy images of structured graphite anodes at magnifications of (**d**) 100, (**e**) 220, and (**f**) 1000; the structures were arranged in a hexagonal pattern with a center distance of 120 μm [30]

upcoming trends from battery production, such as the application of silicon-blended graphite anodes and nickel-rich cathodes, e.g., NMC811, as well as the tendency to high coating layer thicknesses. Furthermore, the transfer of cutting processes on new battery technologies, such as all-solid-state batteries, which also require an adapted process chain, move into the spotlight. The usage of lithium metal anodes is one of the dominating trends necessitating the development of adapted cutting processes [27, 28].

Structuring: A central drawback of current lithium-ion batteries is their limited fast-charging and discharging capability. This issue results from diffusion limitations in a battery cell caused by the porous structures of typical battery electrodes. A promising approach to overcome this drawback is the introduction of microscopic diffusion channels into the electrode coatings using pulsed laser radiation. Especially (ultra-)short-pulsed laser radiation is a versatile tool for creating drillings with micrometer precision at low heat input [29] (see Fig. 7).

Laser structuring of battery electrodes results in an improved fast-charging ability and reduced lithium plating [31] due to the reduction of cell-internal overpotentials [32, 33]. Furthermore, significant lifetime improvements were observed in large-format lithium-ion batteries with laser-structured electrodes [30, 34]. Since graphite anodes typically show higher diffusion limitations than most cathode systems, electrode structuring is especially promising when applied to anodes [35, 36]. Nevertheless, performance enhancements were also reported for lithium-ion batteries containing structured $LiMn_2O_4$ (LMO) [37], $LiCoO_2$ (LCO) [38, 39], $LiNi_xMn_yCo_zO_2$ (NMC) [40–42], and $LiFePO_4$ (LFP) cathodes [43, 44]. The positive effect of electrode structuring on the rate performance is pronounced in thick and highly compressed electrodes [40, 45]. Besides the performance improvements, a facilitated wetting with electrolyte can be achieved through laser structuring of electrodes [46–48].

A central challenge for the industrial application of electrode structuring is increasing the laser processing rate to match the web speeds in roll-to-roll electrode production. Possible approaches include beam-splitting techniques using diffractive optical elements (DOEs) or polygon scanning units [49, 50]. Furthermore, the interdependencies between laser structuring and adjacent processes need to be better
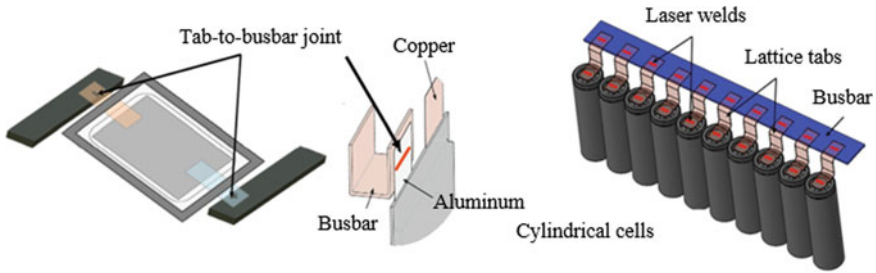
Fig. 8 Example of tab-to-busbar welding for pouch and cylindrical cells [55]

understood, and concepts for integrating laser structuring into the existing process chain of battery production need to be developed.

Battery welding

There are various welding/joining requirements for the three levels of battery systems. As a result of a literature analysis, wire bonding, resistance spot welding, ultrasonic welding, and laser beam welding (LBW) are the most used welding technologies. However, LBW is probably the most promising among these technologies thanks to the advantages of producing a small, precisely targeted deformation, and a confined heat-affected zone [51]. Moreover, LBW has been shown to have the lowest electrical contact resistances and maximum joint strengths compared to the other welding techniques for manufacturing electric vehicle battery packs [51]. Finally, all cell formats of lithium-ion batteries can be welded with lasers [7], which has the maximum flexibility in terms of geometries and configurations that can be assembled (c.f. Figure 8).

However, laser beam welding is typically limited by a low metallurgical affinity between incompatible materials, which can result in significant weaknesses, such as the creation of detrimental intermetallic phases and crack sensitivity. According to studies to date, an optimization of the welding process parameters could enhance joint performance but must take into consideration not only the materials to be welded but also the welding configuration (e.g., butt welding, overlap welding, etc.). Novel laser technologies have also advanced, leading to an increased absorptivity on highly reflective surfaces of metals, such as copper or aluminum, using green and blue lasers [5, 6]. The last generation of lasers with beam-shaping capability establish a more stable keyhole, producing a more controllable penetration depth joint with fewer defects [52].

A weak joint cannot endure challenging driving conditions, dynamic loading, vibrations, and potential crash and may even cause a fire due to short-circuiting. Therefore welding must adhere to a few fundamental requirements:

- Mechanical: Joints need to have high mechanical strength and tightness together with high fatigue resistance and low residual stress. These qualities must be consistent from joint to joint and stable over time.

- Electrical: In order to ensure minimal heat generation and dissipation during the battery's operational life, the joints must possess a very good electrical conductivity.
- Thermal: Heat input must be carefully managed to prevent damage to the cell or its components by residual strains and distortions.
- Metallurgical: Dissimilar metal welds, mixing aluminum and copper, result in the formation of so-called intermetallic compounds (IMCs) characterized by high hardness, high brittleness, and, in many cases, limited electrical conductivity. IMCs must be contained as low as possible with the help of a carefully controlled heat input, which is beneficial for creating joints with favorable mechanical and electrical properties.

According to the previous requirements, in the following paragraphs, the state-of-the-art of LBW for the three levels will be presented:

Cell level: More than 40 extremely thin aluminium and copper foils [53, 54] with a thickness of 10–20 μm serve as the cathode and the anode current collectors, respectively. The joining is highly difficult because of the low single-foil thicknesses and the differing physical properties of the two metals involved.

Module level: Concerning the module level, depending on the cell format and design choices made by the battery producer, this level is characterized by quite varied connecting scenarios. It is impossible to provide a thorough description of all scenarios; however, some typical setups include [55]:

- Tab-on-tab: The positive and negative poles are formed by thin aluminum and copper tabs (0.3–0.4 mm thick) that protrude from pouch cells. These tabs are joined to one another in a lap joint, and, in some cases, a stack of tabs with three or four tabs instead of only two may be present.
- Tab-on-busbar: Tabs are connected in a similar or different configuration to a thicker (2–4 mm) aluminium or copper alloy connecting plate.
- Tab-on-cylindrical cell: This cell has a copper or aluminum tab welded to the top or bottom of the cell, which, in turn, is frequently made with low-carbon steel.
- Tab- or busbar-on-prismatic cell: In a similar or different configuration, a thin (0.3–0.5 mm) or thick (1–2 mm) sheet is welded to the caps of prismatic cells.

One of the most important issues in fusion welding of copper and aluminum is the formation of brittle intermetallic compounds, which are created at the weld interface and, thus, results in poor mechanical characteristics and crack sensitivity. According to studies, these welds are extremely brittle since the intermetallic thickness is greater than 5 μm. Figure 9 displays the properties of essential IMCs between aluminum and copper [56, 57].

The welds with the highest shear strength and the intermetallic layer with a thickness of 3.2 μm had the lowest electrical resistance. Thicker intermetallic compounds showed an increase in joint electrical resistance. Similar findings, showing a linear rise in contact resistance with intermetallic compound thickness, have been published by Dimatteo et al. [58] (Fig. 10).

Phase	Cu content (at.%)	Structure	Microhardness (HV)	Density (gm/cm^3)	Specific resistance (μocm)
CuAl$_2$	33	Body-centered tetragonal	630	4.34	8
CuAl	51	Body-centered othorhombic	905	51.3	11.4
Cu$_4$Al$_3$	55.5	Moniclinic	930	NA	12.2
Cu$_9$Al$_4$	66	Body-centered cubic	770	6.43	14.2

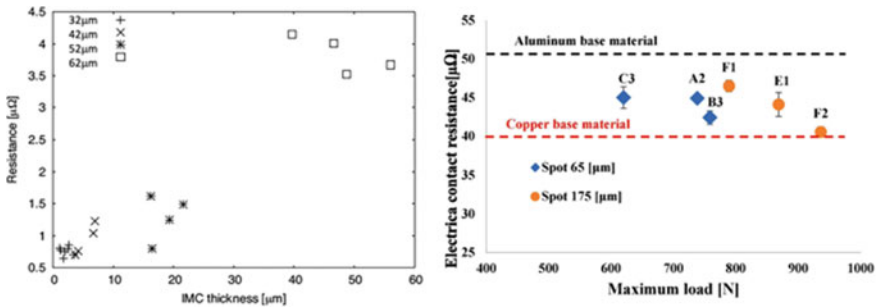**Fig. 9** Copper-aluminum equilibrium intermetallic compounds properties [56, 57]

Fig. 10 Influence of intermetallic compounds (IMCs) on electric resistance [55, 58]

The welding configuration influences the quality of the joint because aluminum usually floats on the copper when used at the top, while copper easily sinks into the aluminum at the bottom. In their study, Lee et al. [56] compared the overlap laser beam welding of copper and aluminum with aluminum at the top and bottom. The IMC AlCu$_2$ of approximately 5 μm thickness formed in the interface region at the top. In contrast, a significant concentration of CuAl$_2$ and Cu$_9$Al$_4$ IMCs were found for aluminum at the bottom, and, for both configurations, the respective sides of the copper solid solution and aluminum solid solution were likewise created. Additionally, the impact of the welding speed on the weld quality was mentioned. For a welding speed of 10 m/min, CuAl$_2$, Cu$_9$Al$_4$, and CuAl IMCs were shown inside the weld zone. However, the formation of IMCs was, inhibited at the faster welding speed of 50 m/min, indicating the significance of process optimization for IMC reductions. Additionally, as the welding speed was increased, the tensile strength also rose, reaching 205 MPa for aluminum at the bottom and 160 MPa for aluminum at the top with a welding speed of 50 m/min. In all samples, the fracture occurred close to the interface of the fusion zone in the intermetallic compound region. In Fig. 11, the composition and the microstructures of a copper-aluminum welding configuration is reported.

The quality as well as the mechanical and electrical properties of welds mainly depend on the heat cycle and, therefore, on the process parameters and strategy used. Moreover, depending on the joint configuration, battery geometries, and module
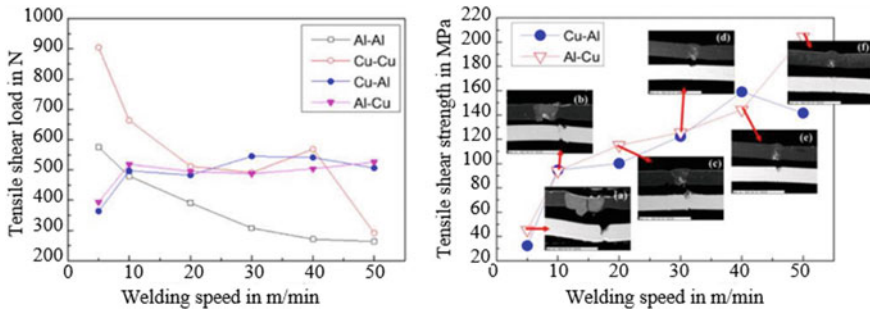
Zone	Concentration (wt% copper)	Phase
1	62.18–64.45	Columnar grain (γ_2-Cu$_9$Al$_4$)
2	45.34–51.95 (white) 30.12 – 41.19 (gray)	Lump (θ-CuAl$_2$) + eutectic (α-Al + θ-CuAl$_2$)
3	30.27–36.61	Eutectic ($\alpha + \theta$)
4	≤ 8.55	Dendrites (α-Al)

Fig. 11 Example of microstructures and chemical composition of phases observed in copper-aluminum laser beam welding [59]

design, there are three typologies of laser power working mode, which are the linear continuous wave (LCW), wobbling continuous wave (WCW) and linear pulsed wave (LPW), whose performance is shown below.

A summary of the performance in LCW, stemming from different authors, is presented in Figs. 12 and 13. They confirm that a reduction of IMCs enhances mechanical properties and, in turn, improves electrical properties.

Wobbling is a more complex process to be optimized due to the involvement of additional process parameters which are mostly interact with each other. However, it has been shown that the wobbling mode allows large joint widths to be obtained and low penetration into the underlying sheet [57], providing good mechanical properties. In Fig. 14, a summary of the performance is provided.

PCW is also used, even if it has lower welding velocity and productivity. Using the latest laser sources, pulses can be designed according to the request of the process. An example is shown in Fig. 15. Finally, in Fig. 16 an example of the temperature measured close to the laser-material interaction zone during welding is given.

Pack level: At the pack level, modules are connected in a variety of methods, but frequently, thick copper or aluminum plates are utilized as connecting components. At this stage, the external enclosure that constitutes the battery's housing is similarly subjected to welding and joining. Lightweight aluminum sheets are frequently used and require hermetical sealing to stop dangerous fume leakage if cells are damaged.
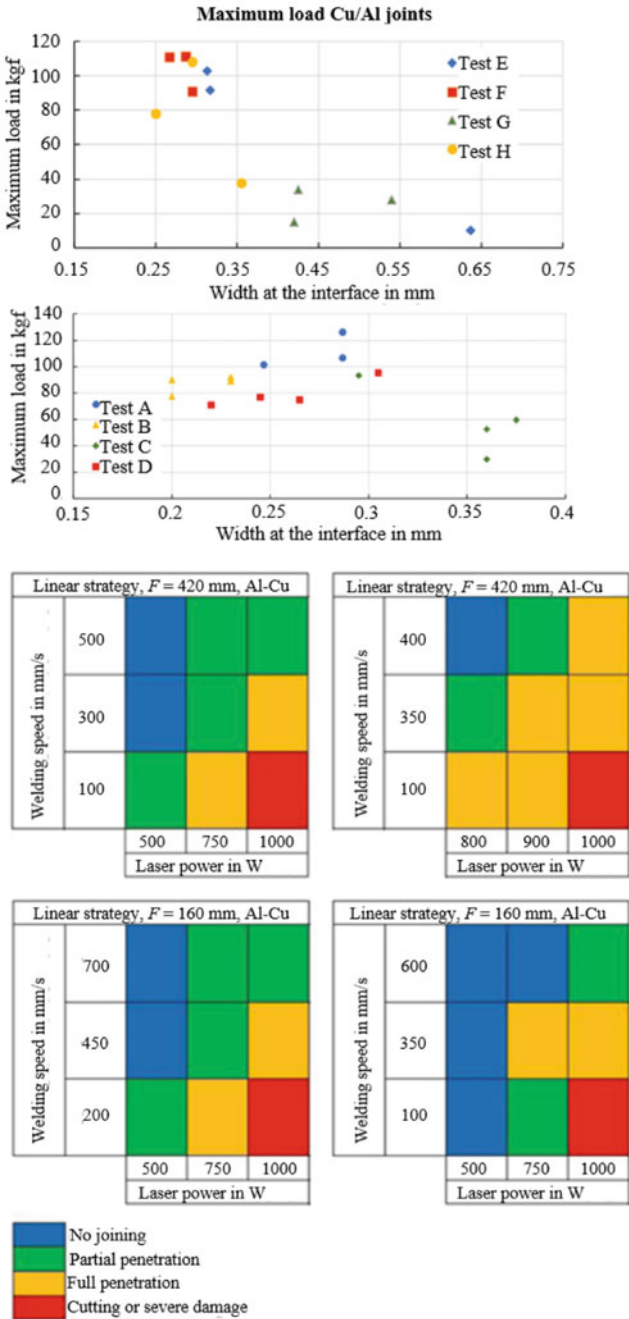
Fig. 12 Mechanical joint strength and process windows for a linear continuous wave (LCW) strategy [60]
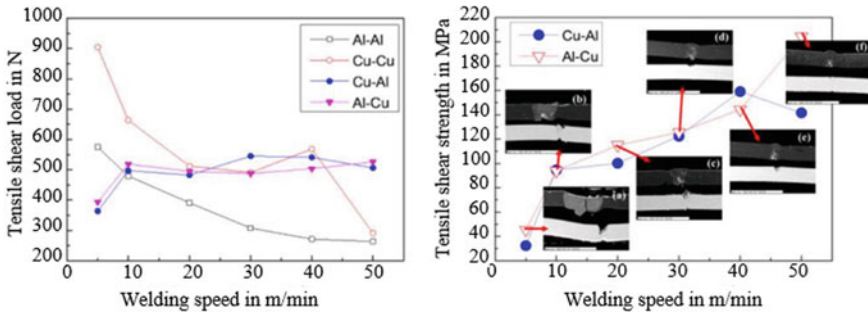
Fig. 13 Mechanical joint strength and process windows for a linear scanning strategy [56]
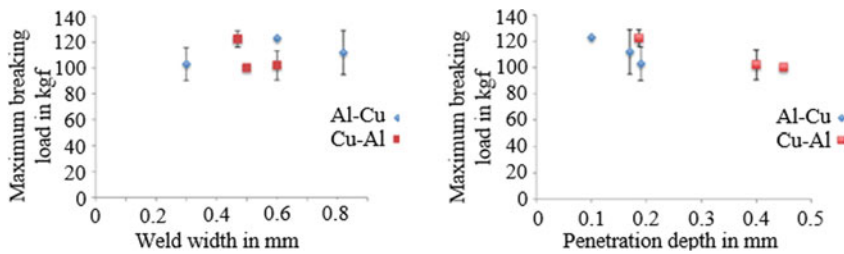
Optimal conditions used for tensile tests.

Configuration	Name	Power (W)	Welding speed (mm/s)	Wobbling amplitude (mm)	Weld width (mm)	Penetration depth (mm)
aluminum-copper	A	600	1566	0.2	0.30	0.19
	B	600	156	0.5	0.60	0.10
	C	800	134	0.7	0.82	0.17
copper-aluminum	D	800	89	0.2	0.50	0.45
	E	900	134	0.5	0.60	0.40
	F	800	134	0.7	0.47	0.187

Fig. 14 Mechanical joint strength for a wobbling scanning strategy [61]

2.4 Laser-Based Manufacturing for Electric Powertrain

Hairpin stripping

The innovative hairpin stator solution promises unique benefits on both the product and process sides but also confronts automotive manufacturers with major challenges. The key for the industrialization of hairpin stators is an effective process development and technology selection. In order to meet the demands and to integrate electric motor production into the value chain, automated solutions with high process stability need to be developed. The technologies necessary for serial production are still partially unknown and need to be selected and optimized considering the final quality conformity of the product. One of them is the stripping of the enameled copper pins in the contacting zone. The identified requirements for the stripping are reproducible
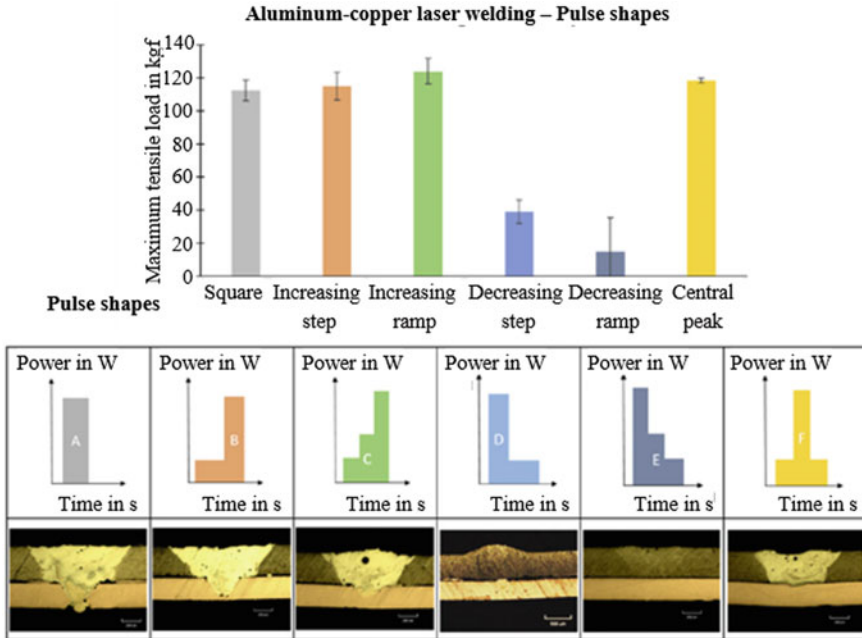
Fig. 15 Seam morphology with E = 13 J and d = 0.32 mm for various pulse shapes: **a** square pulse; **b** increasing step pulse; **c** increasing ramp pulse; **d** decreasing step pulse; **e** decreasing ramp pulse; **f** central peak pulse [62]
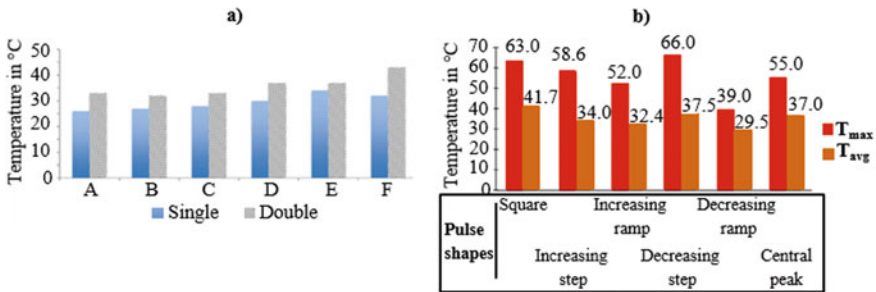
Fig. 16 Temperature in overlap configuration in case of continuous wave (**a**) [60] and pulsed (**b**) [62] laser beam welding

clean surfaces, controllable and accurate removal area, no detrimental effects on the substrate, versatile and precise process, and waste prevention for an environmental-friendly process. Usually, an additional extension of the stripped area is present to prevent heat influences from the weld on the coating of the non-joined hairpin portions (Fig. 17).

Fig. 17 Examples of laser stripped hairpins

Enameled copper wires for the production of windings are mainly insulated with plastics based on polymer hydrocarbons and, therefore, are assigned to organic materials. In addition to good insulating properties, such as high surface resistance, creep resistance, and dielectric strength, these materials feature a high ductility, resulting in good formability and, thus, processability in winding goods. Enamels made of polyurethane, polyetheretherketone, polyimide, polyesterimide, and polyamide-imide can be referred to as common insulation materials. The hairpin insulation is often constituted by combining different of the mentioned materials in layers. Laser stripping induces superior mechanical strength and electrical conductivity, while offering a significant reduction in process time, cost, and a higher flexibility [63]. Aside from the non-contact mode of operation, the advantage of this stripping principle is the small heat input due to the pulsed operation mode of the lasers. For this reason, insulation damage can be prevented in the non-joining areas. A key added benefit is that the radiation removes any oxide layer from the conductor surface, leaving it in the perfect, repeatable state for a more stable and precise contacting process [64]. The first applications and research about laser cleaning processes were characterized by the adoption of excimer UV lasers [65, 66], CO_2 lasers [67], diode lasers [68], and Nd:YAG lasers [69]. Some authors studied the possibility of polymer ablation by emitting at IR wavelengths resonant with the bond fundamental stretching frequencies of polymeric materials [70]. In the stripping process of enameled bar-wound windings, the choice of laser wavelength and process parameters (i.e., laser pulse duration and repetition frequency, spot size, power density, fluence, speed, number of passes, etc.) used to remove the polymer-based insulation from copper are crucial for the stability of the process itself and for the quality of the end result [71, 72]. Firstly, if the wavelength is correctly chosen (strongly absorbed by the insulating material), the laser can vaporize efficiently and effectively. However, the laser beam should not couple strongly with the conductor. Pulsed CO_2 lasers can be used due to the highest reflectivity in copper material and the enhanced absorptivity in organic compounds [73]. The enamel thickness ranges from 20 to 100 μm. It is important to note that the absorption of the light in such films dependents on the film thickness. If the insulating layer reduces to one-fourth of the laser wavelength, then the absorption reduces to a minimum until no further material can be removed. Consequently, when processing the enameled wire with pulsed CO_2 lasers, a thin layer of insulation remains on the conductor (2–3 μm),

sufficient to prevent the subsequent hairpin contacting process [74]. The solution is to change the stripping method by selecting a laser wavelength at which the hairpin coating is largely transparent but absorbed by the substrate, i.e., the antithesis of the previous approach. In this case, a near-infrared pulsed laser with high peak power can release energy at the interface between the coating and substrate. In this way, the insulation is delaminated and ejected at high speed from the hairpin surface due to the creation of a laser-induced plasma at the copper substrate interface, which generates a shock wave able to produce a blank surface [75]. There are also dual IR-based stripping processes, in which a CO_2 laser rapidly vaporizes the majority of the enamel, while the secondary low-power laser ablates the remaining layer. Adopting the same laser system in the subsequent hairpin welding has also been proposed [76]. The interdependencies between process steps have high effects on the later steps in the hairpin process chain and cause error propagations, which lower the stability of the whole manufacturing chain. For example, one error in the welding of hairpins can be traced back to the stripping step. When a high number of pores and air pockets is present, it may be often linked to an insufficient stripping of the material. So, during welding, the not-removed insulation evaporates, impairing the formation of a solid and long-term stable welding joint [77]. In order to check if the organic insulating material is removed reproducibly, a fluorescence measurement is usually executed. The stripping sample body is excited by UV radiation, and the remaining residuals are detected since they are correlated to the fluorescence measured [2]. Another key imperative in the stripping process is that no copper removal or conductor deformation should occur in order to preclude reductions in the conducting cross-section. Pulse overlap must be carefully controlled since high values can lead to an excessive increase in copper substrate temperature, up to surface melting [78]. Furthermore, it must be avoided that the insulation of the conductor outside the stripped area gets damaged or detached and that insulation residues could fall into the winding.

In literature, the removal of the insulating layer from Cu-ETP hairpins is performed with an IR disk laser at 1030 nm with programmable focusing optics, also used for the subsequent contacting process (given that the power output ranged from 160 to 8000 W) [79]. In this case, the PEI insulation is removed by first burning significant parts of the insulation before blasting of residues. The ends of the hairpins are stripped by scanning the laser beam in pulsed mode over the workpiece several times. At first, the insulation is burned with a flame, as the conductor and the insulated material are heated up by the laser. After most of the insulation is removed, the laser radiation is absorbed by the base material. Caused by an abrupt thermal expansion of the conductor, the remaining insulation and combustion residues are blasted off the copper substrate.

Another solution is to use a pulsed IR diode laser for the de-coating of the joining area of the enameled hairpins. In order to meet the series production requirement, there were reported ablation rates in the range of 142–280 mm^3/s [80]. The stripping performance was also analyzed and could be optimized with high powers, reduced feed rates, and reduced fill spaces. The analyses showed that high removal rates could be achieved by CO_2 laser, leaving enamel on the surface. These remains could be removed by a fiber laser in a two-step procedure resulting in low residuals and

mean variations of the process. Then, an optical analysis illustrated that the disk laser generated a distinct structuring of the copper surface and a pronounced transitional area, while the CO_2 and fiber lasers created sharp-edged interfaces. The conclusion was that the most reproducible stripping results with low residues could be achieved with the double IR procedure (CO_2 laser first, fiber radiation after).

Hairpin welding

The process step of contacting is regarded as one of the major challenges in manufacturing hairpin windings. In addition to the high number of contacts, the frequent appearance of faults resulting in high scrap costs needs to be mentioned. Even for contacts that are not classified as defective, an increased contact resistance may cause growing copper losses heating the winding. Large connection cross-sections must be realized and resistances caused by impurity layers must be avoided. In addition, only little space is available in the winding head for the execution of the contacting operation, restricting accessibility. From a wider point of view, the contacting process is the point of interest of many automotive companies because all the previous errors and deviations in the hairpin manufacturing chain, such as the misalignment of the pins, need to be compensated by a winning welding strategy [2]. The laser technology shows potential to realize this joining task as it is an automated and contactless joining process featuring high processing speeds and good process stabilities [81]. Since the failure of one contact point already leads to the loss of function of the electric drive, the contacting operation is a crucial process. One of the main technical challenges concerning this manufacturing step is the high number of contacts that has to be created in a short processing time with high reliability. Apart from long-term stability, it is fundamental that the joints feature large cross sections due to the high currents that flow in the winding of automotive traction drives, which means that reduced conductive cross-sections result in additional undesired ohmic losses, increasing the temperature of the winding. Besides, joining copper material features a strong tendency to spatter formation due to its high thermal conductivity and low viscosity [82]. Moreover, it is necessary to avoid thermal insulation damages outside the skinned area resulting from melt pool ejections or excessive thermal input since this would cause short circuits [83].

Pure copper has always posed high barriers to laser beam welding, especially in the infrared range wavelength [84]. In addition, different from its alloys, pure copper has a melting and boiling point instead of a range. This leads to abrupt liquefaction and vaporization, which obstacle the welding process and may lead to welding defects. One of the recent and widespread introduced techniques is represented by beam wobbling. By moving the beam quickly and repeatedly over the part, the hairpin is first preheated in a controlled manner instead of discharging all the power at once. It enlarges the beam area effectively without reducing the fluence, which stabilizes the melt pool, reducing spatter, defects, and weld porosity compared to traditional welding methods [85, 86] (Fig. 18).

Local power modulation and temporal power modulation techniques applied to hairpin welding were studied by Glaessel et al. [76]. One of the most critical aspects was the effect of the deviations of the contacting process on the electrical resistance of

Fig. 18 Laser welded hairpin windings mounted in an e-drive stator (image courtesy of IMA Automation Atop)

the hairpin connections. It was demonstrated that the presence of pores, the condition of the surface, and the size of the melt pool could result in scattering electrical properties of the joints, as the cross-section of the connection was subjected to deviations due to these instabilities.

Despite several choices in laser beam welding technology, the fundamental studies concerning the laser beam welding of copper hairpins and the influence of the laser processing conditions are lacking in literature. Glaessel et al. studied [87] laser beam welding of copper hairpins with an 8 kW disk laser source and a 255 μm spot size using a linear trajectory. The authors proposed the initial relationships between seam size as well as electrical and mechanical properties. Di Matteo et al. studied laser beam welding of copper hairpins with a 3 kW fiber laser source and a 68 μm spot size using a linear scan strategy with multiple repetitions [88]. The authors showed how defects form related to insufficient and excessive energy input into the seam.

Using novel wavelengths for welding Cu is an emerging topic in literature. The green and blue wavelengths improve absorptivity, while the availability of these laser sources is still scarce. Applying the second harmonic of a high-power disc laser to generate the green wavelength for welding Cu has been reported in the literature [89, 90]. Concerning blue lasers, recent solutions indicate diode lasers with power levels up to 3 kW with 400 μm fiber diameter [91] or 400 W with 50 μm fiber diameter [92]. Wavelength combinations (NIR + visible) with industrial solid-state lasers [93–95] are other possibilities that require fundamental studies.

Stator welding

In an electric drive the stator and rotor stacks are made of thin electrical steel sheets to reduce eddy currents. Most commonly, silicon steel sheets are punched to the desired shape and then joined to form the final stators. An example of this material can be the M330-35, which is also a code for identifying the geometry of the plates. Generally, the sheet thickness varies typically between 0.2 and 0.5 mm [96, 97]. It is well established that each cutting technique affects the properties of the cut zone differently. The most spread technique for sheet separation is punching, while
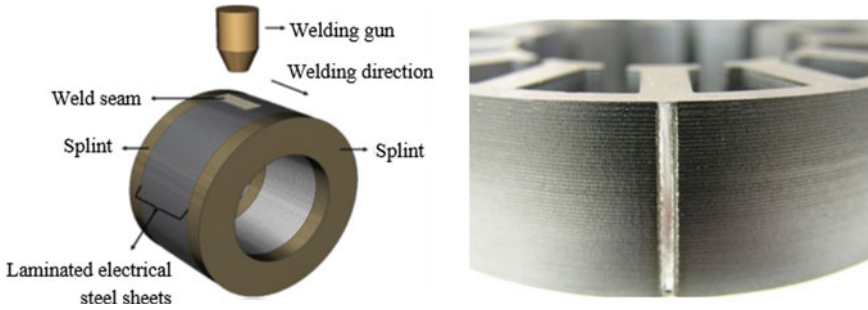
Fig. 19 Schematic description of laser stator welding. Weld gun in the picture gives the impression it is gas metal arc welding which is used [104]

laser cutting has also been explored [96]. After having stacked the several laminates (a common electrical motor contains about 1600 single sheets with a thickness of 0.35 mm [98]), there is the need to weld all the plates together (see Fig. 19). A possible joining process is laser beam welding. Nevertheless, the welded seam geometry influences the magnetic loss during the operation of the motor [99]. The smaller the depth of the seam, the less the magnetic loss. Next to conventional welding, the laser technique is an alternative technology to fix the laminated structure [100]. In this case, the problem obtaining a relatively thin welded zone to achieve a HAZ that does not influence the electromagnetic properties of the stator laminates. Pulsed wave welding and temporal beam modulation strategies provide reduced heat input and better geometrical control over the process [101]. Fiber lasers with relatively low power levels (typically 1–1.5 kW) in continuous and quasi-continuous wave modes are becoming more popular for the stator welding operation due to reduced footprint, higher energetic efficiency, and ease of programmability compared to the Nd:YAG systems [102, 103].

2.5 Laser-Based Manufacturing for Fuel Cells

Polymer electrolyte membrane fuel cells (PEMFCs) are a promising technology for powering a wide range of applications by converting chemically stored energy into electrical energy. However, insufficient durability and difficult water management inside the fuel cell are two main challenges, limiting commercial usage of that technology [105].

As schematically shown in Fig. 20, in a PEMFC, hydrogenn and oxygen react to water ($2H_2 + O_2 \rightarrow 2H_2O$). The water must be dissipated from the fuel cell by passing through the microporous layer (MPL) and the gas diffusion layer (GDL) to the bipolar plate (BPP). The MPL is usually a mixture of carbon particles with hydrophobic additives [106]. The GDL is typically carbon paper, often treated with
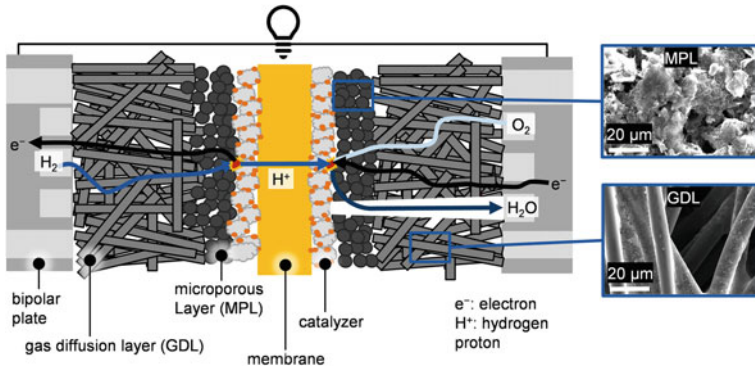
Fig. 20 Schematic illustration of a polymer electrolyte membrane fuel cell (PEMFC) with perforated diffusion layers [112]

hydrophobic fluoropolymers [107]. The in-cell water management is decisive for the performance and the lifetime of PEMFCs. Dry conditions lead to reduced proton conductivity resulting in a decreased lifetime and higher electrical losses [108]. While operating the fuel cell at high current densities removing the water fast enough is challenging, leading to liquid accumulations in the pores of the catalyst and diffusion layers. The transport ways for the oxygen are blocked by the water, which leads to higher losses inside the fuel cell [105].

In previous years, substantial research in improving water management has been conducted [109–111]. The optimization of water management is still challenging due to the complex thermodynamics of the interacting factors, such as gas diffusion, capillary pressure-driven water transport, and phase change within the diffusion media [109].

The structural modification of the MPL and GDL, e.g., with a graded pore structure or micro-drillings introduced into the diffusion layers, has shown promising improvements in water management [109, 111]. In order to introduce micro-drillings into the different layers, laser systems generating pulses with femto- and picosecond pulse durations can be used for a precise material removal with a low thermal impact to the workpiece. So far, the laser process was not the subject of research. Therefore, the complex correlations between laser parameters, material composition, and the resulting ablation behavior have not been understood. This resulted in large heat-affected zones where the polymeric binder evaporated, leading to water accumulations in the vicinity of the holes [105].

Therefore, it can be assumed that a detailed understanding of the laser process using state-of-the-art ultrashort-pulsed laser systems can help to produce micro-drillings with improved characteristics. Using laser pulses with a pulse duration of 8 ps, the area in which the polymeric binder evaporated was considerably smaller compared to longer pulse durations [112].

3 Future Needs and Prospects

The sector's needs and prospects were investigated during the LaserEMobility Workshop held in Bologna on March 10th and 11th, 2022 [113]. The participants from laser components manufacturers, system integrators, and end-users were invited to participate in a brainstorming session to assess the upcoming challenges. The experts contributed to an open discussion over four main topics raised by the organizing committee:

- What innovative combinations of materials and laser processes are envisaged?
- How can laser systems be further integrated into interconnected production systems?
- What are the opportunities and the challenges of laser processes for the production of hydrogen fuel cells?
- What are the potential roles of laser processes in conjunction with alternative methods for energy production, storage, and delivery in electric vehicles?

In the following, the main outcomes of the expert discussions are collected and further developed to better highlight the prospects and trends.

a. Innovative process/material combinations for e-mobility

The electric vehicles will use a wider range of material types, also in a combined manner. Beyond the highly conductive and lightweight metals, the application of polymers, composite materials, ceramics, and glasses will be increased compared to internal combustion engine vehicles. Laser-based manufacturing methods can provide the means for joining materials of different families, such as polymers, metals, and ceramics. Laser surface preparation for bonding [114], transmission welding of polymers to metals [115], and laser cutting for preparing hybrid joints [116] are some of the possibilities. The wider use of engineering ceramics and glasses as insulators but also in displays will require texturing, cutting, and welding techniques where lasers can serve. High power ultra short-pulsed laser sources will potentially provide the means for processing ceramics and glasses for such purposes [117–119]. Concerning the metals, the processing of Lithium-metal will require a great deal of attention for the next generation all-solid-state batteries. Lithium-metal anodes will be largely used in all-solid-state batteries, while the processing of this material by mechanical means is highly difficult. Using laser beam cutting is a straightforward approach to avoid issues related to the material adhesion and toughness [27, 120]. System developers will also have to tackle challenges connected to material handling and atmospheric control due to Lithium's high reactivity.

b. Automation and digitalization needs

Laser systems as digitals lends itself very well to a digitalized manufacturing environment. However, the intrinsic adaptability of the tool does not necessarily provide direct integration. The wide variety of laser-based manufacturing systems renders

it difficult to achieve universal software and control tools. As opposed to a conventional manufacturing tool, such as those used for machining, the laser systems do not employ a universal CAD/CAM language. As a result, each laser station may have a different grade and level of integration to the overall production system. In the case of scanner-based laser manufacturing systems, such differences may be more pronounced, while for robotic and cartesian manipulators, solutions are often adapted from existing machine tools.

Inline monitoring and control systems are highly desired by the laser system end-users. In the case of several millions of welds to be applied in battery system manufacturing or considering the production of e-drives with hairpin welding, the sensorization of the production processes becomes a fundamental need. The sensors are required to monitor the process, identify the defects possibly with the root cause, and move toward real time process control. The use of sensor systems in laser-based manufacturing also allows a means for in-process certification. The signals can be gathered to assess the adequacy of a single weld/cut or an entire part. The laser-based manufacturing processes can contribute to quality insurance and reduce scraps when embedded in the entire quality control of the developed component, such as a battery pack or an e-drive. The used sensor types can be acoustic, mechanical, or often optical, as based on a photonic energy source, laser manufacturing processes lend themselves well to optical monitoring methods. Different sensors allow to observe the process light or probe the process with an external light source [121]. Photodiodes, spectroscopes, and cameras provide different resolution possibilities in space, time, and wavelength domains. Photodiodes have been long used to monitor laser-based manufacturing processes due to their ease of integration, low cost, and high responsivity in time [122]. The performance of such systems highly depend on the optical emission profile of the processed material and the distinct optical transmissivity features of the used laser systems. Recent advancements on the data processing front can provide a better performance even with a relatively low resolution of these devices [123]. Artificial intelligence techniques are expected to improve monitoring performance greatly. As these sensors are more often integrated into the manufacturing systems, the data flow will increase, enlarging the signal database required. Nevertheless, the highest performance gain is related to the opportune choice of the sensor for the given application. Recent advancements in interferometric sensors also provide direct measurements of the process performance. Optical coherence tomography (OCT) is one of these techniques where a probe light measures the workpiece-sensor distance during the laser manufacturing process. OCT provides highly useful information, especially in the case of laser beam welding with partial penetration [124, 125]. The determination of the keyhole depth in laser beam welding of batteries, hairpins, and stators can allow for the correct mechanical properties and avoid excessive penetration. A certain bottleneck of such an approach is the data size, which may slow the overall manufacturing cycle due to the prolonged data transfer and analysis durations [126]. Calculations on-board the sensor and efficient data analysis methods will improve the applicability of these approaches in the field. The big data produced during a single manufacturing operation may generate a second

bottleneck in the phase of storage. Along with the improved data compression techniques, the storage of the certification as per the manufacturing process outcome appears to be one of the most viable future solutions.

With the improved digitalization means, a key requirement for the sector to move forward with digitalization is specialized personnel able to design, construct, and operate laser-based manufacturing systems and knowledgeable in manufacturing, optics, and electronics toward the final engineering application.

c. Laser-based manufacturing for hydrogen-powered vehicles

The hydrogen fuel cell technology has several aspects beyond the assembly of the bipolar plates, as thoroughly discussed in the previous sections. Indeed, laser cutting technology can be used to flexibly separate the bipolar plates to the desired shape and size. Remote cutting can be a possibility combined with remote laser beam welding considering the thickness ranges between 50 and 100 μm.

One of the issues related to the bipolar plate technology is the hydrogen diffusion into the material. Dedicated heat treatments, surface roughening, and oxidation strategies can effectively reduce hydrogen diffusion and related embrittlement [127, 128].

d. Laser processes for alternative methods within energy production, storage and delivery

Laser processing will be extended toward future applications. It can be foreseen that more extensive use of laser-based micromachining will be present in the production of power electronics and the electronic devices used in the dashboard and other control systems. Moreover, laser-based manufacturing for photovoltaic systems and additive manufacturing of battery electrodes are other possibilities.

The use of lasers can also go beyond the manufacturing means. Using photovoltaic systems on vehicles, laser radiation can provide wireless means of energy transfer and a more efficient energy conversion for recharging. Another possibility of using laser radiation is related to the liquid battery chemistries. The use of laser radiation to recombine the required chemistry and hence recharge the battery can be a future possibility.

4 Conclusions

This white paper highlighted the challenges and opportunities of laser materials processing in electric vehicle manufacturing. The paper provided overall insights into the different manufacturing approaches arising from the requirements of the emerging electric vehicles. Throughout the paper, several mainstream applications have been detailed, referring to the literature works. The application of laser-based processes in the production of electric vehicles is a relatively new research field with an increasing knowledge demand from the industry. The theoretical basis of several decades of

laser manufacturing research will be essential to keep up with the requirements. The increased flexibility of next-generation laser sources and integrated manufacturing systems will require expanding the knowledge base. An important aspect that must be underlined is the necessity to collaborate between different disciplines. The manufacturing engineers dealing with the e-mobility sector will have to face challenges coming from the respective application, which might require knowledge from chemistry, physics, or logistics. Moreover, an extensive collaboration between industry and academia is required to comply with the sustainability goals in the targeted time-frame.

References

1. Trenberth KE, Fasullo JT (2012) Tracking earth's energy: from El Niño to global warming. Surv Geophys 33:413–426. https://doi.org/10.1007/s10712-011-9150-2
2. Kampker A, Treichel P, Kreiskother KD, Krebs M, Buning MK (2018) Ex-ante process-FMEA for hairpin stator production by early prototypical production concepts. In: 2018 8th international electric drives production conference, EDPC 2018—Proceedings 2019. https://doi.org/10.1109/EDPC.2018.8658288
3. Lee SS, Kim TH, Hu SJ, Cai WW, Abell JA (2010) Joining technologies for automotive lithium-ion battery manufacturing—a review. In: ASME 2010 international manufacturing science and engineering conference, MSEC, vol 1, pp 541–549. https://doi.org/10.1115/MSEC2010-34168
4. Report T (2019) Smart technologies meet the production requirements of e-Mobility. PhotonicsViews 16:36–37. https://doi.org/10.1002/phvs.201970410
5. Heider A (2022) Laser welding of copper for E-mobility applications. In: EALA—European automotive laser applications 24th European expert conference
6. Lachenmaier M (2022) Laser applications in the new BMW IX—from car body to power train. In: EALA—European automotive laser applications 24th European expert conference.
7. Das A, Li D, Williams D, Greenwood D (2018) Joining technologies for automotive battery systems manufacturing. World Electr Veh J 9. https://doi.org/10.3390/wevj9020022
8. Zwicker MFR, Moghadam M, Zhang W, Nielsen CV (2020) Automotive battery pack manufacturing—a review of battery to tab joining. J Adv Join Process 1:100017. https://doi.org/10.1016/j.jajp.2020.100017
9. Kwade A, Haselrieder W, Leithoff R, Modlinger A, Dietrich F, Droeder K (2018) Current status and challenges for automotive battery production technologies. Nat Energy 3:290–300. https://doi.org/10.1038/s41560-018-0130-3
10. Lutey AHA, Fortunato A, Carmignato S, Ascari A, Liverani E, Guerrini G (2016) Quality and productivity considerations for laser cutting of LiFePO$_4$ and LiNiMnCoO$_2$ battery electrodes. Procedia CIRP 42:433–438. https://doi.org/10.1016/j.procir.2016.02.227
11. Lutey AHA, Fortunato A, Carmignato S, Fiorini M (2017) High speed pulsed laser cutting of Li-ion battery electrodes. Opt Laser Technol 94:90–96. https://doi.org/10.1016/j.optlastec.2017.03.022
12. Kronthaler MR, Schloegl F, Kurfer J, Wiedenmann R, Zaeh MF, Reinhart G (2012) Laser cutting in the production of lithium ion cells. Phys Procedia 39:213–224. https://doi.org/10.1016/j.phpro.2012.10.032
13. Kriegler J, Binzer M, Zaeh MF (2021) Process strategies for laser cutting of electrodes in lithium-ion battery production. J Laser Appl 33:012006. https://doi.org/10.2351/7.0000335
14. Baumann R, Lasagni AF, Herwig P, Wetzig A, Leyens C, Beyer E (2019) Efficient separation of battery materials using remote laser cutting–high output performance, contour flexibility, and cutting edge quality. J Laser Appl 31:022210. https://doi.org/10.2351/1.5096127

15. Lee D, Suk J (2020) Laser cutting characteristics on uncompressed anode for lithium-ion batteries. Energies (Basel) 13:1–12. https://doi.org/10.3390/en13102630

16. Huang J, Shi W, Huang J, Xie Y, Ba Y, He K (2021) High speed pulsed laser cutting of anode material for a Li-ion battery in burst mode. Opt Mater Express 11:2300. https://doi.org/10.1364/OME.425816

17. Zhang Y, Li J, Yang R, Liu T, Yan Y (2019) Analysis of kerf quality on ultrafast laser cutting of anode material for lithium-ion battery. Opt Lasers Eng 118:14–21. https://doi.org/10.1016/j.optlaseng.2019.01.013

18. Patwa R, Herfurth H, Heinemann S, Mazumder J, Lee D (2012) Investigation of different laser cutting strategies for sizing of Li-ion battery electrodes. In: ICALEO 2012—31st international congress on applications of lasers and electro-optics, vol 908, pp 908–914. https://doi.org/10.2351/1.5062562

19. Demir AG, Previtali B (2014) Remote cutting of Li-ion battery electrodes with infrared and green ns-pulsed fibre lasers. Int J Adv Manuf Technol 75:1557–1568. https://doi.org/10.1007/s00170-014-6231-7

20. Lee D (2018) Investigation of physical phenomena and cutting efficiency for laser cutting on anode for Li-Ion batteries. Appl Sci (Switzerland) 8. https://doi.org/10.3390/app8020266

21. Lee D, Ahn S (2017) Investigation of laser cutting width of $LiCoO_2$ coated aluminum for lithium-ion batteries. Appl Sci (Switzerland) 7. https://doi.org/10.3390/app7090914

22. Lee D, Mazumder J (2018) Effects of momentum transfer on sizing of current collectors for lithium-ion batteries during laser cutting. Opt Laser Technol 99:315–325. https://doi.org/10.1016/j.optlastec.2017.09.016

23. Lee D, Patwa R, Herfurth H, Mazumder J (2012) Computational and experimental studies of laser cutting of the current collectors for lithium-ion batteries. J Power Sour 210:327–338. https://doi.org/10.1016/j.jpowsour.2012.03.030

24. Lee D, Patwa R, Herfurth H, Mazumder J (2013) High speed remote laser cutting of electrodes for lithium-ion batteries: anode. J Power Sour 240:368–380. https://doi.org/10.1016/j.jpowsour.2012.10.096

25. Jansen T, Kandula MW, Hartwig S, Hoffmann L, Haselrieder W, Dilger K (2019) Influence of laser-generated cutting edges on the electrical performance of large lithium-ion pouch cells. Batteries 5. https://doi.org/10.3390/batteries5040073

26. Carbonari G, Müller V, Scurtu R-G, Memm M, Hoffmann A, Wohlfahrt-Mehrens M (2020) Communication—edge quality contribution on the electrical impedance of lithium-ion batteries electrodes. J Electrochem Soc 167:080504. https://doi.org/10.1149/1945-7111/ab8875

27. Jansen T, Blass D, Hartwig S, Dilger K (2018) Processing of advanced battery materials—laser cutting of pure lithium metal foils. Batteries 4. https://doi.org/10.3390/batteries4030037

28. Park D (2021) Design and manufacturing of low relative humidity chamber for laser processing of lithium metal

29. Habedank JB, Endres J, Schmitz P, Zaeh MF, Huber HP (2018) Femtosecond laser structuring of graphite anodes for improved lithium-ion batteries: ablation characteristics and process design. J Laser Appl 30:032205. https://doi.org/10.2351/1.5040611

30. Kriegler J, Hille L, Stock S, Kraft L, Hagemeister J, Habedank JB et al (2021) Enhanced performance and lifetime of lithium-ion batteries by laser structuring of graphite anodes. Appl Energy 303:117693. https://doi.org/10.1016/j.apenergy.2021.117693

31. Habedank JB, Kriegler J, Zaeh MF (2019) Enhanced fast charging and reduced lithium-plating by laser-structured anodes for lithium-ion batteries. J Electrochem Soc 166:A3940–A3949. https://doi.org/10.1149/2.1241915jes

32. Habedank JB, Kraft L, Rheinfeld A, Krezdorn C, Jossen A, Zaeh MF (2018) Increasing the discharge rate capability of lithium-ion cells with laser-structured graphite anodes: modeling and simulation. J Electrochem Soc 165:A1563–A1573. https://doi.org/10.1149/2.1181807jes

33. Kraft L, Habedank JB, Frank A, Rheinfeld A, Jossen A (2020) Modeling and simulation of pore morphology modifications using laser-structured graphite anodes in lithium-ion batteries. J Electrochem Soc 167:013506. https://doi.org/10.1149/2.0062001jes

34. Chen KH, Namkoong MJ, Goel V, Yang C, Kazemiabnavi S, Mortuza SM et al (2020) Efficient fast-charging of lithium-ion batteries enabled by laser-patterned three-dimensional graphite anode architectures. J Power Sour 471:228475. https://doi.org/10.1016/j.jpowsour.2020.228475

35. Hille L, Xu L, Keilhofer J, Stock S, Kriegler J, Zaeh MF (2021) Laser structuring of graphite anodes and NMC cathodes—proportionate influence on electrode characteristics and cell performance. Electrochim Acta 392:139002. https://doi.org/10.1016/j.electacta.2021.139002

36. Park J, Jeon C, Kim W, Bong SJ, Jeong S, Kim HJ (2021) Challenges, laser processing and electrochemical characteristics on application of ultra-thick electrode for high-energy lithium-ion battery. J Power Sour 482:228948. https://doi.org/10.1016/j.jpowsour.2020.228948

37. Pröll J, Kim H, Piqué A, Seifert HJ, Pfleging W (2014) Laser-printing and femtosecond-laser structuring of LiMn$_2$O$_4$ composite cathodes for Li-ion microbatteries. J Power Sour 255:116–124. https://doi.org/10.1016/j.jpowsour.2013.12.132

38. Lim DG, Chung D-W, Kohler R, Proell J, Scherr C, Pfleging W et al (2014) Designing 3D conical-shaped lithium-ion microelectrodes. J Electrochem Soc 161:A302–A307. https://doi.org/10.1149/2.013403jes

39. Pfleging W, Gotcu P (2019) Femtosecond laser processing of thick film cathodes and its impact on lithium-ion diffusion kinetics. Appl Sci (Switzerland) 9. https://doi.org/10.3390/app9173588

40. Park J, Hyeon S, Jeong S, Kim HJ (2019) Performance enhancement of Li-ion battery by laser structuring of thick electrode with low porosity. J Ind Eng Chem 70:178–185. https://doi.org/10.1016/j.jiec.2018.10.012

41. Song Z, Zhu P, Pfleging W, Sun J (2011) Electrochemical performance of thick-film Li(Ni0.6Mn0.2Co0.2)O2 cathode with hierarchic structures and laser ablation. Nanomaterials 11:2962. https://doi.org/10.3390/nano11112962

42. Zhu P, Seifert HJ, Pfleging W (2019) The ultrafast laser ablation of Li(Ni$_{0.6}$Mn$_{0.2}$Co$_{0.2}$)O$_2$ electrodes with high mass loading. Appl Sci 9:4067. https://doi.org/10.3390/app9194067

43. Mangang M, Seifert HJ, Pfleging W (2016) Influence of laser pulse duration on the electrochemical performance of laser structured LiFePO4 composite electrodes. J Power Sour 304:24–32. https://doi.org/10.1016/j.jpowsour.2015.10.086

44. Tsuda T, Ando N, Nakamura S, Ishihara Y, Hayashi N, Soma N et al (2019) Improvement of high-rate discharging performance of LiFePO4 cathodes by forming micrometer-sized through-holed electrode structures with a pico-second pulsed laser. Electrochim Acta 296:27–38. https://doi.org/10.1016/j.electacta.2018.11.014

45. Hille L, Toepper H-C, Schriever C, Kriegler J, Keilhofer J, Noecker MP et al (2022) Influence of laser structuring and calendering of graphite anodes on electrode properties and cell performance. J Electrochem Soc 169:060518. https://doi.org/10.1149/1945-7111/ac725c

46. Habedank JB, Günter FJ, Billot N, Gilles R, Neuwirth T, Reinhart G et al (2019) Rapid electrolyte wetting of lithium-ion batteries containing laser structured electrodes: in situ visualization by neutron radiography. Int J Adv Manuf Technol 102:2769–2778. https://doi.org/10.1007/s00170-019-03347-4

47. Pfleging W, Pröll J (2014) A new approach for rapid electrolyte wetting in tape cast electrodes for lithium-ion batteries. J Mater Chem A 2:14918–14926. https://doi.org/10.1039/c4ta02353f

48. Berhe MG, Lee D (2021) A comparative study on the wettability of unstructured and structured lifepo4 with nanosecond pulsed fiber laser. Micromachines 12:1–9. https://doi.org/10.3390/mi12050582

49. Habedank JB, Schwab D, Kiesbauer B, Zaeh MF (2020) Paving the way for industrial ultrafast laser structuring of lithium-ion battery electrodes by increasing the scanning accuracy. J Laser Appl 32:022053. https://doi.org/10.2351/7.0000078

50. Brand MJ, Kolp EI, Berg P, Bach T, Schmidt P, Jossen A (2017) Electrical resistances of soldered battery cell connections. J Energy Storage 12:45–54. https://doi.org/10.1016/j.est.2017.03.019

51. Chen X, Wang X, Liu Z, Hu Z, Huan P, Yan Q et al (2020) Effect of Cu content on microstructure transformation and mechanical properties of Fe–Al dissimilar laser welded joints. Opt Laser Technol 126:106078. https://doi.org/10.1016/j.optlastec.2020.106078

52. NLIGHT (2018) Corona Lasers
53. Grabmann S, Mayr L, Kick MK, Zaeh MF (2022) Enhancing laser-based contacting of aluminum current collector foils for the production of lithium-ion batteries using a nanosecond pulsed fiber laser. Procedia CIRP 111: 778–783,.Elsevier B.V. https://doi.org/10.1016/j.procir.2022.08.127
54. Grabmann S, Kriegler J, Harst F, Günter FJ, Zaeh MF (2022) Laser welding of current collector foil stacks in battery production–mechanical properties of joints welded with a green high-power disk laser. Int J Adv Manuf Technol 118:2571–2586. https://doi.org/10.1007/s00170-021-07839-0
55. Solchenbach T, Plapper P, Cai W (2014) Electrical performance of laser braze-welded aluminum-copper interconnects. J Manuf Process 16:183–189. https://doi.org/10.1016/j.jmapro.2013.12.002
56. Lee SJ, Nakamura H, Kawahito Y, Katayama S (2014) Effect of welding speed on microstructural and mechanical properties of laser lap weld joints in dissimilar Al and Cu sheets. Sci Technol Weld Joining 19:111–118. https://doi.org/10.1179/1362171813Y.0000000168
57. Liu YZ, Zheng BC, Jian YX, Zhang L, Yi YL, Li W (2020) Anisotropic in elasticity, sound velocity and minimum thermal conductivity of Al–Cu intermetallic compounds. Intermetallics (Barking) 124. https://doi.org/10.1016/j.intermet.2020.106880
58. Dimatteo V, Ascari A, Liverani E, Fortunato A (2022) Experimental investigation on the effect of spot diameter on continuous-wave laser welding of copper and aluminum thin sheets for battery manufacturing. Opt Laser Technol 145:107495. https://doi.org/10.1016/j.optlastec.2021.107495
59. Zuo D, Hu S, Shen J, Xue Z (2014) Intermediate layer characterization and fracture behavior of laser-welded copper/aluminum metal joints. Mater Des 58:357–362. https://doi.org/10.1016/j.matdes.2014.02.004
60. Fortunato A, Ascari A (2019) Laser welding of thin copper and aluminum sheets: feasibility and challenges in continuous-wave welding of dissimilar metals. Lasers Manuf Mater Process 6:136–157. https://doi.org/10.1007/s40516-019-00085-z
61. Smith S, Blackburn J, Gittos M, De Bono P, Hilton P (2013) Welding of dissimilar metallic materials using a scanned laser beam. In: ICALEO 2013—32nd international congress on applications of lasers and electro-optics, vol 493, pp 493–502. https://doi.org/10.2351/1.5062921
62. Lerra F, Ascari A, Fortunato A (2019) The influence of laser pulse shape and separation distance on dissimilar welding of Al and Cu films. J Manuf Process 45:331–339. https://doi.org/10.1016/j.jmapro.2019.07.015
63. Razab MKAA, Mohamed Noor A, Suhaimi Jaafar M, Abdullah NH, Suhaimi FM, Mohamed M et al (2018) A review of incorporating Nd:YAG laser cleaning principal in automotive industry. J Radiat Res Appl Sci 11:393–402. https://doi.org/10.1016/j.jrras.2018.08.002
64. Zhu H, Zhang H, Ni X, Shen Z, Lu J (2019) Picosecond laser lift-off method for fracture and debonding of copper oxide layer grown on copper substrate. J Laser Appl 31:042015. https://doi.org/10.2351/1.5121339
65. Shin BS, Oh JY, Sohn H (2007) Theoretical and experimental investigations into laser ablation of polyimide and copper films with 355 nm Nd:YVO4 laser. J Mater Process Technol 187–188:260–263. https://doi.org/10.1016/j.jmatprotec.2006.11.106
66. Yung WKC, Liu JS, Man HC, Yue TM (2000) 355 nm Nd:YAG laser ablation of polyimide and its thermal effect. J Mater Process Technol 101:306–311. https://doi.org/10.1016/S0924-0136(00)00467-2
67. Coutouly JF, Deprez P, Breaban F, Longuemard JP (2009) Optimisation of a paint coating ablation process by CO_2 TEA laser: thermal field modelling and real-time monitoring of the process. J Mater Process Technol 209:5730–5735. https://doi.org/10.1016/j.jmatprotec.2009.06.001
68. Schmidt MJJ, Li L, Spencer JT, Key PH (1999) A comparative study of the effects of laser wavelength on laser removal of chlorinated rubber. Appl Surf Sci 138–139:418–423. https://doi.org/10.1016/S0169-4332(98)00579-0

69. Brygo F, Dutouquet C, Le Guern F, Oltra R, Semerok A, Weulersse JM (2006) Laser fluence, repetition rate and pulse duration effects on paint ablation. Appl Surf Sci 252:2131–2138. https://doi.org/10.1016/j.apsusc.2005.02.143

70. Naithani S, Grisard A, Schaubroeck D, Lallier E, Van SG (2014) Mid-infrared resonant ablation of PMMA. J Laser Micro Nanoeng 9:147–152. https://doi.org/10.2961/jlmn.2014.02.0013

71. Lippert T (2005) Interaction of photons with polymersfrom surface modification to ablation. Plasma Process Polym 2:525–546. https://doi.org/10.1002/ppap.200500036

72. Lu YF, Song WD, Tee CK, Chan DSH, Low TS (1998) Wavelength effects in the laser cleaning process. Jpn J Appl Phys, Part 1: Regul Pa-Pers Short Notes Rev Pap 37:840–844. https://doi.org/10.1143/jjap.37.840

73. Kumar M, Bhargava P, Biswas AK, Sahu S, Mandloi V, Ittoop MO et al (2013) Epoxy-paint stripping using TEA CO_2 laser: determination of threshold fluence and the process parameters. Opt Laser Technol 46:29–36. https://doi.org/10.1016/j.optlastec.2012.04.021

74. Maezono T, Higashiura A, Sano F, Nakamura N (1993) Development of laser strippable new heat resistant magnet wire. In: Proceedings of the 21st electrical electronics insulation conference and electrical manufacturing and coil winding, pp 185–190. https://doi.org/10.1109/eeic.1993.630984

75. Glaessel T, Seefried J, Kuehl A, Franke J (2020) Skinning of insulated copper wires within the production chain of hairpin windings for electric traction drives. Int J Mech Eng Robot Res 9:163–169. https://doi.org/10.18178/ijmerr.9.2.163-169

76. Glaessel T, Baat F, Schwinghammer D, Seefried J, Kuehl A, Franke J (2018) Infrared laser based contacting of bar-wound windings in the field of electric drives production. Procedia CIRP 74:17–22. https://doi.org/10.1016/j.procir.2018.08.005

77. Riedel A, Masuch M, Weigelt M, Glabel T, Kuhl A, Reinstein S et al (2018) Challenges of the hairpin technology for production techniques. In: ICEMS 2018—2018 21st international conference on electrical machines and systems, pp 2471–2476. https://doi.org/10.23919/ICEMS.2018.8549105

78. Jasim HA, Demir AG, Previtali B, Taha ZA (2017) Process development and monitoring in stripping of a highly transparent polymeric paint with ns-pulsed fiber laser. Opt Laser Technol 93. https://doi.org/10.1016/j.optlastec.2017.01.031

79. Glaessel T, Seefried J, Franke J (2018) Challenges in the manufacturing of hairpin windings and application opportunities of infrared lasers for the contacting process. In: 2017 7th international electric drives production conference, EDPC 2017—Proceedings 2018, pp 1–7. https://doi.org/10.1109/EDPC.2017.8328150

80. Rütering M (2019) Hybrid solution moves boundaries of copper welding. PhotonicsViews 16:46–50. https://doi.org/10.1002/phvs.201900044

81. Glaessel T, Pinhal DB, Masuch M, Gerling D, Franke J (2019) Manufacturing influences on the motor performance of traction drives with hairpin winding. In: 2019 9th international electric drives production conference, EDPC 2019–Proceedings. https://doi.org/10.1109/EDPC48408.2019.9011872

82. Kaplan AFH, Powell J (2011) Spatter in laser welding. J Laser Appl 23:032005. https://doi.org/10.2351/1.3597830

83. Kuehl A, Riedel A, Vogel A, Hartl S, Glaessel T, Masuch M et al (2019) Robot-based production of electric motors with hairpin winding technology. In: Lecture notes in engineering and computer science, pp 257–262

84. Auwal ST, Ramesh S, Yusof F, Manladan SM (2018) A review on laser beam welding of copper alloys. Int J Adv Manuf Technol 96:475–490. https://doi.org/10.1007/s00170-017-1566-5

85. Punzel E, Hugger F, Dörringer R, Dinkelbach TL, Bürger A (2020) Comparison of different system technologies for continuous-wave laser beam welding of copper. Procedia CIRP 94:587–591. https://doi.org/10.1016/j.procir.2020.09.081

86. Franco D, Oliveira JP, Santos TG, Miranda RM (2021) Analysis of copper sheets welded by fiber laser with beam oscillation. Opt Laser Technol 133:106563. https://doi.org/10.1016/j.optlastec.2020.106563

87. Glaessel T, Seefried J, Masuch M, Riedel A, Mayr A, Kuehl A et al (2019) Process reliable laser welding of hairpin windings for automotive traction drives. In: 2019 international conference on engineering, science, and industrial applications, ICESI 2019, pp 1–6. https://doi.org/10.1109/ICESI.2019.8863004

88. Dimatteo V, Ascari A, Faverzani P, Poggio L, Fortunato A (2021) The effect of process parameters on the morphology, mechanical strength and electrical resistance of CW laser-welded pure copper hairpins. J Manuf Process 62:450–457. https://doi.org/10.1016/j.jmapro.2020.12.018

89. Kaufmann F, Meier A, Ermer J (2021) Influence of defocusing in deep penetration welding of copper by using visible wavelength

90. Haubold M, Ganser A, Eder T, Zäh MF (2018) Laser welding of copper using a high power disc laser at green wavelength. Procedia CIRP 74:446–449. https://doi.org/10.1016/j.procir.2018.08.161

91. Laserline GmbH (2022) Laserline blue: Diode Lasers for the Processing of High Reflective Metals. https://www.laserline.com/en-int/blue-3kw-diode-laser/. Accessed 5 June 2022

92. Panasonic Industry Co. Ltd. Blue Direct Diode Laser/Laser Welding Robots (2022). https://industrial.panasonic.com/ww/products-fa/welding/industrial-robots/laser-welding-cutting-robot. Accessed 5 June 2022

93. Laserline GmbH (2022) On welding copper components

94. Bocksrocker O, Speker N, Beranek M, Hesse T (2019) Reduction of spatters and pores in laser welding of copper hairpins using two superimposed laser beams. In: Lasers in manufacturing conference 2019 reduction, 1–8

95. Yang H, Tang X, Hu C, Liu S, Fan Y, Xiao Y et al (2021) Study on laser welding of copper material by hybrid light source of blue diode laser and fiber laser. J Laser Appl 33:032018. https://doi.org/10.2351/7.0000386

96. Araujo EG, Schneider J, Verbeken K, Pasquarella G, Houbaert Y (2010) Dimensional effects on magnetic properties of fesi steels due to laser and mechanical cutting. IEEE Trans Magn 46:213–216. https://doi.org/10.1109/TMAG.2009.2034124

97. Adelmann B, Hellmann R (2013) Process optimization of laser fusion cutting of multilayer stacks of electrical sheets. Int J Adv Manuf Technol 68:2693–2701. https://doi.org/10.1007/s00170-013-4884-2

98. Bayraktar Ş, Turgut Y (2018) Effects of different cutting methods for electrical steel sheets on performance of induction motors. Proc Inst Mech Eng B J Eng Manuf 232:1287–1294. https://doi.org/10.1177/0954405416666899

99. El YM, Van Gorp A, Clenet S, Benabou A, Faverolle P, Mipo JC, Slinky stator: The impact of manufacturing process on the magnetic properties. et al (2017) IEEE international electric machines and drives conference. IEMDC 2017:2017. https://doi.org/10.1109/IEMDC.2017.8002159

100. Markovits T, Takács J (2010) Edge welding of laminated steel structure by pulsed Nd:YAG laser. Phys Procedia 5:47–52. https://doi.org/10.1016/j.phpro.2010.08.028

101. Vegelj D, Zajec B, Gregorčič P, Možina J (2014) Adaptive pulsed-laser welding of electrical laminations. Strojniski Vestnik/J Mech Eng 60:106–114. https://doi.org/10.5545/sv-jme.2013.1407

102. Cui R, Li S (2020) Pulsed laser welding of laminated electrical steels. J Mater Process Technol 285:116778. https://doi.org/10.1016/j.jmatprotec.2020.116778

103. Wang H, Zhang Y, Li S (2015) Laser welding of laminated electrical steels. J Mater Process Technol 230:99–108. https://doi.org/10.1016/j.jmatprotec.2015.11.018

104. Wang H, Zhang Y, Lai X (2015) A model for the torsion strength of a laser-welded stator. J Mater Process Technol 223:319–327. https://doi.org/10.1016/j.jmatprotec.2015.04.012

105. Li H, Tang Y, Wang Z, Shi Z, Wu S, Song D et al (2008) A review of water flooding issues in the proton exchange membrane fuel cell. J Power Sour 178:103–117. https://doi.org/10.1016/j.jpowsour.2007.12.068

106. Nanjundappa A, Alavijeh AS, El Hannach M, Harvey D, Kjeang E (2013) A customized framework for 3-D morphological characterization of microporous layers. Electrochim Acta 110:349–357. https://doi.org/10.1016/j.electacta.2013.04.103

107. Manzi-Orezzoli V, Siegwart M, Cochet M, Schmidt TJ, Boillat P (2020) Improved water management for PEFC with interdigitated flow fields using modified gas diffusion layers. J Electrochem Soc 167:054503. https://doi.org/10.1149/2.0062005jes

108. Vengatesan S, Fowler MW, Yuan XZ, Wang H (2011) Diagnosis of MEA degradation under accelerated relative humidity cycling. J Power Sour 196:5045–5052. https://doi.org/10.1016/j.jpowsour.2011.01.088

109. Alink R, Haußmann J, Markötter H, Schwager M, Manke I, Gerteisen D (2013) The influence of porous transport layer modifications on the water management in polymer electrolyte membrane fuel cells. J Power Sour 233:358–368. https://doi.org/10.1016/j.jpowsour.2013.01.085

110. Simon C, Endres J, Nefzger-Loders B, Wilhelm F, Gasteiger HA (2019) Interaction of pore size and hydrophobicity/hydrophilicity for improved oxygen and water transport through microporous layers. J Electrochem Soc 166:F1022–F1035. https://doi.org/10.1149/2.1111913jes

111. Tang H, Wang S, Pan M, Yuan R (2007) Porosity-graded micro-porous layers for polymer electrolyte membrane fuel cells. J Power Sour 166:41–46. https://doi.org/10.1016/j.jpowsour.2007.01.021

112. Geiger C, Kriegler J, Weiss T, Berger A, Zaeh MF (2022) Micro-perforation of the diffusion media for polymer electrolyte membrane fuel cells using short and ultrashort laser pulses. Procedia CIRP

113. LaserEMobility Workshop (2022). https://bi-rex.it/event/laser-emobility-workshop-2022/

114. Maressa P, Anodio L, Bernasconi A, Demir AG, Previtali B (2014) Effect of surface texture on the adhesion performance of laser treated Ti6Al4V alloy. J Adhes 91:518–537. https://doi.org/10.1080/00218464.2014.933809

115. Acherjee B (2020) Laser transmission welding of polymers—a review on process fundamentals, material attributes, weldability, and welding techniques. J Manuf Process 60:227–246. https://doi.org/10.1016/j.jmapro.2020.10.017

116. Stock J, Zaeh MF, Conrad M (2012) Remote Laser cutting of CFRP: improvements in the cut surface. Phys Procedia 39:161–170. https://doi.org/10.1016/j.phpro.2012.10.026

117. Flamm D, Kleiner J, Kaiser M, Zimmermann F, Grossmann D, Kumkar M (2021). Ultrafast laser cutting of transparent materials: the trend towards tailored edges and curved surfaces 15. https://doi.org/10.1117/12.2579329

118. Penilla EH, Devia-Cruz LF, Wieg AT, Martinez-Torres P, Cuando-Espitia N, Sellappan P et al (1979) Ultrafast laser welding of ceramics. Science 2019(365):803–808. https://doi.org/10.1126/science.aaw6699

119. Horn A, Mingaeev I, Werth A, Kachel M (2008) Joining of thin glass with semiconductors by ultra-fast high-repetition laser welding. Laser-Based Micro- and Nanopackaging Assembly II 6880:68800A. https://doi.org/10.1117/12.762337

120. Kriegler J, Nguyen TMD, Tomcic L, Hille L, Grabmann S, Jaimez-Farnham EI et al (2022) Processing of lithium metal for the production of post-lithium-ion batteries using a pulsed nanosecond fiber laser. SSRN Electron J 1–22. https://doi.org/10.2139/ssrn.4108413

121. You DY, Gao XD, Katayama S (2014) Review of laser welding monitoring. Sci Technol Weld Joining 19:181–201. https://doi.org/10.1179/1362171813Y.0000000180

122. Garavaglia M, Demir AG, Zarini S, Victor BM, Previtali B (2020) Fiber laser welding of AA 5754 in the double lap-joint configuration: process development, mechanical characterization, and monitoring. Int J Adv Manuf Technol 111:1643–1657. https://doi.org/10.1007/s00170-020-06128-6

123. Shevchik SA, Le-Quang T, Farahani FV, Faivre N, Meylan B, Zanoli S et al (2019) Laser welding quality monitoring via graph support vector machine with data adaptive kernel. IEEE Access 7:93108–93122. https://doi.org/10.1109/ACCESS.2019.2927661

124. Baader M, Mayr A, Raffin T, Selzam J, Kuhl A, Franke J (2021) Potentials of optical coherence tomography for process monitoring in laser welding of hairpin windings. In: 2021 11th international electric drives production conference (EDPC), pp 1–10. https://doi.org/10.1109/edpc53547.2021.9684210

125. Stadter C, Schmoeller M, von Rhein L, Zaeh MF (2020) Real-time prediction of quality characteristics in laser beam welding using optical coherence tomography and machine learning. J Laser Appl 32:022046. https://doi.org/10.2351/7.0000077
126. Mazzoleni L, Demir AG, Caprio L, Pacher M, Previtali B (2019) Real-time observation of melt pool in selective laser melting: spatial, temporal and wavelength resolution criteria. IEEE Trans Instrum Meas 69:1179–1190
127. Raabe D, Tasan CC, Olivetti EA (2019) Strategies for improving the sustainability of structural metals. Nature 575:64–74. https://doi.org/10.1038/s41586-019-1702-5
128. Kim J, Hall D, Yan H, Shi Y, Joseph S, Fearn S et al (2021) Roughening improves hydrogen embrittlement resistance of Ti–6Al–4V. Acta Mater 220:117304. https://doi.org/10.1016/j.actamat.2021.117304

Digital Twin for Factories: Challenges and Industrial Applications

Walter Terkaj (ID)**, Massimiliano Annoni** (ID)**, Beatriz Olarte Martinez,**
Elena Pessot (ID)**, Marco Sortino** (ID)**, and Marcello Urgo** (ID)

Abstract The widespread adoption of digital technologies in factories has resulted in the generation of a vast amount of data, which has the potential to enhance efficiency and effectiveness in the manufacturing industry. However, collecting and analyzing these data require approaches and tools to design and operate complex digital models and infrastructures, also requiring transversal competencies. The Digital Twin approach can be exploited to couple assets with their digital counterparts to support analyses and decisions. In particular, a Digital Twin can be associated with a product, a specific machine tool or process, a production system, or an entire factory. This paper focuses on the application of Digital Twins in factories, proposing a framework to identify data flows and relevant digital tools for applications throughout the different phases of the factory lifecycle. Despite the great potential, Digital Twin in manufacturing is still hindered by certain limitations. Therefore, by drawing upon relevant literature, we define and highlight the key challenges that need to be

W. Terkaj (✉) · E. Pessot
Institute of Intelligent Industrial Technologies and Systems for Advanced Manufacturing, National Research Council, Milan, Italy
e-mail: walter.terkaj@stiima.cnr.it

E. Pessot
e-mail: elena.pessot@unisi.it

M. Annoni · B. O. Martinez · M. Urgo
Department of Mechanical Engineering, Politecnico di Milano, Milan, Italy
e-mail: massimiliano.annoni@polimi.it

B. O. Martinez
e-mail: beatriz.olarte@polimi.it

M. Urgo
e-mail: marcello.urgo@polimi.it

E. Pessot
Department of Information Engineering and Mathematics, University of Siena, Siena, Italy

M. Sortino
Polytechnic Department of Engineering and Architecture, University of Udine, Udine, Italy
e-mail: marco.sortino@uniud.it

255

addressed. Finally, the framework and the challenges are exploited to characterize three case studies, which demonstrate the application of Digital Twins during the design and execution phases.

Keywords Digital twin · Digital factory · Digital manufacturing · Digital machining

1 Introduction

Digital twin (DT) is recognized as one of the most promising technologies for realizing the paradigm of smart manufacturing and Industry 4.0 [1], which assumes a fully digitized, complex system that affects all units and classes in a factory [2]. The wide adoption of digital technologies in factories yields a large amount of data, but the collection and analysis of these data ask for transversal competencies (mathematics, informatics, engineering) together with approaches and tools to design and operate a complex digital infrastructure. Thus, industrial companies are integrating the ability to access, control, manipulate and thus effectively manage a large amount of data in their strategies [3].

The concept of Digital Twin (DT) entails a digital representation of a physical product, entity or system that comprises its selected properties, conditions, and behaviors using models and data within a single or across multiple life cycle phases, with the coupling between the physical and the digital world [4]. The twinning process is enhanced by the continuous interaction, a constant stream of back-and-forth information, and synchronization between the DT, the physical product and the external environment [5]. The concept of DT was first introduced by Grieves [6, 7] as a concept for product lifecycle management and then exemplified by a case study NASA [8, 9]. DT is used in various application domains such as manufacturing, architecture and construction, agriculture, food, robotics, supply chain, smart cities, and mineral resource acquisition, both in the design and operation phase [10].

The importance of DT for manufacturing is demonstrated by the inclusion of this topic in various industrial and scientific strategic roadmaps [11]. Indeed, industry [12], academy [13] and governments have pushed towards the digitalization of enterprises, especially of SMEs (Small and Medium Enterprises) due to the large amount of them in Europe (approximately 25.1 million in the EU in 2018 [14]). While in the previous industrial revolutions the trend was focused on physical resources, the 4th industrial revolution focuses primarily on creating a digital representation of the physical processes to get better insights into what is going on with the physical processes [15]. The ManuFuture Vision 2030 points out that the increased amount of available data generated by sensors, intelligent control and mechatronics, enables "detailed digital twins for machines, production lines and complete factories" [16]. The initiative Digitising European Industry highlighted the need for Digital Industrial Platforms to cope with the increased use of DT in various sectors, requiring very rich data and semantic models, thus calling for standard development to describe fur-

ther properties of DT for industrial applications to improve interoperability [17]. In particular, among the interoperability layers defined by the European Interoperability Framework (EIF) [18], the semantic interoperability (i.e., the ability to preserve and understand the precise format and meaning of exchanged data and information throughout exchanges between parties) plays a key role in DT development.

Even large companies argue that the next investments will be in DT, but they are still limited by issues. A recent report by Microsoft, Intel, and IoT Analytics, resulting from interviews with more than 500 executives, shows that only one-third of companies implementing smart manufacturing have partially or fully developed DT, and most of them lack a DT strategy as it is considered time-consuming, expensive and lacking standards [19].

Recently, the EIT Manufacturing project LIVE4.0 [20] carried out a survey in four European countries (Czech Republic, Germany, Italy, and Spain) covering the topics of Industry 4.0 solutions and their implementation at SME level. A total number of 67 answers were collected, providing valuable insights into how companies perceive Industry 4.0. Around 75% of the companies are interested in Industry 4.0 hands-on training, even under a payment, thus proving how SMEs are aware of these opportunities. Regarding software tools the companies employ, CAD solutions are still prevalent compared to simulation or CAM (Computer Aided Manufacturing). Although quite common, the production of small batches is still with rigid and traditional systems. Data processing is mainly based on file storage, and only 5% of the companies established automatic process monitoring.

Given their vast capabilities, DT can serve different types of problems in production, such as production and layout planning, process and feedback control, predictive maintenance, efficiency improvement, and validation of the production system [3]. For these reasons, DT technology has been applied in various industries and domains, from healthcare to aerospace and most notably in manufacturing. DT can play a key role in different industrial operations within the product lifecycle, from the design to the manufacturing and (after-sales) services [21]. In manufacturing, a DT can be linked to a product, a specific machine tool or process, a production system, or a whole factory. Virtual models composing a DT can be employed to verify, validate, and evaluate the performance of the physical counterpart along its lifecycle phases using integrated tools for optimization, simulation, monitoring, and control. Herein, the attention is focused on the factory as a whole, seen as the logical aggregation of its main components, i.e. products, processes, resources, and production systems. The IDEF0 diagram shown in Fig. 1, based on the work by Urgo et al. [22], represents the main activities in a factory lifecycle; such activities can also be applied to a single production system composing the factory. This type of diagram helps highlight how a DT must be able to cope with data flows and the heterogeneity of digital tools in manufacturing applications. Based on the requirements to be met and the set of selectable resources, the activity *Design Factory* (*A1* in Fig. 1) deals with the design of a factory (or production system) in terms of hardware configuration, process plans, specific fixtures, and inspection systems. The activity *Construct, Install, and Maintain Factory* (*A2* in Fig. 1) implements the decisions taken during the (re)design phase and continuously updates the state of the factory (or production
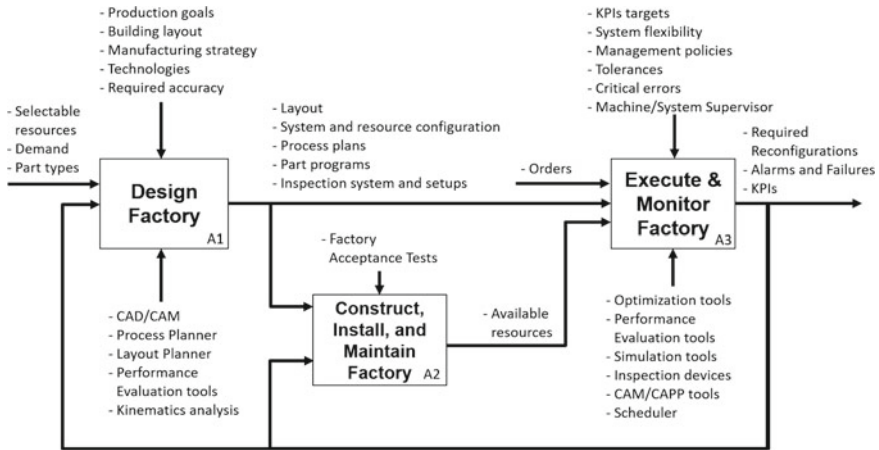
Fig. 1 IDEF0 diagram representing the main activities in a factory lifecycle that can be supported by DT technologies, based on [22]

system) based on possible failures and reconfigurations. The activity *Execute and Monitor Factory* (*A3* in Fig. 1) receives as input the orders and the actual factory (or production system) configuration to plan the manufacturing execution tasks that must be appropriately monitored, thus triggering possible reconfigurations.

This paper aims to provide an overview of the main challenges and foster the development and adoption of DT-based analysis, elaboration, and decision-support tools in academic and industrial contexts.

Section 2 briefly addresses the state of the art in DT for manufacturing. Taking advantage also of the literature, Sect. 3 defines a list of relevant challenges for successfully exploiting DT technologies integrated into the factory digital infrastructure to model the characteristics and evolution of products, processes, and production systems.

Section 4 presents manufacturing case studies showing the implementation of DT integrating methodologies and tools for designing and managing production processes and systems while also exploiting advanced visual DT interfaces for training and evaluations in a virtual environment. Finally, Sect. 5 draws the conclusions.

2   State of the Art

The precursor to what will come to be known as digital twins was the mirror environment which engineers at NASA developed during the disastrous Apollo 13 mission in an attempt, proven successful, to recreate a remote real system in order to determine the correct approach to recreate an air purifier [23]. However, it would take

three to four decades of technological advances, characterized by the development of communication technology, IoT, sensor technology and big data analytics before the digital twin became central in industry [1].

It is difficult to find a universal definition of a digital twin since this varies somewhat depending on its key aspects. A summary of the definitions across literature can be found in the survey by Barricelli et al. [5]. However, it is possible to give a universal description of what a digital twin must be able to do in order to be considered as such, i.e. "A digital twin [âŁ¦] continuously predicts future statuses (e.g., defects, damages, failures), and allows simulating and testing novel configurations, in order to preventively apply maintenance operations" [5]. Tao et al. [1] specified that a complete DT should include five dimensions: physical part, virtual part, connection, data, and service. In addition, the authors define the four main theoretical foundations of DTs: (1) DT modelling, simulation, verification, validation, and accreditation, (2) data fusion, (3) interaction and collaboration, and (4) service.

Considering the vast literature on Digital Twin in manufacturing, this section presents a brief overview of the contributions based on the different integration levels, i.e. the whole factory (Sect. 2.1), production system (Sect. 2.2), and production process at the single machine (Sect. 2.3).

2.1 Digital Twin of Factories

Stark and Damerau [4] proposed a framework for the classification of digital twin applications in manufacturing according to eight criteria: (1) the depth of the integration (e.g. single machine tool or whole factory), (2) the connectivity mode, (3) the update frequency, (4) the degree of intelligence and how automatic and autonomous it is, (5) the simulation capabilities, (6) the richness of the digital model, (7) the way the digital twin interacts with humans, (8) the phase of the lifecycle where it is adopted.

Data modelling and Internet of Things (IoT) play a key role in the uptake of DT technologies. Indeed, several initiatives are addressing the standardization of asset digital information models in the scope of Industry 4.0: IEC (TC 65 and its working group WG16 on Digital Factory), ISO (TC 184), W3C Web of Things,[1] ETSI Smart Appliances,[2] oneM2M,[3] DIN SPEC 91345 (Reference Architecture Model Industrie 4.0-RAMI4.0). Among these initiatives, RAMI4.0 [24] describes a reference architecture model in the form of a cubic layer model, which provides an architecture for technical objects (assets) in the form of layers, and allows them to be described, tracked over their entire lifetime and assigned to technical or organizational hierarchies. It also describes the structure and function of Industry 4.0 components as essential parts of the virtual representation of assets.

---

[1] https://www.w3.org/WoT/.

[2] https://www.etsi.org/technologies/smart-appliances.

[3] https://www.onem2m.org/.

Focusing on the synchronization between physical and digital factories, Modoni et al. [25] highlighted possible benefits and technical challenges. Some relevant benefits are related to the production process management along the product and factory lifecycle, the closed loop optimization between real and virtual, the decentralization of production control, the enhancement of smart products, and the support of teaching factory activities.

Sharma et al. [26] recently presented a review addressing practical applications of DT, in particular, the gap between concept and implementation, the relation with AI, and the impact of the specific domain.

2.2 Digital Twin of Production Systems

Negri et al. [27] proposed a comprehensive review on the application of digital twin in manufacturing industries, summarizing the definitions of DT and possible uses related to production systems (e.g. monitoring, maintenance, predicting performance, virtual commissioning, optimization of design and management).

Uhlemann et al. [28] addressed the potential of real-time data acquisition and simulation based on these data, particularly for learning factory applications.

Cimino et al. [29] reviewed digital twin applications in manufacturing, focusing mainly on manufacturing systems. They classified relevant contributions based on various criteria, namely application purposes, system features, DT implementation features, and DT services defined according to Tao et al. [30]. In addition, the authors provide guidelines for developing a DT, taking as a reference the production line installed in a university lab.

Terkaj et al. [31] developed a prototype digital platform to support the early design of roll shop systems by integrating graphical user interfaces, discrete event simulation, and virtual reality tools by exploiting an underlying ontology data model.

Park et al. [32] analyzed the challenges in DT development for cyber-physical production systems. In particular, the authors identified open problems to be addressed, such as (1) the discrepancy between a digital model and the real system, (2) interaction with Big Data, (3) integration of heterogeneous models, (4) responsiveness in the case of time-critical systems, and (5) security. The typical use case scenarios of DT found in the literature include root-cause failure analysis and predictive maintenance, high-fidelity simulation, closed-loop real-time control, and 3D visualization.

Since production systems are continuously evolving, the generation and update of DT can be time and cost-consuming. Thus, reiterating the centrality of data and models in DT, Lugaresi and Matta [33] proposed a method to automatically discover manufacturing systems and generate digital twins by elaborating more or less structured data such as data logs.

2.3 Digital Twin of Production Processes

The Digital Twin of production processes must be capable of designing and simulating the entire process from a stock part to a finished one, acquiring data from the manufacturing process and taking into consideration the inspection stages of the resulting product and having in mind that optimal design of machining setup, cutting tools and process parameters are of paramount importance [34].

Adeniji and Schoop [35] defined a digital process twin (DPT) as an accurate, fast, and efficient virtual process representation that considers the impact of a unit manufacturing process on the physical characteristics of a workpiece, fusing physically informed models and measured data to optimize a given process. This approach is intended to symbiotically augment the popular DT concept, which acts on a higher "systems" level to integrate the entire product life cycle digitally.

Botkina et al. [36] proposed a methodology for the construction of a digital twin of a cutting tool. The digital twin is based on the ISO 13399 cutting tool data representation and exchange to make it compatible with software servicing cutting tools. In order to enable data exchange between different machines with different protocols, a purpose-made information system architecture was developed.

Digital twins can also be applied for the preliminary study of machine reconditioning to design and validate a machine reconditioning without the need to have the availability of the physical machine, drastically reducing downtime [37].

Liu et al. [38] presented a modelling approach for the design and execution of machining processes by exploiting DT technology. The method was tested in a case study on producing marine diesel engine parts.

Tao et al. [30] proposed an integrated approach exploiting the DT for product design (including conceptual design, detailed design, and virtual verification), product manufacturing, and product service.

Bao et al. [39] defined process digital twins as three-dimensional models that support the manufacturing process, including the manufacturing procedure model, process attribute information and asset digital twins.

Modoni et al. [40] presented a methodology to optimize micromanufacturing processes, specifically micro injection moulding, taking advantage of digital twin technology. The authors tested the approach in a real case study.

3 Challenges

Despite the extensive literature and vast amount of applications and software tools, the full exploitation of DT in manufacturing is still hindered by technical and organizational limitations that must be addressed by research and innovation initiatives. Taking advantage of the literature (Sect. 2), this section lists some of the most relevant challenges that are grouped again according to the integration level, i.e. the

whole factory (Sect. 3.1), production system (Sect. 3.2), and production process at the single machine (Sect. 3.3).

3.1 Challenges for Factory DT

Several challenges should be considered for the definition and implementation of a holistic model and architecture able to effectively lead to broader and at-scale adoption of the DT concept in factories. General challenges to developing and implementing the DT in factories are mainly technical and can be defined as follows:

CF1 Ensuring the connection, synchronization and consistency between the DT and the real factory, including data accuracy and reliability of both realms, while coping with possible discrepancies and exploiting high-speed transmission [3, 25, 26, 32, 41].

CF2 Enabling the efficient harvesting and management of real-time data, together with the persistence and accumulation of the historical data [25], often in the form of Big Data [32].

CF3 Integrating advanced methodologies that can benefit from the DT potential, with the support of Advanced Simulation and Forecasting Tools [25].

CF4 Generation, synchronization, and integration of DT models, thanks to the development and acceptance of communication protocols, a consolidated vocabulary and a universal language to be generally adopted for standardization in modelling [3, 21, 30, 38, 41, 42]. In addition, DT models may have different levels of fidelity [43, 44].

CF5 Enhancing the interoperability between the various parties, and thus the harmonized integration of different software systems used in production lifecycle [25, 26, 32, 41, 45].

CF6 Granularity of the synchronization process. High-Performance Computing and multi-scale models can be breakthrough technologies for representing evolving products, processes, and systems [25, 26, 45].

CF7 Security issues and company concerns regarding data and cybersecurity, including IoT security, cross-industrial partner security, and leak of real-time monitoring data [3, 26, 32, 45, 46]

CF8 Complying with the regulations at the personal, enterprise, local, national, and international level [30].

CF9 Tackling the resistance to change and cost limitations from manufacturing companies, especially small and medium enterprises [30].

CF10 Lack of structured training programs at the university level to prepare engineers with hands-on experience in DT development and use [45, 47].

3.2 Challenges for Production System DT

The challenges for production systems are related to the difficult exploitation of DT in existing manufacturing systems equipped with traditional machinery that is hierarchically based on the automation pyramid, i.e. long-term planning with ERP and operation execution controlled by the MES:

CS1 Connection of the DT environment to the control system of the physical equipment [29] (cf. CF1).

CS2 Use of DT for decision-making in production systems, possibly with autonomy and real-time supervision, integrating an independent and self-governing control decision-making functionality [48].

CS3 Only a limited set of services are offered in one single DT application, also because some services need a 3D graphic interface and others only need data analysis without any visualization [29] (cf. CF5).

CS4 Study of strategies for distributing intelligence and data of the DT close to the various production resources [25].

3.3 Challenges for Production Process DT

Most of the challenges for production processes DT can be defined as a specialization of the general challenges for factories (Sect. 3.1):

CP1 Efficient and robust machining process models are hindered by a lack of realistic model input and a poor understanding of underlying process physics [35, 38]. Ultra-high synchronization, fidelity, and responsiveness between the virtual and physical space [30] are needed to cope with time-critical contexts [32] (cf. CF1).

CP2 Despite the large amount of information generated by the machining process, the machining information is not fully exploited and used in real-time. Operational data are incomplete or missing due to a lack of acquisition systems [38, 42] (cf. CF2).

CP3 Multi-domain and multidisciplinary integration of knowledge stemming from process design, process information management, process execution and process inspection [38] (cf. CF4).

CP4 Connectivity and interoperability problems due to the multi-sourced heterogeneous data [38, 42] (cf. CF5).

CP5 High-performance computing and multi-physics/multi-scale interdisciplinary need to be addressed and improved to realize real-time smart analysis and prediction [30] (cf. CF6).

CP6 Limited understanding of a DT from shop-floor workers, therefore upskilling and learning programs are needed to enable the DT exploitation at the shop-floor level [20, 42] (cf. CF9).

CP7 Decision-making activities at the process level still rely on manual operations
and human interactions. The research challenge is to develop cognitive digital
twins able to interoperate with other digital twins and humans in a seamless
way [21, 42, 49].

4 Case Studies

This section presents industrial and lab case studies demonstrating the potential of
DT in manufacturing applications. These cases help show the relevance of enabling
technologies and provide guidelines for exploiting DT, paying attention to required
competencies and data sources while referring to the challenges defined in Sect. 3.

The case studies tackle manufacturing workflows that can be framed in the factory
lifecycle shown in Fig. 1. Herein, the attention is focused on the *Design Factory* (*A1*
in Fig. 1) and *Execute and Monitor Factory* (*A3* in Fig.1) activities that are further
decomposed in Figs. 2 and 3, respectively.

These diagrams provide a common framework for the case studies. Specifically,
Sects. 4.1 and 4.2 present case studies about process design, execution, and moni-
toring, whereas Sect. 4.3 deals with a case of manufacturing system design.

4.1 Extrusion Male Case Study

The objective of this case study was to virtualise, simulate, and evaluate the outcome
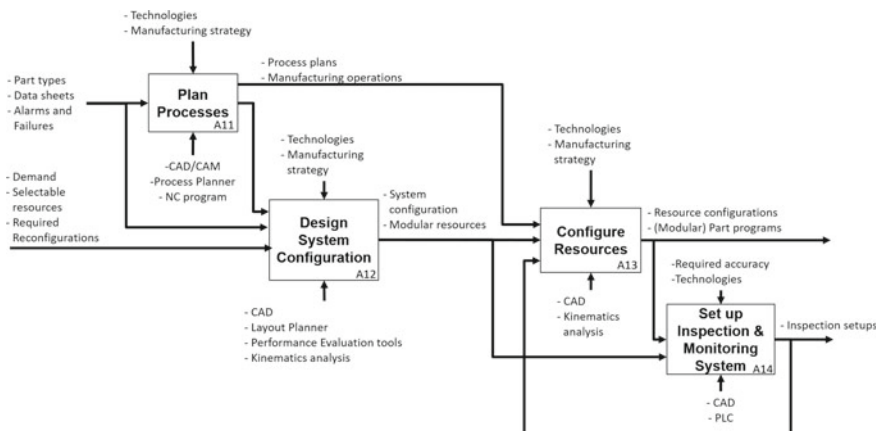from a digital twin of a milling cycle to detect possible defects on the final part

Fig. 2 IDEF0 diagram representing the decomposition of the design factory activity
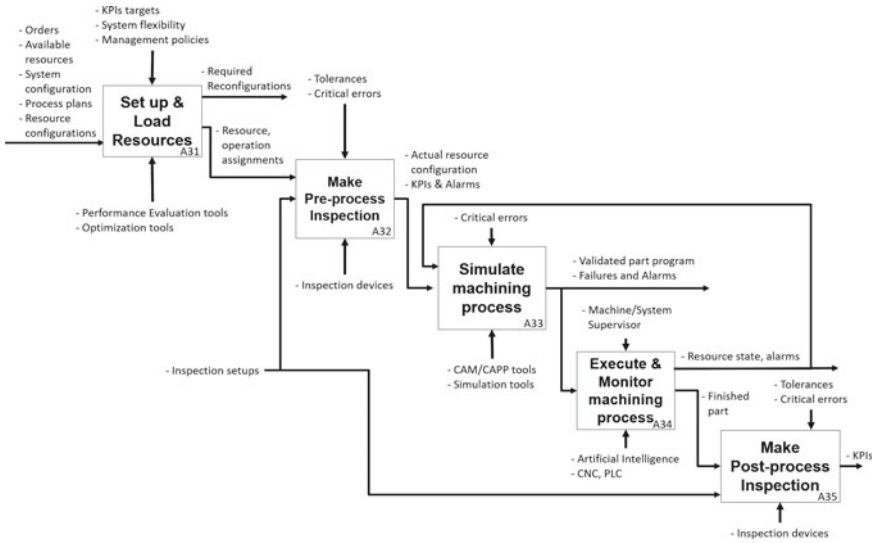
Fig. 3 IDEF0 diagram representing the decomposition of the execute and monitor factory activity

before or after the execution of a trial workpiece (cf. CP3, CP6, CP7) (*A34* in Fig. 3). In this situation, where a correct part program must be prepared for manufacturing the part by 5-axis milling, a CAM software tool should be used for designing the manufacturing cycle by selecting the right tools, strategies and parameters (*A11* in Fig. 2), but also a simulation software (e.g. CGTech Vericut) helps test the obtained and post-processed G-code against collisions, cutting forces and product final quality (*A33* in Fig. 3). It is important in this phase that the simulated final part geometry is compared with the nominal one to detect CAM programming errors and solve them by going back to process planning (*A11* in Fig. 2). When an actual trial is executed on the machine, as it happened in this case study, the real part must be compared with its digital counterpart (*A35* in Fig. 3). If a defect is present in both the physical and digital workpiece, then the defect is not due to malfunctions during its execution on the machine tool, but it was generated during the manufacturing cycle design with CAM; thus, the process plan must be updated. Otherwise, the defect is generated at the machine execution level, and it may be caused by excessive tool runout, tool deflection or wrong process parameters for the machine or tool performance (cf. CP1, CP2). In this case, a more extensive reconfiguration may be needed (*A11*, *A12*, or *A13* in Fig. 2).

The use case workpiece is an extrusion male for plastic materials developed at MI_crolab of Politecnico di Milano [50]. The extrusion male aims to force the material flowing around it and within the die to assume a specific cross-section in the final product, i.e., a catheter in this case. A 3D digital twin of the 5-axis Kern EVO machine, used to process the workpiece, is shown in Fig. 4.
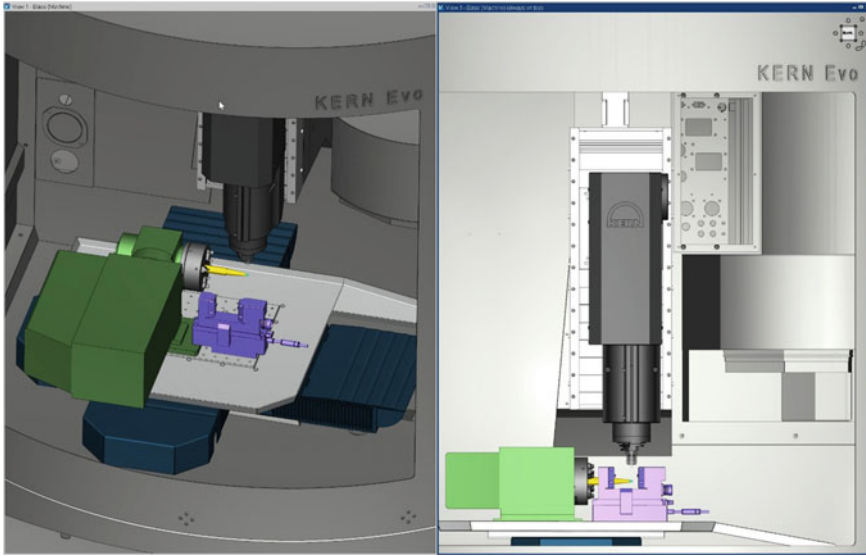
Fig. 4 Indexing head used by the Kern EVO together with the workpiece (in yellow) in a screenshot of Vericut
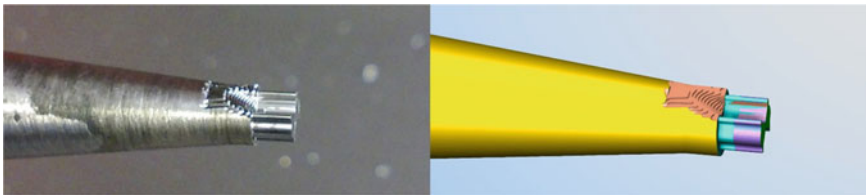

Fig. 5 Extrusion male at the end of the part program number 2.1

The overall machining process consists of 25 part programs. Various pictures were taken at different stages of execution (*A34* in Fig. 3) to enable the comparison of the results from the DT with those obtained during the actual manufacturing. Fig. 5 shows such comparison after the execution of part program number 2.1, which concerns the first roughing of the sides of the extrusion male to produce chamfers that will increase the robustness of the structure. It can be seen that the two images have a very high level of matching. The terracing effect produced by the side roughing matches the one simulated within Vericut, as does the peripheral area to the machined one, which is sometimes cut as the cutting tool disengages from the workpiece.

All 25 part programs were eventually simulated with success, with no collisions detected. The simulation detected a step on the final part that corresponded precisely with the real part (compare left and right pictures in Fig. 6), demonstrating a clear case of an error from the milling strategy designed with the CAM. Furthermore, Fig. 6 shows the presence of material between the six pins because the last six NC
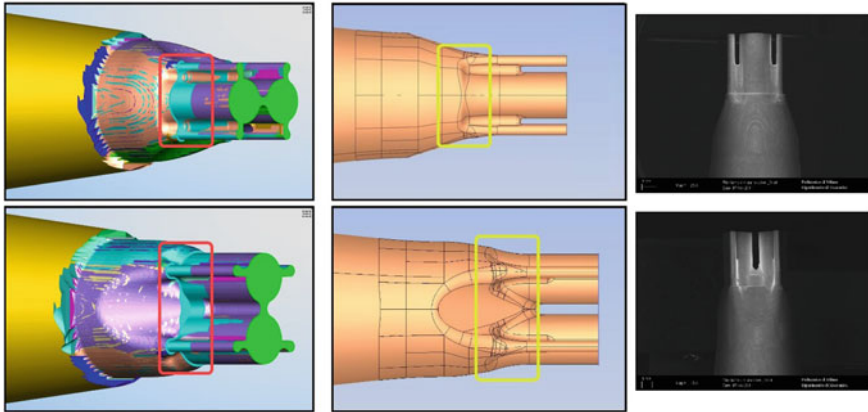
Fig. 6 Vericut-simulated final part (left); CAD model (center); SEM image of the real part (right). Boxes highlight the presence of a step where the geometry should have been smooth according to the CAD model

programs needed to remove such material between them were executed by a hand-written G-code and not simulated, even if Vericut could also do that.

This use case demonstrates how a process digital twin helps detect defects prior to executing the manufacturing cycle on the machine tool. The recommended use of this kind of DT is both before and after machining the first part. Indeed, comparing the simulated part with the machined part enables the detection of the specific type of error applied. However, manufacturing one test part is not always possible, for example, when parts are complex and expensive. In this case, the process DT must be even more accurate and capable of exchanging information with the real twin during the manufacturing cycle execution, thus posing issues with data management (cf. CP3), connectivity (cf. CP4), real-time simulation and interactions (cf. CP5) between twins. Only in this way could issues be solved online while they are taking place.

4.2 Smart Sawing Machine Case Study

The second case study aimed at making smarter an existing sawing machine (i.e. activities *A11, A12* in Fig. 2 are already completed) by reconfiguring this production resource (*A13* in Fig. 2) with a system that is set up (*A14* In Fig. 2) to continuously monitor the cutting process through the collection and analysis of data coming from the servo-drives together with the data collected by a set of sensors installed on the machine head (cf. CP2). The goal was to monitor the evolution of tool wear and avoid critical conditions when sawing tubes or profiles (*A34* in Fig. 3) by integrating data related to process design and process execution (cf. CP3). In these applications, the
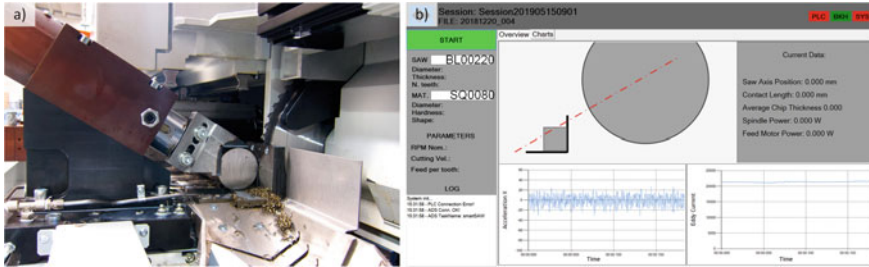
Fig. 7 Development of the smart sawing machine: **a** overview of the cutting area; **b** graphical interface of the real-time simulator and monitoring system
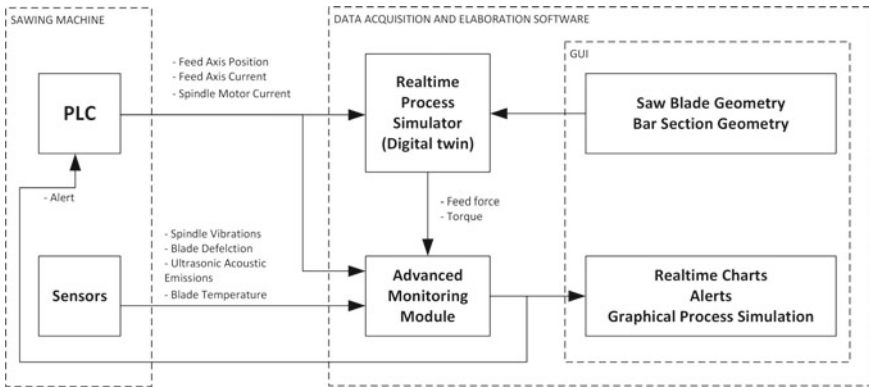

Fig. 8 Smart sawing machine data processing infrastructure

loading conditions and chip formation vary enormously, and the cutting parameters should be carefully designed.

The digital twin was implemented in the panel PC of the sawing machine (Fig. 7a) and consisted of a real-time processor and an additional graphical interface for the user (Fig. 7b). As shown in Fig. 8, the real-time processor continuously receives the feed axis position from the PLC. Given the geometrical configuration of the operation (*A11* in Fig. 2), the process simulator can estimate the cutter engagement and calculate the expected feed force and torque (*A33* in Fig. 3). The advanced monitoring module then used these data to verify whether sensor data and other quantities were consistent with the real-time simulation (*A34* in Fig. 3). In case of significant differences between simulated data and signals, an alert was set for the operator and the PLC that was programmed to stop the operation automatically accordingly (cf. CP1).

Sawing machines are expected to produce high volumes of product without requiring the presence of a human operator. Therefore, it is important to have machines able to detect process deviations and automatically stop when needed (cf. CP7). With the digital twin, the accuracy in the detection of critical conditions was greatly improved

from conventional approaches based on basic thresholds. Moreover, a limited set of machine and tool status indicators were identified and collected, thus enabling future improvements aiming at servitization.

4.3 Celada Case Study

The benefits of Industry 4.0 technologies are often applied to manufacturing execution (e.g. shop-floor data collection, monitoring, maintenance) but can also be exploited for production system design activities. The benefits can be relevant for all stakeholders, including machine tool builders, system integrators, and end users. A typical problem shared by several industrial domains is the concurrent generation of technical and commercial bids after receiving multiple requests for quotation from various potential customers [51]. The preliminary design of *turnkey* production systems is particularly critical because these customized projects involve a large number of stakeholders in a short period while substantially impacting competitiveness and profitability (suitable commercial offer). The high customization levels required by different customers limit frugal innovation and jeopardize standardization for any original equipment manufacturer. Production system design activities are more and more supported by methodologies and digital tools that would benefit from a DT integrated approach (cf. CF5, CS3, CP7) to improve the effectiveness and efficiency of the bid generation phase. In particular, DT can improve success factors [31] such as: (1) speeding up the design phase thanks to semi-automatic workflows, (2) offering the potential customer a set of alternative solutions, (3) performing accurate analysis and simulations to demonstrate the validity of the proposed technical solution and costs, (4) enhancing the design solution with 3D visualization to communicate better and increase the engagement of the customer.

Herein, we present the case of Celada S.p.A designing *turnkey* robotic production cells. Currently, the early design for this type of system is strongly dependent on the involved actors and highly resource-consuming since all the activities in Fig. 2 must be carried out, including process planning, resource configuration (e.g. machine tools, cutting tools, cutting parameters), integration and interconnections between machines and control systems. Developing a comprehensive DT-based design workflow would be a breakthrough solution to manage the evolution of linked models assets, manufacturing operations and parts while exploiting and formalizing the knowledge of operators (cf. CF4). Issues related to this use case are also addressed by the project DIGIMAN4.0 [52].

Figure 9 shows an example of a robotic production cell visualized in a VR environment. The digital model of the cell was developed using digital tools presented in [47] and is available online.[4]

This specific cell produces cylindrical mechanical components and consists of two CNC lathes executing two different sets of machining operations. A 6-axis industrial

---

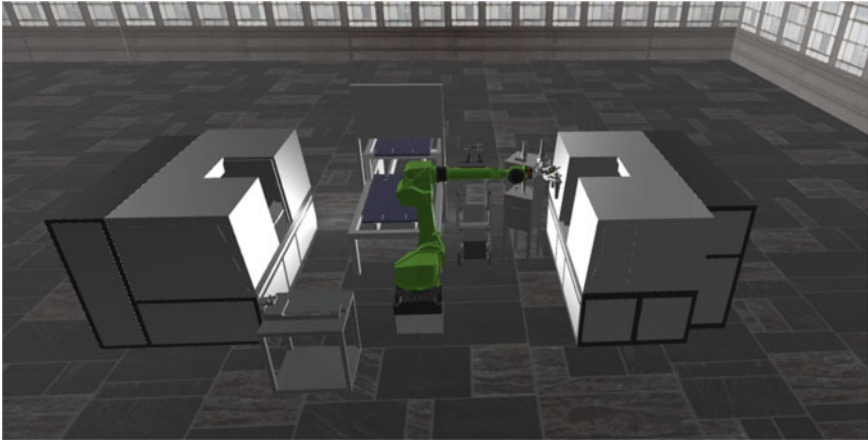[4] https://difactory.github.io/DF/scenes/DFProductionCell/glb.html.

Fig. 9 Virtual reality representation of the production cell (*Courtesy of Celada S.p.A.*)

robot deals with the handling of the work-in-progress parts thanks to an end-effector with three grippers. In addition, the cell includes a cleaning machine that removes dust and metal chips after the turning operations, a poka-yoke jig to check the size of the parts, and a measurement table to perform quality control on the finished part.

The development of an integrated digital model of the robotic production cell also supports virtual commissioning by integrating data from multiple sources and tools: CAD 3D, discrete event simulation, and process simulation (robot simulation) (cf. CF3). After installation, the digital model can be further exploited to create a good DT that supports the manufacturing execution (cf. CS1) and decision-making (cf. CS2).

5   Conclusions and Perspectives

The scientific literature and industrial case studies show that state-of-the-art technologies still provide only partial solutions for DT in manufacturing because of the lack of agreement among actors and tools dedicated to dealing with data related to products, processes, and factories. Even integrated and sophisticated PLM suites can hardly meet the requirements of capturing, representing and sharing a wide range of data along the product/factory life cycle, thus not supporting effective knowledge reuse. Moreover, large PLM suites are not adequate for the needs of Small and Medium Enterprises (SMEs) because they are characterized by high complexity and lack of customization, together with high purchase, management, and training costs.

Research and innovation are necessary to develop innovative solutions (e.g. open, neutral, and scalable digital platforms for data exchange) beyond the state of the art to support the development and management of factory DT while guaranteeing

democratization of the analysis and simulation approaches. New solutions for DT will need to be interoperable and non-disruptive for the existing situation. The upgrade of legacy technologies should be favored so that change management can be properly addressed in a customized way. Small and medium-sized ICT companies can provide complementary solutions for big commercial players in digital factories, mainly to support industrial SMEs. The development of lab-scale or industrial-scale pilot plants can help to assess and appreciate the potential of new digital approaches, thus also representing an opportunity for economic growth.

Moreover, the usability and sharing of DT models can be enhanced by introducing service-oriented architectures (SOA), i.e. solutions that are typically web-based and provide applications as services/functions within a platform with remote access.

Finally, standardization is paramount and requires the collaboration of several stakeholders, i.e. small-medium-large companies, technical committees, universities, research institutes, and ministries. Coordination is needed to reach solutions based on consensus, not partial (commercial) interests. Beyond standardization, guidelines and best practices are also needed to support data interoperability.[5]

References

1. Tao F, Zhang H, Liu A, Nee AYC (2019) Digital twin in industry: State-of-the-art. IEEE Trans Ind Inform 15(4):2405–2415
2. Jaskó S, Skrop A, Holczinger T, Chován T, Abonyi J (2020) Development of manufacturing execution systems in accordance with industry 4.0 requirements: a review of standard-and ontology-based methodologies and tools. Comput Indus 123:103300
3. Atalay M, Murat U, Oksuz B, Parlaktuna AM, Pisirir E, Testik MC (2022) Digital twins in manufacturing: systematic literature review for physical–digital layer categorization and future research directions. Int J Comput Integr Manuf 1–27
4. Stark R, Damerau T (2019) Digital twin. Springer, Berlin, pp 1–8
5. Barricelli BR, Casiraghi E, Fogli D (2019) A survey on digital twin: definitions, characteristics, applications, and design implications. IEEE Access 7:167653–167671
6. Grieves M (2014) Digital twin: manufacturing excellence through virtual factory replication. White Pap 1(2014):1–7
7. Grieves M (2019) Virtually intelligent product systems: digital and physical twins, pp 175–200
8. John Vicker EA (2015) Nasa technology roadmaps ta 12: materials, structures, mechanical systems, and manufacturing

---

[5] https://www.aitem.org/en/sezioni-gruppi/dft/.

9. Grieves M, Vickers J (2017) Digital twin: mitigating unpredictable, undesirable emergent behavior in complex systems. Springer International Publishing, Cham, pp 85–113
10. Liu X, Jiang D, Tao B, Xiang F, Jiang G, Sun Y, Kong J, Li G (2023) A systematic review of digital twin about physical entities, virtual models, twin data, and applications. Adv Eng Inform 55:101876
11. Terkaj W, Tolio T (2019) The Italian flagship project: factories of the future. Springer International Publishing, Cham, pp 3–35
12. Kagermann H, Wahlster W, Helbig J (2013) Recommendations for implementing the strategy initiative industrie 4.0. securing the future of german manufacturing industry [final report of the industrie 4.0. working group]. Acatech–National Academy of Science and Engineering, pp 4–7
13. Issa A, Hatiboglu B, Bildstein A, Bauernhansl T (2018) Industrie 4.0 roadmap: Framework for digital transformation based on the concepts of capability maturity and alignment. Procedia Cirp 72:973–978
14. Statista: Number of small and medium-sized enterprises (SMEs) in the European Union in 2018, by size (2020). https://www.statista.com/statistics/878412/number-of-smes-in-europe-by-size/#statisticContainer
15. Dalzochio J, Kunst R, Pignaton E, Binotto A, Sanyal S, Favilla J, Barbosa J (2020) Machine learning and reasoning for predictive maintenance in industry 4.0: Current status and challenges. Comput Indus 123:103298
16. Manufuture High-Level Group: ManuFuture Vision 2030: Competitive, Sustainable And Resilient European Manufacturing (2018). https://www.manufuture.org/wp-content/uploads/2022/04/Manufuture-Vision-2030_DIGITAL.pdf
17. Digitising European Industry: Working Group 2: Digital industrial platforms (2017). https://ec.europa.eu/futurium/en/system/files/ged/dei_wg2_final_report.pdf
18. The New European Interoperability Framework (2017). https://ec.europa.eu/isa2/sites/default/files/eif_brochure_final.pdf
19. Microsoft, Intel, IoT Analytics: Iot signals—manufacturing spotlight (2022). https://info.microsoft.com/ww-landing-IoT-signals-manufacturing-spotlight.html?lcid=en-us
20. LIVE 4.0 project: Assessment of SMEs' needs and preferred topics through surveys in the four regions of interest (2022). https://www.polimill.polimi.it/wp-content/uploads/2022/11/LIVE4.0-DEL11-D1-ID4342-Assessment-of-SMEs_needs.pdf
21. Semeraro C, Lezoche M, Panetto H, Dassisti M (2021) Digital twin paradigm: a systematic literature review. Comput Indus 130
22. Urgo M, Terkaj W, Giannini F, Pellegrinelli S, Borgo S (2019) Exploiting modular pallet flexibility for product and process co-evolution through zero-point clamping systems. Springer International Publishing, Cham, pp 57–82
23. Hong K, Nagarajah R, Iovenitti P, Dunn M (2007) A sociotechnical approach to achieve zero defect manufacturing of complex manual assemblies. Hum Factors Ergon Manuf Serv Ind 17(2):137–148
24. Reference Architecture Model Industrie 4.0 (RAMI4.0) English translation of DIN SPEC 91345:2016-04 (2016)
25. Modoni GE, Caldarola EG, Sacco M, Terkaj W (2019) Synchronizing physical and digital factory: benefits and technical challenges. Procedia CIRP 79:472–477; (2018) 12th CIRP conference on intelligent computation in manufacturing engineering, Gulf of Naples, Italy
26. Sharma A, Kosasih E, Zhang J, Brintrup A, Calinescu A (2022) Digital twins: State of the art theory and practice, challenges, and open research questions. J Ind Inf Integr 30:100383
27. Negri E, Fumagalli L, Macchi M (2017) A review of the roles of digital twin in cps-based production systems. Procedia Manuf 11:939–948; 27th international conference on flexible automation and intelligent manufacturing, FAIM2017, Modena, Italy
28. Uhlemann THJ, Schock C, Lehmann C, Freiberger S, Steinhilper R (2017) The digital twin: demonstrating the potential of real time data acquisition in production systems. Procedia Manuf 9:113–120; 7th conference on learning factories, CLF

29. Cimino C, Negri E, Fumagalli L (2019) Review of digital twin applications in manufacturing. Comput Indus 113:103130
30. Tao F, Cheng J, Qi Q, Zhang M, Zhang H, Sui F (2018) Digital twin-driven product design, manufacturing and service with big data. Int J Adv Manuf Technol 94(9):3563–3576
31. Terkaj W, Gaboardi P, Trevisan C, Tolio T, Urgo M (2019) A digital factory platform for the design of roll shop plants. CIRP J Manuf Sci Technol 26:88–93
32. Park H, Easwaran A, Andalam S (2019) Challenges in digital twin development for cyber-physical production systems. In: Chamberlain R, Taha W, Törngren M (eds) Cyber physical systems. model-based design. Springer International Publishing, Cham, pp 28–48
33. Lugaresi G, Matta A (2021) Automated manufacturing system discovery and digital twin generation. J Manuf Syst 59:51–66
34. Parenti P, Cacciatore F, Ratti A, Annoni, M (2018) A graphical method for performance mapping of machines and milling tools. Procedia Manuf 26:1500–1508; 46th SME North American manufacturing research conference. NAMRC 46. Texas, USA
35. Adeniji D, Schoop J (2022) In-situ calibrated digital process twin models for resource efficient manufacturing. J Manuf Sci Eng, Trans ASME 144(4)
36. Botkina D, Hedlind M, Olsson B, Henser J, Lundholm T (2018) Digital twin of a cutting tool. Procedia CIRP 72:215–218; 51st CIRP conference on manufacturing systems
37. Ayani M, Ganebäck M, Ng AH (2018) Digital twin: applying emulation for machine reconditioning. Procedia CIRP 72:243–248; 51st CIRP conference on manufacturing systems
38. Liu J, Wen X, Zhou H, Sheng S, Zhao P, Liu X, Kang C, Chen Y (2022) Digital twin-enabled machining process modeling. Adv Eng Inform 54:101737
39. Bao J, Guo D, Li J, Zhang J (2019) The modelling and operations for the digital twin in the context of manufacturing. Enterp Inf Syst 13(4):534–556
40. Modoni GE, Stampone B, Trotta G (2022) Application of the digital twin for in process monitoring of the micro injection moulding process quality. Comput Indus 135:103568
41. Lattanzi L, Raffaeli R, Peruzzini M, Pellicciari M (2021) Digital twin for smart manufacturing: a review of concepts towards a practical industrial implementation. Int J Comput Integr Manuf 34(6):567–597
42. García Á, Bregon A, Martínez-Prieto MA (2022) Towards a connected digital twin learning ecosystem in manufacturing: Enablers and challenges. Comput Indus Eng 171:108463
43. Terkaj W, Qi Q, Urgo M, Scott PJ, Jiang X (2021) Multi-scale modelling of manufacturing systems using ontologies and delta-lenses. CIRP Annals 70(1):361–364
44. Qi Q, Terkaj W, Urgo M, Jiang J, Scott P (2022) A mathematical foundation to support bidirectional mappings between digital models: an application of multi-scale modelling in manufacturing. Proc R Soc A: Math, Phys Eng Sci 478(2264):20220156
45. Mazumder A, Sahed M, Tasneem Z, Das P, Badal F, Ali M, Ahamed M, Abhi S, Sarker S, Das S, Hasan M, Islam M, Islam M (2023) Towards next generation digital twin in robotics: trends, scopes, challenges, and future. Heliyon 9(2):e13359
46. Balduzzi M, Sortino F, Castello F, Pierguidi L (2022) The security risks faced by cnc machines in industry 4.0. https://documents.trendmicro.com/assets/white_papers/wp-the-security-risks-faced-by-cnc-machines-in-industry-4-0.pdf
47. Berardinucci F, Colombo G, Lorusso M, Manzini M, Terkaj W, Urgo M (2022) A learning workflow based on an integrated digital toolkit to support education in manufacturing system engineering. J Manuf Syst 63:411–423
48. Negri E, Berardi S, Fumagalli L, Macchi M (2020) Mes-integrated digital twin frameworks. J Manuf Syst 56:58–71
49. Zheng X, Lu J, Kiritsis D (2021) The emergence of cognitive digital twin: vision, challenges and opportunities. Int J Prod Res 1–23
50. Gerosa S (2011) Progettazione e sviluppo dei cicli di lavorazione di matrici per l'estrusione di cateteri per applicazioni biomedicali. http://hdl.handle.net/10589/31961
51. Philbin SP (2008) Bid management: a systems engineering approach. J High Technol Manag Res 19(2):114–127

52. Early Stage Researchers n.11—Automatic process planning and design of manufacturing cells in Industry 4.0 production. https://www.digiman4-0.mek.dtu.dk/esr
53. DIGItal MANufacturing Technologies for Zero-defect Industry 4.0 Production. https://www.digiman4-0.mek.dtu.dk

White Paper on Innovative Joining Technologies for Naval Applications

Guido Di Bella ⓘ**, Chiara Borsellino** ⓘ**, Gianluca Buffa** ⓘ**,
Michela Simoncini** ⓘ**, Archimede Forcellese** ⓘ**, and Simone Panfiglio**

Abstract This document wants to provide an in-depth framework on the use of innovative joining technologies in the shipbuilding industry that must innovate both its own ship product and production process to maintain high levels of competitiveness, however, it wants also to attract the attention of the shipbuilders, because they often are reluctant to change, to stimulate them to innovation. After an introduction focused on both the impact and the evolution of the industry of European shipbuilding into the contest of the Blue Economy, a state-of-art is developed highlighting the progress in terms not only scientific but also in terms of design and application. Then, the document aims to identify the technological needs and the possible solutions also with the aid of the information provided by some companies such as Intermarine, Fincantieri and Caronte and Tourist.

Keywords Joining · Metal · Composite · Shipbuilding

G. Di Bella (✉) · C. Borsellino
Department of Engineering, University of Messina, Messina, Italy
e-mail: guido.dibella@unime.it

C. Borsellino
e-mail: chiara.borsellino@unime.it

G. Buffa
Department of Engineering, University of Palermo, Palermo, Italy
e-mail: gianluca.buffa@unipa.it

M. Simoncini · A. Forcellese
Marche Polytechnic University, Ancona, Italy
e-mail: m.simoncini@staff.univpm.it

A. Forcellese
e-mail: a.forcellese@staff.univpm.it

S. Panfiglio
NAVTEC, Messina, Italy
e-mail: simone.panfiglio@gmail.com

1 Introduction

The sea is an opportunity for growth to create new jobs, support competitiveness and empower social cohesion [1]. For this, in the last decades, the European Union has pushed the Member States to activate an integrated maritime policy by providing specific financing instruments, firstly, within the 2014/2020 Programs and, in the next, within "Horizon Europe" [2], and by encouraging both the activation of policies such as the Joint Programming Initiative Healthy and Productive Seas and Oceans (JPI Oceans), the EUSAIR strategy and the BLUEMED and WESTMED initiatives, and the creation of clusters as aggregators and centers of excellence for economic, research and innovation activities. Developing a Blue Economy is also in accordance with the goals of the 2030 Agenda for the sustainable development of the United Nations; particularly, with the goal no. 14 "Conserve and sustainably use the oceans, seas and marine resources for sustainable development". This European vision is reflected in the 2021/2027 National Research Program: i.e., in the Italian one, among the intervention areas play a strategic role knowledge, technological innovation and sustainable management of marine ecosystems [3].

Since 2009, the EU Blue Economy fields, characterized by the largest growing in terms of Gross Value Added (i.e., GVA), are Living resources (+31%) and Shipbuilding and repair (+39%). These last also show a positive trend in terms of overall gross investments (i.e., respectively, 12.6 and 8.6% respect to 2009), despite their contribution to the Blue Economy investments is still small compared to other sectors with decreasing investments.

The Shipbuilding and repair industry could become a key sector for the global transition towards a sustainable production paradigm as the market share is around 6% of the global order book in terms of compensated gross tonnage and 19% in terms of value (for marine equipment, the share rises to 50%).

In the global shipbuilding industry, the European Union plays a strategic role due to both the continuous investments in research and innovation and the highly skilled workforce. Its industry is currently composed of about 300 shipyards, which are specialized in building and repairing complex and technologically advanced civilian and military vessels and platforms, generating a production value of about €42.9 billion yearly and directly employing about 300,000 people. The entire supply chain is composed by about 22,000 equipment suppliers and service companies that generate a production value of about €125 billion yearly and create 576,000 direct jobs and 500,000 indirect jobs.

Figure 1 reports, respectively, the trends of persons employed and GVA of EU shipbuilding industry. Particularly, Germany leads the sector with 17% of the jobs and 25% of the GVA, followed closely by France and Italy with 14% of the jobs each and 21 and 19% of the GVA, respectively.

The specialization segments, characterized by high technological level and added value, are cruise ships, offshore support vessels, fishing vessels, ferries, research vessels, dredgers, mega-yachts, tugs, other non-cargo carrying ships, and advanced
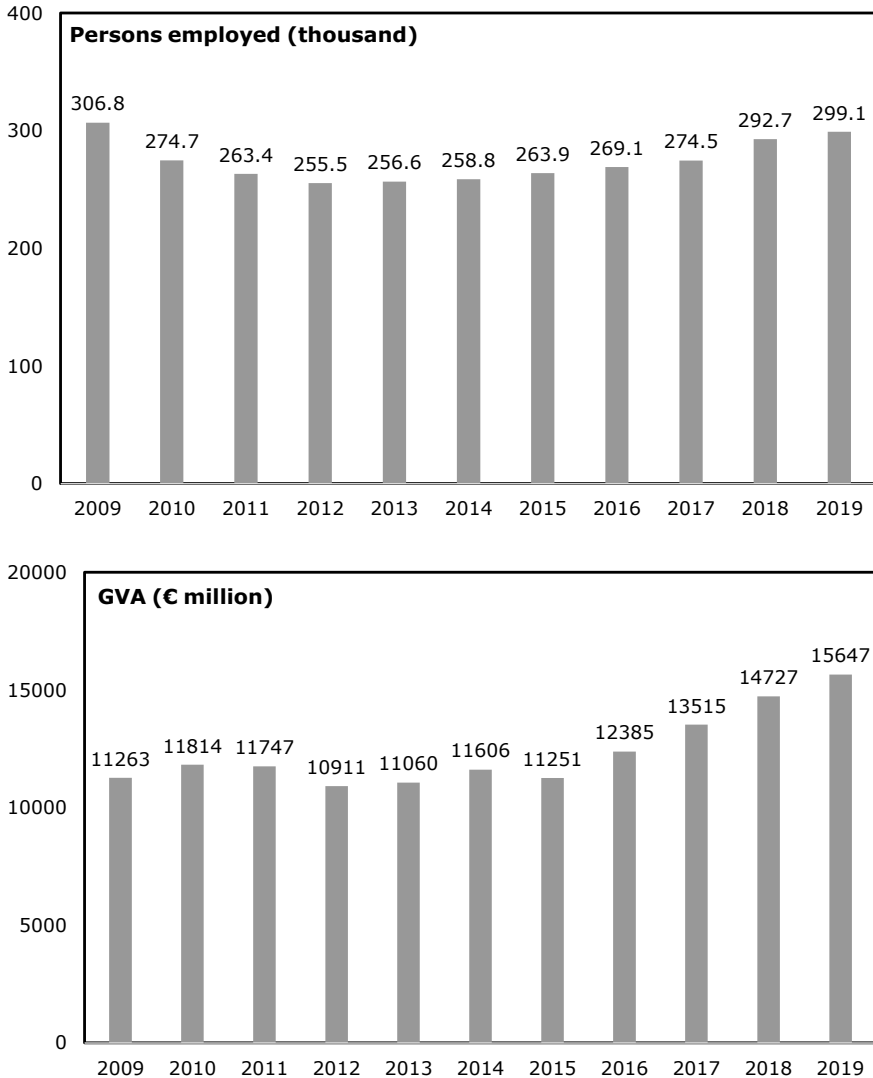
Fig. 1 Persons employed and GVA in EU shipbuilding industry

maritime equipment such as propulsion systems, large diesel engines, environmental, and safety systems, cargo handling and electronics.

The economic and financial crisis of 2008 has changed the business model. Particularly, shipbuilders have externalized part of the workforce and, consequently, part of the activities. Moreover, they have reduced the costs and restructured their capacity by modifying production programs and supply chain.

Moreover, pandemic emergency has severely hit European shipyards both on the demand and production. In the first half of 2020, orders registered a 64% decline in terms of compensated gross tonnage (i.e., CGT). The "ordering freeze" caused by COVID-19 affected particularly the cruise sector [4, 5].

In this context, the main challenges of the EU shipbuilding industry can be identified as follows [6, 7]:

– The Covid-19 crisis which has strongly impacted the sector involving a decrease of 80% in new orders in 2020. It is expected that the niche markets (i.e., the demand for passenger ships) will recover only after 2023–2024. So, it is needed to activate investment to avoid losing key capabilities, talent, and knowhow in the next 5 years.
– The transition toward Shipbuilding 4.0 and the progressive digitalization of the industry (i.e., connection between smart vessels and ports/infrastructure enhancing data flows).
– The EU Green Deal aiming to deliver the first zero-emission short sea ships by 2030.
– The retirement of workforce. It is expected that 40% of the current workers will be retiring in the next 10 years.
– The high intra-EU mobility of workers and the need of having a highly skilled workforce on the whole supply chain.
– The lack of a high-level training offer and the difficulty to adapt it to the technological needs of the industry. So, the companies increase their costs to create their own schools to deliver training.
– The difficulty to attract talent, people with sectoral skills and women. The gender gap issue is evident as women are only 20% of the workforce.

A possible response to the challenges is working on the "Sustainable, safe, connected and autonomous ship" whose goals are:

– By the next three years: evolution toward an autonomy level AL4 (Lloyd classification)/AL6 (Sheridan classification), 10% reduction in greenhouse gas emissions, refitting techniques for 10% reduction in emissions, treatment of 80% waste on shipboard and 90% reduction in the resulting emissions; 3 dB radiated noise reduction in the water for each vessel.
– By the next five years: zero emissions in port.
– By the next ten years: unmanned navigation without remote control also in environments with traffic (i.e., inland waters, coastal navigation, etc.), 10/20% reduction of accidents during the navigation, increase efficiency by 25–30%, 40–50% reduction in greenhouse gas emissions, pollutant reductions by 80%, airborne noise reduction in port areas by 3dB, 10 dB radiated noise reduction in the water for each vessel.

In recent years, also due to the pandemic emergency that has shown the low resilience level of the socio-economic system, sensitivity towards the need to fight climate change has significantly grown. The aim of the European Commission is not only to reduce greenhouse gas emissions by supporting the energy and ecological

transition sectors but also to build a Green Europe, which can protect climate and environment by creating sustainable jobs. This is the basis of the European Green Deal.

In this context, the role of transport industry (i.e., railcar and commercial vehicle manufacturing, shipbuilding, and aircraft construction) is strategic to decarbonize and move forward into a greener future meeting the goals of the EU Green Deal and the Smart and Sustainable Mobility Strategy [8]. Particularly, when looking at the EU's greenhouse gas (GHG) inventory, which is produced under the United Nations Framework Convention on Climate Change (i.e., UNFCCC), the transport sector contributes about one third of the total EU GHG emissions. This contribution can in turn be divided as follows: 0.5% rail, 14.4% aviation, 71% road (11.9% light commercial, 26.2% heavy-duty, 61.9% light-duty), 13.5% marine [9].

In the maritime field, this can involve, for instance, the use of new fuels (i.e., LNG, hydrogen, and biofuel), the installation of more efficient engines, the electrification of the propulsion by batteries, the lightening of the structures. This last allows to: (i) reduce the greenhouse gas emissions, (ii) increase the performance (i.e., higher speed and lower consumptions), (iii) stabilize the ship by lowering the center of gravity and, consequently, to better oppose the roll (i.e., this fact is useful mainly for the vessels characterized by high dimensions such as the cruise ships). These actions create strong innovation needs and lead to a radical change in a sector, characterized by: low technological levels, productions focused on traditional processes and familistic managements (especially when referring to small shipyards).

To reduce the vessel weight, it is necessary to introduce new materials. This involve both new manufacturing techniques and new alternative joining technologies to welding or bolting. For instance, about the introduction of aluminum structures in a vessel, which traditionally is made by steel, it is critical the study of the most suitable joint between steel and aluminum. Consequently, the development of transition joints between aluminum, steel and stainless steel represents an important technological advance.

2 State of the Art

Modern ships are made up of thousands of sub-components and structural elements which are joined together to make the complete assembly. Consequently, the joining processes play a strategic role, and their accuracy and efficiency can significantly impact on the shipbuilding competitiveness [10, 11]:

– Structural joints are extensive, i.e., in a large cruise ship, the total length can be also 400 km. Moreover, they are a source of stress concentration and create discontinuity in the load transfer.
– In terms of both work and cost, joining processes are about 50% due to direct operations, reworks, and potential adjustments. The undirect operations can be also 30% on hull production.

– Under construction, the heat contribution during joining can induce both prema-
  ture damages on preinstalled components and distortions the severity of which is
  connected to the sheet thickness, the complexity of the structures, and the use of
  advanced and/or dissimilar materials
– Applying one technology rather than another can led to structures with different
  mechanical properties, new design solutions, and new properties/lightness ratios.
– The applicability of new materials, such as aluminum alloys, high-tensile steels,
  and composites, and their combination depend on the availability of suitable
  joining technologies.

2.1 Aluminum/Steel

The development of transition joints between aluminum, steel and stainless steel
represents an important technological advance.

The difficulty in welding of these two materials lies in their extremely different
physical properties that hinder the union through conventional arc welding processes.
In fact, usually the carbon steels require temperatures of around 1500–1600 °C, while
the aluminum alloys are often welded at 700–800 °C and although these difficulties
can be overcome, the tendency to form large quantities of brittle iron/aluminum
intermetallic compounds creates a serious problem on the mechanical qualities of
the resulting joint [12].

When comparing Fe-rich and Al-rich intermetallic compounds, these last are
hard and brittle and they generate a worsening effect on mechanical properties, in
particular on the tensile strength of welded structures [13]. Thus, in steel-aluminum
welding it is strongly needed to minimize Al-rich brittle intermetallic compounds.

The fusion welding techniques, due to their high heat input, generate joints char-
acterized to layers of brittle intermetallic compounds, brittle failure, high porosity,
and poor mechanical performance [13–15].

To have good joints, the precautions to be taken are as follows: (i) reduction of heat
input; (ii) reduction of the work time; (iii) use of appropriate of filler materials. The
brazing technique, which reduces the heat introduced during welding, is commonly
combined with spot welding, tungsten inert gas (TIG) welding, metal inert / active
gas (MIG/MAG) welding and laser welding to join alloys of aluminum with steel
[16]. During this hybrid welding, the aluminum part melts and wets the steel. Filler
materials compatible with aluminum and steel, such as zinc-based or Al–12Si-based,
are used to improve the diffusion of aluminum in steel and balance the formation
of Fe-Rich and Al-rich intermetallic compounds during fusion welding. Zinc can
improve the wettability of steel by aluminum [17], while silicon can reduce the
thickness of the layers of intermetallic compounds [18].

The laser beam is an excellent source of heat to join thin aluminum plates to steel
plates, thanks to its ability to act in a very small area; in addition, the metallurgical
interaction between iron and aluminum is reduced due to the high speed of the
process.

An alternative welding technique known as solid-state welding produces a true weld below the melting point between materials of similar and dissimilar nature, normally without the addition of filler material [19]. This process exploits both plastic deformation and atomic diffusion.

The advantages of solid-state welding are connected to the ability to obtain precise welds without the need of other manufacturing processes, and to the ability to weld two or more surfaces during a single cycle. Other advantages are in terms of reduction of the following critical issues: oxidation problems, porosity, hydrogen solubility, and formation of intermetallic compounds due to the relatively low temperatures than the arc welding processes. The disadvantages are connected to a longer welding execution time compared to fusion or brazing welding and a limit on the dimensions of the parts that can be welded. Moreover, the presence of this technology in the industrial field is limited essentially due to the low versatility of the systems, which are not suitable to junctions with a geometry different from that for which they are designed.

The main solid-state welding processes are friction, explosion, diffusion, and ultrasonic [20]. Among these, certainly the most promising techniques for naval applications are the explosion welding and the friction stir welding.

Explosive welding (EXW) is a solid-state welding process, realized by oblique high-velocity impact between two materials caused by an explosive detonation. It is an alternative for joining aluminum and steel alloys since excessive melting can be avoid even for larger sized joints. A distinctive feature of explosively welded joints is the wave-like interfaces [21].

After a wide research program, this technology is used in shipbuilding, typically, on several materials such as steel, aluminum, and titanium [22] for several applications including: joining aluminum superstructures to steel decks, joining aluminum decks or bulkheads to steel hulls, adding permanently connected elements to existing ships during their refitting, such as pillars, bulkheads, equipment containers and even helipads [23].

Friction welding is a solid-state welding process, in which heat is generated by mechanical friction between two pieces when they rotate or move against each other. At the same time a lateral upset force is applied inducing the formation of a joint with the several advantages that include absence of filler metal, flux, and shielding gas, high efficiency, and short operation time.

Rotation speed, friction pressure, friction time, and forging pressure are the process parameters that influence the heat generation, the material flow and, consequently, the microstructure, the residual stresses, and also the possibility to join similar or dissimilar materials [24].

Friction stir welding (FSW) is an updated process of friction welding where a rotating, non-consumable tool generates frictional heat and joins materials. Particularly, the non-consumable tool rotates and plunges into the interface of the workpieces. The tool then moves along the interface line generating a frictional heat that makes the material hot and soften. Then, the rotating tool mechanically mixes the softened material producing high-quality joints in both similar and dissimilar materials in just a short time span [25]. The main advantages are: good mechanical

properties, high safety due to the absence of toxic fumes or spatter of molten material, automation, lower set up costs, less training, possibility to join complex geometries, minimal distortion, low environmental impact.

This process is rapidly replacing all fastening technologies such as riveting. In shipbuilding and marine applications, FSW is used to make panels for decks, sides, bulkheads and floors, hulls and superstructures, helicopter landing platforms, masts, and booms.

Consequently, the most suitable welding methods for joining dissimilar materials are those in the solid state. However, the production of transition joints involves some difficulties. They are not easy to manufacture, they are expensive, and they are available in limited forms. For these reasons, there is a wide literature that studies the application of traditional and/or advanced joining processes to weld dissimilar materials and achieve transition joints in an optimal way.

2.2 Metal/Composite

The introduction of composite materials in the recreational boat industry has leaded to a revolution that has significantly changed the way to design and produce ships. Particularly, composites are widely applied due to the good corrosion resistance, the possibility of making complex shapes, and the high specific strength and stiffness.

Typically, it is possible to identify three different techniques to join composite structures, laminates od sandwiches [11]:

– Over-lamination: some glass fiber fabrics are hand-laminated between the parts to be joined.
– Adhesive bonding: a natural or synthetic mixture in a liquid or semi-liquid state bonds items together.
– Mechanical fastening: the structures are drilled and then assembled by a fastener (i.e., button, zipper, bolt, screw, rivet).

In recent years, is growing the use of composite materials, also in other ship-building fields (i.e., cruises or military), coupled with other materials such as aluminum or steel [26, 27].

Large ships require less weight, more stability, higher speed, more comfort and more safety and the possibility to make components, which are characterized by a significant reduction in the weight without compromising the mechanical performance, promotes the introduction on market of green transport solutions (lighter and, consequently, characterized by lower greenhouse emissions).

To guarantee the efficiency of a multi-material component, the attention of ship-builder must be focused on the joining systems by optimizing the design; the finite element modelling; the surface treatments, and the combination of more technologies (i.e., bonding and riveting). The aim is to develop suitable joining methods to allow the application of composite structures to conventional metallic structures.

In the field of these technological improvements, structural adhesives offer several advantages such as uniform distribution of the stresses, no galvanic corrosion, good manufacturability, and watertightness.

For aluminum alloys, the trend is to combine adhesives with bolting or riveting. For composites, where it may be necessary to avoid drilling or changes in geometry, bonding is becoming predominant. In fact, the drilling process can induce several defects in a composite structure [28]:

– Delamination: the reinforced fiber plies separate due to peel-up or push-out phenomena.
– Burrs: uncut fibers and fiber pull-out occur on the machined edges of composite.
– Tearing: it is a form of delamination damage, which mainly occurs on the outermost material layer.
– Surface cavities: it is a typical cut surface morphology. Particularly, it is a discontinuous surface fracture caused by special fiber fracture mode.
– Glass transition failure: it is a thermal damage of composite matrix, caused by the glass transition of the matrix base, which leads to the degradation of the composite.
– Borehole damages: the drill scrapes the material off with the effect of high feed rather than cutting.

Moreover, the riveted, bolted, or welded components are thick to prevent premature breakage, the bonded elements can be thinner and, consequently, lighter. This is strategic in the choices leading the construction of cruise ships where the lightness of the upper decks, where often are installed swimming pools or other leisure facilities, means to keep lower the vessel center of gravity and, consequently, to give higher stability [26].

For this fact, only the technology of modern industrial bonding makes it possible to safely join aluminum (or another metal) and composites. Structural bonding between dissimilar materials is used, for instance, in the assembly of cruise ships' kitchens, air conditioner floors, deck linings, seating floors and windows.

Generally, adhesive joining technologies for composite and metallic structures are classified into:

– Co-curing, with and without adhesive: it is the process of curing a composite, including resins and adhesive, and simultaneously bonding it to another uncured material. In the co-curing without adhesive, the bonding is guaranteed by the excess of resin used to make the composite structure with a high level of efficiency if the parts are small, simple, or regular.
– Co-bonding: it is the process of curing a composite, including resins and adhesive, and simultaneously bonding it to a dissimilar material (i.e., metal). A careful surface preparation of the metal sheet is required. Also, in this case it is possible to act without adhesive by using the excess of resin.
– Secondary bonding: it is the process of joining together two or more parts with a third material which undergoes the chemical or thermal reactions. This process requires a careful treatment of the substrates, a well-designed fixturing to align and clamp parts.

The secondary bonding, where the adhesion process is promoted by a third material, which for industrial applications consists mainly in a structural resin, offers several advantages: uniform distribution of the stresses, more controlled galvanic corrosion, easy manufacturability and water-resistance [29, 30].

The performance of an adhesive bond depends on many factors:

– external such as temperature, humidity, and load,
– internal such as type of adhesive, type of substrate, overlap length and thickness of the adhesive joint.

The treatment of the substrate surface allows to remove contaminants such as lubricants and oils, control surface topography, and improve surface wettability promoting an intimate contact between substrate and adhesive and influencing the failure modes that can occur at the adhesive-substrate interface (i.e., adhesive failure), in the adhesive (i.e., cohesive failure), or in the substrate. If the failure occurs at the interface, the surface must be treated according to adhesion theories to promote interlocking [26].

Modern adhesives are extremely strong and are becoming increasingly important in modern construction and industry.

3   Challenges

The technological needs connected to the development of components characterized by lightness and high performance, where two or more materials are together combined, are strategic and, based on both the European rules analyzed in Sect. 1 and the state-of-art identified in Sect. 2, National and Regional Programs focused their attention on them by assigning significant resources and funding several research and innovation projects.

Two significant experiences where industry requirements well match with innovation actions are identified as best practices into the following projects:

– "TecHnology And materials for safe Low consumption And low life cycle cost veSSels And crafts" (in the next called THALASSA) [31], funded by the Italian Minister of University and Research on the National Operational Program on Research and Innovation 2014/2020, with a budget of about 10 millions of euros. Partners are the Technological District NAVTEC, the Sicilian Universities of Messina, Catania and Palermo, the National Council of Research with some its Institutes, the CALEF Consortium, the University of Calabria, the University of Salerno, the Polytechnic of Bari, the National Agency for New Technologies, Energy and Sustainable Economic Development, the University of Rome "La Sapienza", the University of Udine, Fincantieri, Caronte & Tourist, the Consortium for the Research and Development of Intermodal Maritime Transport (CTMI), the paint factory Atria, and Azimut Benetti.

– Soluzioni Innovative per Mezzi navali ad Alto Risparmio Energetico (in the next SIMARE), funded by the Sicilian Region on the European Regional Development Fund 2014–2020, with a budget of about 4 million of euros. Partners are the Technological District NAVTEC, the Sicilian Universities of Messina, Catania and Palermo, the National Council of Research with some its Institutes, Ficantieri, and Intermarine.

3.1 THALASSA

The project THALASSA is organized in 5 operative work packages. Particularly, WP1 entitled "Innovative technologies for the implementation of hybrid lightweight structures optimized for design for disassembling" is devoted to test several different joining methods, with regards to the ones connecting different material types (i.e., metal-composite, metal–metal, etc.). WP2 entitled "Bimetal connection systems for high performance vessels" takes into consideration alternative welding processes such as Friction Stir Welding to join different types of metal sheets.

In the last years, large shipyards, such as Fincantieri, have shown high interest to develop multi-material components and, particularly, to use composite materials for naval superstructures, as evinced in preliminary technological audits. The project represents an opportunity to find a solution to their needs. The reference is an application developed in [32], where the French Navy has implemented a superstructure on its La Fayette class frigate in the form of a helicopter hangar by focusing its attention on the joint between steel and composite sandwich with core in balsa for using in the hull-superstructure and hull-bulkhead connection.

Building of this succssfull application, Fincantieri has taken care of the executive planning and the optimisation of two structural joints btween steel hull and composite superstructure, so identified:

– Joint A: double overlapping mechanical adhesive hybrid joint to be made on board. It consists of a steel flange which represents the continuation of the ship's steel planking above the deck on which the composite superstructures are installed.
– Joint C: adhesive hybrid joint with single steel flange to be made on the ground with subsequent installation on board by welding steel/steel. It presents as adhering in steel a single sheet bent suitably to follow the geometry of the sandwich panel. Note that for the construction of the sandwich panel, the steel flange is incorporated within the panel during the layering phase. For this purpose, the type of surface treatment of the steel is of fundamental importance.

The sizing has required a careful analysis of the loads: (i) the total weight of superstructures, equipment, systems and furnishing; (ii) the inertial forces generated by the longitudinal, transverse and vertical accelerations of the ship in operation (ship motions); (iii) the load of deformation of the hull generated by the effect of the wave load. Moreover the joint have to be able to withstand to vibrations generated by the equipment (i.e., up to 80 Hz), variations in the operating temperature ($-20 \div 60$

°C), corrosion phenomena. Finally, for keeping the aesthetic aspect, the presence of discontinuities must be avoided in the planking and the production process must be able to integrate with the conventional processes that take place within the shipyard, i.e. the presence of dust or grease in the environment or the geometric tolerances of shipbuilding processes.

Also in military field the joining plays a significant role. Typically, on the basis of a study performed by CTMI, bonding is preferred to fastening because it allows a more uniform distribution of the stresses due to the larger coupling area. On board of minesweeper and fast patrol units produced by the shipyard, this type of joint is the most used; even if in some cases, where there are large components, bonding and fastening can be coupled. The adhesive can be the same resin of the composite or another structural material as a function of the specific application.

Figure 2 shows a typical section where the component 1 is the superstructure, component 2 is the deck and component 3 is the hull. These can be made combining different materials; i.e., different sandwiches with laminate composites or metal with composite.

The bonding between the parts would be guaranteed by an overlamination that is used to connect bulkheads and other important reinforcing elements to the adjacent structure on both sides, where possible.

It consists of overlapping the layers made of fiber reinforced resin to form a large patch fitted for the corner profile, known as T-joint o corner joint. It is important that each layer is at least 25 mm longer than the previous (if not every layer would act only on the previous layer and not on the surface of the elements to be connected) with the exception of the first which must overlap by at least 50 mm on both the connecting elements. Then the edges of the reinforcements of one layer must not

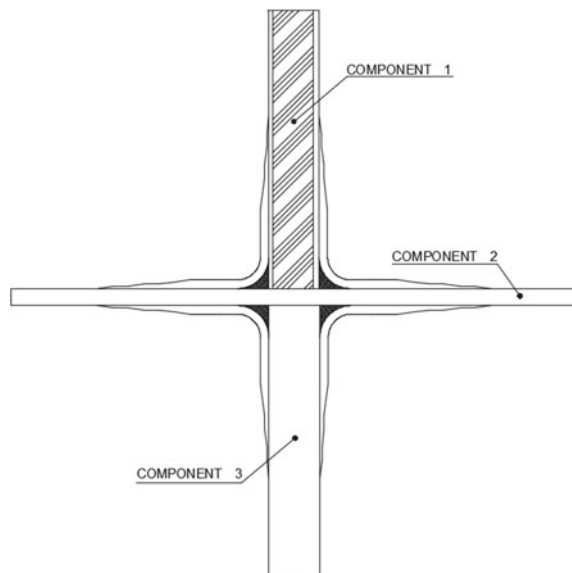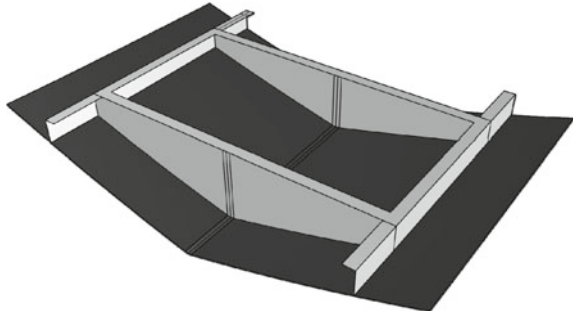**Fig. 2** Typical section

Fig. 3 Diesel tank

only be juxtaposed, instead it is necessary to overlap with the same offset various successive layers. This is in accordance with RINA requirements. A critical area to take into account is the zone under the first layer that usually is not able to fill correctly the corner between the joining elements [20].

Another study performed in the project is related to the connection of a diesel tank to the bottom of the hull using a structural adhesive.

Particularly, Azimut Benetti has focused its attention on the sizing of the joint as a function of the internal pressure, the geometry (i.e., flat or corner flange) and the corrosion resistance in an oil bath. The whole structure, as reported in Fig. 3, has been modeled with a finite elemen code.

3.2 SIMARE

The project SIMARE is organized in 4 operative work packages. Particularly, WP1 entitled "Innovative technologies for the realization of hybrid light structures" is devoted to study and develop the most suitable joining systems for the connection of both hybrid metal composite structures and bimetallic structures. Both types of junctions are of interest of Fincantieri, for applications in mega yachts and cruise ships, and of small shipyards, for small metal boats to be used for decontamination or tourism.

The main studies have focused their attention on steel-aluminum joints realized by Friction Stir Welding and explosion welding. Particularly, single lap friction stir welded joint were realized between a S355J0 steel provided by Fincantieri and an aluminum alloy AA5083.

Steel in quality S355J0 is a non-alloy carbon structural steel suitable for cold forming. The range of use is very wide, ranging from carpentry applications to the production of metal structures, tanks, to use in architecture, etc.

AA5083 is an aluminum alloy with magnesium and traces of manganese and chromium. It is highly resistant in aggressive environments such as seawater and industrial chemicals. It is characterized by exceptional strength after welding. Particularly, it has the highest strength of the non-heat treatable alloys. Its main application

fields are shipbuilding, railroad cars, drilling rigs, coachwork, pressure vessels and aluminum armor.

The process of FWS were realized by RIFTEC GmbH and it was done with welding speed of 300 mm/min at 400 rpm using force control at 30 kN, both in advancing and in retreating.

Figure 4a shows the top of the joint on the side of the aluminum evidencing the friction are characterized by a length of 25 mm. Figure 4b shows the same sample after the tensile test. In this case it is possible to observe the mixing area reduced to a length of 10 mm.

Figure 5 shows the cross section of the joint. Steel particles can be observed in lower area of aluminum weld nugget. At retreating side more steel particles can be observed, reason is material flow direction. There are no imperfections like cavity. Steel particle concentration at retreating side may affect mechanical properties.

Welding tool is pressing material with volume of tool pin upwards during plunging. Part of this material is not ejected and results in higher distance of tool and lower sheet at weld start.

Figure 6 reports the maximum loads for the friction stir welded joints by varying the configuration (i.e., advancing and retreating). The different behavior is connected to different dissipation of the heat generated during the process, in accordance to [33].

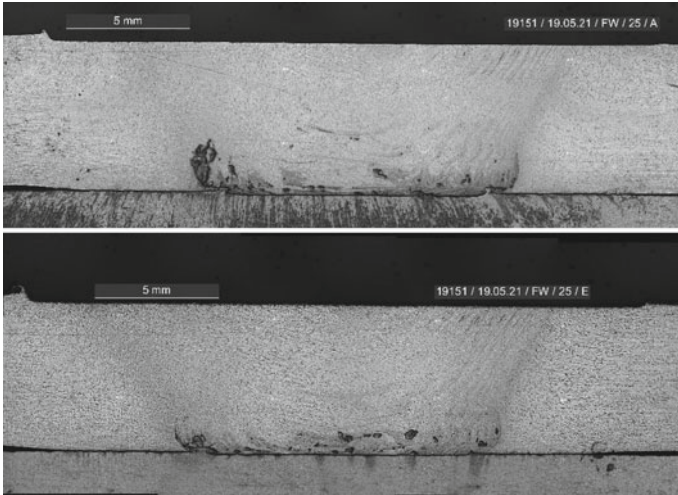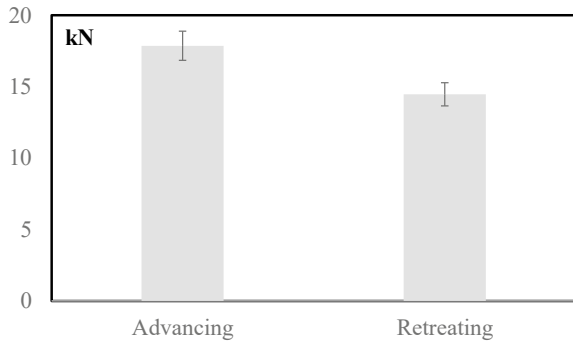**Fig. 4** Friction stir welded joint, before (**a**) and after (**b**) the tensile test
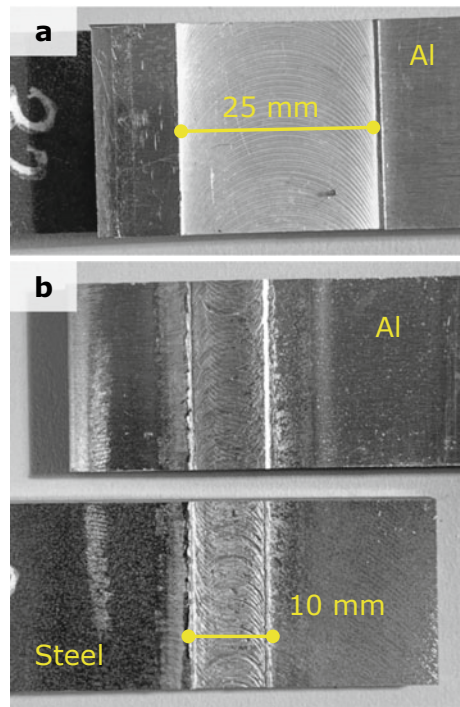
Fig. 5 Cross section of qualification weld (A—start of weld/E—end of weld)

Fig. 6 Maximum loads for friction stir welded joints

A similar study was performed on explosion welded joints provided by Nobelclad. Figure 7 shows the typical failure mode of the joint where the aluminum sheet is in the top and the steel in the bottom. Particularly, a maximum load of about 22 kN was obtained.

4 Case Studies

The substitution of the traditional joining systems with innovative ones is strategic not only for the large shipbuilders but especially for the minor shipbuilding to introduce innovation (i.e., new materials) by reducing the costs and increasing the productivity levels.

Particularly, in this section is presented a case study where a typical welding process is substituted by a FSW process: i.e., the connection by structural elements in the hull of a small ship such as a catamaran.

The most important parts of the structure of a catamaran are the ribs, 8 mm thick construction elements that are located inside the hulls and make up the skeleton. Particularly, these have the function of transversely stiffening the hulls, give it its shape and act as a support for the main deck. To further stiffen the hull, flat bars are welded with Metal-arc Inert Gas welding (MIG) to both locks, which extend longitudinally. For the catamaran, the ribs are spaced from each other by approximately 700 mm and there is only one bar per hull. In construction, the first operation consists in the welding of ribs and bar.

Figure 8 shows the characteristics of the elements that must join with MIG welding. Particularly, the figure focuses on the geometry of the rib, the notch promoting the connection between rib and flat bar and the indication with the corner when welding is applied.

In the case of welding with MIG technique, the flat bars have a section size of 100×4 mm and a length of 8000 mm. To be welded to the ribs, both must undergo preliminary cutting operations, to recreate a suitable notch for promoting the interlocking.

After the assembly, the welding is carried out: the joints are "double T" type, they must be welded in a vertical ascending/descending position and four different passes are required to the success of the welding.

By introducing another joining process, the elements change, and the design must be redefined as evidenced in Fig. 9:

Fig. 8 Design of rib-bar
MIG welded joint
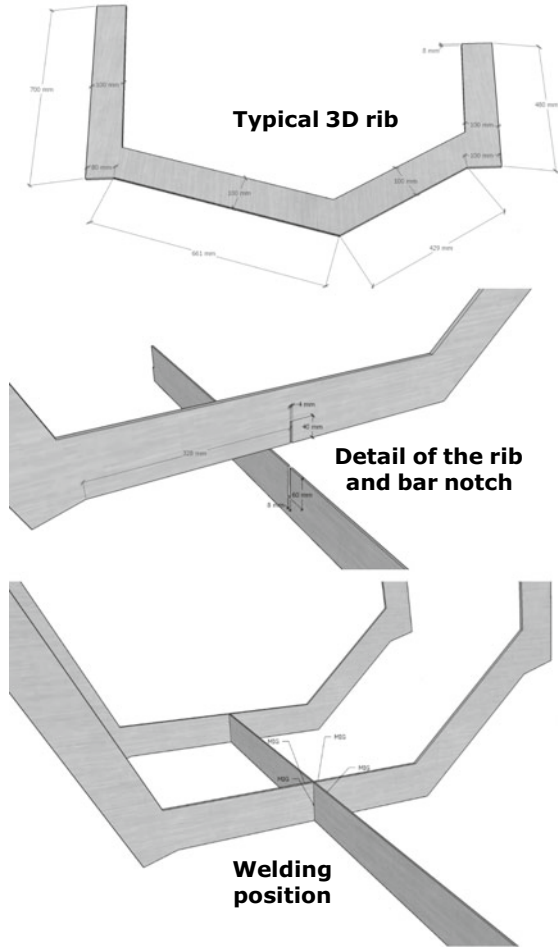
- The geometry of ribs is modified increasing their width.
- The flat bar is substituted by a "L" profilate having $100 \times 100 \times 4$ mm sizes.

After some preliminary operations of cuttnig and bending, the elements are welded in "double T" and simple "T" joints using a Stationary Shoulder Friction Stir Welding process. This consists of a rotating pin having a height of 8 mm inide a non-totating shoulder with a angle equal to 90°. The shaped shoulder holds the agitated material and flows over the surface of the material during welding.

Fig. 9 Design of rib-bar
friction stir welded joint
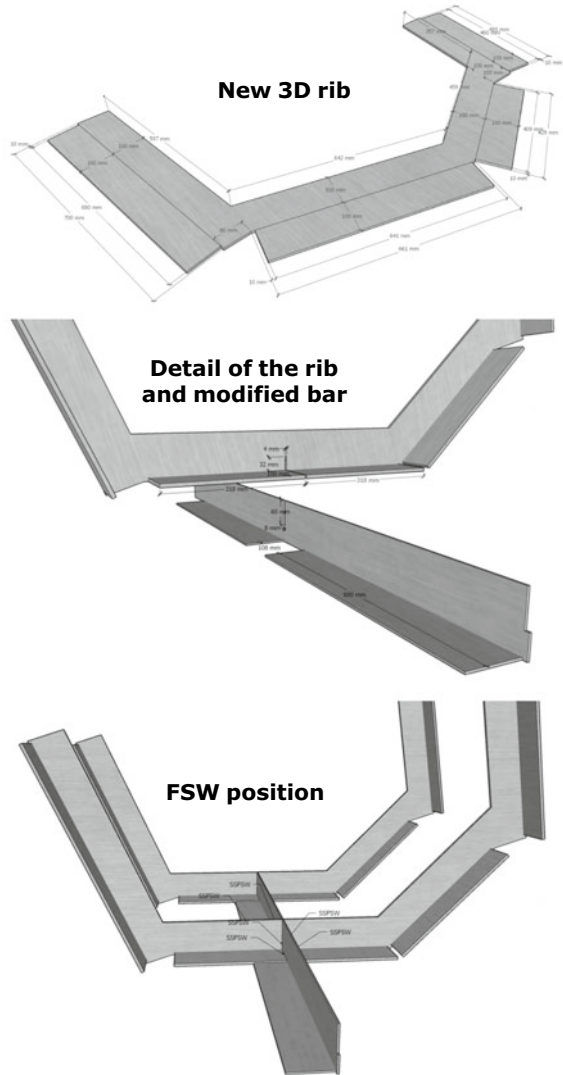
5 Conclusions and Perspectives

This White Paper highlights how the innovation in shipbuilding involves a significant scientific improvement related to the use of new materials and, consequently, to the introduction of innovative joining systems promoting especially the connection between dissimilar materials.

The legislative framework pushes to lead toward the ship of future, sustainable, safe, connected, and autonomous. This requires a significant effort on the part of

both large and small shipbuilders to build vessels characterized by low greenhouse emissions.

The state-of-art evidences the development of some processes such as friction stir welding and explosion welding between dissimilar metals or structural bonding between metals and composites.

The funding of some great research and innovation projects on the part of national or local public administration with on European Programs shows which of technological needs are strategic for shipbuilding and the possible solutions.

Finally, a case study shows how it is possible to substitute the traditional joining technologies.

Consequently, the field of the joining in shipbuilding is in turmoil. In the next ca be interesting not only to present other improvements but also the feasibility in terms economic evaluating, for instance, risk assessment or LCA.

References

1. Blue Italian Growth—BIG (2019) Three-year action plan—2019 Edition, Section 1. Napoli
2. Horizon Europe homepage. https://ec.europa.eu/info/research-and-innovation/funding/funding-opportunities/funding-programmes-and-open-calls/horizon-europe_en. Last accessed 18 June 2022
3. Ministry of University and Research (2020) National Research Program 2021–2027. Roma
4. European Commission: The EU Blue Economy Report (2022) Publications Office of the European Union. Luxembourg
5. Study Center of the Chambers of Commerce Guglielmo Tagliacarne: IX Report on the blue economy (2021). Informare, Latina
6. Pact for skills upskilling shipbuilding and maritime technology workers in Europe homepage. https://ec.europa.eu/social/BlobServlet?docId=24825&langId=de. Last accessed 18 June 2022
7. Waterborne Vision 2030 & 2050 homepage. https://www.waterborne.eu/vision. Last accessed 18 June 2022
8. Romano A, Yang Z (2021) Decarbonisation of shipping: a state of the art survey for 2000–2020. Ocean Coast Manag 214:105936
9. Agency EMS (2021) European environment agency: european maritime transport environmental report 2021. Publications Office of the European Union, Luxembourg
10. Roland F, Manzon L, Kujala P, Brede M, Weitzenbock J (2004) Advanced joining techniques in European shipbuilding. J Ship Prod 20(3):200–210
11. Di Bella G, Galtieri G, Pollicino E, Borsellino C (2012) Joining of GFRP in marine applications. In: Whyters MC (ed) Advances in materials science research, vol 12. Nova Science Publisher, Hauppauge, pp 185–215
12. Ma J, Harooni M, Carlson B, Kovacevic R (2014) Dissimilar joining of galvanized high-strength steel to aluminum alloy in a zero-gap lap joint configuration by two-pass laser welding. Mater Des 58:390–401
13. Rathod MJ, Kutsuna M (2004) Joining of aluminum alloy 5052 and low-carbon steel by laser roll welding. Weld J 83(1):16S-26S
14. Mathieu A, Pontevicci S, Viala JC, Cicala E, Matteï S, Grevey D (2006) Laser brazing of a steel/aluminium assembly with hot filler wire (88% Al, 12% Si). Mater Sci Eng A 435–436:19–28
15. Choi CY, Kim DC, Nam DG, Kim YD, Park YD (2010) A hybrid joining technology for aluminum/zinc coated steels in vehicles. J Mater Sci Technol 26(9):858–864
16. Liu W, Ma J, Atabaki MM, Kovacevic R (2015) Joining of advanced high-strength steel to AA 6061 alloy by using Fe/Al structural transition joint. Mater Des 68(5):146–157

17. Mathieu A, Shabadi R, Deschamps A, Suery M, Matteï S, Grevey D, Cicala E (2007) Dissimilar material joining using laser (aluminum to steel using zinc-based filler wire). Opt Laser Technol 39(3):652–661
18. Sierra G, Peyre P, Beaume FD, Stuart D, Fras G (2008) Steel to aluminium braze welding by laser process with Al–12Si filler wire. Sci Technol Weld Joining 13(5):430–437
19. Mir FA, Khan NZ, Siddiquee AN, Parvez S (2022) Friction based solid state welding—a review. Mater Today: Proc 62(1):55–62
20. Li W, Patel V (2022) Solid state welding for fabricating metallic parts and structures. Encycl Mater: Metals Alloy 4:246–259
21. Chu Q, Xia T, Zhao P, Zhang M, Zheng J, Yan F, Cheng P, Yan C, Liu C, Luo H (2022) Interfacial investigation of explosion-welded Al/steel plate: the microstructure, mechanical properties and residual stresses. Mater Sci Eng A 833:142525
22. Gaines E, Bamker J (1991) Shipyard aluminum/steel welded transition joints. In: Ship production symposium proceedings. San Diego, pp 1–6
23. Boroński D, Skibicki A, Maćkowiak P, Płaczek D (2020) Modeling and analysis of thin-walled Al/steel explosion welded transition joints for shipbuilding applications. Mar Struct 74:102843
24. Gorgheri MS, Kasiri-Asgarani M, Bakhsheshi-Rad HR, Ghayour H, Rafiei M, Mostafa A, Berto F (2022) Friction welding of pure titanium-AZ31 magnesium alloy: Characterization and simulation. Eng Fail Anal 131:105799
25. Stephen Leon J, Jayakumar V (2019) An investigation of analytical modelling of friction stir welding. Int J Mech Prod Eng Res Dev 9:179–190
26. Alderucci T, Borsellino C, Di Bella G (2022) Effect of surface pattern on strength of structural lightweight bonded joints for marine applications. Int J Adhes Adhes 117:103005
27. Di Bella G, Alderucci T, Borsellino C, Miranda R, Valenza A (2022) Comparative analysis between co-curing and adhesive bonding of glass-epoxy composite laminates and AA5083 aluminium sheets for Maritime application: effect of surface pattern. J Adhes Sci Technol. https://doi.org/10.1080/01694243.2022.2054603
28. Xu J, Yin Y, Davim JP, Li L, Ji M, Geier N, Chen M (2022) A critical review addressing drilling-induced damage of CFRP composites. Compos Struct 294:115594
29. Adams RD, Comyn J, Wake WC (1997) Structural adhesive joints in engineering. Chapman & Hall, Londono
30. Renart J, Costa J, Sarrado C, Budhe S, Turon A, Rodríguez-Bellido A (2015) 5—Mode I fatigue behaviour and fracture of adhesively-bonded fibre-reinforced polymer (FRP) composite joints for structural repairs. In: Vassilopoulos AP (ed) Fatigue and fracture of adhesively-bonded composite joints, Woodhead Publishing, Sawston, pp 121–147
31. Panfiglio S, Di Bella G, Proverbio E, Cicala G, Sarasini F, Buffa G, Visco A, Calabrese L (2022) Innovative and sustainable materials for naval applications through national coop-erative research: the experience of the THALASSA project. In: 20th international conference on ship and maritime research (NAV2022). ATENA, Genoa, pp 2A/16
32. Boyd SW, Blake JIR, Shenoi RA (2004) Integrity of hybrid steel-to-composite joints for marine application. Proc Inst Mech Eng, Part M: J Eng MaritE Environ 218(4):235–246
33. Kumar N, Mishra R, Yuan W (2015) Friction stir welding of dissimilar alloys and materials, 1st edn. Butterworth Heinemann, Oxford

Surface Functionalization of Metallic Biomaterials: Present Trend and Future Perspectives

Giovanna Rotella, Vito Basile, Pierpaolo Carlone, Jessica Dal Col, Luigino Filice, Leonardo Orazi, Luca Romoli, Felice Rubino, and Maria Rosaria Saffioti

Abstract Surface functionalization is emerging as one of the most promising methodologies for properly improving surfaces, especially for biomedical applications. The possibility to tune surface properties improving the prosthesis performance and their interaction with the human environment represents a challenging research

G. Rotella (✉)
Department of Management, Finance and Technology, LUM University Giuseppe Degennaro, Casamassima (BA), Italy
e-mail: rotella@lum.it

V. Basile
CNR-STIIMA Institute of Intelligent Industrial Technologies and Systems for Advanced Manufacturing, Bari, Italy
e-mail: vito.basile@stiima.cnr.it

P. Carlone
Department of Industrial Engineering, University of Salerno, Salerno, Italy
e-mail: pcarlone@unisa.it

J. D. Col
Department of Medicine, Surgery and Dentistry, University of Salerno, Scuola Medica Salernitana, Salerno, Italy
e-mail: jdalcol@unisa.it

L. Filice · M. R. Saffioti
Department of Mechanical, Energy and Management Engineering, University of Calabria, Calabria, Italy
e-mail: l.filice@unical.it

M. R. Saffioti
e-mail: mariarosaria.saffioti@unical.it

L. Orazi
Department of Sciences and Methods for Engineering, University of Modena and Reggio Emilia, Reggio Emilia, Italy
e-mail: leonardo.orazi@unimore.it

L. Romoli
Department of Civil and Industrial Engineering, University of Pisa, Pisa, Italy
e-mail: luca.romoli@unipi.it

area. The paper reports the most used surface functionalization for metallic biomaterials highlighting limitations and advantages of such technologies on the actual industrial panorama.

Keywords Surface functionalization · Metallic prostheses · Biomaterials · Biomedical implants · Multifunctional surfaces

1 Introduction

Biomedical implants improve the quality of life for millions of people every day. The development of modern medicine and its technological improvements have led to an increase in the diversity of biological materials [1]. Biomaterials are not a new conceptual field. Linen for stitching, gold and iron for dental applications, and wooden toe replacements were made since ancient times. In another case, some materials such as teflon, silicon, steel and titanium were used after World War II. Thus, a biomaterial is any substance or a complex of several substances, whether natural or synthetic, that can be used as part of a system or alone for a period of time or permanently, to treat, enhance or reduce failure, to replace tissue or organs in the human body [2]. They can be classified as permanent or temporary materials that are compatible with categories such as tissue engineering and synthetic materials [3]. The term biocompatibility is defined as the ability of a material to work with an appropriate host response in a given application. It defines that substances or products derived from them must not cause cell death or chronic impairment of tissue or cell function.

Biomaterials can last longer and must not fail until the individual dies. Therefore, the minimum years of service for elderly patients are 15–20 years, and the years of service for younger patients are more than 20 years. Three key factors are critical to successful implantation: (i) the mechanical, chemical and tribological properties of the biomaterial; (ii) the biocompatibility of the implant; (iii) the physical health of the recipient and the surgeon's skill. The above criteria for currently used materials suggest that although these materials work reasonably well in human systems, it was found that they generally fail in about 12–15 years. This led to reconsider additional surgery to restore the function of the implanted system. The reasons for failure are varied, including mechanical, chemical, tribological, surgical, manufacturing and biocompatibility issues. Implants must not only be biostable with respect to degradation and cytotoxicity, but they must also meet any biological criteria for structural biocompatibility. In other words, the shape and design of the implant

F. Rubino

Department of Chemical, Energetic and Mechanical Technology, Universidad Rey Juan Carlos - Campus de Móstoles, Madrid, Spain
e-mail: frubino@unisa.it

structure must be adapted to the properties of the tissue being replaced, favoring for example, the osseointegration process [4].

The osseintegration can be considered the successful marker of an orthopedic or dental implant. The osseointegration was originally defined as "the direct structural and functional connection between living bone and the surface of the artificial implant" [5]. Currently it has been accepted that osseointegration is a pivotal process of fixation and integration of cementless implants, thus an ever increasing commitment is spent in the development of novel strategies capable to accelerate and enhance it. This process begins immediately after surgery and implant placement [5, 6] and occurs in three step:

- Initial tissue response: it is driven by surgical trauma, it starts few hours after surgery and ends within few days. This phase consists of an initial inflammation with the activation of the complement system and the recruitment of specific immune cells, such as neutrophils and macrophages, concomitantly with the secretion of pro-inflammatory cytokines and the release of growth factors. Calcium ions and serum proteins adhere to implant surface and with platelets and fibrin matrix form a blood clot [7]. The proteins coated on the surface may act as a chemotactic signal for cell migration and successively sustain cell proliferation [8], whereas fibrin matrix becomes a sort of "tracks" for cell migration and attachment [9]. Leukocytes, mesenchymal stem cells, neutrophils and macrophages migrate to the implant and the latest adhere to the implant surface where they provide to the removal of eventual contaminating pathogens, necrotic cells and the blood clot [10, 11] paving the road to the second phase.
- Peri-implant osteogenesis: it occurs between the first and the second week after surgical trauma. The angiogenesis and osteogenesis are the pivotal process of this phase. Angiogenesis occurs in the space between the bone and the implant surface, while new vessels are forming, growth factors and cytokines address mesenchymal stem cells differentiation into osteoblasts in the area adjacent the implant. The osteoblasts produce the primary bone tissue consisting in a fibrillar non collagenous extracellular matrix rich in calcium, phosphorus, osteopontin and bone sialoprotein [12, 13]. At this point, it is possible to distinguish two types of osteogenesis: the contact one and the distance one. In the contact osteogenesis mesenchymal stem cells adhere directly on implant surface and bone formation starts from this point. Conversely, when mesenchymal stem cells migrate along fibrin matrix and the osteogenesis orientation is from bones or tissues surrounding the implant forward the implant itself, it is called distance osteogenesis. However, these two processes can occur contemporary and interact to each other [14].
- Peri-implant bone remodeling: after almost fifteen days from surgery, the final step starts when the space between bone and implant is filled by newborn bone. Bone apposition and remodeling characterize this phase. Bone remodeling begins in the primary osteoid. Osteoclasts direct the remodeling process from immature bone to highly mineralized lamellar bone by binding to the mineralized collagen matrix. Osteoclasts resorb the newly formed bone to eliminate the microcracks and optimize the surface for lamellar bone [15] creating a zone where the bone is

deposited directly on the implant surface. Osteoclasts and osteoblasts cooperate in a coordinate way, and the fragile provisional woven bone transforms gradually into parallel fiber bone and then into the lamellar bone. This dynamic process exists continuously over 1 year or longer, which is necessary for long-term fixation [6, 16, 17].

Several factors can affect the whole process and they depend on both, the molecular and cellular microenvironment of the bone-implant interface and the intrinsic characteristics of implant itself.

The environmental factors include loading conditions, host bone properties, interface distance, the concentration of local osteoblast and osteoclast, and systemic illness (diabetes, rheumatoid arthritis, cancer and smoking) [18–20]. The second aspect consists of materials; surface coating; topology; macro-, micro-, and nanostructure of the implants, and so on [21].

In line with these considerations and thank to the increasing knowledge in cell and molecular biology, materials science, chemistry, and engineering we have assisted to an evolution in the fabrication of biomaterials. Indeed, the first generation biomaterials were developed to combine the functional features to acceptably meet the biocompatibility. In particular, the biomaterial was required to be safe without any detrimental behavior of the surrounding biological environment. In this context the inertness of the materials was consider very important. The second generation biomaterials can be considered an advance in the first generation. The driven idea was to generate implants or device able to develop an uninterrupted reaction with the adjacent tissue, therefore the bioactivity became the most important characteristic. In addition, biodegradable materials such as polymeric biomaterials were also evolved in that period. Further, the expanding state-of-the-art gave rise to the fabrication of the third generation biomaterials, intending to stimulate the regeneration of functional or living tissues.

In this regard, surface functionalization of biomaterials is a potential solution not only to secure the biomaterial's surface against harmful reactions and elements and to improve its existing attributes/properties remarkably, but also a strategy to enhance the responsiveness of the damage tissue accelerating the healing process.

Among the large family of biomaterials, metallic biomaterials are chosen herein because of their wide range of applications in musculoskeletal implants, such as artificial hip joint and knee prostheses, screws, plates, pins, intramedullary fastenings parts, and dental implants [22].

Along with metals, technologies widely employed for surface functionalization are described in this work highlighting their limitations and potentials. The actual challenge of fabricating high performance implants by surface functionalization is also analyzed here with the aim to also highlight future trends in biomedical surface manufacturing.

2 State of the Art

Biomedical components made of natural or synthetic materials are often used as implanted biological structures to replace missing or damaged biological ones in humans or to improve their quality of life [23, 24]. The elderly are diseases such as joint pain and arthritis, leading to an increased demand for artificial devices made of biomedical materials to replace dysfunctional tissues [25]. Therefore, materials with biological functions have attracted great interest in recent years. Biomedical materials can be used in various parts of the human body (Fig. 1) [26–30].

For example, implants for replacing knee and hip joints place high demands because osteoporosis, arthropathy and trauma can lead to pain or loss of tissue functions [31]. For decades, great efforts in research has been devoted to the production of biomaterials since those used for implants must have many concurrent characteristics, such as sufficient mechanical properties, corrosion resistance, excellent tribological properties, biocompatibility, osseointegration and non-toxicity [32]. The medical goal of a biomedical material is the most important factor to consider in its design and development. After implantation of a biomedical prosthesis, various reactions occur at the interface between the living host tissue and the prosthesis. These responses define the biocompatibility of the implant, which in turn affects its success [31]. In order to be biocompatible, materials containing toxic elements are not expected to be used in biomedical materials [33]. Therefore, it is particularly important to handle non-toxic and biocompatible components in the production of biomedical materials [34]. The mechanical properties of biomedical materials now determine

Fig. 1 Example of different types of medical devices in human body
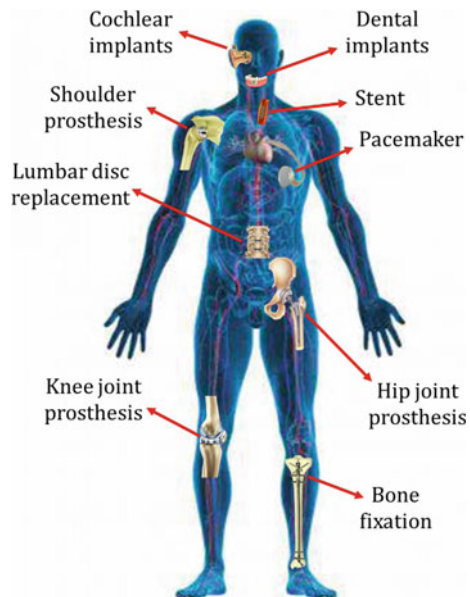
which implants are suitable for which purposes. The tensile strength, fatigue strength, elongation, and elastic modulus of biomedical materials are critical for load-bearing applications in hard tissue implants. For example, the elasticity of implant materials depends on their strength [35]. In addition, the corrosion and wear resistance of the implant affects its service life. Implants in vivo have limited corrosion and wear resistance, turning into premature wearing and/or release of inappropriate metal ions, leading to allergic and cytotoxic reactions [36]. Therefore, the developed biomedical materials should have significant wear and corrosion resistance properties to prolong the lifespan of implants in the human body. Finally, the most important criteria for the use of orthopaedic implants are excellent antimicrobial and osseointegration properties, which basically refers to the establishment of reliable contact between adjacent bones and the implant without the formation of fibrous tissue or infection [37]. Under functional load, effective osseointegration is defined as the absence of relative motion between the surrounding bone and the implant [38]. Therefore, biomedical prostheses must have suitable surfaces to effectively integrate with the surrounding bone.

Due to the above considerations, researchers have developed a variety of metallic biomaterials for orthopedic applications such as scaffolds and hard tissue implants [39]. Stainless steel, magnesium and its alloys, cobalt-chromium alloys, titanium and its alloys are by far the most commonly used metallic biomedical implant materials [40]. Biomaterials have been developed using a variety of advanced manufacturing techniques, including powder metallurgy, arc melting, friction stir technology, and additive manufacturing [41].

It is critical that material surfaces that are fully exposed to living organisms must be biocompatible. Therefore, it is crucial to modify the surface properties in terms of chemical, mechanical, biological and morphological properties. The goal of implant surface engineering is not only to meet criteria for avoiding adverse effects of implant materials on adjacent tissues, but also to enhance the interaction of specific materials with living matter. Surface modification of biomedical devices has become increasingly popular in recent years. The goal of many techniques in materials processing is to improve corrosion resistance (preventing the release of toxic elements into the body), wear resistance, biocompatibility (through the addition of additives such as nano-hydroxyapatite or ceramic oxides) and microbial properties. Various parts of the human body, such as shoulders, hips, joints, bones, etc., can be treated with biomaterials. These biomaterials are exposed to the body's fluid environment after implantation [42]. In general, the interaction between the implant surface and the human body dictates the biomaterial classification as illustrated in Fig. 2.

A biotolerant material is characterized by the formation of a fibrous layer while a bioinert material does not interact with the surrounding environment which, in turn, chemically reacts with a bioactive material. Finally, a biodegradable biomaterial degrades in time releasing into the bone tissue.

The processing of biomaterials is a difficult task as it requires not only mechanical properties but also the preservation of unique properties such as the shape memory

Fig. 2 Classification of biomaterials based on different interactions with human body
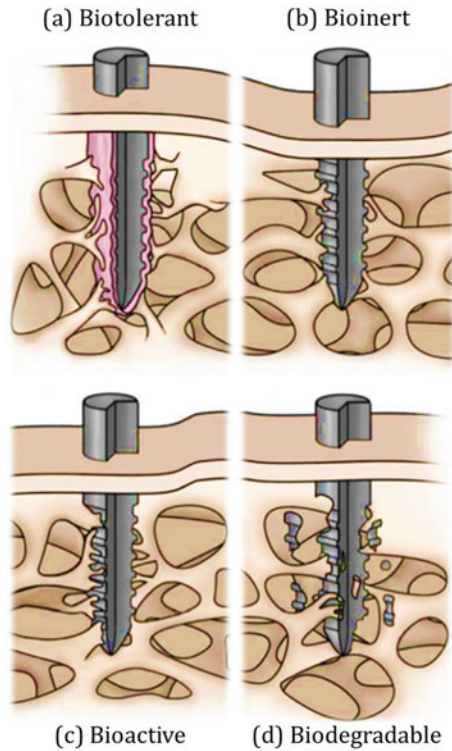
effect in shape memory alloys (SMA). Techniques work with intense plastic deformation to refine the grains of the material being processed. Compared with coarse-grained materials, ultrafine-grained materials generally have strong mechanical properties, high wear resistance, high corrosion resistance, and excellent biocompatibility. Ultrafine-grained materials, especially micro and nano-grained materials, have fewer atoms per grain and therefore more surface atoms, resulting in higher surface energies. As a result, bone cells more readily adhere to the surface of these materials, leading to increased osseointegration. Furthermore, these surfaces have been shown to prevent bacterial adhesion and reduce biofilm formation [43].

2.1 Metallic Biomaterials and Need for Functionalization

In many ways, the use of metals in the body has accompanied and driven advances in medicine in the twentieth and twenty-first centuries. Medical devices often require metals because they have mechanical properties required for many applications that cannot be replicated by other biological materials. The human body is essentially a fatigue machine, producing millions to tens of millions of stress cycles in specific

locations each year. For example, at 70 beats per minute, the human heart contracts about 37 million times a year, while a typical person walking 10.000 steps per day (5.000 steps per leg) puts pressure on the joints about 1.8 million times a year. These pressures can be very large, resulting in pressures that can reach hundreds of megapascals. Cyclic loading can lead to fatigue failure modes, persistent wear mechanisms, the potential for mechanically assisted corrosion mechanisms, and other effects. No other class of biomaterials can cause as much stress and degradation as metals. Metallic biomaterials provide the medical device community with a large and successful toolkit of alloys to perform many desired functions, and new alloys continue to be explored. These facts are likely to remain true for decades to come, and metals and alloys will remain an important part of the biomaterial recipient for the foreseeable future.

The adaptability of metals and alloys for bone repair and dentistry dates back thousands of years. In 1959, Bechtol, Fergusson, and Laing [44] provided an excellent overview of the development and use of metals in the human body during the first half of the twentieth century. This monograph provided an overview of many concepts and research directions related to metal biomaterials, many of which are the subject of ongoing in vivo research. Wire for internal fracture fixation was explored as early as 1775, and tests on dogs with platinum, gold, silver and lead in 1829 showed promising results. As early as 1908, people began to study the cell's response to metal fragments. Furthermore, co-implantation of copper and zinc were demonstrated to induce cyclical muscle contractions.

Early research identified scientific issues including corrosion of magnesium (Mg) alloys and their ability to induce bone formation or inhibit cancerous tumors, as well as copper (Cu), silver (Ag), and other elements that can limit infection. By the 1920s, major advances in metallurgy began with stainless steel (AISI-302, AISI-304, AISI-316 and AISI-317 versions) and Stellite and/or vitalium (cobalt-chromium-molybdenum CoCrMo alloys) introduced for use in internal fracture fixation devices (screws, plates).

Titanium and its alloys were also discovered in the late 1950 and 1970s for their excellent strength, corrosion resistance, and biocompatibility for various medical device applications, and were subsequently introduced into medical devices. Platinum-related alloys (eg Pt-10% Ir for electrodes), gold (Au–Cu alloys for dentistry), silver amalgam (Ag–Hg amalgam), etc. have been used in various applications, for a decade or more, and has resulted in significant improvements in the health and quality of life for millions of patients.

Due in part to the passage of the Medical Device Amendments of 1976 [45] and the limited number of alloys with the right combination of mechanical, corrosion and biocompatibility properties, only a limited number of alloys are currently used in the human body. Experience with the main alloy bodies used since 1976 sheds light on the safety and effectiveness of these alloys in most applications. It also raises new questions related to the degradation and interactions between organisms and biomaterials, including immune responses, hypersensitivity reactions, and allergic reactions, which are often multifactorial and interacting degradation processes.

The main alloys in use today include metals intended for indefinite use in the body (permanently implantable) and those intended to be temporary, degrade over time, or biocorrosive (biodegradable alloys). Permanently implantable alloys are primarily used in various medical devices currently available, while biodegradable alloys are being developed or used in a small number of approved applications.

The three main permanent implant alloy systems used for various medical devices in the body are: (1) stainless steel, mainly 316L stainless steel, (2) CoCrMo and (3) titanium and its alloys. Other permanently implantable alloys include Pt, Au and Ag alloys. Degradable alloys considered include magnesium, tin (Sn), iron (Fe), and zinc (Zn) alloys. However, there are a variety of metallic elements that could serve as potential biomedical alloys. Some of the more promising are zirconium (Zr), niobium (Nb), palladium (Pd) and tantalum (Ta). There are other elements, such as rhenium (Re), molybdenum (Mo), and alloys of the two, which are beginning to be considered for medical devices. Recent research is evaluating these alloys, and while there may be some advantages in strength or other properties, the three main alloy systems described previously (stainless steel, CoCrMo, and Ti alloys) remain the workhorse alloys in biomaterials.

The main concern with degradable alloys is to find alloys that can withstand the applied stress and wear process until the body heals to the point where they are no longer needed, then corrode away and be absorbed and excreted by the body. Magnesium alloys are best studied [46].

This alloy is known to corrode rapidly in physiological solutions and the oxidation products are mainly relatively harmless magnesium oxide (MgO or $Mg(OH)_2$) and hydrogen gas, which can be problematic. Other alloy systems including Sn, Fe, and Zn are also considered as degradable alloys for biomaterial applications.

Alloys composed of Au, Ag, and Pt as noble alloys often use their electrical properties as electrodes, their valuable electrochemical properties to resist corrosion or degradation, and/or other properties that play a role in certain dental applications. Silver is also used for its antimicrobial properties, often as coatings, nanoparticles, or other methods of placing silver on the surface of medical devices. It is also used for amalgam in dentistry. Other alloys are also considered for their antimicrobial properties. These include alloys that corrode rapidly, produce significant reduction reaction products (active oxygen intermediates), and can also produce killing effects.

Stainless Steel, CoCrMo, and Ti have a variety of alloy systems that are widely used in in vivo applications. Stainless steel is used in surgical instruments, but importantly, in many medical devices, including screws, rods, and plates for bone fixation and spinal fusion instruments. Cobalt-chromium-molybdenum alloys are commonly used in applications requiring high strength, fatigue strength, and wear resistance.

CoCrMo is one of the most wear-resistant alloys known and has been used in full-joint applications for decades. Titanium and its primary alloys (Ti–6Al–4V) are used in dental implants and total joint replacements. This alloy has high strength and low modulus, making it particularly suitable as an interface for biological systems. The growth of bone into a porous titanium surface, called biofixation, is the primary way orthopaedic implants attach directly to bone.

For titanium implants, surface roughness is one of the most important surface properties to reduce osseointegration time, stimulate greater bone regeneration, and improve mechanical stability by interlocking the surrounding bone tissue with the implant. In fact, the modifications introduced by surface treatments developed for uncemented and intraosseous implants are based on empirical evidence that there is a range of surface roughness's that optimize osseointegration. Among the various surface treatments used on biomaterials in order to improve osseointegration and shorten healing time, sandblasting, acid etching, and a combination of the two (sandblasting + acid etching) are currently commonly used. Implants are often subjected to cyclic loading during their lifetime, so the fatigue resistance of materials plays a very important role in evaluating the long-term performance of the device [47, 48]. Furthermore, the surface condition of the implant is one of the main features affecting the fatigue performance, mainly the cracking stage. Surface factors that affect the fatigue life of implants can be broadly classified into three categories: (i) surface roughness or surface stress increase; (ii) changes in surface metal fatigue strength; (iii) surface residual stress state. In general, a notch in a loaded specimen accelerates the initial stage of crack propagation due to stress-increasing effects and triaxiality at the root of the notch, resulting in high local stress and material yielding lower capacity. On the other hand, introducing compressive residual stress on the surface (by sandblasting, thermomechanical treatment, etc.) can greatly increase the fatigue strength. Thus, although surface treatments applied to bone-engaging implants produced important improvements in tissue response, since treated implants suffered from residual stress, surface roughness, generation of defects, surface hardening introduced during treatment, the fatigue life may be significantly reduced from plastic deformations. Thus, it is necessary to functionalize the surfaces according to the specific need and applications.

To meet different clinical needs, different synthetic functionalization methods (mechanical, chemical and physical) for metal biomaterials have been proposed and validated in previous studies [48, 49]. In addition to these methods, nature has developed fascinating strategies over millions of years to specify nearly perfect multifunctional surfaces [50]. Biological materials and structures, determined by evolution, environmental constraints, and limited material availability, have unique properties that distinguish them from their synthetic counterparts. These natural functions and strategies have recently emerged as new sources of inspiration for creating multifunctional surfaces with high potential for biomaterial applications. In the case of bone implants, it is generally believed that osteoprogenitor cells migrate to the implantation site and differentiate into bone-forming osteoblasts. The biocompatibility requirement is that the material should integrate into the bone (i.e. osseointegration) [51]. Stainless steel and titanium alloys are commonly used for fracture fixation in clinical practice, and new bone formation can be observed on the surface of fixation devices made of titanium alloys. The natural TiO_2 layer minimizes the release of metal ions and unwanted body reactions, thereby improving the biocompatibility of titanium alloys [52, 53].

However, this native passive oxide layer cannot provide the desired osseointegration [48] so various surface functionalization methods have been proposed to

improve osteoconductivity or bioactivity. Surface properties such as morphology, roughness, and wettability are known to influence the response of osteoblasts to Ti implants [54].

Singer et al. Micron and submicron topographies on titanium implants were found to promote osteoblast differentiation and the production of osteogenic local factors [55]. There is a synergistic effect between the high surface energy and topography of Ti substrates, and micro- and sub-micron structural features are necessary for this synergistic response of osteoblasts [56]. Recently, taking inspiration from the natural hierarchical micro/nanostructure in rat alveolar bone, a combined hierarchical structure composed of micropits, interwoven, self-assembled TiO_2 nanotubes on the Ti surface was developed [57]. The larger surface energy and preferential hydrophilicity of the biomimetic micro/nanosurfaces can provide superior osteoblast attachment and growth, and thus better bioactivity and biocompatibility, compared to their smooth and purely micro treated counterparts. This biomimetic metal implant micro/nanofabrication has been successfully used in clinical studies for 12 months [58] and provides a new strategy for osteopathic applications of metal biomaterials.

2.2 Functionalization by Micro-Texturing

Micro-texturing is an effective solution to functionalize surfaces and enhance specific performance of parts in its working environment. Typical functional properties are wettability (hydrophilicity or hydrophobicity), tribological properties (low friction and wear), load capacity, optical properties (refraction, diffraction, and light absorption), adhesion, strength, etc. The effects of micro texturing on several surface characteristics have been widely investigated [59]. Many successfully applications of this technique have been found in different fields, from biomedical implants to high-performance mechanical components operating in tough and aggressive environments (impellers, aircraft engine components, sliding piston-cylinder, etc.). Micro-texturing is typically used to refer engineered surfaces characterized by single- or multi-array of micro features (grooves, holes, dimples or pillars/protrusions, channels, hairs, needles) at micro scale. Table 1 briefly summarizes functionalization and surface micro-textures.

Many surface micro-textures have been gathered by nature observation by nature. The shark skin has a 3D micro-ribs pattern which reduces the drag and turbulent wall shear stress. The Nelumbo nucifera (lotus) plant has super-hydrophobic leaves thanks to its particular surface micro-texturing made by two levels of surface roughness obtained by combining nano- and micro-texturing: nano-hairs on micro-pillars. Similar microstructures can be found on the surfaces of Dahlia flowers and leaves, with micro-pillars with superimposed nano-spheres, which enable the super-hydrophobic function.

Industrially, the most common surface micro-textures are:

Table 1 Functionalization by surface micro-texturing

Functions	Micro-texture
Tribological properties (low friction and wear)	Micro-dimples, micro-channels, micro-grooves
Hydrophilicity, adhesion	Micro-dimples, micro-channels, micro-grooves
Hydrophobicity, anti-fouling, anti-icing, self-cleaning, protection against pathogens	Micro-pillars, nano-hairs on micro-pillars (super-hydrophobicity)
Optical properties (refraction, diffraction, light absorption)	Micro- and macro-grooves and porosity
Biological properties: cell adhesion and proliferation, foster osseointegration of surgical implants	Nano- and micro-grooves and pores
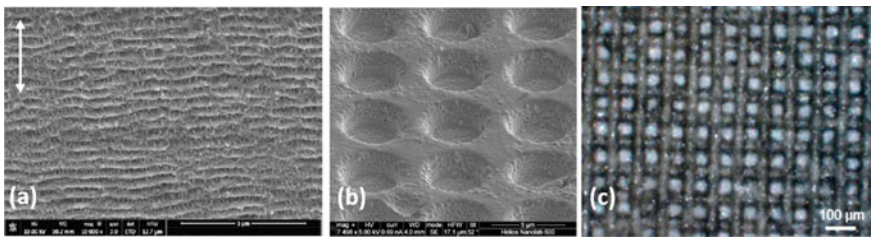
Fig. 3 Surface micro-texturing: **a** micro-grooves [60]; **b** micro-dimples [61]; **c** micro-pillars [62]

– Micro- grooves, channels and ribs: continuous grooves or ribs are realized on the target surface typically oriented along one or more directions or according to a designed geometrical scheme (Fig. 3a);
– Micro-dimples/cavities and micro-pillars/protrusions arrays: micro-features (dimples or pillars) are uniformly distributed according to a pattern (Fig. 3b, c).

The above-mentioned micro-textures can be combined together to obtain more complex multi-array surface micro texturing, thus obtaining enhanced function performance. In these cases, a hierarchy of micro-textures can be defined and, typically, micro-features are characterized by different scale, i.e. nano-features on micro-features. For example, the Dahlia and Lotus leaves have hierarchical structures, where micro-pillars enable hydrophobicity, but the nano-features (nano-hairs o nano-spheres) on the micro-pillars allow super-hydrophobicity.

Continuous oriented micro-textures change the roughness of the surface at values that comes from the geometrical parameters (type and shape, grooves depth/ribs height diameter, pitch, density/cavity or protruded area fraction, etc.). Discrete micro-textures obtained as an array of micro-features, are typically characterized by more geometrical parameters (micro-feature type and 3D-shape, dimple depth/ pillar height, array type, pitch between micro-features, etc.). In this latter case— arrays of micro-features—the surface micro-texture can be seen as a combination

of three main components: (i) micro-feature, which is the elementary component (dimples/pillar); (ii) array, that is the geometrical scheme of repetition of micro-features; (iii) hierarchy, intended as the combination of more arrays (i.e. nano-hairs on micro-pillars, micro-channels between micro-dimples).

Considering the complexity of the involved phenomena, the design of the surface micro-texture is a challenging step, often to be accomplished with a multi-modal (theoretical, numerical, experimental) and a multi-disciplinary (i.e. medical applications) approach. In many cases, the study of natural surface micro-textures has allowed to define design criteria and guidelines. From the theoretical point of view, each property, to be activated or enhanced, has its peculiar physical and chemical parameters, which can be translated in geometrical (morphological) parameters of the micro-texture. Hydrophobicity is promoted by micro protrusions having diameters and heights in the range of 20–30 µm and pitch between protrusions of 30–40 µm. Super-hydrophobicity is achieved adding micro- or nano-protrusions (i.e. hairs or needles, 500–800 nm diameter) on the base micro-protrusions (hierarchal micro-textures). Improved tribological properties are obtained by: (i) interposing a liquid lubricant between the interface components, thus promoting hydrodynamic friction; (ii) creating reservoirs (micro-dimples) for a stable liquid micro-film and for micro-debris trap; (iii) promote surface wettability and hydrophilicity. If interface components exchange significant loads, such as in artificial joint implants, then a suitable cavity area fraction, typically below 40%, is required to guarantee the load bearing capacity [62]. With these guidelines, several surface micro-textures have been proposed in literature. Usami et al. presented a surface micro-dimples array (Fig. 4) with diameter Ø 200–300 µm and depth 5–10 µm, and area fractions in the range 10–40% on aluminum alloy for casting (AC8A–T6) samples [63].

Dong et al. [64] proposed a micro-dimples array with diameter in the range 55–190 µm, depth of 1.5–9.5 µm, distance between micro-dimples of 37–58 µm (Fig. 5).

Dougherty et al. [65] fabricated a surface micro-texture with micro-dimples array (Fig. 6) having diameter in the range 100–400 µm, depth of 10–40 µm, distance of 500 µm and cavity area fraction up to 50%. In all works, improved tribological properties have been experimentally verified. Thus concluding that enhanced tribological properties can be achieved with a micro-dimple array with diameters of 100–400
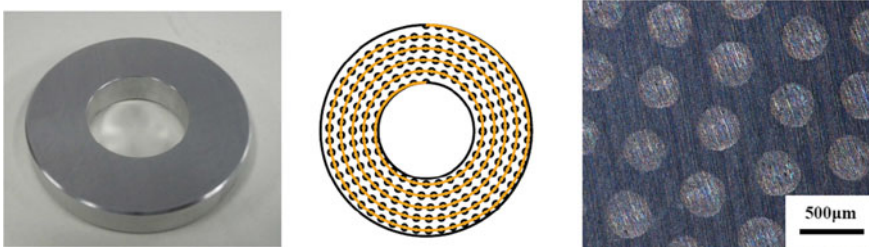

Fig. 4 Textures on aluminum alloy for casting (AC8A–T6) samples: Array of Micro-dimples diameter Ø 200–300 µm, depth 5–10 µm, area fraction 10–40% [63]
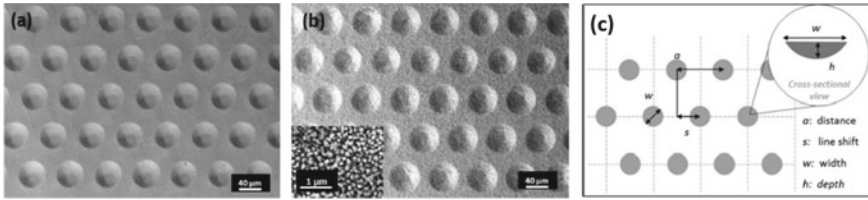
Fig. 5 SEM images of micro-features (dimples) on CoCrMo femoral head of hip joint implant: **a** with **b** and without (**a**) plasma carburizing. Dimple density of 37–58%; depth 1.5–9.5 μm; diameter 55–190 μm; pitch between dimples 37–58 μm [64]
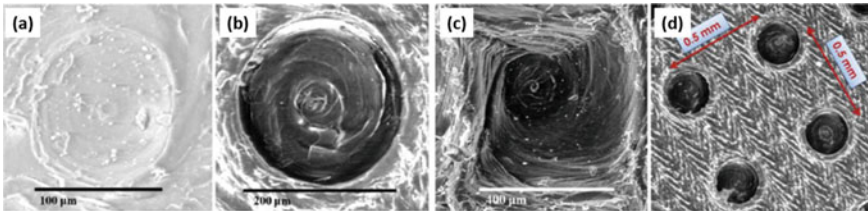

Fig. 6 SEM images of the surface micro-texturing on Ultra-High Molecular Weight Polyethylene (UHMWPE) via CNC micro-milling machining: **a** Dimple, diameter Ø 100 μm, depth 10 μm, Area fraction (AF) 3.1%; **b** Dimple Ø 200 μm, depth 20 μm, AF = 12.6%; **c** Dimple Ø 400 μm, depth 40 μm, AF = 50.2%; **d** Pattern and measurement of the distance between dimples, 500 μm [65]

μm, depth of 10–40 μm, distance between micro-dimples up to 500 μm, cavity area fraction up to 40–50%.

Starting from an accurate assessment of material properties and geometry of the surface micro-texture, the selection of the most suitable manufacturing technology and optimum machining parameters is crucial. Some of the most commonly used micro-manufacturing technologies for surface micro-texturing are reported below:

– CNC micro-milling machining is an important and reliable cutting process, which allow high dimensional accuracy and surface integrity improvement. Leveraging high-performance multi-axis control, this technology enables complex machining and challenging structures. Furthermore, it can be applied to a wide-range of materials. CNC micro-milling machining is a successful technology for surface micro-texturing [66].
– Laser Surface Texturing (LST) has been successfully applied for surface micro texturing, especially for tribological properties enhancement and mechanical sealing. Both accuracy and repeatability on micro-features are high but this technology has important limitations in terms of large-scale production and costs. Furthermore, distortions can occur due to the laser thermal treatment [67, 68].
– Micro-Electrical Discharge Machining (μ-EDM) has advantages and disadvantages similar to LST, but the application of this technology is limited to electrical

conductive materials such as metals. Furthermore, the thermal energy applied in machining can induce residual stresses and micro-cracks[68, 69].

– Micro-Electro Chemical Machining (μ-ECM) is a promising technology which implements a non-thermal process. Compared with μ-EDM, it is not affected by thermal drawbacks and it has a higher material removal rate (MRR). This technology is quite recent for these applications and more developments are required, especially on process parameters optimization [70, 71].

– Electron Beam Machining (EBM) and Focused ion beam milling (FIBM) are suitable manufacturing process for texturing having features at micro- and nanoscale, but it lacks in terms of machining time and resources [72].

– Chemical texturing (CT) is suitable for large area machining but it has the relevant drawback of low control of process parameters and variables. Its complexity limits its application for surface micro-texturing [59].

In many cases, surface micro-texturing must be accomplished on complex 3D curved surfaces. This can limit the application of some micro-manufacturing technology, since it requires high accuracy in motion and position control.

2.3 Functionalization by Laser Modifications

Laser can be used as a method to modify surfaces basically in three ways: phases and microstructural changes induced by laser hardening and remelting [73] onset of compressive residual stress through laser shock peening [74] and change of the 3D topography at the micro and nanoscale thanks to laser texturing [75] (Fig. 7).

Laser modifications can be extremely selective in term of the areas to be treated and advanced laser source controllers will usually guarantee a fine and dynamic control of the parameters. This permits the modification of the mechanical properties of the surfaces only where required such as, for example, areas where hertzian pressure reaches its peak, areas subjected to sliding contacts and subject to wear, notches root where fatigue cracks could nucleate and propagate.

Biomedical devices are intrinsically characterized by complex, free-form surfaces, in many cases they are customized and patient specific, this fits well with the flexibility that characterize laser processes.

Compared to other more conventional peening processes, laser shock peening offers the great advantage to be contactless, there is not surface contamination with the mix of glasses, ceramics and hard metals normally used in peening.

Biocompatibility aspects play a fundamental role for biomedical applications and laser shock peening can also alter the viability response of the surface.

Although the detailed mechanisms are still unclear, they are evidently correlated to the modification of wettability, electrochemical and corrosion properties of the treated surfaces [77]. These aspects are further enhanced when applied to degradable material like AZ31 magnesium alloy [78] where corrosion and mechanical properties can be strongly influenced by residual stress near the surface (Fig. 8).
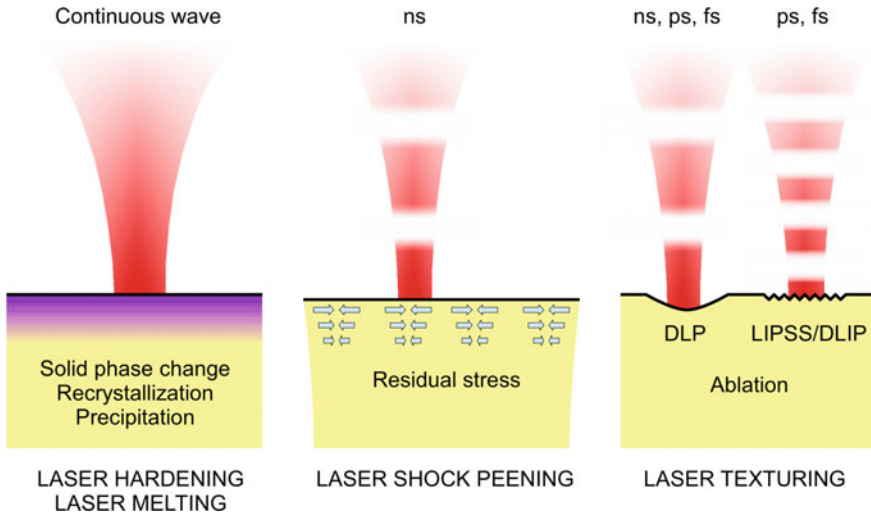
Fig. 7 Schematic of the main laser modification processes for metallic biomaterials**.** The first two methods increase mechanical properties as hardness, strength and fatigue limits and could be effectively adopted for the treatment of material and parts employed under several conditions as prosthesis and implants for joint replacement [76]

Fig. 8 Effect of LSP on fatigue life of Mg AZ31 alloy [78]
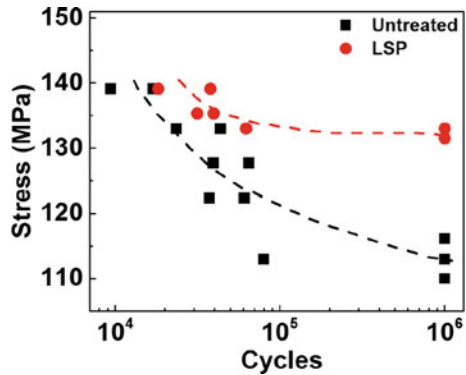
Laser ablation is the main mechanism involved in laser texturing. By using short and ultrashort pulsed laser the surface of metallic materials can be easily melt, vaporized and ionized to plasma condition. Phases transition occurs suddenly with a great efficiency in energy coupling, efficiency that roughly increases with the decrease of pulse duration. The strong spatial gradient of the temperature and the conditions inside the affected volume, very far from thermodynamic equilibrium, results in a series of micro-explosion with material removal.

The availability of highly efficient, more powerful and reliable laser source, and relatively cheap strongly affected the use of laser texturing for biomedical applications [75].

A rough classification of laser-based texturing can be done with respect pulse duration, we can refer to short or ultrashort pulsation regimes, the last one can be defined as the regime with "*a pulse with a duration shorter than the coupling time between the electrons (carriers) and the material lattice*" [79]. The use of ultrafast lasers is related to the generation of LIPSS, Laser Induced Periodic Surface Structure. LIPSS are topographic reliefs, with the presence of a linear pattern, with a periodicity lower than the wavelength of the employed laser light, roughly between 100 nm and 1 µm depending by frequency of the laser source, applied fluence and number of passes. This overcome the diffraction limit that affects far field laser propagation, LIPSS direction can be moreover controlled by a proper orientation of the polarization plane. Laser operating in ns regime can be used for Direct Laser Patterning (DLP) generating structures with dimensions of the same order of the focal spot, usually in the range between 10 and 100 µm. A further method for the treatment of surfaces is the use of DLIP, Direct Laser Interference Patterning, this method requires more complex devices to operate but guarantee high throughput for mass scale production, structures periodicity can range in between those the other two methods.

In case of orthopedic applications osseointegration is one of the main properties that affect the outcomes. The most part of the scientific literature concerns at the moment results in-vitro and with animal models. The majority of the metallic alloys employed in biomedical applications were tested. in particular Ti alloys, the most widely used class of alloys for orthopedic applications were investigated both for osseointegration [80–82] and for reduced bacterial proliferation [83].

Although their decreasing use as material for prosthetics and implants, AISI 316L and similar stainless steels were deeply tested in term of biocompatibility, cell viability and antibacterial properties [83, 84].

Laser texturing of NiTi was used to increase osseointegration of wires, nevertheless for this particular geometry mechanical interlocking can play a fundamental role (see Fig. 9), ex-vivo push-out results clearly show a strong increase for textured samples [85].
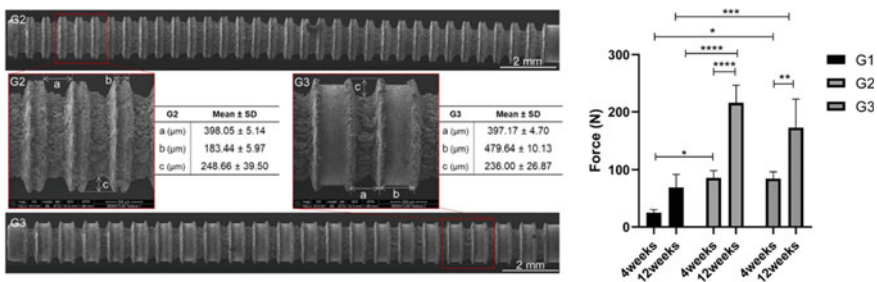

Fig. 9 Left) laser textured surface of 1.4 mm in diameter NiTi wires. Right) Push-out results for different groups, G1 represented untreated wire group (Adapted from [85])

The improvement of reendothelialization properties is one of the main objective in the manufacturing of stents, in-vitro and in-vivo tests already demonstrated the effectiveness of femtosecond laser treatment on cells adhesion, proliferation and migration of cells on AISI 316L [86] and CoCr [87] stents.

Actually, few clinical trials were performed mainly on dental implants [88]. These trials evaluate the effects on laser micro-texturing in term of different outcomes as: Marginal Bone Level (MBL); Peri-implant Probing Depths (PPD); Bleeding on Probing (BOP) and Marginal Tissue Height (MTH). Results are quite specific and oriented to dentistry and surgery audience but the preliminary conclusion is that laser micro texturing can slightly increase some of the controlled outcomes but authors agree that further study should be assessed for a real statistical significance.

2.4 Functionalization by Chemical Treatments

From chemical point of view, clinical applications of metal alloys are governed by the chemical composition of the materials surfaces. Chemical treatments currently employed are classified according to their goals and mechanisms of action. Therefore, it possible to distinguish chemical treatment for topographical modification, which aim to improve the physical interaction and promote the biological one (such as bone-metallic implant osteogenic processes), and chemical treatments for surface chemical tuning, where the surface composition of a device is modified at atomic/molecular scale to modulate the chemical and biochemical response of the tissues [48]. The chemical treatments falling in the former category are mainly subtraction processes, where the required topography is obtained by selectively removing material from the target surface. Electrochemical etching and electro-chemical polishing are the main processes, which are able to obtain rough or smooth surfaces ranging from nanometer to millimeter scale. In particular, these processes are mainly used as surface preparation techniques prior the application of a biomedical coating to improve the adhesion on the target substrate [89].

In the electropolishing process the metal sample and an electrode are placed in an electrolyte bath and connected to the opposite poles of a direct current generator. The passage of current causes the formation of an oxide layer on the surface of the metal sample, which then dissolve in the electrolyte solution. The degree of polishing and, hence, the roughness of the surface can be tuned by controlling the current intensity and the duration of the process. In fact, the total mass of removed materials is directly linked to the total charge consumed during the electropolishing. Composition of electrolyte as well as working temperature also influence the performance of the process [89]. Any metals or alloys can be processed by electropolishing, therefore, considering the high versatility of the technique, it has been employed on several metallic medical devices, like dental implants [90] and coronary stents [91–93]. Remarkable improvements in the adhesion strength of biomedical coating and corrosion resistance of stainless steel stents have been achieved after the electropolishing, by selectively modifying the roughness and eliminating the oxide impurities

in the former case [94], and by promoting the formation of chromiumrich protective oxide layer in the second case [93].

In chemical etching, layers of a material surface are removed under the action of chemicals, usually acids, alkalis or their mixtures [95]. Chemical etching proved to be more effective than other surface treatments, like mechanical polishing or sonication, to enhance the bond strength of biomedical coatings on the devices. Promising results have been obtained in case of polymeric coatings, such as high-density polyethylene (HDPE) or other polymers on the metallic and ceramic dental implants, where the increased adhesion strength is connected to the roughness and the surface porosities produced by the etching [95–98]. Chemical etching has been also employed for the functionalization of titanium surface to promote the adhesion and the growth of hydroxyapatite biomedical coating using different type of chemicals, like sodium hydroxide (NaOH), acids or alkalis [99–101]. Photochemical etching, where the effect of chemicals on the material is enhanced by the action of light generated from an arc lamp, has been successfully tested to treat chemically inert materials, e.g., Co-Cr alloys [102]. Obviously, chemical etching must be carefully used depending on the materials to be treated. Indeed, negative results in terms of flexural strength for alumina samples etched with acids or adhesion strength of resin cement coating on human teeth have been observed [103, 104].

Chemical surface functionalization is used to vary the composition of device surface without altering the surface topography in order to improve implant biocompatibility, bioactivity, and bone conductivity, as well as to promote specific cell or tissue response. The main processes used for the surface modification of Ti alloy (but not limited to them) are anodic oxidation, cathodic polarization, and electro-phoretic deposition. These electrochemical treatments have been widely used in the production of several commercial medical devices and other applications (e.g., color-coding for osteosynthesis plates and electropolishing of joint prostheses) [105].

In anodic polarization, the target metal is immersed in an electrolytic bath and connected to the anode of a power supply. By applying an electrical field, the diffusion of metal and oxygen ions is driven resulting in the formation and growth of an oxide layer on the metal surface [48]. Anodization is successfully used to produce films with increased oxide thickness, porous coatings, and desired crystallographic forms on surface of titanium alloys devices [106]. The thickness of the obtained TiO_2 film can easily be tuned by the growing parameters mainly depending on electrical polarization (current density, final voltage, etc.) and electrolytic bath composition. For instance, an increase in electrolyte concentration and electrolyte temperature were found to decrease the anodic forming voltage, the anodic forming rate and the current efficiency, while an increase in current density and in surface area of anode to cathode ratio leads to an increase in the anodic forming voltage, the anodic forming rate and the current efficiency [107]. By appropriate choice of these parameters, in addition, different surface properties can be obtained that can be exploited in various biomedical applications; namely:

– Colorization;
– Insertion of specific inorganic ions;

– Creation of specific crystalline TiO$_2$ structures;
– Cathodic deposition;
– Electrophoresis deposition (EPD).

By colorization, specific colors can be obtained on the titanium oxide by exposing the titanium and titanium alloy to low voltage electrical fields. It is used mainly for the identification of dimension or parts in prostheses, or medical devices. Phosphoric and sulphuric acids or other electrolytes have been commonly adopted as suitable for growing oxide films in the correct range for determining colorization effects on the titanium. Beside electrolyte composition and current voltage, the corresponding colors of the titanium oxide can vary according to the current density, electrolyte concentration and surface pre-treatment, which induce the occurrence of non-uniformities or stoichiometric defects in the oxide film [107]. The second cate-gory is employed to improve corrosion resistance by exposing the titanium surface to high voltage (above a specific threshold value), leading to anodic spark deposition (ASD). The formation of sparks causes the incorporation of ions within the oxide structure obtaining doped oxide surface as result of local melting and re-crystallization of the oxide film. It has been observed that the incorporation of Ca and P ions promoted the bone calcification, while Ag ions improved the antibacterial properties of the titanium implant [108]. Incorporation of Ca, P Ag and Pt ions by using electrolytic solution during the ASD process on Ti-based implants improved the biocompatibility and provide, at the same time, antibacterial activity [108]. The ASD also generates peculiar surface morphology on the oxide film with microscale porosities, which is advantageous for the bone consolidation [109, 110]. Creation of specific crystalline TiO$_2$ structures can be obtained by tuning the anodization process. Thus, different titanium oxide species can be produced, e.g., anatase and rutile (both tetragonal), or Ti$_3$O$_5$ and brookite (orthorhombic or tetragonal). Is has been observed that the presence of anatase phase reduce the bacterial colonization on the surface of the device [111].

In cathodic deposition, the target metal is placed in the electrolytic solution and used as cathode of an electrical circuit. Once the voltage between the cathode (the workpiece) and the anode is applied, several chemical reactions are triggered. Cathodic deposition is mainly used in biomaterial application to produce calcium phosphate coating, which has a crucial role in the bone/implant contact. The generation of Ca/P precipitates from the solution to form a thin film on the target metal depends on several factors. The main parameters governing the cathodic electrolytic deposition are in fact: (i) electrolytic bath composition, (ii) pH of the electrolyte solution, (iii) voltage and current density applied, (iv) process temperature and (v) deposition duration (which in turn depends on the passed current). By understanding the basic mechanisms and parameters involved in coating deposition kinetics, different functionalities can be achieved, such as the formation of crystalline and chemical structures at surfaces capable of improving and modulating bone response [112]. For instance, studies have pointed out that by adjusting the working temperatures and the treatment duration it possible to regulate the Ca/P coating thickness, while specific Ca/P phases (DCPD, OCP, TCP, HA) can be obtained by appropriate tuning of

pH, current density, chemical bath composition, and applied potential [112]. Finally, temperature and other parameters (e.g., voltage, pH and current density) can influence the crystallinity of the coating as well as the grain size and the porosity [113, 114].

Electrophoresis deposition (EPD) is used in biomedical application to produce ceramic or hybrid inorganic/organic coating on the medical devices, regardless their geometries or shapes. The technique is based on the movement of electrically charged particles immersed in a fluid: suspended particles move toward the cathode if they bear positive charge, and to the anode if they are negatively charged. Coating deposition is achieved via particle coagulation on the target surface. Coating thickness and morphology can be easily altered and that the corrosion resistance of the coatings is enhanced by adjusting the deposition voltage and process duration [115]. The process can be applied on any solid, including metals, polymers, carbides, oxides, nitrides, and glasses [116]. EPD has recently experienced a growing attention in the case of the titanium alloy devices to improve the bone/material interaction and bioactivity [116].

The limits in the spreading of EPD technique in biomaterials applications are related to the low density of the manufactured coatings, which require post-deposition treatments, like sintering or curing, to obtain a more dense material.

2.5 Coatings

Metal implants (mostly made in stainless steel, cobalt-chromium alloys, or titanium and titanium alloys) are used as orthopedic devices or prostheses being able to provide the suitable mechanical properties. The success of such devices is linked to the ability of the metal to create a strong interface with the bone and to be incorporated into the natural structure of the bone [117]. Deposition of various types of coating is a successful method to achieve this goal and has widely explored in the last decades. Calcium-phosphate coatings, for instance, enhance the mechanical attachment between the new bone and the implant, promote a faster growth of the bone and can protect the biological environment from the release of ions from the metallic substrate, hence increasing the longevity of the implant [117].

Surface coating techniques (thermal spray, physical and chemical vapor deposition, glow discharge plasma treatments, sol–gel technique) are employed as additive processes to modify the topography and/or the chemical composition of the sur-face of a bulk structure (also called substrate) and impart specific selective proper-ties to the material surface. Surface coatings are usually in the 10^{-6} to 10^{-3} m range depending on the specific process used. The choice of a specific coating deposition process depends on the type and the material of the coating to produce as well as the final application. In order to exploit the potential advantages of coating systems, they have to possess specific properties. The degree of crystallinity of the coatings is linked to their solubility within the physiological environment. Amorphous hydroxyapatite, for example, is more soluble in aqueous solution than crystalline HA and, therefore, has a higher rate of dissolution than the highly crystalline form [118, 119].

To enhance the bone bonding, and avoid loosening and failure of the implant, it has been suggested that coatings should be as crystalline as possible (approximately 80%); however, a certain degree of dissolution is beneficial to the bone forming due to the re-precipitation of calcium phosphate back onto the coating in the form of new bone. Thickness and roughness of coatings vary depending on the deposition process and the parameters configurations. Sputtering, sol–gel or vapor deposition can produce coatings ranging from nanometer up to 1 μm, while with plasma spray or other thermal spray process it possible to obtain coating 50 μm thick or higher [120]. The optimal value of coating thickness balance two competitive effects: thinner coating dissolve faster leading to a reduced longevity and risk of exposing areas of the substrate to the physiological environment, with potential release of metallic ions. Thicker coatings dissolve slower resulting the formation of a good interfacial bonding with the bone. However, they are more prone to generate high residual stresses and occur in internal failure. Roughness has a dramatic effect on the response of bone as well [121]. Human osteoblasts attach more readily to surfaces with a roughness less than 0.5 μm than to rougher surfaces (>2 μm), despite, rougher or more porous surfaces enhance the mechanical attachment of surrounding bone [122]. The adhesion strength of a coating is paramount for the effectiveness of the implants. The deposition method, the processing parameters and the coating/substrate materials pair are responsible of the resulting adhesion strength of the coating [123–125]. To enhance the coating adhesion, a boning layer is commonly applied on the substrate prior the deposition of the actual coating. Titanium oxide or zirconia, for instance, are used to improve the adhesion strength of hydroxyapatite coating [126]. Other mechanical properties, Young's modulus, residual stress and hardness, together influence the resistance of the coating and are paramount to prevent the internal failure of the coating [127].

In case of metal implants, the commonly applied systems are mineral or carbon-based coatings by using thermal spray process (TS). TS processes, such as plasma spray (PS), high velocity oxygen fuel spray (HVOF), or flame spray, are mainly used to produce hydroxyapatite-based mineral coatings on metallic surfaces (stainless steel, cobalt-chromium alloys, titanium and titanium alloys). Hydroxyapatite, indeed, has composition similar to the main component in bones and the coatings can promote the consolidation and the growth of bone tissue on the implant. Several thermal spray processes are currently employed in biomedical applications, and they operate on similar principles: powder particles are melted in the high temperature by flame or plasma, high velocity gas is used to accelerate the powder particles towards the substrate. On impact, the individual powder particles cool as splats, solidifying together to form the final coating. The substrate surface remains relatively cool during this process, generally reaching temperatures no greater than 300 K. It allows the substrate to retain its pristine properties. Thin or thick coatings can be obtained by changing the processing parameters and controlling the number of passes. The properties of the final coating differ from the starting powders: as the layers of splats build up, partially melted particles, oxides and pores can become trapped within the thickness of the coating. They consequently produce a multiphase structure, whose
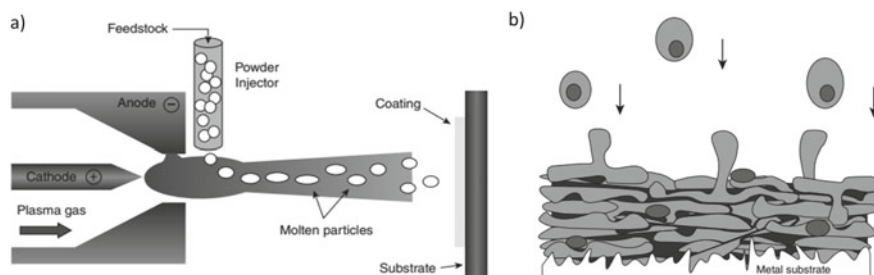
Fig. 10 a Representative scheme of plasma spray process; **b** schematic description of TS coating build-up

properties are influence by the composition and the distribution of all the phases (Fig. 10 reports a schematic representation of process and coating).

The most common method of producing coatings for metal implants is by plasma spraying. Hydroxyapatite is used as calcium phosphate precursor in the plasma spraying process to produce the bioactive coating. In vitro and in vivo studies of plasma sprayed hydroxyapatite coatings demonstrated the ability of the coatings to improve the bone-to-implant contact and the fixation of the implant [128].

Positive effect on the osteoblast growth has been observed [129, 130]. Two techniques are used: atmospheric plasma spraying, which is carried out in normal air, and vacuum plasma spraying, which is performed in a low-pressure inert gas atmosphere.

The latter is preferred because it reduces the in-flight oxidation of the particles, increases the particle velocity and allow obtained denser and uniform coatings. Numerous variables and factors can be modified to adjust the plasma spraying process allowing producing a wide array of coatings. Figure 11 shows an overview of the parameters affecting the plasma spray.

Amorphous hydroxyapatite is formed during the plasma spraying process due to the high temperatures and high cooling rate, resulting in crystallinities in the range of 65–70% [131]. Post-deposition heat treatment is a suitable method to control the crystallinity of plasma-sprayed hydroxyapatite coatings: treatment at 600/700 °C for 1 h raised the crystallinity of the coatings, while treatment at 700 °C or above converted almost all amorphous phases to crystalline phases [131]. Surface roughness of plasma sprayed hydroxyapatite coating is in the range of 5–30 μm, rougher than other deposition processes with a positive trend with crystallinity degree and particle size [132, 133]. Adhesion strength ranging from 8 to 80 MPa and Young's modulus of 5.5 GPa, which more closely resemble that of human bone, have been reported for the hydroxyapatite coating [131]. The plasma sprayed coating usually presents a multiphase structure with a number of distinct calcium phosphate phases, which differ from the pure hydroxyapatite and can weaken the coating. Heat treatments are suggested as suitable method to decrease the presence of these impurities [131].

Magnetron sputtering is also used to deposit bioactive coatings. It is an extremely versatile process able to deposit coating on different materials (polymers, metals and ceramics). The coatings are dense, homogenous and well adherent to the substrates.
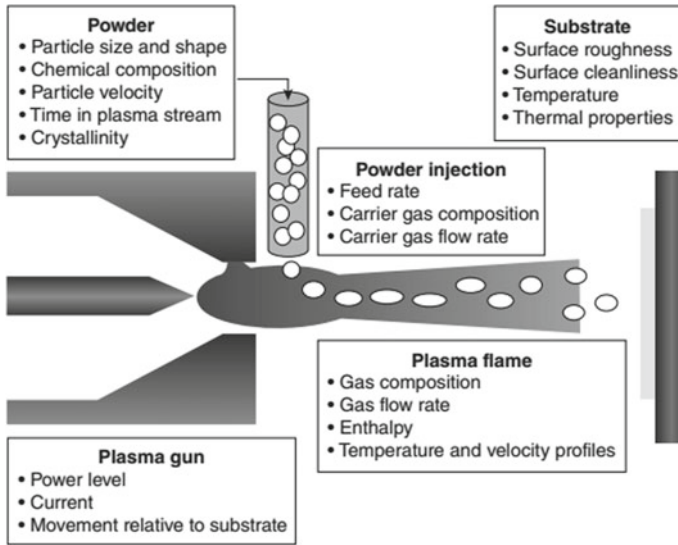
Fig. 11 Summary of the main parameters in PS process

Studies on coatings produced by magnetron sputtering indicated an enhanced bioactivity of the calcium phosphate coating and an improved osseointegration compared to plasma sprayed coating (Fig. 12) [134]. Other in vivo studies demonstrated an increase in the bond strength between bone and coated implants [135–137].

Fig. 12 Schematic representation of the magnetron sputtering process
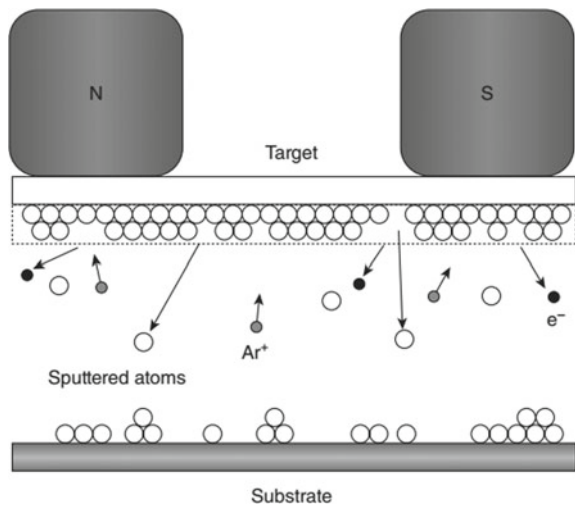
However, differently from plasma spray, it is very slow, with a deposition rate of 1–1.5 μm/h and can work only on small, flat and fine polished substrate. The coatings are thin, usually around 1 μm and never above 10 μm. In addition, the hydroxyapatite coatings are intrinsically amorphous and this, together with the very small thickness, leads to a rapid dissolution of the coating in biological conditions, failing to provide a surface for biological attachment. Substrate heating or post-deposition heat treatments have been suggested as methods to increase the crystallinity of the coating [138, 139]. These factors, together with the relatively higher costs, impede a wider diffusion of such a process, if compared to the plasma spray.

The deposition of coating by magnetron sputtering relies on the acceleration of positively charged ions on a target material under the action of a magnetic field. The ions are extracted from the target material from a plasma generated in an inert gas. These atoms are then deposited on the substrate, forming the coating. The magnetic field increases the sputtering of the target by confining the electrons close to the surface of the target and preventing them from recombining with ions near the walls of the chamber. The process is carried out in vacuum to avoid interaction of ions with the environment.

The physical and chemical surface properties of magnetron-sputtered mineral coatings can have a significant influence on biological performance. As deposited coating surfaces are very smooth with roughness around 30–50 nm [139]. The roughness can be increased, together with the crystallinity, by applying a heat treatment on the coating, reaching values in the range of 1–2 μm [140, 141].

Magnetron-sputtered hydroxyapatite coatings are characterized by a strong adhesion to the substrate over those using other coating methods, capable to withstand significant loads without showing signs of bursting after penetration of the indenter into the substrate [123]. Hardness of a coating was found to be approximately 10 GPa, while the Young's modulus of sputtered hydroxyapatite coatings was measured to be between 100 and 150 GPa [123, 139]. As mentioned, magnetron-sputtered coatings are relatively thin compared to plasma-sprayed deposits. Generally, magnetron-sputtered coatings range between 0.5 and 3.0 μm in thickness. Usually, coatings thicker than 1.6 μm have been shown to exhibit poor mechanical properties [123, 129]. The deposition rate for the hydroxyapatite target stands at 0.2–2.0 μm per hour depending on the sputtering conditions.

Other deposition techniques reported in literature to produced hydroxyapatite coating on metal implant are high velocity oxygen-fuel spraying (HVOF) [133], biomimetic deposition [142], Sol–gel deposition [143] and electrophoretic deposition [144]. Those processes are promising techniques, however because they are relatively slower and usually require a post deposition treatment to achieve a good consolidation of the coating, manufacturers prefer plasma spray over them, and a limited number of studies are available in literature dealing with their optimization for the deposition of mineral coatings.

3   Case Studies

3.1   Cell Adhesion and Proliferation on Severely Plastic Deformed Additively Manufactured Zr–702

In the context of surface changes and biocompatibility by combining severe plastic deformation processes with cell culture and additively manufactured metal materials a concrete application was performed [145]. In particular, the main objective was to evaluate the cell adhesion and proliferation on severely plastic deformed additively manufactured Zr–702, using the turning process under different environmental and process conditions by varying cutting speed and feed rate and working under dry and cryogenic state. Then, a cell culture of MC3T3–E1 osteoblast cells was seeded on the machined samples in order to assess cell adhesion and proliferation after 24 h and three days of culture. Finally based on the machined surface characteristics and the cells behavior was investigated the potential of machining process to modulate biocompatibility of the material.

As a new kind of biomaterial, the metal zirconium is becoming more attractive thanks to its properties as high corrosion resistance, low elastic modulus and magnetic susceptibility, good mechanical strength and often it could be used in hip and knee implants because of its satisfactory biocompatibility. Pure Zirconium is employed to encourage the osseointegration, thus it is important to properly treat the surface with the right processes in order to obtain a positive tissue response. Nowadays, the introduction of new technologies has meant that advanced manufacturing methods have come up, as the additive manufacturing technologies, which for example were used to produce such sample through laser powder bed fusion. In depth analysis, in particular a study performed by Aristizabal et al. [146], focussed on additive manufacturing parameters were carried out in order to achieve good mechanical properties comparable with the conventionally produced one. Assessing the cellular behavior, also in this case, through adhesion and proliferation of MC3T3 osteoblast precursor cells. However, it must be highlighted that additively manufactured products need to undergo surface finishing processes before being put into operation, especially in the biomedical field. Therefore, in an industrial perspective comes the necessity to evaluate the cell behavior on Zirconium after finishing operations, such as turning, finding the influence of process parameters and cells adhesion and proliferation.

More in detail, the sample used for the experimental campaign were Zr–702 bars with 10 mm as initial diameter. The cylindrical bars were produced by Selective Laser Melting (SLM). The optimum process parameters were defined based on the results of the previous work [146].

In Fig. 13 is reported the as printed surface shows typical additive manufacturing defects such as unmelted powder particles and balling. Turning tests have been performed using the following process parameters: 0.05 mm of depth of cut, three different speed and feed rate levels: 60, 75, 90 m/min and 0.05, 0.1, 0.15 mm/rev, at varying cooling conditions, namely dry and cryogenic. Afterwards, the arithmetical mean height (Sa), the maximum height (Sz) and the reduced valley depth (Svk) on
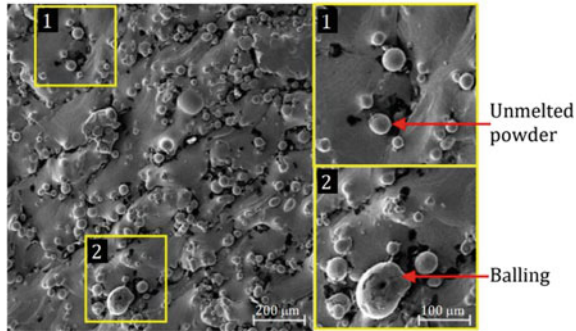
Fig. 13 High-magnification scanning electron microscope (SEM) of as printed Zr–702 [145]

the surface, were measured using a contact profilometer. Part of the samples were used for cell culture with a MC3T3–E1 preosteoblast cell-line to test the biocompatibility after surface modifications. The surface roughness trend after turning and at varying process parameters is visible in Fig. 14 where turning process significantly improved the surface quality. Concerning cell adhesion and proliferation the vitality of the seeded osteoblasts on the machined samples confirmed the biocompatibility and non-toxicity of the material.

Cell culture results for selected cases are visible in Fig. 15. In particular, a good cell adhesion favored by the high roughness conditions is observed on the as printed sample, but such level of roughness did not enhance the growth of the osteoblasts since the cell proliferation and cell size after three days did not show significant changes. Thus, it can be concluded that AP surface conditions are not suitable for long term applications. Regarding machined surfaces despite are less prone to cell adhesion during the early stage of the culture at the end (after 3 days) start a faster process of proliferation. Furthermore, the different topography obtained due to the several process conditions employed lead to different cell behavior in terms of adhesion and proliferation allowing to demonstrate that it is possible to modulate, with finishing parameters, the biomedical surface interaction with human cells.

3.2 Micro-Texturing of Mold Surfaces for the Fabrication of High-Performance Medical Components

In current artificial joint implants, titanium alloys components are typically employed as the structural components, for load bearing and bones integration, while polymeric inserts, as cartilages in natural joints, are generally used as interface components. High-performance polymers are preferred over other materials (ceramics or metals) due to the reduced friction coefficient and wear. These inserts allow a reduced risk of debris formation and biologic reactions such as inflammation, bone resorption
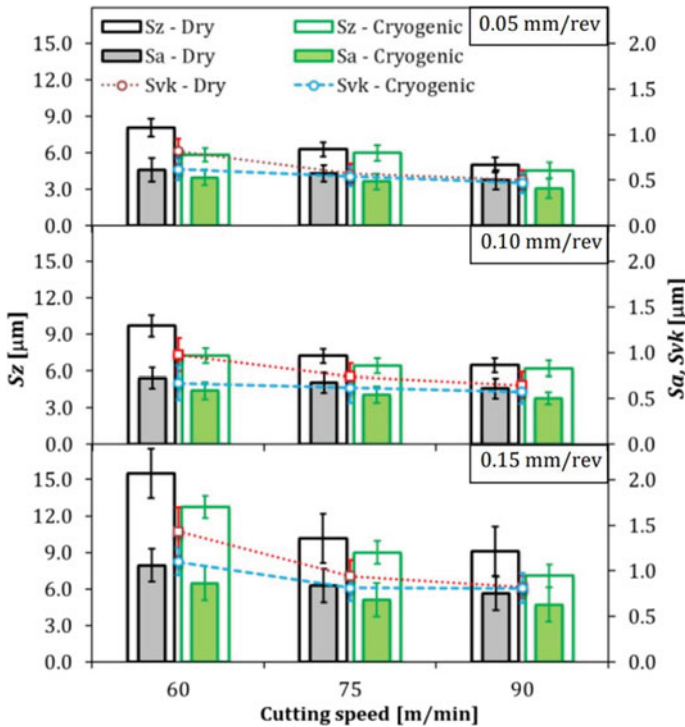
Fig. 14 Height (Sa, Sz) and functional (Svk) parameters on machined samples under dry and cryogenic cooling conditions at varying turning process conditions (the error bars indicate standard deviation) [145]

or periprosthetic osteolysis [147]. Common names of these components are: Radiocapitellum in elbow implants, patella prostheses in knee implants, acetabular cup in hip joint implants, humerosocket liner in shoulder implants. Main requirements for these components are: biocompatibility, low friction and wear, high load bearing capacity and stiffness.

Among biopolymers, Ultra High Molecular Weight Polyethylene (UHMWPE) has wide application. In fact, it has excellent resistance to stress and cracking, abrasion wear, chemical resistance, excellent dielectric properties and self-lubricating. Furthermore, the non-porosity of UHMWPE prevents the growth of fungi or bacteria. In order to extend the life of the artificial joint implants (Fig. 16), polymeric interface components should exhibit reduced friction and wear, by fostering the hydrostatic friction of the synovial fluid as lubricant in natural joints. The surface micro-texturing of UHMWPE interface components is a valid strategy to enhance the tribological properties.

From the manufacturing viewpoint, a successful approach is the manufacturing of molds with micro-texturing for injection molding [149–152].
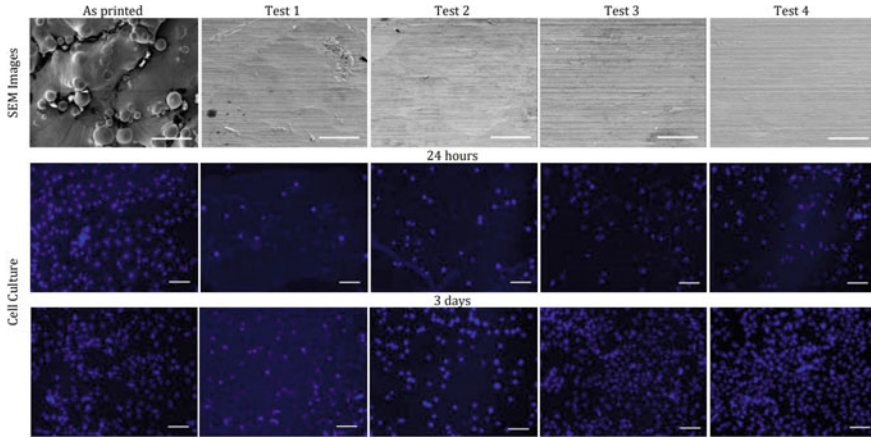
Fig. 15 SEM images of as printed and machined samples: tests 1 and 2 correspond to samples machined at 60 m/min, 0.15 mm/rev under dry and cryogenic cooling condition respectively; tests 3 and 4 correspond to samples machined at 90 m/min, 0.05 mm/rev under dry and cryogenic cooling condition respectively. Samples surface seeded with the osteoblastic MC3T3-E1 cells for 24 h and three days. The fluorescence micrographs illustrate the viability of the seeded and proliferated cells over the duration of the experiment (scale bar = 100 μm) [145]
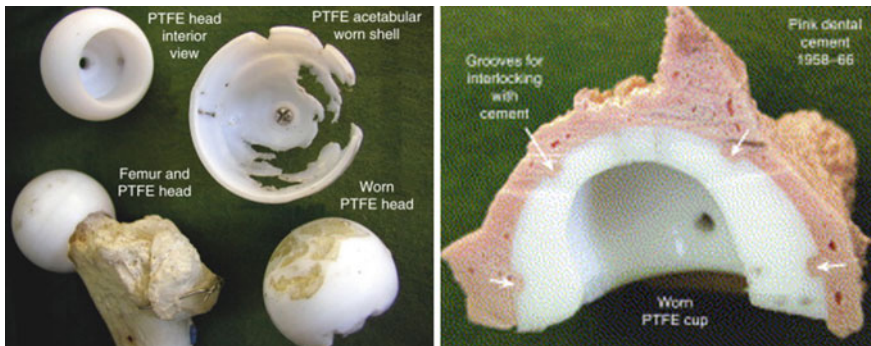

Fig. 16 Wear processes of a polymeric Acetabular cup in hip joint implant [148]

On Celanese GUR5113 UHMWPE samples via injection molding. Four different micro-textures (MT) were realized via micro Electrical Discharge Machining (μ-EDM) on a steel mold insert. The micro-textures were characterized by confocal microscopy. UHMWPE samples were then produced by micro-Injection Molding (μ-IM) and molded parts were characterized to assess the overall process-chain feasibility. Figure 17 shows the geometrical parameters of the micro-textures.

The mold micro-textures were fabricated via μ-EDM in milling mode by means of a Sarix SX200 machine. Tool electrodes adopted for the micro-milling are two tungsten carbide cylindrical rods with diameters of 0.4 and 0.15 mm, while the dielectric
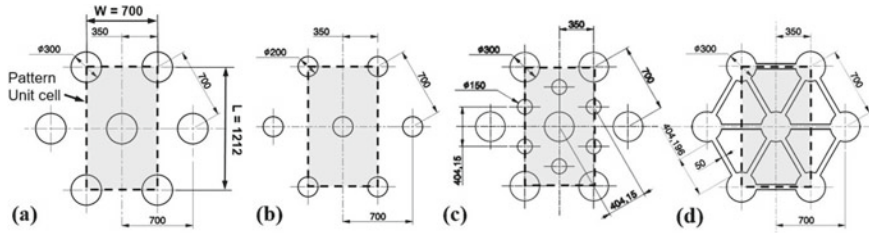
Fig. 17 Micro-textures and geometrical parameters (µm). **a** MT1; **b** MT2; **c** MT3; **d** MT4

fluid is a hydrocarbon oil. The µ-IM was performed by DesmaTec FormicaPlast 1 K machine. Profiles and surface roughness of inserts and samples were acquired via confocal microscope Zeiss CSM700. The Fig. 18 shows images of the steel mold insert and UHMWPE samples with surface micro-textures. Figure 19 reports the graphs of the errors on the micro-textures measured on samples.
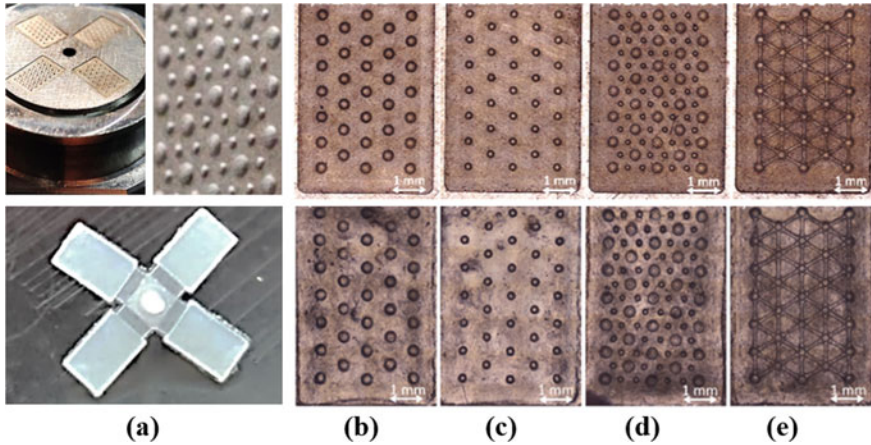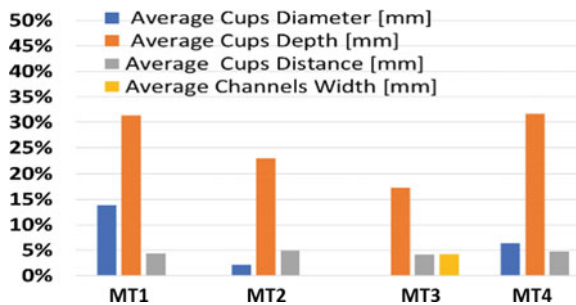

Fig. 18 Micro-textures on steel mold surfaces, HDPE and GUR5113 UHMWPE samples: **a** Steel mold and samples; Detail of the micro-textures: MT1 **b**, MT2 **c**; MT3 **d**, MT4 **e** [151]

Fig. 19 Errors on micro-features measured on UHMWPE samples [151]

The present case study investigates the manufacturing feasibility of a production process chain, combining μ-EDM and μ-IM, for fabricating parts with micro-textured surfaces for high-performance medical components. The experimental results show that μ-EDM is a valid technology for surface texturing at micro-scale of steel molds with good dimensional accuracy and surface roughness. The Celanese UHMWPE GUR5113 material can be processed but the process requires further optimization.

3.3 Biomolecules Surface Functionalization to Improve Osseointegration Process

Biomolecule surface functionalization exploit bone organic components to improve bone regeneration, such as extracellular matrix proteins (e.g. collagen) or peptide sequences for bone cell adhesion [153, 154], and bone growth factors for new bone formation [155]. In the preclinical models, other components have been evaluated, such as deoxyribonucleic acid (DNA) fragments for structural reinforcement [156] and enzymes involved in bone mineralisation [157]. Biomolecule immobilization onto metallic surfaces can be obtained mainly by physical adsorption, physical barrier entrapment, and covalent attachment [158].

In addition, the use of other natural compound, such as the self-polymerization mussel-inspired polydopamine (DOPA) has been preclinically investigated. It was found to form a thin and surface-adherent coating onto a wide range of inorganic and organic materials [159, 160]. The polydopamine coating can also further enhance subsequent surface-mediated reactions implementing the cell-adhesive, osteoconductive, and osteoinductive performance of Ti implants. Indeed, it was reported that the addition of Arginylglycylaspartic acid (RGD)-conjugated polymers, HA nanoparticles, bone morphogenic protein-2 (BMP-2) during the polymerization process of DOPA coating, results in functionalized surfaces able to induce the transition from mesenchymal stem cells to osteoblasts and to promote osteogenic differentiation and mineralisation [161]. Figure 20 summarizes the whole process [161].
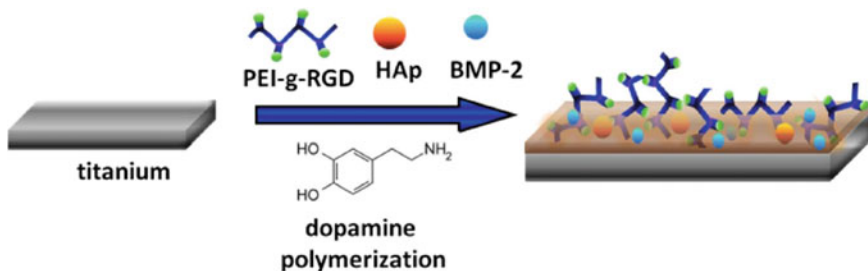

Fig. 20 A schematic illustration of dopamine-assisted immobilization of PEI-g-RGD, hydroxyapatite (HAp) nanoparticles and rhBMP-2 on a titanium substrate

In addition, considering that the natural bone is mainly composed of organic proteins and inorganic CaP-based materials, where the extracellular organic matrix consists of 90% collagenous proteins and of 10% non-collagenous proteins and HA, the development of composite coatings has become a hot topic for implant surface functionalization. Several independent studies demonstrated superior properties of the biomolecules–CaP composite coatings over the individual components together with the opportunity to overcome technical problems related to the difficult control of loading efficiency and of release kinetics of the superficially adsorbed biomolecules [162, 163]. For example, the ductile properties of collagen can compensate for the poor fracture toughness of CaPs [164], and also promote the CaP coating adhesion, the cell adhesion and thus the fixation of the metallic implant [158]. Immobilization of growth factors such as bone morphogenetic protein (BMP)-2 and trasforming growth factor (TGF)-β to the CaP coating significantly enhanced the osteoconductivity and bone regeneration at the tissue–implant interface [165]. Moreover, CaP or collagen coating can help to create a delayed and sustained delivery profile or a higher stability of the growth factors and DNA [166]. As for the coating technologies of the organic–inorganic composite coatings, electrolytic deposition (ELD), spin coating, and biomimetic coating methods have been used to generate homogeneous collagen–CaP composite coatings onto metallic implants [164–167], but these coating procedures are time-consuming and have poor control over the produced coating thickness [168]. The electrospray deposition (ESD) is among the most promising techniques because its low processing temperatures allow for simultaneous deposition of both biomolecules and CaP [169]. This method incorporates the growth factors directly into the inorganic layer, which is conducive to a sustained biological activity for a considered period of time. However, the reproduction of the mechanical properties and the intricately structured organization of bone have not yet been achieved for the bioinspired organic–inorganic composite coatings [170]. Moreover, the high cost of pure type I collagen and the risk associated with the animal primary source of extracted collagen restrict its applications [171]. Therefore, the organic–CaP composite coatings could provide an advantage over other materials for bone repair application, but further clinical studies are required to validate its effectiveness.

3.4 Laser Texturing and Analysis of Cellular/Surface Interaction for Dental Applications

Laser modifications of metallic biomaterials is a process involving several different physical aspects, by these quantum physics, electromagnetism and optics, chemistry, fluid dynamics, thermodynamics and metallurgy. On the other hand, interaction between living cells, bacteria, virus and treated surfaces are of the same order of complexity so, in the most part of research works activities are mainly experimental following the trial and errors paradigm.

The simulation of the interaction between cells and artificial surfaces is of utmost importance in the field of metallic biomaterials. Therefore, many modelling studies have been devoted to better understand how cells, interpreted as colloid particles, behave in close proximity with textured surfaces. The interpretation of such peculiar surface feature is believed to play a key role in adhesion/repulsion phenomena which can significantly influence the performance of biomedical devices.

In the case of individual colloidal particles interacting with perfectly flat substrates, the effects of surface chemistry have traditionally been described by the Derjaguin–Landau–Verwey–Overbeek (DLVO) theory, accounting for interplay between Lifshitz–Van der Waals and electrostatic forces. The more recent extended DLVO theory also accounts for acid–base (AB) interactions, which are considered the dominant contribution to attractive interactions [172, 173]. The Derjaguin approximation typically employed for DLVO representations of extended objects, however, does not allow the description of interactions with rough substrates. Surface Element Integration (SEI) has been introduced to calculate the interaction energy between colloidal particles and textured surfaces [174, 175]. Within this approach, the cell behaviour of textured surfaces is accounted for in terms of a reduction in the interaction energy for increasing values of average roughness [175]. The role of surface protrusion density in decreasing the cell-substrate contact area has also been predicted [176]. Other models have been developed to account for cell deformation in attempts to interpret bactericidal behaviour for non-rigid bodies [176–178], describing contact between a cell wall and patterned surface in terms of the minimisation of surface free energy. All of these models, however, are based on adaptation of the cell wall to well-defined textures, typically inspired by bactericidal biological surfaces and modelled as regular arrays of simple geometric shapes. As a result, these approaches are inadequate when considering more irregular textures such as those produced via large scale processing in industrial contexts. Moreover, local non-covalent interactions with the substrate, considered in the DLVO-based approaches, are not taken into account, while fluid surrounding the cell, one of the most important mediators in the interaction [179], is often neglected.

To provide a more robust theoretical framework accounting for the cellular properties of industrially-relevant textured surfaces, a model of cell-substrate interactions was proposed in [180] where bacterial cells are described as deformable objects in the framework of molecular dynamics (MD), overcoming limitations associated with the aforementioned approaches in view of a unified theory for the cell properties of textured surfaces (Fig. 21). Cells immersed in a computational fluid representing the surrounding environment interacted with a computational substrate via specifically tailored physicochemical processes. Owing to the spatial resolution enabled by the MD framework, the model allowed the interaction energy of cells and surfaces to be determined in a manner that closely resembled experiments, without the need for geometric approximations.

The feasibility of the approach was assessed by simulating the interaction of cells with surfaces chosen to represent stainless steel substrates textured with ultrashort laser pulses (LIPSS), shown to exhibit antibacterial properties in the literature. A statistical analysis was carried out considering a wide range of surface morphologies

Fig. 21 Local stress on the cell wall. Example of a spherocylindrical cell adhered to a substrate characterised by LIPSS. The false colour map represents the local stresses on the cell walls in an adhesion experiment and example of normalised frequency histogram of the maximum local stresses produced with 200 simulations [79]
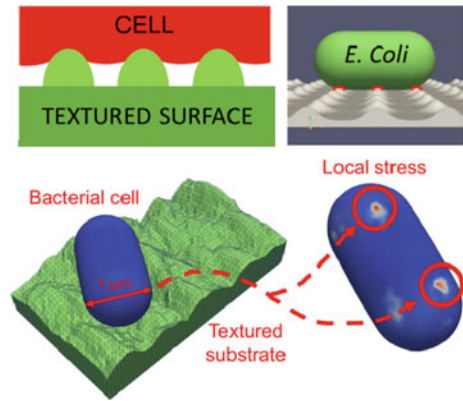
and different shaped cells. The mechanical properties of the latter were assigned based on currently available experimental data, with the antibacterial properties of each surface quantified in terms of local stresses acting on the bacterial cell walls. Dependence of simulation outcomes on parameters relating to surface chemistry leads to a novel interpretation of the antibacterial effects of textured surfaces.

Applications of laser texturing for dental applications can be found in different works. The majority of then refer to titanium-based alloys that capture the largest market share. In [181] the response of osteoblast cells to textured Ti-6Al-7Nb samples, in that work both polished and sandblasted samples were textured with a picosecond laser to over impose LIPSS on the original topography, authors measured a significant increase of osteoblast proliferation and an appreciable retardation of initial bacterial adhesion of textured surfaces compared to bare ones (Fig. 22).

A second harmonic picosecond laser was employed in [182] to generate LIPSS on Ti6Al4V on dental abutments and the positive effects on the biofilm formation, precursor to the osteointegration, was assessed.

From a manufacturing point of view, dental implants are characterized by complex geometries highly customized. In [183] authors propose methods for efficient generation of LIPSS on screw like geometries looking forward for future mass production (see Fig. 23).

DLP method, that employ cheaper and simple nanosecond pulsating laser was successfully employed in [184] and [185] to generate crosshatched and hexagonal patterns with the final double aim to improve biological colonization in the osteointegration process and to induce a favorable strain and stress field at the implant/bone interface to increase the implantation success rate.
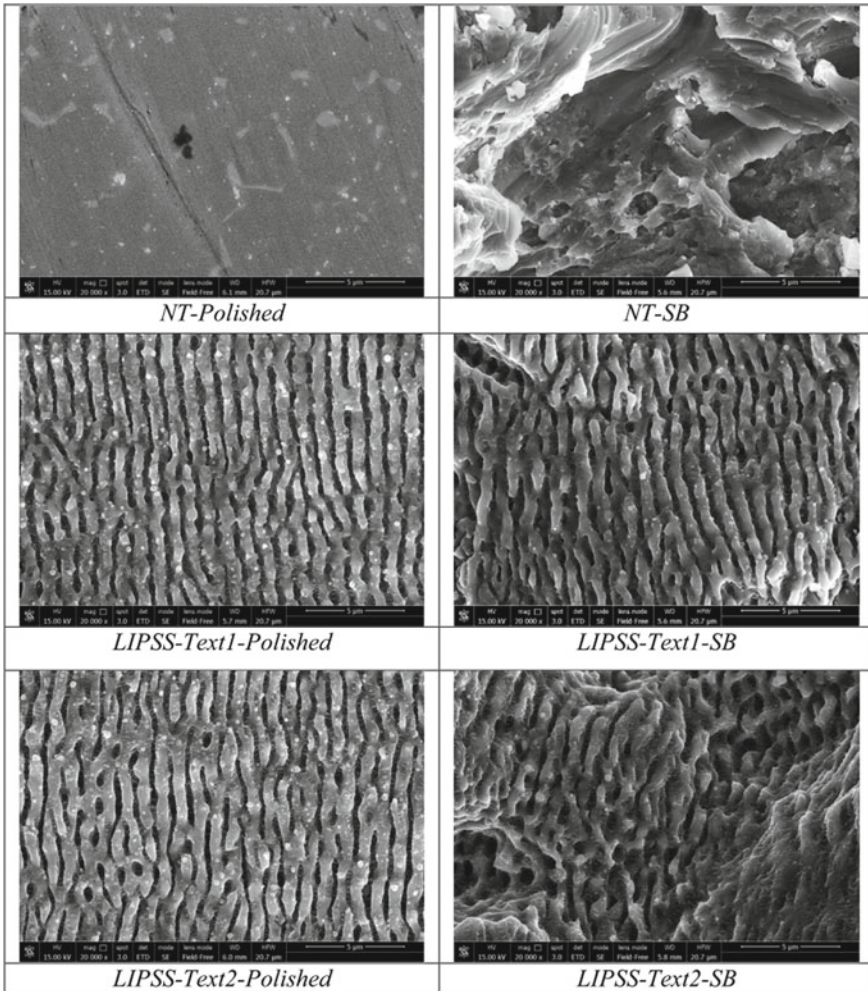
Fig. 22 Example of LIPSS based texturing of Ti-6Al-7Nb surfaces for dental implants. On the left untreated and textured examples starting from polished surface, on the right the over impose of LIPSS texturing on the sandblasted initial surface is shown [181]

4 Challenges

The future step in the orthopedic implants' development uses bioinspired multi functional surfaces derived from human-made components. Human bones' remarkable and extraordinary qualities come from their multi-faceted, multi-scale and hetero-geneous tissue structure that's hierarchical in nature. The reason these traits are so impressive is because of human evolution over thousands of years—which is
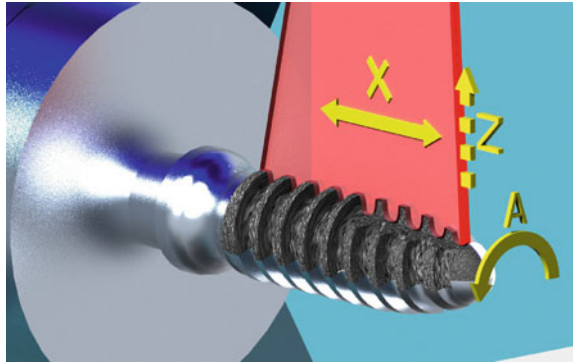
why transitioning bone structures into artificial implants that mimics these properties is highly beneficial. The development and repair of bone requires a detailed understanding of the interplay between its structure and properties. Consequently, providing an insight into the bone's fundamentally hierarchical nature will be extremely helpful when creating appropriate bone-replicating implants for regeneration and repair. This can be achieved by thoroughly examining the formation and repair of bone at the molecular and cellular level. Thus, to fabricate reliable surfaces, it is crucial to consider many factors including size, surface properties, drug absorption and cellular interaction.

Additionally, characterizing and testing these systems in vitro and in vivo is challenging. This is because it is difficult to create a system that is both easy to prepare, affordable and biocompatible. In particular, it is challenging to obtain proper surface characteristics according to the following lack of knowledge and needs:

– Selecting surface functionalities in order to correctly confer to the right surface area the desired property.
– Selection of the right modality to achieve the required surface functionalization.
– Having a uniform standard for characterizing the functionalized surfaces for biomedical applications.
– Optimize the density and arrangement of surface functionalities.
– Maintaining the surface efficiency in vivo.

Thus, it is necessary to work in order to fill the gap between the actual know-how and the trend of high specialized surfaces for fabricating the fourth generation implants.

5   Conclusions and Future Perspectives

Decades of research and development in medical fields and materials technologies can be summarized into three development phases: (i) first-generation implants (bio-inert) with tremendous mechanical properties for replacing injured bones; (ii) second-generation implants (biocompatible) characterized by high-affinity with surrounding tissue structure supporting osteoconductivity; (iii) third-generation implants (bioactive) equipped with excellent osteoconductivity, osteoinductivity, osteointegration and superb anti-infection ability. Thus, we are now seeking for the possibility to develop and fabricate the fourth-generation implants with advanced multifunctional surface functionalization able to produce devices that replace defective tissues responding, at the same time, to external stimuli (e.g. mechanical, chemical and biological).

Case studies reported herein explain how progress in surface functionalization and post-manufacturing integrity seriously influence the overall implant characteristics dictating its success or failure for clinical use. In particular, each functionalization methodology reported in this work influences the overall implant surface characteristics based on the desired specifications. The lack of metrics in measuring surface characteristics in biomedical applications represents a serious obstacle to an effective research progress in this field.

Thus, numerous questions are emerging in order to prove clinical application of innovative functionalized implants:

– How to strike a perfect balance between different properties of anti-infection, os-teointegration and anti-inflammation.
– How to standardize surface characterization techniques in order to systematically compare different surface modifications and their effects on surfaces' performance.
– Understanding the intricate relationship between the surface structure build-up and the bone properties.
– How to determine optimal concentrations of various surface functionalization re-sults to maximize bone healing and avoid tissue malformation.
– How to select the right combination of functionalization parameters to obtain the desired surface state and characteristics.

It is vital to consider the long-term stability, durability and cost effectiveness of prospective medical implants when fabricating them. The same applies to their large-scale reproducibility. Additionally, it's crucial to consider the durability and stability of biomaterials when designing implants. Once designed, the next step is to fabricate these implants for clinical practice. In order for future implants to cost-effectively serve patients throughout their lives, researchers need to provide detailed instructions. These instructions should include methods of use, indications and potential complications. Additionally, surgeons should have easy access to these instructions so they can perform effectively. With these considerations, surgeons

and patients will have access to next-generation implants with improved bioinspired surfaces.

References

1. Moghadasi K, Mohd Isa MS, Ariffin MA, Mohd Jamil MZ, Raja S et al (2022) A review on biomedical implant materials and the effect of friction stir based techniques on their mechanical and tribological properties. J Mater Res Technol 17:1054–1121. https://doi.org/10.1016/j.jmrt.2022.01.050

2. Bergmann CP, Stumpf A (2013) Dental ceramics: microstructure, properties and degradation. In: Dental ceramics: microstructure, properties and degradation, pp 1–84. https://doi.org/10.1007/978-3-642-38224-6

3. Ratner BD, Hoffman AS, Lemons JE (2006) Biomaterials science : an introduction to materials in volume I : basic concepts 3rd annual microscopy workshop in microscopy for materials these topics will be covered, pp 25–27

4. Zadpoor AA (2013) Open forward and inverse problems in theoretical modeling of bone tissue adaptation. J Mech Behav Biomed Mater 27:249–261. https://doi.org/10.1016/j.jmbbm.2013.05.017

5. Brånemark R, Brånemark PI, Rydevik B, Myers RR (2001) Osseointegration in skeletal reconstruction and rehabilitation: a review. J Rehabil Res Dev

6. Lee JWY, Bance ML (2019) physiology of osseointegration, otolaryngologic clinics of North America

7. Terheyden H, Lang NP, Bierbaum S, Stadlinger B (2012) Osseointegration–communication of cells. Clin Oral Implant Res 23(10):1127–1135. https://doi.org/10.1111/J.1600-0501.2011.02327.X

8. Rivera-Chacon DM, Alvarado-Velez M, Acevedo-Morantes CY, Singh SP, Gultepe E et al (2013) Fibronectin and vitronectin promote human fetal osteoblast cell attachment and proliferation on nanoporous titanium surfaces. J Biomed Nanotechnol 9(6). https://doi.org/10.1166/jbn.2013.1601

9. Mavrogenis AF, Dimitriou R, Parvizi J, Babis GC (2009) Biology of implant osseointegration. J Musculoskelet Neuronal Interact

10. Davies JE (2003) Understanding peri-implant endosseous healing. J Dent Educ 67(8). https://doi.org/10.1002/j.0022-0337.2003.67.8.tb03681.x

11. Caplan AI, Dennis JE (2006) Mesenchymal stem cells as trophic mediators. J Cell Biochem

12. Pellegrini G, Francetti L, Barbaro B, Del Fabbro M (2018) Novel surfaces and osseointegration in implant dentistry. J Investig Clin Dent

13. Kim J, Adachi T (2021) Cell-fate decision of mesenchymal stem cells toward osteocyte differentiation is committed by spheroid culture. Sci Rep 11(1). https://doi.org/10.1038/s41598-021-92607-z

14. Choi JY, Sim JH, Luke IS (2017) Characteristics of contact and distance osteogenesis around modified implant surfaces in rabbit tibiae. J Periodontal Implant Sci 47(3). https://doi.org/10.5051/jpis.2017.47.3.182

15. Mulari MTK, Qu Q, Härkönen PL, Väänänen HK (2004) Osteoblast-like cells complete osteoclastic bone resorption and form new mineralized bone matrix in vitro. Calcif Tissue Int 75(3):253–261. https://doi.org/10.1007/s00223-004-0172-3

16. Rupp F, Liang L, Geis-Gerstorfer J, Scheideler L, Hüttig F (2018) Surface characteristics of dental implants: a review Dent Mater

17. Irandoust S, Müftü S (2020) The interplay between bone healing and remodeling around dental implants. Sci Rep 10(1). https://doi.org/10.1038/s41598-020-60735-7

18. Annibali S, Pranno N, Cristalli MP, La Monaca G, Polimeni A (2016) Survival analysis of implant in patients with diabetes mellitus: a systematic review. Implant Dent

19. Li Y, He S, Hua Y, Hu J (2017) Effect of osteoporosis on fixation of osseointegrated implants in rats, J Biomed Mater Research Part B Appl Biomater 105(8). https://doi.org/10.1002/jbm.b.33787

20. Shibamoto A, Ogawa T, Duyck J, Vandamme K, Naert I et al (2018) Effect of high-frequency loading and parathyroid hormone administration on peri-implant bone healing and osseointegration. Int J Oral Sci 10(1). https://doi.org/10.1038/s41368-018-0009-y

21. Rasouli R, Barhoum A, Uludag H (2018) A review of nanostructured surfaces and materials for dental implants: surface coating, patterning and functionalization for improved performance. Biomater Sci

22. Pazos L, Corengia P, Svoboda H (2010) Effect of surface treatments on the fatigue life of titanium for biomedical applications. J Mech Behav Biomed Mater 3(6). https://doi.org/10.1016/j.jmbbm.2010.03.006

23. Geetha M, Singh AK, Asokamani R, Gogia AK (2009) Ti based biomaterials, the ultimate choice for orthopaedic implants—a review. Prog Mater Sci 54(3):397–425. https://doi.org/10.1016/j.pmatsci.2008.06.004

24. Abdel-Hady Gepreel M, Niinomi M (2013) Biocompatibility of Ti-alloys for long-term implantation. J Mech Behav Biomed Mater 20:407–415. https://doi.org/10.1016/j.jmbbm.2012.11.014

25. Navarro M, Michiardi A, Castaño O, Planell JA (2008) Biomaterials in orthopaedics. J R Soc Interface 5(27):1137–1158. https://doi.org/10.1098/rsif.2008.0151

26. Zhang LC, Klemm D, Eckert J, Hao YL, Sercombe TB (2011) Manufacture by selective laser melting and mechanical behavior of a biomedical Ti–24Nb–4Zr–8Sn alloy. Scripta Mater 65(1):21–24. https://doi.org/10.1016/j.scriptamat.2011.03.024

27. Liao B, Xia RF, Li W, Lu D, Jin ZM (2021) 3D-printed Ti–6Al–4V scaffolds with graded triply periodic minimal surface structure for bone tissue engineering. J Mater Eng Perform 30(7):4993–5004. https://doi.org/10.1007/s11665-021-05580-z

28. Martinez-Marquez D, Delmar Y, Sun S, Stewart RA (2020) Exploring macroporosity of additively manufactured titanium metamaterials for bone regeneration with quality by design: a systematic literature review. Materials 13(21):1–44. https://doi.org/10.3390/ma13214794

29. Barba D, Alabort E, Reed RC (2019) Synthetic bone: design by additive manufacturing. Acta Biomater 97:637–656. https://doi.org/10.1016/j.actbio.2019.07.049

30. Dobrzański LA, Dobrzańska-Danikiewicz AD, Dobrzański LB (2021) Effect of biomedical materials in the implementation of a long and healthy life policy. Processes 9(5). https://doi.org/10.3390/pr9050865

31. Kaur M, Singh K (2019) Review on titanium and titanium based alloys as biomaterials for orthopaedic applications. Mater Sci Eng, C 102:844–862. https://doi.org/10.1016/j.msec.2019.04.064

32. Zhang LC, Chen LY (2019) A review on biomedical titanium alloys: recent progress and prospect. Adv Eng Mater 21(4):1–29. https://doi.org/10.1002/adem.201801215

33. Warburton A, Girdler SJ, Mikhail CM, Ahn A, Cho SK (2020) Biomaterials in spinal implants: a review. Neurospine 17(1):101–110. https://doi.org/10.14245/ns.1938296.148

34. Sezer N, Evis Z, Kayhan SM, Tahmasebifar A, Koç M (2018) Review of magnesium-based biomaterials and their applications. J Magnes Alloy 6(1):23–43. https://doi.org/10.1016/j.jma.2018.02.003

35. Kunčická L, Kocich R, Lowe TC (2017) Advances in metals and alloys for joint replacement. Prog Mater Sci 88(April):232–280. https://doi.org/10.1016/j.pmatsci.2017.04.002

36. Kopova I, Kronek J, Bacakova L, Fencl J (2019) A cytotoxicity and wear analysis of trapeziometacarpal total joint replacement implant consisting of DLC-coated Co–Cr–Mo alloy with the use of titanium gradient interlayer. Diam Relat Mater 97:107456. https://doi.org/10.1016/j.diamond.2019.107456

37. Mughal MP, Farooq MU, Mumtaz J, Mia M, Shareef M et al (2021) Surface modification for osseointegration of Ti6Al4V ELI using powder mixed sinking EDM. J Mech Behav Biomed Mater 113:104145. https://doi.org/10.1016/j.jmbbm.2020.104145

38. Cao N-J, Zhu Y-H, Gao F, Liang C, Wang Z-B et al (2021) Gradient nanostructured titanium stimulates cell responses in vitro and enhances osseointegration in vivo. Ann Transl Med 9(7):531–531. https://doi.org/10.21037/atm-20-7588

39. Wang ZX, Chen GQ, Chen LY, Xu L, Lu S (2018) Degradation behavior of micro-arc oxidized ZK60 magnesium alloy in a simulated body fluid. Metals 8(9):1–17. https://doi.org/10.3390/met8090724

40. Hu X, Neoh KG, Zhang J, Kang ET (2014) Bacterial and osteoblast behavior on titanium, cobalt-chromium alloy and stainless steel treated with alkali and heat: A comparative study for potential orthopedic applications. J Colloid Interface Sci 417:410–419. https://doi.org/10.1016/j.jcis.2013.11.062

41. West P, Shunmugasamy VC, Usman CA, Karaman I, Mansoor B (2021) Part II.: dissimilar friction stir welding of nickel titanium shape memory alloy to stainless steel–microstructure, mechanical and corrosion behavior. J Adv Join Process 4. https://doi.org/10.1016/j.jajp.2021.100072

42. Ødegaard KS, Torgersen J, Elverum CW (2020) Structural and biomedical properties of common additively manufactured biomaterials: a concise review. Metals 10(12):1–23. https://doi.org/10.3390/met10121677

43. Raja S, Muhamad MR, Jamaludin MF, Yusof F (2020) A review on nanomaterials reinforcement in friction stir welding. J Market Res 9(6):16459–16487. https://doi.org/10.1016/j.jmrt.2020.11.072

44. Bechtol F, Laing, (1959) Metals and engineering in bone and joint surgery. Williams and Wilkins, Baltimore, p 582

45. Wizemann, T. (ed) (2010) Institute of Medicine (US) Committee on the Public Health Effectiveness of the FDA 510(k) Clearance Process. Public Health Effectiveness of the FDA 510(k) Clearance Process: Balancing Patient Safety and Innovation: Worksh

46. Witte F (2010) The history of biodegradable magnesium implants: a review. Acta Biomater 6(5):1680–1692. https://doi.org/10.1016/j.actbio.2010.02.028

47. Javier Gil F, Planell JA, Padrós A, Aparicio C (2007) The effect of shot blasting and heat treatment on the fatigue behavior of titanium for dental implant applications. Dent Mater 23(4):486–491. https://doi.org/10.1016/j.dental.2006.03.003

48. Liu X, Chu PK, Ding C (2004) Surface modification of titanium, titanium alloys, and related materials for biomedical applications. Mater Sci Eng R Rep 47(3–4):49–121. https://doi.org/10.1016/J.MSER.2004.11.001

49. Hornberger H, Virtanen S, Boccaccini AR (2012) Biomedical coatings on magnesium alloys–a review. Acta Biomaterialia

50. Koch K, Bhushan B, Barthlott W (2009) Multifunctional surface structures of plants: an inspiration for biomimetics. Prog Mater Sci

51. Ratner BD, Hoffman AS, Schoen FJ, Lemons JE (2013) Biomaterials science: an introduction to materials, 3rd edn.

52. Lorenzetti M, Dakischew O, Trinkaus K, Susanne Lips K, Schnettler R et al (2015) Enhanced osteogenesis on titanium implants by UVB photofunctionalization of hydrothermally grown TiO_2 coatings. J Biomater Appl 30(1). https://doi.org/10.1177/0885328215569091

53. Wang G, Li J, Lv K, Zhang W, Ding X et al (2016) Surface thermal oxidation on titanium implants to enhance osteogenic activity and in vivo osseointegration. Sci Rep 6. https://doi.org/10.1038/srep31769

54. Rosales-Leal JI, Rodríguez-Valverde MA, Mazzaglia G, Ramón-Torregrosa PJ, Díaz-Rodríguez L et al (2010) Effect of roughness, wettability and morphology of engineered titanium surfaces on osteoblast-like cell adhesion. Colloids SurfS A: PhysChemical Eng Asp 365(1–3). https://doi.org/10.1016/j.colsurfa.2009.12.017

55. Zinger O, Zhao G, Schwartz Z, Simpson J, Wieland M et al (2005) Differential regulation of osteoblasts by substrate microstructural features. Biomaterials 26(14). https://doi.org/10.1016/j.biomaterials.2004.06.035

56. Zhao G, Raines AL, Wieland M, Schwartz Z, Boyan BD (2007) Requirement for both micron- and submicron scale structure for synergistic responses of osteoblasts to substrate

surface energy and topography. Biomaterials 28(18). https://doi.org/10.1016/j.biomaterials.2007.02.024

57. Wang F, Shi L, He WX, Han D, Yan Y et al (2013) Bioinspired micro/nano fabrication on dental implant-bone interface. Appl Surf Sci 265. https://doi.org/10.1016/j.apsusc.2012.11.032

58. Huang MS, Chen LK, Ou KL, Cheng HY, Wang CS (2015) Rapid Osseointegration of titanium implant with innovative nanoporous surface modification: animal model and clinical trial. Implant Dent 24(4). https://doi.org/10.1097/ID.0000000000000258

59. Patel D, Jain VK, Ramkumar J (2018) Micro texturing on metallic surfaces: state of the art. Proc Inst Mech Eng, Part B: J Eng Manuf

60. Biondani F, Benassi L, Bissacco G, Orazi L, Tang PT (2020) Surface micro and nanostructuring of three-dimensional components of micro medical devices. Procedia CIRP

61. Zhang Y, Hansen HN, Bissacco G, Biondani F (2018) Comparison of selected processes for surface microstructuring of complex mould for an implanted device. Int J Adv Manuf Technol 97(5–8). https://doi.org/10.1007/s00170-018-2152-1

62. Lu P, Wood RJK (2020) Tribological performance of surface texturing in mechanical applications-a review. Surf Topogr: Metrol Prop

63. Usami H, Sato T, Kanda Y, Nishio S (2017) Applicability of interrupted micro cutting process "Tilling" as surface texturing. Key Eng Mater

64. Dong Y, Svoboda P, Vrbka M, Kostal D, Urban F et al (2016) Towards near-permanent CoCrMo prosthesis surface by combining micro-texturing and low temperature plasma carburizing. J Mech Behav Biomed Mater 55. https://doi.org/10.1016/j.jmbbm.2015.10.023

65. Dougherty PSM, Srivastava G, Onler R, Ozdoganlar OB, Higgs CF (2015) Lubrication enhancement for uhmwpe sliding contacts through surface texturing. Tribol Trans 58(1). https://doi.org/10.1080/10402004.2014.933935

66. Chen N, Li HN, Wu J, Li Z, Li L et al (2021) Advances in micro milling: from tool fabrication to process outcomes. Int J Mach Tools Manuf

67. Mao B, Siddaiah A, Liao Y, Menezes PL (2020) Laser surface texturing and related techniques for enhancing tribological performance of engineering materials: a review. J Manuf Process

68. Chen K, Yang X, Zhang Y, Yang H, Lv G et al (2021) Research progress of improving surface friction properties by surface texture technology. Int J Adv Manuf Technol

69. Rajurkar KP, Sundaram MM, Malshe AP (2013) Review of electrochemical and electrodischarge machining. Procedia CIRP

70. Patel DS, Jain VK, Shrivastava A, Ramkumar J (2019) Electrochemical micro texturing on flat and curved surfaces: simulation and experiments. Int J Adv Manuf Technol 100(5–8). https://doi.org/10.1007/s00170-016-9700-3

71. Kumar A, Kumar M, Alok A, Das M (2020) Surface texturing by electrochemical micromachining: a review. In: IOP conference series: materials science and engineering

72. Kim J, Lee WJ, Park HW (2016) The state of the art in the electron beam manufacturing processes. Int J Precis Eng Manuf 17(11). https://doi.org/10.1007/s12541-016-0184-8

73. Yang Z, Wen F, Sun Q, Chai L, Ma X et al (2022) Strength-ductility improvement achieved by introducing heterostructured martensite in a Ti–6Al–4V alloy. Mater Charact 192:112230. https://doi.org/10.1016/j.matchar.2022.112230

74. Wang H, Jürgensen J, Decker P, Hu Z, Yan K et al (2020) Corrosion behavior of NiTi alloy subjected to femtosecond laser shock peening without protective coating in air environment. Appl Surf Sci 501:144338. https://doi.org/10.1016/j.apsusc.2019.144338

75. Shivakoti I, Kibria G, Cep R, Pradhan BB, Sharma A (2021) Laser surface texturing for biomedical applications: a review. Coatings 11(2):1–15. https://doi.org/10.3390/coatings11020124

76. Shen X, Shukla P, Subramaniyan AK, Zammit A, Swanson P et al (2020) Residual stresses induced by laser shock peening in orthopaedic Ti–6Al–7Nb alloy. Opt Laser Technol 131:106446. https://doi.org/10.1016/j.optlastec.2020.106446

77. Vishnu J, Ansheed AR, Hameed P, Praveenkumar K, Pilz S et al (2022) Insights into the surface and biocompatibility aspects of laser shock peened Ti–22Nb alloy for orthopedic implant applications. Appl Surf Sci 586:152816. https://doi.org/10.1016/j.apsusc.2022.152816

78. Zhang R, Zhou X, Gao H, Mankoci S, Liu Y et al (2018) The effects of laser shock peening on the mechanical properties and biomedical behavior of AZ31B magnesium alloy. Surf Coat Technol 339(February):48–56. https://doi.org/10.1016/j.surfcoat.2018.02.009

79. Orazi L, Romoli L, Schmidt M, Li L (2021) Ultrafast laser manufacturing: from physics to industrial applications. CIRP Ann 70(2):543–566. https://doi.org/10.1016/j.cirp.2021.05.007

80. Yu Z, Yin S, Zhang W, Jiang X, Hu J (2020) Picosecond laser texturing on titanium alloy for biomedical implants in cell proliferation and vascularization. J Biomed Mater Res Part B Appl Biomater 108(4). https://doi.org/10.1002/jbm.b.34497

81. Gnilitskyi I, Pogorielov M, Viter R, Ferraria AM, Carapeto AP et al (2019) Cell and tissue response to nanotextured Ti–6Al–4V and Zr implants using high-speed femtosecond laser-induced periodic surface structures. Nanomedicine: Nanotechnol, Biol, Med 21. https://doi.org/10.1016/j.nano.2019.102036

82. Costa MM, Miranda A, Bartolomeu F, Carvalho Ó, Matos S et al (2022) Osseointegration assessment of multi-material Ti6Al4V–β TCP implants: an experimental study in rats. Adv Mater Technol 7(6). https://doi.org/10.1002/admt.202101117

83. Shaikh S, Kedia S, Singh D, Subramanian M, Sinha S (2019) Surface texturing of Ti6Al4V alloy using femtosecond laser for superior antibacterial performance. J Laser Appl 31(2). https://doi.org/10.2351/1.5081106

84. Purnama A, Furlan V, Dessi D, Demir AG, Tolouei R et al (2020) Laser surface texturing of SS316L for enhanced adhesion of HUVECs. Surf Eng 36(12). https://doi.org/10.1080/02670844.2018.1495408

85. Costa MM, Miranda A, Bartolomeu F, Carvalho O, Matos S et al (2022) NiTi laser textured implants with improved in vivo osseointegration: an experimental study in rats. J Mater Sci Technol 114. https://doi.org/10.1016/j.jmst.2021.11.014

86. Liang C, Hu Y, Wang H, Xia D, Li Q et al (2016) Biomimetic cardiovascular stents for in vivo re-endothelialization. Biomaterials 103. https://doi.org/10.1016/j.biomaterials.2016.06.042

87. Schieber R, Lasserre F, Hans M, Fernández-Yagüe M, Díaz-Ricart M et al (2017) Direct laser interference patterning of cocr alloy surfaces to control endothelial cell and platelet response for cardiovascular applications. Adv Healthc Mater 6(19). https://doi.org/10.1002/adhm.201700327

88. Carrigy J, Perrotti V, Franciotti R, Sharma A, Quaranta A (2021) A randomized pilot clinical and microbiological study comparing laser microtextured implants with and without platform switching. Appl Sci (Switzerland) 11(9). https://doi.org/10.3390/app11094140

89. Driver M (2012) Coatings for biomedical applications, p 366

90. Degidi M, Petrone G, Iezzi G, Piattelli A (2003) Bone contact around acid-etched implants: a histological and histomorphometrical evaluation of two human-retrieved implants. J Oral Implant 29(1). https://doi.org/10.1563/1548-1336(2003)029<0013:BCAAIA>2.3.CO;2

91. Gellér ZE, Albrecht K, Dobránszky J (2008) Electropolishing of coronary stents. Mater Sci Forum

92. Raval A, Choubey A, Engineer C, Kothwala D (2005) Surface conditioning of 316LVM slotted tube cardiovascular stents. J Biomater Appl 19(3). https://doi.org/10.1177/0885328205046564

93. Bhuyan A, Gregory B, Lei H, Seow YY, Gianchandani YB (2005) Pulse and DC electropolishing of stainless steel for stents and other devices. Proc IEEE Sens

94. Haïdopoulos M, Turgeon S, Sarra-Bournet C, Laroche G, Mantovani D (2006) Development of an optimized electrochemical process for subsequent coating of 316 stainless steel for stent applications. J Mater Sci: Mater Med 17(7). https://doi.org/10.1007/s10856-006-9228-4

95. Laberger M, Drouin G, Gélinas C, Champagne B, Bobyn JD (1990) Adherence of HDPE powder coating on Co–Cr surfaces: effect of substrate preparation and gas sterilization. J Biomed Mater Res 24(11). https://doi.org/10.1002/jbm.820241103

96. Burke M, Clarke B, Rochev Y, Gorelov A, Carroll W (2008) Estimation of the strength of adhesion between a thermoresponsive polymer coating and nitinol wire. J Mater Sci: Mater Med 19(5). https://doi.org/10.1007/s10856-007-3274-4

97. Bona AD, Shen C, Anusavice KJ (2004) Work of adhesion of resin on treated lithia disilicate-based ceramic. Dent Mater 20(4). https://doi.org/10.1016/S0109-5641(03)00126-X
98. Schmage P, Nergiz I, Herrmann W, Özcan M (2003) Influence of various surface-conditioning methods on the bond strength of metal brackets to ceramic surfaces. Am J Orthod Dentofac Orthop 123(5). https://doi.org/10.1016/S0889-5406(02)56911-0
99. Kono H, Miyamoto M, Ban S (2007) Bioactive apatite coating on titanium using an alternate soaking process. Dent Mater J 26(2). https://doi.org/10.4012/dmj.26.186
100. Maitz MF, Pham MT, Matz W, Reuther H, Steiner G et al (2002) Ion beam treatment of titanium surfaces for enhancing deposition of hydroxyapatite from solution. Biomol Eng
101. De Andrade MC, Sader MS, Filgueiras MRT, Ogasawara T (2000) Microstructure of ceramic coating on titanium surface as a result of hydrothermal treatment. J Mater Sci: Mater Med 11(11). https://doi.org/10.1023/A:1008984030540
102. Adlkofer K, Tanaka M (2001) Stable surface coating of gallium arsenide with octadecylthiol monolayers. Langmuir 17(14). https://doi.org/10.1021/la001507q
103. Addison O, Marquis PM, Fleming GJP (2007) Resin strengthening of dental ceramics-the impact of surface texture and silane. J Dent 35(5). https://doi.org/10.1016/j.jdent.2006.11.012
104. Wilson D, Xu C, Hong L, Wang Y (2009) Effects of different preparation procedures during tooth whitening on enamel bonding. J Mater Sci: Mater Med 20(4). https://doi.org/10.1007/s10856-008-3657-1
105. Besra L, Liu M (2007) A review on fundamentals and applications of electrophoretic deposition (EPD). Prog Mater Sci
106. Oh SH, Finõnes RR, Daraio C, Chen LH, Jin S (2005) Growth of nano-scale hydroxyapatite using chemically treated titanium oxide nanotubes. Biomaterials 26(24). https://doi.org/10.1016/j.biomaterials.2005.01.048
107. Sul YT, Johansson CB, Jeong Y, Albrektsson T (2001) The electrochemical oxide growth behaviour on titanium in acid and alkaline electrolytes. Med Eng Phys 23(5). https://doi.org/10.1016/S1350-4533(01)00050-9
108. Yerokhin AL, Nie X, Leyland A, Matthews A, Dowey SJ (1999) Plasma electrolysis for surface engineering. Surf CoatS Technol
109. Dong Q, Chen C, Wang D, Ji Q (2006) Research status about surface modification of biomedical Ti and its alloys by micro-arc oxidation. Surf Rev Lett 13(1). https://doi.org/10.1142/S0218625X06007792
110. Chiesa R, Sandrini E, Santin M, Rondelli G, Cigada A (2003) Osteointegration of titanium and its alloys by anodic spark deposition and other electrochemical techniques: a review. J App Biomat Biomechanics
111. Del Curto B, Brunella MF, Giordano C, Pedeferri MP, Valtulina V et al (2005) Decreased bacterial adhesion to surface-treated titanium. Int J Artif Organs 28(7). https://doi.org/10.1177/039139880502800711
112. Lopez-Heredia MA, Weiss P, Layrolle P (2007) An electrodeposition method of calcium phosphate coatings on titanium alloy. J Mater Sci: Mater Med 18(2). https://doi.org/10.1007/s10856-006-0703-8
113. Zhang JM, Lin CJ, Feng ZD, Tian ZW (1998) Mechanistic studies of electrodeposition for bioceramic coatings of calcium phosphates by an in situ pH-microsensor technique. J Electroanal Chem 452(2). https://doi.org/10.1016/S0022-0728(98)00107-7
114. Park JH, Lee DY, Oh KT, Lee YK, Kim KM et al (2006) Bioactivity of calcium phosphate coatings prepared by electrodeposition in a modified simulated body fluid. Mater Lett 60(21–22). https://doi.org/10.1016/j.matlet.2005.07.091
115. Balamurugan A, Balossier G, Michel J, Ferreira JMF (2009) Electrochemical and structural evaluation of functionally graded bioglass-apatite composites electrophoretically deposited onto Ti–6Al–4V alloy. Electrochim Acta 54(4):1192–1198. https://doi.org/10.1016/j.electacta.2008.08.055
116. Van Der Biest OO, Vandeperre LJ (1999) Electrophoretic deposition of materials
117. Hench LL (1980) Biomaterials 208

118. Porter AE, Rea SM, Galtrey M, Best SM, Barber ZH (2004) Production of thin film silicon-doped hydroxyapatite via sputter deposition. J Mater Sci 39(5):1895–1898. https://doi.org/10.1023/B:JMSC.0000016213.77001.71

119. Sun L, Berndt CC, Gross KA, Kucuk A (2001) Material fundamentals and clinical performance of plasma-sprayed hydroxyapatite coatings: a review. J Biomed Mater Res

120. Massaro C, Baker MA, Cosentino F, Ramires PA, Klose S et al (2001) Surface and biological evaluation of hydroxyapatite-based coatings on titanium deposited by different techniques. J Biomed Mater Res 58(6). https://doi.org/10.1002/jbm.1065

121. Deligianni DD, Katsala ND, Koutsoukos PG, Missirlis YF (2000) Effect of surface roughness of hydroxyapatite on human bone marrow cell adhesion, proliferation, differentiation and detachment strength. Biomaterials 22(1). https://doi.org/10.1016/S0142-9612(00)00174-5

122. Anselme K, Bigerelle M, Noel B, Dufresne E, Judas D et al (2000) Qualitative and quantitative study of human osteoblast adhesion on materials with various surface roughnesses. J Biomed Mater Res 49(2). https://doi.org/10.1002/(SICI)1097-4636(200002)49:2<155::AID-JBM2>3.0.CO;2-J

123. Pichugin VF, Surmenev RA, Shesterikov EV, Ryabtseva MA, Eshenko EV et al (2008) The preparation of calcium phosphate coatings on titanium and nickel-titanium by rf-magnetron-sputtered deposition: Composition, structure and micromechanical properties. Surf Coat Technol 202(16). https://doi.org/10.1016/j.surfcoat.2008.01.038

124. Zhang S, Xianting Z, Yongsheng W, Kui C, Wenjian W (2006) Adhesion strength of sol-gel derived fluoridated hydroxyapatite coatings. Surf Coat Technol 200/22–23 SPEC. ISS. https://doi.org/10.1016/j.surfcoat.2005.11.033

125. Yang YC, Chang E (2003) The bonding of plasma-sprayed hydroxyapatite coatings to titanium: effect of processing, porosity and residual stress. Thin Solid Films 444(1–2). https://doi.org/10.1016/S0040-6090(03)00810-1

126. Liu DM, Chou HM, Wu JD (1994) Plasma-sprayed hydroxyapatite coating: effect of different calcium phosphate ceramics. J Mater Sci: Mater Med 5(3). https://doi.org/10.1007/BF00053335

127. Morks MF, Kobayashi A (2007) Effect of gun current on the microstructure and crystallinity of plasma sprayed hydroxyapatite coatings. Appl Surf Sci 253(17). https://doi.org/10.1016/j.apsusc.2007.02.183

128. Soballe K, Hansen ES, Brockstedt-Rasmussen H, Bunger C (1993) Hydroxyapatite coating converts fibrous tissue to bone around loaded implants. J Bone Jt Surg-Ser B 75(2). https://doi.org/10.1302/0301-620x.75b2.8444949

129. Yang CY, Yang YC (2002) The biological response of human osteoblasts on plasma sprayed hydroxyapatite coatings

130. Labat B, Chamson A, Frey J (1995) Effects of γ-alumina and hydroxyapatite coatings on the growth and metabolism of human osteoblasts. J Biomed Mater Res 29(11):1397–1401. https://doi.org/10.1002/jbm.820291111

131. Tsui YC, Doyle C, Clyne TW (1998) Plasma sprayed hydroxyapatite coatings on titanium substrates. Part 2: Optim Coat Prop Biomater 19(22). https://doi.org/10.1016/S0142-9612(98)00104-5

132. Sun L, Berndt CC, Khor KA, Cheang HN, Gross KA (2002) Surface characteristics and dissolution behavior of plasma-sprayed hydroxyapatite coating. J Biomed Mater Res 62(2). https://doi.org/10.1002/jbm.10315

133. Lima RS, Khor KA, Li H, Cheang P, Marple BR (2005) HVOF spraying of nanostructured hydroxyapatite for biomedical applications. Mater Sci Eng A 396(1–2). https://doi.org/10.1016/j.msea.2005.01.037

134. Best SM, Porter AE, Thian ES, Huang J (2008) Bioceramics: past, present and for the future. J Eur Ceram Soc 28(7). https://doi.org/10.1016/j.jeurceramsoc.2007.12.001

135. Hulshoff JEG, Van Dijk K, Van Der Waerden JPCM, Wolke JGC, Kalk W et al (1996) Evaluation of plasma-spray and magnetron-sputter Ca-P-coated implants: an in vivo experiment using rabbits. J Biomed Mater Res 31(3):329–337. https://doi.org/10.1002/(SICI)1097-4636(199607)31:3%3c329::AID-JBM6%3e3.0.CO;2-O

136. Hulshoff JEG, van Dijk K, van Der Waerden JPCM, Wolke JGC, Ginsel LA et al (1995) Biological evaluation of the effect of magnetron sputtered Ca/P coatings on osteoblast-like cells in vitro. J Biomed Mater Res 29(8). https://doi.org/10.1002/jbm.820290808

137. Cooley DR, Van Dellen AF, Burgess JO, Windeler AS (1992) The advantages of coated titanium implants prepared by radiofrequency sputtering from hydroxyapatite. J Prosthet Dent 67(1). https://doi.org/10.1016/0022-3913(92)90057-H

138. Mello A, Hong Z, Rossi AM, Luan L, Farina M et al (2007) Osteoblast proliferation on hydroxyapatite thin coatings produced by right angle magnetron sputtering. Biomed Mater 2(2). https://doi.org/10.1088/1748-6041/2/2/003

139. Nelea V, Morosanu C, Iliescu M, Mihailescu IN (2003) Microstructure and mechanical properties of hydroxyapatite thin films grown by RF magnetron sputtering. Surf CoatS Technol 173(2–3). https://doi.org/10.1016/S0257-8972(03)00729-1

140. Wolke JGC, Van Der Waerden JPCM, Schaeken HG, Jansen JA (2003) In vivo dissolution behavior of various RF magnetron-sputtered Ca-P coatings on roughened titanium implants. Biomaterials 24(15). https://doi.org/10.1016/S0142-9612(03)00067-X

141. Yang Y, Kim KH, Ong JL (2005) A review on calcium phosphate coatings produced using a sputtering process—an alternative to plasma spraying. Biomaterials

142. Zhang Q, Leng Y, Xin R (2005) A comparative study of electrochemical deposition and biomimetic deposition of calcium phosphate on porous titanium. Biomaterials 26(16). https://doi.org/10.1016/j.biomaterials.2004.08.016

143. Balamurugan A, Balossier G, Torres P, Michel J, Ferreira JMF (2009) Sol-gel synthesis and spectrometric structural evaluation of strontium substituted hydroxyapatite. Mater Sci Eng C 29(3). https://doi.org/10.1016/j.msec.2008.09.005

144. Xiao XF, Liu RF, Tang XL (2008) Electrophoretic deposition of silicon substituted hydroxyapatite coatings from n-butanol-chloroform mixture. J Mater Sci: Mater Med 19(1). https://doi.org/10.1007/s10856-007-0161-y

145. Umbrello D, Saffioti MR, Imbrogno S (2022) Surface modifications induced by turning on additively manufactured Zr–702 and their effects on cell adhesion and proliferation for biomedical applications. CIRP Ann 71(1):457–460. https://doi.org/10.1016/j.cirp.2022.04.079

146. Aristizabal M, Jamshidi P, Saboori A, Cox SC, Attallah MM (2020) Laser powder bed fusion of a Zr-alloy: Tensile properties and biocompatibility. Mater Lett 259:126897. https://doi.org/10.1016/j.matlet.2019.126897

147. Dumbleton JH, Manley MT, Edidin AA (2002) A literature review of the association between wear rate and osteolysis in total hip arthroplasty. J Arthroplast 17(5). https://doi.org/10.1054/arth.2002.33664

148. Kurtz SM (2015) UHMWPE biomaterials handbook: ultra high molecular weight polyethylene in total joint replacement and medical devices

149. Sorgato M, Masato D, Lucchetta G, Orazi L (2018) Effect of different laser-induced periodic surface structures on polymer slip in PET injection moulding. CIRP Ann 67(1):575–578. https://doi.org/10.1016/j.cirp.2018.04.102

150. Orazi L, Sorgato M, Piccolo L, Masato D, Lucchetta G (2020) Generation and characterization of laser induced periodic surface structures on plastic injection molds content courtesy of springer nature , terms of use apply. Rights reserved. Content courtesy of Springer Nature, terms of use apply. Rights reserved, pp 207–221.

151. Modica et al (2022) Replication study of molded micro-textured samples made of ultra-high molecular weight polyethylene for medical application. In: World congress on micro and nano manufacturing WCMNM 2022. Leuven

152. Basile V, Modica F, Surace R, Fassi I (2022) Micro-texturing of molds via Stereolithography for the fabrication of medical components. Procedia CIRP 110(C):93–98. https://doi.org/10.1016/j.procir.2022.06.019

153. Hinderer S, Layland SL, Schenke-Layland K (2016) ECM and ECM-like materials—Biomaterials for applications in regenerative medicine and cancer therapy. Adv Drug Deliv Rev

154. Zhao N, Zhu D (2014) Collagen self-assembly on orthopedic magnesium biomaterials surface and subsequent bone cell attachment. PLoS ONE 9(10). https://doi.org/10.1371/journal.pone.0110420

155. Ronga M, Fagetti A, Canton G, Paiusco E, Surace MF et al (2013) Clinical applications of growth factors in bone injuries: experience with BMPs. Injury 44(SUPPL):1. https://doi.org/10.1016/S0020-1383(13)70008-1

156. van den Beucken JJJP, Walboomers XF, Leeuwenburgh SCG, Vos MRJ, Sommerdijk NAJM et al (2007) Multilayered DNA coatings: in vitro bioactivity studies and effects on osteoblast-like cell behavior. Acta Biomaterialia 3(4). https://doi.org/10.1016/j.actbio.2006.12.007

157. Douglas T, Wlodarczyk M, Pamula E, Declercq H, de Mulder E et al (2014) Enzymatic mineralization of gellan gum hydrogel for bone tissue-engineering applications and its enhancement by polydopamine. J Tissue Eng Regen Med 8(11). https://doi.org/10.1002/term.1616

158. De Jonge LT, Leeuwenburgh SCG, Wolke JGC, Jansen JA (2008) Organic-inorganic surface modifications for titanium implant surfaces. Pharm Res

159. Lee H, Dellatore SM, Miller WM, Messersmith PB (2007) Mussel-inspired surface chemistry for multifunctional coatings. Science 318(5849). https://doi.org/10.1126/science.1147241

160. Lynge ME, Schattling P, Städler B (2015) Recent developments in poly(dopamine)-based coatings for biomedical applications. Nanomedicine

161. Chien CY, Tsai WB (2013) Poly(dopamine)-assisted immobilization of Arg-Gly-Asp peptides, hydroxyapatite, and bone morphogenic protein-2 on titanium to improve the osteogenesis of bone marrow stem cells. ACS Appl Mater Interfaces 5(15). https://doi.org/10.1021/am401071f

162. Siebers (2006) Transforming growth factor-b1 release from a porous electrostatic spray deposition–derived calcium phosphate coating MARIJKE 12(9):1–8

163. Goodman SB, Yao Z, Keeney M, Yang F (2013) The future of biologic coatings for orthopaedic implants. Biomaterials 34(13). https://doi.org/10.1016/j.biomaterials.2013.01.074

164. Fan Y, Duan K, Wang R (2005) A composite coating by electrolysis-induced collagen self-assembly and calcium phosphate mineralization. Biomaterials 26(14). https://doi.org/10.1016/j.biomaterials.2004.06.019

165. Liu Y, De Groot K, Hunziker EB (2005) BMP-2 liberated from biomimetic implant coatings induces and sustains direct ossification in an ectopic rat model. Bone 36(5). https://doi.org/10.1016/j.bone.2005.02.005

166. He J, Huang T, Gan L, Zhou Z, Jiang B et al (2012) Collagen-infiltrated porous hydroxyapatite coating and its osteogenic properties in vitro and in vivo study. J Biomed Mater Res Part A 100 A(7). https://doi.org/10.1002/jbm.a.34121

167. Teng SH, Lee EJ, Park CS, Choi WY, Shin DS et al (2008) Bioactive nanocomposite coatings of collagen/hydroxyapatite on titanium substrates. J Mater Sci: Mater Med 19(6). https://doi.org/10.1007/s10856-008-3370-0

168. de Jonge LT, Leeuwenburgh SCG, van den Beucken JJJP, te Riet J, Daamen WF et al (2010) The osteogenic effect of electrosprayed nanoscale collagen/calcium phosphate coatings on titanium. Biomaterials 31(9). https://doi.org/10.1016/j.biomaterials.2009.11.114

169. de Jonge LT, van den Beucken JJJP, Leeuwenburgh SCG, Hamers AAJ, Wolke JGC et al (2009) In vitro responses to electrosprayed alkaline phosphatase/calcium phosphate composite coatings. Acta Biomaterialia 5(7). https://doi.org/10.1016/j.actbio.2009.03.019

170. Roach P, Eglin D, Rohde K, Perry CC (2007) Modern biomaterials: a review—Bulk properties and implications of surface modifications. J Mater Sci: Mater Med

171. Lee CH, Singla A, Lee Y (2001) Biomedical applications of collagen. Int J Pharm 221(1–2). https://doi.org/10.1016/S0378-5173(01)00691-3

172. Florence A, van Oss C (2007) Interfacial forces in aqueous media, 2nd edn. CRC Press. ISBN: 1–57444–482; Int J Pharm 331(1). https://doi.org/10.1016/j.ijpharm.2006.11.036

173. Farahat M, Hirajima T, Sasaki K, Doi K (2009) Adhesion of Escherichia coli onto quartz, hematite and corundum: Extended DLVO theory and flotation behavior. Colloids SurfS B: Biointerfaces 74(1). https://doi.org/10.1016/j.colsurfb.2009.07.009

174. Bendersky M, Davis JM (2011) DLVO interaction of colloidal particles with topographically and chemically heterogeneous surfaces. J Colloid Interface Sci 353(1). https://doi.org/10.1016/j.jcis.2010.09.058

175. Siegismund D, Undisz A, Germerodt S, Schuster S, Rettenmayr M (2014) Quantification of the interaction between biomaterial surfaces and bacteria by 3-D modeling. Acta Biomaterialia 10(1). https://doi.org/10.1016/j.actbio.2013.09.016

176. Pogodin S, Hasan J, Baulin VA, Webb HK, Truong VK et al (2013) Biophysical model of bacterial cell interactions with nanopatterned cicada wing surfaces. Biophys J 104(4). https://doi.org/10.1016/j.bpj.2012.12.046

177. Xue F, Liu J, Guo L, Zhang L, Li Q (2015) Theoretical study on the bactericidal nature of nanopatterned surfaces. J Theor Biol 385. https://doi.org/10.1016/j.jtbi.2015.08.011

178. Li X, Chen T (2016) Enhancement and suppression effects of a nanopatterned surface on bacterial adhesion. Phys Rev E, 93(5). https://doi.org/10.1103/PhysRevE.93.052419

179. Cheng Y, Feng G, Moraru CI (2019) Micro-and nanotopography sensitive bacterial attachment mechanisms: a review. Front Microbiol

180. Lazzini G, Lutey AHA, Romoli L, Fuso F (2021) Molecular dynamics model for the antibactericity of textured surfaces. Colloids SurfS B: Biointerfaces 199. https://doi.org/10.1016/j.colsurfb.2020.111504

181. Orazi L, Pogorielov M, Deineka V, Husak E, Korniienko V et al (2019) Osteoblast cell response to LIPSS-modified Ti-implants, in key engineering materials

182. Uhlmann E, Schweitzer L, Cunha A, Polte J, Huth-Herms K et al (2019) Application of laser surface nanotexturing for the reduction of peri-implantitis on biomedical grade 5 Ti–6Al–4V dental abutments. https://doi.org/10.1117/12.2509701

183. Orazi L, Pelaccia R, Mishchenko O, Reggiani B, Pogorielov M (2020) Fast LIPSS based texturing process of dental implants with complex geometries. CIRP Annals 69(1). https://doi.org/10.1016/j.cirp.2020.04.065

184. Dabbagh GR, Sadrnezhaad SK, Shoja Razavi R, Nourbakhsh AA, Hassanzadeh Nemati N (2021) Laser textured novel patterns on Ti–6Al–4V alloy for dental implants surface improvement. J Laser Appl 33(4). https://doi.org/10.2351/7.0000418

185. Çelen S, Özden H (2012) Laser-induced novel patterns: as smart strain actuators for new-age dental implant surfaces. Appl Surf Sci 263. https://doi.org/10.1016/j.apsusc.2012.09.112